GUSTAVO HENRIQUE NALON

SELF-SENSING CONCRETE BLOCKS AND MORTAR JOINTS FOR HEALTH MONITORING OF STRUCTURAL MASONRY BEFORE AND AFTER EXPOSURE TO HIGH TEMPERATURES

Thesis submitted to the Universidade Federal de Viçosa, in partial fulfillment of the requirements of the Civil Engineering Graduate Program, for the degree of *Doctor Scientiae*.

Advisor: José Carlos Lopes Ribeiro

Co-advisors: Leonardo Gonçalves Pedroti
Roberto Marcio da Silva
Eduardo Nery Duarte de Araújo

VIÇOSA - MINAS GERAIS
2024

Ficha catalográfica elaborada pela Biblioteca Central da Universidade Federal de Viçosa - Campus Viçosa

T
N172s
2024

Nalon, Gustavo Henrique, 1993-
Self-sensing concrete blocks and mortar joints for health monitoring of structural masonry before and after exposure to high temperatures / Gustavo Henrique Nalon. – Viçosa, MG, 2024.
1 tese eletrônica (366 f.): il. (algumas color.).

Texto em inglês.
Inclui apêndices.
Orientador: José Carlos Lopes Ribeiro.
Tese (doutorado) - Universidade Federal de Viçosa, Departamento de Engenharia Civil, 2024.
Inclui bibliografia.
DOI: https://doi.org/10.47328/ufvbbt.2024.094
Modo de acesso: World Wide Web.

1. Estabilidade estrutural. 2. Alvenaria. 3. Materiais nanoestruturados. 4. Detectores. 5. Incêndios. 6. Deformações e tensões. I. Ribeiro, José Carlos Lopes, 1977-. II. Universidade Federal de Viçosa. Departamento de Engenharia Civil. Programa de Pós-Graduação em Engenharia Civil. III. Título.

CDD 22. ed. 624.171

Bibliotecário(a) responsável: Alice Regina Pinto Pires CRB-6/2523

GUSTAVO HENRIQUE NALON

SELF-SENSING CONCRETE BLOCKS AND MORTAR JOINTS FOR HEALTH MONITORING OF STRUCTURAL MASONRY BEFORE AND AFTER EXPOSURE TO HIGH TEMPERATURES

Thesis submitted to the Universidade Federal de Viçosa, in partial fulfillment of the requirements of the Civil Engineering Graduate Program, for the degree of *Doctor Scientiae*.

APPROVED: February 23, 2024.

Assent:

Documento assinado digitalmente
gov.br
GUSTAVO HENRIQUE NALON
Data: 01/03/2024 10:29:48-0300
Verifique em https://validar.iti.gov.br

Gustavo Henrique Nalon
Author

Documento assinado digitalmente
gov.br
JOSE CARLOS LOPES RIBEIRO
Data: 01/03/2024 18:32:27-0300
Verifique em https://validar.iti.gov.br

José Carlos Lopes Ribeiro
Advisor

ACKNOWLEDGMENTS

I thank God for blessing me with the strength, well-being, wisdom, and peace needed to progress on this path and accomplish this research project.

I express my profound gratitude to my parents, Sebastião and Rogéria, for their constant encouragement and heartfelt prayers. Their unwavering support has provided me with the strength to overcome challenges along the way.

I am significantly grateful to my advisor, Prof. Dr. José Carlos Lopes Ribeiro, for the friendly guidance, valuable insights and dedicated support shared during the research process. His expertise in mechanics of structures and fire safety engineering was indispensable in accomplishing the crucial stages of this thesis.

I also thank the guidance provided by my co-advisor, Prof. Dr. Leonardo Gonçalves Pedroti, who promptly addressed my inquiries and made relevant contributions to make this research possible. His expertise in construction materials played a crucial role in overcoming challenges and enhancing the depth of our investigations.

I wish to extend my sincere thanks to my co-advisor, Prof. Dr. Roberto Marcio da Silva, for his consistent suggestions and essential guidance in overcoming challenges faced during this research. His profound expertise in masonry structures not only facilitated our progress but also added a significant richness to our investigations.

I express my gratitude to my co-advisor, Prof. Dr. Eduardo Nery Duarte de Araújo, for generously sharing his expertise in generating insightful ideas and conducting essential laboratory analyses. His profound understanding of conductive nanomaterials played a pivotal role in shaping the foundation of this research and ensuring its successful outcome.

I would like to thank the collaboration and insights from the thesis committee members, Prof. Dr. Gihad Mohamad, Prof. Dr. Guilherme Aris Parsekian and Prof. Dr. White José dos Santos. Their constructive comments significantly contributed to the improvement of the quality of this research.

I extend my sincere appreciation for the support provided by the members of the Civil Engineering Department at the Universidade Federal de Viçosa (UFV), especially Prof. Dr. José Maria Franco de Carvalho, Prof. Dr. Gustavo de Souza Veríssimo, and Prof. Dr. Flávio Antônio Ferreira. Their friendship, valuable assistance and generous sharing of knowledge significantly contributed to the success of this research. Additionally, I would like to thank Prof. Dr. Rita de Cássia Silva Sant'Anna Alvarenga *(in memoriam*), who guided my first steps in science and fostered my academic development.

I extend my special acknowledges to Robson, José Carlos, André, José Dias, Marcelo, Nathália, and Wellington, for their friendly engagement and vital support in managing the laboratory activities.

I wish to thank my friends Gustavo Emilio, Rodrigo, Márcia, Guilherme, Cíntia, Roziani, Beatryz, Caio, Gabriel, Hellen, Géssica, and others for their friendship, consistent support, and collaborations that significantly eased the challenges faced throughout this project.

I would like to acknowledge the Nucleus of Microscopy and Microanalysis at the Universidade Federal de Viçosa for providing the equipment and technical support for experiments involving electron microscopy. I extend my gratitude to the Department of Physics at UFV for their support in conducting analyses of X-ray diffraction and field emission scanning electron microscopy. Additionally, I appreciate the assistance provided by the Department of Chemistry at UFV in the development of Fourier transform infrared spectroscopy analyses. Special thanks go to the Laboratório de Materiais de Construção at the Civil Engineering Department of the Universidade Federal de Ouro Preto (UFOP) for their support in the development of X-ray fluorescence analyses. I also express my thanks to the Laboratório de Embalagens at the Department of Food Technology of UFV for their contribution to the development of thermogravimetric analyses.

I express my appreciation to the financial support that enabled the completion of this doctoral thesis. This study was financed in part by the Coordenação de Aperfeiçoamento de Pessoal de Nível Superior - Brasil (CAPES) - Finance Code 001.

I express gratitude for the carbon black nanoparticles supplied by Birla Carbon and RESIDROX Chemical Solutions, the shrinkage-compensating admixture donated by Chimica Edile do Brasil, the thermal-resistant electrodes provided by Kanthal, the hollow concrete blocks donated by BLOJAF, the sonicator provided by the Instituto de Biotecnologia Aplicada à Agropecuária (BIOAGRO) of UFV, and the samples of PowerFlow 4001, Nafufill KMH, and MC-Proof 2200 donated by MC Bauchemie. Their support has been instrumental in the success of my research.

ABSTRACT

NALON, Gustavo Henrique, D.Sc., Universidade Federal de Viçosa, February, 2024. **Self-sensing concrete blocks and mortar joints for health monitoring of structural masonry before and after exposure to high temperatures.** Advisor: José Carlos Lopes Ribeiro. Co-advisors: Leonardo Gonçalves Pedroti, Roberto Marcio da Silva and Eduardo Nery Duarte de Araújo.

Self-sensing cementitious materials are emerging technologies for stress/strain monitoring and damage detection in structural members. This research presents the development and validation of innovative technology for Structural Health Monitoring (SHM) of concrete masonry: self-sensing concrete blocks and mortar joints containing carbon-black nanoparticles (CBN). A factorial experiment was carried out to evaluate the effects of lime/cement ratio and CBN dosage on the self-sensing, mechanical and microstructural behavior of masonry mortars. Different approaches for producing self-sensing concrete units were also investigated. The results indicated that epoxy-based structural adhesives provided the best bonding performance between cementitious sensors and concrete substrates. In addition, concrete units could be successfully cast around hardened cement-based sensors. When an expansive agent was added to the self-sensing matrix, the fresh cementitious sensor was successfully embedded into hardened concrete units. The effects of different types of shrinkage-reducing admixtures and expansive agents on the drying shrinkage, self-sensing properties, microstructure and strength of cementitious materials were also reported. Finally, a validation study was carried out to investigate the mechanical and piezoresistive behavior of self-sensing masonry units and joints applied to masonry prisms under uniaxial compression. This study covered the use of different types of concrete units, mortar bedding approaches, bonding arrangements, relative strengths of mortar and units, joint thicknesses, and locations of self-sensing regions. The self-sensing units and joints were found to be promising alternatives for stress and strain monitoring of structural masonry elements, before and after high temperatures. The self-sensing masonry also demonstrated the ability for real-time detection and quantification of damage due to exposure to elevated temperatures. The electrical response of the self-sensing masonry also provided valuable insights into the recovery of damage due to rehydration procedures. This research enabled the effective design and application of smart units and joints in SHM systems of concrete masonry.

Keywords: Structural masonry; Structural Health Monitoring; self-sensing concrete unit; self-sensing masonry joint; high temperatures.

RESUMO

NALON, Gustavo Henrique, D.Sc., Universidade Federal de Viçosa, fevereiro de 2024. **Blocos de concreto e juntas de argamassa autossensoras para monitoramento da integridade da alvenaria estrutural antes e após exposição a elevadas temperaturas.** Orientador: José Carlos Lopes Ribeiro. Coorientadores: Leonardo Gonçalves Pedroti, Roberto Marcio da Silva e Eduardo Nery Duarte de Araújo.

Materiais cimentícios autossensores são tecnologias emergentes aplicadas no monitoramento de tensões/deformações e detecção de danos em elementos estruturais. Esta pesquisa apresenta a criação e validação de novas tecnologias para Monitoramento da Integridade Estrutural (SHM) da alvenaria estrutural: blocos de concreto e juntas autossensores contendo nanopartículas de *carbon black* (CBN). Um experimento fatorial foi realizado para avaliar os efeitos da razão cal/cimento e do teor de CBN no comportamento autossensor, mecânico e microestrutural de argamassas de assentamento. Diferentes abordagens para produção de unidades de concreto autossensoras também foram estudadas. Adesivos estruturais à base de epóxi forneceram a melhor aderência entre sensores cimentícios e substratos de concreto. Unidades de concreto puderam ser moldadas em torno de sensores cimentícios no estado endurecido. Utilizando um aditivo expansor na matriz autossensora, também foi possível embutir o sensor cimentício no estado fresco em unidades de concreto no estado endurecido. Foram relatados os efeitos de aditivos redutores de retração e expansores na retração por secagem, propriedades autossensoras, microestrutura e resistência de materiais cimentícios. Finalmente, foi realizado um estudo de validação para investigar o comportamento mecânico e piezoresistivo de unidades e juntas autossensoras incorporadas em prismas de alvenaria sob compressão uniaxial, considerando-se diferentes tipos de unidades de concreto, padrões de assentamento, arranjos de blocos, resistências relativas argamassa/blocos, espessuras de juntas e posições das regiões autossensoras. Observou-se que unidades e juntas autossensoras são alternativas promissoras para monitorar tensões e deformações em elementos de alvenaria estrutural, antes e após elevadas temperaturas. A alvenaria autossensora também demonstrou a capacidade de detecção e quantificação em tempo real de danos por exposição a altas temperaturas, além de fornecer importantes informações sobre a recuperação de danos devidos ao procedimento de reidratação. A presente pesquisa permitiu a efetiva produção e aplicação de unidades e juntas autossensoras em sistemas de SHM de elementos de alvenaria.

Palavras-chave: Alvenaria estrutural; Monitoramento da Integridade Estrutural; unidade de concreto autossensora; junta autossensora; temperatura elevada.

TABLE OF CONTENTS

PART I:

INTRODUCTION AND THEORETICAL FRAMEWORK

1 GENERAL INTRODUCTION

1.1. INTRODUCTION

Improvements in the safety level, durability and preservation of the reliability of civil structures are some important tasks of designers, contractors, maintenance teams and operators of the construction industry. These professionals must deal with different natural forces and human activities that can affect the integrity of civil structures, such as chemical and biological attacks, humidity and temperature variations, soil vibration and movements, wind erosion, fire disasters, overload due to inappropriate use and other deleterious effects (Baloch et al., 2018; Mustapha et al., 2021; Shlyakhova et al., 2021). Therefore, Structural Health Monitoring (SHM) systems have been proposed for continuous real-time monitoring of operational status, assessment of mechanical behavior and damage detection in civil structures during their service life (Dong and Catbas, 2021; Taheri, 2019; Wang et al., 2021).

In recent years, various types of sensing technologies have been rapidly developed for SHM of new and existing masonry structures. In the case of heritage masonry, SHM technologies can indirectly extend the service life of historical structural elements, predict damage propagation associated with unforeseen events and detect external factors that can accelerate masonry deterioration (Medeiros et al., 2020; Mishra, 2021; Scuro et al., 2021). In the case of modern masonry structures, SHM of masonry elements is very important to improve the expansion of 'smart structures' in urban areas, define the possibility of changing the typical use of masonry buildings, identify vulnerability factors and improve the structural safety on a large territorial scale (La Mendola et al., 2021; Medeiros et al., 2020).

Different equipment and techniques can be used to investigate the health status of masonry, such as acoustic emission sensors for damage assessment in masonry walls (Figure 1a), digital image correlation to obtain the field deformation on the masonry surface (Figure 1b), linear variable differential transformers to measure crack amplitude (Figure 1c), ceramic and capacitive sensors embedded in masonry joints to measure compressive stresses (Figure 1d and Figure 1e), accelerometers to track the evolution of masonry's vibration modal properties (Figure 1f), infrared cameras to inspect structural integrity (Figure 1g) and flat-jack tests to investigate the stress-strain behavior of masonry walls (Figure 1h). Although

these conventional approaches can provide interesting insights on the management and maintenance of masonry structures, they have many disadvantages that limit a large-scale application, such as short service life, high cost, poor performance in aggressive environments, limited sensitivity, low authenticity, implementation complexity, low robustness and poor compatibility with civil structures (Das and Saha, 2018; Han et al., 2020; Sarwary et al., 2019; Ubertini and D'Alessandro, 2018).

Figure 1 - Different systems used for monitoring the structural masonry behavior.

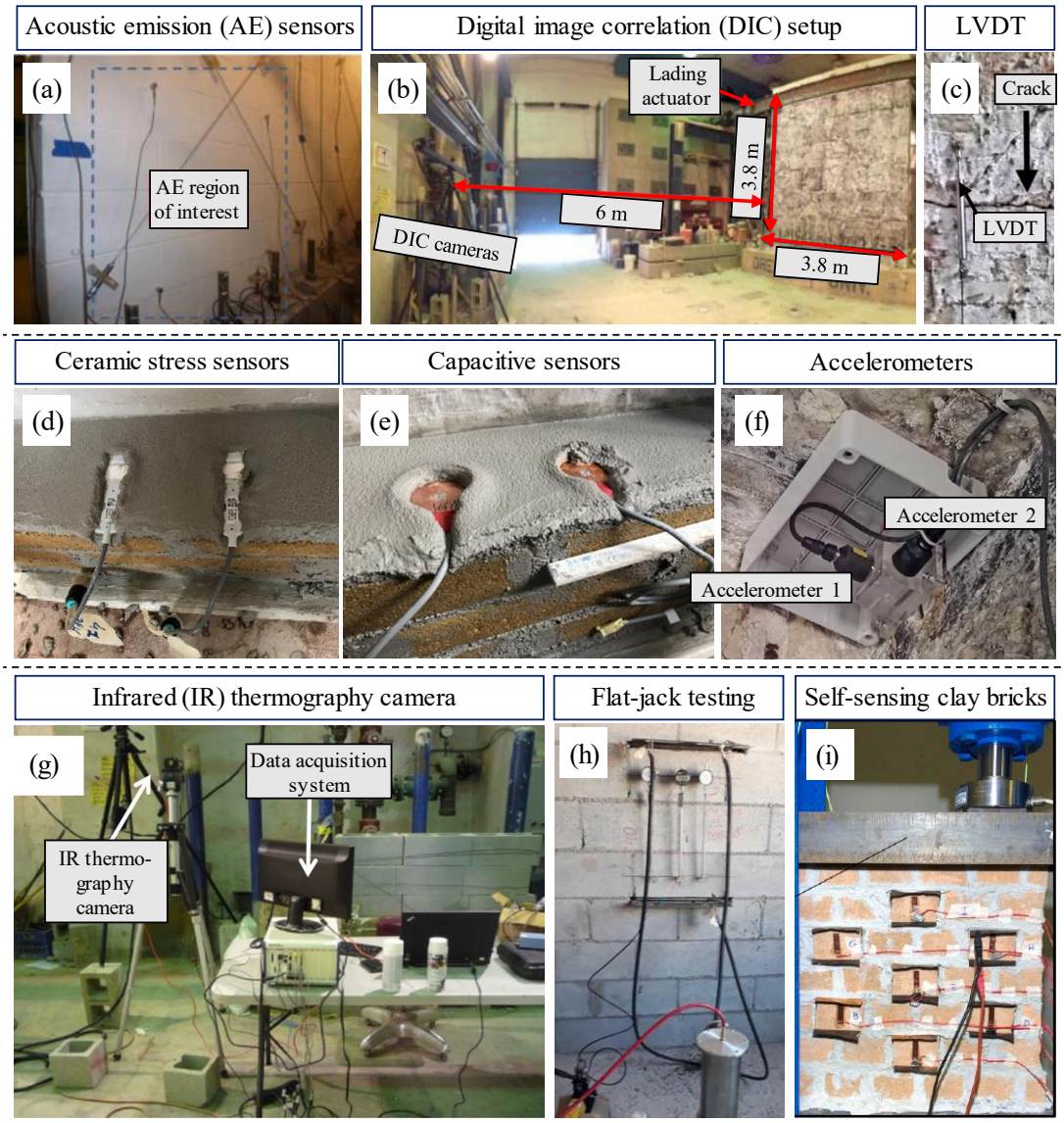

Source: (a) and (b) adapted from Vanniamparambil et al. (2014), as permitted under the Creative Commons Attribution License Agreement; (c) and (f) adapted from Kita (2019), Copyright 2019, with permission from Elsevier; (d) and (e) adapted from La Mendola et al. (2021), Copyright 2021, with permission from Elsevier; (g) adapted from Khan et al. (2015), Copyright 2015, with permission from Wiley Company; (h) adapted from Ferreira Junior (2020), as permitted under the Creative Commons Attribution License Agreement); (i) adapted from Meoni et al. (2021), Copyright 2021, with permission from Elsevier.

The development of self-sensing cementitious matrices with inherent intelligence and their incorporation into SHM architectures are gathering increasing attention in the SHM community. These smart cement-based materials exhibit natural sensitivity to external stimuli and changes in their surrounding environment, in addition to noticeable robustness, low cost, high gauge factor, durability and mechanical properties. Based on the piezoresistivity phenomenon, these materials have a natural strain/stress-sensing ability, as they exhibit changes in their electrical resistivity due to the application of mechanical loading. Based on irreversible changes in electrical resistivity, they can also detect cracking propagation in structural elements. Among the different types of admixtures used to construct the composites' conductive network, carbon-based nanomaterials are commonly used in self-sensing cementitious materials (Dong et al., 2019). In the present work carbon black nanoparticles (CBN) were used to construct the conductive network inside the mortars.

Figure 2 - (a) Fusion of carbon black nanoparticles (CBN) to form aggregates and agglomerates; and (b) sketch of CBN consisting of concentrically arranged graphitic-like domains.

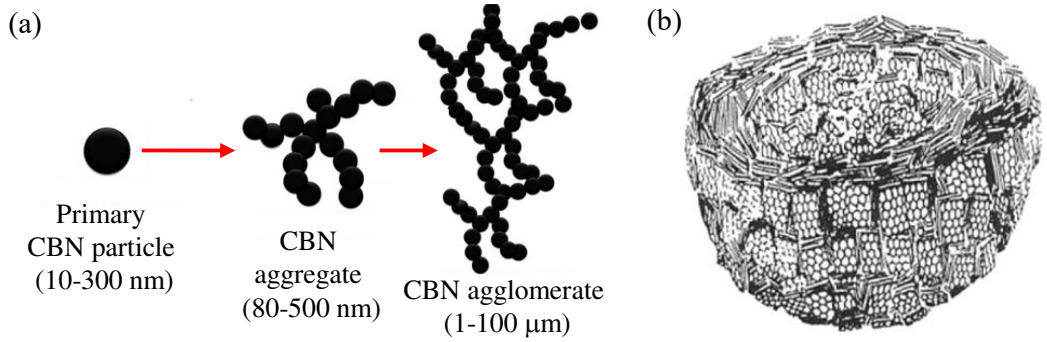

Source: (a) adapted from Kausar and Taherian (2019), Copyright 2019, with permission from Elsevier; and (b) reproduced from Pawlyta et al. (2015), Copyright 2015, with permission from Elsevier.

In the last years, a novel class of self-sensing construction materials called smart bricks (Figure 1i) was found to be a cost-effective solution for SHM of masonry structures, as these clay bricks are able to self-monitor deformations, load paths changes and development of damages (Birgin et al., 2023; Downey et al., 2018; García-Macías and Ubertini, 2019; Meoni, D'Alessandro and Ubertini, 2021). Although solid concrete bricks and hollow concrete blocks have been widely used in masonry structures, there is no previous investigation on the application of self-sensing cementitious materials for SHM of concrete masonry.

A severe fire is a big threat to human life and structural safety. Catastrophic life losses and substantial damage to structural elements associated with severe fires have stimulated the development of diverse studies on the field of structural and fire safety assessment. To

avoid the demolition and rebuilding of fire-damaged structures, their repair and refurbishment are interesting alternatives from a technical, ecological and economic point of view. However, a careful and accurate assessment of the damage status of fire-damaged elements is required to ensure a good structural safety level (Cho et al., 2017; Ha et al., 2016).

The recent progress on the understanding of electrical and self-sensing properties of cementitious composites exposed to high temperatures provided important insights on the development of smart structural elements that are able to (i) work as a fire alarm sensor, (ii) provide a self-detection/quantification of damage due to fire exposure, or (iii) self-monitor stresses and strains of structures after fire incidents (Demircilioğlu et al., 2019; Dong et al., 2020; Jang et al., 2022; Nalon et al., 2021).

Although significant progress has been made on the design, evaluation and optimization of self-sensing pastes, mortars and concretes, there is no previous experimental investigation of their potential application in the realm of SHM of concrete block masonry. In response to the growing concern about the progressive degradation of masonry structures, this thesis deals with the use of CBN for production of self-sensing concrete blocks and self-sensing cement-lime mortars that can provide a cost-effective solution for SHM of concrete masonry elements before and after fire hazards.

1.2. OBJECTIVES

1.2.1. General objective

The main goal of this thesis was the development and evaluation of concrete blocks and mortar joints with the ability to self-monitor strain/stress and self-detect damage in masonry prisms, before and after exposure to elevated temperatures.

1.2.2. Specific objectives

The specific objectives of this thesis are outlined below:

(1) determining the electrical and self-sensing behavior of cement-lime laying mortars with different lime/cement ratios and various CBN contents;

(2) evaluation of various embedding approaches to produce self-sensing concrete units and the effects of distinct types of interface agent types between concrete units and self-sensing cementitious matrices;

(3) analyses of the effects of shrinkage-reducing admixtures and expansive agents on self-sensing properties and shrinkage control of cementitious materials;
(4) verification of the viability of using self-sensing concrete blocks and self-sensing cement-lime mortars for strain/stress monitoring, damage detection and prediction of masonry failure modes before exposure to high temperatures;
(5) numerical analyses of temperature distributions in masonry exposed to different maximum temperature levels and subjected to distinct boundary conditions;
(6) verification of the viability of using self-sensing concrete blocks and self-sensing cement-lime mortars for strain/stress monitoring, damage detection and prediction of failure mechanisms of masonry prisms exposed to different high temperature levels, before or after the application of a rehydration process.

1.3. JUSTIFICATION

Improvements in SHM systems applied to masonry structures are of fundamental importance for safety of users. Solid clay bricks with self-sensing ability have been recently proposed as cost-effective solutions for SHM of clay and earth masonry (Birgin et al., 2023; D'Alessandro et al., 2018; Downey et al., 2018; García-Macías and Ubertini, 2019; Meoni, D'Alessandro and Ubertini, 2021; Meoni et al., 2019, 2020, 2021, 2022; Ubertini et al., 2017). However, the design and testing of concrete blocks and cement-lime mortar joints with self-sensing properties were not investigated in previous literature. One of the motivations for the present thesis was the development of concrete masonry components with intrinsic sensing abilities that solve some issues associated with the limited scalability of SHM architectures traditionally used to monitor the mechanical behavior of concrete masonry. The experimental campaign of this thesis is justified by the need for studies to design concrete blocks and cement-lime mortars with self-sensing capability to monitor strain/stresses of masonry within its linear-elastic regime. Another justification for this work was the evaluation of the possible use of smart masonry components to identify changes in load paths and detect incipient or critical damages, such as those associated with progressive cracking of units or eventual pore-collapse of joints. It would allow a prognosis of damage evolution that could culminate in some failure mode typically observed in masonry elements.

In the context of structural fire safety, this thesis is also justified by the need for new technologies that can provide an accurate and cost-effective assessment of the residual mechanical performance and damage status of fire-damaged masonry structures. Severe fires

cause more significant deterioration and decreases in strength and stiffness of concrete blocks masonry, compared to other types of masonry elements (Bošnjak et al., 2020; Daware and Naser, 2021). Despite this, sometimes the rehabilitation of concrete masonry can be an interesting alternative in terms of technical, environmental and economic perspectives (Aseem et al., 2019; Cho et al., 2017; Ha et al., 2016; Nalon et al., 2021). There is no previous study that evaluated the piezoresistive behavior of self-sensing masonry structures after exposure to high temperatures. The ability of these structures to self-detect damage due to exposure to elevated temperatures has also not been reported in previous papers. Then, another justification for developing this research is the analysis of the applicability of self-sensing concrete blocks and mortar joints to monitor stress and strains of fire-damaged masonry elements, as well as to verify their ability to self-detect the damage associated with the exposure of the masonry to high temperatures. Moreover, the effects of post-fire rehydration on the recovery of mechanical properties of masonry prisms exposed to high temperatures is still unknown. Therefore, another motivation for the present research is the characterization of mechanical and piezoresistive properties of masonry prisms subjected to post-fire rehydration. Finally, the self-detection of damage recovery in masonry due to this rehydration process is another contribution of this thesis.

1.4. THESIS STRUCTURE

This thesis is organized into ten chapters, strategically distributed across five parts, ensuring a coherent and systematic presentation of the research content. Figure 3 shows a flowchart that represents the different stages of this thesis. This flowchart serves as a roadmap, offering a structured overview of the various stages comprising the content of the present thesis. A brief description of the content of each part is provided below.

(1) Part I: Introduction and theoretical framework

Part I is composed of Chapters 1, 2 and 3. It offers an in-depth exploration of the research's introductory aspects and provides the theoretical framework for the subsequent parts. In Chapter 1, the context of this research is presented, based on an introduction about SHM of masonry structures, self-sensing cementitious materials and fire safety assessment. The objectives, motivations and the structure of this thesis are also described in this chapter.

Figure 3 - Thesis structure flowchart.

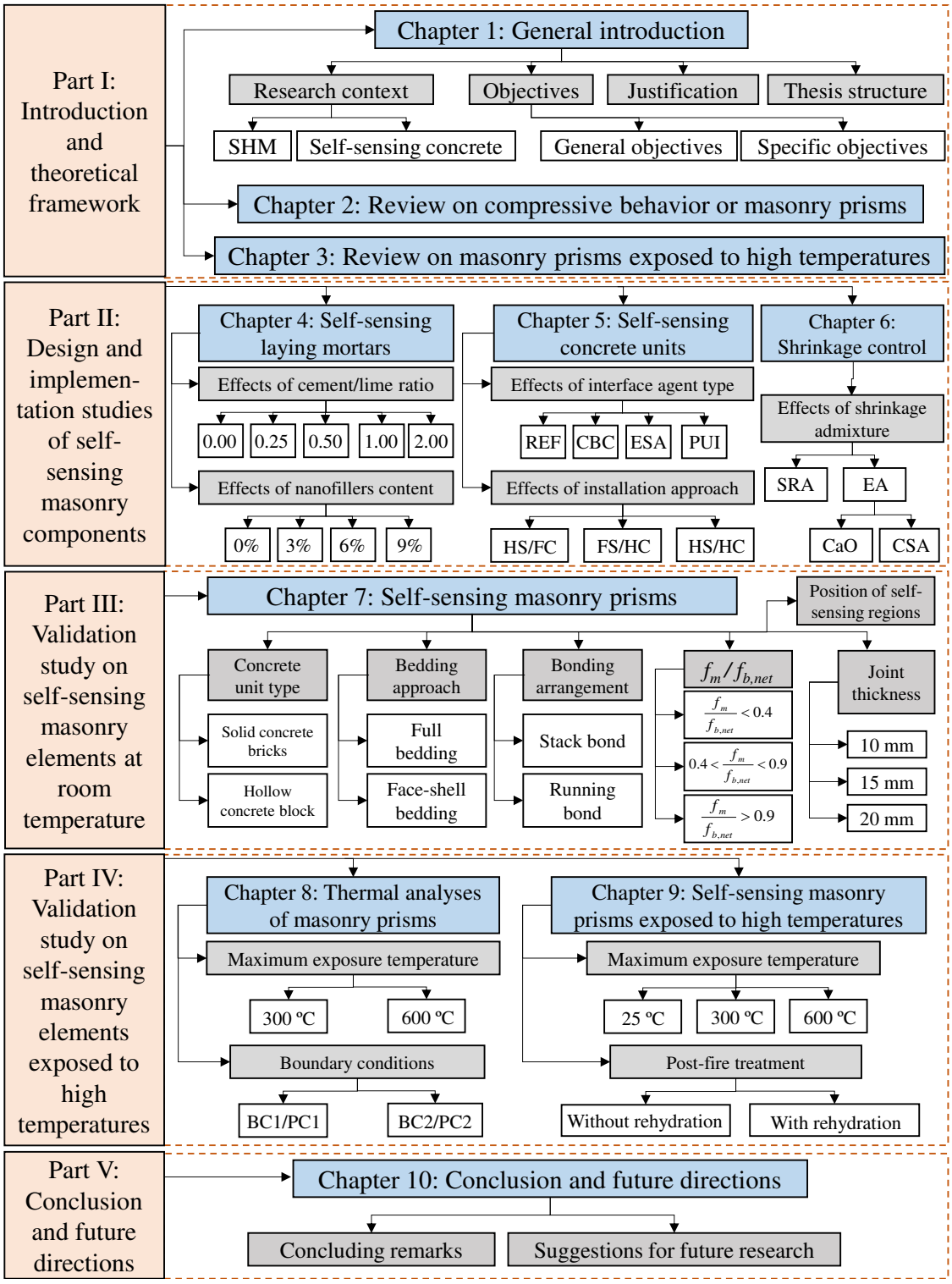

Note: SHM = Structural Health Monitoring, REF = reference series, CBC = cement-based bonding coat, ESA = epoxy-based structural adhesive, PUI = polyurethane-based resin in the interface, HS/FC = hardened sensor/fresh concrete, FS/HC = fresh sensor/hardened concrete, HS/HC = hardened sensor/hardened concrete, SRA = shrinkage-reducing admixture, EA = expansive agent, CaO = calcium oxide, CSA = calcium sulfoaluminate, f_m = compressive strength of mortar, $f_{b,net}$ = net area compressive strength of concrete units, BC1/PC1 and BC2/PC2 = boundary conditions type 1 and 2, respectively.

Source: Author (2024).

Chapter 2 presents a comprehensive literature review of the recent progress on the compressive behavior of masonry prisms, in addition to the identification of future research directions in this area. It includes a careful revision of the failure mechanisms and mechanical properties of prisms constructed with conventional and innovative masonry components, the mutual dependency of different factors that affect the compressive behavior of masonry prisms, some model predictions of their mechanical performance and novel minor-destructive and non-destructive tests applied to monitor strain/stress and damage status of masonry prisms.

In Chapter 3, the current state-of-the-art on the effects of elevated temperatures on the mechanical behavior of masonry prisms is revised. Residual strength, stiffness and failure modes of fire-damaged masonry prisms produced with different types of units, mortars and/or grout were presented. Then, this literature review is used to detect promising topics to be addressed in future studies in this scientific field.

(2) Part II: Design and implementation studies of self-sensing masonry components

Comprising Chapters 4, 5, and 6, Part II presents design and implementation studies related to self-sensing masonry units and self-sensing mortar joints. This section describes the conceptualization and implementation planning stages, evaluating different alternatives to integrate sensing abilities into masonry components.

Chapter 4 is devoted to the design of self-sensing cement-lime mortars for SHM of masonry structures. It reports the first experimental investigation of the effects of different lime/cement ratios and distinct CBN concentrations on electrical resistivity, self-sensing properties, compressive strength and microstructure of masonry mortars.

Chapter 5 focus on evaluations of promising strategies to obtain self-sensing concrete units. Different interface agent types for embedding self-sensing cementitious composites into concrete units are evaluated, in terms of interface bond strength. In addition, advantages and limitations of distinct installation approaches are analyzed, in terms of the mechanical and piezoresistive response of the obtained self-sensing concrete units.

Chapter 6 presents an implementation study crucial for addressing shrinkage issues that could arise during the practical application of self-sensing masonry components. This study explores the viability of using a polypropylene glycol-based shrinkage-reducing admixture,

a calcium oxide expansive agent, or a calcium sulphoaluminate expansive agent for shrinkage control of self-sensing cementitious composites. These admixtures are promising alternatives to solve shrinkage issues associated with the practical application of the cement-based sensors in SHM of existing masonry elements. The effects of these different types of admixtures on the electrical resistivity, self-sensing properties, compressive strength, microstructure and shrinkage behavior of nanomodified mortars are evaluated.

(3) Part III: Validation study on self-sensing masonry elements at room temperature

Part III primarily consists of Chapter 7 and systematically examines the mechanical and self-sensing performance of masonry prisms containing the smart concrete units and cement-lime mortar joints developed in Part II of the present thesis, before exposure to elevated temperatures.

A validation study of the developed self-sensing components is presented in Chapter 7, taking into account the promising results and the limitations identified in Chapters 4, 5 and 6. The self-sensing performance of nanomodified units and mortar joints is investigated in compression tests of masonry elements. In this validation, many different variables that affect the prism compressive behavior revised in Chapter 2 are explored, such as the relative strength between units and mortar, the type of masonry unit, the mortar bedding approach, the bonding arrangement and the mortar joint thickness.

(4) Part IV: Validation study on self-sensing masonry elements exposed to high temperatures

Part IV of this thesis is composed of Chapters 8 and 9. This part presents a comprehensive exploration of the mechanical and self-sensing performance of masonry prisms containing the smart concrete blocks and cement-lime mortar joints, after exposure to elevated temperatures.

Thermal analyses are developed in Chapter 8 to assess the temperature distribution in concrete masonry prisms exposed to different temperature levels and boundary conditions during heating tests. Numerical simulations are carried out for examination of the influence

of convection mechanisms inside the voids on the temperature homogenization in prisms subjected to predefined test conditions.

Chapter 9 presents another validation study, considering the impact of elevated temperatures on the mechanical and self-sensing performance of masonry prisms that exhibited appropriate functionality in Part III. In this validation, different variables that affect the prism residual compressive behavior revised in Chapter 3 are explored, such as the maximum exposure temperature level and the application of post-fire rehydration.

(5) Part V: Conclusions and future directions

Part V is composed by Chapter 10 and presents the main conclusions obtained from the studies developed in Parts I, II, III and IV. A comprehensive summary of key findings is presented, highlighting implications, limitations and the overall significance of the present research. Additionally, Part V lists recommendations for future research in the field of self-sensing masonry technology. Potential directions for addressing existing limitations are indicated, thereby serving as a bridge to guide future advancements in the development of self-sensing construction materials for improved SHM of masonry structures.

REFERENCES

Aseem, A., Latif Baloch, W., Khushnood, R. A., & Mushtaq, A. (2019). Structural health assessment of fire damaged building using non-destructive testing and micro-graphical forensic analysis: A case study. *Case Studies in Construction Materials*, *11*, e00258. https://doi.org/10.1016/j.cscm.2019.e00258

Baloch, W. L., Khushnood, R. A., & Khaliq, W. (2018). Influence of multi-walled carbon nanotubes on the residual performance of concrete exposed to high temperatures. *Construction and Building Materials*, *185*, 44–56. https://doi.org/10.1016/j.conbuildmat.2018.07.051

Birgin, H. B., D'Alessandro, A., Meoni, A., & Ubertini, F. (2023). Self-Sensing Eco-Earth Composite with Carbon Microfibers for Sustainable Smart Buildings. *Journal of Composites Science*, *7*(2), 63. https://doi.org/10.3390/jcs7020063

Bošnjak, J., Gambarelli, S., Sharma, A., & Mešković, A. (2020). Experimental and numerical studies on masonry after exposure to elevated temperatures. *Construction and Building Materials*, *230*, 116926. https://doi.org/10.1016/j.conbuildmat.2019.116926

Cho, H., Lee, D., Ju, H., Park, H., Kim, H., & Kim, K. (2017). Fire Damage Assessment of Reinforced Concrete Structures Using Fuzzy Theory. *Applied Sciences*, *7*(5), 518. https://doi.org/10.3390/app7050518

D'Alessandro, A., Meoni, A., García-Macías, E., Cavalagli, N., Gioffrè, M., & Ubertini, F. (2018). Full-scale testing of a masonry building monitored with smart brick sensors. *Proceedings of 5th International Electronic Conference on Sensors and Applications*, 5764. https://doi.org/10.3390/ecsa-5-05764

Das, S., & Saha, P. (2018). A review of some advanced sensors used for health diagnosis of civil engineering structures. *Measurement*, *129*, 68–90. https://doi.org/10.1016/j.measurement.2018.07.008

Daware, A., & Naser, M. Z. (2021). Fire performance of masonry under various testing methods. *Construction and Building Materials*, *289*, 123183. https://doi.org/10.1016/j.conbuildmat.2021.123183

Demircilioğlu, E., Teomete, E., Schlangen, E., & Baeza, F. J. (2019). Temperature and moisture effects on electrical resistance and strain sensitivity of smart concrete. *Construction and Building Materials*, *224*, 420–427. https://doi.org/10.1016/j.conbuildmat.2019.07.091

Dong, & Catbas, F. N. (2021). A review of computer vision–based structural health monitoring at local and global levels. *Structural Health Monitoring*, *20*(2), 692–743. https://doi.org/10.1177/1475921720935585

Dong, W., Li, W., Tao, Z., & Wang, K. (2019). Piezoresistive properties of cement-based sensors: Review and perspective. *Construction and Building Materials*, *203*, 146–163. https://doi.org/10.1016/j.conbuildmat.2019.01.081

Dong, W., Li, W., Wang, K., Han, B., Sheng, D., & Shah, S. P. (2020). Investigation on physicochemical and piezoresistive properties of smart MWCNT/cementitious composite exposed to elevated temperatures. *Cement and Concrete Composites*, *112*, 103675. https://doi.org/10.1016/j.cemconcomp.2020.103675

Downey, A., D'Alessandro, A., Laflamme, S., & Ubertini, F. (2018). Smart bricks for strain sensing and crack detection in masonry structures. *Smart Materials and Structures*, *27*(1), 015009. https://doi.org/10.1088/1361-665X/aa98c2

Ferreira Junior, J. B. (2020). *Validation of the flat jack technique in assessing the strength of existing masonry performed with hollow concrete blocks* [Dissertation]. Universidade Federal de São Carlos.

García-Macías, E., & Ubertini, F. (2019). Earthquake-induced damage detection and localization in masonry structures using smart bricks and Kriging strain reconstruction: A numerical study. *Earthquake Engineering & Structural Dynamics*, *48*(5), 548–569. https://doi.org/10.1002/eqe.3148

Ha, T., Ko, J., Lee, S., Kim, S., Jung, J., & Kim, D.-J. (2016). A Case Study on the Rehabilitation of a Fire-Damaged Structure. *Applied Sciences*, *6*(5), 126. https://doi.org/10.3390/app6050126

Han, J., Pan, J., Cai, J., & Li, X. (2020). A review on carbon-based self-sensing cementitious composites. *Construction and Building Materials*, *265*, 120764. https://doi.org/10.1016/j.conbuildmat.2020.120764

Jang, D., Yoon, H. N., Seo, J., & Yang, B. (2022). Effects of exposure temperature on the piezoresistive sensing performances of MWCNT-embedded cementitious sensor. *Journal of Building Engineering*, *47*, 103816. https://doi.org/10.1016/j.jobe.2021.103816

Kausar, A., & Taherian, R. (2019). Electrical Conductivity Behavior of Polymer Nanocomposite with Carbon Nanofillers. In *Electrical Conductivity in Polymer-Based Composites: Experiments, Modelling and Applications* (pp. 41–72). Elsevier. https://doi.org/10.1016/B978-0-12-812541-0.00003-3

Khan, F., Rajaram, S., Vanniamparambil, P. A., Bolhassani, M., Hamid, A., Kontsos, A., & Bartoli, I. (2015). Multi-sensing NDT for damage assessment of concrete masonry walls. *Structural Control and Health Monitoring*, *22*(3), 449–462. https://doi.org/10.1002/stc.1680

Kita, A., Cavalagli, N., & Ubertini, F. (2019). Temperature effects on static and dynamic behavior of Consoli Palace in Gubbio, Italy. *Mechanical Systems and Signal Processing*, *120*, 180–202. https://doi.org/10.1016/j.ymssp.2018.10.021

La Mendola, L., Oddo, M. C., Papia, M., Pappalardo, F., Pennisi, A., Bertagnoli, G., Di Trapani, F., Monaco, A., Parisi, F., & Barile, S. (2021). Performance of two innovative stress sensors imbedded in mortar joints of new masonry elements. *Construction and Building Materials*, *297*, 123764. https://doi.org/10.1016/j.conbuildmat.2021.123764

Medeiros, W. A., Soriani, M. de O., & Parsekian, G. A. (2020). Innovation in flat-jack application to evaluate modern high-strength hollow concrete block masonry. *Construction and Building Materials*, *255*, 119341. https://doi.org/10.1016/j.conbuildmat.2020.119341

Meoni, A., D'Alessandro, A., Cavalagli, N., Gioffré, M., & Ubertini, F. (2019). Shaking table tests on a masonry building monitored using smart bricks: Damage detection and localization. *Earthquake Engineering & Structural Dynamics*, *48*(8), 910–928. https://doi.org/10.1002/eqe.3166

Meoni, A., D'Alessandro, A., Kruse, R., De Lorenzis, L., & Ubertini, F. (2021). Strain field reconstruction and damage identification in masonry walls under in-plane loading using dense sensor networks of smart bricks: Experiments and simulations. *Engineering Structures*, *239*, 112199. https://doi.org/10.1016/j.engstruct.2021.112199

Meoni, A., D'Alessandro, A., & Ubertini, F. (2020). Characterization of the strain-sensing behavior of smart bricks: A new theoretical model and its application for monitoring of masonry structural elements. *Construction and Building Materials*, *250*, 118907. https://doi.org/10.1016/j.conbuildmat.2020.118907

Meoni, A., D'Alessandro, A., & Ubertini, F. (2021). *Recent Advances and Open Issues on the Use of Smart Bricks for Seismic Monitoring of Masonry Buildings: Experimental Tests and Numerical Simulations* (pp. 851–860). https://doi.org/10.1007/978-3-030-64594-6_82

Meoni, A., Fabiani, C., D'Alessandro, A., Pisello, A. L., & Ubertini, F. (2022). Strain-sensing smart bricks under dynamic environmental conditions: Experimental investigation and new modeling. *Construction and Building Materials*, *336*, 127375. https://doi.org/10.1016/j.conbuildmat.2022.127375

Mishra, M. (2021). Machine learning techniques for structural health monitoring of heritage buildings: A state-of-the-art review and case studies. *Journal of Cultural Heritage*, *47*, 227–245. https://doi.org/10.1016/j.culher.2020.09.005

Mustapha, S., Lu, Y., Ng, C.-T., & Malinowski, P. (2021). Sensor Networks for Structures Health Monitoring: Placement, Implementations, and Challenges—A Review. *Vibration*, *4*(3), 551–584. https://doi.org/10.3390/vibration4030033

Nalon, G. H., Ribeiro, J. C., Pedroti, L. G., Duarte de Araújo, E., Franco de Carvalho, J., Soares de Lima, G., & de Moura Guimarães, L. (2021). Residual piezoresistive properties of mortars containing carbon nanomaterials exposed to high temperatures. *Cement and Concrete Composites*, *121*, 104104. https://doi.org/10.1016/j.cemconcomp.2021.104104

Pawlyta, M., Rouzaud, J.-N., & Duber, S. (2015). Raman microspectroscopy characterization of carbon blacks: Spectral analysis and structural information. *Carbon*, *84*, 479–490. https://doi.org/10.1016/j.carbon.2014.12.030

Sarwary, M. H., Yıldırım, G., Al-Dahawi, A., Anıl, Ö., Khiavi, K. A., Toklu, K., & Şahmaran, M. (2019). Self-Sensing of Flexural Damage in Large-Scale Steel-Reinforced Mortar Beams. *ACI Materials Journal*, *116*(4), 209–221. https://doi.org/10.14359/51715581

Scuro, C., Lamonaca, F., Porzio, S., Milani, G., & Olivito, R. S. (2021). Internet of Things (IoT) for masonry structural health monitoring (SHM): Overview and examples of innovative systems. *Construction and Building Materials*, *290*, 123092. https://doi.org/10.1016/j.conbuildmat.2021.123092

Shlyakhova, E. A., Serebryanaya, I. A., Egorochkina, I. O., Matrosov, A. A., & Soloviev, A. N. (2021). Compositions Based on Expansion Additive for the Repair of Reinforced Concrete Structures. *IOP Conference Series: Materials Science and Engineering*, *1029*(1), 012047. https://doi.org/10.1088/1757-899X/1029/1/012047

Taheri, S. (2019). A review on five key sensors for monitoring of concrete structures. *Construction and Building Materials*, *204*, 492–509. https://doi.org/10.1016/j.conbuildmat.2019.01.172

Ubertini, F., & D'Alessandro, A. (2018). Concrete with self-sensing properties. In *Eco-Efficient Repair and Rehabilitation of Concrete Infrastructures* (pp. 501–530). Elsevier. https://doi.org/10.1016/B978-0-08-102181-1.00018-6

Ubertini, F., D'Alessandro, A., Materazzi, A., Laflamme, S., & Downey, A. (2017). Novel nanocomposite clay brick for strain sensing in structural masonry. *2017 IEEE International Conference on Environment and Electrical Engineering and 2017 IEEE Industrial and Commercial Power Systems Europe (EEEIC / I&CPS Europe)*, 1–4. https://doi.org/10.1109/EEEIC.2017.7977598

Wang, X., Chakraborty, J., & Niederleithinger, E. (2021). Noise Reduction for Improvement of Ultrasonic Monitoring Using Coda Wave Interferometry on a Real Bridge. *Journal of Nondestructive Evaluation*, *40*(1), 14. https://doi.org/10.1007/s10921-020-00743-9

2 REVIEW OF RECENT PROGRESS ON THE COMPRESSIVE BEHAVIOR OF MASONRY PRISMS

This chapter has been published as the following paper: Nalon, G. H.; Ribeiro, J. C. L.; Pedroti, L. G.; Silva, R. M.; Araújo, E. N. D.; Santos, R. F.; Lima, G. E. S. Review of recent progress on the compressive behavior of masonry prisms. ***Construction and Building Materials*** *320 (2020) 1296181. https://doi.org/10.1016/j.conbuildmat.2021.126181*

Abstract: *Masonry prisms have been widely used in research and quality control of masonry structures, as they are simplified models that can represent the interaction between different masonry components. Although much progress has been recently made on the compressive behavior of masonry prisms, review papers on this topic were published many years ago. Then, this work aimed to investigate the current state-of-the-art on this topic. The following contributions derived from this review: identification and comparison of the compressive behavior of prisms constructed with innovative materials created in recent years; detection of topics for improvement of masonry design codes, associated with the mutual dependency of many factors affecting the mechanical performance of prisms; discussions of prism case scenarios often neglected in past literature; compilation of advances in model predictions of prisms' compressive behavior; emerging technologies for assessment of safety of masonry elements is discussed based on minor-destructive tests (MDT) and non-destructive tests (NDT) for strain monitoring and damage detection in masonry prisms. Future development trends for studies on this topic were also presented.*

Keywords: *Masonry prisms; mechanical performance; failure mode; strain and damage monitoring.*

2.1. INTRODUCTION

Structural masonry has been widely used for construction of monumental, administrative, and residential buildings due to different reasons, such as resource availability, social constraints, cultural affinity, and economic viability (Parajuli et al., 2020;

Parsekian et al., 2018; Ramalho and Corrêa, 2003). The mechanical properties of masonry have been investigated based on experimental tests of non-homogeneous, inelastic, and orthotropic masonry-assemblages produced with a combination of units, mortar, grout, and/or reinforcement (Lumantarna et al., 2014). Indeed, masonry design codes (ABNT, 2020a; ASA, 2018; CEN, 2005; CSA, 2014; MSJC, 2016) state two main methods to determine the mechanical properties of structural masonry: tabulated design values based on unit, mortar, and grout designations; and experimental tests of masonry assemblages built with site representative materials.

Experimental tests of complex masonry elements have practical limitations in terms of cost, time, sample transportation, capacity and size of available testing machines, among others (Sarhat and Sherwood, 2014). Then, the masonry prism has been proposed as a simple assemblage of masonry components, usually 2–5 units in height. Experimental tests of prisms are widely used in masonry research and practical quality control because prisms are simplified models that are easy to construct and test, considering operational and economic aspects. They can represent the actual masonry behavior, including effects of constituent properties and quality of workmanship (Nalon et al., 2020; Parsekian et al., 2012; Thaickavil and Thomas, 2018).

Compressive strength and elastic modulus of masonry prisms under compression have been extensively studied because they are important design parameters, on which the derivation of masonry mechanical properties are largely based (Drougkas et al., 2016). Although much progress has been made on the compressive behavior of masonry prisms over the recent years, comprehensive review papers on this topic were published many years ago (Ganesan and Ramamurthy, 1992; Mohamad et al., 2007). Actually, recent review manuscripts have mainly focused on experimental investigations on the shear and flexural behavior of masonry walls (Anić et al., 2020; Chang et al., 2020; El-Dakhakhni and Ashour, 2017), computational modeling techniques of masonry elements (Asteris et al., 2017; D'Altri et al., 2020; Shadlou et al., 2020), and masonry strengthening methods (Furtado et al., 2020; Gupta and Singhal, 2020; Marques and Lourenço, 2019; Thamboo, 2020).

Given that many different findings concerning the compressive behavior of masonry prisms have been published during the last years, the present work aimed to investigate the current state-of-the-art on this subject, identify knowledge gaps, and provide recommendations for future research on this topic. The main contributions of this research include: (i) identification and comparison of compressive behavior of masonry prisms

constructed with innovative materials developed over the last decades (e.g., eco-efficient masonry components, high-strength concrete blocks, polymer adhesive mortars, pre-blended mortars and grout, etc); (ii) detection of topics of special importance for improvement of masonry design codes, associated with the mutual dependency of a large number of factors affecting the structural performance of masonry prisms; (iii) discussions of test results of prisms within case scenarios often neglected in past literature; (iv) compilation of advances in model predictions of prisms compressive behavior; (v) emerging technologies consisting of minor-destructive tests (MDT) and non-destructive tests (NDT) were discussed, based on strain monitoring and damage detection in masonry prisms; (vi) comparisons between mechanical properties predicted by formulations of current masonry design codes and mechanical properties obtained in the revised literature; and (vii) identification of future development trends for studies on the compressive behavior of masonry prisms.

This review was structured in different sections that deal with key pioneering studies reporting relevant knowledge and modern advances on the compressive behavior of masonry prisms. Section 2.1 presents a brief background information on this topic, in addition to the objectives and contributions of this chapter. Section 2.2 presents a compilation of discussions and illustrations of failure mechanisms observed in ungrouted and grouted prisms under compression. Section 2.3 revises the compressive strength and modulus of elasticity of masonry prisms produced with different innovative types of masonry components. The mutual dependency of distinct factors affecting the strength and stiffness of masonry prisms is also discussed in this section. The predictive ability of formulations and tables of current masonry codes is also evaluated in this section, in the view of a large number of studies. Section 2.4 discusses recent advances on models that represent the stress-strain relationship of prisms subjected to compression. Modern technologies for characterization of prisms with MDT and NDT are discussed in Section 2.5. Finally, conclusions and future development trends for studies on this topic were prospected in Sections 2.6 and 2.7, respectively.

2.2. FAILURE MECHANISMS OF MASONRY PRISMS

The mechanical performance of prisms under compression is directly affected by failure modes associated with the mechanical properties of their constituent materials. The structural behavior of units, mortar and grout in a composite masonry element is significantly different from that observed in stand-alone specimens subjected to uniaxial compression

tests. The mechanical response of each individual component is a function of a triaxial behavior resulted from the complex interaction between them. Thus, the failure mechanisms of a masonry prism is a sequence of effects directly related to the relative strength of mortar, units, and grout (Drougkas et al., 2019; Llorens et al., 2020; Mohamad et al., 2017, 2018).

2.2.1. Ungrouted prisms

Structural masonry is mainly constructed with stiffer units and relatively low-strength mortar (Shi et al., 2021). In ungrouted prisms produced with units stiffer than mortars and subjected to axial compression, the mortar joint tends to present a lateral expansion ($\Delta_{h,m}$) higher than the tendency of lateral expansion of units ($\Delta_{h,u}$), as indicated in Figure 1a. These differential movements are restrained due to the mortar/unit adhesion, so that the actual lateral expansion is an intermediate value ($\Delta_{h,p}$) between the amounts that each component tended to deform. Consequently, the mortars are subjected to vertical compressive stresses ($\sigma_{v,m}$) and lateral compressive stresses ($\sigma_{h,m}$) that mobilize their strength under multiaxial confinement, while the units are subjected to vertical compressive stresses ($\sigma_{v,u}$) and lateral tensile stresses ($\sigma_{h,u}$) (Alvarenga et al., 2017a; Drougkas et al., 2019; Nalon et al., 2020), as indicated in Figure 1a.

Figure 1 - States of stress in (a) prisms produced with units stiffer than the mortar under a compressive stress σ_v and (b) prisms produced with units softer than the mortar under a compressive stress σ_v.

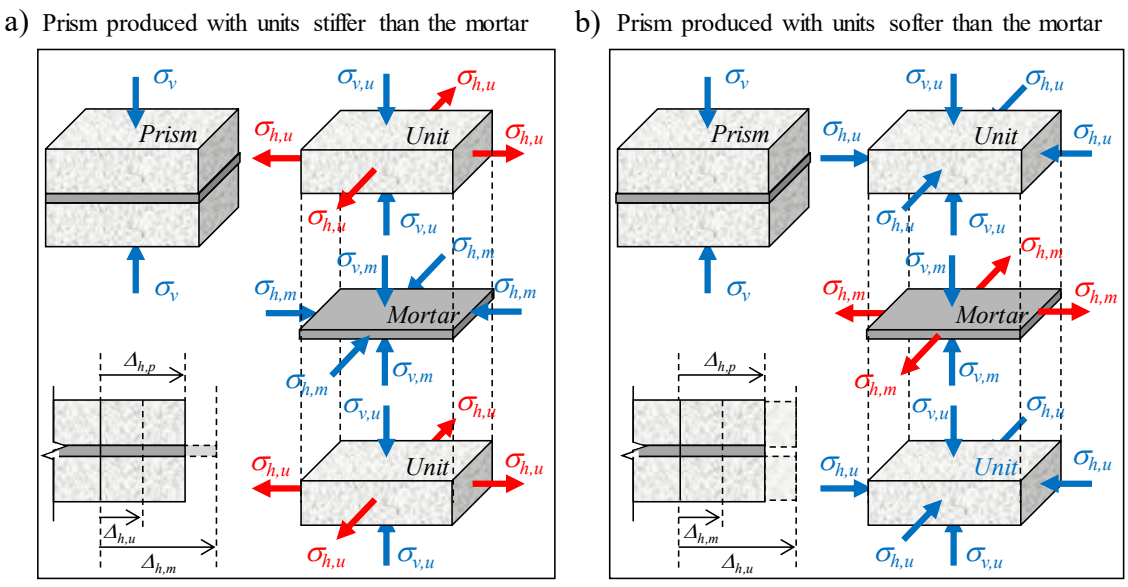

Source: Author (2024).

In this situation, two different mechanisms have been elucidated by Mohamad et al. (2017, 2018):

(i) When the compressive strength of the mortar in its confined state was higher than the units' tensile strength, vertical cracking of units initiated at a net area compressive stress around 60% of the net area compressive strength of the prism. Despite this, an almost linear stress-strain relationship was observed before and after units' cracking. The vertical tensile splitting cracks in the units immediately propagated somewhat horizontally along the mortar joint, as presented in Figure 2a. Then, a tensile splitting failure happened after crack propagation across the multiple joints.

Figure 2 - Cracking development in masonry prism: (a) propagation of vertical tensile splitting cracks in the units along the mortar joint, and (b) localized crushing of the mortar joint causing tensile stress concentration and vertical cracks in the units.

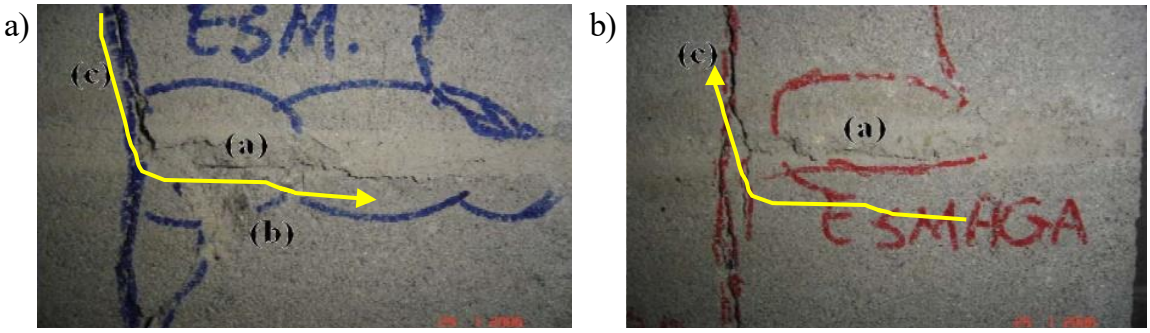

Source: Adapted from Mohamad et al. (2017), Copyright 2017, with permission from Elsevier.

(ii) When the compressive strength of mortar in the confined state was lower than the tensile strength of the units, the prism failure started with mortar crushing and localized spalling of mortar. A nonlinear stress-strain relationship initiated at a prism compressive stress/strength ratio of approximately 40%, and an internal failure mechanism by mortar crushing started at the onset of the masonry nonlinear behavior. The yellow arrow of Figure 2b shows that the localized mortar crushing produced tensile stress concentration and crack in the units. Consequently, mortar crushing is eventually followed by tensile stress concentration and development of vertical cracks in the units. In Figure 3, Mohamad et al. (2017) represented the sequence of failure mechanisms verified in prisms produced with a weak mortar. When the vertical compressive load on the prism increased, the mortar at the upper interface of the joint experienced more lateral expansion than the mortar at the bottom interface (interface 2 of Figure 3), due to its higher porosity. It caused higher tensile stresses on the top block, so that vertical cracks eventually caused the total failure of the prism.

Figure 3 - Sequence of failures mechanisms in prisms produced with weak mortar.

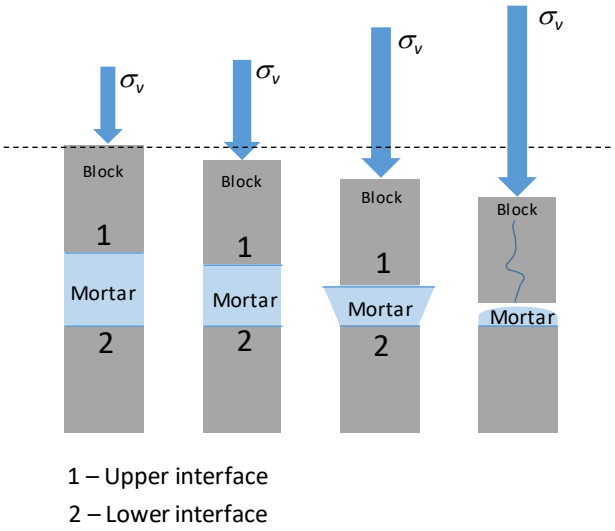

Source: Adapted from Mohamad et al. (2017), Copyright 2017, with permission from Elsevier.

Mohamad et al. (2017) concluded that the mortar governed the failure mode of prisms. Further research is recommended to develop strength prediction models that take into account the nonlinear behavior of crushed mortar. Design codes must be adjusted in order to establish a more appropriate way to account for the effects of low-strength mortars on the masonry failure mechanism.

The necessity of using soft units due to availability limitations and the steady improvements in cement properties justify the development of experimental investigations on the use of mortars stiffer than units.

Figure 1b shows that in this case, $\Delta_{h,u}$ tends to be higher than $\Delta_{h,m}$, so that the units are under triaxial compression and the mortar is under vertical compression with lateral tension. A brittle failure of the prisms is usually observed, based on the crushing of units at compressive stresses close to the compressive strength of the units (Nalon et al., 2020; Ravula and Subramaniam, 2017).

To better understand the failure mode of masonry prisms produced with units softer than mortars and vice versa, the present review compiled the failure mechanisms observed in ungrouted prisms produced with different ratios between mortar compressive strength (f_m) and unit compressive strength (f_b) as summarized in Table 1. The net area of the units was used to calculate all values of compressive strength of units ($f_{b,net}$). In face-shell bedded prisms, the effective area consists of the area of the face shells only, as recommended in TMS 402/ACI 530/ASCE 5 (2016). In previous literature, mortar compressive strength has been determined with either cubic or cylindrical specimens. To unify the experimental database,

mortar strength values were always represented in terms of cubic mortar compressive strength ($f_{m,cub}$), since mortar cubes were the most used types of specimens (a cube/cylinder strength ratio of 1.25 (Neville, 2011) was used to convert strength of mortar cylinders to mortar cubes).

Table 1 - Failure mode of ungrouted prisms.

Authors	$f_{m,cub}/f_{b,net}$ (%)	Failure mode
Zahra et al. (2021)	14.9 - 25.0	Mortar crushing leading to block cracking.
	20.2 - 34.0	Minor mortar crushing, block spalling and web splitting.
	35.7 - 60.0	Block spalling and web splitting.
Padalu and Singh (2021)	56.4	Vertical splitting cracks caused face shell separation, cone and split break, or semi-conical failure of prisms.
Behera and Nanda (2021)	48.4	Face shell separation through the bed joints of masonry prisms.
Krishnaraj et al. (2020a)	-	Brick crushing, mortar crushing, and failure at the brick/mortar interface.
Darwish et al. (2020)	-	Loss of bond between mortar and units (sometimes, cracks were observed in the mortar joint), followed by crack propagation in the units.
Mahamid et al. (2020)	13.3 - 99.9	In face-shell bedded prisms, failure mode varied between splitting and face shell separation, shear break, split and shear. In full-bedded prisms, failure modes varied between conical break, cone and shear, cone and split, tension break, semi conical break, shear break, and face shell separation.
Abdel-Rahman et al. (2020)	57.3	Vertical cracks close to the unit's web when approaching the peak stress; formation of diagonal cracks along the face shells until the failure.
Nalon et al. (2020)	26.2; 34.5	Localized mortar crushing started at 80% of the peak stress. Sometimes, it was followed by vertical cracking of the units due to stress concentration close to the regions where the crushed mortar was expelled.
	49.6; 54.4	At about 80% of the peak stress, vertical cracks were visible in the block's shells and webs. The cracking increased progressively up to the failure.
	87.2; 100.0	The prism failed in a brittle and explosive way by crushing of the block.
Thamboo (2020)	72.8 - 263.0	Vertical cracking initiated at the unit-mortar interface followed by cracks in the masonry units parallel to the direction of compression loading.
Caldeira et al. (2020)	34.4	Prisms with the highest joint thickness failed by mortar crushing under lower compression levels. In the others, mortar crushing was prevented and vertical cracks in blocks' shells and webs caused the failure.
	40.1	Mortar crushing was the failure mode observed in all prisms.
	62.6; 68.1	Tensile splitting failure of the units happened before mortar crushing.
	108.6	Prisms failed by blocks crushing in a brittle rupture mechanisms.
Mohamad et al. (2020)	29.8	The authors only mentioned a ductile failure in prisms made of weak mortar and hollow clay blocks with solid face shells.
	68.8	The authors only mentioned a brittle failure in prisms made of strong mortar and hollow clay blocks with solid face shells.
Yang et al. (2019)	249.1 - 353.9	The first crack started at the unit near the steel loading plates at 40-50% of the peak stress. It developed along the loading direction up to 85% of the peak stress. Then, the cracks from one surface of the specimen were able to reach the other surface to conclude the failure.
Thamboo and Dhanasekar (2019)	25.2 - 121.9	Vertical cracks parallel to the loading direction were observed. Most of them initiated at the unit-mortar interfaces at 70–85% of the peak stress.

Sajanthan et al. (2019)	13.5 - 149.7	When unit was stronger than mortar, tensile splitting failure was observed. When unit was weaker than mortar, the unit failed by crushing ahead of the splitting failure. In most of the prisms, units were stronger than mortar.
Kanchidurai et al. (2019)	106.8	Face shell separation and conical splitting failure were identified in the masonry prisms. In specimens containing mortar joint reinforcement, crack propagation was lowered after crossing the mesh layer embedded into the mortar joint.
Thaickavil and Thomas (2018)	203.6 - 778.5	Failure was governed by units, as they were the weaker constituents. Then, deformation and failure of units caused the failure of prisms.
Guo et al. (2018)	-	The failure mechanism was mainly dependent on the mortars. After failure, cracks were observed in a direction parallel to the load application.
Martins et al. (2018)	54.3 - 74.3	Vertical cracks extended over the shells and webs of the units and the prisms failed by transverse block splitting.
Fortes et al. (2018)	31.6 - 42.0	The failure mode was a typical compression failure initiated by vertical splitting cracks through both the web and face shells of specimens.
Sathiparan et al. (2018)	113.2; 275.2	Compression failures initiated in the unit and propagated through the joints.
	57.5	Cracks initiated from mortar, and then propagated to the brick units.
Segura et al. (2018a)	10.6	Thin vertical cracks appeared near the specimen edges. Then, they became later apparent across the joints and propagated over the prisms. Vertical cracks also affected the central part of their faces after the peak load.
Kazempour et al. (2017) and Kazempour (2014)	23.3 - 153.3	Vertical cracks propagated along the webs and shells of the units of all prisms.
Alvarenga et al. (2017b)	35.5	The prism failed when the lateral tensile stresses reached the tensile strength of the blocks, so that vertical cracks appeared at the blocks' shells.
	72.3	Lateral compressive stresses occurred in the blocks, since the tendency of lateral deformation of mortar was not so substantial. The prism presented a very brittle failure, by crushing of the units.
Mohamad et al. (2017)	24.4; 40.0	An internal failure mechanism due to pore collapse of the mortar and internal mortar cracking was verified. Vertical cracks in the units were eventually observed after mortar crushing.
	109.8	Instantaneous failure after the development of tensile splitting cracks in the units, which propagated somewhat horizontally along the lower interface of the mortar joints.

Note: $f_{b,net}$ is the net area compressive strength of units, $f_{m,cub}$ is the compressive strength of mortar obtained from cubic specimens.

Source: Author (2024).

Table 1 shows that tensile splitting failure modes have been observed in prisms constructed with different types of units, when their tensile strength was lower than the compressive strength of the mortar in its confined state. Zahra et al. (2021) compared the development of vertical cracks in both solid and hollow concrete blocks. They observed that prisms made with solid concrete bricks presented higher mechanical performance, which was partially attributed to the improved bonding with mortar due to their larger contact area, in comparison to that of hollow concrete blocks. In prisms made with hollow concrete blocks,

Nalon et al. (2020) observed that the transverse block splitting failure started when the compressive load reached about 80% of the ultimate capacity of the prisms and then increased progressively up to the their rupture. Since the mortar was not extremely stiff ($f_{m,cub}/f_{b,net}$ ratio of 49.6 - 54.4%), a sudden failure by unit crushing could be avoided. A typical failure by vertical splitting cracks through web and face shells of hollow concrete blocks was also observed in the ungrouted prisms tested by Fortes et al. (2018) and AbdelRahman and Galal (2020), as illustrated in Figure 4a.1. The development of vertical cracking on the front and lateral faces of the specimens was also the failure mode observed in solid clay brick prisms tested by Padalu and Singh (2021) (Figure 4a.2), Thamboo and Dhanasekar (2019) (Figure 4a.3). Table 1 indicates that these prisms presented $f_{m,cub}/f_{b,net}$ ratios pretty close to those of hollow concrete block prisms tested by Nalon et al. (2020), so that most of the vertical cracks also initiated at compressive stresses around 70-85% of the compressive strength of the prisms. Vertical cracks in units were also observed in hollow clay block prisms (Figure 4a.4) tested by Alvarenga et al. (2017b) and solid earth brick prisms (Figure 4a.5) tested by Sajanthan et al. (2019), when the units were stronger than the mortar. Moreover, Sajanthan et al. (2019) reported that when the block-mortar interface eventually failed in shear due to loss of bond, the solid earth bricks also failed in tensile splitting.

The mortar bedding approach used in the construction of the prisms can affect their failure mode. In the full bedding pattern, shell and web areas of the units are fully covered with mortar. In the face-shell bedding pattern, mortar only covers the face shell areas of the units. The face-shell bedding approach is commonly used in masonry construction to facilitate easy and faster production and decrease the mortar consumption (Ganesan and Ramamurthy, 1992). Zahra et al. (2021) investigated the effects of both bedding approaches on the failure mechanisms of masonry prisms produced with mortar with compressive strength in the confined state higher than the tensile strength of the units. They verified that full bedded prisms failed by vertical parallel cracks developed on all sides of the prisms (Figure 4b.1), due to the incompatibility between the deformation properties of units and mortar. Web-splitting failure was observed in face-shell bedded prisms produced with face-shell capping, due to deep-beam action effects at the unmortared webs (Figure 4b.2).

Details on the mutual influence of mortar joint thickness, mortar/unit strength ratio, and type of mortar on the failure mechanisms of hollow concrete block prisms were investigated by Caldeira et al. (2020). Although increases in the joint thickness decreased the lateral confinement of the mortar and its compressive strength, the tensile strength of their

normal-strength concrete blocks was not high enough to avoid the transverse block splitting, as indicated in Figure 4c.1 and Figure 4c.2. Consequently, variations in the value of the joint thickness (5-20 mm) caused negligible effects on the mechanical performance of these prisms, regardless of the type of mortar (job site mixed or preblended mortar).

Figure 4 - Ungrouted prisms whose failure mode was mainly due to block tensile splitting: (a) effects of different types of units; (b) effects of mortar bedding approach; and (c) effects of type of mortar.

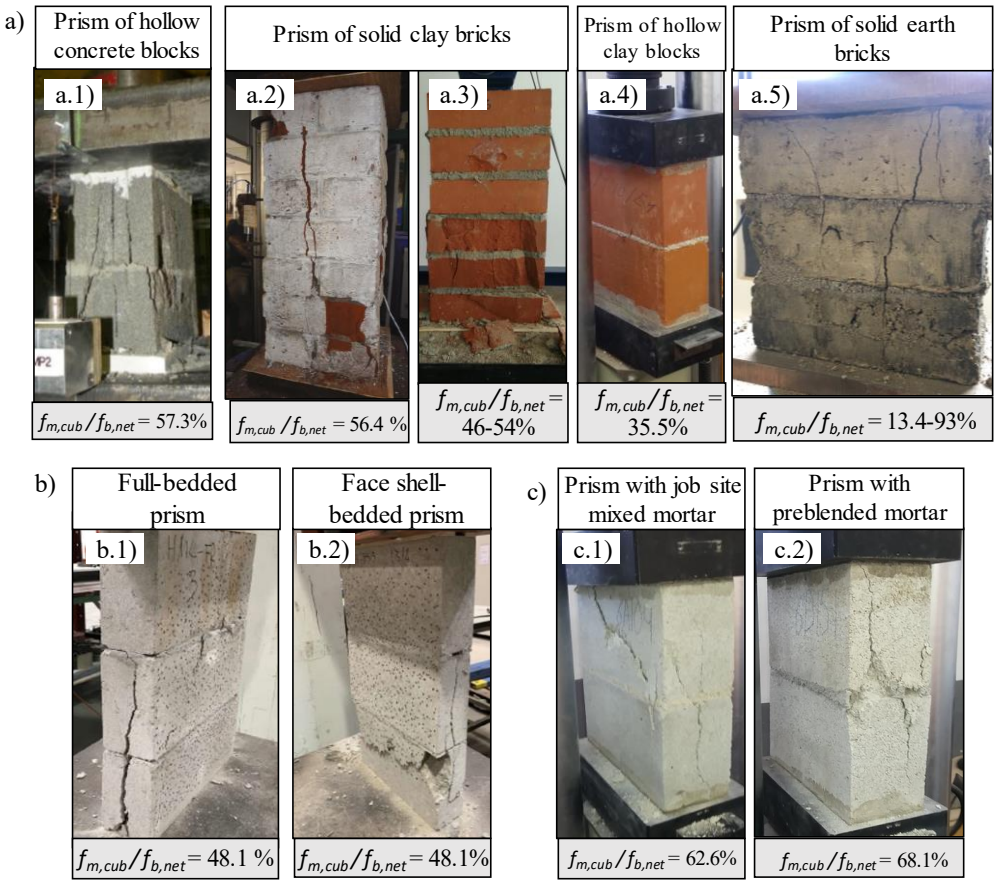

Source: (a) Adapted from AbdelRahman and Galal (2020), Copyright 2020, with permission from Elsevier; Padalu and Singh (2021), Copyright 2021, with permission from Elsevier; Thamboo and Dhanasekar (2019), Copyright 2019, with permission from Elsevier; Alvarenga et al. (2017b), Copyright 2017, with permission from Springer Nature Customer Service Centre GmbH; Sajanthan et al. (2019), as permitted under the Creative Commons Attribution License Agreement; (b) Zahra et al. (2021), Copyright 2021, with permission from Elsevier; and (c) Caldeira et al. (2020), Copyright 2020, with permission from Elsevier.

Hence, information reviewed in Table 1 indicates that tensile splitting failure of masonry units has been the predominant failure mechanism in ungrouted prisms with $f_{m,cub}/f_{b,net}$ ratios between 31.6% and 121.9%. Since this phenomenon is initiated by the restrained deformation of the mortar in the bed joints, it follows that tensile splitting failure can be delayed with the increase in the bonding between solid units and mortar joint due to their larger contact area, in comparison to that of hollow masonry blocks. In contrast, changes

in joint thickness are not expected to cause significant impact on the rupture of masonry constructed with $f_{m,cub}/f_{b,net}$ ratio in this range. Also, it can be inferred that particular attention must be paid to the use of the face-shell bedding approach, since deep-beam action effects were found to anticipate the tensile splitting failure at the center of the unmortared webs of the units.

The studies listed in Table 1 also mentioned mortar crushing as a failure mechanism of masonry prisms, when the tensile strength of the units was higher than the compressive strength of the confined mortar. Figure 5a shows the failure mode observed in prisms produced with weak mortars and different types of units. Zahra et al. (2021) observed mortar crushing along with block splitting failure in prisms constructed with solid concrete blocks and normal-strength hollow concrete blocks (Figure 5a.2). The use of a low-strength mortar caused crushing of mortar joint and eventual propagation of parallel cracks on the face shells of the concrete units. However, cracking over the units was not as significant as that observed in the concrete block prisms presented in Figure 4a.1, Figure 4a.2, Figure 4b.1, and Figure 4b.2. Caldeira et al. (2020) verified that mortar crushing is commonly observed in prisms made with high-strength concrete blocks, since their tensile strength is very high. The authors also observed cracks in the high-strength units due to stresses concentration close to regions where the crushed mortar was expelled (Figure 5a.3). Although Segura et al. (2018b) tested solid clay brick prisms with a very low $f_{m,cub}/f_{b,net}$ ratio (10.6%, as indicated in Table 1), they did not report signs of mortar joint crushing. The failure mode was characterized by the development of thin vertical cracks in the bricks, particularly close to the specimens' edges. These cracks became later apparent across the mortar joints and propagated over the whole height of the prisms, so that the authors observed a remaining core with a sandglass shape (Figure 5a.4). It was probably associated with the interference of shear stresses developed at the ends of the specimens due to friction effects with the plates of the press (Bezerra et al., 2016). Since the prisms tested by Segura et al. (2018b) (Figure 5a.4) presented lower values of height-to-thickness ratio and length-to-thickness ratio than the prisms of Zahra et al. (2021) (Figure 5a.1 and Figure 5a.2) and Caldeira et al. (2020) (Figure 5a.3), they exhibited higher lateral confinement at their ends (Abasi et al., 2020) (refer to Section 2.3.2).

Zahra et al. (2021) also carried out a recent exploration of the influence of different bedding approaches on the failure mode of prisms constructed with very weak mortars. The authors observed that full and face-shell bedded prisms exhibited mortar crushing under compression, sometimes accompanied by block splitting failure in the prism. Figure 5b.1 and

Figure 5b.2 show that web-shell splitting was not prominent in most of the prisms because the weak mortar failed quite earlier than the units, and the webs and shells of the blocks did not experience failure tensile strain levels. A comparison between Figure 4b and Figure 5b indicates that the failure mode of full and face-shell bedded prisms changed from mortar joints crushing to block splitting, as the magnitude of the $f_{m,cub}/f_{b,net}$ ratio increased.

Figure 5 - Ungrouted prisms whose failure mode exhibited mortar crushing: (a) effects of different types of units; (b) effects of bedding approach; and (c) effects of mortar thickness.

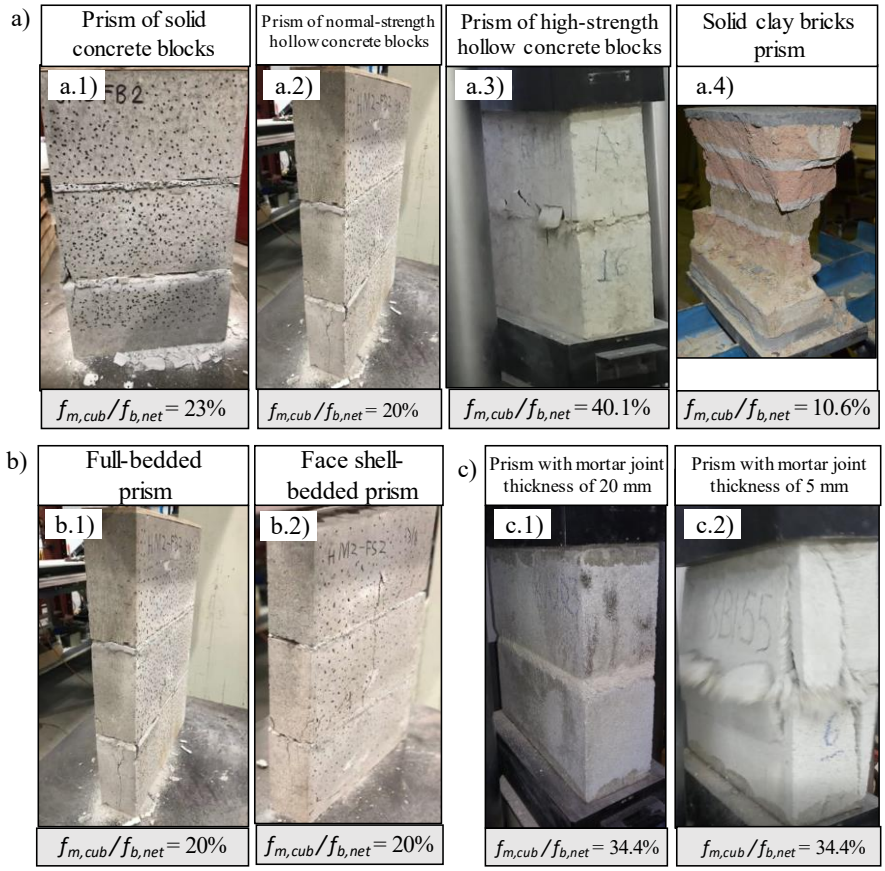

Source: (a) Adapted from Zahra et al. (2021), Copyright 2021, with permission from Elsevier; Caldeira et al. (2020), Copyright 2020, with permission from Elsevier; Segura et al. (2018a), Copyright 2018, with permission from Elsevier); (b) Zahra et al. (2021), Copyright 2021, with permission from Elsevier; and (c) Caldeira et al. (2020), Copyright 2020, with permission from Elsevier.

Results of Caldeira et al. (2020) indicated that the influence of the joint thickness on the structural performance and failure mode of masonry prisms depends on the deformation properties of blocks and mortars used to produce them. The effects of joint thickness were more significant when the mortar strength was much lower than the blocks' strength, since mortar crushing was observed in this situation. Consequently, increases in the joint thickness from 0.5 cm to 2 cm decreased the lateral confinement of the mortar and its strength. Therefore, joint thickness variations could increase or decrease the probability of mortar

crushing development, which specially impacts the structural performance of masonry constructed with high-strength concrete blocks, which is discussed in Section 2.3.2.

Therefore, mortar joint crushing has been observed in ungrouted prisms with $f_{m,cub}/f_{b,net}$ ratios ranging from 13.5% to 40.1%. Localized mortar crushing is often followed by tensile stress concentration and propagation of vertical cracks through the units, which highlights the need for careful monitoring of the sequence of events that take place during the increase in the compression load. It may be inferred that mortar crushing greatly affects the compressive behavior of masonry prisms. For instance, the use of low-strength mortars was able to change the expected failure mode of face-shell bedded prisms from web-splitting to localized mortar crushing. In addition, strict control of workmanship quality is needed when dealing with such low $f_{m,cub}/f_{b,net}$ ratios in the construction site, since slight increases in joint thickness can decrease the lateral confinement of the joints and anticipate the mortar crushing phenomenon.

Table 1 also indicates that unit crushing has characterized the failure mechanism of prisms constructed with different types of units softer than the mortar joint. For example, Yang et al. (2019) observed that the first crack started at the units in solid concrete brick prisms (Figure 6a.1) with very high $f_{m,cub}/f_{b,net}$ ratio (249.1- 353.9%, as indicated in Table 1). Nalon et al. (2020) verified a sudden failure by crushing of units in hollow concrete block prisms (Figure 6a.2) produced with strong mortars. Such brittle separation of the prisms' face shells should be avoided when designing masonry walls under compressive stresses. Thamboo (2020) also reported that the mismatch tangential deformation at the unit-mortar interfaces led to vertical cracks in the masonry units, so that the brick strength governed the load bearing capacity of masonry prisms produced with strong mortar (Figure 6a.3). Finally, crushing of units was also observed in hollow clay block prisms tested by Alvarenga et al. (2017b). The authors observed that the very stiff mortar was not able to effectively accommodate differential lateral movements between masonry components and could not prevent a brittle failure by units crushing.

Thaickavil and Thomas (2018) investigated the effects of prism height and geometric arrangement of units on the failure mode of prisms made with mortar stronger than units ($f_{m,cub}/f_{b,net}$ ratio of 203.6-778.5%, as indicated in Table 1). Figure 6b shows the crack pattern observed in prisms with 2, 3, 4 and 6 courses, prepared with stack bond and staggered bond (running bond), in a total of eight different configurations. The failure mode was controlled by the bricks, since they were the weakest constituents of the prisms. Vertical cracks were

formed at units at the middle of the prisms, due to explosive forces developed in the components by Poisson's effect. Inclined cracks were observed close to the ends of the specimens, due to the resultant forces of the bursting force and the frictional force between specimen and plates of the testing machine. According to previous literature (Berto, 2005; Hendry, 1997), masonry prisms constructed with mortars with high stiffness usually exhibit diagonal cracks associated with a phenomenon of shear failure that is commonly observed in compression tests of brittle materials. Thaickavil and Thomas (2018) observed a higher number of inclined cracks in prisms with lower height, as they presented a smaller region of pure bursting force. In running bonded prisms, cracks extended to the vertical joints, due to the debonding at the weak vertical unit-brick interfaces. In prisms with high number of courses, cracks extended across the bed joint to the next course, since the bed joint mortar and its interface were relatively stronger than the units.

Figure 6 - Failure mode of ungrouted prisms produced with mortar stronger than units: (a) effects of different types of units; (b) effects of bonding pattern and number of courses; and (c) effects of type of mortar.

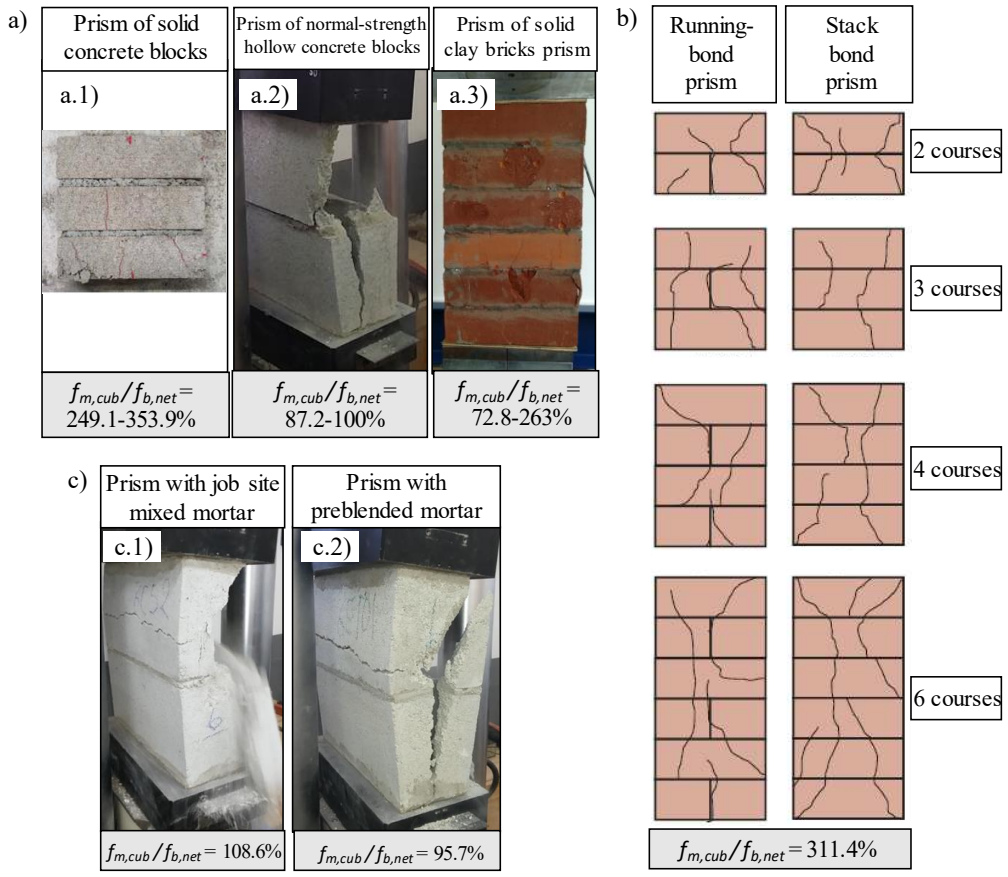

Source: (a) Adapted from Yang et al. (2019), as permitted under the Creative Commons Attribution License Agreement; Nalon et al. (2020), Copyright 2020, with permission from Elsevier; Thamboo (2020), Copyright 2020, with permission from Elsevier; (b) Thaickavil and Thomas (2018), as permitted under the Creative Commons Attribution License Agreement; and (c) Caldeira et al. (2020), Copyright 2020, with permission from Elsevier.

The effects of joint thickness on the failure mechanisms of masonry prisms produced with job site mixed mortar (Figure 6c.1) and preblended mortar (Figure 6c.2) stronger than the units were recently investigated by Caldeira et al. (2020). In both cases, triaxial compression tends to occur in the blocks' region close to the mortar joints. However, block's lateral confinement did not change very much with the variation of joint thickness, as the blocks' height was always significantly higher than the mortar thickness. Consequently, changes in the value of joint thickness from 5 mm to 20 mm did not cause significant impacts in the failure mode and mechanical properties of prisms produced with strong mortars.

Therefore, sudden failure by crushing of units has been the predominant rupture mechanism in ungrouted prisms with $f_{m,cub}/f_{b,net}$ ratios between 87.2% and 778.5%. Although brittle failure mechanisms should be avoided in masonry structures, manual process is often used for brick production in many countries around the world, so that geographical limitations lead to the need for the use of units softer than the mortar. However, there is a limited amount of studies dealing with these distinct case scenarios. Future studies are strongly recommended to better understand the effects of the mismatch of the elastic properties of masonry components. Further research should investigate alternatives to increase the ductility of masonry elements made with such contrasting variations in unit and mortar's deformation characteristics.

2.2.2. Grouted prisms

The failure mode of grouted prisms has also been widely investigated in previous literature, in terms of the interaction of units, mortar, and grout under multiaxial states of stress. Earlier studies (Drysdale and Hamid, 1979; Hamid and Drysdale, 1979; Khalaf, 1996) on compressed grouted prisms reported that when the units were stiffer than the grout, significant lateral expansion of grout caused a premature tensile splitting failure of the blocks' shells. When a grout stiffer than the units was used, the grout cores remained intact and were able to withstand additional loading, despite the failure of the blocks' shells. However, matching the deformation characteristics of grout and units was found to be more efficient than increasing the grout strength. In this situation, grout and blocks tend to work and fail together as a single entity, improving the mechanical performance of the masonry.

The failure mechanisms of grouted prisms under compression reported in recent studies are summarized in Table 2. They investigated the effects of various combinations between f_m, $f_{b,net}$, and compressive strength of grout (f_g) on the failure mode of grouted masonry

elements. All studies of Table 2 used cylindrical specimens to determine the compressive strength of grout ($f_{g,cyl}$).

Table 2 - Failure mode of grouted prisms.

Authors	$f_{m,cub}/f_{b,net}$ (%)	$f_{g,cyl}/f_{b,net}$ (%)	Type of grout	Failure mode
Zahra et al. (2021)	30.4	235.7	Conventional grout	Web splitting and face shell spalling and cracking.
Abdel-Rahman et al. (2020)	57.3	56.3	Prepacked grout (prisms subjected to drying before grouting)	Vertical cracks were verified in the face shells shortly before reaching the peak stress. The authors also observed excessive crushing of the grout cores and spalling of the face shell (due to excessive lateral strains exerted by the grout core on the masonry face shell) after the peak stress.
	57.3	153.1	Conventional grout (prisms subjected to drying before grouting)	
	57.3	153.1	Conventional grout (covered with paper towel)	Lateral tensile strains exerted by the isolated grout cores on the masonry shell caused its premature failure. Most of the grout cores remained intact even after the prism failure.
	57.3	153.1	Conventional grout (wetting of prisms before grouting)	Premature failure of face shells was not verified up to peak stress. A conical shaped diagonal shear failure was verified. Vertical and diagonal cracks propagated after the peak stress. Face shell spalling was not observed up to the failure.
Nalon et al. (2020)	26.2	104.3	Conventional grout	Lateral strains of the blocks were mostly restrained by the adhesion in the mortar joint. Cracks on the block's shells and webs initiated at the block/mortar interface, so that the prism behaved as strong grout cores with weak shells.
	49.6	109.9		
	87.2	104.3		
	34.5	85.4		Cracks in units and mortar crushing configured a premature tensile splitting failure. Lateral tensile stresses in units resulted from lateral expansion of grout were added to those derived from the elastic mismatch between units and mortar.
	54.4	80.7		A noticeable rupture warning was not verified. Grout and units failed almost together (the system acted homogeneously).
	100.0	91.8		
Ouyang et al. (2019)	47.4 - 50.3	58.4 - 105.3	Conventional grout	Cracks initiated on the narrow side of the prism and propagated gradually on their wide side. Obvious signs of outward bulging along the normal direction of the wide side appeared. At the final loading stage, the web of the block became crushed due to its interaction with the grout cores.
Fonseca et al. (2019)	34.2 - 42.7	47.8 - 113.3	Conventional grout and grout with shrinkage-compensating admixture	Shear failure was observed. Grout cores did not remain intact. Then, the components acted somewhat homogeneously.

Martins et al. (2018)	49.4	87.5	Conventional grout	Cracks propagated through the blocks' shells and webs, starting from the region of the block/mortar interface.
	55.8	156.4		
	49.2	184.6		
	54.1	118.5		
	57.0	151.9		
	74.3	96.4		
	54.5	80.9		
	74.4	86.4		Homogeneity of grout and units allowed them to work together as a monolithic resistant system and both failed together.
	64.6	63.0		Lateral expansion of grout induced lateral tensile stresses in the blocks' shell and webs. These stresses were added to stresses resulted from differential lateral strains in blocks and mortar. Then, rupture occurred by blocks' transverse splitting.
Fortes et al. (2018)	31.6 - 42.0	58.2 - 74.8	Conventional grout	Typical compression failure initiated by vertical splitting cracks through both the web and face shells of the specimens.

Note: $f_{b,net}$ is the net area compressive strength of units, $f_{m,cub}$ is the compressive strength of mortar obtained from cubic specimens, $f_{g,cyl}$ is the compressive strength of grout obtained from cylindrical specimens.

Source: Authors (2024).

Figure 7 shows some images representing the failure mode of the grouted prisms reported in these studies. Recent studies have been developed to provide a better understanding of the influence of the mechanical properties of grout, mortar, and blocks on the failure mechanisms of grouted masonry. When Martins et al. (2018) produced hollow concrete block prisms (Figure 7a.1) with strong grout ($f_{g,cyl}/f_{b,net}$ ratio from 87.5% to 184.6%), blocks and mortar tended to expand laterally more than the grout. Therefore, the lateral stresses developed on blocks and mortar mainly depended on their own deformation properties. Since Martins et al. (2018) used a mortar softer than the blocks ($f_{m,cub}/f_{b,net}$ ratio from 49.2% and 74.3%), visual vertical cracks were observed in the blocks' shells and webs, starting from the region of the block-mortar interface. Nalon et al. (2020) complemented this investigation with an exploration of grouted prisms with similar values of $f_{g,cyl}/f_{b,net}$ ratio (104.3-109.9%), but lower and higher values of $f_{m,cub}/f_{b,net}$ ratio (26.2% and 87.2%, respectively), as indicated in Table 2. Regardless of the mortar strength, the authors obtained prisms with very similar mechanical performance and failure mode, characterized by cracks on the block's shells and webs close to the block-mortar interface. Then, the use of weaker or stronger mortars did not cause significant effects on the failure mode of grouted prisms. In these different block-mortar combinations, the prism was not a homogeneous material, but a strong grout column with weak shells.

In contrast, when Martins et al. (2018) produced hollow concrete block prisms with a weak grout ($f_{g,cyl}/f_{b,net}$ ratio of 63%), the high deformations of the grout core induced lateral

tensile stresses in the blocks' shell and webs. Since the authors used a mortar softer than the blocks ($f_{m,cub}/f_{b,net}$ ratio of 64.6%), these lateral tensile stresses were added to those resulted from the distinct deformation properties of blocks and mortar, so that premature vertical cracks were developed in the blocks' shells and webs.

Figure 7 - Failure mode of grouted prisms (a) produced with hollow concrete blocks and I-shaped concrete blocks; and (b) subjected to different grouting procedures.

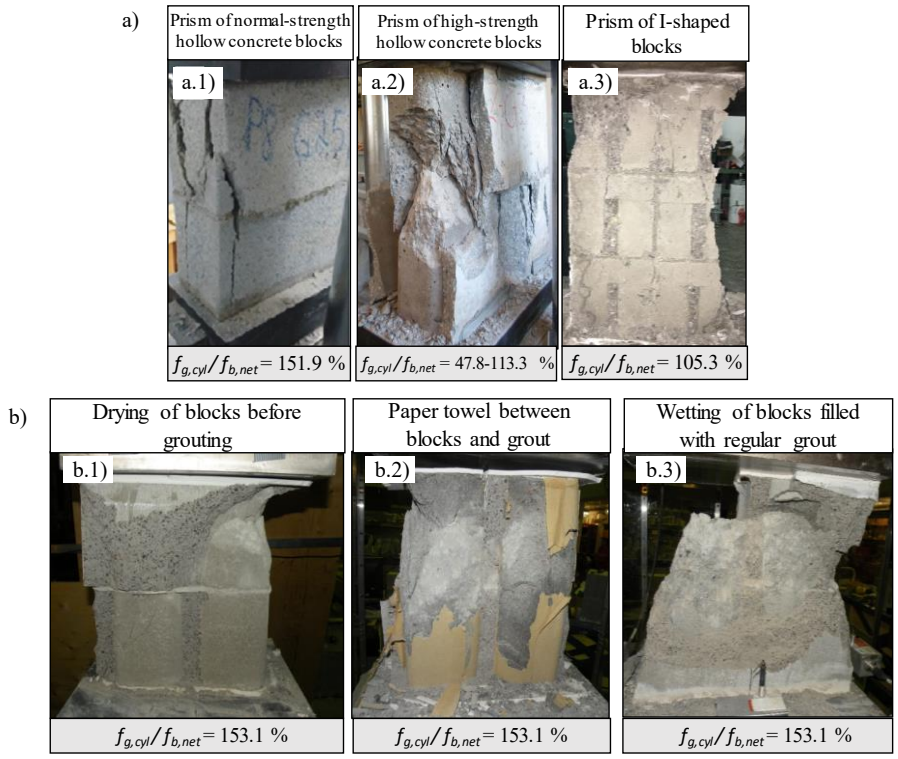

Source: (a) Adapted from Martins et al. (2018), Copyright 2018, with permission from Elsevier; Fonseca et al. (2019), Copyright 2019, with permission from Elsevier; Ouyang et al. (2019), Copyright 2019, with permission from Elsevier; and AbdelRahman and Galal (2020), Copyright 2020, with permission from Elsevier.

Table 2 shows that Nalon et al. (2020) and Fortes et al. (2018) also observed this failure mechanism in grouted prisms with $f_{g,cyl}/f_{b,net}$ ratio of 85.4% and 58.2 - 74.8%, respectively, but lower values of $f_{m,cub}/f_{b,net}$ ratio (34.5% and 31.6 - 42.0%, respectively). Both works did not report impacts associated with mortar joint crushing. Despite this, further investigations are recommended to clarify the effects of the use of weak mortars on the failure mode of grouted prisms. Sipp (2019) also observed a huge amount of vertical cracks in hollow clay block prisms ($f_{g,cyl}/f_{b,net}$ ratio of 58.4-105.3% and $f_{m,cub}/f_{b,net}$ ratio of 29.9-48.4%), which suggests possible effects of excessive lateral strain of the grout column on the clay units.

According to Ouyang et al. (2019), the interaction between I-shaped substructures inside grouted masonry makes them the ideal mechanical element prototype. The authors

observed that the characteristics of grouted masonry prisms constructed with I-type concrete blocks (Figure 7a.3) are basically consistent with the characteristics published in previous literature, in terms of failure mode. When a $f_{g,cyl}/f_{b,net}$ ratio of 58.4 - 105.3% was used, the first cracks mainly appeared on the narrow side of the prisms, and then propagated on the wide side. As the load increased, obvious signs of outward bulging along the normal direction of the wide side appeared. At the final loading stage, the web of the I-type blocks became crushed. Ouyang et al. (2019) also reported that within a reasonable range, the influence of mortar strength was insignificant. According to the authors, as long as the mortar joint could transfer the stresses between the units, its influence on the mechanical behavior of the grouted prisms could be neglected.

When Martins et al. (2018) tested hollow concrete block prisms with $f_{g,cyl}/f_{b,net}$ ratio of 80.9% and 86.4%, grout and blocks failed practically together, since they worked as a monolithic resistant system. Similar results were reported by Nalon et al. (2020) for prisms with $f_{g,cyl}/f_{b,net}$ ratio of 80.7% and 91.8%. Although Fonseca et al. (2019) tested hollow concrete block prisms (Figure 7a.2) with a wide range of $f_{g,cyl}/f_{b,net}$ ratios (47.8 - 113.3%), they could identify a similar general trend: grout cores did not remain intact and the masonry components acted somewhat homogeneously.

The failure modes of hollow concrete block prisms subjected to different treatments before grouting were recently studied by AbdelRahman and Galal (2020). Some prisms were air-dried for two hours before grouting, other prisms were lined with paper towel before grouting, and the others were immersed in water for two hours before grouting. Significant discrepancy was observed between the failure modes of dry and wet grouted prisms. In dry prisms, lateral shrinkage of grout provided a masonry assemblage with two separate elements: the grout core and the face shell. Consequently, excessive crushing of the grout cores and spalling of the face shell happened after the peak stress (Figure 7b.1). Lining of prisms with a paper towel as a means of eliminating the initial tensile cracks due to restrained dry shrinkage was not as significant as expected. This procedure was not able to prevent the water absorption of the grout cores by the surrounding dry units. Consequently, the isolated grout cores caused lateral tensile strains on the masonry shell, leading to a premature failure of the masonry shell (Figure 7b.2). In wet prisms, a suitable bond between the masonry shell and the grout core was observed. This enabled the masonry shell and the grout core to maintain their strengths up to the peak stress with no premature failure of the face shell. Then,

a conical shaped diagonal shear failure was observed, without significant face shell spalling up to the failure (Figure 7b.3).

Thus, important aspects on the failure mechanisms of grouted masonry prisms derived from the dataset presented in Table 2. These include, firstly, the observation that the use of $f_{g,cyl}/f_{b,net}$ ratios from 87.5% to 235.7% led to non-homogeneous prisms composed of a strong grout column with weak shells. Secondly, it has been reported that prisms with $f_{g,cyl}/f_{b,net}$ ratios from 56.3% to 85.4% presented premature vertical cracks in masonry shells due to the excessive lateral expansion of the grout core. Premature failure of the masonry shell was also reported in prisms subjected to drying before grouting and prisms lined with a paper towel before grouting, although they presented a $f_{g,cyl}/f_{b,net}$ ratio of 153.1%. Finally, most of the investigators affirmed that they were able to match the deformation characteristics of grout and units when the $f_{g,cyl}/f_{b,net}$ ratios were between 80.7% and 113.3%, situation in which grout and units worked as a monolithic resistant system, failing practically together.

2.3. STRENGTH AND STIFFNESS OF MASONRY PRISMS

The failure mechanisms reviewed in Section 2.2 support the understanding of different factors affecting the strength and stiffness of masonry prisms discussed in the present section. The load-bearing capacity and the elastic modulus of masonry prisms are directly associated with (i) the characteristics of their basic components (units, mortar, and grout) and (ii) the relative strength of masonry components, production/testing methods, and geometric characteristics of the prisms, as discussed in Sections 2.3.1 and 2.3.2, respectively. Then, Section 2.3.3 presents comparisons between prism mechanical properties obtained in previous literature and predicted by current masonry design codes.

2.3.1. Effects of types of masonry components on strength and stiffness of prisms

To understand the complex interaction between various masonry components, researchers have investigated prisms with units, mortar, and grout with different compositions and geometries. Characteristics of components used in current research for the construction of masonry prisms were summarized in Table 3. A review of this inventory indicates that different types of units (e.g., hollow concrete blocks, solid concrete bricks, hollow clay blocks, solid pressed earth bricks, and solid burnt clay bricks), job-site mixed and preblended mortars (e.g., cement mortar, cement-lime mortars, earth-based mortars, and

polymer adhesive mortars), and grout (e.g., conventional cement grout, prepacked grout, and grout containing shrinkage-compensating admixtures) have been recently investigated. Table 3 also summarizes the effects of different components characteristics on the gross area compressive strength and elastic modulus of prisms ($f_{p,gross}$ and $E_{p,gross}$, respectively).

2.3.1.1. Unit

Figure 8 shows the values of net area compressive strength of units and ungrouted prisms reported in Table 3. In general, recent findings are in accordance with the well-known fact that increases in unit strength lead to the enhancement of the mechanical properties of ungrouted masonry made with various types of units (Parsekian et al., 2012; Zahra and Dhanasekar, 2016; Zhou et al., 2017). Nevertheless, current studies indicate that this enhancement is mutually affected by many other factors, as discussed in Section 2.3.2.

Figure 8 - Plot of net area compressive strength of units against compressive strength of ungrouted prisms reviewed in this chapter.

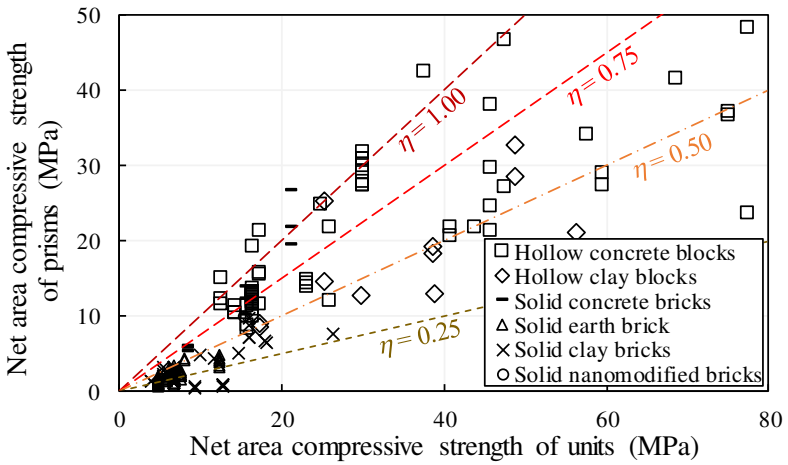

Source: Author (2024).

Studies compiled in this review indicated that the type of unit significantly affects the compressive strength of masonry prisms. Figure 8 shows that most of the prisms produced with concrete units (AbdelRahman and Galal, 2020; Caldeira et al., 2020; Guo et al., 2018; Mahamid and Westin, 2020; Martins et al., 2018; Nalon et al., 2020; Yang et al., 2019) exhibited net area compressive strength values (5.2-41.8 MPa) usually higher than the net area compressive strengths of prisms produced with clay units (1.1-32.9 MPa) (Segura et al., 2018a; Thaickavil and Thomas, 2018; Thamboo, 2020; Thamboo and Dhanasekar, 2019) or pressed earth units (0.83-4.73 MPa) (Darwish et al., 2020; Sajanthan et al., 2019; Thaickavil and Thomas, 2018).

Table 3 - Characteristics of units, mortars, and grout investigated in recent research papers

Authors	Unit				Mortar		Filling material (grout or mortar)		Prism's strength and stiffness	
	Type	Material	Length x width x height (mm)	$f_{b,net}$ (MPa)	Material	$f_{m,cub}$ (MPa)	Material	$f_{g,cyl}$ (MPa)	$f_{p,gross}$ (MPa)	$E_{p,gross}$ (MPa)
Zahra et al. (2021)	Solid and hollow blocks	Conventional concrete	390 x 90 x 190	15.4; 15.6	Cement-lime mortar	3.13; 4.25; 7.5	-	-	3.9 - 13.9	458 - 8490
Padalu and Singh (2021)	Solid bricks	Clay	229 x 109 x 72	26.2	Cement mortar	14.8	-	-	7.6	3375
Behera and Nanda (2021)	Solid bricks	Clay	250 x 125 x 75	9.1	Cement mortar (with or without joint reinforcement)	4.4	-	-	0.5; 0.6	-
Zhara et al. (2021)	Hollow blocks	Conventional concrete	390 x 190 x 190	14	Cement-lime mortar	4.25	Conventional grout	33.0	2.8 - 9.1	-
Krishnaraj et al. (2020a)	Solid bricks	Clay; fly ash	215 x 100 x 75	-	Cement mortar; cement-fly ash mortar; nanomodified mortar	35.9 - 48.0	-	-	5.4 - 9.2	-
Darwish et al. (2020)	Solid bricks	Pressed earth	300 x 140 x 90	-	Cement or earth mortar	1.15	-	-	0.6 - 1.1	-
Mahamid et al. (2020)	Hollow blocks	Light/normal weight concrete	407 x 203 x 203	16.3; 25.9	Cement-lime mortar	10.3 - 19.9	-	-	8.7 - 21.8	-
Thamboo (2020)	Solid bricks	Clay	200 x 90 x 65; 210 x 100 x 60	5.4; 15.8	Polymeric mortar; cement mortar	11.5 - 14.2	-	-	2.8 - 9.8	1555 - 6546
AbdelRahman and Galal (2020)	Hollow blocks	Conventional concrete	390 x 190 x 190	37.4	Preblended mortar	21.4	Prepacked grout; conventional grout	21.0 - 57.3	23.4 - 39.3	10804 - 15288

Nalon et al. (2020)	Hollow blocks	Conventional concrete	390 x 140 x 190	14.1; 17.1	Cement-lime mortar	3.7 - 17.1	Conventional grout	13.8 - 15.7	5.6 - 18.3	1858 - 4717
Caldeira et al. (2020)	Hollow blocks	Conventional concrete	390 x 140 x 190	16.3; 45.6	Cement-lime mortar; preblended mortar	5.6 - 18.3	-	-	5.6 - 22.5	3041 - 8847
Mohamad et al. (2020)	Hollow blocks	Clay	290 x 140 x 190	9.8; 23.9	Cement-lime mortar	7.5 - 33.5	-	-	5.7 – 16.1	-
Yang et al. (2019)	Solid bricks	Conventional concrete	190 x 90 x 57	8.2	Cement mortar	20.5 - 29.1	-	-	5.3 - 5.9	2633 - 2714
Thamboo and Dhanasekar (2019)	Solid bricks	Clay	200 x 90 x 65; 210 x 100 x 60; 225 x 150 x 90; 220 x 140 x 90; 280 x 140 x 90	3.8 - 15.8	Cement mortar	4.0; 6.5	-	-	1.4 - 7.3	954 - 5544
Ouyang et al. (2019)	Hollow blocks (I-type)	Conventional concrete	190 x 200 x 190	24.7 - 28.8	Cement-lime mortar	12.4 - 13.7	Conventional grout	14.4 - 29.6	16.9 - 24.3	13558 - 22410
Sajanthan et al. (2019)	Solid bricks	Pressed earth	205 x 105 x 65	4.6 - 12.2	Cement mortar	1.6 - 6.9	-	-	1.4 - 4.7	-
García et al. (2019)	Solid bricks	Clay	241 x 115 x 68.5	9.8 - 17.8	Cement mortar	13.2	-	-	3.2 - 6.6	Question-able
Fonseca et al. (2019)	Hollow blocks	High-strength concrete	390 x 140 x 190	40.7 - 74.9	Cement-lime mortar	14.0 - 32.0	Conventional grout; grout produced with shrinkage-compensating admixture	27.0 - 52.0	9.6 - 32.4	-
Sipp (2019)	Hollow blocks	Clay	290 x 140 x 190	29.7 - 56.2	Preblended mortar	11.6; 18.6	Conventional grout	20.3; 33.6	5.8 - 21.5	7016 - 26968
Nascimento et al. (2019)	Hollow blocks	Clay	290 x 140 x 190	27.0	Preblended mortar	3.1 - 12.7	Prepacked grout; conventional grout; preblended mortar	2.5 - 40.3	6.5 - 24.3	2900 - 11800

Kanchidurai et al. (2019)	Solid bricks	Clay	225 x 105 x 82	12.6	Cement mortar (with or without joint reinforcement)	13.5	-	-	0.6 – 1.0	-
Thaickavil and Thomas (2018)	Solid bricks	Pressed earth; clay	190 x 113 x 100; 210 x 96 x 50	4.6; 6.7	Cement mortar	13.6 - 35.5	-	-	0.7 - 2.9	-
Guo et al. (2018)	Hollow blocks	Concrete with recycled concrete aggregates	390 x 190 x 190	-	Cement mortar	4.7 - 8.1	-	-	4.3 - 4.9	3201 - 4718
Martins et al. (2018)	Hollow blocks	Conventional concrete	390 x 140 x 190	14.2 - 24.7	Cement-lime mortar	7.0 - 18.4	Conventional grout	12.4 - 26.2	5.6 - 23.8	2650 - 6540
Fortes et al. (2018)	Hollow blocks	High-strength concrete	390 x 140 x 190	43.7 - 68.6	Cement-lime mortar	13.8 - 28.1	Conventional grout	32.7 - 42.5	10.1 - 28.4	-
Sathiparan et al. (2018)	Solid bricks	Clay	205 x 105 x 55	6.6	Cement mortar	3.8 - 18.1	-	-	2.1 - 3.0	-
Segura et al. (2018a)	Solid bricks	Clay	311 x 149 x 45	18.0	Premixed lime mortar	1.9	-	-	6.5	2494
Kazempour et al. (2017) and Kazempour (2014)	Hollow blocks	Conventional concrete	390 x 190 x 190	30.0	Cement mortar; nanomodified mortar	7.0 - 46.0	-	-	27.5 - 32.0	16780 - 26300
Alvarenga et al. (2017b)	Hollow blocks	Clay	390 x 140 x 190	17.2	Cement-lime mortar	6.6; 12.4	-	-	3.2; 3.4	1064; 1167
Mohamad et al. (2017)	Hollow blocks	Conventional concrete	390 x 140 x 190	23.1	Cement-lime mortar	5.6 - 25.4	-	-	8.9 - 9.2	12537 - 14880
Mahamood et al. (2016)	Solid bricks	Nanomodified rubbercrete	210 x 110 x 65	15.2	-	-	-	-	10.0	-

Note: $f_{b,net}$ is the net area compressive strength of units, $f_{m,cub}$ is the compressive strength of mortar obtained from cubic specimens, $f_{g,cyl}$ is the compressive strength of grout obtained from cylindrical specimens, $f_{p,gross}$ is the gross area compressive strength of prisms, and $E_{p,gross}$ is the gross area modulus of elasticity of prisms.

Source: Author (2024).

In general, most of the concrete units presented a η value (ratio between the prism's net area compressive strength and the unit's net area compressive strength) ranging between 0.50 and 1.00, whereas most of the clay and earth solid units exhibited η values lower than 0.50. For concrete units with $f_{b,net} \leq 30$ MPa, 30 MPa $< f_{b,net} \leq 60$ MPa, and 60 MPa $< f_{b,net} \leq 80$ MPa, Figure 8 shows values of $0.47 \leq \eta \leq 1.25$, $0.46 \leq \eta \leq 1.14$, and $0.47 \leq \eta \leq 1.25$, respectively. For clay units with $f_{b,net} \leq 20$ MPa, 20 MPa $< f_{b,net} \leq 40$ MPa, and 40 MPa $< f_{b,net} \leq 60$ MPa, Figure 8 indicates values of $0.05 \leq \eta \leq 0.56$, $0.29 \leq \eta \leq 1.00$, and $0.38 \leq \eta \leq 0.68$, respectively. Figure 8 also shows that the pressed earth solid units used in the papers revised in this chapter always presented $f_{b,net} \leq 15$ MPa, whereas the prisms constructed with these units exhibited $0.14 \leq \eta \leq 0.54$.

Over the last years, the challenge to build taller masonry structures has led to a robust construction industry that can deliver high-quality units of high strength and different geometries (Parsekian et al., 2018). However, existing masonry codes do not provide design procedures to account for the use of high-strength units. Then, current advances in the characterization of masonry constructed with high-strength blocks have become of special importance (Caldeira et al., 2020; Castro et al., 2016; Fonseca et al., 2019; Fortes et al., 2017, 2018). Figure 8 shows that masonry elements built with high-strength blocks present η values ranging from 0.46 to 0.65. These η values are directly related to the combination of high-strength blocks and low-strength mortars, limiting the prism compressive strength, as discussed in Section 2.1.

The effects of specific unit types on the masonry compressive strength were not taken into account in tables of current design codes that correlate properties of units and mortar to masonry strength. For example, Mahamid et al. (2020) observed that table-based methods of the American standard provide conservative estimates for average strength of prisms made of normal-weight concrete block. However, they are not applicable for lightweight block masonry, since the authors reported that compressive strength values of lightweight block prisms were lower than values predicted by design code tables. Thaickavil and Thomas (2018) discovered that prisms constructed with pressed earth bricks had lower strength than clay brick prisms, even though this difference decreased with the increase in the height to thickness ratio of the prisms.

The current knowledge in nanoscience allowed a better understanding and control of the matter at the nanoscale, which enabled the development of novel nanotechnology-based construction materials. In this context, the application of nanotechnology for the fabrication

of innovative masonry units has emerged as a very promising research field. Nanosilica is one of the most reported nanoadmixtures incorporated into concrete matrices. This interest can be attributed to the high reactivity and filler effects of nanosilica, as compared to other nanomaterials (Birgisson et al., 2012a; Sikora et al., 2018). Mahamood et al. (2016) produced stack-bond masonry prisms with solid concrete bricks containing 4.35% of nanosilica (by mass of binder). The authors observed that nanosilica provided strength increases to the solid concrete bricks due to the densification of their interfacial transition zone. The physical effects of nanosilica were mainly associated with the refinement of their pore system at the nano level, while the chemical effects are associated with improvements in cement hydration and pozzolanic reactions.

Moreover, different contents of colloidal nanosilica (2.5% and 3.5% by mass of cement) were recently used by Dawood et al. (2021) to enhance the mechanical properties of sustainable concrete masonry bricks containing waste glass and steel slag powders. The authors did not test masonry prisms, but observed that the colloidal nanosilica provided masonry units with a denser microstructure through silica chains growth in calcium silicate hydrates. It resulted in increases in compressive strength of about 12-24% and in flexural strength of about 2-10%, at early and late ages.

2.3.1.2. Mortar

Figure 9 plots the values of compressive strength of mortars against the net area compressive strength of the ungrouted prisms reported in Table 3. Prisms made with cement-lime mortars and preblended mortars presented the highest values of net area compressive strength, ranging from 3.35 MPa to 42.64 MPa. Caldeira et al. (2020) observed that concrete block prisms produced with job site mixed cement-lime mortars and preblended mortars with similar compressive strengths presented very similar mechanical properties, regardless of the mortar joint thickness.

The dataset presented in Figure 9 also indicates that prisms made with cement mortar and polymer adhesive mortar exhibited lower compressive strength (ranging between 0.96 MPa and 9.80 MPa), in comparison to cement-lime and preblended mortars. Cement mortars are usually very stiff and may not ensure suitable strain accommodation, while cement-lime mortars present reasonable strength along with appropriate workability and water retention (Hernoune et al., 2020; Kaczmarek, 2019; Parsekian and Soares, 2010; Pavia and Brennan, 2019). Moreover, Thamboo (2020) reported that polymer adhesive mortar

provided strength increases of 10-18% to clay brick prisms, compared to cement mortar, due to the relatively higher bond strength of specimens constructed with polymeric mortar.

Figure 9 - Plot of compressive strength of mortars against compressive strength of ungrouted prisms reviewed in this chapter.

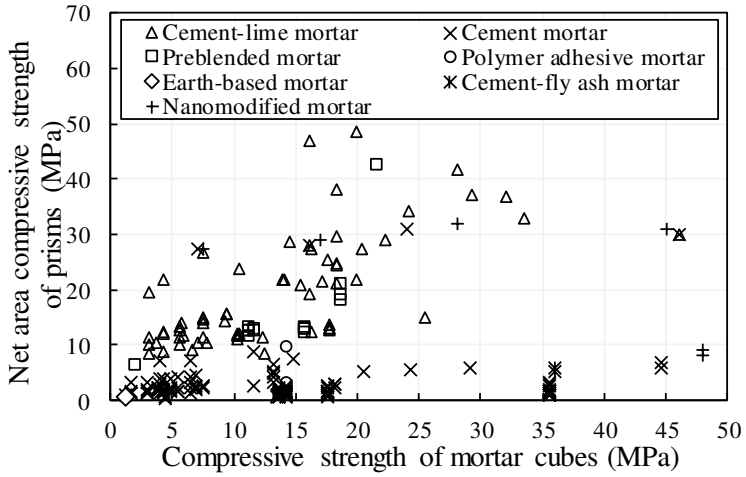

Source: Author (2024).

Darwish et al. (2020) compared the use of cement mortar and earth-based mortar to pressed earth bricks. In Figure 9, the lowest prism strength (0.56 MPa) was obtained for the prisms constructed with earth-based mortar. Darwish et al. (2020) observed that prisms fabricated with cement mortar were about 80% stronger than their counterparts constructed with earth-based mortar, although all of them presented a similar level of ductility.

Mortar joint reinforcement techniques have been used to arrest crack propagation in masonry elements (Sadek and Lissel, 2013; Saenger and Raupach, 2019; Valluzzi et al., 2005). Recent works have studied the compressive behavior of masonry prisms containing different types of meshes in the bed joints. For example, brick masonry prisms with geogrid reinforcement embedded in the mortar joints were recently investigated by Behera and Nanda (2021). The authors observed that the reinforcement provided better distribution of stresses, making the mortar joint stiffer. Consequently, the compressive strength of geogrid-embedded prisms was 32.7% higher than that of the unreinforced brick prisms. Kanchidurai et al. (2019) also reported an absence of mortar failure in masonry prisms with different types of joint reinforcement. The average compressive strength of prisms with embedded mesh was 42%, 51%, and 31% higher than that of unreinforced prisms, for expanded wire mesh, stainless steel wire mesh, and poultry net mesh, respectively.

The structural performance of nanomodified mortars for masonry construction has been demonstrated by several investigations. For example, masonry mortars containing 0%

or 4% of nanosilica (by mass of binder) were used by Kazempour et al. (2014; 2017) to produce three and four course high masonry prisms assembled and cured at cold weather. Although the 28-days compressive strength of masonry prisms was not significantly affected by the incorporation of the nanomaterials, the nanosilica shortened the setting time of the laying mortars at 5 ± 1 °C and increased their compressive strength up to 72 h, compared to the control mixture. Consequently, nanosilica accelerated the kinetics of hydration at early-age, which is a promising approach for controlling the effects of cold weather on masonry construction, without the need for heating practices.

The impact of using ultrafine fly ash (UFFA) on the nanostructure of masonry mortars was investigated by Krishnaraj et al. (2020b), based on the development of compression tests of masonry prisms produced with Class C fly ash or UFFA, in addition to clay or fly ash bricks. The voids of the mortar matrices produced with UFFA were highly reduced, in comparison to the mortars made with Class C fly ash, which was attributed to the huge availability of particles size ranges from micro to nano level. The compression tests of the masonry prisms indicated that the use of UFFA mortar provided increases in masonry strength. The use of mortars containing UFFA provided strength increases of about 33%, in comparison to conventional masonry prisms, due to the nanosize and irregular shape of UFFA and the greater interlocking of cement hydrated products.

Erdogmus et al. (2015) did not obtain improvements in the masonry mortars' structural performance due to the incorporation of different volume fractions of carbon nanofibers (0%; 0.25%, and 0.5% per unit volume of composite material). According to the authors, the presence of nanofibers reduced the strength of the mortars due to breaking bonds between cement hydrates.

The effects of various contents of ZrO_2 nanoparticles on cement masonry mortars (0%, 0.15%, 0.20%, 0.25%, and 0.30% by weight of cement) were investigated by Mohammed Rawoof et al. (2015) by performing compression tests on mortar cubes and brick masonry prisms. The nanomodified mortar provided masonry prisms with compressive strength nearly 20% higher than conventional mortars, which suggests strong possibilities of incorporating nano ZrO_2 particles in masonry materials to enhance their mechanical properties.

Masonry mortars with nanoalumina were also evaluated in previous research. Different nanoalumina contents (0%, 2%, 4%, and 6% by mass of cement) were used by Kazempour et al. (2014; 2017) to produce masonry mortars applied in masonry construction at cold weather. The overall trends suggested that contents of 6% of nanoalumina could alleviate the

effects of low temperatures on the masonry mortar mixtures, in terms of accelerating the kinetics of hydration and rate of hardening.

2.3.1.3. Grout

Various effects of grout on the mechanical properties of masonry prisms were reported in past literature. Some authors (Bolhassani et al., 2015; Hamid and Chukwunenye, 1986; Huang et al., 2014; Heydariha et al., 2017) mentioned significant increases in masonry strength when the units were filled with grout. Other works (Camacho et al., 2015; Köksal et al., 2005; Parsekian et al., 2012) stated that grouting does not necessarily lead to significant increases in masonry strength and increasing grout strength leads to minor variations in prism strength. Consequently, the superposition of strengths of grout and units was found to overestimate the compressive strength of grouted prisms. It is mainly attributed to effects of plastic and drying shrinkage of grout, effects of unit geometry, inappropriate construction procedures, differences in the stress-strain relationship of grout and units, among others (AbdelRahman and Galal, 2020; Drysdale and Hamid, 1979; Parsekian et al., 2012). Strength improvements due to grouting can be interpreted from the general trend observed in Figure 10, which plots the compressive strength of grout against the compressive strength of the masonry prisms reviewed in Table 3.

Advances in the field of chemical admixtures for concrete materials have provided new alternatives of shrinkage compensating admixtures for masonry grout. The dataset presented in Figure 10 shows that prisms filled with conventional grout presented gross area compressive strengths ranging from 10.4 MPa to 39.3 MPa, whereas the gross area compressive strength of prisms filled with non-shrink grout was between 16.7 MPa and 27.5 MPa. AbdelRahman and Galal (2020) verified that masonry prisms fabricated with non-shrink grout presented a slightly higher compressive strength and modulus of elasticity, lower strain at the peak strength, and similar post-peak behavior, in comparison to prisms produced with regular grout. Fonseca et al. (2019) also observed small increases in the compressive strength of concrete masonry, which indicates that the admixture was effective in decreasing the grout shrinkage and inducing the block-grout to act more homogeneously. However, they also observed slight strength reductions with increases in the admixture percentage. Future research is recommended to evaluate suitable shrinkage-compensating admixture dosage, especially because excessive lateral expansion due to inappropriate admixture contents can result in damage to the masonry blocks.

Figure 10 - Plot of compressive strength of filling material (grout or mortar) against compressive strength of masonry prisms reviewed in this chapter.

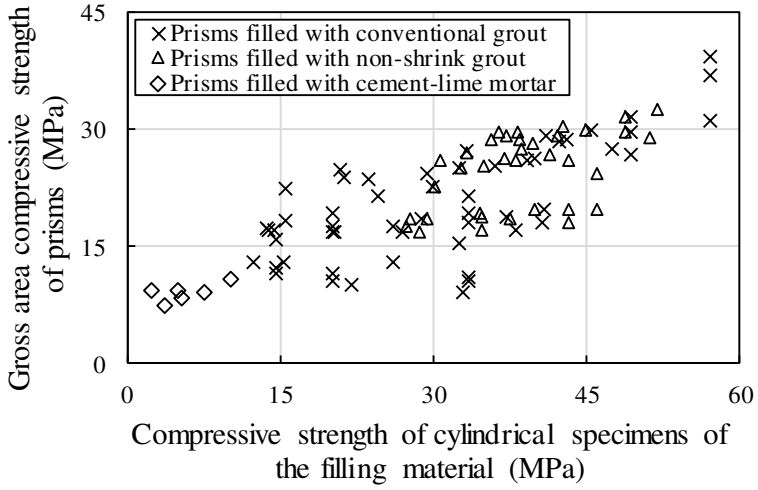

Source: Author (2024).

Nascimento et al. (2019) recently carried out an experimental investigation of the behavior of structural masonry prisms with cells filled with the same mortar used in the bed joints, aiming at attaining greater agility and flexibility in the construction process of unreinforced masonry. Compressive strength results suggested the viability of using bedding mortar with the same structural function as grout. The best mechanical performance was obtained when the mortar compressive strength was 10-24% of the net area compressive strength of the blocks. Despite this, comparisons between the experimental data reviewed in this chapter (Figure 10) indicated that the values of gross area compressive strength of prisms filled with bedding mortar (7.4-10.7 MPa) were lower than those observed in prisms filled with grout (10.4-39.3 MPa), which can be mainly attributed to the small values of compressive strength of the cement-lime mortars used as filling material (2.5-10.2 MPa).

Recent studies have also investigated nanomodified grout for masonry construction. For example, Papayianni et al. (2012) reported increases in compressive and flexural strength provided by different concentrations of nanosilica (0.5% and 1% by mass of cement) with distinct gradations (average particle size of 14 nm and 150 nm) to lime-based grout for filling and strengthening of masonry. In addition, 150-nm nanosilica positively affected the fresh state properties of the grout mixtures and stabilized their volume changes. On the other hand, negative effects provided by 14-nm nanosilica (concerning mainly water-binder ratio increases and shrinkage induction) could be limited with the addition of superplasticizer.

Grout has also been produced with carbon nanomaterials, which are basically composed of carbon particles with low density, high surface area to volume ratio, and present

unique mechanical, electrical, and thermal properties (Du et al., 2020a; Han et al., 2015; Sikora et al., 2018). Restuccia et al. (2018) investigated masonry grouts with different concentrations of carbon nanotubes (0%, 0.025%, 0.05%, 0.08%, 0.12%, 0.25%, 0.5%, and 0.8% by mass of binder) and observed that small contents of these nanocarbons (up to 0.12% by mass of binder) provided increases of up to 73%, 35%, and 80% in the flexural strength, compressive strength, and fracture energy of grout specimens, respectively. These results were attributed to different factors, such as the reduction in the grout porosity, the crack bridging mechanism provided by the nanofillers, and the formation of nucleation sites for the development of hydration products.

The effects of different grouting procedures have also been explored over the last years. AbdelRahman and Galal (2020) reported that wetting concrete block prisms before grouting provided a well-bonded masonry shell and grout core, with significant increases in their compressive strength. The superposition of strengths of grout core and blocks' shells and webs was found to provide a good prediction of the compressive strength of wet grouted prisms. Wetting masonry prisms before grouting was found to be a promising construction procedure to improve the mechanical properties of grouted masonry, which is already recommended in different masonry codes.

2.3.2. Mutual effects of different characteristics of masonry prisms on their strength and stiffness

The mechanical properties of masonry prisms are not only affected by the types of mortars, units, and grout, as previously presented in Section 2.3.1. They are also mutually affected by different characteristics of the masonry prisms, such as the relative strength between the masonry components ($f_{m,cub}/f_{b,net}$ and $f_{g,cyl}/f_{b,net}$ ratios), their preparation/testing conditions (e.g., arrangement of units within the prisms, mortar bedding approach, capping method, curing procedures, loading rate, and workmanship quality), and geometric properties (e.g., number of courses, thickness of the mortar joints, and dimensions of the prisms) (Ganesan and Ramamurthy, 1992; Mohamad et al., 2007; Parsekian et al., 2012). Table 4 presents a review of different preparation/testing conditions and geometric properties of prisms investigated in latest research, in addition to the corresponding components' strength ratios. Due to the lack of combined studies on different parameters affecting the compressive behavior of masonry, relevant progress has been recently made on the understanding of the mutual influence of various factors on the compressive strength and elastic modulus of

prisms, which are discussed in the present section. Moreover, novel prediction models for compressive strength and elastic modulus of ungrouted and grouted masonry prisms have been proposed over the last years, such as those proposed by Thaickavil and Thomas (2018), Sharafati et al. (2021), Martins et al. (2018), Nalon et al. (2020), and Ouyang et al. (2019).

Masonry elements are traditionally constructed with stiffer units and relatively low strength mortar (mortar compressive strength in the range between 0.4 $f_{b,net}$ and 0.7 $f_{b,net}$) (Nalon et al., 2020; Parsekian et al., 2012; Shi et al., 2021). However, engineers around the world recently deal with some distinct case scenarios. Sometimes, mortar must be stronger than units due to different reasons, such as the recent improvements in mortar cement properties, and the need for the application of locally available soft units for construction of low-cost housing in developing countries (Prakash et al., 2016; Sathiparan and Rumeshkumar, 2018; Thaickavil and Thomas, 2018; Thamboo, 2020; Thamboo and Dhanasekar, 2019; Yang et al., 2019). Sometimes, units must be significantly stronger than mortar, especially with the recent progress on the development of high-strength masonry blocks (Caldeira et al., 2020; Castro et al., 2016; Fonseca et al., 2019; Fortes et al., 2017, 2018). Studies published in the last couple years have improved the understanding of the influence of the relative strength of mortars and units on the masonry prisms' mechanical behavior. In order to summarize the experimental findings of these works, mutual effects of mechanical properties of mortar and units on the compressive strength of ungrouted prisms are represented in the 3D surface plot and contour plot of Figure 11a and Figure 11b, respectively.

Table 4 - Characteristics of masonry prisms tested in recent studies.

Authors	Preparation and testing conditions					Geometric properties					Components' strength ratios		Prism's strength and stiffness	
	Prism type	Mortar joint's bedding pattern	Capping in top and bottom surfaces of prisms	Curing conditions	Loading rate	Number of courses	Average joint thickness (mm)	Average height of block to mortar thickness ratio	Average height to thickness ratio	Average length to thickness ratio	$f_{m,cub}$ / $f_{b,net}$ (%)	$f_{g,cyl}$ / $f_{b,net}$ (%)	$f_{p,gross}$ (MPa)	$E_{p,gross}$ (MPa)
Zahra et al. (2021)	Stack bond	Face-shell bedding; full bedding	10 mm plywood capping	Covered with cling wraps	1 mm/min	3	10.0	19.0	6.56	4.33	14.9 - 60.0	-	3.9 - 13.9	458 - 8490
Padalu and Singh (2021)	English bond	Full bedding	3 mm plywood sheets	Wet bags	1.2 mm/min	6	10.0	7.2	2.39	2.40	56.4	-	7.6	3375
Behera and Nanda (2021)	Stack bond	Full bedding	-	-	0.013 MPa/s	8	12.5	6.0	1.30	0.65	48.4	-	0.5; 0.6	-
Zahra et al. (2021)	Stack bond	Face-shell bedding	6 mm plywood capping	Wrapped in plastic sheet	1 mm/min	4	10.0	19.0	4.16	2.05	30.4	235.7	2.8 - 9.1	-
Krishnaraj et al. (2020a)	Stack bond	Full bedding	-	-	-	3	10.0	7.5	2.45	1.14	-	-	5.4 - 9.2	-
Darwish et al. (2020)	Flemish bond	Full bedding	-	-	25 mm/min; 12 mm/min	6	12.0	7.5	2.00	1.50	-	-	0.6 - 1.1	-
Mahamid et al. (2020)	Stack bond	Face-shell bedding; full bedding	Sulfur mixture and gypsum cement	Covered with plastic bags	-	2	9.5	21.4	2.05	2.00	13.3 - 99.9	-	8.7 - 21.8	-

Thamboo (2020)	Stack bond	Full bedding	5 mm plywood capping	Air curing	0.5 mm/min	6	1.0-3.0	32.5; 30.0	4.44; 3.70	2.22; 2.10	72.8 - 263.0	-	2.8 - 9.8	1555 - 6546
Abdel-Rahman et al. (2020)	Stack bond	Full bedding	Gypsum capping	Covered with plastic bags	0.3 mm/min; 0.18 mm/min	2	10.0	19.0	2.05	2.05	57.3	56.3 - 153.1	23.4 - 39.3	10804 - 15288
Nalon et al. (2020)	Stack bond	Full bedding	3 mm cement mortar	-	-	2	10.0	19.0	2.80	2.80	26.2 - 100.0	80.7 - 109.9	5.6 - 18.3	1858 - 4717
Caldeira et al. (2020)	Stack bond	Full bedding	2 mm cement mortar	Protected from rain and wind	-	2	5; 10; 15; 20	9.4 - 41.3	2.80	2.80	34.4 - 108.6	-	5.6 - 22.5	3041 - 8847
Mohamad et al. (2020)	Stack bond	Full bedding	Cement paste	-	0.05 MPa/s	2	10.0	19.0	2.79	2.07	29.8; 68.8	-	5.7 - 16.1	-
Yang et al. (2019)	Stack bond	Full bedding	-	-	0.1 mm/min	3	10.0	5.7	2.12	2.11	249.1 - 353.9	-	5.3 - 5.9	2633 - 2714
Thamboo and Dhana-sekar (2019)	Stack bond	Full bedding	5 mm plywood capping	Air curing	0.25 mm/min	5; 6	10.0	6.0; 6.5; 9.0	3.27 - 4.89	1.50 - 2.22	25.2 - 121.9	-	1.4 - 7.3	954 - 5544
Ouyang et al. (2019)	Stack bond	Full bedding	10 mm cement mortar	-	0.02 MPa/s	3	10.0	19.0	2.95	1.95	47.4 - 50.3	58.4 - 105.3	16.9 - 24.3	13558 - 22410
Sajanthan et al. (2019)	Stack bond	Full bedding	-	Indoor lab environment	2 mm/min	3	10.0	6.5	2.05	1.95	13.5 - 149.7	-	1.4 - 4.7	-
García et al. (2019)	Stack bond	Full bedding	-	-	0.30 MPa/s	5	10.0	6.9	3.19 - 3.54	2.09 - 2.23	74.2 - 200.0	-	3.2 - 6.6	Ques-tionable
Fonseca et al. (2019)	Stack bond	Full bedding	Cement paste	-	0.01 MPa/s	2	10.0	19.0	2.80	2.79	34.2 - 42.7	47.8 - 113.3	9.6 - 32.4	-
Sipp (2019)	Stack bond	Full bedding	Cement paste	-	-	2	10.0	19.0	2.79	1.34	29.9 - 48.4	36.2 - 113.3	5.8 - 21.5	7016 - 26968
Nascimento et al. (2019)	Stack bond	Full bedding	Cement paste	-	-	3	10.0	19.0	2.79	1.34	11.5 - 47.0	9.2 – 149.3	6.5 - 24.3	2900 - 11800
Kanchidurai et al. (2019)	Stack bond	Full bedding	-	-	0.013 MPa/s	2	10.0	8.2	1.60	0.78	106.8	-	0.6 - 1.0	-

Thaickavil & Thomas (2018)	Running bond; stack bond	Full bedding	1-2 mm dental plaster	Spraying water at regular intervals	-	2; 3; 4; 6	10.0	5.0; 10.0	1.15 - 5.75	1.68; 2.19	203.6 - 778.5	-	0.7 - 2.9	-
Guo et al. (2018)	Stack bond	Full bedding	Cement paste	-	0.07 MPa/s	3	10.0	19.0	3.11	2.05	-	-	4.3 - 4.9	3201 - 4718
Martins et al. (2018)	Stack bond	Full bedding	Cement paste	Protected from sun and wind	0.15 MPa/s	2	10.0	19.0	2.80	2.80	49.2 - 74.4	63.0 - 184.6	5.6 - 23.8	2650 - 6540
Fortes et al. (2018)	Running bond	Full bedding	Cement mortar	-	0.92 MPa/s	5	10.0	19.0	7.07	2.79	31.6 - 42.0	58.2 - 74.8	10.1 - 28.4	-
Sathiparan et al. (2018)	Stack bond	Full bedding	-	Oven-dry, air-dry or wet conditions	0.21 MPa/s	4	10.0	5.5	2.38	1.95	57.5 - 275.2	-	2.1 - 3.0	-
Segura et al. (2018b)	Stack bond	Full bedding	Cement mortar	Covered with polyethylene sheets	0.02 MPa/s	5	10.0	3.0	1.91	2.09	10.6	-	6.5	2494
Kazempour et al. (2017) and Kazempour (2014)	Stack bond	Full bedding	-	Walk-in environmental chamber at (5 ± 1) ºC	-	3	10.0	19.0	3.11	1.51	23.3 - 153.3	-	27.5 - 32.0	16780 - 26300
Alvarenga et al. (2017b)	Stack bond	Full bedding	Cement mortar	-	0.05 MPa/s; 0.15 MPa/s	2	10.0	19.0	2.79	2.79	38.5; 72.3	-	3.2; 3.4	1064; 1167
Mohamad et al. (2017)	Stack bond	Full bedding	-	-	0.0027 MPa/s; 0.037 MPa/s	2	-	-	-	2.79	24.4 - 109.8	-	8.9 - 9.2	12537 - 14880
Mahamood et al. (2016)	Stack bond	Full bedding	-	-	-	4	-	-	-	-	-	-	10.0	-

Note: $f_{b,net}$ is the net area compressive strength of units, $f_{m,cub}$ is the compressive strength of mortar obtained from cubic specimens, $f_{g,cyl}$ is the compressive strength of grout obtained from cylindrical specimens, $f_{p,gross}$ is the gross area compressive strength of prisms, and $E_{p,gross}$ is the gross area modulus of elasticity of prisms.

Source: Author (2024).

Figure 11 - Influence of compressive strength of mortar and units on the strength of ungrouted prisms.

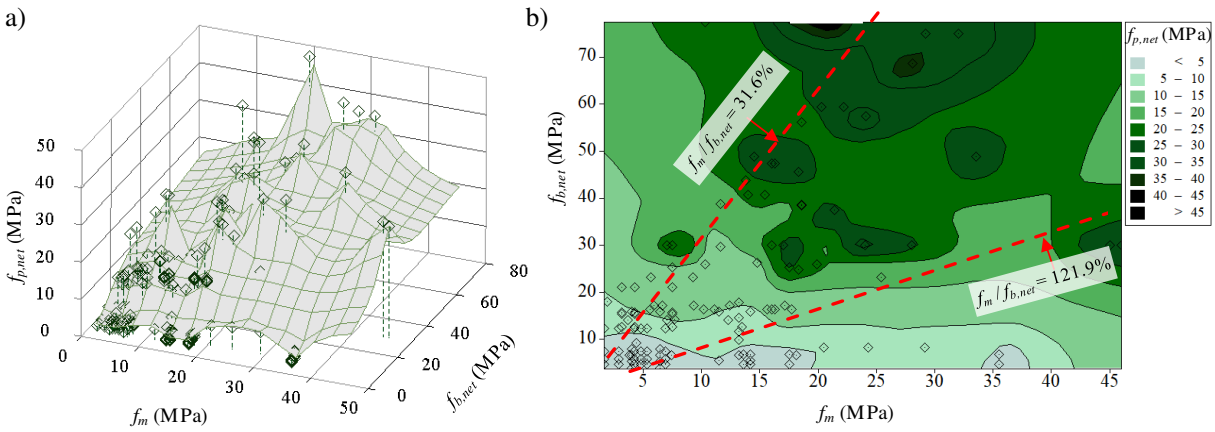

Source: Author (2024).

Both images of Figure 11 suggested that when low-strength units are used, increases in the mortar compressive strength cause only marginal increases in the masonry prisms' compressive strength. This happened because unit failure governed the failure mode of the masonry prisms, since high values of $f_{m,cub} / f_{b,net}$ ratios were used and the typical rupture mechanisms were those summarized in Figure 6. Moreover, Figure 11 indicates that strength gains due to the enhancement in unit strength were lower when softer mortars were used. This behavior is in agreement with the failure modes of prisms made with low-strength mortars presented in Figure 5, in which the rupture was mainly governed by mortar crushing. Interestingly, most of the darker regions (highest values of prisms mechanical performance) of Figure 11b are within the red dashed lines that represent the range of $f_{m,cub} / f_{b,net}$ ratios (between 31.6% and 121.9%, according to data revised in Section 2.2.1) in which tensile splitting of masonry units was the observed failure mechanism (Figure 4).

Negligible effects of mortar strength on the mechanical properties of grouted prisms have been reported in previous literature (Köksal et al., 2005; Parsekian et al., 2012; Ramalho and Corrêa, 2003). Then, the influence of mechanical properties of grout and units on the compressive strength of grouted prisms were represented in the 3D surface plot and contour plot of Figure 12a and Figure 12b, respectively. In this regard, recent experimental studies carried out by Martins et al. (2018) and Nalon et al. (2020) analyzed the mechanical behavior of masonry prisms made of concrete units with three different strength levels, cement-lime mortar with three different strength levels (in relation to the unit strength), and grout of three strength levels. Regardless of the unit strength, the authors did not verify a linear proportionality between the increase in grout strength and the enhancement of prism strength, which justifies

the non-linear patterns observed in Figure 12a. Figure 12b evidences light colors when strong grout is combined with significantly weak units, and vice versa, suggesting that using a grout much stronger than the blocks or vice versa is not effective.

Figure 12 - Influence of compressive strength of grout and units on the strength of grouted prisms.

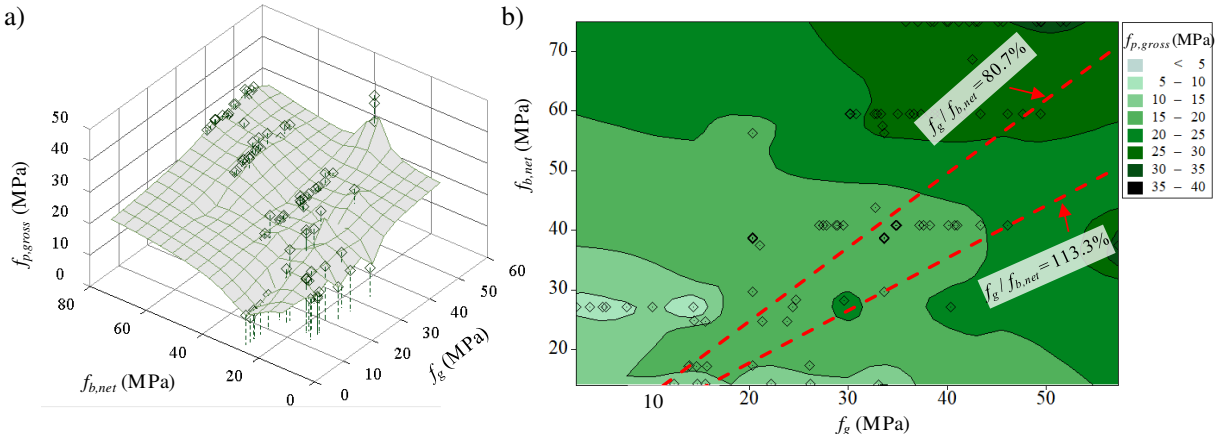

Source: Author (2024).

Most studies revised in this chapter concluded that the best prism mechanical performance is usually observed within the red dashed lines of Figure 12b, i.e., when the grout compressive strength is reasonably close to the blocks' net area compressive strength ($f_g / f_{b,net}$ ratios between 80.7% and 113.3%, according to data revised in Section 3.2.2). However, Figure 12b also indicates that high compressive strength values can be observed in some regions outside the limits of this range. For example, some dark regions of Figure 12b are also associated with prisms constructed with $f_g / f_{b,net}$ ratios lower than 80.7% and high-strength blocks. It clearly shows the efficiency of modern high-strength units to avoid premature vertical cracks of masonry shells due to excessive lateral expansion of the grout. Similarly, Figure 12b also exhibits small dark regions associated with prisms constructed with $f_g / f_{b,net}$ ratios higher than 113.3% and high-strength grout. These regions represent specific situations in which a strong grout core was able to withstand increasing compressive load, despite the rupture of the blocks' shells and webs.

The effects of bonding pattern (stack bond vs. running bond approach) on the compressive strength of masonry prisms with 2, 3, 4, and 6 courses were investigated by Thaickavil and Thomas (2018). The authors reported increases in prism compressive strength with the increase in volume fraction of units (VF_b). They also observed strength increases with the increase in the volume ratio of bed joint to total mortar (VR_{mH}), since the prepend joints were weak links in the prism when subjected to friction effects imposed by the loading platens of the testing

machine. Prisms with greater volume of bed joint mortar presented a lower number of weak links. Therefore, Thaickavil and Thomas (2018) suggested the consideration of both VF_b and VR_{mH} for the development of a prediction strength model for masonry prisms. Since prepend joints contribute to reductions in the strength of masonry elements, Thamboo and Dhanasekar (2019) reported a pioneering study to compare strength and deformation characteristics of both stack-bond prisms and wallettes under compression, since stress-strain relationships reported in previous works have been developed from prism or wallettes testing and not from both in a single experimental study.

The ratio between height and thickness of masonry prisms also affects their compressive strength. Thaickavil and Thomas (2018) observed decreases in prism compressive strength with increases in their slenderness ratio. When the ratio between height and thickness increased from 1.86 to 5.85, compressive strength decreases of 35-40% were observed in prisms constructed with solid clay bricks with compressive strength of 4.56 MPa. When the ratio between height and thickness increased from 1.15 to 3.65, strength decreases of about 50% were observed in prisms constructed with solid clay bricks with compressive strength of 6.68 MPa. When the height to thickness ratio increased from 3.27 to 4.89, strength decreases from 30-40% were also observed by Thamboo and Dhanasekar (2019) in prisms made with low-strength bricks (compressive strength of 3.8-5.3 MPa). The loading platens of the testing machines used in uniaxial compression tests of masonry prisms impose friction that causes lateral confinement to their top and bottom ends. The zone subjected to lateral tensile stresses increases with the increases in the slenderness ratio of the prisms. Consequently, strength reductions with increases in the slenderness ratio of the prisms are directly associated with reductions in friction effects at the ends of the specimens.

However, effects of variations in unit compressive strength were found to be higher than the effects of variations in slenderness ratio of masonry prisms. For instance, experimental results of Thamboo and Dhanasekar (2019) indicated that prisms made with units with compressive strength of 15.8 MPa and height to thickness ratio of 4.10 presented compressive strength values 67-82% higher than those of prisms made with units with compressive strength of 3.8-5.3 MPa and height to thickness ratio of 3.27-4.89. These results demonstrated that increases in unit strength were able to mitigate the effects of increasing lateral tensile stresses due to increases in the slenderness ratio of the prisms.

The mechanical properties of prisms are not only a function of their height to thickness ratio, but also a function of their length to thickness ratio. Since research into the effects of

prism length on compressive strength remained limited, Abasi et al. (2020) recently developed a systematic investigation of the effects of prisms' length on their compressive strength. They concluded that the effects of length to thickness ratio of prisms on their strength are significant and must be considered together with the well-understood effect of height to thickness ratio on the determination of strength correction factors. Actually, strength correction factors provided in current masonry design codes often lead to overestimated strength values. Therefore, Abasi et al. (2020) elaborated new correction factors to account for the effects of height to thickness ratio and length to thickness ratio on the prisms compressive strength.

The influence of mortar joint thickness on the masonry behavior has also been investigated in the past. Most previous research reported increases in masonry strength and stiffness due to reductions in the mortar joint thickness (Cassinello, 2006; Francis et al., 1972; Lima et al., 2012; Reddy et al., 2009; Thamboo et al., 2013). Distinct results were also reported. For instance, Nwofor and Sule (2012) proposed a model with increases in strength with the increase in thickness up to 10 mm, after which the strength started to decrease. In contrast, Rao et al. (1995) reported increases in strength with the increase in joint thickness up to 15 mm in tests of masonry produced with soil-cement units weaker than the mortar. Recently, Caldeira et al. (2020) investigated the mutual effects of joint thickness, mortar/unit strength ratio, and type of mortar on the compressive strength and modulus of elasticity of prisms made of hollow concrete blocks. They verified that the influence of joint thickness on the mechanical properties of masonry elements is higher when the mortar strength is much lower than the blocks' strength, since decreases in joint thickness provided increases in mortar strength with the enhancement of the joint confinement effect, so that the prism's early rupture by mortar crushing could be avoided. When stronger mortars were used, failure occurred by transverse blocks splitting or blocks crushing and, consequently, the impact of joint thickness on the prism strength and elastic modulus was not very significant. The authors also mentioned that prisms made of job site mixed mortars and preblended mortars presented similar structural behaviors, regardless of the joint thickness level. Another interesting experimental result reported by Caldeira et al. (2020) was that the reductions in compressive strength and elastic modulus with the increase in joint thickness are significantly greater in prisms produced with high-strength blocks. Then, strict control of workmanship quality is recommended when dealing with these novel unit types, in order to avoid significant variability of joint thickness. Thamboo (2020) also presented some findings on the modern thin layer mortared masonry construction system: improvements in

prisms compressive strength were observed due to the relatively higher bond strength provided by a polymeric mortar, combined to the use of a very small mortar joint thickness (1-3 mm).

The mortar bedding approach also affects the mechanical properties of prisms under compression. Although face-shell-bedded prisms only have mortar in the face shell areas, the full net cross-sectional area of the blocks is commonly used to determine their net compressive strength. Mahamid et al. (2020) explained that this approach provides more representative values of the ultimate load carrying capacity of the elements, since the compressive strength of face-shell bedded prisms would be higher than that of full-bedded prisms if only face shell-bedded mortar area was used for strength calculations. This is not valid, since prism compression tests clearly indicate that full-bedded prisms have a greater load-carrying capacity than face-shell bedded prisms. Previous studies (Ganesan and Ramamurthy, 1992; Mahamid and Westin, 2020; Parsekian et al., 2012) reported that high local lateral tensile stresses are developed at the center of the webs of face-shell-bedded prisms by a mechanism analogous to the deep-beam bending, so that their compressive strength is lower than that of full-bedded prisms. A recent study conducted by Mahamid et al. (2020) observed that the face-shell bedding approach causes a greater reduction in compressive strength for lightweight concrete block prisms than for conventional concrete block ones.

Zahra et al. (2021) reported the compressive strength and elastic modulus of masonry prisms resulted from the combination of mortars with three different strength levels, two distinct mortar bedding types (full and face-shell mortar bedding), and two types of units (solid and hollow concrete blocks). No significant variation in the masonry strength reductions due to face-shell bedding approach with respect to the mortar strength grades was observed. It happened because full bedded and face-shell-bedded prisms constructed with soft mortars failed by crushing of mortar joints, whereas prisms produced with stiffer mortars presented web splitting failure for face-shell bedding and cracking/spalling in blocks and mortar for full bedding. On the other hand, full bedding was found to be more effective for solid concrete units, while face-shell bedding was more efficient for hollow concrete units. Zahra et al. (2021) also observed that despite of variations in mortar strength and unit type, face-shell-bedded prisms presented relatively lower ultimate axial strains than full-bedded prisms. It was attributed to the earlier failure observed in face-shell-bedded prisms, due to the stronger bond provided by a larger bedding area in fully-bedded prisms, which prevented high tensile stresses in the web-shells.

2.3.3. Comparisons between strength and stiffness obtained in previous studies and predictions of masonry codes

Some current design codes propose empirical equations to estimate the compressive strength of some types of masonry structures, such as EN 1996-1-1 (2005) and AS 3700 (2018). In contrast, TMS 402/602 (2016) proposes the application of the unit strength method (USM), which consists of using an existing strength table that correlates unit strength and mortar type to masonry strength. CSA S304 (2014) also recommends tabulated values of compressive strength to be used in the design of masonry constructed with clay, concrete, or calcium silicate units. The values of prism compressive strength reviewed in the present work were compared to masonry strength values predicted by formulations proposed by EN 1996-1-1 (2005) and AS 3700 (2018), and tabulated values of TMS 402/602 (2016) and CSA S304 (2014). It was needed to calculate values of equivalent prism compressive strength (f_p) based on the values of masonry compressive strength (f_k) predicted by these codes [f_k/f_p ratios of 0.7 and 0.6 were used for masonry made with hollow and solid units, respectively, as prescribed by the ABNT NBR 16868-1 (2020a) standard]. In Figure 13a, compressive strengths obtained in the experimental programs reviewed in this chapter were plotted against prism compressive strengths predicted by masonry codes.

Figure 13 - Comparisons between compressive strength (a) and modulus of elasticity (b) of prisms obtained in previous literature and values predicted by masonry codes.

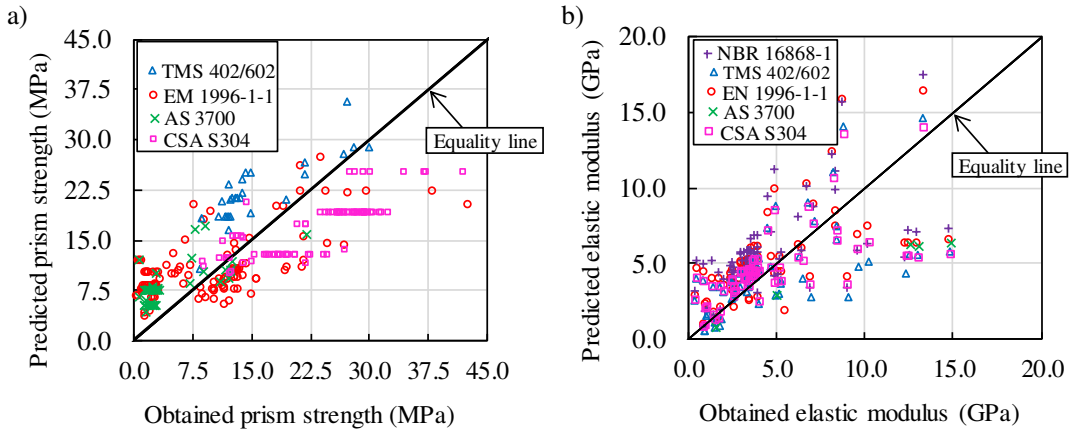

Source: Author (2024).

Limitations and comments on specific parameters used in formulations of EN 1996-1-1 (2005) and AS 3700 (2018) are presented in Table 5. Values tabulated in CSA S304 (2014) were not used to predict the compressive strength of prisms made with mortars that could not be classified as type S or N, according to CAN/CSA-A179 (2014). Moreover, tabulated values

of TMS 402/602 (2016) could not be applied to prisms constructed with mortars that could not be classified as type N, S, or M, according to ASTM C270-19a (2019). Many studies used type O mortars (mortars recommended for construction of non-load bearing walls) to produce masonry prisms for structural purposes, situation that was not covered by the USM (2016). USM tables were not applied when the thickness of the bed joints exceeded 15.9 mm, as recommended in TMS 402/602 (2016). Finally, predictions were not applied to prisms made with mortar, units or grout with strength classes and types that were not covered by CSA S304 (2014) and TMS 402/602 (2016).

Figure 13a indicates that strength formulations proposed by EN 1996-1-1 (2005) and CSA S304 (2014) are more conservative than those prescribed by AS 3700 (2018) and TMS 402/602 (2016). In general, EN 1996-1-1 (2005) provided the best overall agreement with experimental data reported in previous literature. However, significant amount of data was reasonably far from the equality line presented in Figure 13a. In most of the cases, AS 3700 (2018) and TMS 402/602 (2016) overestimated the compressive strength of the prisms, whereas CSA S304 (2014) underestimated their compressive strength.

Table 5 - Formulations for prediction of masonry compressive strength and comments about their application in comparisons developed in the present study.

Equation	Formulation	Specific comments		Source
(1)	$f_k = K\left(f_b\right)^{0.70}\left(f_m\right)^{0.30}$	Equation applied to masonry made with general purpose mortar and lightweight mortar.	These equations could not be applied to hollow block prisms of studies that did not report the thickness of blocks' webs and shells, as this information was required to determine the coefficient *K*. Moreover, they were not applied to prisms made with fly ash bricks or pressed earth bricks, as these types of units were beyond the application scope of the code. Finally, the application of shape factors defined in EN 772-1 (2000) were required to determine the normalized compressive strength of masonry units.	EN 1996-1-1 (2005)
(2)	$f_k = K\left(f_b\right)^{0.85}$	Equation applied to masonry made with thin layer mortar and clay units of Groups 1 and 4 of EN 1996-1-1 (2005), calcium silicate, aggregate concrete, and autoclaved aerated concrete units.		
(3)	$f_k = K\left(f_b\right)^{0.70}$	Equation applied to masonry made with thin layer mortar and c1ay units of Group 2 and 3 of EN 1996-1-1 (2005).		
(4)	$f_k = k_h k_m \sqrt{f_b}$	This equation could not be applied to studies that used mortars that could not be classified as M2, M3 or M4 mortars prescribed by AS 3700 (2018), as this information was required to determine k_m. In addition, they could not be applied to prisms constructed with unit types and unit-mortar combinations that were not covered by this standard.		AS 3700 (2018)

Source: Author (2024).

These comments are in agreement with discussions recently published by Zahra et al. (2021), which indicated that current design codes are inconsistent and non-conservative in their masonry strength predictions. Zahra et al. (2021) recommended the inclusion of the use of low-strength mortars to strength prediction formulations, in addition to modifications of face-shell bedding correction factors, since they exhibited high inconsistency between the predictions. Caldeira et al. (2020) also observed that strength formulations proposed by masonry codes did not account for the significant influence of joint thickness on the compressive behavior of prisms made with high-strength blocks. Mahamid et al. (2020) reported that that the USM should not be used for lightweight block or face-shell bedded masonry because it is not sufficiently conservative. Padalu et al. (2021) and Nalon et al. (2020) also observed that available strength formulations mainly deal with masonry elements constructed with stiffer/stronger units in comparison to the mortar, which greatly limits their predictive ability. Accordingly, Mohamad et al. (2017) verified that formulations of current masonry codes do not account for different failure mechanisms of masonry elements and the onset of their nonlinear stress-strain response.

The studies reviewed in the present chapter highlight significant limitations of empirical equations and tabulated values of current design codes, which calls for their careful and urgent revision. The dataset revised in the present work suggests that the estimation of the compressive strength of masonry by the prism test method would be more appropriate than the application of formulations and tables proposed in current masonry codes. In this regard, the new Brazilian masonry code ABNT NBR 16868-1 (2020a) presents a table that includes reference values of prism compressive strength based on block, mortar, and grout strength. However, they must be confirmed with experimental tests of masonry prisms during the previous characterization of the masonry materials and during the site control of masonry construction. Site control by the prism test method is required by ABNT NBR 16868-2 (2020b), except when the characteristic compressive strength of the prisms obtained in initial characterization tests is greater than or equal to twice the design characteristic compressive strength. The requirements of experimental tests of masonry prisms of these masonry standards were needed because masonry construction has been one of the most preferred high-rise building systems in Brazil, due to its cost-effectiveness and ease of construction (Parsekian et al., 2018).

Furthermore, the values of secant elastic modulus of elasticity reviewed in this chapter were compared to values of modulus of elasticity predicted by formulations proposed by EN 1996-1-1 (2005), TMS 402/602 (2016), AS 3700 (2018), and CSA S304 (2014), as presented

in Figure 13b. Table 6 shows models proposed in different masonry codes to determine the short-term secant modulus of elasticity of masonry (E_k), in addition to specific comments on their application to the experimental dataset of the present review. When necessary, values of prism strength were used to estimate the masonry strength [f_k/f_p ratios of 0.7 and 0.6 were used for masonry made with hollow and solid units, respectively, as prescribed by the ABNT NBR 16868-1 (2020a) standard].

Figure 13b indicates that formulations to predict the modulus of elasticity proposed by CSA S304 (2014) are more conservative than those prescribed by EN 1996-1-1 (2005), ABNT NBR 16868-1 (2020a), and TMS 402/602 (2016). Although AS 3700 (2018) could be applied to very few works revised in this chapter, it was possible to realize that this standard provided conservative stiffness predictions, since most of the points were located under the equality line. Again, significant amount of data was reasonably far from the equality line of Figure 13b. The worst predictions of modulus of elasticity were observed in masonry prisms with high stiffness. Thus, future studies should mainly focus on improvements of the predictive ability of masonry prisms constructed with high-strength components.

Table 6 - Formulations for prediction of masonry compressive strength and comments about their application in comparisons developed in the present study.

Equation	Formulation	Specific comments		Source
(5)	$E_k = 1000 f_k$	-		EN 1996-1-1 (2005)
(6)	$E_k = 700 f_k$	Equation applied to clay masonry		TMS 402/602 (2016)
(7)	$E_k = 900 f_k$	Equation applied to concrete masonry		
(8)	$E_k = 700 f_k$	Equation applied to masonry constructed with M2 or M3 mortars, and clay units with characteristic compressive strength from 5 to 30 MPa	These formulations could not be applied to studies that used mortars that could not be classified as M2, M3 or M4 mortars prescribed by AS 3700 (2018), as this information was required to choose the suitable equation. Moreover, they could not be applied when the density of concrete units was not provided	AS 3700 (2018)
(9)	$E_k = 1000 f_k$	Equation applied to masonry constructed with M3 or M4 mortars, and clay units with characteristic compressive strength ≥ 30 MPa		
(10)	$E_k = 1000 f_k$	Equation applied to masonry constructed with M3 or M4 mortars, and concrete units with density ≥ 1800 kg/m³ and calcium silicate units		
(11)	$E_k = 750 f_k$	Equation applied to masonry constructed with M2 or M3 mortars, and concrete units with density < 1800 kg/m³		
(12)	$E_k = 500 f_k$	Equation applied to masonry constructed with thin mortar bed and aerated autoclaved concrete units		CSA S304 (2014)

(13)	$E_k = 850 f_k \leq 20\,\text{GPa}$	Equation applied to masonry constructed with concrete or clay units	ABNT NBR 16868-1 (2020a)
(14)	$E_k = 800 f_p$	Equation applied to masonry constructed with concrete units with characteristic gross area compressive strength ≤ 20 MPa	
(15)	$E_k = 750 f_p$	Equation applied to masonry constructed with concrete units with characteristic gross area compressive strength of 22 and 24 MPa	
(16)	$E_k = 700 f_p$	Equation applied to masonry constructed with concrete units with characteristic gross area compressive strength ≥ 26 MPa	
(17)	$E_k = 600 f_p$	Equation applied to clay masonry	

Source: Author (2024).

2.4. STRESS-STRAIN RELATIONSHIP OF MASONRY PRISMS

The stress-strain relationship is one of the most important parameters for the design of masonry elements under compression. It depends on some interrelated test parameters, including the mechanical properties of units, mortar, and grout (Yang et al., 2019). Theoretical methods for masonry design and analysis of its structural behavior usually assume mechanical properties or constitutive equations obtained from standard test methods of units (Barbosa and Hanai, 2005). The reproduction of the actual masonry conditions for suitable laboratory characterization of the units is challenging. For example, the uniaxial compression tests of units do not reproduce their interaction with mortar and grout. In addition, these tests do not reproduce the state of stress of the units inside a masonry element due to the existing confinement effects of the press loading platens on the ends of the specimens (Barbosa et al., 2010). Other strategy proposed in previous works was the mechanical characterization of samples extracted from the units, even though some uncertainties may appear due to the geometry of these samples (Barbosa and Hanai, 2005; Barbosa and Hanai, 2009).

Uniaxial compression tests of mortar specimens casted in non-absorbent molds also do not represent the mechanical behavior of the actual mortar in masonry prisms, as the mortar is laid in-between the units, which are absorbent and are subjected to a triaxial stress state (Lakshani et al., 2020; Mohamad et al., 2007, 2018). Lakshani et al. (2020) recently reported the results of an experimental program carried out to empirically correlate the unconfined compressive strengths of different types of masonry mortar specimens (e.g., mortar cubes of 50 mm and 70 mm, prisms of 160 mm x 40 mm x 40 mm, cylinders with diameters of 100 mm and 200 mm, and slates extracted from masonry joints measuring 50 mm x 50 mm x 10 mm). In complement, Makoond et al. (2020) recently found the relationship between the static and

dynamic modulus of elasticity of cement and lime mortars (prismatic specimens of 160 mm x 40 mm x 40 mm) used for construction of masonry elements. However, the compaction degree of mortar specimens casted in prismatic and cylindrical molds is higher than that applied in the masonry joints. Strength and stiffness of mortar usually increases with furthering compaction, as it increases the density and decreases the porosity of the cementitious matrix (Patterson and Pavía, 2012). Consequently, numerical models of masonry elements usually present bed mortar with values of modulus of elasticity that are slightly lower than those obtained from prismatic or cylindrical mortar specimens.

Since masonry elements are made of different constituents, they can exhibit typical non-elastic and anisotropic behavior. Previous works (Mohamad et al., 2007, 2017) reported that the stress-strain curves of masonry prisms made with units stiffer than the mortar exhibited significantly higher non-linearity up to the peak load than prisms constructed with mortar comparatively stiffer than units. Figure 14 shows the vertical compressive stress-strain curves of three different prisms constructed with hollow concrete blocks ($f_{b,net}$ equal to 23.1 MPa) and three types of mortars (mortar type I with f_m of 19.8 MPa, mortar type II with f_m of 7.2 MPa, and mortar type III with f_m of 4.4 MPa). The prism produced with mortar type I presented an almost linear stress-strain curve before and after a slight release of strain due to a sudden crack at a stress/strength ratio of about 60%. The crack propagated through the unit, and the prism finally split into two halves, without crushing of the mortar joint. The prisms with mortar types II and III presented a gradual non-linear increase in compressive strains with an increase in stress. Although a sudden crack at a stress/strength ratio of 60% was also observed in the prism with mortar type II, the strong non-linear behavior is an indication of changes in stress state of the mortar and/or propagation of micro cracks inside the mortar. In fact, localized crushing and crumbling of mortar joint were verified in prisms with mortar types II and III. These findings were complemented by Camacho et al. (2015), based on the determination of stress-strain curves of ungrouted prisms and prisms filled by grout and/or steel reinforcement.

Similar trends were observed by Ravula et al. (2017) in the stress-strain curves of prisms constructed with solid clay bricks with compressive strength of 7.4 MPa, combined to different mortar types: a weak mortar (1:6) with f_m of 5.80 MPa, and a strong mortar (1:3) with f_m of 7.95 MPa. They observed that prisms produced with the 1:6 mortar exhibited a significantly higher level of pre-peak non-linearity, in comparison to specimens made with the 1:3 mortar. These results also indicated that the prisms with mortar stiffer than the units presented a more brittle failure mode, since a very rapid load decrease occurred in the post-peak.

Figure 14 - Stress-strain curves of prisms produced with different combinations of mortar and unit strengths.

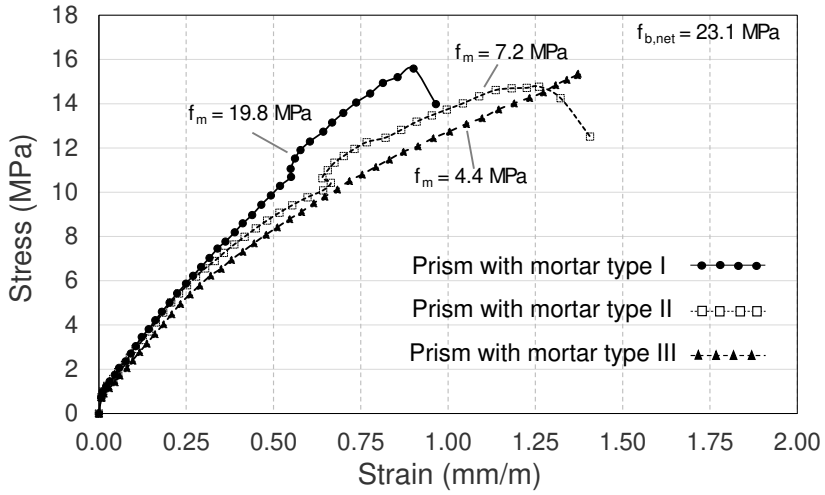

Source: Adapted from Mohamad et al. (2018), as permitted under the Creative Commons Attribution License Agreement.

In addition, the Poisson's ratio of the mortar joint cannot be determined as an elasticity theory parameter in a straightforward manner (Drougkas et al., 2019). At first, the Poisson's ratio decreases with the increase in the compressive load, until reaching a minimum value β_1. After that, the Poisson's ratio increases to very high values up to the failure, so that it is significantly influenced by the existing triaxial stress state (Mohamad et al., 2007).

A novel rational model for non-linear stress-strain curves of concrete brick masonry under compression was also proposed by Yang et al. (2019). The proposed stress-strain relationship accounts for mortar strength values higher than the strength of the units ($f_{m,cub}/f_{b,net}$ ratio ranging between 249.1% and 353.9%, as indicated in Table 4). The model provided results very close to those observed in the experimental tests from the beginning, through the ascending branch, to the 50% of the peak stress in the descending branch. In the final stage of the descending branch, the model provided lower ductility than the experimental test results, which was attributed to the effects of the confined condition of the specimens in the tests. Therefore, further experimental tests of prisms subjected to different test set-ups are required to explain the differences. Despite this, the proposed models were found to contribute towards the mathematical simplicity of analytical modeling in such specific case scenarios.

A new methodology for determination of the compressive stress-strain curves of grouted masonry produced with I-type concrete units was also proposed by Ouyang et al. (2019), based on the softened compression constitutive law of concrete. The authors observed that this theory was able to provide a reliable and accurate prediction of the stress-strain relationship when the compressive strength of grout was lower or close to the block strength. However, the proposed

model presented good applicability and modifiability, since it can be modified with different constitutive laws and deformation ratios within the proposed theoretical frame.

Drougkas et al. (2019) expanded a model for micro-mechanical analysis of prisms and wallettes under compression, in order to include shifting values for the Poisson's ratio of mortar under increasing vertical load. It was possible to realize the inadequacy of considering a constant mortar Poisson's ratio for the accurate micro modeling of masonry. Moreover, the development of damage was found to change significantly when the variations in the Poisson's ratio of mortar were taken into account. Detailed studies about the development of the Poisson's ratio in mortar joints under different levels of confinement are strongly recommended.

2.5. MONITORING OF STRUCTURAL PERFORMANCE AND INTEGRITY OF MASONRY PRISMS UNDER COMPRESSION

The integrity and the resistance of structural masonry elements is compromised due to degradation and worn-away processes associated with fatigue, aging and weathering conditions. Monitoring the damage evolution and the structural behavior of masonry elements is significantly important. Cracks may be caused by excessive loads or different imposed deformations (e.g., soil settlements, temperature variations, shrinkage, irreversible expansion, moisture changes, among others) (Luchin et al., 2020; Pulatsu et al., 2020).

The application of performance-based design methodologies and adequate techniques for monitoring of structural behavior of existing masonry require a deep understanding of nonlinear mechanical properties of their components, in addition to the structural morphology of the buildings (Caprili et al., 2017; Formisano et al., 2018; Luchin et al., 2020). It becomes particularly relevant in historical structures, as they are usually constructed with specific constitutive materials, resulting in very irregular elements and great variety of masonry typologies (Caprili et al., 2017; Luchin et al., 2020; Sarhosis et al., 2018).

2.5.1. Minor-destructive tests of masonry prisms

Many studies have proposed the application of minor-destructive tests (MDT) for the investigation of performance and integrity of masonry elements, since they provide a direct evaluation of masonry properties by only causing negligible damage to small or superficial portions of the structural member. MDT techniques are classified into two different categories: (i) in-situ experiments performed directly on masonry structural elements, and (ii) laboratory

testing of small field-extracted samples (Pelà et al., 2018a). Some examples of MDT applied to masonry prisms are presented in Figure 15.

Figure 15: Minor-destructive tests (MDT) applied for characterization of masonry prisms: (a) mechanical tests of field-extracted prisms; (b) prisms made with field-extracted units; (c) double punch test of mortar joints; (d) penetrometer test of mortar joints of prisms; (e) pneumatic pin penetration test of mortar joints of prisms; and (f) flat-jack test of masonry prisms.

Source: Adapted from (a) Almesfer et al. (2014), as permitted under the Creative Commons Attribution License Agreement; (b) Russo et al. (2008), with permission from the International Masonry Society; (c) Łątka and Matysek (2020), as permitted under the Creative Commons Attribution License Agreement; (d) Łątka and Matysek (2018), as permitted under the Creative Commons Attribution License Agreement; (e) Oliveira et al. (2012), as permitted under the Creative Commons Attribution License Agreement; and (f) Medeiros et al. (2020), Copyright 2020, with permission from Elsevier.

Regarding the first category of MDT, previous studies have proposed the extraction of masonry prisms from existing masonry buildings to be tested in laboratory (Lumantarna et al.,

2014; Song et al., 2018). In this context, the experimental tests carried out by Almesfer et al. (2014) and Lumantarna et al. (2014) indicated that laboratory-constructed clay masonry prisms adequately replicated those from the field-extracted samples (Figure 15a), so that predictive equations and a numerical compression stress-strain model could be developed based on the results of compression tests. These experimental prism results were recently used by Müller and Graubner (2021) to develop a practice-oriented method for determining characteristic values and partial safety factors for the compressive strength of existing masonry.

Compression tests of prisms made with field-extracted units, diametral compression tests of small core samples removed from existing brickwork, and double punch test (DPT) of on-site extracted mortar joints are other examples of MDT (Łątka and Matysek, 2018, 2020; Marastoni et al., 2016; Pelà et al., 2015, 2018b). For example, Russo et al. (2008) developed a mechanical characterization of stack-bond prisms produced with fire-damaged clay bricks extracted from a historic masonry structure that was partially destroyed by a fire accident (Figure 15b). Although mechanical and thermal properties of masonry units and mortar exposed to elevated temperatures vary considerably and may not be easily determined (Maraveas et al., 2013, 2014), the MDT of field-extracted prisms developed by Russo et al. (2008) were able to provide reasonable estimation of the residual compressive strength of the fire-damaged structure. Drougkas et al. (2016) tested stack-bond prisms made with cylindrical cores from solid clay units and pure lime mortar. Their experimental results indicated that the application of the coring method for extracting samples from masonry units is an interesting choice for investigation of existing structures. Łątka et al. (2019) constructed stack-bond prisms with solid clay units and cement-lime mortars and developed a mortar mechanical characterization based on DPT tests of 5 cm x 5 cm x 1.2 cm cut out from the bed joints of the prisms (Figure 15c).

The second category of MDT includes the use of portable instruments for the development of in-situ experiments that are easily carried out on the construction site and are minimally invasive to the structure (Pelà et al., 2018a). Many laboratory studies have investigated the application of these MDT for characterization of masonry prisms under compression. For example, Łątka and Matysek (2018) estimated the compressive strength of the mortar joint of clay brick prisms subjected to uniaxial compression, based on correlations with physical magnitudes obtained from a penetrometer test (PT). This test provides the value of the immersion of a steel needle in the mortar joint of the masonry prism, due to the repeated loading of the needle with a constant force, as presented in Figure 15d.1 (dredging of the PT hole) and Figure 15d.2 (penetrometric deep measurements). Łątka and Matysek (2018) stated

that the penetration distribution obtained from the PT indicated that the mortar in the bed joints was characterized by high homogeneity and an average compressive strength of about 2.41 MPa. The authors also reported a very small difference (0.13 MPa) between the compressive strength of the mortar joints determined by DPT and PT methods.

Oliveira et al. (2012) applied a pneumatic pin penetration test (PPPT) to evaluate the penetration depths of steel probes into the mortar joints of prisms made with hollow concrete blocks (Figure 15e.1) subjected to uniaxial compression. A total of ten depth measurements were performed over each one of the two mortar joints of the prism (Figure 15e.2) and then correlated with the compressive strength of the material. The authors observed a good correlation between the penetration depth of pins and the compressive strength of the prism's mortar, so that PPPT was considered a practical test for characterization of masonry mortars with compressive strength ranging between 1.5 MPa and 20 MPa.

Another popular slightly destructive method for structural diagnosis of masonry elements is the flat-jack testing (Alecci et al., 2021; Guadagnuolo et al., 2020; Łątka and Matysek, 2020). In a very recent paper, Medeiros et al. (2020) investigated the mechanical behavior of hollow-concrete prisms produced in laboratory and subjected to uniaxial compression (Figure 15f.1), hollow-concrete prisms removed from a masonry wall (Figure 15f.2) and subjected to uniaxial compression, and hollow-concrete masonry subjected to flat-jack testing (Figure 15f.3). The elastic modulus obtained from the flat-jack tests was extremely close to the elastic modulus of prisms removed from walls (the difference was about 2%). Moreover, a maximum difference of 3.3% was observed between the elastic modulus estimated with the flat-jack tests and the elastic modulus of the stack-bond prisms produced in laboratory. The authors developed a novel flat-jack equipment that solved some limitations (geometry and maximum applied pressure) and allowed the application of this technique for investigation of modern masonry structures constructed with high-strength concrete blocks.

2.5.2. Non-destructive tests of masonry prisms

Sometimes, the extraction of masonry prisms or masonry components for prediction of the mechanical properties of masonry structures cannot be carried out due to site conditions. In the cases of heritage masonry structures, experimental investigations must respect their intrinsic cultural value (Łątka and Matysek, 2020; Luchin et al., 2020; Marastoni et al., 2017; Mishra et al., 2020; Pelà et al., 2018b). In these situations, one must rely on the data collected from non-destructive tests (NDT). NDT are not invasive to the structure and provide safety, enhance the

life of masonry elements, and reduce diagnostic uncertainties (Marastoni et al., 2017; Mishra et al., 2019, 2020; Pelà et al., 2018b). Then, they are technical alternatives that can successfully meet requirements of preservation, safeguard, and valorization of masonry architectural heritage (Lacidogna et al., 2016).

Despite being an advanced technology, the application of NDT on masonry structures can be frustrating because the interpretation of NDT results of highly heterogeneous elements is often difficult (Martini et al., 2020). In this regard, artificial neural networks have been successfully used in recent studies (Armaghani et al., 2021; Martini et al., 2020) for interpretation of NDT dataset and mechanical characterization of anisotropic materials, such as granite stone masonry panels. Mishra (2021) carried out a very recent review of various machine learning techniques applied to analyze NDT data and assess the health condition of masonry buildings.

NDT techniques can rely on different theoretical principles and provide various information about the physical properties of masonry elements. Different acquisition techniques with non-destructive nature (e.g., unmanned aerial vehicles, laser scanning, ground penetrating radar, interferometric synthetic aperture radar, infrared thermography, electrical impedance tomography, among others) can provide a geometric basis for structural analysis of masonry structures and contribute to the quantification of structural damage (Alani et al., 2020; Biscarini et al., 2020; Cavalagli et al., 2020; Kassotakis and Sarhosis, 2021; Riveiro et al., 2016). However, previous studies on the application of NDT for characterization of masonry prisms have focused on acoustic and digital image correlation techniques.

Many NDT methods are based on the transmission of sonic or electromagnetic waves through the masonry elements (Luchin et al., 2020; Marastoni et al., 2017). Various recent studies (Dizhur et al., 2017; Makoond et al., 2020; Marques et al., 2020; Nalon et al., 2018; Vasanelli et al., 2020) have reported results of ultrasonic pulse velocity (UPV) tests of different types of masonry units and mortars. Since the formation and development of damage release energy inside masonry materials, acoustic emission (AE) techniques have also been used to detect elastic wave released by damaged masonry prisms (De Santis and Tomor, 2013; Wu et al., 2019). De Santis and Tomor (2013) recorded signals from AE sensors (L1 and L2) installed at the mid-height of stack-bond clay prisms subjected to uniaxial compression (Figure 16a and Figure 16b). AE amplitude and energy values suggested three different crack stages associated with compaction, micro-cracking, and macro-cracking prior to failure (Figure 16c and Figure 16d). Approximate AE amplitudes and energy levels observed in mortar and brick specimens

suggested that early cracking occurred in the mortar joints, whereas damage in the units only appeared close to the failure. In a recent work developed by Wu et al. (2019), AE sensors were arranged in the middle of sides of clay brick prisms subjected to uniaxial compression and were able to qualitatively reflect their damage condition. High amplitude and energy values in the low-frequency band could be used as symptoms of loss of bearing capacity, which offers promising application for crack monitoring and damage assessment of masonry structure buildings.

Figure 16 - Non-destructive tests (NDT) applied for characterization of masonry prisms: (a) acoustic emission tests and (b) digital image correlation tests.

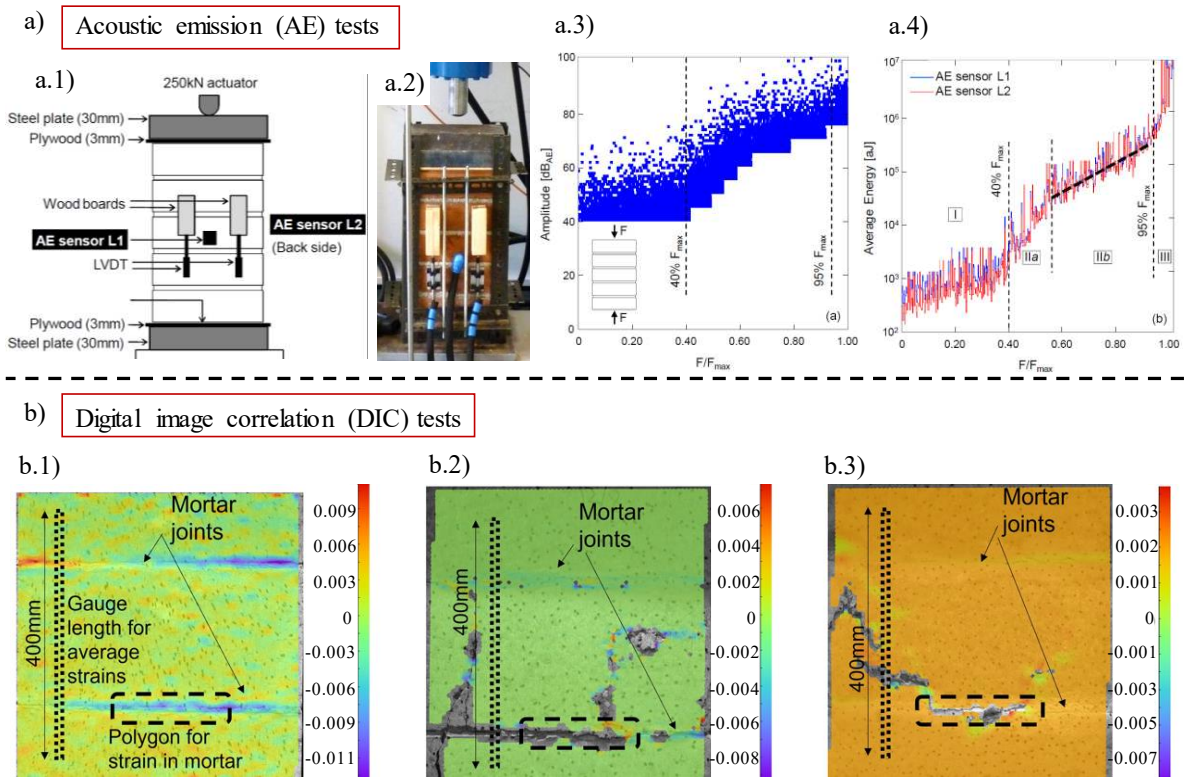

Source: Adapted from (a) De Santis and Tomor (2013), Copyright 2013, with permission from Elsevier and (b) Zahra et al. (2021), Copyright 2021, with permission from Elsevier.

An optical technique known as digital image correlation (DIC) has been proposed to monitor the deformations at the surface of masonry prisms, by tracking random speckle patterns assigned to their surface, based on fundamental photogrammetry and digital image processing rules. The gauge length used for calculation of the deformations can be assumed between any set of points captured by DIC. Consequently, it is possible to perform spatially continuous measurements of displacements across the surface area of units and/or mortar joints of masonry prisms (Bolhassani et al., 2016; Kumar et al., 2019; Ravula and Subramaniam, 2017; Zahra,

Thamboo and Asad, 2021). Used DIC to monitor the average longitudinal strain on the surface of prisms produced with a weak mortar (Figure 16b.1), a medium-strength mortar (Figure 16b.2), and a strong mortar (Figure 16b.3). The technique was able to indicate that increases in mortar strength have slightly reduced the axial deformation capacity of masonry prisms.

Damage can also be evaluated with the DIC technique, based on the analysis of the development of cracks on the surface of the prisms. Ravula et al. (2017) indicated that cracks can be identified as closed contours with very high strain gradient in a given area of interest of the surface of masonry prisms. They observed that the initiation of a vertical crack close to the brick-mortar interface of a compressed prism specimen coincided with the onset of non-linearity in its stress-strain curve. Therefore, the authors concluded that DIC images can be used to monitor crack propagation and predict the manifestation of a failure mode of masonry prisms.

The incorporation of nanomaterials into construction materials to provide them with multifunctional properties has received considerable attention over the last years (Birgisson et al., 2012b; Du et al., 2019, 2020b). Conductive carbon nanomaterials have been recently used to produce smart materials with an intrinsic ability to monitor strain and detect structural elements' damage (Dong et al., 2019; Nalon et al., 2020; Tian et al., 2019). To produce smart masonry elements, Ubertini et al. (2017) doped solid clay masonry bricks with different contents of carbon nanotubes (0%, 0.5%, 0.75% and 1% by total composite weight). The bricks with nanomaterials presented an evident intrinsic sensitivity to external loads, whereas the normal clay bricks do not exhibit any relevant stress sensitivity. Therefore, the authors concluded that the electrical output of their nanomodified self-sensing bricks seem to a promising novel NDT method to characterize masonry elements.

2.6. CONCLUSIONS

This chapter presented a careful review on the significant progress on the understanding of the compressive behavior of masonry prisms. Many conclusions derived from the present review can be drawn as follows:

(1) The failure mode of ungrouted masonry depends on whether the mortar joint is weak or strong relative to the masonry units. The dataset evaluated in the present review revealed that mortar crushing has been observed in prisms with $f_{m,cub}/f_{b,net}$ ratio ranging between 13.5% and 40.1%, tensile splitting failure of units has been

predominant in prisms with $f_{m,cub}/f_{b,net}$ from 31.6% to 121.9%, and unit crushing has been the failure mode of prisms with $f_{m,cub}/f_{b,net}$ from 87.2% to 778.5%.

(2) The rupture mechanisms of grouted prisms with $f_{g,cyl}/f_{b,net}$ ratios from 87.5% to 235.7% are mainly characterized by tensile failure of weak block shells around a strong grout core. In contrast, prisms with $f_{g,cyl}/f_{b,net}$ ratios from 56.3% to 85.4% typically fail by premature vertical cracks in the block shells due to excessive lateral expansion of the grout core. When previous studies used $f_{g,cyl}/f_{b,net}$ ratios from 80.7% to 113.3%, it was possible to match the deformation properties of blocks and grout, so that they worked together as a monolithic resistant system.

(3) Numerous types of masonry components (e.g., eco-efficient masonry components, nanomodified masonry components, high-strength concrete blocks, lightweight units, I-type blocks, polymer adhesive mortars, non-shrink grout, preblended cement-based materials, among others) affect the mechanical properties and failure mechanisms of masonry prisms. Other parameters such as new curing, mortar bedding, and grouting procedures also influence the compressive behavior of masonry prisms. This chapter revised some details that demonstrate that the compressive behavior of prisms constructed with innovative components is very complex, and explanations of different phenomena have been obtained through experimental investigations of many variables.

(4) Mutual effects of unit and mortar strength on mechanical properties of ungrouted prisms were observed in 3D surfaces and contour graphs constructed with the reviewed dataset. When low-strength units were used, increases in mortar strength caused marginal increases in ungrouted prism strength, since unit failure usually governed the failure mode. Moreover, gains of ungrouted compressive strength due to the enhancement in unit strength were lower when low-strength mortars were used, since the rupture was mainly governed by mortar crushing. Improved mechanical performance of ungrouted prisms was graphically observed when the $f_{m,cub}$ / $f_{b,net}$ ratios were between 31.6% and 121.9%, situation in which tensile splitting of masonry units was the observed failure mechanism.

(5) Analyses of 3D surfaces and contour graphs were also used to visualize the mutual effects of unit and grout strength on mechanical properties of grouted prisms. From these observations, it may be inferred that lower values of mechanical properties have been reported when strong grout is combined with significantly weak units,

and vice versa. The best mechanical performance has been reported when the $f_g/f_{b,net}$ ratio is between 80.7% and 113.3%. However, high compressive strength values were also observed in some regions outside the limits of this range. For example, in prisms constructed with $f_g/f_{b,net}$ ratio lower than 80.7%, the use of modern high-strength units was able to prevent the premature vertical cracks of masonry shells due to excessive lateral expansion of the grout. In prisms constructed with $f_g/f_{b,net}$ ratios higher than 113.3% and high-strength grout, a strong grout column could withstand increasing compressive load, despite the rupture of the blocks' shells and webs.

(6) Values of compressive strength and modulus of elasticity experimentally obtained in different studies reviewed in this research were plotted against predicted values of European, American, Canadian, Australian, and Brazilian codes. Significant amount of data was reasonably far from the equality line of predicted versus obtained compressive strength (or modulus of elasticity). Then, the dataset revised indicated that the estimation of the compressive strength and modulus of elasticity of masonry by the prism test method would be more appropriate than the application of empirical equations and tabulated values proposed in current masonry codes. The significant limitation of the formulations of current design codes calls for their careful and urgent revision.

(7) Analyses and comparisons of previous studies demonstrated the mutual dependency of different factors affecting the compressive behavior of masonry prisms (e.g.; mutual effects of joint thickness, mortar/unit strength ratio, and type of mortar; mutual effects of grouting and mortar/unit strength ratio; mutual effects of bedding approach, type of unit, and mortar/unit strength ratio; mutual effects of prism bonding arrangement, type and size of units; length to thickness ratio and height to thickness ratio of prisms, among others). Available models for prediction of prism strength and stiffness usually consider only a few factors, so that poor predictive ability has been observed in different situations.

(8) The present assessment has proved the relevance of elucidating and summarizing the mechanical performance of masonry prisms associated with case scenarios that are not conventionally applied in masonry construction. This review addresses issues often neglected in past literature, such as new insights on the use of mortar joints significantly stronger than the units and vice versa.

(9) Novel stress-strain models of masonry elements have been developed to reflect a series of different aspects, such as the non-linear behavior of masonry components, geometry of masonry specimen, mutual factors affecting the prism structural behavior, changes in Poisson's ratio with the confinement level of mortar joint, among others.

(10) Strategies for structural investigation of existing masonry buildings were demonstrated in this manuscript, based on previous studies dealing with the characterization of in-situ extracted masonry prisms and application of various MDT and NDT for strain monitoring and damage detection in masonry prisms. It was possible to conclude that masonry prisms can be successfully used to study existing and innovative MDT and NDT that are essential to characterize existing masonry structures and monitor stress, strain and damage propagation.

2.7. LIMITATIONS AND FUTURE DIRECTIONS

The review of the current state-of-the-art on the compressive behavior of masonry prisms allowed the identification of different limitations, knowledge gaps, and uncertainties that can be interesting research directions in future studies, as follows:

(1) Most studies have only investigated factors affecting the compressive behavior of prisms constructed with normal-strength units. Then, relevant future investigations should focus on explorations of ungrouted and grouted prisms made of high-strength units, considering different bedding approaches, bonding arrangement, production and curing methods, among other factors.

(2) The incorporation of wastes into building materials for the development of eco-friendly masonry components will positively improve the sustainability of the construction industry. However, many uncertainties remain in the effects of reusing different types of recycled admixtures on the compressive behavior of masonry elements. Therefore, future studies are needed to investigate the eco-efficiency of prisms constructed with waste-based components, considering their mechanical, environmental, and durability performance.

(3) Previous studies mainly revealed and predicted the short-term response of masonry prisms under compression, so that detailed analyses are required to better understand their long-term structural behavior.

(4) Different uncertainties have been observed in the stress and strain states of the mortar joints of prisms under perpendicular compression. Particularly, future studies on Poisson's ratio variations in prisms' mortar joints under different confinement levels are of significant importance.

(5) Many uncertainties in the mechanical behavior of masonry prisms are associated with the application of inappropriate models to describe the mechanical behavior of masonry constructed with soft units and relatively high-strength mortars. Further studies are recommended to develop applicable stress-strain curve models and strength/stiffness predictions to prisms produced with mortar stronger than units.

(6) Most studies revised in this research tested six or more specimens to determine the mechanical properties of masonry prisms. High degree of scatter was observed in these tests, which is mainly due to the heterogeneous nature of masonry components and the high complexity of unit/mortar interfacial effects. Future studies on this field should test six or more specimens to get representative strength and stiffness values and estimate the natural variability of compression test of masonry prisms.

(7) In-depth studies on the durability properties of masonry prisms are strongly recommended, since the previous studies have mainly focused on their mechanical performance.

(8) Measurement, processing, and classification of UPV and AE signal parameters obtained from masonry prisms and comparisons with field experiments would be of great interest for the development of experimental database and continuous detection of damage in masonry elements.

(9) Experimental research on nanomodified masonry elements are still in their initial phase. It is pertinent to expand comprehensive and comparable studies investigating the compressive strength, modulus of elasticity, and failure mechanisms of masonry prisms constructed with various types of nanomodified units, mortars, and grout. Future works are also recommended to explore synergistic effects of potential combinations of various nanomaterials on the compressive behavior of prisms made with nanomodified components.

REFERENCES

Abasi, A., Hassanli, R., Vincent, T., & Manalo, A. (2020). Influence of prism geometry on the compressive strength of concrete masonry. *Construction and Building Materials*, *264*, 120182. https://doi.org/10.1016/j.conbuildmat.2020.120182

AbdelRahman, B., & Galal, K. (2020). Influence of pre-wetting, non-shrink grout, and scaling on the compressive strength of grouted concrete masonry prisms. *Construction and Building Materials*, *241*, 117985. https://doi.org/10.1016/j.conbuildmat.2019.117985

ABNT. (2020a). *NBR 16868-1: Structural masonry Part 1 - Design* (p. 70).

ABNT. (2020b). *NBR 16868-2: Structural masonry Part 2 - Execution and site control* (p. 23).

Afanador García, N., Farelo Alvarez, K. A., & Calderon, F. (2019). A numerical model of the behavior of the resistance to compression in prisms of solid masonry. *Journal of Physics: Conference Series*, *1386*, 012131. https://doi.org/10.1088/1742-6596/1386/1/012131

Alani, A. M., Tosti, F., Ciampoli, L. B., Gagliardi, V., & Benedetto, A. (2020). An integrated investigative approach in health monitoring of masonry arch bridges using GPR and InSAR technologies. *NDT & E International*, *115*, 102288. https://doi.org/10.1016/j.ndteint.2020.102288

Alecci, V., De Stefano, M., Luciano, R., Marra, A. M., & Stipo, G. (2021). Numerical Investigation on the Use of Flat-Jack Test for Detecting Masonry Deformability. *Journal of Testing and Evaluation*, *49*(1), 20190781. https://doi.org/10.1520/JTE20190781

Almesfer, N., Dizhur, D. Y., Lumantarna, R., & Ingham, J. M. (2014). Material properties of existing unreinforced clay brick masonry buildings in New Zealand. *Bulletin of the New Zealand Society for Earthquake Engineering*, *47*(2), 75–96. https://doi.org/10.5459/bnzsee.47.2.75-96

Alvarenga, R. C. S. S., Nalon, G. H., Fioresi, L. A. F., Pinto, M. C., Pedroti, L. G., & Ribeiro, J. C. L. (2017a). Experimental Evaluation of the Influence of Mortar's Mechanical Properties on the Behavior of Clay Masonry. In *Characterization of Minerals, Metals, and Materials 2018* (pp. 671–679). https://doi.org/10.1007/978-3-319-51382-9_74

Alvarenga, R. C. S. S., Nalon, G. H., Fioresi, L. A. F., Pinto, M. C., Pedroti, L. G., & Ribeiro, J. C. L. (2017b). Experimental Evaluation of the Influence of Mortar's Mechanical Properties on the Behavior of Clay Masonry. *Minerals, Metals and Materials Series*, *Part F7*, 671–679. https://doi.org/10.1007/978-3-319-51382-9_74

Anić, F., Penava, D., Abrahamczyk, L., & Sarhosis, V. (2020). A review of experimental and analytical studies on the out-of-plane behaviour of masonry infilled frames. *Bulletin of Earthquake Engineering*, *18*(5), 2191–2246. https://doi.org/10.1007/s10518-019-00771-5

Armaghani, D. J., Mamou, M., Maraveas, C., Roussis, P. C., Siorikis, V. G., Skentou, A. D., & Asteris, P. G. (2021). Predicting the unconfined compressive strength of granite using only two non-destructive test indexes. *Geomechanics and Engineering*, *25*(4), 317–330. https://doi.org/10.12989/gae.2021.25.4.317

ASA. (2018). *AS 3700: Masonry Structures*.

Asteris, P. G., Cavaleri, L., Di Trapani, F., & Tsaris, A. K. (2017). Numerical modelling of out-of-plane response of infilled frames: State of the art and future challenges for the equivalent strut macromodels. *Engineering Structures*, *132*, 110–122. https://doi.org/10.1016/j.engstruct.2016.10.012

ASTM. (2019). *C270: Standard Specification for Mortar for Unit Masonry* (p. 14).

Barbosa, C., & Hanai, J. (2005). Strength and deformability of hollow concrete blocks and their correlations with mechanical properties of constituent material. *10th Canadian Masonry Symposium*.

Barbosa, C. S., & Hanai, J. B. (2009). Strength and deformability of hollow concrete blocks: correlation of block and cylindrical sample test results. *Revista IBRACON de Estruturas e Materiais*, *2*(1), 85–99. https://doi.org/10.1590/S1983-41952009000100005

Barbosa, C. S., Lourenço, P. B., & Hanai, J. B. (2010). On the compressive strength prediction for concrete masonry prisms. *Materials and Structures*, *43*(3), 331–344. https://doi.org/10.1617/s11527-009-9492-0

Behera, B., & Nanda, R. P. (2021). In-plane shear strengthening of brick masonry panel with geogrid reinforcement embedded in bed and bed-head joints mortar. *Engineering Structures*, *227*, 111411. https://doi.org/10.1016/j.engstruct.2020.111411

Berto, L. (2005). Failure mechanism of masonry prism loaded in axial compression: computational aspects. *Materials and Structures*, *38*(276), 249–256. https://doi.org/10.1617/14096

Bezerra, U. T., Alves, S. M. S., Barbosa, N. P., & Torres, S. M. (2016). Hourglass-shaped specimen: compressive strength of concrete and mortar (numerical and experimental analyses). *Revista IBRACON de Estruturas e Materiais*, *9*(4), 510–524. https://doi.org/10.1590/S1983-41952016000400003

Birgisson, B., Mukhopadhyay, B., Geary, A., Khan, G., & Sobolev, K. (2012a). *Nanotechnology in Concrete Materials*. Transportation Research Board of the National Academies.

Birgisson, B., Mukhopadhyay, B., Geary, A., Khan, G., & Sobolev, K. (2012b). *Nanotechnology in Concrete Materials*. Transportation Research Board of the National Academies.

Biscarini, C., Catapano, I., Cavalagli, N., Ludeno, G., Pepe, F. A., & Ubertini, F. (2020). UAV photogrammetry, infrared thermography and GPR for enhancing structural and material degradation evaluation of the Roman masonry bridge of Ponte Lucano in Italy. *NDT & E International*, *115*, 102287. https://doi.org/10.1016/j.ndteint.2020.102287

Bolhassani, M., Hamid, A. A., Lau, A. C. W., & Moon, F. (2015). Simplified micro modeling of partially grouted masonry assemblages. *Construction and Building Materials*, *83*, 159–173. https://doi.org/10.1016/j.conbuildmat.2015.03.021

Bolhassani, M., Rajaram, S., Hamid, A. A., Kontsos, A., & Bartoli, I. (2016). Damage detection of concrete masonry structures by enhancing deformation measurement using DIC. In T. Yu, A. L. Gyekenyesi, P. J. Shull, & H. F. Wu (Eds.), *Nondestructive Characterization and Monitoring of Advanced Materials, Aerospace, and Civil Infrastructure* (p. 980411). https://doi.org/10.1117/12.2218368

Caldeira, F. E., Nalon, G. H., Oliveira, D. S. de, Pedroti, L. G., Ribeiro, J. C. L., Ferreira, F. A., & Carvalho, J. M. F. de. (2020). Influence of joint thickness and strength of mortars on the compressive behavior of prisms made of normal and high-strength concrete blocks. *Construction and Building Materials*, *234*, 117419. https://doi.org/10.1016/j.conbuildmat.2019.117419

Camacho, J. S., Logullo, B. G., Parsekian, G. A., & Soudais, P. R. N. (2015). The influence of grouting and reinforcement ratio in the concrete block masonry compressive behavior. *Revista IBRACON de Estruturas e Materiais*, *8*(3), 341–364. https://doi.org/10.1590/S1983-41952015000300006

CAN/CSA. (2014). *A179-14: Mortar and grout for unit masonry* (p. 76).

Caprili, S., Mangini, F., Paci, S., Salvatore, W., Bevilacqua, M. G., Karwacka, E., Squeglia, N., Barsotti, R., Bennati, S., Scarpelli, G., & Iannelli, P. (2017). A knowledge-based approach for the structural assessment of cultural heritage, a case study: La Sapienza Palace in Pisa. *Bulletin of Earthquake Engineering*, *15*(11), 4851–4886. https://doi.org/10.1007/s10518-017-0158-y

Cassinello, M. J. (2006). Influencia del espesor de la junta de mortero en la deformabilidad de las fábricas pétreas medievales. *Materiales de Construcción*, *56*(284). https://doi.org/10.3989/mc.2006.v56.i284.19

Castro, L. O., Alvarenga, R. C. S. S., Silva, R. M., & Ribeiro, J. C. L. (2016). Experimental evaluation of the interaction between strength concrete block walls under vertical loads. *Revista IBRACON de Estruturas e Materiais*, *9*(5), 643–681. https://doi.org/10.1590/S1983-41952016000500002

Cavalagli, N., Gioffrè, M., Grassi, S., Gusella, V., Pepi, C., & Volpi, G. M. (2020). On the accuracy of UAV photogrammetric survey for the evaluation of historic masonry structural damages. *Procedia Structural Integrity*, *29*, 165–174. https://doi.org/10.1016/j.prostr.2020.11.153

CEB. (2000). *EN 772-1: Methods of test for masonry units - Part 1: Determination of compressive strength*.

CEN. (2005). *Eurocode 6: Design of masonry structures - General rules for reinforced and unreinforced masonry structures*.

Chang, L.-Z., Messali, F., & Esposito, R. (2020). Capacity of unreinforced masonry walls in out-of-plane two-way bending: A review of analytical formulations. *Structures*, *28*, 2431–2447. https://doi.org/10.1016/j.istruc.2020.10.060

CSA. (2014). *S304-14: Design of masonry structures*.

D'Altri, A. M., Sarhosis, V., Milani, G., Rots, J., Cattari, S., Lagomarsino, S., Sacco, E., Tralli, A., Castellazzi, G., & de Miranda, S. (2020). Modeling Strategies for the Computational Analysis of Unreinforced Masonry Structures: Review and Classification. *Archives of Computational Methods in Engineering*, *27*(4), 1153–1185. https://doi.org/10.1007/s11831-019-09351-x

Darwish, M., Khedr, S., Halim, F., & Khalil, R. (2020). Novel Simplified Construction of Walls and Prisms Made of CEBs and Earth-Based Mortar. *Practice Periodical on Structural Design and Construction*, *25*(4), 04020041. https://doi.org/10.1061/(ASCE)SC.1943-5576.0000525

Dawood, E. T., & Mahmood, M. S. (2021). Production of Sustainable concrete brick units using Nano-silica. *Case Studies in Construction Materials*, *14*, e00498. https://doi.org/10.1016/j.cscm.2021.e00498

De Santis, S., & Tomor, A. K. (2013). Laboratory and field studies on the use of acoustic emission for masonry bridges. *NDT & E International*, *55*, 64–74. https://doi.org/10.1016/j.ndteint.2013.01.006

Dizhur, D., Lumantarna, R., Biggs, D. T., & Ingham, J. M. (2017). In-situ assessment of the physical and mechanical properties of vintage solid clay bricks. *Materials and Structures*, *50*(1), 63. https://doi.org/10.1617/s11527-016-0939-9

Dong, W., Li, W., Tao, Z., & Wang, K. (2019). Piezoresistive properties of cement-based sensors: Review and perspective. *Construction and Building Materials*, *203*, 146–163. https://doi.org/10.1016/j.conbuildmat.2019.01.081

Drougkas, A., Roca, P., & Molins, C. (2016). Compressive strength and elasticity of pure lime mortar masonry. *Materials and Structures*, *49*(3), 983–999. https://doi.org/10.1617/s11527-015-0553-2

Drougkas, A., Verstrynge, E., Hayen, R., & Van Balen, K. (2019). The confinement of mortar in masonry under compression: Experimental data and micro-mechanical analysis. *International Journal of Solids and Structures*, *162*, 105–120. https://doi.org/10.1016/j.ijsolstr.2018.12.006

Drysdale, R., & Hamid, A. (1979). Behavior of Concrete Block Masonry Under Axial Compression. *ACI Journal Proceedings*, *76*(6), 707–722. https://doi.org/10.14359/6965

Du, M., Jing, H., Gao, Y., Su, H., & Fang, H. (2020a). Carbon nanomaterials enhanced cement-based composites: advances and challenges. *Nanotechnology Reviews*, *9*(1), 115–135. https://doi.org/10.1515/ntrev-2020-0011

Du, M., Jing, H., Gao, Y., Su, H., & Fang, H. (2020b). Carbon nanomaterials enhanced cement-based composites: advances and challenges. *Nanotechnology Reviews*, *9*(1), 115–135. https://doi.org/10.1515/ntrev-2020-0011

Du, S., Wu, J., AlShareedah, O., & Shi, X. (2019). Nanotechnology in Cement-Based Materials: A Review of Durability, Modeling, and Advanced Characterization. *Nanomaterials*, *9*(9), 1213. https://doi.org/10.3390/nano9091213

El-Dakhakhni, W., & Ashour, A. (2017). Seismic Response of Reinforced-Concrete Masonry Shear-Wall Components and Systems: State of the Art. *Journal of Structural*

Engineering, *143*(9), 03117001. https://doi.org/10.1061/(ASCE)ST.1943-541X.0001840

Erdogmus, E. (2015). Use of Fiber-Reinforced Cements in Masonry Construction and Structural Rehabilitation. *Fibers*, *3*(4), 41–63. https://doi.org/10.3390/fib3010041

Fonseca, F. S., Fortes, E. S., Parsekian, G. A., & Camacho, J. S. (2019). Compressive strength of high-strength concrete masonry grouted prisms. *Construction and Building Materials*, *202*, 861–876. https://doi.org/10.1016/j.conbuildmat.2019.01.037

Formisano, A., Vaiano, G., Fabbrocino, F., & Milani, G. (2018). Seismic vulnerability of Italian masonry churches: The case of the Nativity of Blessed Virgin Mary in Stellata of Bondeno. *Journal of Building Engineering*, *20*, 179–200. https://doi.org/10.1016/j.jobe.2018.07.017

Fortes, E. S., Parsekian, G. A., Camacho, J. S., & Fonseca, F. S. (2017). Compressive strength of masonry constructed with high strength concrete blocks. *Revista IBRACON de Estruturas e Materiais*, *10*(6), 1273–1319. https://doi.org/10.1590/s1983-41952017000600008

Fortes, E. S., Parsekian, G. A., Fonseca, F. S., & Camacho, J. S. (2018). High-Strength Concrete Masonry Walls under Concentric and Eccentric Loadings. *Journal of Structural Engineering*, *144*(6), 04018055. https://doi.org/10.1061/(ASCE)ST.1943-541X.0001978

Francis, A., Horman, C., & Jerrems, L. (1972). The effect of joint thickness and other factors on the compressive strength of brickwork. *2nd International Brick Masonry Conferemce*.

Furtado, A., Rodrigues, H., Arêde, A., & Varum, H. (2020). Experimental tests on strengthening strategies for masonry infill walls: A literature review. *Construction and Building Materials*, *263*, 120520. https://doi.org/10.1016/j.conbuildmat.2020.120520

Ganesan, T. P., & Ramamurthy, K. (1992). Behavior of Concrete Hollow-Block Masonry Prisms under Axial Compression. *Journal of Structural Engineering*, *118*(7), 1751–1769. https://doi.org/10.1061/(ASCE)0733-9445(1992)118:7(1751)

Guadagnuolo, M., Aurilio, M., Basile, A., & Faella, G. (2020). Modulus of Elasticity and Compressive Strength of Tuff Masonry: Results of a Wide Set of Flat-Jack Tests. *Buildings*, *10*(5), 84. https://doi.org/10.3390/buildings10050084

Guo, Z., Tu, A., Chen, C., & Lehman, D. E. (2018). Mechanical properties, durability, and life-cycle assessment of concrete building blocks incorporating recycled concrete

aggregates. *Journal of Cleaner Production*, *199*, 136–149. https://doi.org/10.1016/j.jclepro.2018.07.069

Gupta, A., & Singhal, V. (2020). Strengthening of Confined Masonry Structures for In-plane Loads: a Review. *IOP Conference Series: Materials Science and Engineering*, *936*, 012031. https://doi.org/10.1088/1757-899X/936/1/012031

Hamid, A. A., & Chukwunenye, A. O. (1986). Compression Behavior of Concrete Masonry Prisms. *Journal of Structural Engineering*, *112*(3), 605–613. https://doi.org/10.1061/(ASCE)0733-9445(1986)112:3(605)

Hamid, A., & Drysdale, R. (1979). Suggested Failure Criteria for Grouted Concrete Masonry Under Axial Compression. *ACI Journal Proceedings*, *76*(10), 1047–1062. https://doi.org/10.14359/6973

Han, B., Sun, S., Ding, S., Zhang, L., Yu, X., & Ou, J. (2015). Review of nanocarbon-engineered multifunctional cementitious composites. *Composites Part A: Applied Science and Manufacturing*, *70*, 69–81. https://doi.org/10.1016/j.compositesa.2014.12.002

Hendry, A. (1997). *Structural masonry* (2nd ed.). MACMILLAN PRESS LTD.

Hernoune, H., Benabed, B., Alshugaa, M., Abousnina, R., & Guettala, A. (2020). Strengthening of masonry walls with CFRP composite: experiments and numerical modeling. *Epitoanyag - Journal of Silicate Based and Composite Materials*, *72*(1), 2–11. https://doi.org/10.14382/epitoanyag-jsbcm.2020.1

Huang, L., Liao, L., Yan, L., & Yi, H. (2014). Compressive Strength of Double H Concrete Block Masonry Prisms. *Journal of Materials in Civil Engineering*, *26*(8), 06014019. https://doi.org/10.1061/(ASCE)MT.1943-5533.0001084

Kaczmarek, A. (2019). Technical Evaluation of Construction Mortars with Various Lime Quantity Additions. *IOP Conference Series: Materials Science and Engineering*, *471*, 032037. https://doi.org/10.1088/1757-899X/471/3/032037

Kanchidurai, S., Krishanan, P. A., Baskar, K., & Mohan, K. S. R. (2019). Strength characteristic of novel mesh embedment technique for new brick construction with least expensive material. *Engineering Structures*, *178*, 484–492. https://doi.org/10.1016/j.engstruct.2018.10.062

Kassotakis, N., & Sarhosis, V. (2021). Employing non-contact sensing techniques for improving efficiency and automation in numerical modelling of existing masonry

structures: A critical literature review. *Structures*, *32*, 1777–1797. https://doi.org/10.1016/j.istruc.2021.03.111

Kazempour, H. (2014). *Effect of Nanoparticles on the Properties of Masonry Mortars and Assemblages at a Cold Temperature*. University of Manitoba.

Kazempour, H., Bassuoni, M. T., & Hashemian, F. (2017). Masonry mortar with nanoparticles at a low temperature. *Proceedings of the Institution of Civil Engineers - Construction Materials*, *170*(6), 297–308. https://doi.org/10.1680/jcoma.15.00054

Khalaf, F. M. (1996). Factors influencing compressive strength of concrete masonry prisms. *Magazine of Concrete Research*, *48*(175), 95–101. https://doi.org/10.1680/macr.1996.48.175.95

Köksal, H. O., Karakoç, C., & Yildirim, H. (2005). Compression Behavior and Failure Mechanisms of Concrete Masonry Prisms. *Journal of Materials in Civil Engineering*, *17*(1), 107–115. https://doi.org/10.1061/(ASCE)0899-1561(2005)17:1(107)

Krishnaraj, L., Niranjan, R., Kumar, G. P., & Kumar, R. S. (2020a). Numerical and experimental investigation on mechanical and thermal behaviour of brick masonry: An efficient consumption of ultrafine fly ash. *Construction and Building Materials*, *253*, 119232. https://doi.org/10.1016/j.conbuildmat.2020.119232

Krishnaraj, L., Niranjan, R., Kumar, G. P., & Kumar, R. S. (2020b). Numerical and experimental investigation on mechanical and thermal behaviour of brick masonry: An efficient consumption of ultrafine fly ash. *Construction and Building Materials*, *253*, 119232. https://doi.org/10.1016/j.conbuildmat.2020.119232

Kumar, S. L., Aravind, H. B., & Hossiney, N. (2019). Digital image correlation (DIC) for measuring strain in brick masonry specimen using Ncorr open source 2D MATLAB program. *Results in Engineering*, *4*, 100061. https://doi.org/10.1016/j.rineng.2019.100061

Lacidogna, G., Accornero, F., & Carpinteri, A. (2016). Masonry Structures. In M. Ohtsu (Ed.), *Innovative AE and NDT Techniques for On-Site Measurement of Concrete and Masonry Structures* (pp. 27–46). RILEM State-of-the-Art Reports. https://doi.org/10.1007/978-94-017-7606-6

Lakshani, M. M. T., Jayathilaka, T. K. G. A., & Thamboo, J. A. (2020). Experimental investigation of the unconfined compressive strength characteristics of masonry mortars. *Journal of Building Engineering*, *32*, 101558. https://doi.org/10.1016/j.jobe.2020.101558

Łątka, D., & Matysek, P. (2018). Assessment of the compressive strength of lime mortar in the joints of brick walls - case study. *MATEC Web of Conferences*, *163*, 02006. https://doi.org/10.1051/matecconf/201816302006

Łątka, D., & Matysek, P. (2020). Determination of Mortar Strength in Historical Brick Masonry Using the Penetrometer Test and Double Punch Test. *Materials*, *13*(12), 2873. https://doi.org/10.3390/ma13122873

Łątka, D., Seręga, S., & Matysek, P. (2019). Estimation of Mortar Compressive Strength Based on Specimens Extracted from Masonry Bed Joints. *Structural Analysis of Historical Constructions*, 577–586. https://doi.org/10.1007/978-3-319-99441-3_62

Lima, F., Lima, A., & Assis, W. (2012). Study of the influence of compressive strength and thickness of capping-mortar on compressive strength of prisms of structural clay blocks. *15th International Brick and Block Masonry Conference*.

Llorens, J., Llorens, M., Chamorro, M. A., Gómez, J., & Barris, C. (2020). Experimental study on the vertical interface of thin-tile masonry. *Construction and Building Materials*, *261*, 119976. https://doi.org/10.1016/j.conbuildmat.2020.119976

Luchin, G., Ramos, L. F., & D'Amato, M. (2020). Sonic Tomography for Masonry Walls Characterization. *International Journal of Architectural Heritage*, *14*(4), 589–604. https://doi.org/10.1080/15583058.2018.1554723

Lumantarna, R., Biggs, D. T., & Ingham, J. M. (2014). Uniaxial Compressive Strength and Stiffness of Field-Extracted and Laboratory-Constructed Masonry Prisms. *Journal of Materials in Civil Engineering*, *26*(4), 567–575. https://doi.org/10.1061/(ASCE)MT.1943-5533.0000731

Mahamid, M., & Westin, N. (2020). Reevaluation of fm′ for the Unit-Strength Method with Application to Lightweight Concrete Block Masonry and Face Shell–Bedded Mortar Joints. *Practice Periodical on Structural Design and Construction*, *25*(3), 04020019. https://doi.org/10.1061/(ASCE)SC.1943-5576.0000494

Mahamood, N., Mohammed, B., Shafiq, N., & Eisa, S. (2016). Development of nano silica modified solid rubbercrete bricks. In *Civil, Offshore and Environmental Engineering* (pp. 443–446). CRC Press. https://doi.org/10.1201/b21942-90

Makoond, N., Cabané, A., Pelà, L., & Molins, C. (2020). Relationship between the static and dynamic elastic modulus of brick masonry constituents. *Construction and Building Materials*, *259*, 120386. https://doi.org/10.1016/j.conbuildmat.2020.120386

Marastoni, D., Benedetti, A., Pelà, L., & Pignagnoli, G. (2017). Torque Penetrometric Test for the in-situ characterisation of historical mortars: fracture mechanics interpretation and experimental validation. *Construction and Building Materials*, *157*, 509–520. https://doi.org/10.1016/j.conbuildmat.2017.09.120

Marastoni, D., Pelà, L., Benedetti, A., & Roca, P. (2016). Combining Brazilian tests on masonry cores and double punch tests for the mechanical characterization of historical mortars. *Construction and Building Materials*, *112*, 112–127. https://doi.org/10.1016/j.conbuildmat.2016.02.168

Maraveas, C., Wang, Y. C., & Swailes, T. (2013). Thermal and mechanical properties of 19th century fireproof flooring systems at elevated temperatures. *Construction and Building Materials*, *48*, 248–264. https://doi.org/10.1016/j.conbuildmat.2013.06.084

Maraveas, C., Wang, Y. C., & Swailes, T. (2014). Fire resistance of 19th century fireproof flooring systems: A sensitivity analysis. *Construction and Building Materials*, *55*, 69–81. https://doi.org/10.1016/j.conbuildmat.2014.01.022

Marques, A. I., Morais, J., Morais, P., Veiga, M. do R., Santos, C., Candeias, P., & Ferreira, J. G. (2020). Modulus of elasticity of mortars: Static and dynamic analyses. *Construction and Building Materials*, *232*, 117216. https://doi.org/10.1016/j.conbuildmat.2019.117216

Marques, R., & Lourenço, P. B. (2019). Structural behaviour and design rules of confined masonry walls: Review and proposals. *Construction and Building Materials*, *217*, 137–155. https://doi.org/10.1016/j.conbuildmat.2019.04.266

Martini, R., Carvalho, J., Arêde, A., & Varum, H. (2020). Non-destructive Method of the Assessment of Stone Masonry by Artificial Neural Networks. *The Open Construction and Building Technology Journal*, *14*(1), 84–97. https://doi.org/10.2174/1874836802014010084

Martins, R. O. G., Nalon, G. H., Alvarenga, R. D. C. S. S., Pedroti, L. G., & Ribeiro, J. C. L. (2018). Influence of blocks and grout on compressive strength and stiffness of concrete masonry prisms. *Construction and Building Materials*, *182*, 233–241. https://doi.org/10.1016/j.conbuildmat.2018.06.091

Medeiros, W. A., Soriani, M. de O., & Parsekian, G. A. (2020). Innovation in flat-jack application to evaluate modern high-strength hollow concrete block masonry. *Construction and Building Materials*, *255*, 119341. https://doi.org/10.1016/j.conbuildmat.2020.119341

Mishra, M. (2021). Machine learning techniques for structural health monitoring of heritage buildings: A state-of-the-art review and case studies. *Journal of Cultural Heritage*, *47*, 227–245. https://doi.org/10.1016/j.culher.2020.09.005

Mishra, M., Bhatia, A. S., & Maity, D. (2019). Support vector machine for determining the compressive strength of brick-mortar masonry using NDT data fusion (case study: Kharagpur, India). *SN Applied Sciences*, *1*(6), 564. https://doi.org/10.1007/s42452-019-0590-5

Mishra, M., Bhatia, A. S., & Maity, D. (2020). Predicting the compressive strength of unreinforced brick masonry using machine learning techniques validated on a case study of a museum through nondestructive testing. *Journal of Civil Structural Health Monitoring*, *10*(3), 389–403. https://doi.org/10.1007/s13349-020-00391-7

Mohamad, G., Fonseca, F. S., Roman, H. R., Ottoni, T., & Lubeck, A. (2020). Determination of Ritter constant for hollow clay prisms under compression. In *Brick and Block Masonry - From Historical to Sustainable Masonry* (pp. 860–865). CRC Press. https://doi.org/10.1201/9781003098508-122

Mohamad, G., Fonseca, F. S., Vermeltfoort, A. T., & Lubeck, A. (2018). Stiffness plasticity degradation of masonry mortar under compression: preliminar results. *Revista IBRACON de Estruturas e Materiais*, *11*(2), 279–295. https://doi.org/10.1590/s1983-41952018000200004

Mohamad, G., Fonseca, F. S., Vermeltfoort, A. T., Martens, D. R. W., & Lourenço, P. B. (2017). Strength, behavior, and failure mode of hollow concrete masonry constructed with mortars of different strengths. *Construction and Building Materials*, *134*, 489–496. https://doi.org/10.1016/j.conbuildmat.2016.12.112

Mohamad, G., Lourenço, P. B., & Roman, H. R. (2007). Mechanics of hollow concrete block masonry prisms under compression: Review and prospects. *Cement and Concrete Composites*, *29*(3), 181–192. https://doi.org/10.1016/j.cemconcomp.2006.11.003

Mohammed Rawoof, F., Santhi, M., & Ponraj, C. (2015). Beneficial Influence of Nano ZrO2 in Brick Masonry Construction. *International Journal of Applied Engineering Research*, *10*(27), 21638–21642.

MSJC. (2016). *TMS402/ACI530/ASCE5: Building Code Requirements and Specification for Masonry Structures* (p. 389).

Müller, D., & Graubner, C.-A. (2021). Assessment of Masonry Compressive Strength in Existing Structures Using a Bayesian Method. *ASCE-ASME Journal of Risk and*

Uncertainty in Engineering Systems, Part A: Civil Engineering, *7*(1), 04020057. https://doi.org/10.1061/AJRUA6.0001113

Nalon, G. H., Martins, R. O. G., Alvarenga, R. de C. S. S., Lima, G. E. S. de, Pedroti, L. G., & Santos, W. J. dos. (2018). Effect of Specimens' Shape and Size on the Determination of Compressive Strength and Deformability of Cement-lime Mortars. *Materials Research*. https://doi.org/10.1590/1980-5373-mr-2016-1006

Nalon, G. H., Santos, C. F. R., Pedroti, L. G., Ribeiro, J. C. L., Veríssimo, G. de S., & Ferreira, F. A. (2020). Strength and failure mechanisms of masonry prisms under compression, flexure and shear: Components' mechanical properties as design constraints. *Journal of Building Engineering*, *28*, 101038. https://doi.org/10.1016/j.jobe.2019.101038

Nalon, G., Ribeiro, J., Araújo, E., Pedroti, L., Carvalho, J., Santos, R., & Aparecido-Ferreira, A. (2020). Effects of different kinds of carbon black nanoparticles on the piezoresistive and mechanical properties of cement-based composites. *Journal of Building Engineering*, *32*, 101724. https://doi.org/10.1016/j.jobe.2020.101724

Nascimento, M. R., Roman, H. R., & Fonseca, F. S. (2019). Testing and analysis of masonry hollow clay block prisms filled with mortar. *International Journal of Masonry Research and Innovation*, *4*(4), 312. https://doi.org/10.1504/IJMRI.2019.102537

Neville, A. (2011). *Properties of concrete* (Pearson, Ed.; 5th Ed.).

Nwofor, T., & Sule, S. (2012). A mathematical model for the prediction of optimum mortar joint thickness in brick-mortar couplet. *Advances in Applied Science Research*, *3*, 1767–1771.

Oliveira, A. L., Damiani, P. L., Ribeiro, I. F. R., Souza, R. A., & Calçada, L. M. L. (2012). Ensaio de cravação pneumática de pino para avaliação da resistência à compressão de juntas de assentamento de alvenaria estrutural. Pneumatic pin penetration test to evaluate the compressive strength of mortar bedding on structural masonry (in Portuguese). *Ambiente Construído*, *12*(2), 175–188. https://doi.org/10.1590/S1678-86212012000200012

Ouyang, J., Wu, F., Lü, W., Huang, H., & Zhou, X. (2019). Prediction of compressive stress-strain curves of grouted masonry. *Construction and Building Materials*, *229*, 116826. https://doi.org/10.1016/j.conbuildmat.2019.116826

Padalu, P. K. V. R., & Singh, Y. (2021). Variation in compressive properties of Indian brick masonry and its assessment using empirical models. *Structures*, *33*, 1734–1753. https://doi.org/10.1016/j.istruc.2021.05.063

Papayianni, I., Pachta, V., & Stefanidou, M. (2012). Experimental study of nano-modified lime-based grouts. *World Journal of Engineering*, *9*(6), 501–508. https://doi.org/10.1260/1708-5284.9.6.501

Parajuli, R. R., Furukawa, A., & Gautam, D. (2020). Experimental characterization of monumental brick masonry in Nepal. *Structures*, *28*, 1314–1321. https://doi.org/10.1016/j.istruc.2020.09.065

Parsekian, G. A., Medeiros, W. A., & Sipp, G. (2018). High-rise concrete and clay block masonry building in Brazil. *Mauerwerk*, *22*(4), 260–272. https://doi.org/10.1002/dama.201800010

Parsekian, G., Hamid, A., & Drysdale, G. (2012). *Behavior and design of structural masonry (in Portuguese)*. EdUFSCar.

Parsekian, G., & Soares, M. (2010). *Clay blocks structural masonry - design, execution and control (in Portuguese)* (Telo Melo, Ed.; 1st ed.).

Patterson, R., & Pavía, S. (2012). Influence of loading rate and specimen geometry on lime mortar strength. In Caprani & O'Connor (Ed.), *Bridge and Concrete Research in Ireland (BCRI) Conference* (pp. 361–365).

Pavia, S., & Brennan, O. (2019). Portland Cement-Lime Mortars for Conservation. In *Historic Mortars* (pp. 129–142). Springer International Publishing. https://doi.org/10.1007/978-3-319-91606-4_10

Pelà, L., Roca, P., & Aprile, A. (2018a). Combined In-Situ and Laboratory Minor Destructive Testing of Historical Mortars. *International Journal of Architectural Heritage*, *12*(3), 334–349. https://doi.org/10.1080/15583058.2017.1323247

Pelà, L., Roca, P., & Aprile, A. (2018b). Combined In-Situ and Laboratory Minor Destructive Testing of Historical Mortars. *International Journal of Architectural Heritage*, *12*(3), 334–349. https://doi.org/10.1080/15583058.2017.1323247

Pelà, L., Roca, P., & Benedetti, A. (2015). Mechanical Characterization of Historical Masonry by Core Drilling and Testing of Cylindrical Samples. *International Journal of Architectural Heritage*, 150817093153002. https://doi.org/10.1080/15583058.2015.1077906

Prakash, S. S., Aqhtarudin, M., & Dhara, J. S. (2016). Behaviour of soft brick masonry small assemblies with and without strengthening under compression loading. *Materials and Structures*, *49*(7), 2919–2934. https://doi.org/10.1617/s11527-015-0695-2

Pulatsu, B., Erdogmus, E., Lourenço, P. B., Lemos, J. V., & Hazzard, J. (2020). Discontinuum analysis of the fracture mechanism in masonry prisms and wallettes via discrete element method. *Meccanica*, *55*(3), 505–523. https://doi.org/10.1007/s11012-020-01133-1

Ramalho, M., & Corrêa, M. (2003). *Projeto de edifícios de alvenaria estrutural. Design of Structural Masonry Buildings (in Portuguese)* (Pini, Ed.).

Rao, S., Reddy, B., & Jagadish, K. (1995). Strength characteristics of soil-cement block masonry. *Indian Conc. J.*, *69*, 127–131.

Ravula, M. B., & Subramaniam, K. V. L. (2017). Experimental investigation of compressive failure in masonry brick assemblages made with soft brick. *Materials and Structures*, *50*(1), 19. https://doi.org/10.1617/s11527-016-0926-1

Reddy, B. V. V., Lal, R., & Rao, K. S. N. (2009). Influence of Joint Thickness and Mortar-Block Elastic Properties on the Strength and Stresses Developed in Soil-Cement Block Masonry. *Journal of Materials in Civil Engineering*, *21*(10), 535–542. https://doi.org/10.1061/(ASCE)0899-1561(2009)21:10(535)

Restuccia, L., Lopez, A., Ferro, G. A., Liberatore, D., & Tulliani, J. M. (2018). An investigation of the beneficial effects of adding carbon nanotubes to standard injection grout. *Fatigue & Fracture of Engineering Materials & Structures*, *41*(1), 119–128. https://doi.org/10.1111/ffe.12663

Riveiro, B., DeJong, M. J., & Conde, B. (2016). Automated processing of large point clouds for structural health monitoring of masonry arch bridges. *Automation in Construction*, *72*, 258–268. https://doi.org/10.1016/j.autcon.2016.02.009

Russo, S., Boscato, G., & F., Sciarretta. (2008). Behaviour of a historical masonry structure subjected to fire. *Masonry International*, *21*(1), 1–14.

Sadek, H., & Lissel, S. (2013). Seismic performance of masonry walls with GFRP and Geogrid Bed joint reinforcement. *Construction and Building Materials*, *41*, 977–989. https://doi.org/10.1016/j.conbuildmat.2012.07.005

Saenger, D., & Raupach, M. (2019). Experimental Investigation on Masonry with Textile Reinforcement in Thin Bed Joints. *Key Engineering Materials*, *817*, 404–411. https://doi.org/10.4028/www.scientific.net/KEM.817.404

Sajanthan, K., Balagasan, B., & Sathiparan, N. (2019). Prediction of Compressive Strength of Stabilized Earth Block Masonry. *Advances in Civil Engineering*, *2019*, 1–13. https://doi.org/10.1155/2019/2072430

Sarhat, S. R., & Sherwood, E. G. (2014). The prediction of compressive strength of ungrouted hollow concrete block masonry. *Construction and Building Materials*, *58*, 111–121. https://doi.org/10.1016/j.conbuildmat.2014.01.025

Sarhosis, V., Milani, G., Formisano, A., & Fabbrocino, F. (2018). Evaluation of different approaches for the estimation of the seismic vulnerability of masonry towers. *Bulletin of Earthquake Engineering*, *16*(3), 1511–1545. https://doi.org/10.1007/s10518-017-0258-8

Sathiparan, N., & Rumeshkumar, U. (2018). Effect of moisture condition on mechanical behavior of low strength brick masonry. *Journal of Building Engineering*, *17*, 23–31. https://doi.org/10.1016/j.jobe.2018.01.015

Segura, J., Pelà, L., & Roca, P. (2018a). Monotonic and cyclic testing of clay brick and lime mortar masonry in compression. *Construction and Building Materials*, *193*, 453–466. https://doi.org/10.1016/j.conbuildmat.2018.10.198

Segura, J., Pelà, L., & Roca, P. (2018b). Monotonic and cyclic testing of clay brick and lime mortar masonry in compression. *Construction and Building Materials*, *193*, 453–466. https://doi.org/10.1016/j.conbuildmat.2018.10.198

Shadlou, M., Ahmadi, E., & Kashani, M. M. (2020). Micromechanical modelling of mortar joints and brick-mortar interfaces in masonry Structures: A review of recent developments. *Structures*, *23*, 831–844. https://doi.org/10.1016/j.istruc.2019.12.017

Sharafati, A., Haji Seyed Asadollah, S. B., & Al-Ansari, N. (2021). Application of bagging ensemble model for predicting compressive strength of hollow concrete masonry prism. *Ain Shams Engineering Journal*, *(IN PRESS)*. https://doi.org/10.1016/j.asej.2021.03.028

Shi, T., Zhang, X., Hao, H., & Chen, C. (2021). Experimental and numerical investigation on the compressive properties of interlocking blocks. *Engineering Structures*, *228*, 111561. https://doi.org/10.1016/j.engstruct.2020.111561

Sikora, P., Abd Elrahman, M., & Stephan, D. (2018). The Influence of Nanomaterials on the Thermal Resistance of Cement-Based Composites—A Review. *Nanomaterials*, *8*(7), 465. https://doi.org/10.3390/nano8070465

Sipp, G. (2019). *Avaliação do comportamento de aderência entre blocos cerâmicos e grautes. Evaluation of the bonding behavior between ceramic blocks and grouts (in Portuguese)*. Universidade Federal de São Carlos, São Carlos, Brazil.

Song, M., Yousefianmoghadam, S., Mohammadi, M.-E., Moaveni, B., Stavridis, A., & Wood, R. L. (2018). An application of finite element model updating for damage assessment of a two-story reinforced concrete building and comparison with lidar. *Structural Health Monitoring*, *17*(5), 1129–1150. https://doi.org/10.1177/1475921717737970

Thaickavil, N. N., & Thomas, J. (2018). Behaviour and strength assessment of masonry prisms. *Case Studies in Construction Materials*, *8*, 23–38. https://doi.org/10.1016/j.cscm.2017.12.007

Thamboo, J. (2020). Performance of masonry columns confined with composites under axial compression: A state-of-the-art review. *Construction and Building Materials*, 121791. https://doi.org/10.1016/j.conbuildmat.2020.121791

Thamboo, J. A. (2020). Material characterisation of thin layer mortared clay masonry. *Construction and Building Materials*, *230*, 116932. https://doi.org/10.1016/j.conbuildmat.2019.116932

Thamboo, J. A., & Dhanasekar, M. (2019). Correlation between the performance of solid masonry prisms and wallettes under compression. *Journal of Building Engineering*, *22*, 429–438. https://doi.org/10.1016/j.jobe.2019.01.007

Thamboo, J., Dhanasekar, M., & Yan, C. (2013). Effects of joint thickness, adhesion and web shells to the face shell bedded concrete masonry loaded in compression. *Australian Journal of Structural Engineering*, *14*(3). https://doi.org/10.7158/S12-035.2013.14.3

Tian, Z., Li, Y., Zheng, J., & Wang, S. (2019). A state-of-the-art on self-sensing concrete: Materials, fabrication and properties. *Composites Part B: Engineering*, *177*, 107437. https://doi.org/10.1016/j.compositesb.2019.107437

Ubertini, F., D'Alessandro, A., Materazzi, A., Laflamme, S., & Downey, A. (2017). Novel nanocomposite clay brick for strain sensing in structural masonry. *2017 IEEE International Conference on Environment and Electrical Engineering and 2017 IEEE Industrial and Commercial Power Systems Europe (EEEIC / I&CPS Europe)*, 1–4. https://doi.org/10.1109/EEEIC.2017.7977598

Valluzzi, M. R., Binda, L., & Modena, C. (2005). Mechanical behaviour of historic masonry structures strengthened by bed joints structural repointing. *Construction and Building Materials*, *19*(1), 63–73. https://doi.org/10.1016/j.conbuildmat.2004.04.036

Vasanelli, E., Micelli, F., Colangiuli, D., Calia, A., & Aiello, M. A. (2020). A non destructive testing method for masonry by using UPV and cross validation procedure. *Materials and Structures*, *53*(6), 134. https://doi.org/10.1617/s11527-020-01568-8

Wu, Y., Li, S., & Wang, D. (2019). Characteristic analysis of acoustic emission signals of masonry specimens under uniaxial compression test. *Construction and Building Materials*, *196*, 637–648. https://doi.org/10.1016/j.conbuildmat.2018.11.148

Yang, K.-H., Lee, Y., & Hwang, Y.-H. (2019). A Stress-Strain Model for Brick Prism under Uniaxial Compression. *Advances in Civil Engineering*, 1–10. https://doi.org/10.1155/2019/7682575

Zahra, T., & Dhanasekar, M. (2016). Prediction of masonry compressive behaviour using a damage mechanics inspired modelling method. *Construction and Building Materials*, *109*, 128–138. https://doi.org/10.1016/j.conbuildmat.2016.01.048

Zahra, T., Thamboo, J., & Asad, M. (2021). Compressive strength and deformation characteristics of concrete block masonry made with different mortars, blocks and mortar beddings types. *Journal of Building Engineering*, *38*, 102213. https://doi.org/10.1016/j.jobe.2021.102213

Zahra, T., Thamboo, J., Asad, M., & Song, M. (2021). Experimental investigation on the effectiveness of lateral restrainers to the vertical steel in reinforced masonry walls under axial compression. *Construction and Building Materials*, *297*, 123790. https://doi.org/10.1016/j.conbuildmat.2021.123790

Zhou, Q., Wang, F., Zhu, F., & Yang, X. (2017). Stress–strain model for hollow concrete block masonry under uniaxial compression. *Materials and Structures*, *50*(2), 106. https://doi.org/10.1617/s11527-016-0975-5

Zohreh Heydariha, J., Das, S., & Banting, B. (2017). Effect of grout strength and block size on the performance of masonry beam. *Construction and Building Materials*, *157*, 685–693. https://doi.org/10.1016/j.conbuildmat.2017.09.130

3 REVIEW OF RECENT PROGRESS ON THE EFFECTS OF HIGH TEMPERATURES ON THE MECHANICAL BEHAVIOR OF MASONRY PRISMS

This chapter has been published as the following paper: Nalon, G. H.; Ribeiro, J. C. L.; Pedroti, L. G.; Silva, R. M.; Araújo, E. N. D.; Santos, R. F.; Lima, G. E. S. Review of recent progress on the effects of high temperatures on the mechanical behavior of masonry prisms. ***Infrastructures*** *8 (2023) 112. https://doi.org/10.3390/infrastructures8070112*

Abstract: *The structural performance of civil structures exposed to elevated temperatures has been investigated in many recent works. Some of these studies evaluated the residual mechanical behavior of masonry prisms subjected to high temperatures, as these specimens are simplified models (2–5 units in height) that can be easily produced and tested, in terms of operational and economic factors. However, there is no previous literature review on the mechanical properties of fire-damaged masonry prisms. Therefore, this chapter presents an investigation of the current state-of-the-art on this topic. It provided a careful review of the recent knowledge on the failure mechanisms, residual compressive strength, modulus of elasticity, and stress-strain behavior of masonry prisms made with different types of units, mortars and/or grout, after exposure to different types of thermal treatments. Based on the revised information, future research directions on the scientific field of masonry structures were reported.*

Keywords: *Masonry prisms, mechanical performance, fire.*

3.1. INTRODUCTION

The high complexity of the structural behavior of masonry elements is significantly increased when they are exposed to high temperatures. The combination between mechanical behavior of fire-damaged units and mortars governs the overall performance of masonry elements under fire conditions (Bosnjak et al., 2020; Medeiros et al., 2021). The importance of studying the effects of fire on structural elements is justified by the fact that high temperatures change the physical, chemical and mechanical properties of the materials,

leading to possible strength/stiffness losses and building collapse risks (Neves et al., 2022; Pires et al., 2018; Rodrigues and Moreno Júnior, 2017).

Since the masonry elements are mainly subjected to compressive loads, the determination of the compressive behavior of fire-damaged masonry provides a valuable dataset for the development of strategies for preservation of human lives and structural diagnosis of masonry structures. Based on the residual strength and stiffness of fire-damaged structures, the engineers can check their loadbearing capacity and decide whether they can be repaired for reuse or not (Cho et al., 2017; Ha et al., 2016; Nalon et al., 2021).

Some studies on the effects of high temperatures on masonry structures have been developed over the last decades and reviewed by some authors (Russo and Sciarretta, 2013; Torregrosa and Diez, 2015; Yassin et al., 2018). Other works have focused on investigations of masonry components (e.g., units, mortar and grout) exposed to elevated temperatures (Bamonte et al., 2021; Fernandes Neto et al., 2022; Leal et al., 2022; Medeiros et al., 2022, 2023; Sciarretta et al., 2021; Yassin et al., 2020). Despite this, scarce information is still available to provide quantitative data regarding the effects of fire on the structural performance of masonry elements.

The post-fire behavior of masonry elements has been rarely investigated due to the peculiarities of masonry as a composite material, high variability of geometry and type of masonry components, and high complexity of testing programs (Bošnjak et al., 2020; Russo and Sciarretta, 2013). Fire tests of walls and small walls are expensive and time consuming, require complex equipment and must be developed by qualified personnel with appropriate training. The lack of standard test methods and reliable equipment have led to a large scatter of thermal and mechanical results of masonry components (Daware and Naser, 2021). To solve some of these issues, fire tests of masonry prisms have been carried out due to operational and economic benefits provided by these simple types of specimens.

The mechanical behavior of masonry prisms can simulate many important mechanisms that characterize the complex structural behavior of full-scale masonry elements. They are simplified models (2–5 units in height) that can be easily produced and tested (Nalon et al., 2020; Parsekian et al., 2012; Thaickavil and Thomas, 2018). Although many review papers have already revised the behavior of masonry walls under fire conditions (Daware and Naser, 2021; Ismaiel et al., 2022; Russo and Sciarretta, 2013; Sciarretta et al., 2021; Torregrosa and Diez, 2015; Yassin et al., 2020), there is no previous review focused on reviewing the residual compressive behavior of masonry prisms after exposure to elevated temperatures. To bridge

this knowledge gap, the present work revised the current state-of-the-art on this topic, summarizing results of residual compressive strength, static elastic modulus, stress-strain curves, and failure modes of masonry prisms made with different types of units, mortars and/or grout, after exposure to different types of thermal treatments.

The present chapter provided important contributions for the area of design, diagnosis, and maintenance of masonry structures subjected to fire events, such as the (i) evaluation and comparison of the post-fire performance of masonry prisms produced with different types of masonry components (e.g., clay bricks, solid calcium silicate bricks, concrete blocks, cement mortar, lime mortar, pre-blended mortar, cement-lime mortar, conventional grout, etc.); (ii) recommendations for improvement of masonry design codes, based on the effects of the mutual dependency of different variables that affect the post-fire behavior of masonry prisms (e.g., maximum exposure temperature, type of unit or mortar, specimens rendering type, cooling method, etc.); (iii) compilation of new test methods and masonry components investigated in recent research dealing with masonry prisms exposed to elevated temperatures; (iv) recommendations for practical application of fire tests of masonry prisms as cost-effective alternatives for estimation of the residual mechanical performance of fire-damaged masonry; and (v) recommendations of future research in this scientific field.

This chapter was structured in four sections, as indicated in Figure 1. Section 3.1 presents the introduction of the chapter, which covers the research context and the original contributions of this work. Section 3.2 presents the literature review about the effects of high temperatures on the failure mode, strength and stiffness of masonry prisms. Section 3.3 summarizes the conclusions obtained from the content revised in this chapter. Finally, Section 3.4 shows the limitations and recommendations for future works.

3.2. EFFECTS OF HIGH TEMPERATURES ON MASONRY PRISMS

This section presents a literature review about the effects of high temperatures on the compressive behavior of masonry prisms. To ensure the reliability and accuracy of the content of this review work, only research papers, dissertations and thesis with high standards of critical appraisal were revised. Research was made using reliable search engines (Scopus, Google Scholar, and Periódicos CAPES). Various combinations of keywords were investigated in each database. Keywords related to the structural masonry field (e.g., masonry, masonry prisms, masonry wallettes, masonry walls) were combined to keywords

often used in studies dealing with structural fire performance (e.g., fire, high temperatures, elevated temperatures). After a careful reading, the relevant studies (experimental works of fire-damaged masonry prisms) were selected, important information was extracted for review and Table 1 was constructed to summarize the main findings of the present review.

Figure 1 - Structure diagram of the present literature review chapter ($f_{b,net}$ is the net area compressive strength of the units, $f_{m,cub}$ is the compressive strength of the mortar and $f_{g,cyl}$ is the compressive strength of the grout).

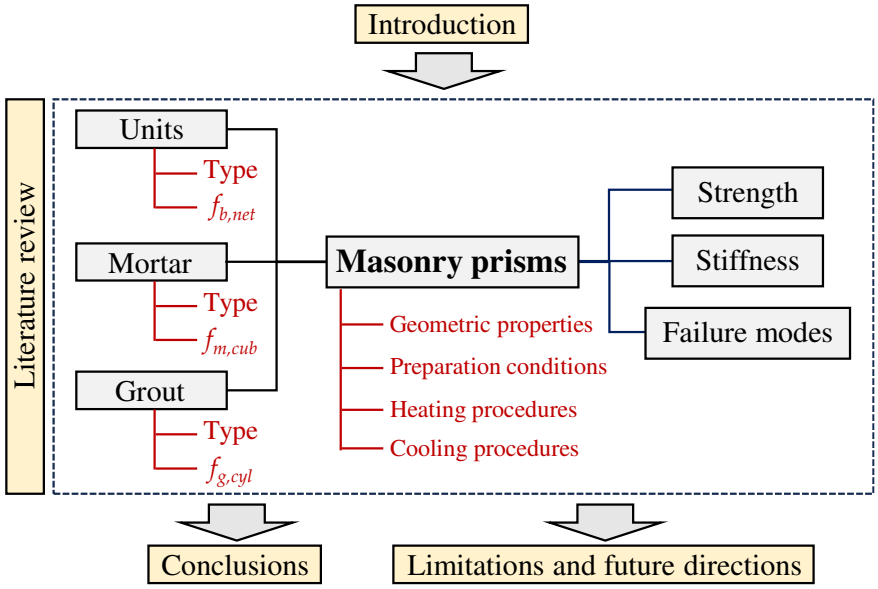

Source: Author (2024).

It is important to highlight that the previous research on the compressive behavior of masonry prisms exposed to elevated temperatures is still limited. Great efforts were made to select relevant references for the present review, avoiding the lack of transparency and scientific evidence in the revised studies. Another limitation of the review process was the lack of presentation of some methodological details in some papers, such as standard deviation (SD) values, heating rate used in fire tests, and prism capping procedures. Consequently, it was not able to present some of these results in Table 1. Since the authors of some papers did not provide the ratio between net and gross area of the blocks, it was estimated as 0.50 (Ramalho and Corrêa, 2003), for estimation of the net area strength of hollow masonry blocks and prisms. Other limitation that must be highlighted is the use of different types of specimens for determination of mortar compressive strength. When cylindrical specimens were used for mortar characterization, a cube/cylinder strength ratio equal to 1.25 (Neville, 2011) was applied as a correction factor.

Table 1 - Previous investigations of residual compressive behavior of fire-damaged masonry prisms

Authors	Units [a]			Mortar		Grout		Prisms								
	Type	Length x width x height (mm)	$f_{b,net}$ [b,c] (MPa)	Material	$f_{m,cub}$ [c,d] (MPa)	Material	$f_{g,cyl}$ [c,e] (MPa)	Rendering	Joint thickness (mm)	Heating rate (ºC/min)	Time at maximum temperature (h)	Maximum exposure temperature (ºC)	Cooling method	Mechanical properties of prisms studied by the authors of the paper	Capping of prisms after fire and before mechanical tests
Gao et al. (2023)	Solid clay brick	240 x 115 x 53	16.32 (0.47)	Cement mortar	29.38 (0.73)	-	-	Various reinforced layer types [f] (15 mm)	10	16	2	200; 400; 600	Natural cooling	f_c, load-displacement curves	Quick-hardening cement layer (3 mm)
Kiran et al. (2022)	Solid clay brick	255 x 100 x 100	7.85 (SD was not presented)	Cement mortar	13.65 (SD was not presented)	-	-	Manu-factured sand, vermiculite or perlite mortar (20 mm)	10	Standard ISO 834-1 (1999) curve (30; 60; 90; 120 min)			Natural cooling (outside the oven)	f_c, E_s, stress-strain curves	Gypsum plaster (10 mm) and plywood sheets (20 mm)
Leal et al. (2021)	Hollow concrete blocks	390 x 140 x 190	7.7 (SD was not presented)	Cement-lime mortar	6.13 (SD was not presented)	-	-	-	10	Standard ISO 834-1 (1999) curve (70 min)			Natural cooling (inside the oven)	f_c (tests at 7 days after fire)	Mineral fiber capping board (20 mm)
Bošnjak et al. (2019, 2020)	Solid clay brick / Solid calcium silicate brick	240 x 115 x 71	32.6 (SD was not presented) / 28.3 (SD was not presented)	Cement mortar	23.4-25.9 (SD was not presented) / 25.9-27.5 (SD was not presented)	-	-	-	10	2	2	100-1100	Natural cooling (inside the oven)	f_c, E_s, stress-strain curves	Without capping (bricks' surface polished before heating)

Neto (2020)	Hollow clay blocks	290 x 140 x 190	24.3 (3.5); 27.9 (5.5)	Cement-lime mortar	4.38 (0.9)	-	-	-	10	Standard ISO 834-1 (1999) curve (120 min)			Fan cooling	f_c, E_s, stress-strain curves	Mineral fiber capping board
Bitten-court and Antunes (2019)	Hollow clay blocks	290 x 140 x 190	14.9 (3.6)	Not reported	11.4 (0.5)	Conven-tional grout	67.7 (23.2)	-	-	3	0.5	300; 600; 900	Natural cooling (inside the oven)	f_c	Not reported
Dupim (2019)	Hollow concrete blocks	290 x 140 x 190	42.2 (2.4); 14.3 (1.2)	Cement-lime mortar	11.5 (1.0)	-	-	Gypsum plaster layer (5 mm)	10	Standard ISO 834-1 (1999) curve (70; 120 min)			Fan cooling	f_c	Mineral fiber capping board
		290 x 190 x 190	38.1 (2.0); 11.6 (0.8)												
Zhang et al. (2019)	Perfora-ted clay brick	240 x 115 x 90	12.9 (0.3)	Cement-lime mortar	2.5 (0.2); 5.6 (0.3); 10.0 (0.1)	-	-	-	15	Standard ISO 834-1 (1999) curve (90; 150 min)			Air cooling (opened oven door if < 400 ºC); water cooling	f_c, stress-strain curve	Not reported
Rigão (2012)	Hollow clay blocks	290 x 140 x 190	11.5 (1.1)	Pre-blended mortar	4 (SD was not presented)	-	-	-	-	-	0.5	400; 900	Natural cooling (inside the oven)	f_c	Not reported
Russo et al. (2008)	Solid clay brick	Around 60 x 60 x 60	11.4-39.2 (SD was not presented)	Lime mortar	3.0-31.5 (SD was not presented) [g]	-	-	-	-	Real fire event in a historic brick masonry structure in Venice, 2003				f_c, E_s, stress-strain curves	Not reported

Notes: [a] Masonry unit: preformed component used in masonry construction (EN 1996 1-1, 2005). [b] $f_{b,net}$ is the average value of the net area compressive strength of the masonry units. [c] Standard deviation (SD) values (in MPa) were provided in parentheses. [d] $f_{m,cub}$ is the average value of the compressive strength of the mortar obtained from equivalent cubic specimens. [e] $f_{g,cyl}$ is the average value of the compressive strength of grout obtained from cylindrical specimens. [f] Reinforced layer types: PVA (polyvinyl alcohol) fibers, mixed PVA/basalt fibers reinforced layer, mixed PVA/steel fibers reinforced layer, and ordinary plaster mortar. [g] Predictions of mortar compressive strength, based on non-destructive tests with energy dissipation penetrometer.

Source: Author (2024)

Different characteristics (e.g., material type, length, width, height, strength, etc.) of masonry units, mortar, grout, and prisms used in previous works dealing with this topic (Bittencourt and Antunes, 2019; Bosnjak et al., 2019, 2020; Dupim, 2019; Kiran et al., 2022; Leal et al., 2021; Neto, 2020; Rigão, 2012; Russo et al., 2008; Zhang et al., 2019) are displayed in Table 1. The residual compressive behavior of prisms exposed to high temperatures was mainly investigated in these experimental studies based on their residual stress-strain relationships, failure mechanisms, residual compressive strength (f_c), and residual static elastic modulus (E_s).

Different methodologies were used to test the masonry prisms at high temperatures. In some studies (Dupim, 2019; Kiran et al., 2022; Leal et al., 2021; Neto, 2020; Zhang et al., 2019), they were exposed to a standard temperature increase defined by the ISO 834-1:1999 fire curve (ISO, 1999), which is represented in Figure 2a and Equation (1). In this formulation, θ_g is the gas temperature in the fire compartment, θ_0 is the initial room temperature, and t is the time of the heating process. In other works (Bittencourt and Antunes, 2019; Bosnjak et al., 2019, 2020; Rigão, 2012), the masonry prisms were subjected to a heating ramp (constant heating rate) up to a maximum temperature, as indicated in Figure 2b. After reaching the maximum test temperature, it was maintained for a period of 0.5-2 h (Table 1). Table 1 shows that different maximum temperatures levels have been used to cause severe damage conditions to masonry prisms: 900 ºC (Bittencourt and Antunes, 2019; Rigão, 2012), 1100 ºC (Bosnjak et al., 2019, 2020), or application of the ISO 834-1:1999 fire curve (ISO, 1999) up to ~970 ºC (Leal et al., 2021), ~1050 ºC (Dupim, 2019; Kiran et al., 2022; Neto, 2020), or ~1080 ºC (Zhang et al., 2019).

Figure 2 - Temperature versus time curves used in different methods for tests of masonry prisms.

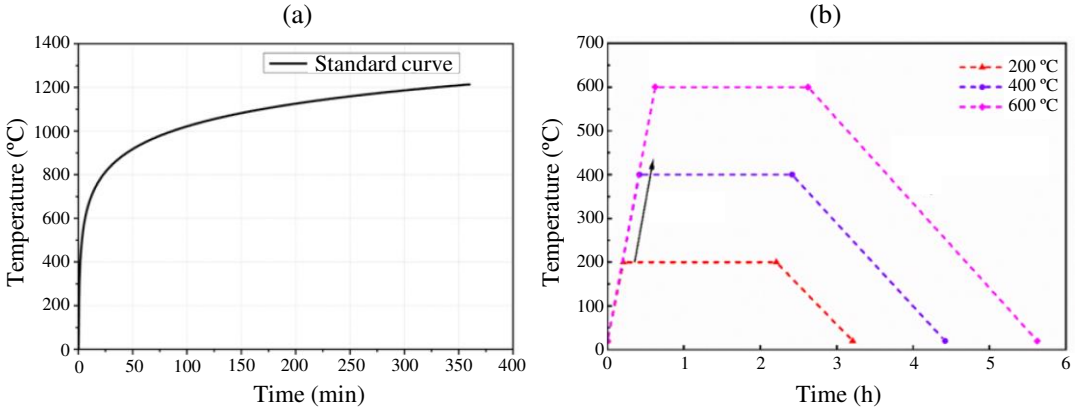

Source: (a) and (b) adapted from Gao et al. (2023) Copyright 2023, with permission from Springer.

$$\theta_g = \theta_0 + 345 \log (8t + 1) \qquad \text{Equation (1)}$$

In addition, Table 1 shows that different types of cooling methods have been applied to masonry prisms, such as natural cooling inside the furnace, natural cooling outside the furnace, fan cooling, and water cooling. The effects of these different methodologies on the residual mechanical behavior of the specimens are discussed in the following sections.

In most of the cases, the fire tests of masonry prisms were carried out in computer-controlled electrical furnaces, as indicated in the experimental setup of Gao et al. (2023) of Figure 3a. In modern experimental programs, masonry prisms were also subjected to heating/cooling procedures in gas furnaces with high heating capacity. For example, Figure 3b shows the gas furnace used by Leal et al. (2021) to heat masonry prisms and small walls.

Figure 3 - Equipment used in tests of prims exposed to high temperatures.

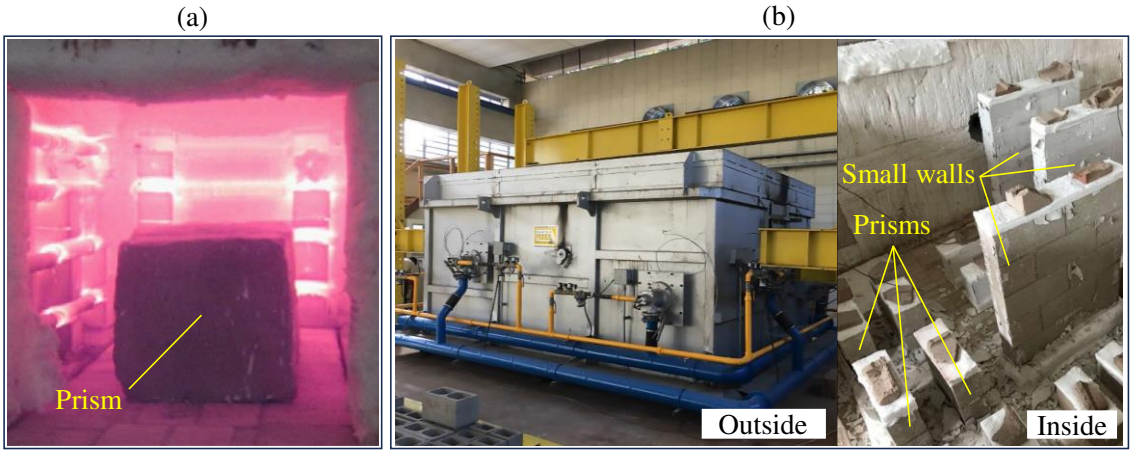

Source: (a) adapted from Kiran et al. (2022), Copyright 2022, with permission from Wiley Company; (b) adapted from Leal et al. (2022; 2021) as permitted under the Creative Commons Attribution License Agreement.

3.2.1. Failure mechanisms of prisms exposed to high temperatures

Bošnjak et al. (2019, 2020) reported an experimental evaluation of ungrouted prisms fabricated with solid clay and calcium silicate units, after exposure to temperatures up to 1100 ºC and slow cooling. The failure mode of fire-damaged prisms made with clay bricks (Figure 4a) and calcium silicate bricks (Figure 4f and Figure 4g) was governed by the mortar joint. It happened because the mortar was the least stiff and weakest component of the prisms, regardless of the type of unit (Table 1). At first, the joint was compressed by the units, leading to increased deformation in the mortar joint. Consequently, high transversal tensile stresses happened in both types of bricks, so that they failed after propagation of vertical cracks.

Figure 4 - Failure mechanisms of masonry prisms subjected to different exposure temperature levels (T_{max}).

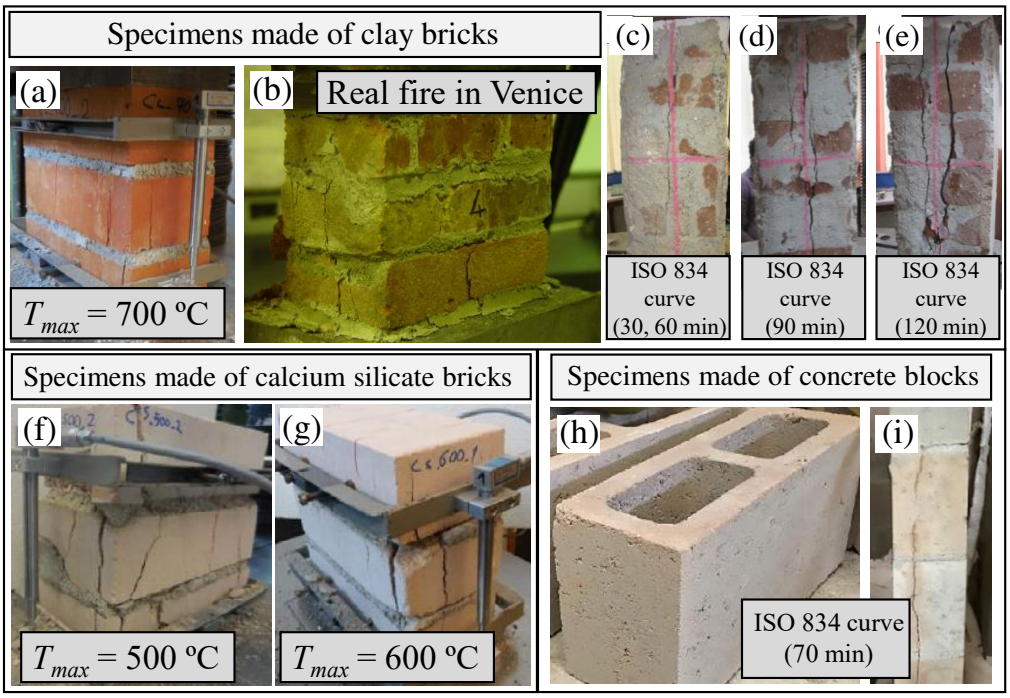

Source: (a), (f) and (g) adapted from Bošnjak et al. (2020), Copyright 2020, with permission from Elsevier; (b) adapted from Russo et al. (2008) with permission from the International Masonry Society; (c), (d), (e) adapted from Kiran et al. (2022), Copyright 2022, with permission from Wiley Company; (h) and (i) adapted from Leal et al. (2021), as permitted under the Creative Commons Attribution License Agreement.

The exposure to high temperatures increased the difference in the stiffness of bricks and mortar, especially for clay brick prisms. This increase may be attributed to the significant thermal degradation of the mortar joint (physical and chemical changes happened in the hydrated cement paste, aggregates, and interfacial transition zone) and minor damage in clay and calcium silicate units after exposure to high temperatures. After exposure to 500 ºC, crushing of mortar joints was visible in the outer portions of the prisms. The significant degradation of the mortar joint caused significant losses of compressive strength and modulus of elasticity with increasing temperature, which are discussed in the next section.

Masonry prisms produced with fire-damaged clay bricks were tested by Russo et al. (2008). The authors constructed these prisms with fire-damaged units collected from a historic brick masonry structure in Venice after a fire event. The typical collapse of the prisms is reproduced in Figure 4b. Localized spalling of mortar joints and vertical cracks in the clay bricks can be observed in this image, as also reported by Bošnjak et al. (2019, 2020).

Kiran et al. (2022) investigated the post-fire behavior of clay brick prisms. After exposure to the ISO 834-1:1999 standard fire curve (ISO, 1999) for different periods (30, 60, 90, or 120 min), the prisms plastering portion was chipped-off, in order to observe existing

crack patterns. In specimens subjected to 30 or 60 min exposure (Figure 4c), cracking was only visible at the point of the ultimate compressive load. In prisms subjected to 90 min exposure (Figure 4d), most cracks were developed at the brick/mortar interface, at 70-85% of the prism compressive strength. In these prisms, the final failure was observed at the mortar joints. After a 120 min exposure (Figure 4e), vertical cracks close to the vertical joints were visible at the loading stage, due to the de-bonding at the weak brick-mortar interface.

The rupture modes of ungrouted prisms made of hollow clay blocks were investigated by Rigão (2012). Prisms that were not exposed to high temperatures and prisms exposed to 400 ºC failed by transverse block splitting. In contrast, mortar crushing was observed in prisms exposed to 900 ºC. These results evidence that the significant degradation of the joints at higher temperatures was able to change the masonry rupture mechanisms. Therefore, the failure mode of clay masonry prisms was remarkably affected by the thermal treatments.

Failure mode modifications due to increased exposure temperature were also verified by Zhang et al. (2019) in clay brick prisms exposed to different times of exposure of the ISO 834-1:1999 standard fire curve (ISO, 1999). According to the authors, the first crack appeared at 65-75%, 30-40%, and 15-20% of the failure load in specimens subjected to 0, 90 and 150 min of standard fire exposure, respectively. These authors also reported the first experimental investigation of the effects of different cooling methods (air cooling vs. water cooling) on the failure mode of masonry prisms. As previously observed in plain concrete specimens subjected to fast cooling procedures, the thermal shock associated with the application of the water-cooling method generated tensile stresses in the bricks, resulting in severe crack and permanent deformation in the center of the specimens.

The application of a reinforced layer to the surface of masonry prisms also changed their failure mechanisms. According to the recent work developed by Gao et al. (2023), the different types of reinforced layers (PVA fibers reinforced layer, mixed PVA/basalt fibers reinforced layer, mixed PVA/steel fibers reinforced layer, and ordinary plaster mortar) delayed the failure of the internal clay-brick structure. Prisms produced with the PVA/steel fibers reinforced layer presented the lower amount of cracks after exposure to 200 ºC. After 400 °C and 600 °C, the brittleness and the damage of the different types of specimens increased significantly. The use of steel fibers improved the bonding performance between the reinforced layer and the masonry prism.

Leal et al. (2021) recently compared the compressive behavior of masonry blocks, prisms and small walls after exposure to high temperatures. These different types of

specimens were subjected of the ISO 834-1:1999 (ISO, 1999) standard fire for 70 min. Differently from the minor thermal damage observed in clay and calcium silicate units previously mentioned in this section, Leal et al. (2021) observed that fire-damage concrete blocks showed superficial cracks (Figure 4h) and noticeable degradation, so that some units could be easily broken when handled after fire exposure. A similar cracking pattern was observed in masonry prisms and small walls, which was mainly characterized by the formation of vertical cracks at the unit's webs (Figure 4). Localized mortar crushing and spalling of block portions were observed by Dupim (2019), in masonry prisms produced with hollow concrete blocks and subjected to the ISO 834-1:1999 standard fire curve (ISO, 1999) for 70 min.

3.2.2. Strength and stiffness of prisms exposed to high temperatures

Experimental results of the compression tests carried out by Bošnjak et al. (2019, 2020) indicated that the compressive strength of masonry prisms made with solid clay or calcium silicate units remained at least the same as the original compressive strength (before heating) up to temperature levels of 700 °C, which shows the excellent fire resistance of masonry produced with clay and calcium silicate bricks. For temperature levels higher than 700 °C, clay brick prisms presented strength reductions up to 22%, while strength reductions higher than 55% were observed in calcium silicate prisms. In contrast, stiffness reductions higher than 50% were observed in both types of prisms when the maximum exposure temperature was higher than 600 ºC. The residual stiffness of the prisms reduced progressively with the increase in the maximum temperature, mainly for temperatures higher than 300 ºC, due to the strong thermal degradation of the cement mortar joint of the prisms.

Kiran et al. (2022) evaluated the residual mechanical performance of clay brick prisms plastered with the different lightweight mortars indicated in Table 1 (manufactured sand mortar, vermiculite mortar, or perlite mortar), after exposure to 30, 60, 90, or 120 min of the ISO 834-1:1999 standard fire curve (ISO, 1999). Reference prisms (without plaster) could not resist exposure temperatures periods ≥ 60 min. In contrast, interesting residual values of strength and stiffness were observed in specimens plastered with lightweight mortars. Prisms plastered with perlite mortar had better fire resistance, since they did not present strength reductions when subjected to any heating duration. After 120 min of fire exposure, prisms with vermiculite plaster and perlite plaster presented values of axial compressive strength 31.6% and 86.1% higher than that of prisms with sand plaster, respectively. After the same

thermal treatment, prisms with perlite, vermiculite, and sand mortar presented elastic modulus losses of 15%, 25%, and 60%, respectively. These results indicated that lightweight minerals such as vermiculite and perlite behaved like sacrificial materials that can provide an adequate thermal protection to clay brick masonry.

A trend of compressive strength decreases with temperature increases was observed by Russo et al. (2008) in masonry prisms produced with fire-damaged clay bricks resulted from a real fire event in Venice. The joints of these prisms were made with mortar with mechanical properties close to those obtained from in-situ non-destructive tests with an energy dissipation penetrometer. The compressive strength of these prisms was about 39% lower than that of reference prisms produced with units and mortar that were not exposed to high temperatures. In contrast, stress-strain curves revealed that reference prisms presented greater deformability than the fire-damage prisms, which is not in agreement with the results of Bošnjak et al. (2019, 2020). Based on micro-destructive tests with flat jacks carried out in the field, the authors observed that the production of mortar in laboratory to simulate fire-damage conditions can be the cause of those unexpected stiffness results.

The effects of different cooling methods on the residual compressive strength of clay brick prisms exposed to 90 min of the ISO 834-1:1999 standard fire curve (ISO, 1999) were reported by Zhang et al. (2019). Water-cooled masonry prisms presented a compressive strength loss 10% greater than that of the air-cooled prisms. This result was attributed to the sudden drop in temperature associated with the water-cooling process, which resulted in cracks in units and mortar joints, reducing the load-bearing capacity of the specimens.

The residual mechanical properties of ungrouted prisms produced with hollow clay blocks were studied by Rigão (2012). The residual strengths of clay block prisms exposed to 400 ºC and 900 ºC were 73.0% and 48.7% of their original compressive strength (before the heating treatments), respectively. The different strength losses observed by the authors are attributed to the changes in the rupture mode from tensile block splitting to mortar crushing, as discussed in the previous section.

Neto (2020) evaluated the residual mechanical properties of ungrouted prisms constructed with hollow clay blocks. However, they were subjected to the ISO 834-1:1999 standard fire curve (ISO, 1999) for 120 min. After being exposed to temperatures higher than 900 ºC, the prisms exhibited reductions in compressive strength and elastic modulus up to 93.5% and 98.5%, respectively. Comparisons between the results of Neto (2020), Rigão

(2012), and Bošnjak et al. (2019, 2020) suggest that prisms made with hollow clay blocks seem to be more affected by the fire exposure than prisms constructed with solid clay bricks.

The residual compressive strength of hollow clay blocks filled with conventional grout was recently investigated by Bittencourt and Antunes (2019). Considering a 5% significance level, no statistical difference was observed between the original strength of the grouted prisms and their residual strength after exposure to 300 ºC, 600 ºC, and 900 ºC. Although deleterious effects on the grout/unit adherence and decreases in grout strength were observed since the exposure to 300 ºC, the high thermal resistance of hollow clay units provided excellent residual mechanical properties to the masonry prisms.

All types of reinforced layers (PVA fibers reinforced layer, mixed PVA/basalt fibers reinforced layer, mixed PVA/steel fibers reinforced layer and ordinary plaster mortar) investigated by Gao et al. (2023) also increased the residual compressive strength of clay brick prisms exposed to temperatures of 200 ºC, 400 ºC or 600 ºC. The best residual strength improvements were provided by the PVA/steel fibers reinforced layer. In addition, the load-displacement curves obtained from compression tests of these specimens revealed that the specimens with fiber-reinforced layers presented the highest initial residual stiffness after exposure to 200 ºC or 400 ºC. On the other hand, prisms covered with ordinary plaster mortar exhibited the largest initial stiffness after exposure to 600 ºC.

Dupim (2019) carried out an experimental program that investigated the residual compressive strength of prisms made with hollow concrete blocks. After exposure to the ISO 834-1:1999 standard fire curve (ISO, 1999) for 70 min, their compressive strength was only 14% of their original compressive strength, since both concrete and mortar joints presented significant degradation due to the exposure to elevated temperatures. Other prisms were covered with a 5 mm plaster layer and then exposed to the ISO 834-1:1999 standard fire curve (ISO, 1999) for 120 min. They presented residual compressive strength values ranging between 6% and 9% of their initial compressive strength. Comparisons between the results of Dupim (2019) and Neto (2020) indicated that prisms made with hollow concrete blocks were more affected by the fire exposure than prisms constructed with hollow clay blocks.

Values of compressive strength of masonry prisms and small walls of hollow concrete blocks, after exposure for 70 min to the ISO 834-1:1999 curve (ISO, 1999), were recently compared by Leal et al. (2021). The fire-damaged prisms and small walls yielded a compressive strength of approximately 14% of their initial strength. According to the authors, these results suggest that using simpler specimens (such as stack-bond prisms) can provide

satisfactory results in the evaluation of the residual masonry compressive strength, considering slenderness effects separately. Since prisms are specimens easier to construct and test, the results of Leal et al. (2021) indicate that prisms are promising candidates for future experimental analyses of masonry exposed to elevated temperatures.

3.3. CONCLUSIONS

This study reviews the effects of high temperature exposure on the compressive behavior of masonry prisms, which is an important topic in the research field of resilient civil structures. The following conclusions were obtained from the content re-vised in this study:

(1) The exposure to high temperatures can cause remarkable changes in the failure mode of prisms produced with clay or calcium silicate units, due to increases in the difference between the residual stiffness of the units and the mortar. This increase has been attributed to the significant thermal degradation of the joint compared to the units, so that a premature crushing of the fire-damaged mortar joint was usually observed.

(2) The effects of fire on the failure mode of concrete block prisms were less remarkable compared to those verified in prisms produced with clay or calcium silicate units. In concrete block prisms, units and mortar joints were all severely affected by the elevated temperatures, leading to slight changes in the difference between their residual stiffness. Then, tensile block splitting, spalling of block portions, and localized mortar crushing were reported in prisms of concrete units.

(3) Comparisons between the residual strength and stiffness of masonry prisms demonstrated an excellent fire resistance of prisms produced with clay and calcium silicate units, compared to prisms constructed with concrete units. The mechanical performance after exposure to high temperatures was improved when concrete grout was poured into the hollow block prisms. The mechanical properties of ungrouted hollow clay block prisms seemed to be more affected by fire exposure than prisms constructed with solid units.

(4) Experimental tests of masonry prisms have been successfully used to evaluate the effects of different factors on the behavior of masonry exposed to high temperatures. The following factors have been investigated in previous studies: maximum expo-sure temperature of the prisms (using constant heating rate or

standard fire curve), type of unit or mortar (solid clay bricks, solid calcium silicate bricks, hollow clay blocks, hollow concrete blocks, cement mortar, lime mortar, and cement-lime mortar), specimens rendering type (PVA fibers reinforced layer, mixed PVA/basalt fibers reinforced layer, mixed PVA/steel fibers reinforced layer and ordinary plaster mortar, manufactured sand mortar, vermiculite mortar, or perlite mortar), and cooling method (air cooling, water cooling).

(5) The good agreement between the compressive strength results of masonry prisms and small walls (before and after exposure to fire) suggested that prisms can be considered simple types of specimens that may provide interesting insights on the residual strength of fire-damaged masonry.

3.4. LIMITATIONS AND FUTURE DIRECTIONS

Based on the information revised in this study, some limitations and open questions could be identified. Many issues associated with the compressive behavior of masonry prisms exposed to high temperature need future studies:

(1) The effects of numerous variables on the post-fire mechanical properties of masonry prisms have not yet been investigated in previous literature. Then, it is pertinent to evaluate the influence of the following factors on the structural behavior of prisms subjected to high temperatures: time and rate of heating, type of aggregates used in concrete units and mortar joint, geometry of hollow blocks, different slow and fast cooling procedures, moisture content of the prism, relative strength of units and mortar, bedding approach, and bonding arrangement.

(2) Previous studies have only explored the mechanical performance of fire-damaged masonry prisms made with conventional types of units and mortars. Therefore, future studies are recommended to investigate the effects of high temperatures on mechanical properties of prisms produced with high-strength blocks, units and mortars incorporating wastes and recycled admixtures, nanomodified units and mortars, polymer adhesive mortars, fiber-modified units and mortars, and other unconventional masonry components.

(3) The current knowledge on the mechanical behavior of grouted masonry prisms exposed to high temperatures is very limited. Thus, relevant future studies should focus on the compressive behavior of prisms produced with different grouting

procedures, prisms made of hollow blocks filled by grout of different mechanical properties, and grout containing different types and dosages of shrinkage-compensating admixtures.

(4) Future experimental works should be developed to increase the available dataset on residual mechanical strength and elastic modulus of masonry prisms, which can be used to develop more representative stress–strain curve models and empirical formulations for prediction of prism strength and stiffness.

REFERENCES

Bamonte, P., Gambarova, P. G., & Sciarretta, F. (2021). Thermo-mechanical properties and stress-strain curves of ordinary cementitious mortars at elevated temperatures. *Construction and Building Materials*, *267*, 121027. https://doi.org/10.1016/j.conbuildmat.2020.121027

Bittencourt, B., & Antunes, E. (2019). Mechanical behavior of grouted prisms exposed to high temperatures: aid to future standardization (in Portuguese). *Repositório UNESC*, 1–18.

Bosnjak, J., Gambarelli, S., Sharma, A., & Meskovic, A. (2019). Experimental and numerical studies on masonry after exposure to elevated temperatures. *Otto-Graf-Journal*, *18*, 41–52.

Bosnjak, J., Gambarelli, S., Sharma, A., & Mešković, A. (2020). Experimental and numerical studies on masonry after exposure to elevated temperatures. *Construction and Building Materials*, *230*, 116926. https://doi.org/10.1016/j.conbuildmat.2019.116926

Cho, H., Lee, D., Ju, H., Park, H., Kim, H., & Kim, K. (2017). Fire Damage Assessment of Reinforced Concrete Structures Using Fuzzy Theory. *Applied Sciences*, *7*(5), 518. https://doi.org/10.3390/app7050518

Daware, A., & Naser, M. Z. (2021). Fire performance of masonry under various testing methods. *Construction and Building Materials*, *289*, 123183. https://doi.org/10.1016/j.conbuildmat.2021.123183

Dupim, R. (2019). *Resistência residual de compressão de blocos, prismas e pequenas paredes de alvenaria estrutural de blocos de concreto submetidos à situação de incêndio* [MSc. Thesis]. University of São Paulo, São Carlos, Brazil.

EN 1996 1-1. (2005). *Eurocode 6 - Design of masonry structures - Part 1-1: General rules for reinforced and unreinforced masonry structures*.

Fernandes Neto, J. A. D., Sombra, T. N., Haach, V. G., & Corrêa, M. R. S. (2022). Effects of post-fire curing on the residual mechanical behavior of cement-lime masonry mortars. *Construction and Building Materials*, *327*, 126613. https://doi.org/10.1016/j.conbuildmat.2022.126613

Gao, S., Hao, D., Zhu, Y., & Wang, Z. (2023). Compression and Shear Properties of Unreinforced Masonry Structures Reinforced by ECC/HECC subjected to High Temperatures. *KSCE Journal of Civil Engineering*, *27*(2), 751–768. https://doi.org/10.1007/s12205-022-1260-5

Ha, T., Ko, J., Lee, S., Kim, S., Jung, J., & Kim, D.-J. (2016). A Case Study on the Rehabilitation of a Fire-Damaged Structure. *Applied Sciences*, *6*(5), 126. https://doi.org/10.3390/app6050126

Ismaiel, M., Chen, Y., Cruz-Noguez, C., & Hagel, M. (2022). Thermal resistance of masonry walls: a literature review on influence factors, evaluation, and improvement. *Journal of Building Physics*, *45*(4), 528–567. https://doi.org/10.1177/17442591211009549

ISO. (1999). *834 - Fire-resistance tests - Elements of building construction* (p. 25).

Kiran, T., N, A., Andrushia, A. D., Kodur, V., Mathews, M. E., & Arulraj, G. P. (2022). Performance of clay masonry prisms with light weight plaster exposed to standard fire exposure. *Fire and Materials*, 1–21. https://doi.org/10.1002/fam.3081

Leal, D. (2022). *Análise experimental e numérica sobre alvenaria estrutural de blocos de concreto, com e sem revestimento, em situação de incêndio* [PhD Thesis]. University of São Paulo.

Leal, D. F., Dupim, R. H., Munaiar Neto, J., & Corrêa, M. R. S. (2021). Experimental investigation on structural concrete masonry in fire: emphasis on the thermal behavior and residual strength. *Revista IBRACON de Estruturas e Materiais*, *14*(4), 1–16. https://doi.org/10.1590/s1983-41952021000400008

Leal, Medeiros, W., Maebara, A., da Silva, D., Parsekian, G., & Christoforo, A. (2022). Aggregate type influence on strength and deformability of structural zero-slump concrete blocks: numerical, experimental, and statistical study. *Matéria (Rio de Janeiro)*, *27*(3). https://doi.org/10.1590/1517-7076-rmat-2022-0050

Medeiros, W. A., Parsekian, G. A., & Jr., A. L. M. (2021). Critical analysis of the use of international codes and standards to design Brazilian structural masonry in fire situation. *International Journal of Masonry Research and Innovation*, *6*(3), 285. https://doi.org/10.1504/IJMRI.2021.116202

Medeiros, W. A., Parsekian, G. A., & Moreno, A. L. (2022). Test methodology for determining the mechanical properties of concrete blocks at high temperatures. *Materials and Structures*, *55*(2), 61. https://doi.org/10.1617/s11527-022-01892-1

Medeiros, W. A., Parsekian, G. A., & Moreno, A. L. (2023). Residual mechanical properties of hollow concrete blocks with different aggregate types after exposure to high temperatures. *Construction and Building Materials*, *377*, 131085. https://doi.org/10.1016/j.conbuildmat.2023.131085

Nalon, G. H., Ribeiro, J. C., Pedroti, L. G., Duarte de Araújo, E., Franco de Carvalho, J., Soares de Lima, G., & de Moura Guimarães, L. (2021). Residual piezoresistive properties of mortars containing carbon nanomaterials exposed to high temperatures. *Cement and Concrete Composites*, *121*, 104104. https://doi.org/10.1016/j.cemconcomp.2021.104104

Nalon, G. H., Santos, C. F. R., Pedroti, L. G., Ribeiro, J. C. L., Veríssimo, G. de S., & Ferreira, F. A. (2020). Strength and failure mechanisms of masonry prisms under compression, flexure and shear: Components' mechanical properties as design constraints. *Journal of Building Engineering*, *28*, 101038. https://doi.org/10.1016/j.jobe.2019.101038

Neto, J. (2020). *Estudo experimental do comportamento de elementos de alvenaria estrutural com blocos cerâmicos em situação de incêndio* [MSc. Thesis]. University of São Paulo, São Carlos, Brazil.

Neves, N. S. das, Camargo, R. S., & Azevedo, M. S. de. (2022). Finite element computational development for thermo-mechanical analysis of plane steel structures exposed to fire. *REM - International Engineering Journal*, *75*(1), 9–18. https://doi.org/10.1590/0370-44672021750006

Neville, A. (2011). *Properties of concrete* (Pearson, Ed.; 5th Editio).

Parsekian, G., Hamid, A., & Drysdale, G. (2012). *Behavior and design of structural masonry (in Portuguese)*. EdUFSCar.

Pires, D., Barros, R. C., Rocha, P. A. S., & Silveira, R. A. da M. (2018). Thermal analysis of steel-concrete composite cross sections via CS-ASA/FA. *REM - International Engineering Journal*, *71*(2), 149–157. https://doi.org/10.1590/0370-44672016710155

Ramalho, M., & Corrêa, M. (2003). *Projeto de edifícios de alvenaria estrutural. Design of Structural Masonry Buildings (in Portuguese)* (Pini, Ed.).

Rigão, A. (2012). *Comportamento de pequenas paredes de alvenaria estrutural frente a altas temperaturas*. Federal University of Santa Maria, Santa Maria, Brazil.

Rodrigues, F. M., & Moreno Júnior, A. L. (2017). Temperature field of concrete-filled steel tubular columns in fire. *REM - International Engineering Journal*, *70*(2), 137–147. https://doi.org/10.1590/0370-44672015700172

Russo, S., Boscato, G., & F., Sciarretta. (2008). Behaviour of a historical masonry structure subjected to fire. *Masonry International*, *21*(1), 1–14.

Russo, S., & Sciarretta, F. (2013). Masonry exposed to high temperatures: Mechanical behaviour and properties—An overview. *Fire Safety Journal*, *55*, 69–86. https://doi.org/10.1016/j.firesaf.2012.10.001

Sciarretta, F., Eslami, J., Beaucour, A.-L., & Noumowé, A. (2021). State-of-the-art of construction stones for masonry exposed to high temperatures. *Construction and Building Materials*, *304*, 124536. https://doi.org/10.1016/j.conbuildmat.2021.124536

Thaickavil, N. N., & Thomas, J. (2018). Behaviour and strength assessment of masonry prisms. *Case Studies in Construction Materials*, *8*, 23–38. https://doi.org/10.1016/j.cscm.2017.12.007

Torregrosa, M. E. M., & Diez, J. C. (2015). Heat Transfer Mechanism and Thermomechanical Analysis of Masonry Structures (Mortars and Bricks) Subjected to High Temperatures. In *Reactions and Mechanisms in Thermal Analysis of Advanced Materials* (pp. 437–466). John Wiley & Sons, Inc. https://doi.org/10.1002/9781119117711.ch18

Yassin, Adnan, S., Shahidan, S., & Ayop, S. (2020). Strength and Physical Properties of Concrete Brick at Elevated Temperature. *IOP Conference Series: Earth and Environmental Science*, *498*(1), 012054. https://doi.org/10.1088/1755-1315/498/1/012054

Yassin, M., Adnan, S., Shahidan, S., Ali, N., Kamarulzaman, N., & Roni, N. (2018). Strength and physical properties of sustainable concrete masonry at elevated temperature: A review. *Malaysian Construction Research Journal*, *4*(5), 45–55.

Zhang, J., Zhang, Q., Zhang, D., Xu, Q., & Li, W. (2019). Experimental and numerical study on compressive performance of perforated brick masonry after fire exposure. *Fire and Materials*, *43*(2), 200–218. https://doi.org/10.1002/fam.2688

PART II:

DESIGN AND IMPLEMENTATION STUDIES OF SELF-SENSING MASONRY COMPONENTS

4 SMART BEDDING MORTARS FOR MASONRY STRUCTURES: EFFECTS OF LIME/CEMENT RATIO AND CARBON NANOMATERIALS CONTENT ON SELF-SENSING BEHAVIOR

This chapter has been published as the following paper: Nalon, G. H.; Ribeiro, J. C. L.; Pedroti, L. G.; Silva, R. M.; Araújo, E. N. D.; Lima, G. E. S. Smart laying mortars for masonry structures: effects of lime/cement ratio and carbon nanomaterials content on self-sensing behavior. ***Cement and Concrete Composites*** *145 (2024) 105351. https://doi.org/10.1016/j.cemconcomp.2023.105351*

Abstract: *The mechanical behavior of mortar joints directly affects the structural performance and failure mechanisms of masonry. Since previous research did not evaluate the effects of different lime/cement ratios on intrinsic self-sensing properties, this study developed a factorial experiment to investigate the electrical resistivity, gauge factor, stress sensitivity and compressive strength of mortars with different lime/cement proportions (0.25, 0,50, 1.00, 2.00, by volume) and carbon black nanoparticles (CBN) contents (0%, 3%, 6%, 9% by weight of binders). Results were explained based on X-ray fluorescence (XRF), X-ray diffraction (XRD), Fourier transform infrared spectroscopy (FTIR) and scanning electron microscopy (FEGSEM) analyses. Increases in lime content delayed the percolation threshold and decreased the mortars' strength. Portlandite and calcite structures of lime increased the distance between CBN, modifying the electron conduction mechanisms. At the end of the percolation zone, the addition of lime increased self-sensing properties, whereas the opposite behavior was observed at the beginning of the percolation zone.*

Keywords: *Structural Health Monitoring, cement-lime mortars, smart materials, mechanical properties, piezoresistivity, microstructure.*

4.1. INTRODUCTION

In the field of Structural Health Monitoring (SHM) of new and existing masonry structures, mortar joints deserve special attention in terms of investigation of mechanical behavior and integrity, as they are directly related to the failure mechanisms of masonry elements. When strong mortar is used for masonry construction, cracks associated with the

tensile splitting failure of units usually propagate through the masonry joints. In contrast, the masonry failure mode is initiated by the mortar crushing phenomenon when weak mortar is used (Mohamad et al., 2017, 2018; Nalon et al., 2020; Zahra et al., 2021).

Different methods have been proposed for the evaluation of mortar joints, such as mechanical and microstructural tests of mortar samples extracted from the masonry walls, installation of ceramic piezoelectric or capacitive sensors inside the joints, in addition to in-situ experiments based on determining the penetration depth of a steel needle or quantifying the energy required to drill small cavities in mortar bed joints (La Mendola et al., 2021; Łątka and Matysek, 2018, 2020; Marastoni et al., 2017; Oliveira et al., 2012). These characterization methods are constrained by scalability issues and can be invasive to the structure. Most of them do not allow continuous real-time monitoring of the structural masonry behavior.

A new generation of multifunctional construction materials has been proposed for SHM approaches: smart composites with stress/strain self-monitoring and damage self-detection abilities. These composites can be produced with distinct types of conductive admixtures that decrease their electrical resistivity, such as carbon fiber (CF), steel fiber (SF), carbon nanotubes (CNT), graphene (G), carbon black nanoparticles (CBN), among others. Consequently, they demonstrate detectable changes in electrical resistivity in response to variations in stress/strain and propagation of cracks, which makes them promising alternatives to SHM architectures (Chung, 2021; Ding et al., 2019; Dong et al., 2021; Nalon et al., 2022; Vlachakis et al., 2020).

Most of the previous works dealt with the design, fabrication and application of self-sensing cementitious mortars for SHM of reinforced concrete structures (Castañeda-Saldarriaga et al., 2021; Cholker, 2021; Dinesh et al., 2022; Ding et al., 2019, 2021; Meoni et al., 2021; Rao and Sasmal, 2020). Other recent works studied smart clay bricks for stress/strain field assessment and damage identification in structural masonry elements (D'Alessandro et al., 2018; Dong et al., 2020; Downey et al., 2018; García-Macías and Ubertini, 2019; Meoni et al., 2019, 2020, 2021). Monitoring mortar joints is of great importance to evaluate the mechanical performance and integrity of masonry elements. Despite this, few papers investigated the self-sensing properties of masonry mortars. Dimou et al. (2022) recently observed a good self-sensing in nanomodified composites produced with cement, metakaolin and lime (constant cement/lime ratio of 1.00, by weight). In contrast, Drougkas et al. (2023a, 2023b) focused on the evaluation of self-sensing properties

of pure lime mortars (cement/lime ratio of 0.00) containing different types of micro/nano conductive admixtures. Although the combination of cement and lime is highly attractive for production of masonry mortars, there is no systematic study about the evaluation of self-sensing cement-lime mortars for SHM of masonry structures.

The mechanical and rheological properties of mortars with different lime/cement ratios are widely reported in previous literature (Hernoune et al., 2020; Kaczmarek, 2019; Parsekian and Soares, 2010; D. Zhang et al., 2018). According to these studies, cement mortars present high strength, high impermeability and may not ensure suitable strain accommodation, whereas pure lime mortars typically exhibit low strength, good water vapor transmission performance and high durability. The increase in the lime/cement ratio reduces the stiffness, improves the ability to accommodate strains, enhances the base adhesion, increases the water retention and improves the workability of mortars.

However, there is no previous analysis of the effects of different lime/cement ratios on compressive strength, electrical resistivity, self-sensing properties and microstructure of nanomodified masonry mortars. The present chapter reports a pioneering experimental analysis of the mechanical and self-sensing performance of CBN-based mortars produced with various lime/cement ratios covered by ASTM C270 (2019), which deals with mortars used in the construction of masonry structures. X-ray fluorescence (XRF), X-ray diffraction (XRD), Fourier transform infrared spectroscopy (FTIR) and scanning electron microscopy (FEGSEM) analyses were used to clarify the experimental results at the microstructural level. The findings of the present study provide important insights that can be used for further design of smart self-sensing mortar joints for SHM of masonry elements.

The structure of this chapter includes four sections. Section 4.1 introduces the development of self-sensing construction materials and their potential application in SHM systems of masonry structures. Section 4.2 shows the materials and methods used in experiments for determination of compressive strength, electrical resistivity, self-sensing properties, and microstructural behavior of cement-lime mortars containing CBN. In Section 4.3, the experimental findings are presented and comprehensively discussed, after different statistical analyses. Section 4.4 presented the concluding remarks, limitations of the present study and some recommendations for future investigations.

4.2. MATERIALS AND METHODS

4.2.1. Materials

Portland cement CP V-ARI with density of 3.05 g/cm³ was used in this study, which is equivalent to the ASTM C150 (2022) Type III portland cement (Mehta and Monteiro, 2005). The hydrated lime had a density of 2.51 g/cm³ and contents of CaO and MgO (nonvolatile basis) > 90%, carbon dioxide < 10% and unhydrated oxides ~0%. Table 1 shows the chemical composition of cement and lime determined by X-Ray Fluorescence (XRF) spectrometry, using a Panalytical Epsilon 3^x equipment.

Table 1 - Chemical composition (wt.%) of cement and lime determined by XRF analysis.

Oxides	CaO	SiO_2	Al_2O_3	Fe_2O_3	MgO	K_2O	SO_3	TiO_2	Other oxides
Cement	68.15	16.94	5.16	3.44	0.53	0.85	3.89	0.27	0.77
Lime	89.35	1.73	0.95	0.74	0.52	0.12	5.82	0.04	0.73

Source: Author (2024).

Natural quartzite sand with specific gravity of 2.64, maximum grain size of 2.38 mm and fineness modulus of 2.52 was also used. The conductive admixtures used in the present experimental program were CBN provided by Birla Carbon, with average particle size of 20 nm and with specific surface area of 120 m^2/g. Polycarboxylate-based superplasticizer (SP) with density of 1.12 g/cm³ was used to improve the dispersion of the carbon nanomaterials, as recommended in previous literature (Monteiro et al. 2017a, 2017b; Nalon et al., 2021).

4.2.2. Experimental design and production of specimens

A factorial experiment was carried out in this research, according to a completely randomized design, in order to identify not only the effect of individual factors but also interactions between them on different response variables, namely (i) electrical resistivity, (ii) gauge factor (GF), (iii) stress sensitivity (SS) and (iv) compressive strength.

The two factors of this factorial experiment were (i) the conductive network structure (designated as CNS factor) and (ii) the type of masonry mortar (designated as TMM factor). The four levels of the CNS factor aimed to characterize the insulation zone and different parts of the percolation zone of cementitious composites with CBN (Han et al., 2015; Hwang et al., 2011; Nalon et al., 2021). The five levels of the TMM factor covered various binder compositions defined by ASTM C270 (2019).

As indicated in Table 2, the conductive network structures associated with the CNS factor were produced using different CBN contents: 0%, 3%, 6% and 9% (by weight of binders). Table 2 also shows that the binder composition variations that characterize the different levels of the TMM factor were achieved using lime/cement ratios (l/c) of 2.00, 1.00, 0.50 and 0.25 (by volume), which characterize Type O, Type N, Type S and Type M cement-lime mortars of ASTM C270 (2019), in addition to a series of cement mortars (lime/cement ratio equal to 0.00), which was associated in the present work with the acronym "TC". Each type of mortar was designated as Tx-y to provide a fast identification of the characteristics of the materials. The term “x” indicates the lime/cement ratio (O, N, S, M and C indicate lime/cement ratio equal to 2.00, 1.00, 0.50, 0.25 and 0.00, respectively) and the term “y” indicates the percentage content of CBN (by weight of binders). Since the aggregate fraction acted as an electrical insulator, a low sand/cement ratio of 0.75 (by volume) was used in all mixtures, following a recommendation of Wen and Chung (2007) for attaining high electrical conductivity. The use of higher sand/cement ratios would require high concentrations of conductive admixtures to attain the same level of conductivity, which compromises the mortar compressive strength, as discussed in the next section.

Table 2 - Raw materials consumption and mini-slump flow of each different series of composites.

Series	CBN/binder ratio (by mass) associated with the CNS factor	Lime/cement ratio (by volume) associated with the TMM factor	Proportions (kg/m³)						Flow index (mm)
			Cement	Sand	Lime	Water	CBN	SP	
TO-0%	0.00	2.00	437.90	284.27	720.73	461.60	0.00	0.00	84
TO-3%	0.03		401.20	260.45	660.34	477.65	31.85	12.74	77
TO-6%	0.06		377.19	244.86	620.82	481.59	59.88	23.95	71
TO-9%	0.09		355.95	231.08	585.86	484.99	84.76	33.91	71
TN-0%	0.00	1.00	633.76	411.42	521.55	428.58	0.00	0.00	85
TN-3%	0.03		594.16	385.71	488.96	434.63	32.49	13.00	81
TN-6%	0.06		551.42	357.97	453.79	447.77	60.31	24.12	70
TN-9%	0.09		492.90	319.98	405.63	481.77	80.87	32.35	69
TS-0%	0.00	0.50	833.72	541.24	343.06	384.96	0.00	0.00	82
TS-3%	0.03		781.41	507.27	321.53	393.35	33.09	13.24	73
TS-6%	0.06		707.68	459.42	291.19	423.24	59.93	23.97	70
TS-9%	0.09		652.76	423.76	268.60	442.77	82.92	33.17	67
TM-0%	0.00	0.25	955.44	620.25	196.57	373.48	0.00	0.00	80
TM-3%	0.03		905.29	587.70	186.25	376.48	32.75	13.10	74
TM-6%	0.06		793.47	515.10	163.25	427.30	57.40	22.96	67
TM-9%	0.09		757.40	491.69	155.83	428.33	82.19	32.88	66
TC-0%	0.00	0.00	1083.29	703.25	0.00	378.44	0.00	0.00	80
TC-3%	0.03		1046.05	679.07	0.00	371.17	31.38	12.55	76
TC-6%	0.06		942.15	611.62	0.00	407.83	56.53	22.61	71
TC-9%	0.09		864.30	561.09	0.00	433.09	77.79	31.11	65

Source: Author (2024).

A nanosuspension of CBN, water and SP was produced with ultrasound sonication, using a probe sonicator with a frequency of 20 kHz and a power of 50 W. A constant SP/CBN ratio of 0.4 (by mass) and sonication energy of 450 J/mL were used in this process, which provided appropriate dispersion of CBN in water and polycarboxylate-based SP, according to preliminary studies. After that, the nanosuspension was mixed with cement, lime and sand in a mechanical mixer for about 10 minutes.

To ensure that the workability of the mixtures was appropriate for masonry construction, the water consumption increased with the increase in the concentrations of lime and CBN. Mini-slump tests were carried out for workability control, using a Kantro cone mold (truncated cone with top inner diameter of 19 mm, base inner diameter of 38 mm and height of 57 mm). The Kantro cone mold was placed at the center of a flow table and filled with three equal layers of fresh mortar. After that, it was removed and the flow table was dropped 30 times through a height of 12.5 mm within 30 seconds. Then, the flow index was calculated based on the spread diameter of the fresh mixture measured in three distinct directions. The water content was adjusted to obtain a flow index (Table 2) of (70 ± 15) mm with the Kantro cone mold, which is equivalent to the flow index of (230 ± 10) mm obtained with the methodology prescribed by ABNT NBR 13276 (2005). According to previous literature (Parsekian et al., 2012; Parsekian and Soares, 2010), a flow index of (230 ± 10) mm is recommended for bedding mortars used in the construction of masonry structures.

The fresh mixture was poured into oiled molds in two equal layers. Each layer was appropriately compacted with 30 strokes of a steel tamping rod. For each series presented in Table 2, three mortar prisms of 20 mm × 20 mm × 60 mm were produced for piezoresistive tests (designated as S1, S2 and S3), three mortar cubes of 20 mm were prepared to determine the compressive strength of the material and one mortar cylinder of 35 mm × 70 mm was cast for microstructural analysis. The shape and size of the specimens are in good agreement with the recommendations of EN 12390-1 (CEN, 2019), which specify that the basic dimension of cubic specimens must be at least three and a half times the nominal size of the aggregates. An extra mortar prism was also produced for estimation of the load amplitude applied in the piezoresistive tests. Copper plates of 14 mm × 30 mm × 1 mm were used as electrodes. They were embedded into the central region of the mortar prisms in a straight line and distance of 0.8 cm from each other. The specimens were conditioned for 72 h inside the molds in a controlled environment room with a temperature of 20 ± 5 ºC and a relative humidity of at least 85%, in order to prevent moisture loss. The specimens were demolded

after 72 hours and subjected to air-curing for 28 days in a moisture room (relative humidity higher than 85% and ambient temperature of 20 ± 5 ºC).

4.2.3. Electrical/mechanical tests

Before the electrical/mechanical tests, the specimens were dried at 60 ± 10 ºC for 72 hours and then cooled down to ambient temperature. These drying procedures were recommended in previous literature (Han et al., 2021; Wang et al., 2019, 2021) to eliminate the pore water and avoid undesirable effects of ionic conduction on results of electro-mechanical tests.

The prismatic mortar specimens (with electrodes) were subjected to direct current (DC) tests for measurements of electrical resistivity, in addition to biphasic DC measurements for evaluation of their piezoresistive response. The cubic mortar specimens (without electrodes) were subjected to uniaxial compression tests. An EMIC DL-60000 universal testing machine and a constant loading rate of 0.50 MPa/s were used in these tests.

In both DC and biphasic DC tests, each mortar prism was series-connected with a reference resistor of 1000 Ω (R_{ref}), as indicated in Figure 1. In DC tests, a constant voltage source of 5 V was applied using a microcontroller board (Arduino Mega 2560 R3). In biphasic DC tests, the microcontroller board was used to apply a ±5 V square wave voltage signal with frequency of 6 Hz and duty cycle of 50%, in order to remove polarization effects.

Figure 1 - Experimental apparatus used in DC and biphasic DC tests.

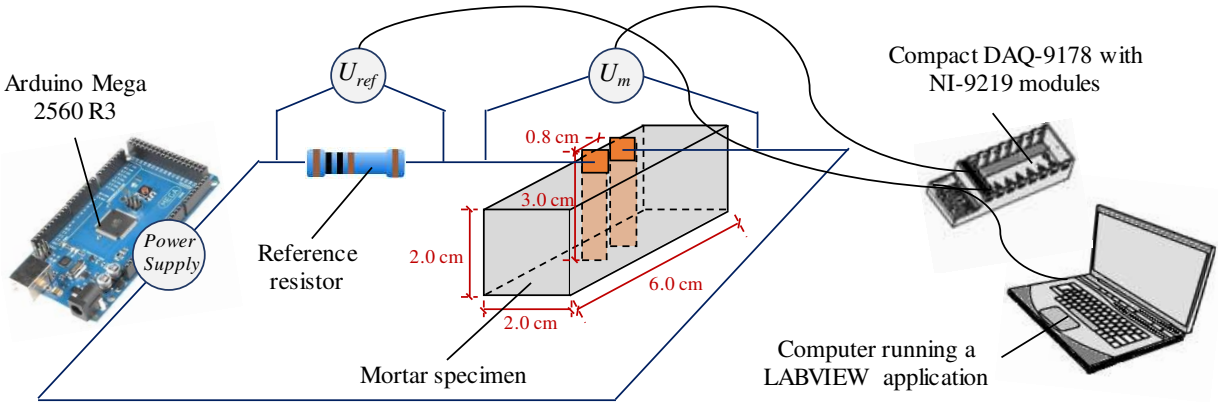

Source: Author (2024).

A LabVIEW application and an NI compact DAQ-9178 chassis with NI-9219 modules were used to determine the voltage drop across the prismatic mortar specimen (U_m) and the reference resistor (U_{ref}). Ohm's law was used to calculate the circuit's electrical current (i)

and the mortar electrical resistance (R_m), as indicated in Equation (1) and Equation (2), respectively. In the case of biphasic DC tests, U_m and U_{ref} were measured at 80% of the cyclic positive constant part of the square wave (Downey et al., 2017; Meoni et al., 2021; Nalon et al., 2021). In addition, the distance (L) and the effective area (A) between the copper electrodes were used to estimate the electrical resistivity ρ, according to Equation (3).

$$i = \frac{U_{ref}}{R_{ref}} \quad (1)$$

$$R_m = \frac{U_m}{i} \quad (2)$$

$$\rho = \frac{R_m \ A}{L} \quad (3)$$

The piezoresistive response of the mortars was evaluated in cyclic compressive loading tests. To determine the loading amplitude used in the piezoresistive tests of each series, the extra mortar prism mentioned in the previous section was subjected to a uniaxial compression test for estimation of the specimens' strength. After that, the other mortar prisms were subjected to three loading/unloading cycles with amplitude of about 30% of the estimated specimen strength. Then, a final loading cycle with load steps at 10%, 20% and 30% of the estimated strength was carried out. As presented in Figure 2, thin insulating films of low-density polyethylene were placed between the mortar prism and the loading plates to avoid unwanted electrical conduction. Longitudinal strains were measured during the tests by EMIC clip-gauges symmetrically arranged with respect to the central axis of the specimen.

Figure 2 - Experimental apparatus used in piezoresistive tests.

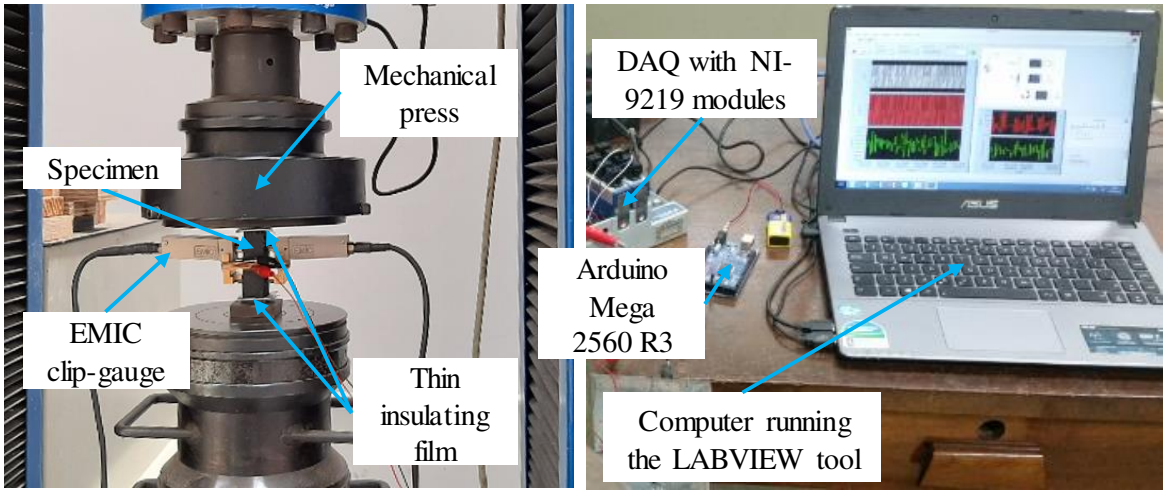

Source: Author (2024).

Fractional changes in electrical resistivity (FCRs) due to the compressive loads were obtained from the biphasic DC measurements described above. Values of FCR, compressive strain (ε) and compressive stress (σ) were used to calculate the GF and SS of mortars that exhibited a coherent self-sensing response. The GF and SS [Equation (4) and Equation (5), respectively] of these mortars were calculated through the linear stretch of FCR versus strain and FCR versus stress curves, respectively.

$$GF = \frac{FCR}{\varepsilon} = \frac{\frac{\Delta R}{R_0}}{\varepsilon} \approx \frac{\frac{\Delta \rho}{\rho_0}}{\varepsilon} \quad (4)$$

$$SS = \frac{FCR}{\sigma} = \frac{\frac{\Delta R}{R_0}}{\sigma} \approx \frac{\frac{\Delta \rho}{\rho_0}}{\sigma} \quad (5)$$

where R_0 and ρ_0 indicate the initial electrical resistance and resistivity of the specimen, respectively, and ΔR and $\Delta \rho$ indicate the changes of electrical resistance and resistivity due to the compressive loading, respectively.

The three mortar cubes of 2.0 cm were used to determine the average compressive strength of the mortar (f_m), based on the maximum compressive load supported by the specimen (P_{max}) and its cross-sectional area (S), as indicated in Equation (6).

$$f_m = \frac{P_{max}}{S} \quad (6)$$

4.2.4. Statistical analyses

The experimental results of electrical resistivity, GF, SS and compressive strength were subjected to Grubb's test analyses for identification of outliers, Shapiro-Wilk tests of normality and Bartlett tests of homoscedasticity. When required assumptions were satisfied, a factorial analysis of variance (ANOVA) was carried out to identify the effect of different factors and interactions between them on each response variable. After the identification of significant differences between average values being compared, Tukey's multiple comparison tests were used to identify which averages differ from the rest. The null hypotheses (H_0), alternative hypotheses (H_a) and significance levels considered in all of these statistical analyses were presented in APPENDIX 4A.

4.2.5. Microstructural analyses

After the 28-days curing period, two slices for microstructural investigation (thickness of about 0.4 cm) were cut from the hardened cylinders using a disk saw (top and bottom slices of the cylinders were discarded, as they might not be representative), following the recommendations of Scrivener, Snellings and Lothenbach (2016). After that, the cut slices were subjected to hydration stoppage by solvent exchange using isopropanol. The hydration stoppage enabled the study of comparatively steady microstructures, reducing the chances of slight subsequent alterations that could eventually impact the discussions presented in the following section. It is important to highlight that hydration stoppage makes the sample less sensitive to the carbonation phenomenon during the sample preparation procedures, and that different microstructural investigation techniques require dried samples to obtain reliable data (Scrivener et al., 2016; Snellings et al., 2018).

For microscopy analysis, a small ~0.4 cm cube was cut from the center of one of the slices to avoid wall effects. The sample was mounted on microscope stubs with double-sided carbon tape and sputter coated with gold to improve electrical conductivity, using a Quorum Q150RS equipment. A CBN-based paint was also used to create a conductive path from the surface of the sample to the microscope stub. Field emission gun scanning electron microscopy (FEGSEM) analysis was used to obtain secondary electron images of the samples, using a TESCAN MIRA's microscope with FEG Schottky electron emission source (1.2 nm resolution at 30 keV).

To obtain powder samples for X-ray diffraction (XRD) analysis, the other slice was finely ground using a No. 200 mesh (75 μm) standard sieve. The powder was placed on a sample holder and measured by XRD, using CuKα radiation (λ = 1.5418 Å) in a Bruker D8-Discover diffractometer, working at 40 kV and 40 mA. Data were collected from 5° to 70° 2θ with a time per step of 1 second and 0.05º increments, resulting in a total measurement time of approximately 20 minutes. In addition, Fourier transform infrared spectroscopy (FTIR) analyses of the samples were carried out in a Varian 660 equipment (range of 400-4000 cm^{-1} and resolution of 4 cm^{-1}).

4.3. RESULTS AND DISCUSSIONS

4.3.1. Electrical resistivity

Figure 3a and Figure 3b present the variation of DC electrical resistivity with the CBN volume fraction and lime/cement ratio of the masonry mortars, respectively. To enable the comparison of results presented in these figures, all DC measurements were taken 5 minutes after the initiation of each DC test. It is important to highlight that the polarization phenomenon was mitigated as all specimens were dried before the DC tests (~60 ºC for 72 hours), ensuring that no significant water content remained in the composites' pores to allow for any relevant ionic current flow. Results presented in APPENDIX 4A indicated that the electrical resistivity data presented in these figures could not be subjected to an ANOVA because normality and homoscedasticity assumptions were not met at the 5% significance level. It can be attributed to the very sharp reduction in electrical resistivity provided by the addition of the conductive nanomaterials and the significant difference between the standard deviation of plain mortars and mortars produced with high contents of CBN.

Figure 3 - DC electrical resistivity of the composites versus lime/cement ratio (a) and DC electrical resistivity versus CBN volume fraction.

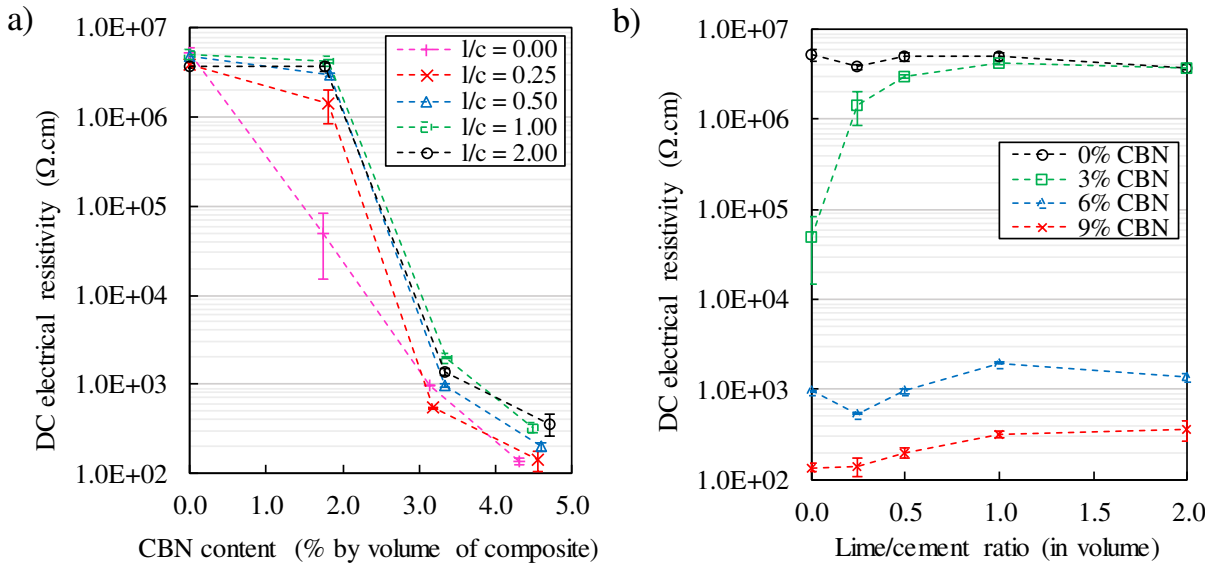

Source: Author (2024).

It was possible to observe that mortars without nanomaterials always presented very high values of electrical resistivity (between 1.5×10^{6} Ω.cm and 1.0×10^{7} Ω.cm), regardless of their lime content. In fact, such high values of electrical resistivity have been widely observed in dried cementitious materials without conductive admixtures (Hou and Lynch, 2005; Yoo

et al., 2017; You et al., 2017). In contrast, contents of 6% and 9% of CBN (by mass of binders) enabled the production of very conductive composites with electrical resistivity values (between 1.4×10^2 Ω.cm and 2.0×10^3 Ω.cm) up to five orders of magnitude lower than the values of electrical resistivity of plain mortars.

Since significant and progressive reductions in electrical resistivity were provided by contents of 6% or 9% of CBN (by mass of binders), it is possible to infer that these concentrations were beyond the percolation threshold. The high electrical conductivity of these mortars can be attributed to electronic and contact conduction phenomena. Electronic conduction is associated with the flow of electrons through thin layers of insulating cementitious matrix between CBN that are closely spaced, based on the quantum tunneling effect. In contrast, contact conduction is characterized by the movement of electrons due to direct contact between neighboring CBN aggregates (Li et al., 2006; Nalon et al., 2021; Xiao et al., 2010).

The addition of a small concentration of CBN (3% by mass of binders) caused negligible or small variation in the electrical resistivity of the cement-lime mortars (l/c > 0.00). It happened because the small amounts of CBN aggregates were not close enough to form conductive pathways within the composites. On the other hand, the addition of 3% of CBN to the cement mortar (l/c = 0.00) caused resistivity decreases of about two orders of magnitude. These results clearly indicate that the incorporation of lime into the mortars changed their conductive network and delayed the percolation threshold. Figure 3a shows that the percolation threshold for mortars with l/c = 0.00 and l/c = 0.25 occurred at CBN concentrations below 1.74% and 1.82% (by volume of composite), respectively. In mortars with l/c = 0.50, l/c = 1.00 and l/c = 2.00, the percolation threshold was delayed, as it was observed within the range of CBN concentrations between 1.84% and 3.33% (by volume of composite).

Figure 3b evidenced that nanomodified mortars generally exhibited increases in electrical resistivity with increasing lime/cement ratio. The reasons for these modifications are discussed in the next subsection. According to Figure 3b, the electrical resistivity of mortars containing only 3% of CBN (by weight of binders) increased by about two orders of magnitude when the lime/cement ratio increased from 0.00 to 2.00. In contrast, mortars with higher CBN concentration (6% and 9%, by weight of binders) presented lower resistivity increases with the addition of lime. For example, specimens with 9% of CBN presented small electrical resistivity increases for any increment in the l/c ratio. The electrical resistivity of

specimens with 6% of CBN fluctuated around 1.0×10^3 Ω.cm (initially, the electrical resistivity of these mortars decreased, then increased, and finally decreased again with the addition of lime). The limited impact of lime on the conductive network of composites containing 6% or 9% of CBN is a result of the position of these specimens at end of the percolation zone. Their well-established conductive network was significantly dense and hard to be changed by the incorporation of lime. Consequently, in mortars containing high dosages of CBN, some stretches of the conductive network were obstructed by non-conductive crystalline compounds, but the electrons could flow through many other paths still available in the conductive network of these composites.

In mortars containing 3% of CBN (by weight of binders), the increase in the lime/cement ratio from 0.00 to 1.00 caused significant increases in the electrical resistivity, i.e., from 4.9×10^4 Ω.cm to 3.6×10^6 Ω.cm). In this case, most of the conductive network stretches were separated when lime was incorporated. The great impact of lime on the conductive network of specimens containing 3% of CBN is a result of the position of these specimens at the beginning of the percolation zone. The conductive network of these mortars was very sparse, so that the addition of lime had a substantial impact on the obstruction of pathways for electrical conductivity. When the lime/cement ratio increased from 1.00 to 2.00, the electrical resistivity remained within the same order of magnitude, i.e., it varied from 4.2×10^6 Ω.cm to 3.6×10^6 Ω.cm. These electrical resistivity values are typically observed in dried cementitious materials without conductive admixtures. For example, Figure 3b shows that the electrical resistivity of mortars containing 0% of CBN fluctuated between 1.5×10^6 Ω.cm and 1.0×10^7 Ω.cm.

4.3.2. Microstructural analyses

This section presents the results of microstructural analyses of TO-3%, TO-9%, TC-3%, TC-9% samples (only these samples were analyzed because they represent typical contrasting situations associated with the addition of low and high contents of CBN and lime to the cementitious matrix). At first, the microstructural mechanisms behind the effects of these materials on the behavior of the masonry mortars can be elucidated with the results of XRD analyses presented in Figure 4.

Figure 4 - XRD diffractograms of TO-3%, TO-9%, TC-3%, TC-9% samples.

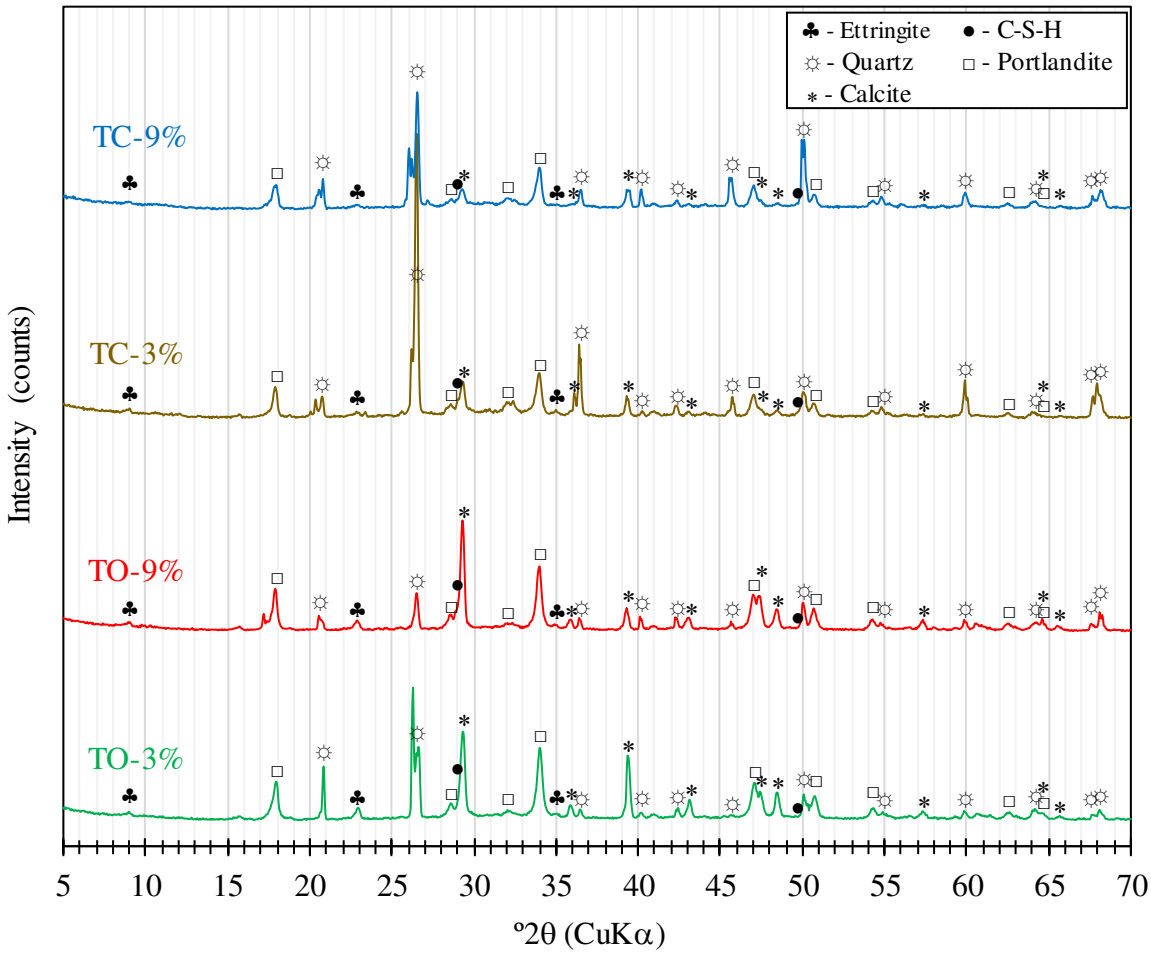

Source: Author (2024).

There are two main differences between the XRD diffractogram of mortars with high lime content (TO-3% and TO-9%) and mortars without lime (TC-3% and TC-9%). At first, TO-3% and TO-9% samples exhibited intense calcium hydroxide (CH) peaks (e.g., 2θ = 18.1º, 34.2º, 47.3º and 50.9º). In addition, TO-3% and TO-9% mortars presented intense peaks of calcite (e.g., 2θ = 29.4º, 39.5º, 47.6º and 48.7º). These results suggested that many conductive paths between CBN were inevitably obstructed by the high amounts of non-conductive CH and calcite compounds associated with the increase in the content of hydrated lime, as also evidenced by the high CaO content verified in the XRF results of Table 1. In fact, the separation of aggregates of CBN [85-500 nm aggregates composed of nanospheres with diameters of 10-150 nm (ICBA, 2016)] by calcite structures and plate-like CH crystals [compounds with particle size of 0.7-3.0 μm (Mehta and Monteiro, 2005)] was typically observed in FEGSEM analyses, as indicated in Figure 5a and Figure 5c of TO-3% and TO-9% samples, respectively. Dong et al. (2021) also reported the separation between CBN and

slaked lime within the cementitious matrix, as the nanoparticles were typically attached to the surface of lime compounds.

Figure 5 - FEGSEM images of (a) TO-3%, (b) TC-3%, (c) TO-9% and (d) TC-9% samples.

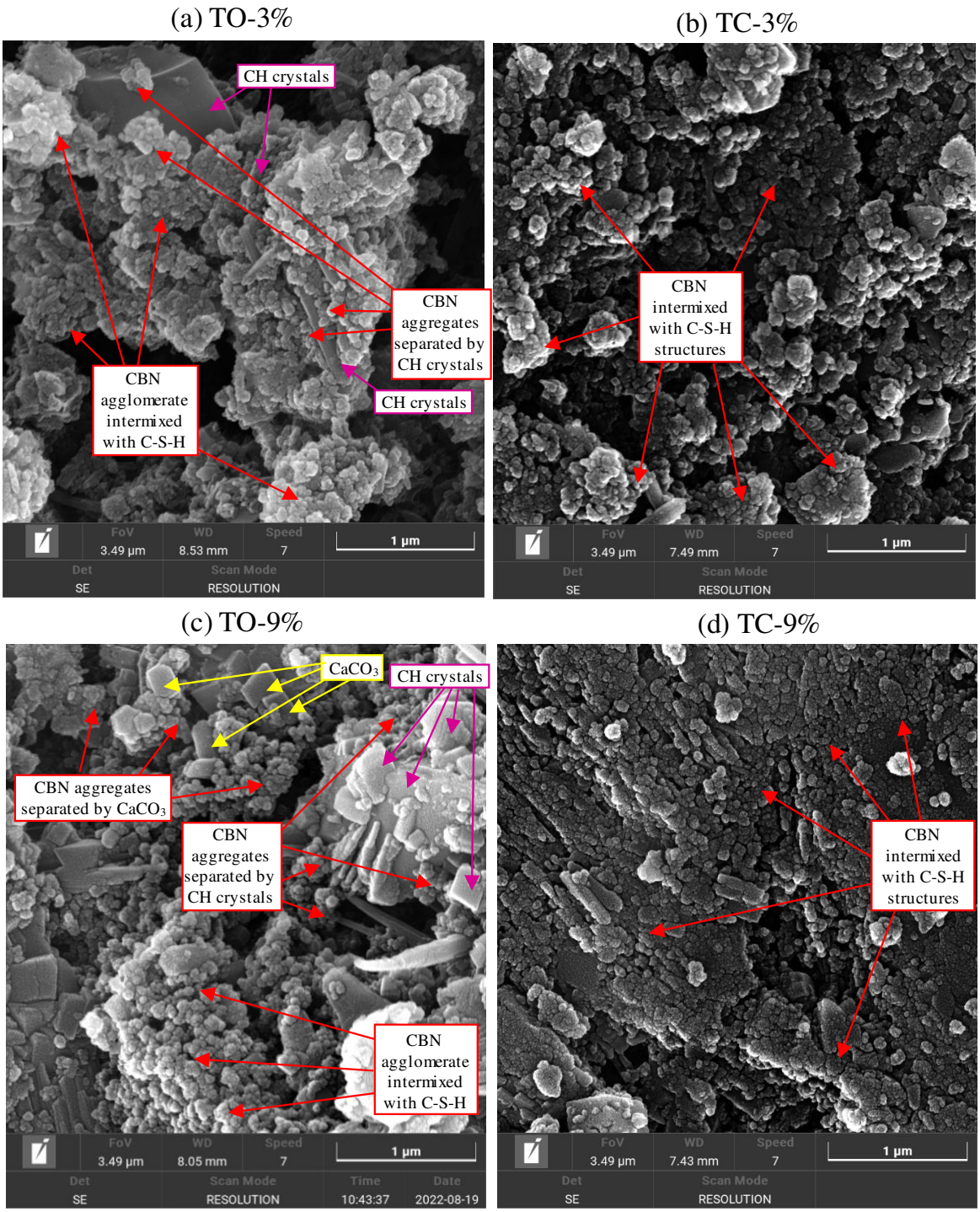

Source: Author (2024).

The lime compounds evidenced in Figure 5 tended to increase the distance between adjacent conductive particles, making contact conduction impossible and changing the

probability of tunneling conduction mechanisms. Consequently, the addition of lime tends to compromise the conductive network inside the nanomodified mortars. On the other hand, since the high surface area of CBN is able to provide many locations for the growth of hydration products (Lima et al., 2021; Parvan et al., 2020; Zhang et al., 2022), cement hydrates existing in mortars without lime would not cause such significant interruptions in their conductive network. Actually, cement mortars were mainly composed by CBN (spherical particles with diameters of 10-150 nm indicated in Figure 5b and Figure 5d) intrinsically intermixed with the C-S-H gel due to nucleation effects.

The vibration bands associated with different compounds of the self-sensing materials were evaluated based on the FTIR spectra illustrated in Figure 6. For example, the stretching of $(OH)^-$ in CH structures led to noticeable absorption bands at 3640 cm^{-1}, especially in the spectra of TO-3% and TO-9% (Horgnies et al., 2013; Tantawy, 2017; Vaičiukynienė et al., 2013; Yaseen et al., 2019; Ylmén and Jäglid, 2013). These spectra also revealed high-intensity bands related to the presence of calcite at 713 cm^{-1}, 874 cm^{-1} and 1300-1600 cm^{-1}, which can be attributed to symmetric (ν_2 and ν_4) and asymmetric (ν_3) vibrations of CO_3^{2-} (Medina et al., 2018; Nasrazadani et al., 2016; Tantawy, 2017; Vaičiukynienė et al., 2013). Therefore, results of the FTIR analyses also corroborate the hypotheses that the CBN-based conductive network was obstructed by the incorporation of non-conductive CH and calcite structures derived from high contents of hydrated lime.

Figure 6 - Fourier transform infrared (FTIR) spectroscopy results of TO-3%, TO-9%, TC-3% and TC-9% samples.

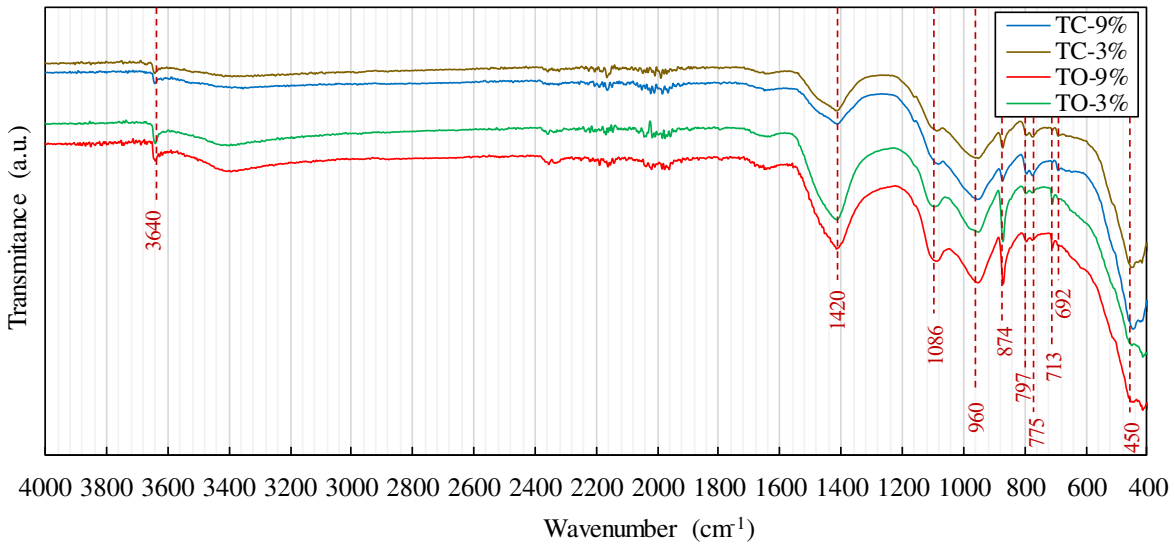

Source: Author (2024).

Signatures of Si-O modes at approximately 450 cm^{-1}, 775 cm^{-1}, 797 cm^{-1}, 692 cm^{-1} and 1086 cm^{-1} can be attributed to the quartzite aggregates (Malathy et al., 2022; Sekhaneh et al., 2020; Tyagi et al., 2006), whereas the band at about 900-1050 cm^{-1} has been usually associated with Si-O asymmetric stretching vibrations in the C-S-H gel (Horgnies et al., 2013; Malathy et al., 2022; Medina et al., 2018).

4.3.3. Self-sensing behavior

The piezoresistive performance of the composites was tested using the biphasic DC measurements proposed by Downey et al. (2017), in which a square-wave signal induces depolarization effects through current polarity reversal. A piezoresistive response was not observed in cement mortars and cement-lime mortars with 0% or 3% of CBN (by mass of binders). As discussed in the previous subsections, electronic conduction was not observed in these specimens, as they always presented very high values of electrical resistivity that were not well correlated with compressive stress/strain levels. In contrast, coherent and reversible FCRs were observed in the cyclic loading tests of cement and cement-lime mortars containing 6% or 9% of CBN (by mass of binders). Since these CBN-based mortars were designed within the percolation zone, compressive/tensile loading changed the inter-particle distance between nanomaterials, leading respectively to decrements/increments of electrical resistivity, which evidences the promising self-sensing ability of these composites to monitor stresses and strains of civil structures (Li et al., 2006; Monteiro et al., 2017a, 2017b; Nalon et al., 2020).

APPENDIX 4B shows the FCR *vs* compressive strain and FCR *vs* compressive stress curves obtained from the piezoresistive tests of the cement and cement-lime mortars investigated in the present work. It also shows linear regression models that provided the best fit to the dataset associated with the linear stretch of each curve, in addition to the coefficients of determination (R^2) of the developed models. The GF and SS of these mortars were calculated as the slope of the initial part (linear stretch) of these curves, as recommended by Chung (2020). Examples of construction of these regression models are represented in the diagrams of Figure 7, using the experimental data of the specimen S2 of the TC-9% series. Figure 8 plots these self-sensing properties against the lime/cement ratio of the composites.

Figure 7 - Examples of linear regression models obtained from the FCR *vs* compressive strain (a) and FCR *vs* compressive stress curves (b).

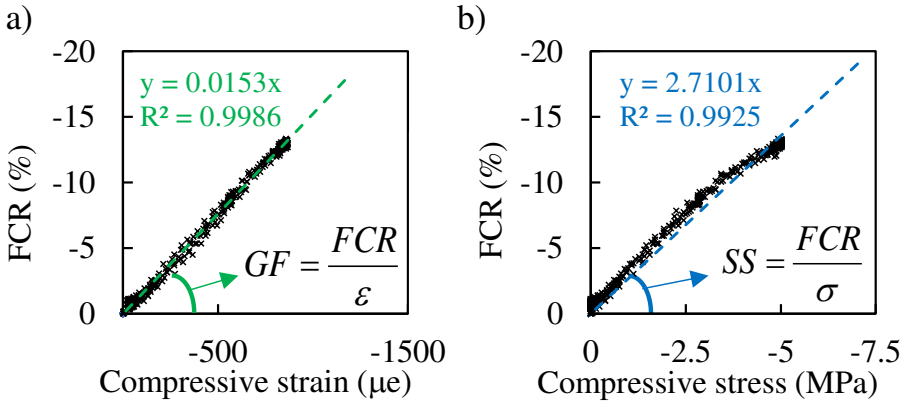

Source: Author (2024).

Figure 8 - Effects of lime/cement ratio on the GF (a) and SS (b) of mortars with self-sensing behavior.

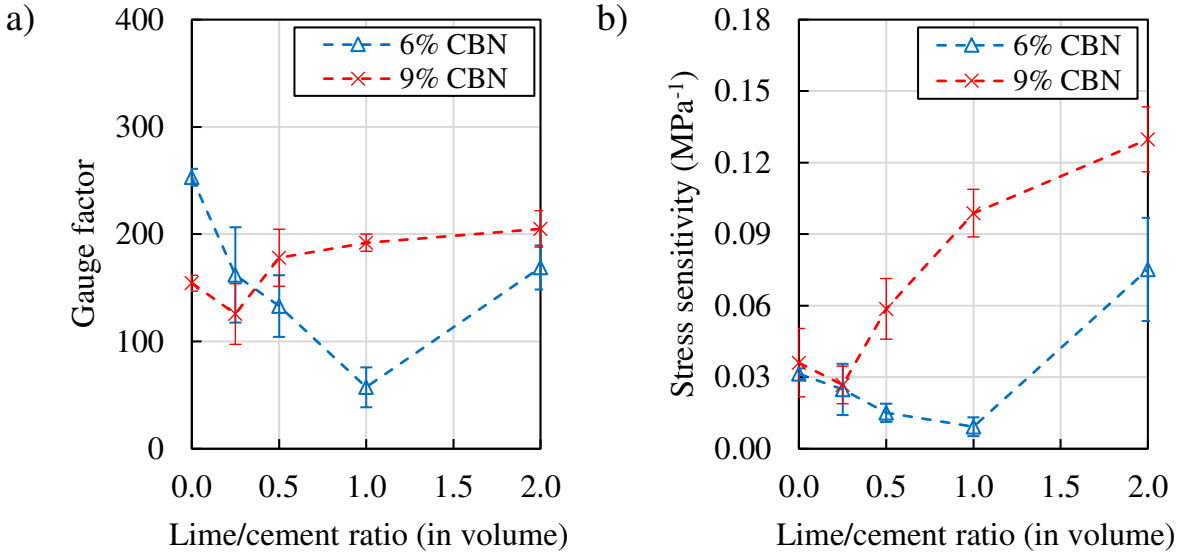

Source: Author (2024).

The statistical analyses of the results of GF and SS are presented in APPENDIX 4A. In this case, ANOVA assumptions were satisfied for both response variables, so that a factorial ANOVA could be carried out. P-values of 1.3×10^{-5} and 1.3×10^{-4} were obtained when evaluating the interaction effects between the TMM and CNS factors on the GF and SS of the mortars, respectively. These results proved that the influence of lime/cement ratio on the self-sensing properties of masonry mortars depends on their conductive network structure. Consequently, the TMM × CNS interaction was unfolded to analyze the effects of each independent variable within each level of the other independent variable. Table 3 and Table 4 show the results of Tukey's multiple comparison tests, which indicate which values of average self-sensing properties differ from the rest. Figure 9 summarizes the notation

guidelines related to the use of uppercase and lowercase letters presented with the two-way ANOVA results of these tables. These letters were added to represent the effects of the independent variables and their interactions, which resulted in various pairwise comparisons. For a significance level equal to 5%, values followed by the same lowercase letter within each column or the same uppercase letter within each row are not considered significantly different according to the Tukey test.

Table 3 - Results of ANOVA and Tukey test for gauge factor (GF) of self-sensing masonry mortars with different lime/cement ratios (l/c) and carbon nanomaterials contents.

Nanomaterials content	Lime/cement ratio				
	l/c = 2.00	l/c = 1.00	l/c = 0.50	l/c = 0.25	l/c = 0.00
6% CBN	169.0 **Ba**	57.3 **Cb**	133.0 **Ba**	162.0 **Ba**	253.0 **Aa**
9% CBN	205.0 **Aa**	192.0 **ABa**	178.0 **ABa**	125.7 **Bb**	154.3 **ABb**

Note: Means sharing a lowercase letter within each column or an uppercase letter within each row are not significantly different by the Tukey test at the 5% significance level.

Source: Author (2024).

Table 4 - Results of ANOVA and Tukey test for stress sensitivity (SS) of self-sensing masonry mortars with different lime/cement ratios (l/c) and carbon nanomaterials contents (in MPa^{-1}) .

Nanomaterials content	Lime/cement ratio				
	l/c = 2.00	l/c = 1.00	l/c = 0.50	l/c = 0.25	l/c = 0.00
6% CBN	0.0752 **Ab**	0.0093 **Bb**	0.0151 **Ba**	0.0249 **Ba**	0.0315 **Ba**
9% CBN	0.1297 **Aa**	0.0988 **Aa**	0.0586 **Bb**	0.0268 **Ba**	0.0361 **Ba**

Note: Means sharing a lowercase letter within each column or an uppercase letter within each row are not significantly different by the Tukey test at the 5% significance level.

Source: Author (2024).

Figure 9 - Notation guidelines related to the use of uppercase and lowercase letters for reporting the results of a two-way ANOVA.

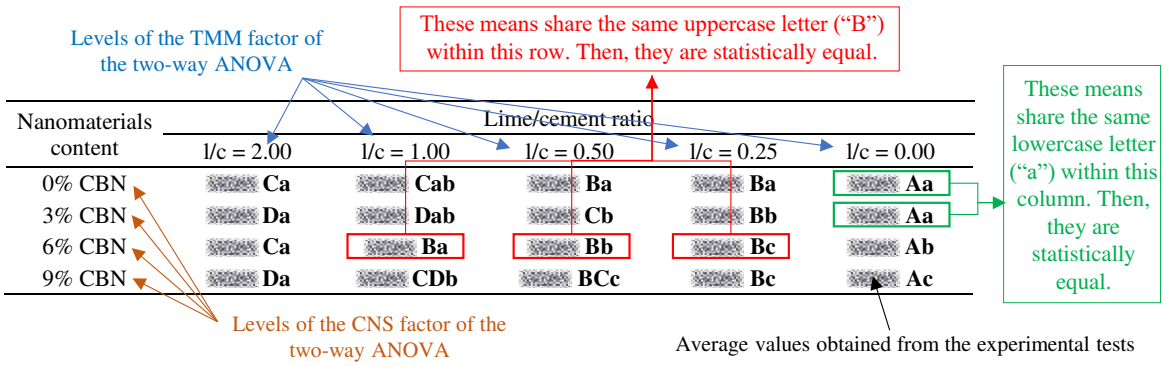

Source: Author (2024).

In mortars with 9% of CBN (by mass of binders), the addition of lime provided statistically significant increases in self-sensing properties. In fact, Tukey test results of Table 3 and Table 4 revealed that 9%-CBN mortars with l/c = 2.00 and l/c = 1.00 share the same uppercase letter (A), whereas the others share a different uppercase letter (B). Increases in GF and SS of mortars with 9% of CBN (by weight of binder) can be explained based on the impacts of lime on their very dense conductive network. Since these mortars had a high concentration of nanomaterials, they exhibited conductive mechanisms typically observed at the end of the percolation zone (tunneling and contact conduction played leading roles in electrical conduction). The microstructural analyses discussed in the previous section indicated that the inclusion of the non-conductive CH and calcite structures caused interruptions in the direct contact between many CBN. It not only reduced contact conduction mechanisms, but also increased the amount of tunneling gaps and enhanced the probability of tunneling conduction between CBN. Since the dominancy of tunneling conduction over contact conduction increases the FCRs associated with external loading (Han et al., 2010, 2015; Nalon et al., 2021), the self-sensing properties of masonry mortars with high concentration of CBN increased with the incorporation of lime.

The percentage increases in the average GF of mortars with 9% of CBN (by mass of binders) due to the addition of lime were lower than the percentage increases in SS. For example, the average GF of TO-9% mortars was 32.8% higher than that of TC-9% mortars, whereas the average SS of TO-9% mortars was 259.7% higher than that of TC-9% mortars. This difference is justified by the high deformability of cement-lime mortars compared to cement mortars (Arandigoyen and Alvarez, 2007; Sébaïbi et al., 2006; Silva and Campiteli, 2008). The elastic modulus of these materials is expected to decrease with the increase in the lime/cement ratio. Consequently, the SS enhancement due to lime incorporation is attributed not only to improvements in tunneling conduction mechanisms (FCR increases), but also to the decreases in the stiffness of the material.

A distinct behavior was observed in mortars with 6% of CBN (by mass of binders). In these composites, the increase in the lime/cement ratio from 0.00 to 1.00 caused statistically significant reductions in GF and negligible changes in SS. According to the Tukey's test results of Table 3, the average GF of 6%-CBN mortars with l/c = 0.0 is higher than the average GF values of mortars with l/c = 0.25 or l/c = 0.50, which are higher than the average GF of mortars with l/c = 1.00. These GF decreases with lime addition are directly related to the sparse conductive network of mortars with 6% of CBN (by mass of binders). Since these

composites were produced with nanoadmixtures content slightly higher than the percolation threshold concentration (within the percolation zone), tunneling conduction played a leading role in their conductivity (Han et al., 2015). In this case, the incorporation of non-conductive lime compounds mentioned in the previous section inevitably increased the thickness of the insulating matrix between CBN. In consequence, lime incorporation decreased the amount of tunneling gaps within the composites, decreasing the FCR amplitude and the GF of the materials.

Although the GF of mortars with 6% of CBN (by mass of binders) decreased when the lime/cement ratio increased from 0.00 to 1.00, their SS did not change in this range. For instance, Table 4 shows that the average SS values of TC-6%, TM-6%, TS-6% and TN-6% mortars share the same uppercase letter (B), which means that they are statistically equal. It is also attributed to the expected reductions in elastic modulus of mortars with the increase in the lime content (Arandigoyen and Alvarez, 2007; Sébaïbi et al., 2006; Silva and Campiteli, 2008). Variations of SS due to lime incorporation were not observed because the FCR reductions associated with decreases in tunneling conduction mechanisms were compensated by the increases in the deformability of the material.

The GF and SS of 6%-CBN mortars increased when the lime/cement ratio increased from 1.00 to 2.00. It probably happened because a high stress amplitude (up to 57% of the strength of the specimens) was unfortunately used in the piezoresistive tests of TO-6% mortars (the uniaxial compression test of the extra mortar prism of this series provided an overestimation of the ultimate strength of the prisms of this series). The application of excessive compressive loading resulted in damage of the cementitious matrix and irreversible changes in electrical resistivity. According to Chung (2020), the GF is incorrectly obtained if reversible and irreversible FCRs are combined in piezoresistive tests beyond the elastic regime of cementitious composites. In addition, it is important to highlight that such high lime/cement ratio (2.00) is only used in non-loadbearing masonry structures.

In summary, the addition of lime enhanced the probability of tunneling conduction mechanisms in mortars designed at the end of the percolation zone, resulting in statistically significant increases in GF and SS values. Furthermore, the percentage increase in SS due to lime incorporation was higher than the percentage increase in GF because the elastic modulus of the mortars decreases with the increase in the lime/cement ratio. On the other hand, the incorporation of lime in mortars designed at the beginning of the percolation zone caused reductions in GF and negligible changes in SS. This is associated with increases in the

thickness of the insulating matrix between CBN, which leads to reductions in the number of tunneling gaps between nanomaterials and in the FCR values.

4.3.4. Compressive strength

The effects of lime/cement ratio and CBN content on the compressive strength of the masonry mortars are presented in Figure 10. The statistical analyses of compressive strength results were detailed in APPENDIX 4A. Since all ANOVA assumptions were met, a factorial ANOVA could be carried out in this case. A P-value equal to 9.3×10^{-8} was obtained when analyzing the interaction effects between the TMM and CNS factors on the compressive strength of the mortars. Therefore, the effects of lime/cement ratio on the mechanical performance of masonry mortars depend on the distribution of carbon nanomaterials in the composite matrix. For the compressive strength dataset, the interaction TMM × CNS was also unfolded for analyses of the influence of each independent variable within each level of the other independent variable.

Figure 10 - Compressive strength of the composites versus lime/cement ratio (a) and compressive strength versus CBN volume fraction.

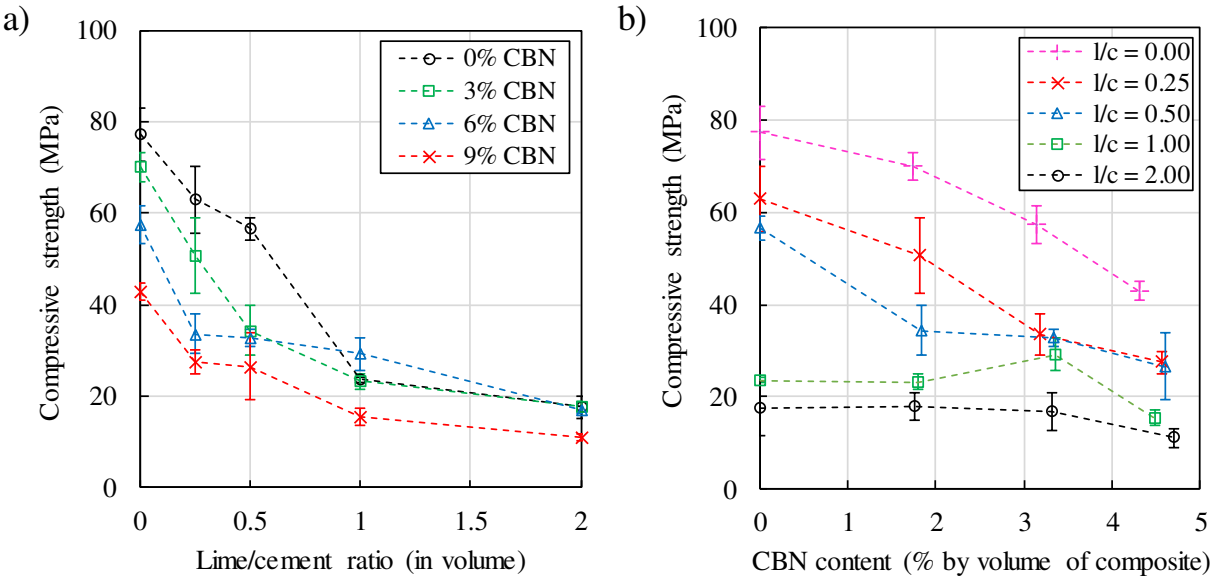

Source: Author (2024).

Table 5 shows the results of post-hoc comparison tests carried out after the development of the factorial ANOVA. Regardless of the CBN concentration, increases in lime content caused similar reductions in the compressive strength of all mortars. In general, Table 5 shows that the average compressive strength of cement mortars (l/c = 0.00) was

statistically higher than the average strengths of cement-lime mortars with l/c = 0.25 and l/c = 0.50, which were statistically higher than the average strengths of mortars with l/c = 1.00 and l/c = 2.0. In fact, Figure 10a indicated that a variation in the lime/cement ratio from 0.00 to 2.00 (by volume) caused percentage reductions in strength ranging between 70.5% and 77.2% in all mortars. These mechanical strength decreases can be explained based on the microstructural changes caused by the increase in lime content, which are mainly characterized by the observations of a less amorphous C-S-H phase, noticeable porosity and higher amount of CH and calcite crystals (Cizer et al., 2008).

Table 5 - Results of ANOVA and Tukey test for compressive strength (MPa) of masonry mortars with different lime/cement ratios (l/c) and carbon nanomaterials contents.

Nanomaterials content	Lime/cement ratio				
	l/c = 2.00	l/c = 1.00	l/c = 0.50	l/c = 0.25	l/c = 0.00
0% CBN	17.59 **Ca**	23.66 **Cab**	56.62 **Ba**	63.01 **Ba**	77.31 **Aa**
3% CBN	17.87 **Da**	23.32 **Dab**	34.42 **Cb**	50.82 **Bb**	70.13 **Aa**
6% CBN	16.95 **Ca**	29.29 **Ba**	32.81 **Bb**	33.57 **Bc**	57.46 **Ab**
9% CBN	11.13 **Da**	15.48 **CDb**	22.06 **BCc**	27.44 **Bc**	42.97 **Ac**

Note: Means sharing a lowercase letter within each column or an uppercase letter within each row are not significantly different by the Tukey test at the 5% significance level.

Source: Author (2024).

Increases in the CBN dosage also caused gradual reductions in the mechanical performance of all mortars. The strength decreases due to the addition of CBN were slightly more evident in mortars with lower lime contents. For instance, Table 5 indicates that all mortars with lime/cement ratio of 2.00 share the same lowercase letter (a), which means that they are statistically equal. For the other lime/cement ratios, a statistical difference was observed between the average strengths of mortars with distinct CBN contents. In fact, Figure 10b shows that mortars produced with a lime/cement ratio of 0.00 and 0.25 presented high percentage reductions in strength (44.4% and 56.5%, respectively) due to the increase in the CBN dosage from 0% to 9% (by weight of binders). In contrast, lower percentage strength decreases were verified in mortars with lime/cement ratio of 1.00 and 2.00 (34.6% and 36.7%, respectively).

According to previous studies dealing with cement mortars containing CBN (Lima et al., 2021; Monteiro et al., 2017a; Zhang et al., 2022), agglomerates of CBN within the cementitious matrix can form weak zones that cause reductions in the mechanical strength of the composites. The FEGSEM analysis of Figure 5d revealed that CBN were usually

intermixed with the flocculated C-S-H structures. Therefore, the addition of CBN seems to impair the cohesion between the hydrates of the masonry mortars, which probably caused the decrease in their mechanical performance.

Although the CBN contents investigated in this study did not provide strength improvements, they ensured significant increases in electrical conductivity and self-sensing properties, which were discussed in the previous subsections. For the contents of CBN and lime investigated in this study, the inclusion of lime caused higher decreases in mechanical strength than the addition of CBN. These effects on the compressive strength must be considered when designing self-sensing masonry mortars for SHM of masonry elements.

4.4. CONCLUSIONS

The present study comprises an experimental investigation of the mutual effects of binder composition and conductive network structure on electrical resistivity, microstructure, self-sensing properties and compressive strength of masonry mortars. The following conclusions were obtained from this work:

(1) The electrical resistivity of dry masonry mortars can be reduced by more than four orders of magnitude with the addition of CBN contents higher than 6% (by mass of binders). However, increases in lime content were found to delay the percolation threshold of cementitious composites. Microstructural analyses suggested that CH and calcite structures increased the distance between adjacent conductive nanomaterials, changing the electron conduction mechanisms.

(2) Plain masonry mortars and masonry mortars with 3% of CBN (by mass of binders) did not exhibit a piezoresistive behavior, whereas a coherent and repeatable self-sensing response was observed in masonry mortars containing 6% or 9% of CBN (by mass of binders).

(3) In mortars designed at the end of the percolation zone, the addition of lime provided statistically significant increases in self-sensing properties (GF and SS). It happened because the inclusion of the non-conductive CH and calcite structures caused interruptions in the direct contact between CBN, reducing contact conduction mechanisms, enhancing the probability of tunneling conduction between CBN and increasing the FCRs associated with external loading.

(4) In mortars designed at the beginning of the percolation zone, the inclusion of lime caused reductions in GF and negligible changes in SS. In this case, the incorporation of non-conductive lime compounds increased the thickness of the insulating matrix between CBN, decreasing the amount of tunneling gaps and decreasing their FCR amplitude.

(5) The compressive strength of masonry mortars decreased with the increase in the contents of lime or CBN. Strength reductions due to increases in CBN concentration were slightly more evident in mortars with lower lime contents. Strength reductions were associated with the agglomeration of CBN, which impaired the cohesion between cementitious compounds and led to the formation of weak zones within the composites.

Some details must be considered before a larger-scale application of the findings reported in the present research. Future investigations should involve specimens with shape and sizes similar to those used in real-life applications (cement-lime mortar joints of masonry structures), in order to examine the geometrical correction factors associated with the electrical and mechanical properties of the self-sensing composites. Future research is also recommended to study the interface between self-sensing mortars and masonry blocks with distinct deformation properties, as the stress/strain compatibility between these masonry components may affect the electromechanical response of the material. Indeed, the self-sensing mortars developed in this research show great potential as materials for monitoring the complex triaxial state of stress/strain of masonry joints. A detailed investigation is also needed to detect the minimum and maximum CBN dosages that could provide an appropriate balance between self-sensing and mechanical properties.

These conclusions provide new insights for the design of smart self-sensing mortars used in SHM systems of masonry elements. Since this work was limited to the development and evaluation of self-sensing cement-lime mortars, the investigation of the piezoresistive response of other different types of masonry mortars (e.g., polymer adhesive mortars, earth mortars, preblended mortars) containing conductive admixtures is the logical follow-up to the present study. Future works are also recommended to elaborate theoretical models that can describe the self-sensing behavior of cement-lime mortars with CBN, based on the investigation of the effects of hydrated lime on tunnel effect theory-based piezoresistivity models available in the literature.

REFERENCES

ABNT. (2005). *NBR 13276: Preparation of mortar for unit masonry and rendering with standard consistence index*.

Arandigoyen, M., & Alvarez, J. I. (2007). Pore structure and mechanical properties of cement–lime mortars. *Cement and Concrete Research*, *37*(5), 767–775. https://doi.org/10.1016/j.cemconres.2007.02.023

ASTM. (2019). *C270: Standard Specification for Mortar for Unit Masonry* (p. 14).

ASTM. (2022). *C150/C150M-22: Standard Specification for Portland Cement*.

Castañeda-Saldarriaga, D. L., Alvarez-Montoya, J., Martínez-Tejada, V., & Sierra-Pérez, J. (2021). Toward Structural Health Monitoring of Civil Structures Based on Self-Sensing Concrete Nanocomposites: A Validation in a Reinforced-Concrete Beam. *International Journal of Concrete Structures and Materials*, *15*(1), 3. https://doi.org/10.1186/s40069-020-00451-8

CEN. (2019). *EN 12390-1: Testing hardened concrete - Part 1: Shape, dimensions and other requirements for specimens and moulds*.

Cholker, A. K. (2021). Incorporation of Smart Concrete in Large-Scale RC Beams for Evaluating Self-Sensing and structural Properties. *Arabian Journal for Science and Engineering*. https://doi.org/10.1007/s13369-021-05517-7

Chung, D. D. L. (2020). A critical review of piezoresistivity and its application in electrical-resistance-based strain sensing. *Journal of Materials Science*, *55*(32), 15367–15396. https://doi.org/10.1007/s10853-020-05099-z

Chung, D. D. L. (2021). Self-sensing concrete: from resistance-based sensing to capacitance-based sensing. *International Journal of Smart and Nano Materials*, *12*(1), 1–19. https://doi.org/10.1080/19475411.2020.1843560

Cizer, O., Van Balen, K., Van Gemert, D., & Elsen, J. (2008). Blended lime-cement mortars for conservation purposes: Microstructure and strength development. In *Structural Analysis of Historic Construction* (pp. 965–972). Taylor & Francis Group.

D'Alessandro, A., Meoni, A., & Ubertini, F. (2018). Stainless Steel Microfibers for Strain-Sensing Smart Clay Bricks. *Journal of Sensors*, *2018*, 1–8. https://doi.org/10.1155/2018/7431823

Dimou, A., Metaxa, Z., Alexopoulos, N., & Kourkoulis, S. (2022). Assessing the potential of nano-reinforced blended lime-cement pastes as self-sensing materials for restoration

applications. *Materials Today: Proceedings*, *62*, 2482–2487. https://doi.org/10.1016/j.matpr.2022.02.623

Dinesh, A., Suji, D., & Pichumani, M. (2022). Electro-mechanical investigations of steel fiber reinforced self-sensing cement composite and their implications for real-time structural health monitoring. *Journal of Building Engineering*, *51*, 104343. https://doi.org/10.1016/j.jobe.2022.104343

Ding, S., Ruan, Y., Yu, X., Han, B., & Ni, Y.-Q. (2019). Self-monitoring of smart concrete column incorporating CNT/NCB composite fillers modified cementitious sensors. *Construction and Building Materials*, *201*, 127–137. https://doi.org/10.1016/j.conbuildmat.2018.12.203

Ding, Y., Li, D., Ma, Y., Liu, G., Song, S., Zhang, D., & Ding, G. (2021). Self-localization of the flexural cracks of fiber reinforced concrete beams. *Construction and Building Materials*, *302*, 124364. https://doi.org/10.1016/j.conbuildmat.2021.124364

Ding, Y., Yang, Y., Liu, R., Xiao, T., & Tian, J. (2019). Study on pressure sensitivity of smart polymer concrete based on steel slag. *Measurement*, *140*, 14–21. https://doi.org/10.1016/j.measurement.2019.03.040

Dong, W., Li, W., Luo, Z., Long, G., Vessalas, K., & Sheng, D. (2020). Structural response monitoring of concrete beam under flexural loading using smart carbon black/cement-based sensors. *Smart Materials and Structures*, *29*(6), 065001. https://doi.org/10.1088/1361-665X/ab7fef

Dong, W., Li, W., Shen, L., Zhang, S., & Vessalas, K. (2021). Integrated self-sensing and self-healing cementitious composite with microencapsulation of nano-carbon black and slaked lime. *Materials Letters*, *282*, 128834. https://doi.org/10.1016/j.matlet.2020.128834

Downey, A., D'Alessandro, A., Laflamme, S., & Ubertini, F. (2018). Smart bricks for strain sensing and crack detection in masonry structures. *Smart Materials and Structures*, *27*(1), 015009. https://doi.org/10.1088/1361-665X/aa98c2

Downey, A., D'Alessandro, A., Ubertini, F., Laflamme, S., & Geiger, R. (2017). Biphasic DC measurement approach for enhanced measurement stability and multi-channel sampling of self-sensing multi-functional structural materials doped with carbon-based additives. *Smart Materials and Structures*, *26*(6), 065008. https://doi.org/10.1088/1361-665X/aa6b66

Drougkas, A., Sarhosis, V., Basheer, M., D'Alessandro, A., & Ubertini, F. (2023a). Design of a smart lime mortar with conductive micro and nano fillers for structural health monitoring. *Construction and Building Materials*, *367*, 130024. https://doi.org/10.1016/j.conbuildmat.2022.130024

Drougkas, A., Sarhosis, V., Basheer, M., D'Alessandro, A., & Ubertini, F. (2023b). Electromechanical Testing of Smart Lime Mortars for Structural Health Monitoring. In *European Workshop on Structural Health Monitoring* (pp. 755–763). Springer. https://doi.org/10.1007/978-3-031-07254-3_76

García-Macías, E., & Ubertini, F. (2019). Earthquake-induced damage detection and localization in masonry structures using smart bricks and Kriging strain reconstruction: A numerical study. *Earthquake Engineering & Structural Dynamics*, *48*(5), 548–569. https://doi.org/10.1002/eqe.3148

Han, B., Ding, S., & Yu, X. (2015). Intrinsic self-sensing concrete and structures: A review. *Measurement*, *59*, 110–128. https://doi.org/10.1016/j.measurement.2014.09.048

Han, B., Yu, X., & Ou, J. (2010). Effect of water content on the piezoresistivity of MWNT/cement composites. *Journal of Materials Science*, *45*(14), 3714–3719. https://doi.org/10.1007/s10853-010-4414-7

Han, J., Cai, J., Pan, J., & Sun, Y. (2021). Study on the conductivity of carbon fiber self-sensing high ductility cementitious composite. *Journal of Building Engineering*, *43*, 103125. https://doi.org/10.1016/j.jobe.2021.103125

Hernoune, H., Benabed, B., Alshugaa, M., Abousnina, R., & Guettala, A. (2020). Strengthening of masonry walls with CFRP composite: experiments and numerical modeling. *Epitoanyag - Journal of Silicate Based and Composite Materials*, *72*(1), 2–11. https://doi.org/10.14382/epitoanyag-jsbcm.2020.1

Horgnies, M., Chen, J. J., & Bouillon, C. (2013). Overview about the use of Fourier Transform Infrared spectroscopy to study cementitious materials. *WIT Transactions on Engineering Sciences*, 251–262. https://doi.org/10.2495/MC130221

Hou, T.-C., & Lynch, J. P. (2005). *Conductivity-based strain monitoring and damage characterization of fiber reinforced cementitious structural components* (M. Tomizuka, Ed.; p. 419). https://doi.org/10.1117/12.599955

Hwang, S.-H., Park, Y.-B., Han, K., & Suk, D. (2011). Smart Materials and Structures Based on Carbon Nanotube Composites. In *Carbon Nanotubes - Synthesis, Characterization, Applications*. InTech. https://doi.org/10.5772/17374

ICBA. (2016). *Carbon Black User's Guide - Safety, Health, & Environmental Information* (p. 32). International Carbon Black Association.

Kaczmarek, A. (2019). Technical Evaluation of Construction Mortars with Various Lime Quantity Additions. *IOP Conference Series: Materials Science and Engineering*, *471*, 032037. https://doi.org/10.1088/1757-899X/471/3/032037

La Mendola, L., Oddo, M. C., Papia, M., Pappalardo, F., Pennisi, A., Bertagnoli, G., Di Trapani, F., Monaco, A., Parisi, F., & Barile, S. (2021). Performance of two innovative stress sensors imbedded in mortar joints of new masonry elements. *Construction and Building Materials*, *297*, 123764. https://doi.org/10.1016/j.conbuildmat.2021.123764

Łątka, D., & Matysek, P. (2018). Assessment of the compressive strength of lime mortar in the joints of brick walls - case study. *MATEC Web of Conferences*, *163*, 02006. https://doi.org/10.1051/matecconf/201816302006

Łątka, D., & Matysek, P. (2020). Determination of Mortar Strength in Historical Brick Masonry Using the Penetrometer Test and Double Punch Test. *Materials*, *13*(12), 2873. https://doi.org/10.3390/ma13122873

Li, H., Xiao, H., & Ou, J. (2006). Effect of compressive strain on electrical resistivity of carbon black-filled cement-based composites. *Cement and Concrete Composites*, *28*(9), 824–828. https://doi.org/10.1016/j.cemconcomp.2006.05.004

Lima, G. E. S. de, Nalon, G. H., Santos, R. F., Ribeiro, J. C. L., Carvalho, J. M. F. de, Pedroti, L. G., & Araújo, E. N. D. de. (2021). Microstructural Investigation of the Effects of Carbon Black Nanoparticles on Hydration Mechanisms, Mechanical and Piezoresistive Properties of Cement Mortars. *Materials Research*, *24*(4). https://doi.org/10.1590/1980-5373-mr-2020-0539

Malathy, R., Shanmugam, R., Chung, I.-M., Kim, S.-H., & Prabakaran, M. (2022). Mechanical and Microstructural Properties of Composite Mortars with Lime, Silica Fume and Rice Husk Ash. *Processes*, *10*(7), 1424. https://doi.org/10.3390/pr10071424

Marastoni, D., Benedetti, A., Pelà, L., & Pignagnoli, G. (2017). Torque Penetrometric Test for the in-situ characterisation of historical mortars: fracture mechanics interpretation and experimental validation. *Construction and Building Materials*, *157*, 509–520. https://doi.org/10.1016/j.conbuildmat.2017.09.120

Medina, C., Sáez del Bosque, I. F., Frías, M., & Sánchez de Rojas, M. I. (2018). Design and characterisation of ternary cements containing rice husk ash and fly ash. *Construction and Building Materials*, *187*, 65–76. https://doi.org/10.1016/j.conbuildmat.2018.07.174

Mehta, P., & Monteiro, P. (2005). *Concrete: Microstructure, Properties and Materials (Portuguese version)* (McGraw-Hill Professional, Ed.).

Meoni, A., D'Alessandro, A., Cavalagli, N., Gioffré, M., & Ubertini, F. (2019). Shaking table tests on a masonry building monitored using smart bricks: Damage detection and localization. *Earthquake Engineering & Structural Dynamics*, *48*(8), 910–928. https://doi.org/10.1002/eqe.3166

Meoni, A., D'Alessandro, A., Kruse, R., De Lorenzis, L., & Ubertini, F. (2021). Strain field reconstruction and damage identification in masonry walls under in-plane loading using dense sensor networks of smart bricks: Experiments and simulations. *Engineering Structures*, *239*, 112199. https://doi.org/10.1016/j.engstruct.2021.112199

Meoni, A., D'Alessandro, A., Mancinelli, M., & Ubertini, F. (2021). A Multichannel Strain Measurement Technique for Nanomodified Smart Cement-Based Sensors in Reinforced Concrete Structures. *Sensors*, *21*(16), 5633. https://doi.org/10.3390/s21165633

Meoni, A., D'Alessandro, A., & Ubertini, F. (2020). Characterization of the strain-sensing behavior of smart bricks: A new theoretical model and its application for monitoring of masonry structural elements. *Construction and Building Materials*, *250*, 118907. https://doi.org/10.1016/j.conbuildmat.2020.118907

Mohamad, G., Fonseca, F. S., Vermeltfoort, A. T., & Lubeck, A. (2018). Stiffness plasticity degradation of masonry mortar under compression: preliminar results. *Revista IBRACON de Estruturas e Materiais*, *11*(2), 279–295. https://doi.org/10.1590/s1983-41952018000200004

Mohamad, G., Fonseca, F. S., Vermeltfoort, A. T., Martens, D. R. W., & Lourenço, P. B. (2017). Strength, behavior, and failure mode of hollow concrete masonry constructed with mortars of different strengths. *Construction and Building Materials*, *134*, 489–496. https://doi.org/10.1016/j.conbuildmat.2016.12.112

Monteiro, A., Cachim, P., & Costa, P. (2017). Self-sensing piezoresistive cement composite loaded with carbon black particles. *Cement and Concrete Composites*, *81*, 59–65. https://doi.org/10.1016/j.cemconcomp.2017.04.009

Monteiro, A., Loredo, A., Costa, P., Oeser, M., & Cachim, P. (2017). A pressure-sensitive carbon black cement composite for traffic monitoring. *Construction and Building Materials*, *154*, 1079–1086. https://doi.org/10.1016/j.conbuildmat.2017.08.053

Nalon, G. H., Ribeiro, J. C., Pedroti, L. G., Duarte de Araújo, E., Franco de Carvalho, J., Soares de Lima, G., & de Moura Guimarães, L. (2021). Residual piezoresistive

properties of mortars containing carbon nanomaterials exposed to high temperatures. *Cement and Concrete Composites*, *121*, 104104. https://doi.org/10.1016/j.cemconcomp.2021.104104

Nalon, G. H., Ribeiro, J., Pedroti, L., de Araújo, E., Franco de Carvalho, J. M., Lima, G., & Oliveira, D. (2021). Self-Sensing Mortars: Effect of Moisture and Nanocarbon Black Content. *ACI Materials Journal*, *118*(3), 131–141. https://doi.org/10.14359/51732636

Nalon, G. H., Santos, C. F. R., Pedroti, L. G., Ribeiro, J. C. L., Veríssimo, G. de S., & Ferreira, F. A. (2020). Strength and failure mechanisms of masonry prisms under compression, flexure and shear: Components' mechanical properties as design constraints. *Journal of Building Engineering*, *28*, 101038. https://doi.org/10.1016/j.jobe.2019.101038

Nalon, G. H., Santos, R. F., Lima, G. E. S. de, Andrade, I. K. R., Pedroti, L. G., Ribeiro, J. C. L., & Franco de Carvalho, J. M. (2022). Recycling waste materials to produce self-sensing concretes for smart and sustainable structures: A review. *Construction and Building Materials*, *325*, 126658. https://doi.org/10.1016/j.conbuildmat.2022.126658

Nalon, G., Ribeiro, J., Araújo, E., Pedroti, L., Carvalho, J., Santos, R., & Aparecido-Ferreira, A. (2020). Effects of different kinds of carbon black nanoparticles on the piezoresistive and mechanical properties of cement-based composites. *Journal of Building Engineering*, *32*, 101724. https://doi.org/10.1016/j.jobe.2020.101724

Nasrazadani, S., Eghtesad, R., Sudoi, E., Vupputuri, S., Ramsey, J. D., & Ley, M. T. (2016). Application of Fourier transform infrared spectroscopy to study concrete degradation induced by biogenic sulfuric acid. *Materials and Structures*, *49*(5), 2025–2034. https://doi.org/10.1617/s11527-015-0631-5

Oliveira, A. L., Damiani, P. L., Ribeiro, I. F. R., Souza, R. A., & Calçada, L. M. L. (2012). Pneumatic pin penetration test to evaluate the compressive strength of mortar bedding on structural masonry (in Portuguese). *Ambiente Construído*, *12*(2), 175–188. https://doi.org/10.1590/S1678-86212012000200012

Parsekian, G., Hamid, A., & Drysdale, G. (2012). *Behavior and design of structural masonry (in Portuguese)*. EdUFSCar.

Parsekian, G., & Soares, M. (2010). *Clay blocks structural masonry - design, execution and control (in Portuguese)* (Telo Melo, Ed.; 1st ed.).

Parvan, M.-G., Voicu, G., Badanoiu, A.-I., & Fruth, V. O. (2020). Self-sensing Piezoresistive Composites Based on Cement Incorporating Low Dosage of Carbon Black Used as

Multifunctional Construction Materials. *Revista de Chimie*, *71*(5), 30–44. https://doi.org/10.37358/RC.20.5.8110

Rao, R. K., & Sasmal, S. (2020). Smart nano-engineered cementitious composite sensors for vibration-based health monitoring of large structures. *Sensors and Actuators A: Physical*, *311*, 112088. https://doi.org/10.1016/j.sna.2020.112088

Scrivener, K., Snellings, R., & Lothenbach, B. (2016). *A Practical Guide to Microstructural Analysis of Cementitious Materials*. CRC.

Sébaïbi, Y., Dheilly, R. M., Beaudoin, B., & Quéneudec, M. (2006). The effect of various slaked limes on the microstructure of a lime–cement–sand mortar. *Cement and Concrete Research*, *36*(5), 971–978. https://doi.org/10.1016/j.cemconres.2005.12.021

Sekhaneh, W., Shiyyab, A., Arinat, M., & Gharaibeh, N. (2020). Use of FTIR and thermogravimetric analysis of ancient mortar from the church of the cross in Gerasa (Jordan) for conservation purposes. *Mediterranean Archaeology and Archaeometry*, *20*(3), 159–174. https://doi.org/10.5281/zenodo.4016073

Silva, N., & Campiteli, V. (2008). Correlação entre módulo de elasticidade dinâmico e resistências mecânicas de argamassas de cimento, cal e areia. *Ambiente Construído*, *8*(4), 21–35.

Snellings, R., Chwast, J., Cizer, Ö., De Belie, N., Dhandapani, Y., Durdzinski, P., Elsen, J., Haufe, J., Hooton, D., Patapy, C., Santhanam, M., Scrivener, K., Snoeck, D., Steger, L., Tongbo, S., Vollpracht, A., Winnefeld, F., & Lothenbach, B. (2018). Report of TC 238-SCM: hydration stoppage methods for phase assemblage studies of blended cements—results of a round robin test. *Materials and Structures*, *51*(4), 111. https://doi.org/10.1617/s11527-018-1237-5

Tantawy, M. A. (2017). Effect of High Temperatures on the Microstructure of Cement Paste. *Journal of Materials Science and Chemical Engineering*, *05*(11), 33–48. https://doi.org/10.4236/msce.2017.511004

Tyagi, B., Chudasama, C. D., & Jasra, R. V. (2006). Determination of structural modification in acid activated montmorillonite clay by FT-IR spectroscopy. *Spectrochimica Acta Part A: Molecular and Biomolecular Spectroscopy*, *64*(2), 273–278. https://doi.org/10.1016/j.saa.2005.07.018

Vaičiukynienė, D., Skipkiūnas, G., Daukšys, M., & Sasnauskas, V. (2013). Cement hydration with zeolite-based additive. *Chemija*, *24*(4), 271–278.

Vlachakis, C., Perry, M., & Biondi, L. (2020). Self-Sensing Alkali-Activated Materials: A Review. *Minerals*, *10*(10), 885. https://doi.org/10.3390/min10100885

Wang, H., Shen, J., Liu, J., Lu, S., & He, G. (2019). Influence of carbon nanofiber content and sodium chloride solution on the stability of resistance and the following self-sensing performance of carbon nanofiber cement paste. *Case Studies in Construction Materials*, *11*, e00247. https://doi.org/10.1016/j.cscm.2019.e00247

Wang, H., Shi, F., Shen, J., Zhang, A., Zhang, L., Huang, H., Liu, J., Jin, K., Feng, L., & Tang, Z. (2021). Research on the self-sensing and mechanical properties of aligned stainless steel fiber-reinforced reactive powder concrete. *Cement and Concrete Composites*, *119*, 104001. https://doi.org/10.1016/j.cemconcomp.2021.104001

Wen, S., & Chung, D. D. L. (2007). Double percolation in the electrical conduction in carbon fiber reinforced cement-based materials. *Carbon*, *45*(2), 263–267. https://doi.org/10.1016/j.carbon.2006.09.031

Xiao, H., Li, H., & Ou, J. (2010). Modeling of piezoresistivity of carbon black filled cement-based composites under multi-axial strain. *Sensors and Actuators A: Physical*, *160*(1–2), 87–93. https://doi.org/10.1016/j.sna.2010.04.027

Yaseen, S. A., Yiseen, G. A., & Li, Z. (2019). Elucidation of Calcite Structure of Calcium Carbonate Formation Based on Hydrated Cement Mixed with Graphene Oxide and Reduced Graphene Oxide. *ACS Omega*, *4*(6), 10160–10170. https://doi.org/10.1021/acsomega.9b00042

Ylmén, R., & Jäglid, U. (2013). Carbonation of Portland Cement Studied by Diffuse Reflection Fourier Transform Infrared Spectroscopy. *International Journal of Concrete Structures and Materials*, *7*(2), 119–125. https://doi.org/10.1007/s40069-013-0039-y

Yoo, D.-Y., You, I., & Lee, S.-J. (2017). Electrical Properties of Cement-Based Composites with Carbon Nanotubes, Graphene, and Graphite Nanofibers. *Sensors*, *17*(5), 1064. https://doi.org/10.3390/s17051064

You, I., Yoo, D.-Y., Kim, S., Kim, M.-J., & Zi, G. (2017). Electrical and Self-Sensing Properties of Ultra-High-Performance Fiber-Reinforced Concrete with Carbon Nanotubes. *Sensors*, *17*(11), 2481. https://doi.org/10.3390/s17112481

Zahra, T., Thamboo, J., & Asad, M. (2021). Compressive strength and deformation characteristics of concrete block masonry made with different mortars, blocks and mortar beddings types. *Journal of Building Engineering*, *38*, 102213. https://doi.org/10.1016/j.jobe.2021.102213

Zhang, D., Zhao, J., Wang, D., Xu, C., Zhai, M., & Ma, X. (2018). Comparative study on the properties of three hydraulic lime mortar systems: Natural hydraulic lime mortar, cement-aerial lime-based mortar and slag-aerial lime-based mortar. *Construction and Building Materials*, *186*, 42–52. https://doi.org/10.1016/j.conbuildmat.2018.07.053

Zhang, Q., Luan, C., Yu, C., Huang, Y., & Zhou, Z. (2022). Mechanisms of carbon black in multifunctional cement matrix: Hydration and microstructure perspectives. *Construction and Building Materials*, *346*, 128455. https://doi.org/10.1016/j.conbuildmat.2022.128455

APPENDIX 4A: RESULTS OF STATISTICAL ANALYSES

4A.1. GRUBB'S TEST FOR OUTLIER DETECTION

Experimental results of electrical resistivity, gauge factor, stress sensitivity and compressive strength obtained in this work were subjected to Grubb's tests for detection of statistical outliers (Table A1, A2, A3 and A4).

4A.1.1. Hypothesis and significance level

- Null hypothesis (H_0): all values belong to the same population.
- Alternative hypothesis (H_a): the smallest or the largest value is an outlier.
- Significance level (α): 5%.

4A.1.2. Results of the statistical tests

Table A1 - Grubb's test statistical summary for the electrical resistivity dataset.

Series	Mean (Ω.cm)	Standard deviation (Ω.cm)	Minimum (Ω.cm)	Maximum (Ω.cm)	Grubb's test statistic	P-value
TO-0%	3772638	320400	3445827	4086218	1.02	0.932
TO-3%	3671302	453501	3224466	4131187	1.01	0.952
TO-6%	1374	154	1207	1509	1.09	0.649
TO-9%	357	115	270	488	1.14	0.351
TN-0%	4976777	725140	4275566	5723684	1.03	0.896
TN-3%	4267676	260776	4068220	4562768	1.13	0.383
TN-6%	1982	89	1886	2061	1.08	0.668
TN-9%	319	38	284	359	1.07	0.740
TS-0%	4935395	600388	4242451	5300203	1.15	0.058
TS-3%	3021604	177844	2835447	3189767	1.05	0.832
TS-6%	971	74	918	1055	1.14	0.281
TS-9%	199	31	177	233	1.14	0.287
TM-0%	3814952	304086	3488117	4089511	1.07	0.715
TM-3%	1422325	709223	861827	2219661	1.12	0.440
TM-6%	540	5	536	546	1.09	0.657
TM-9%	141	43	104	188	1.09	0.645
TC-0%	5210872	983083	4097723	5960126	1.13	0.377
TC-3%	49995	42811	24156	99412	1.15	0.050
TC-6%	960	12	946	968	1.14	0.274
TC-9%	137	16	122	154	1.05	0.821

Source: Author (2024).

Table A2 - Grubb's test statistical summary for gauge factor results.

Series	Mean	Standard deviation	Minimum	Maximum	Grubb's test statistic	P-value
TO-6%	169.0	25.2	140	186	1.150	0.189
TO-9%	205.0	20.7	186	227	1.060	0.759
TN-6%	57.3	22.8	37	82	1.080	0.684
TN-9%	192.0	9.9	181	200	1.120	0.490
TS-6%	133.0	35.2	96	166	1.050	0.812
TS-9%	178.0	32.5	145	210	1.020	0.949
TM-6%	162.0	54.3	123	224	1.140	0.282
TM-9%	125.7	34.5	97	164	1.110	0.532
TC-6%	253.0	9.5	247	264	1.150	0.100
TC-9%	154.3	9.1	146	164	1.070	0.756

Source: Author (2024).

Table A3 - Grubb's test statistical summary for stress sensitivity results.

Series	Mean (MPa^{-1})	Standard deviation (MPa^{-1})	Minimum (MPa^{-1})	Maximum (MPa^{-1})	Grubb's test statistic	P-value
TO-6%	0.075	0.027	0.045	0.092	1.15	0.108
TO-9%	0.130	0.017	0.117	0.149	1.13	0.369
TN-6%	0.009	0.005	0.005	0.015	1.08	0.704
TN-9%	0.099	0.012	0.090	0.113	1.15	0.210
TS-6%	0.015	0.005	0.010	0.019	1.12	0.452
TS-9%	0.059	0.016	0.041	0.070	1.14	0.320
TM-6%	0.025	0.013	0.015	0.040	1.14	0.283
TM-9%	0.027	0.010	0.016	0.035	1.08	0.689
TC-6%	0.031	0.003	0.030	0.035	1.15	0.141
TC-9%	0.036	0.018	0.025	0.056	1.15	0.125

Source: Author (2024).

Table A4 - Grubb's test statistical summary for compressive strength results.

Series	Mean (MPa)	Standard deviation (MPa)	Minimum (MPa)	Maximum (MPa)	Grubb's test statistic	P-value
TO-0%	17.59	2.96	14.47	20.36	1.05	0.807
TO-3%	17.87	1.33	16.35	18.77	1.15	0.193
TO-6%	16.95	0.87	16.14	17.87	1.06	0.798
TO-9%	11.13	0.88	10.19	11.94	1.06	0.758
TN-0%	23.66	0.79	22.89	24.48	1.03	0.879
TN-3%	23.32	2.05	21.65	25.61	1.12	0.493
TN-6%	29.29	4.27	24.97	33.51	1.01	0.963
TN-9%	15.48	2.10	13.07	16.88	1.15	0.173
TS-0%	56.62	3.12	53.31	59.52	1.06	0.790
TS-3%	34.42	6.57	26.86	38.73	1.15	0.152
TS-6%	32.81	2.16	31.20	35.27	1.14	0.342
TS-9%	22.06	4.37	17.72	26.45	1.01	0.978

TM-0%	63.01	8.80	53.38	70.63	1.09	0.620
TM-3%	50.82	10.05	44.38	62.41	1.15	0.124
TM-6%	33.57	5.26	27.73	37.92	1.11	0.525
TM-9%	27.44	3.18	23.96	30.19	1.09	0.621
TC-0%	77.31	7.19	69.34	83.30	1.11	0.542
TC-3%	70.13	3.74	65.82	72.61	1.15	0.168
TC-6%	57.46	5.03	51.76	61.26	1.13	0.362
TC-9%	42.97	2.40	40.35	45.04	1.1	0.614

Source: Author (2024).

4A.1.3. Conclusions of the statistical tests

Since all analyses provided a P-value higher than 0.050, the null hypothesis was not rejected. Therefore, outliers were not found in the experimental dataset.

4A.2. SHAPIRO-WILK TEST OF NORMALITY

Experimental results of electrical resistivity, gauge factor, stress sensitivity and compressive strength obtained in this work were subjected to the Shapiro-Wilk test for verification of normality of residuals (Table A5), which is one of the assumptions of each analysis of variance (ANOVA) presented in Section A.4.

4A.2.1. Hypothesis and significance level

- Null hypothesis (H_0): residuals are normally distributed.
- Alternative hypothesis (H_a): residuals are not normally distributed.
- Significance level (α): 5%.

4A.2.2. Results of the statistical tests

Table A5 - Shapiro-Wilk's test statistical summary for all response variables.

Response variable	Shapiro-Wilk's test statistic	P-value
Electrical resistivity	0.816	3.5×10^{-7}
Gauge factor	0.976	0.699
Stress sensitivity	0.971	0.580
Compressive strength	0.974	0.218

Source: Author (2024).

4A.2.3. Conclusions of the statistical tests

Analyses of results of gauge factor, stress sensitivity and compressive strength provided a P-value higher than 0.050, which indicates that the null hypothesis was not rejected. For these response variables, the residuals are normally distributed. On the other hand, residuals associated with the electrical resistivity dataset are not normally distributed because a P-value lower than 0.050 was obtained.

4A.3. BARTLETT TEST OF HOMOSCEDASTICITY

Experimental results of electrical resistivity, gauge factor, stress sensitivity and compressive strength obtained in this work were subjected to the Bartlett test for verification of homoscedasticity (Table A6), which is one of the assumptions of each ANOVA presented in Section A.4.

4A.3.1. Hypothesis and significance level

- Null hypothesis (H_0): all population variances are equal.
- Alternative hypothesis (H_a): at least two population variances are different.
- Significance level (α): 5%.

4A.3.2. Results of the statistical tests

Table A6 - Bartlett's test statistical summary for all response variables.

Response variable	Bartlett's K-squared	P-value
Electrical resistivity	316.34	2.2×10^{-16}
Gauge factor	9.768	0.370
Stress sensitivity	11.213	0.261
Compressive strength	29.033	0.065

Source: Author (2024).

A.3.3. Conclusions of the statistical tests

Analyses of results of gauge factor, stress sensitivity and compressive strength provided a P-value higher than 0.050, which indicates that the null hypothesis was not rejected. Thus, homogeneity of variances was observed in these cases. In contrast,

homogeneity of variances was not verified in the electrical resistivity dataset because a P-value lower than 0.050 was obtained.

4A.4. ANOVA OF MAIN FACTORS AND INTERACTION BETWEEN THEM

A factorial analysis of variances (ANOVA) of results of gauge factor, stress sensitivity and compressive strength was carried out to identify (i) the effect of individual factors and (ii) interactions between different factors on each response variable (Table A7, A8 and A9). Factorial ANOVA of electrical resistivity results was not carried out because the ANOVA assumptions of normality of residuals and homogeneity of variances were not verified in this dataset, as reported in Sections A.2 and A.3, respectively.

4A.4.1. Hypothesis and significance level

For the CNS factor:

- Null hypothesis (H_0): there is no significant difference on the response variable based on the conductive network structure of the mortar.
- Alternative hypothesis (H_a): there is some difference on the response variable based on the conductive network structure of the mortar.
- Significance level (α): 5%.

For the TMM factor:

- Null hypothesis (H_0): there is no significant difference on the response variable based on the type of masonry mortar.
- Alternative hypothesis (H_a): there is some difference on the response variable based on the type of masonry mortar.
- Significance level (α): 5%.

For the interaction between CNS and TMM factors:

- Null hypothesis (H_0): there is no significant interaction effect between the conductive network structure and the type of masonry mortar on the response variable.
- Alternative hypothesis (H_a): there is a significant interaction effect between the conductive network structure and the type of masonry mortar on the response variable.
- Significance level (α): 5%

4A.4.2. Results of the statistical tests

Table A7 - Factorial ANOVA statistical summary for the gauge factor dataset.

Source		Degrees of freedom	Sum of squares	Mean Square	F test statistics	P-value
Main factors	TMM	4	24737.00	6184.20	7.46	7.6×10^{-4}
	CNS	1	1952.00	1952.10	2.36	0.141
Interaction	TMM × CNS	4	46815.00	11703.70	14.12	1.3×10^{-5}
Residuals		20	16576.00	828.80	-	-

Source: Author (2024).

Table A8 - Factorial ANOVA statistical summary for the stress sensitivity dataset.

Source		Degrees of freedom	Sum of squares	Mean Square	F test statistics	P-value
Main factors	TMM	4	0.0227	0.0057	28.34	5.5×10^{-8}
	CNS	1	0.0113	0.0113	56.42	3.1×10^{-7}
Interaction	TMM × CNS	4	0.0081	0.0020	10.06	1.3×10^{-4}
Residuals		20	0.0040	0.0002		

Source: Author (2024).

Table A9 - Factorial ANOVA statistical summary for the compressive strength dataset.

Source		Degrees of freedom	Sum of squares	Mean Square	F test statistics	P-value
Main factors	TMM	4	15707.30	3926.80	183.03	$< 2.2 \times 10^{-16}$
	CNS	3	4478.30	1492.80	69.58	6.3×10^{-16}
Interaction	TMM × CNS	12	2217.10	184.80	8.61	9.3×10^{-8}
Residuals		40	858.20	21.50	-	-

Source: Author (2024).

4A.4.3. Conclusions of the statistical tests

The ANOVA of individual factors only provided a P-value higher than 0.05 (P-value = 0.141) when evaluating the effects of the conductive network structure on the gauge factor of self-sensing mortars. This result initially suggested that there was no significant difference on the gauge factor based on the conductive network structure of mortars containing 6% or 9% of CBN. In contrast, all of the other ANOVAs of individual factors provided P-values lower than 0.05, which indicated that the null hypothesis should be rejected, i.e., there was some difference on the response variable based on the corresponding individual factor. Although these main effects analyses are valid from a mathematical point of view, it is important to highlight that additional analyses were required because significant interaction effects between the TMM and CNS factors were also verified. In fact, the

ANOVA of the interactions always provided a P-value lower than 0.05. Consequently, the null hypothesis must be rejected, i.e., there was a significant interaction effect between the conductive network structure and the type of masonry mortar on the gauge factor, stress sensitivity and compressive strength of the masonry mortars. The effect of one factor on the response variable can be different dependent on the level of the factor. In order to properly identify statistical differences between response variables (considering the interaction effects), complementary analyses were required, as presented in Section A.5.

4A.5. ANOVA OF FACTORIAL EXPERIMENT WITH SIGNIFICATIVE INTERACTION

Since the statistical analyses presented in Section A.4 suggested significant interaction effects between the TMM and CNS factors on all response variables, Tukey's multiple comparison tests must not be applied separately for each factor, neglecting the interaction effects. Actually, it is necessary to unfold the interaction TMM × CNS based on two different methods (Table A10, A11, A12, A13, A14 and A15): (i) analysis of the effects of masonry mortar type within each type of conductive network structure and (ii) analysis of the effects of the conductive network structure within each type of masonry mortar.

4A.5.1. Hypothesis and significance level

Unfolding the interaction TMM × CNS for analysis of the effects of the CNS within each level of the TMM factor:

- Null hypothesis (H_0): within the corresponding level of the TMM factor, there is no significant difference on the response variable based on the conductive network structure of the mortar.
- Alternative hypothesis (H_a): within the corresponding level of the TMM factor, there is some difference on the response variable based on the conductive network structure of the mortar.
- Significance level (α): 5%.

Unfolding the interaction TMM × CNS for analysis of the effects of the TMM within each level of the CNS factor:

- Null hypothesis (H_0): within the corresponding level of the CNS factor, there is no significant difference on the response variable based on the type of mortar.

- Alternative hypothesis (H_a): within the corresponding level of the CNS factor, there is some difference on the response variable based on the type of mortar.
- Significance level (α): 5%.

4A.5.2. Results of the statistical tests

Table A10 - Unfolding the interaction TMM × CNS for analysis of the effects of the CNS within each level of the TMM factor on the gauge factor of the mortars.

Source	Degrees of freedom	Sum of squares	Mean Square	F test statistics	P-value
CNS/TMM_1	1	1944.00	1944.00	2.35	0.1413
CNS/TMM_2	1	27202.67	27202.67	32.82	~ 0.000
CNS/TMM_3	1	3037.50	3037.50	3.66	0.0700
CNS/TMM_4	1	1980.17	1980.17	2.39	0.1379
CNS/TMM_5	1	14602.67	14602.67	17.62	0.0004
Residuals	20	16576.00	828.80	-	-

Note: TMM_1: cement-lime mortar with l/c = 2.00, TMM_2: cement-lime mortar with l/c = 1.00, TMM_3: cement-lime mortar with l/c = 0.50, TMM_4: cement-lime mortar with l/c = 0.25, TMM_5: cement mortar.

Source: Author (2024).

Table A11 - Unfolding the interaction TMM × CNS for analysis of the effects of the TMM within each level of the CNS factor on the gauge factor of the mortars.

Source	Degrees of freedom	Sum of squares	Mean Square	F test statistics	P-value
TMM/CNS_1	4	59615.07	14903.77	17.98	~ 0.000
TMM/CNS_2	4	11936.67	2984.17	3.60	0.0229
Residuals	20	16576.00	828.80	-	-

Note: CNS_1: mortars with 6% of CBN, CNS_2: mortars with 9% of CBN.

Source: Author (2024).

Table A12 - Unfolding the interaction TMM × CNS for analysis of the effects of the CNS within each level of the TMM factor on the stress sensitivity of the mortars.

Source	Degrees of freedom	Sum of squares	Mean Square	F test statistics	P-value
CNS/TMM_1	1	0.0045	0.0045	22.2581	~ 0.000
CNS/TMM_2	1	0.0120	0.0120	59.9974	~ 0.000
CNS/TMM_3	1	0.0029	0.0029	14.2060	0.001
CNS/TMM_4	1	0.0000	0.0000	0.0270	0.871
CNS/TMM_5	1	0.0000	0.0000	0.1584	0.695
Residuals	20	0.00	0.00	-	-

Note: TMM_1: cement-lime mortar with l/c = 2.00, TMM_2: cement-lime mortar with l/c = 1.00, TMM_3: cement-lime mortar with l/c = 0.50, TMM_4: cement-lime mortar with l/c = 0.25, TMM_5: cement mortar.

Source: Author (2024).

Table A13 - Unfolding the interaction TMM × CNS for analysis of the effects of the TMM within each level of the CNS factor on the stress sensitivity of the mortars

Source	Degrees of freedom	Sum of squares	Mean Square	F test statistics	P-value
TMM/CNS_1	4	0.0082	0.0020	10.1681	~ 0.000
TMM/CNS_2	4	0.0226	0.0057	28.2331	~ 0.000
Residuals	20	0.0040	0.0002	-	-

Note: CNS_1: mortars with 6% of CBN, CNS_2: mortars with 9% of CBN.

Source: Author (2024).

Table A14 - Unfolding the interaction TMM × CNS for analysis of the effects of the CNS within each level of the TMM factor on the compressive strength of the mortars.

Source	Degrees of freedom	Sum of squares	Mean Square	F test statistics	P-value
CNS/TMM_1	3	91.80	30.60	1.43	0.249
CNS/TMM_2	3	289.75	96.58	4.50	0.008
CNS/TMM_3	3	1893.17	631.06	29.41	~ 0.000
CNS/TMM_4	3	2371.81	790.60	36.85	~ 0.000
CNS/TMM_5	3	2048.87	682.96	31.83	~ 0.000
Residuals	40	858.20	21.50	-	-

Note: TMM_1: cement-lime mortar with l/c = 2.00, TMM_2: cement-lime mortar with l/c = 1.00, TMM_3: cement-lime mortar with l/c = 0.50, TMM_4: cement-lime mortar with l/c = 0.25, TMM_5: cement mortar.

Source: Author (2024).

Table A15 - Unfolding the interaction TMM × CNS for analysis of the effects of the TMM within each level of the CNS factor on the compressive strength of the mortars

Source	Degrees of freedom	Sum of squares	Mean Square	F test statistics	P-value
TMM/CNS_1	4	8025.51	2006.38	93.51	~ 0.000
TMM/CNS_2	4	5463.94	1365.99	63.67	~ 0.000
TMM/CNS_3	4	2594.21	648.55	30.23	~ 0.000
TMM/CNS_4	4	1840.73	460.18	21.45	~ 0.000
Residuals	40	858.20	21.50	-	-

Note: CNS_1: mortars without CBN, CNS_2: mortars with 3% of CBN, CNS_3: mortars with 6% of CBN, CNS_4: mortars with 9% of CBN.

Source: Author (2024).

4A.5.3. Conclusions of the statistical tests

For the gauge factor dataset, the ANOVAs only provided a P-value higher than 0.05 in the following processes: CNS unfolding within cement-lime mortars with l/c = 2.00, CNS unfolding within cement-lime mortars with l/c = 0.50, CNS unfolding within cement-lime mortars with l/c = 0.25. For the stress sensitivity dataset, it was only observed in the following

processes: CNS unfolding within cement-lime mortars with l/c = 0.25 and CNS unfolding within cement mortars. For compressive strength, it was only verified in the CNS unfolding within cement-lime mortars with l/c = 2.00. In these cases, the null hypothesis was not rejected. A P-value lower than 0.05 was obtained in the other cases, which indicated that there was a significant difference between the averages. Tukey tests at the 5% significance level were used to identify which average values differ from the others. Results of these tests were tabulated in the main text of the present work.

Figure B1 - FCR *vs* compressive strain curves of mortars containing 6% of CBN (by mass of binders).

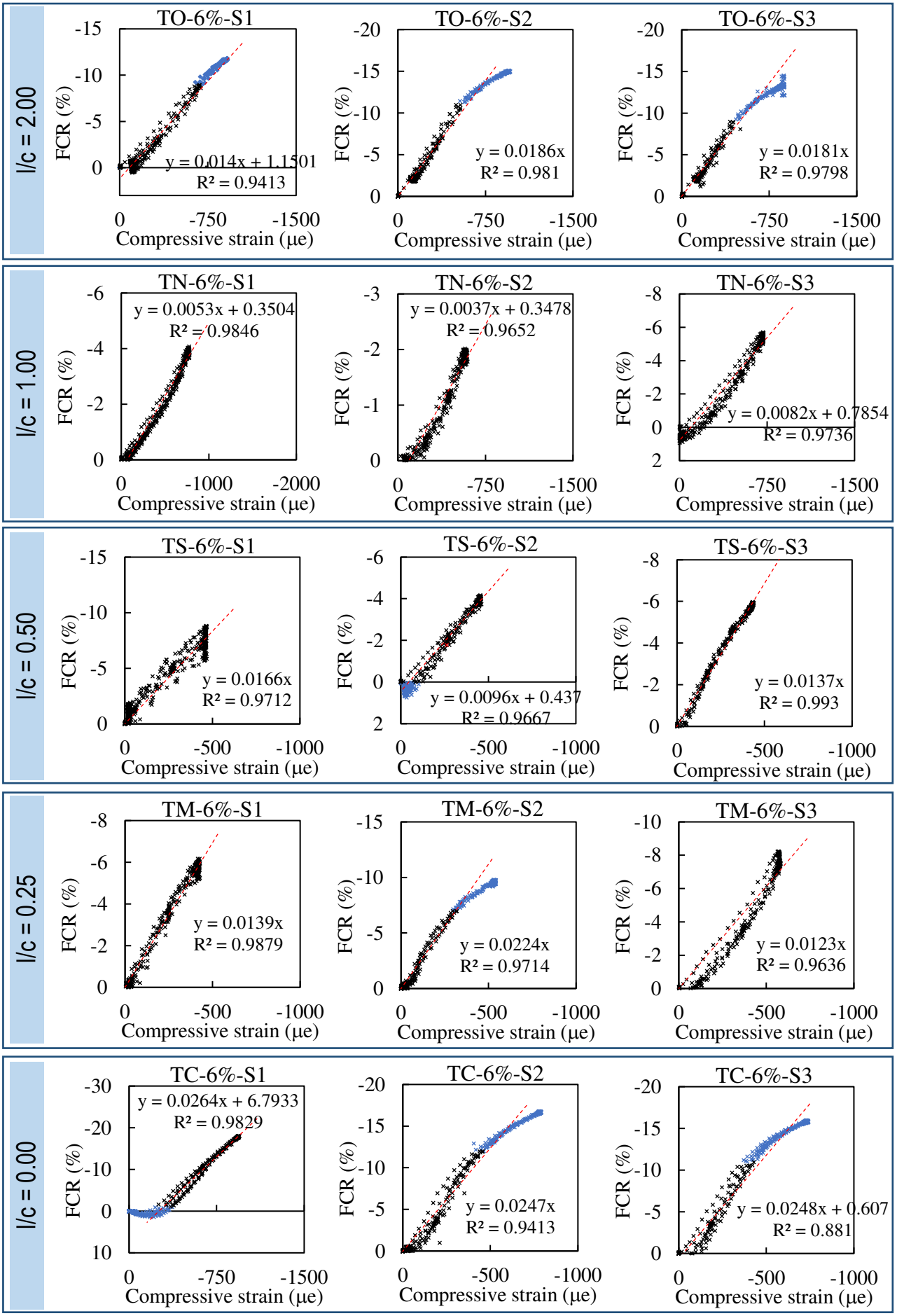

Source: Author (2024)

Figure B2 - FCR *vs* compressive stress curves of mortars containing 6% of CBN (by mass of binders).

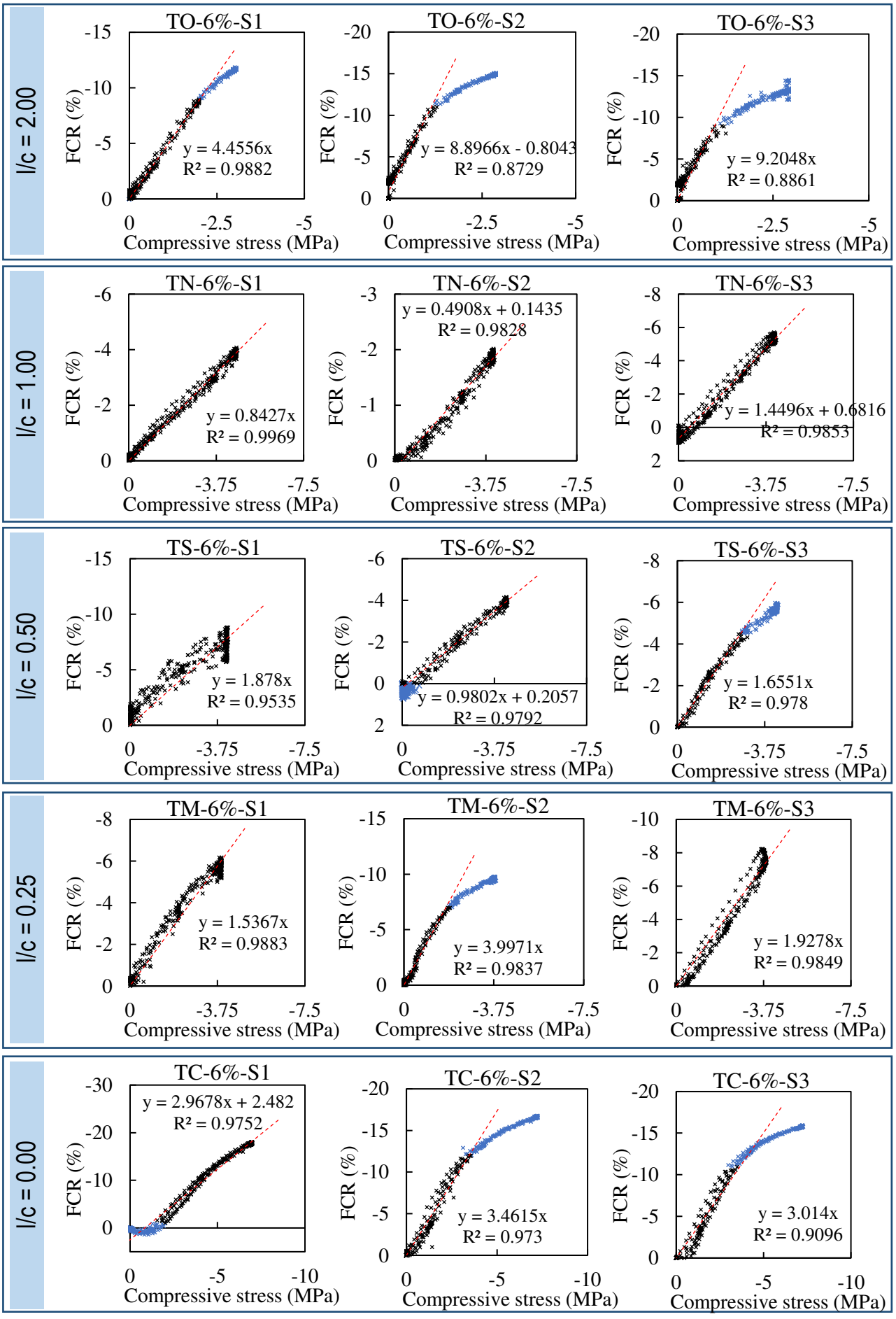

Source: Author (2024)

Figure B3 - FCR *vs* compressive strain curves of mortars containing 9% of CBN (by mass of binders).

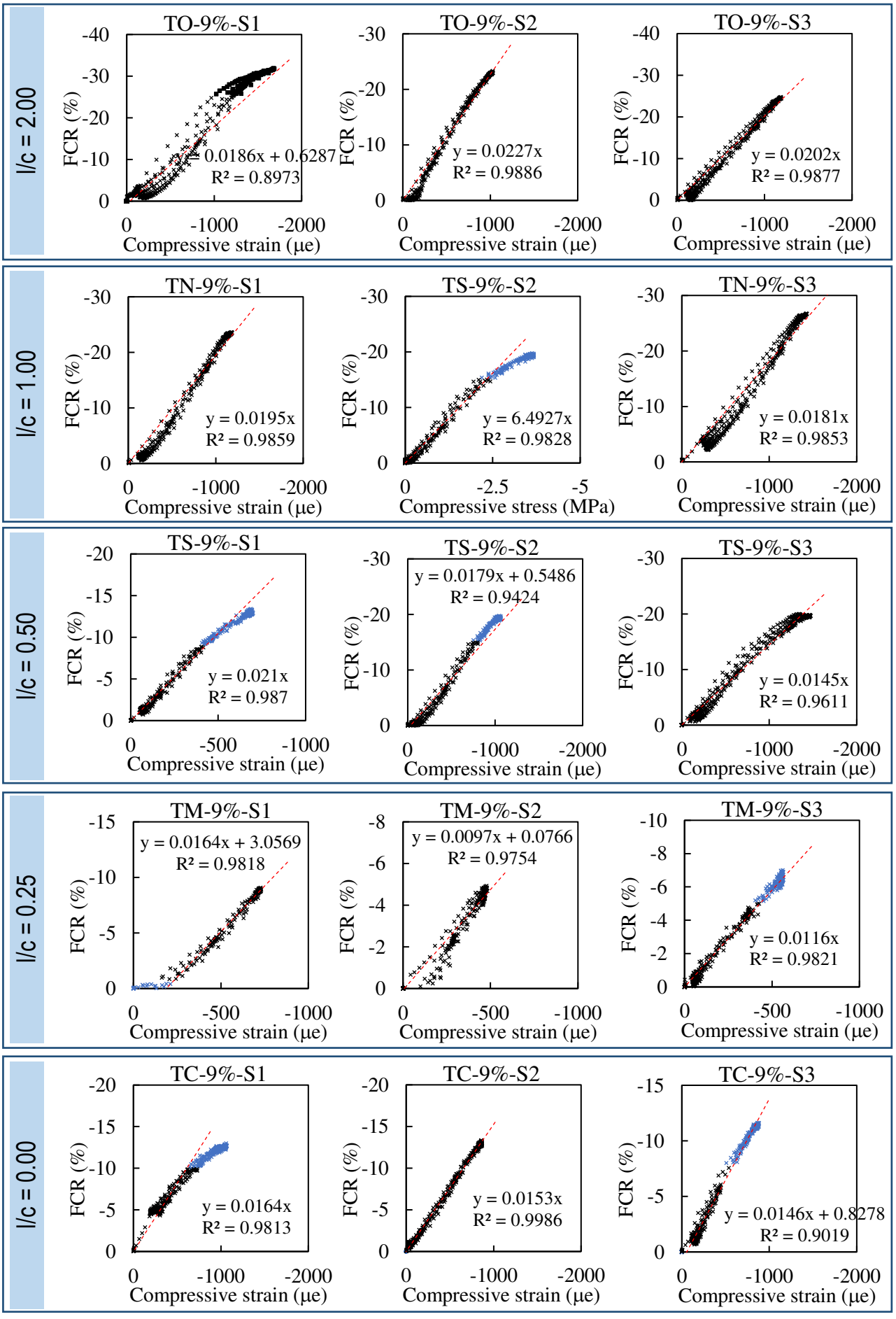

Source: Author (2024)

Figure B4 - FCR *vs* compressive stress curves of mortars containing 9% of CBN (by mass of binders).

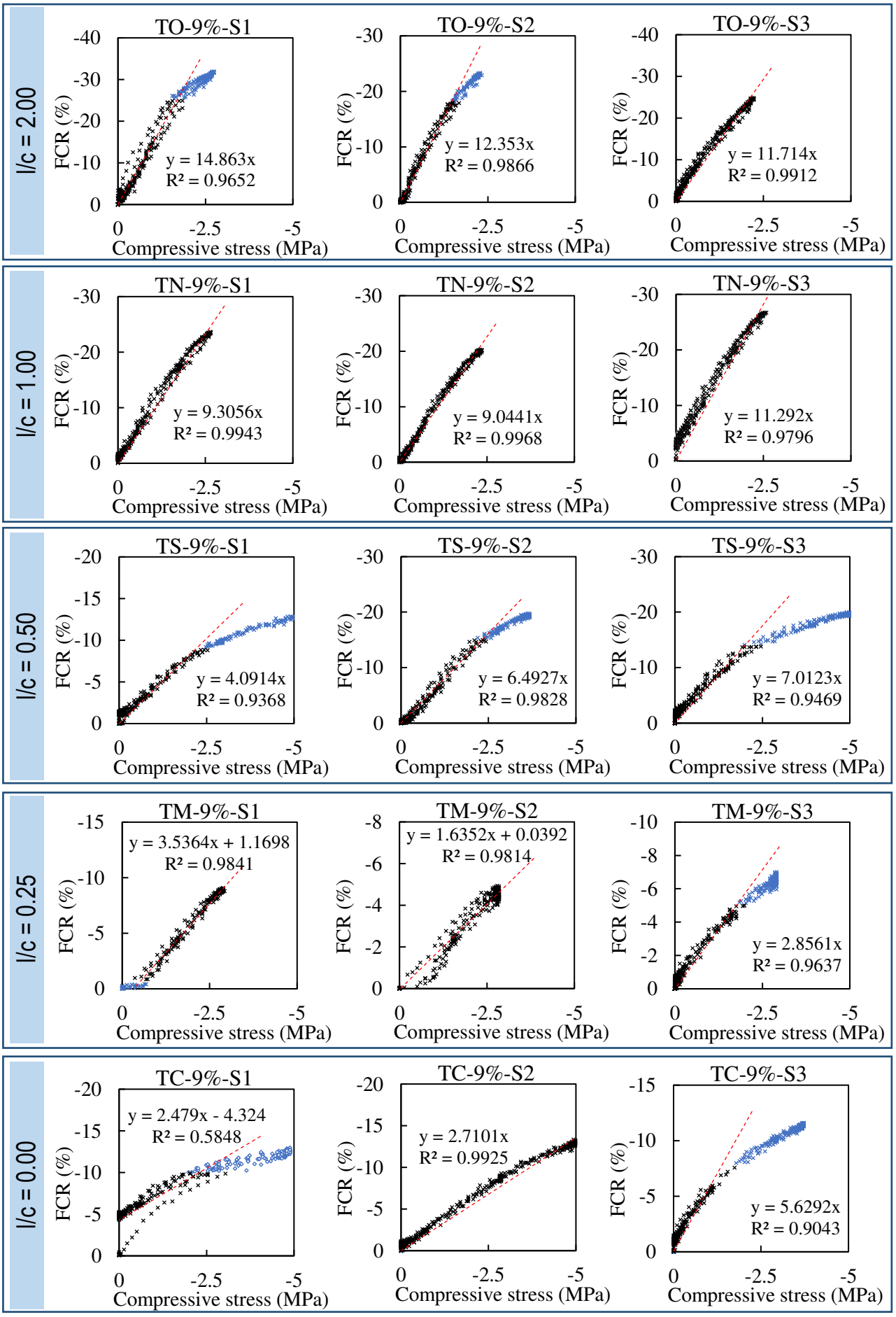

Source: Author (2024)

5 CONCRETE UNITS FOR STRAIN-MONITORING IN CIVIL STRUCTURES: INSTALLATION OF CEMENT-BASED SENSORS USING DIFFERENT APPROACHES

This chapter has been published as the following paper: Nalon, G. H.; Ribeiro, J. C. L.; Araújo, E. N. D.; Silva, R. M.; Pedroti, L. G.; Lima, G. E. S. Concrete units for strain-monitoring in civil structures: Installation of cement-based sensors using different approaches. ***Construction and Building Materials*** *394 (2023) 132169. https://doi.org/10.1016/j.conbuildmat.2023.132169*

Abstract: *Cementitious materials with self-sensing properties have been recently proposed for strain-monitoring of civil structures. Although different methods have been used to install cement-based sensors in concrete elements, there is a lack of systematic experimental comparisons between self-sensing mechanisms provided by different procedures. This work investigated the bonding performance of different interface agent types (cement-based bonding agent, polyurethane-based interface and epoxy-based structural adhesive) between self-sensing cementitious materials and concrete substrates. It also reported the strain-monitoring performance and the compressive behavior of cement sensors embedded into masonry units using three methods: (i) the cement sensor was in the hardened state and the concrete structural element was in the fresh state during the installation process (HS/FC - hardened sensor/fresh concrete); (ii) the fresh cement sensor was installed in hardened concrete units (FS/HC - fresh sensor/hardened concrete); and (iii) both components were in the hardened state during the installation process (HS/HC - hardened sensor/hardened concrete). Results indicated that the epoxy-based structural adhesive provided the best bonding performance and ensured suitable transference of stresses between cement-based sensors and the monitored concrete element. The HS/FC and the FS/HC approaches were found to be appropriate for future cement-based sensors installations because they provided composites with appropriate values of average gauge factor and mechanical performance.*

Keywords: *Structural Health Monitoring, concrete units, smart cement-based composites, carbon black nanoparticles, embedding approaches.*

5.1. INTRODUCTION

Recent improvements in the understanding of piezoresistive properties of cementitious materials containing conductive admixtures enabled the development of multifunctional concretes with intrinsic abilities of stress, strain and damage sensing. The traditional sensing technologies used in Structural Health Monitoring (SHM) systems are usually expensive, have poor long-term durability, do not exhibit a natural compatibility with infrastructures, require skilled workers for installation, demand high maintenance costs, and do not support frequent service loads and harsh environmental conditions (Ding et al., 2022; Han et al., 2015b; Hussain et al., 2022). The large-scale application of conventional SHM systems is often limited by the lack of scalability, as numerous sensors are required for damage diagnosis, localization, and prognosis of large structures (Laflamme et al., 2016). Compared to the traditional sensors used in SHM, the practical use of self-sensing cementitious materials is advantageous in many different aspects, including low cost, natural compatibility with civil structures, in addition to high mechanical strength, durability, sensitivity, authenticity and robustness (Chung, 2021; Dong et al., 2022; Han et al., 2020; Ubertini and D'Alessandro, 2018).

Previous papers reported an appropriate self-sensing response for monitoring stress and strain in different types of cementitious composites subjected to quasi-static loadings (Birgin et al., 2023; Dong et al., 2021a, 2021b, 2020; Nalon et al., 2020, 2021a; Suchorzewski et al., 2020; Xu et al., 2021) or dynamic loadings in the frequency range of 0.1-5 Hz, covering the typical frequency content of the dynamic response of large civil engineering structures (Adresi et al., 2021; D'Alessandro et al., 2021; García-Macías et al., 2017; Materazzi et al., 2013; Meoni et al., 2018). Therefore, the self-sensing materials can successfully detect loading redistributions associated with the development of structural damages (Meoni et al., 2021a, 2019). In addition, the conductive network inside the smart composites is broken down when severe damage occurs in the self-sensing cementitious matrix, increasing their electrical resistivity (Han et al., 2015b). Consequently, the self-sensing materials are able to demonstrate a response to the initial propagation of cracks, progressive and sudden damage events, which suggests another interesting potential for SHM of civil infrastructures (Ding et al., 2023). Different multichannel measurement techniques have also been investigated for practical field implementations of smart cement-based sensors. These methodologies are

based on various configurations of circuit diagrams containing reference resistors and self-sensing composites whose electrical outputs are obtained by direct current (DC) methods (Han et al., 2015b, 2007), alternating current (AC) methods (Kang et al., 2018; Machan and Steffan, 2015), or biphasic DC methods (Downey et al., 2017; Meoni et al., 2021b).

According to previous literature (Abedi et al., 2021; Han et al., 2015a; Horszczaruk et al., 2016), self-sensing cementitious composites can be applied to structural elements using different configurations, such as the bulk, coating/sandwich, bonded and embedded forms. In the bulk approach, structural elements are exclusively made of self-sensing concrete. In the other configurations, the self-sensing cementitious materials are only applied to key locations of civil structures. Previous works have proposed different key locations for self-sensing composites such as the top and bottom of middle span or side span of concrete beams (Liu et al., 2018; Xiao et al., 2011a); center of concrete columns (Ding et al., 2019; Xiao and Li, 2006); sleepers and ballasts of railway systems (Lee et al., 2020; Xu et al., 2020); lintel supports, connections and arches of masonry structures (Downey et al., 2018); sections of track slabs (Ding et al., 2022; Han et al., 2013); among others. Compared to the other configurations, the bulk form has some drawbacks such as lower monitoring efficiency, higher construction cost and higher susceptibility of steel reinforcement to corrosion mechanisms (Abedi et al., 2021; Han et al., 2015a; Horszczaruk et al., 2016). In fact, previous research (Garcés et al., 2012, 2005; Hassan et al., 2019; Li et al., 2020) reported that steel corrosion rates were higher in cementitious matrices containing carbonaceous admixtures, due to the higher electrical conductivity of the composites and destruction of the passivating layer on the steel rebar surface. Moreover, Han et al. (2022) verified that the embedded approach improved the sensitivity, signal-to-noise ratio and repeatability of the cement-based sensors, compared to the bulk and coating/sandwich configurations.

When the bulk approach is not used, three main installation methods (Figure 1) have been applied to incorporate self-sensing cementitious composites into key locations of structural elements (Baeza et al., 2013; Ding et al., 2019; Han et al., 2013; Meoni et al., 2021b; Sun et al., 2014; Ubertini and D'Alessandro, 2018). In the first method, the cement-based sensor is in the hardened state and the concrete structural element is in the fresh state during the installation process (HS/FC method - hardened sensor/fresh concrete). In the second approach, the fresh cement-based sensor is installed on hardened concrete elements (FS/HC method - fresh sensor/hardened concrete). In the last case, both cement-based sensor and structural element are in the hardened state during the installation procedures (HS/HC

method - hardened sensor/hardened concrete). For practical application purposes, previous studies (Baeza et al., 2013; Han et al., 2013; Monteiro et al., 2017; Sun et al., 2014; Xiao et al., 2011a) have also proposed different types of interfaces between the self-sensing cementitious materials and the structural concrete element, such as epoxy resin or cementitious bonding agents. These interface types improved bonding and/or waterproofing performances.

Figure 1 - Installation methods used to apply self-sensing cementitious composites to structural elements.

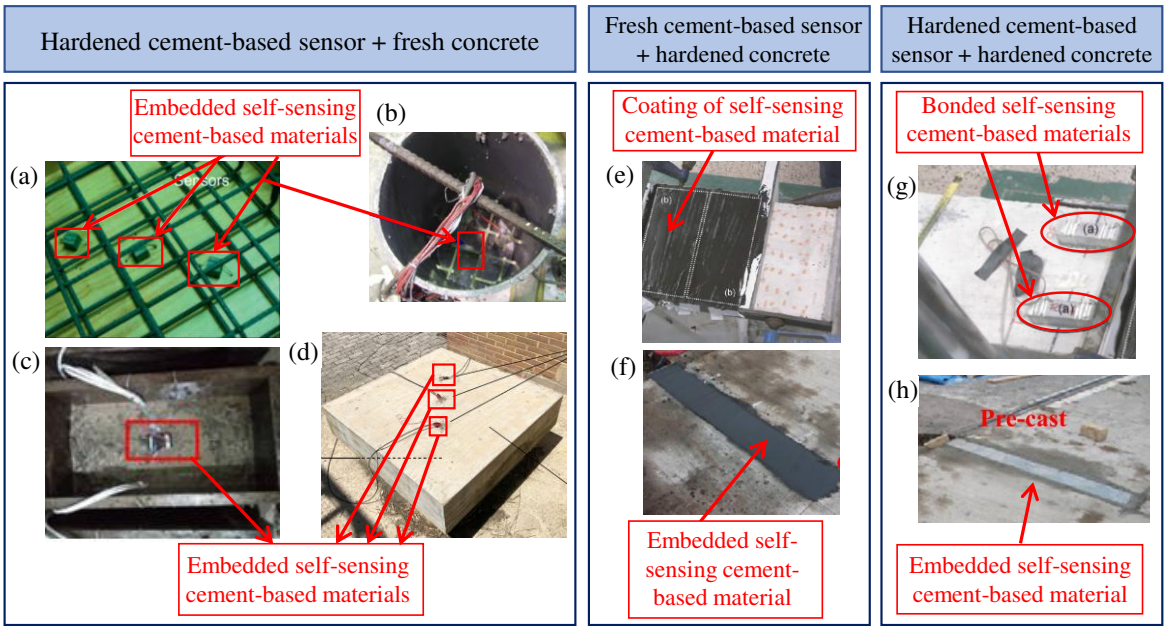

Source: Source: (a) adapted from Ubertini and D'Alessandro (2018), Copyright 2018, with permission from Elsevier; (b) adapted from Sun et al. (2014), Copyright 2014, with permission from Elsevier; (c) adapted from Ding et al. (2019), Copyright 2019, with permission from Elsevier; (d) adapted from Meoni et al. (2021b) as permitted under the Creative Commons Attribution License Agreement; (e) and (g) adapted from Baeza et al. (2013), as permitted under the Creative Commons Attribution License Agreement; (f) and (h) adapted from Han et al. (2013), Copyright 2013, with permission from IOP Publishing.

The HS/FC method is used for construction of new self-sensing structures. For example, Figure 1a shows small-size cementitious sensors that were prefabricated by Ubertini and D'Alessandro (2018) and placed in the rebar cage before casting of reinforced concrete elements. In Figure 1b, a fixture frame was used by Sun et al. (2014) to place a cementitious sensor in the mid-height region of a column's cylindrical mold before concrete pouring. In this case, the surface of the cementitious sensor was coated with epoxy resin (826 Epoxy) with curing agent (Polyisocyanate) for waterproofing. The embedded sensor was able to sense strain and stress of the column up to a compressive stress of 154 MPa. In addition, column damage was monitored based on irreversible changes in the electrical resistance of the cementitious sensor. Similarly, Ding et al. (2019) used the HS/FC method by placing

their cementitious sensor at the center of a prismatic concrete column during the pouring process (Figure 1c). The embedded sensors exhibited stable and repeatable self-sensing properties under cyclic and monotonic compression. Figure 1d shows a reinforced concrete plate with embedded cubic cementitious sensors tested by Meoni et al. (2021b). Six electrical measurements per hour were obtained from the sensors embedded into this concrete plate for three days. The authors observed that the electrical output was mainly affected by temperature changes and all cement sensors exhibited consistent temperature sensitivity.

In contrast, the FS/HC method has been mainly proposed for SHM of existing civil structures. For instance, Baeza et al. (2013) covered the surface of a reinforced concrete beam with the cementitious sensor in the fresh state (Figure 1e), after surface cleaning and application of an epoxy-based bonding agent (Sikadur-32 Fix). The cement paste was able to act as a strain sensor attached to the concrete beam, even when the structure was close to the failure. Han et al. (2013) also used the FS/HC method to integrate cast-in-place cementitious sensors into a concrete pavement test section. As indicated in Figure 1f, the fresh cementitious sensor was poured into a groove that was cut in an existing concrete pavement. After that, it was surface-smoothed and covered with a plastic film for curing. The self-sensing material was able to monitor the passing of different vehicles under different vehicular speeds and test environments.

Self-sensing cementitious materials can be also installed in existing structures using the HS/HC method. As exemplified in Figure 1g, Baeza et al. (2013) attached some hardened self-sensing cementitious composites to the surface of a reinforced concrete beam using a thin layer of an epoxy resin to ensure suitable strain transmission between the sensor and the beam. The cementitious composites were also able to monitor strain of the concrete beam. Han et al. (2013) also installed precast cementitious sensors in a groove cut in a road concrete pavement (Figure 1h), using a cement mortar as bonding agent. Road test results indicated that these cementitious sensors could develop a real-time online detection of vehicle passing.

Although a self-sensing response was reported in papers dealing with all installation methods (HS/FC, FS/HC and HS/HC), many practical drawbacks have been observed in these different approaches. For instance, Baeza et al. (2013) observed that cementitious sensors installed in a reinforced concrete beam using the FS/HC and HS/HC methods were not applicable as damage sensors. Another example was provided by Azhari (2008), who observed that the bond between the concrete beam and the sensor embedded using the HS/FC method was not adequate, leading to unreliable FCR measurements. Han et al. (2022) also

reported a weak interface between the self-sensing coating and the concrete substrate (HS/FC method), eventually leading to the peeling of the coating. After the peeling, the coating was unable to monitor the strain. Although these issues have always been a concern for researchers, direct comparisons between the efficiency of different bonding agents used in the installation of self-sensing cementitious materials have not been reported to date. Although three different methods (HS/FC, FS/HC and HS/HC) have been extensively used to incorporate self-sensing cementitious materials into structural elements, a systematic comparison between the mechanisms of strain-sensing behavior provided by these different methodologies was not reported in previous works.

Considering these gaps in the literature, the present experimental investigation provided the following contributions to the current state-of-the-art: (i) comparison of the bonding performance of different interface agent types (cement-based bonding agent, polyurethane-based interface and epoxy-based structural adhesive) between the self-sensing cementitious materials and the structural concrete element; (ii) strain-monitoring performance of a self-sensing cementitious composite embedded into a concrete unit using the HS/FC, FS/HC or HS/HC approaches; and (iii) mechanical performance in compression tests of concrete units containing a cement-based sensor that was installed with the HS/FC, FS/HC or HS/HC methods.

This chapter is structured in four sections. Section 5.1 introduces the use of self-sensing cementitious materials and reviews different installation methods applied to incorporate them into structural elements. Section 5.2 presents the materials and methods used in bond strength tests, piezoresistive tests and uniaxial compressive strength tests. In Section 5.3, the experimental results are presented, evaluated via statistical analyses of variance (ANOVA) and carefully discussed. Then, Section 5.4 shows the final remarks and the recommendations for future studies.

5.2. MATERIALS AND METHODS

5.2.1. Materials

Self-sensing cementitious composites were produced with portland cement CP V-ARI (specific mass of 3.05 g/cm³) similar to the Type III (ASTM, 2022) portland cement (Mehta and Monteiro, 2005); river quartz sand (specific mass of 2.64 g/cm³ and maximum particle

size of 2.38 mm), carbon black nanoparticles (CBN) supplied by Birla Carbon (particle size of 20 nm, surface area of 120 m^2/g and dibutyl phthalate absorption number of 124.7 $cm^3/100g$); and polycarboxylate-based superplasticizer PowerFlow 4001 (density of 1.12 g/cm^3). CBN were selected as conductive admixtures because they combine many advantages, such as high electrical conductivity, low cost, high specific surface area, and good dispersibility in the presence of water and superplasticizer (Han et al., 2020; Huang et al., 2018; Monteiro et al., 2017).

Concrete units (average dimensions of 20 cm × 10 cm × 8 cm, average compressive strength of 26.98 MPa and average water absorption of 8.37%) were used as structural elements in which the self-sensing cementitious composites were embedded. These units were produced with the same cement and fine aggregates used to produce the self-sensing mortars, in addition to gneiss coarse aggregates (specific mass of 3.00 g/cm^3 and maximum particle size of 9.50 mm).

Finally, three different interface agent types were investigated in this work: (i) a cement-based bonding coat (Nafufill KMH, with density of 2.10 g/cm^3); (ii) a polyurethane-based resin (MC-Proof 2200, with density of 1.39 g/cm^3); and (iii) an epoxy-based structural adhesive (Tecbond MF Quartzolit, with density of 1.70 g/cm^3).

5.2.2. Production of self-sensing cementitious composites

The self-sensing cementitious composites were produced with a sand/cement ratio equal to 0.75 (in volume), following suggestions of previous literature for getting cementitious materials with low electrical resistivity (Wen and Chung, 2007). Their water/cement ratio was 0.50 (in mass) and the concentration of CBN was 9% (by weight of cement). Initially, a mixture between water, CBN and superplasticizer was subjected to ultrasonication procedures (frequency of 20 kHz, power of 50 W). The superplasticizer/CBN ratio was equal to 0.40 (in mass) and the sonication energy was 450 J/mL (these parameters can improve the dispersion of the nanomaterials, according to results of some preliminary trials). Then, cement and fine aggregates were added to the nanosuspension (CBN dispersed in water and superplasticizer) and mixed for approximately 10 min. After that, the fresh self-sensing mortar was ready to be used to produce the different types of self-sensing specimens described in Section 5.2.3 and Section 5.2.4.

5.2.3. Methods for evaluating the bonding performance of distinct interface agent types

To investigate the bonding performance of different types of agents applied to the interface between the self-sensing cementitious composite and the structural concrete element, twelve prismatic specimens were prepared, using the procedures indicated in Figure 2. Each specimen consisted of a concrete substrate (5.0 cm cube with the same material of the concrete units) bonded to a self-sensing cementitious composite (5.0 cm cube produced with the procedures described in Section 5.2.2).

Figure 2 - Methods for determining the bonding performance between cement sensors and concrete substrate.

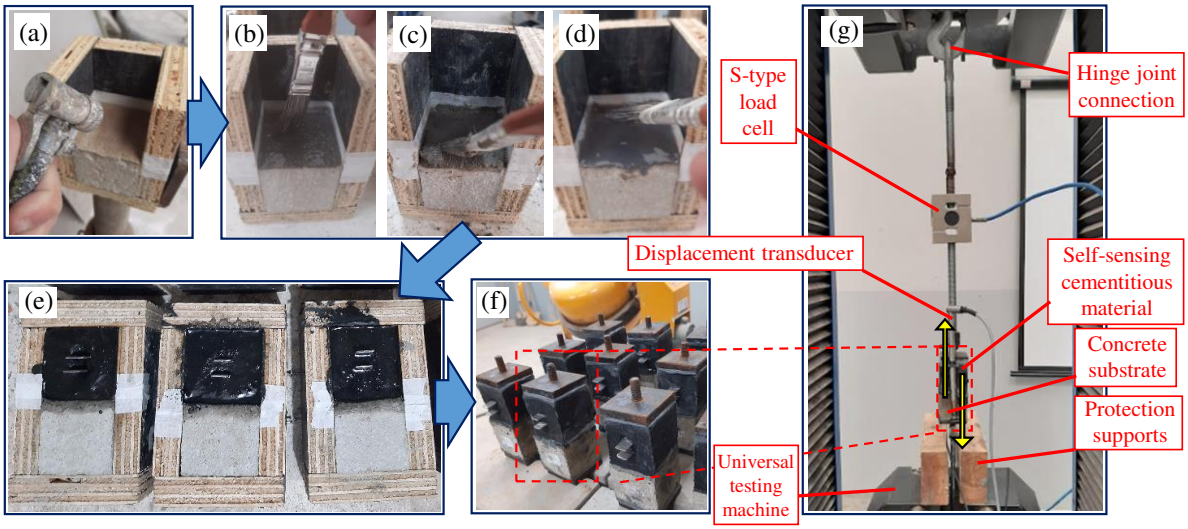

Source: Author (2024).

Firstly, the surface of the concrete substrate was cleaned with compressed air (Figure 2a). Following the recommendations of the manufacturer, each different interface agent type was applied to the concrete surface. In three specimens (ESA series), the epoxy-based structural adhesive (ESA) was used (Figure 2b). Three samples (CBC series) were produced with the cement-based bonding coat (CBC) (Figure 2c). Three specimens (PUI series) were fabricated using the polyurethane-based resin in the interface (PUI) (Figure 2d). Some reference specimens (REF series) were fabricated without any type of interface agent. Therefore, for each different type of specimen, three replicates were prepared. Each specimen was designated as x-Sy, in which the term "x" indicates the series of the specimen (ESA, CBC, PUI or REF) and the term "y" refers to the specimens' replications (1, 2 or 3).

After that, the fresh self-sensing mortar was poured into the molds (Figure 2e) in two layers of equal height. Each layer was compacted with 30 strokes of a steel tamping rod. After that, the electrodes were placed at the central region of the cement sensor cube (the

spacing between the electrodes was about 10 mm). After 72 hours, the prisms were demolded and placed in a moist room (relative humidity higher than 85% and temperature of 20 ± 5 ºC). The total curing period of the self-sensing mortar was 28 days. The specimens were covered with a plastic film to prevent water evaporation during the curing process. Around 24 hours before the tensile bond tests, two metal plates were bonded to the top and bottom surfaces of the specimens using epoxy adhesive (Figure 2f).

The bonding performance was evaluated by applying a tensile force on the top and bottom metal plates of the specimen at a rate of 0.5 mm/min, using an EMIC DL-60000 universal testing machine (Figure 2g). The tensile force was measured using an S-type load cell. The relative displacement between the top and bottom surfaces of the specimen was measured using a linear variable differential transformer (LVDT). Force and displacement data were acquired at a rate of 2 Hz, using the QuantumX MX1615 and the QuantumX MX840A data acquisition systems, respectively.

5.2.4. Methods for analyzing distinct methods to install cement-based sensors

To investigate the strain-monitoring ability and the compressive behavior of a self-sensing cementitious composite embedded into a concrete unit using the HS/FC, FS/HC or HS/HC approaches, other specimens were prepared using the methods of Figure 3. Three equal specimens were produced for each installation approach (three replicates for each different series). Each specimen was designated as z-Sw, in which the term “z” indicates the series of the specimen (HS/FC, FS/HC or HS/HC) and the term “w” refers to the specimens’ replications (1, 2 or 3). Since the epoxy-based structural adhesive provided the best bonding performance (results presented in the next section), this type of interface agent was used in all of these specimens. In addition, three prismatic specimens of non-embedded cementitious sensors (NES series) were tested for comparison purposes, as discussed in the next section.

Firstly, prismatic self-sensing mortars of 2.0 cm × 2.0 cm × 4.0 cm were produced (Figure 3a) to be incorporated into solid concrete units. To support some of the discussions in the next section regarding the specimens’ confinement effects on piezoresistive properties, NES samples were produced with dimensions of 2.0 cm × 2.0 cm × 6.0 cm. All self-sensing composites were cast in two equal layers compacted with 30 strokes of a steel tamping rod. Two electrodes were placed at the mid-height of the specimens (the spacing between the electrodes was approximately 10 mm). Concrete units of 20.0 cm × 10.0 cm × 8.0 cm with a central hole (Figure 3b) of approximately 2.3 cm × 2.3 cm × 4.3 cm were also produced.

These specimens were covered with plastic film and subjected to a curing period of 28 days (relative humidity higher than 85% and temperature of 20 ± 5 ºC). After the curing period, the self-sensing mortars were dried at 60 ± 10 ºC for 72 h to mitigate ionic conduction mechanisms and meet the suggestions of previous studies (Han et al., 2021; Wang et al., 2021, 2019). After that, the surface of the self-sensing mortar specimens (Figure 3c and Figure 3d) and the internal surface of the concrete units' holes (Figure 3e) were covered with the structural adhesive.

Figure 3 - Different methods used to install a self-sensing cementitious material in concrete units.

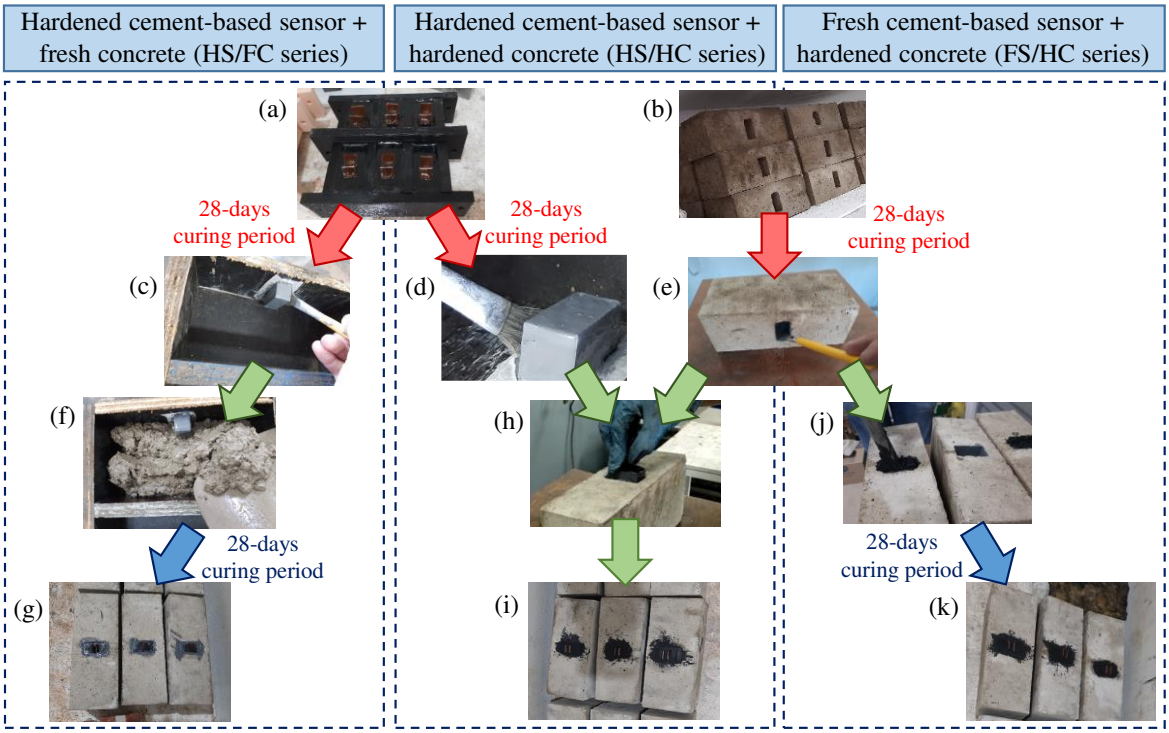

Source: Author (2024).

To produce the HS/FC specimens, each prefabricated cement sensor was fixed at the lateral wall of a mold used to cast concrete units (Figure 3f). After 48 hours, the specimens of this series were demolded. These specimens were also subjected to a curing time of 28 days (Figure 3g). In contrast, HS/HC specimens were produced by manually inserting the prefabricated cement sensors into the hole of the concrete units (Figure 3h and Figure 3i). The FS/HC specimens were fabricated by molding the self-sensing mortars inside the hole of the concrete units and using the previously mentioned compaction methods (Figure 3j). The specimens of this series were also cured for 28 days in moist room (Figure 3k) and then

subjected to the previously mentioned drying procedures (Han et al., 2021; Wang et al., 2021, 2019), avoiding undesirable effects of ionic conduction during the electro-mechanical tests.

The self-sensing ability of all specimen types was investigated with quasi-static cyclic compressive loading tests (Figure 4). These tests were composed of three loading-unloading cycles with amplitude of 30% of the estimated specimens' strength, in addition to a final loading cycle with load steps at 10%, 20% and 30% of the estimated specimens' strength. Insulating films were placed between the specimens and the steel plates of the EMIC DL-60000 testing machine, in order to prevent unwanted electrical conduction. EMIC clip-gauges symmetrically arranged with respect to the central axis of the cement-based sensors were used for compressive strain measurements. The self-sensing composite was connected in series with a reference resistor (R_{ref} = 1000 Ω) and a ±5 V square wave voltage signal (50% duty cycle and 6 Hz frequency) was applied to the system by a microcontroller board (Arduino Mega 2560 R3). To deal with polarization effects, voltage drops across the self-sensing mortar (U_m) and the reference resistor (U_{ref}) were acquired using a NI compact DAQ-9178 chassis with NI-9219 modules. These voltage measurements were obtained at specific time instants (80% of the positive constant part of the square wave signal), following recommendations of previous works (Downey et al., 2017; Meoni et al., 2021a; Nalon et al., 2021b). Since the frequency of the square wave was 6 Hz, the sampling frequency of the voltage measurements was also 6 Hz. Equation (1) was used to calculate the electrical current of the circuit (i). The electrical resistance of the self-sensing composite (U_m) was calculated with Equation (2). Specimen geometrical properties (distance between electrodes, L, and effective area between electrodes, A) were used to estimate the electrical resistivity ρ of the material, as indicated in Equation (3). Then, the fractional changes in electrical resistivity (FCRs) of the cement sensors (percentage changes in electrical resistivity related to the initial electrical resistivity) could be determined during the compressive loading. The values of FCR and compressive strain obtained in these piezoresistive tests were used to determine the gauge factor of the specimens.

$$i = \frac{U_{ref}}{R_{ref}} \tag{1}$$

$$R_m = \frac{U_m}{i} \tag{2}$$

$$\rho = \frac{R_m \ A}{L} \tag{3}$$

Figure 4 - Experimental setup used in piezoresistive tests.

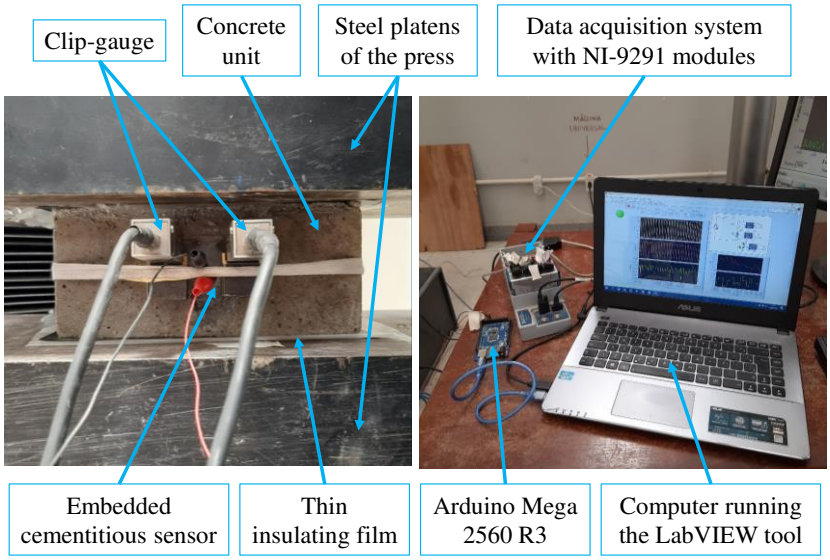

Source: Author (2024).

After the piezoresistive tests, the specimens were subjected to uniaxial compression tests to investigate the compressive strength and the failure mode associated with the different approaches used to embed the cement sensors within the concrete units. The deformation properties of the materials used to cast the concrete units and the self-sensing cementitious composites were experimentally determined. The modulus of elasticity of specimens with a high height/width (or height/length) ratio (prisms of 2.0 cm × 2.0 cm × 6.0 cm) was determined, using three replicates and the load-time history of the methodology A of ABNT NBR 8522 (2017). In the case of the solid concrete units, the prismatic samples with the appropriate dimensions were directly cut from the units. All mechanical tests were also carried out in an EMIC DL-60000 universal testing machine, using a constant loading rate of 0.50 MPa/s.

5.2.5. Statistical analyses

The maximum tensile force, gauge factor and compressive strength results were subjected to different statistical analyses: (i) Grubb's test for outlier detection, (ii) Shapiro-Wilk test for evaluation of normality of residuals, (iii) Bartlett test for verification of homogeneity of variances, (iv) analysis of variance (ANOVA) for evaluation of differences between average values, and (v) Tukey's test for pairwise comparisons between average values. APPENDIX 5A shows the null and alternative hypotheses used in all these tests. A significance level equal to 5% was used in all statistical analyses.

5.3. RESULTS AND DISCUSSIONS

5.3.1. Bonding performance of different interface agent types

The average values of maximum tensile force obtained in the tensile tests of specimens with different bonding agent types are presented in Figure 5a. For this response variable, statistical analyses of APPENDIX 5A indicated that ANOVA assumptions were not violated. Then, a P-value equal to 1.1×10^{-3} was obtained in the ANOVA of the maximum tensile force dataset, which indicates that the type of interface bond agent statistically affected the bonding between the self-sensing cementitious composite and the concrete substrate.

Figure 5 - (a) Maximum tensile force (bars that share the same uppercase letter are not significantly different by the Tukey's test at the 5% significance level) and (b) force-displacement curves of specimens fabricated with different bonding agent types.

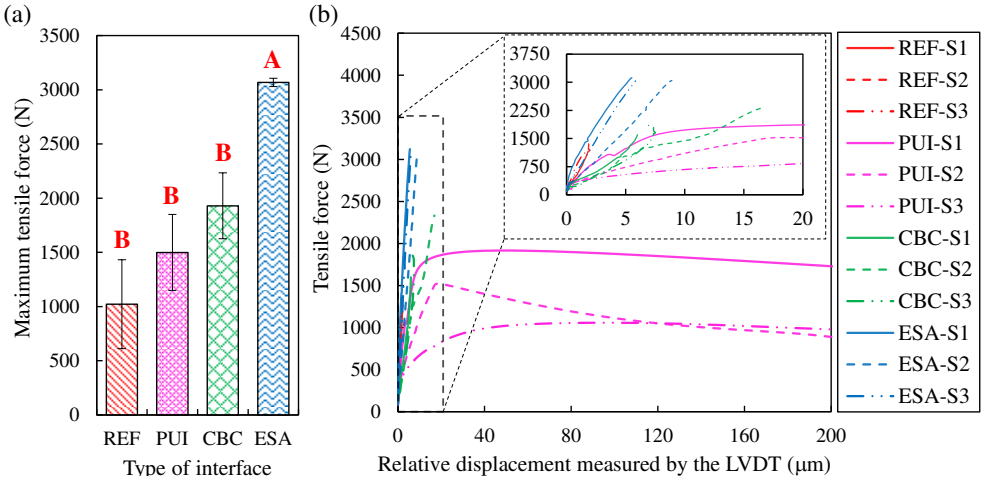

Source: Author (2024).

The standard deviation observed in the ESA series was significantly lower than the standard deviation of the other series. Consequently, the post-hoc Tukey's test did not detect statistical difference between the average values of maximum tensile force of CBC, PUI and REF series (these series share the same uppercase letter "B" in Figure 5a). In contrast, the maximum tensile force of the ESA series was statistically higher than that observed in the other series. The average value of maximum tensile force of the ESA series was 58.1%, 105.7% and 202.2% higher than the maximum tensile force observed in the CBC, PUI and REF series, respectively. Some papers published in recent literature did not use interface bond agents between self-sensing materials and concrete substrate, which may cause questionable experimental results due to issues in the transference of stresses between the materials and/or premature failure at the interface.

According to Figure 5b, small displacement values up to the failure (< 17 μm) were measured by the LVDT attached to the specimens of the REF, CBC and ESA series, whereas high displacement values were observed in specimens of the series PUI. The brittle behavior observed in REF, CBC and ESA series and the ductile behavior verified in PUI specimens can be explained based on the three different typical failure modes indicated in Figure 6.

Figure 6 - Failure modes observed in tensile bond tests of specimens with different bonding agent types

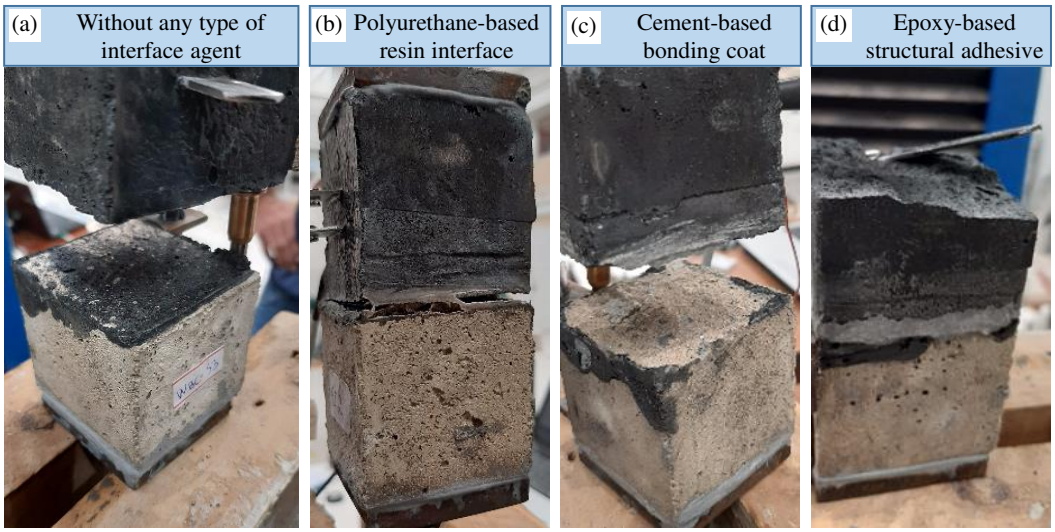

Source: Author (2024).

Debonding between the self-sensing mortar and the concrete substrate was observed in specimens of the REF and CBC series (Figure 6a and Figure 6b, respectively). Since the debonding phenomenon was observed in the absence of an interface agent bond or with the use of cement-based bonding coat, low levels of tensile force (Figure 5a) were able to cause a brittle detachment of the cement-based sensor. Since the average maximum tensile force of the CBC series was 91.2% higher than that verified in the REF series, the cement-based bonding coat may help to delay the debonding phenomena. However, high variability was observed in REF and CBC series (statistical difference was not observed between the average values of maximum tensile force of these series), so that the percentage adhesion benefits provided by the cement-based bonding coat could not be proved statistically.

When the polyurethane-based resin was used, a brittle failure was not observed. However, the specimen was not able to withstand high load levels because large deformations and partial debonding (Figure 6b) happened at the interface when tensile forces between 1055 N and 1920 N were applied (Figure 5b). Although complete debonding was not verified in these specimens, the high deformation of the polyurethane-based interface can be a

limitation for practical application of self-sensing cementitious materials. In this situation, the deformations monitored by the cement sensor will not reflect the actual deformations of the monitored structural element.

In contrast, the use of the epoxy-based structural adhesive was able to prevent debonding mechanisms at the interface between the cementitious sensor and the monitored concrete, so that Figure 6d indicates that the failure mechanism of ESA specimens series was characterized by tensile rupture in the region of the specimen with lower net area available to support the tensile loading (region close to the electrodes). Thus, the epoxy-based structural adhesive was found to be the best alternative to prevent debonding mechanisms between self-sensing composites and the concrete substrate, ensuring an appropriate transference of stresses between these materials, so that the failure mode was not related to limitations associated with the mechanical properties of the interface.

It is important to highlight that the mechanical strength of the self-sensing mortar used in this study was higher than the mechanical strength of the concrete substrate (detailed discussions about the strength of these different materials are presented at the end of Section 5.3.2). The tensile rupture of Figure 6 did not happen at the concrete cube because the net area to withstand the applied tensile force in the tests of the present study was significantly lower at the horizontal plane in which the electrodes of the self-sensing material were located. If possible, the preferred orientation of electrodes in monitored structures should not be in the same direction of maximum tensile stresses, preventing undesirable effects related to the loss of contact between the electrodes and the self-sensing cementitious matrix. Electrodes should preferably be oriented in the direction of compressive strains and theoretical models of piezoresistivity of composites under multi-axial strain (Liu et al., 2015; Xiao et al., 2015, 2010) can be applied to interpret the electrical response of the cement sensors.

5.3.2. Self-monitoring and compressive behavior of cement-based sensors embedded into concrete units using different methods

Strain-sensing behavior was observed in the piezoresistive tests of all specimens investigated in the present study, except for the HS/HC-S3 specimen (reasons for the distinct behavior of this specimen are discussed below). The FCRs due to cyclic compressive loading are associated with changes in the inter-particle distance between the CBN incorporated in the cement-based sensors and their effects on tunneling conduction mechanisms within the cementitious matrix. Changes in the distance between conductive spots and variations in the

tunneling resistance become the dominant mechanisms of pressure-sensitivity (Deng and Li, 2018; Ding et al., 2020; Li et al., 2006; Nalon et al., 2020; Xiao et al., 2016). In Figure 7, the FCRs were plotted against the strain measurements. Linear regression analyses were used to elaborate models that provided the best fit to the experimental data associated with the linear part (Chung, 2020) of the FCR *vs* compressive strain curves. Reversible FCR variations upon loading and unloading cycles were also observed in previous research investigating different types of self-sensing materials (Ding et al., 2021; Dong et al., 2021b; Han et al., 2022; Lima et al., 2020; Nalon et al., 2021a).

Figure 7 - FCR *vs* compressive strain curves of self-sensing cementitious composites installed with the (a) HS/FC method, (b) HS/HC method, (c) FS/HC method and (d) non-embedded cementitious sensors.

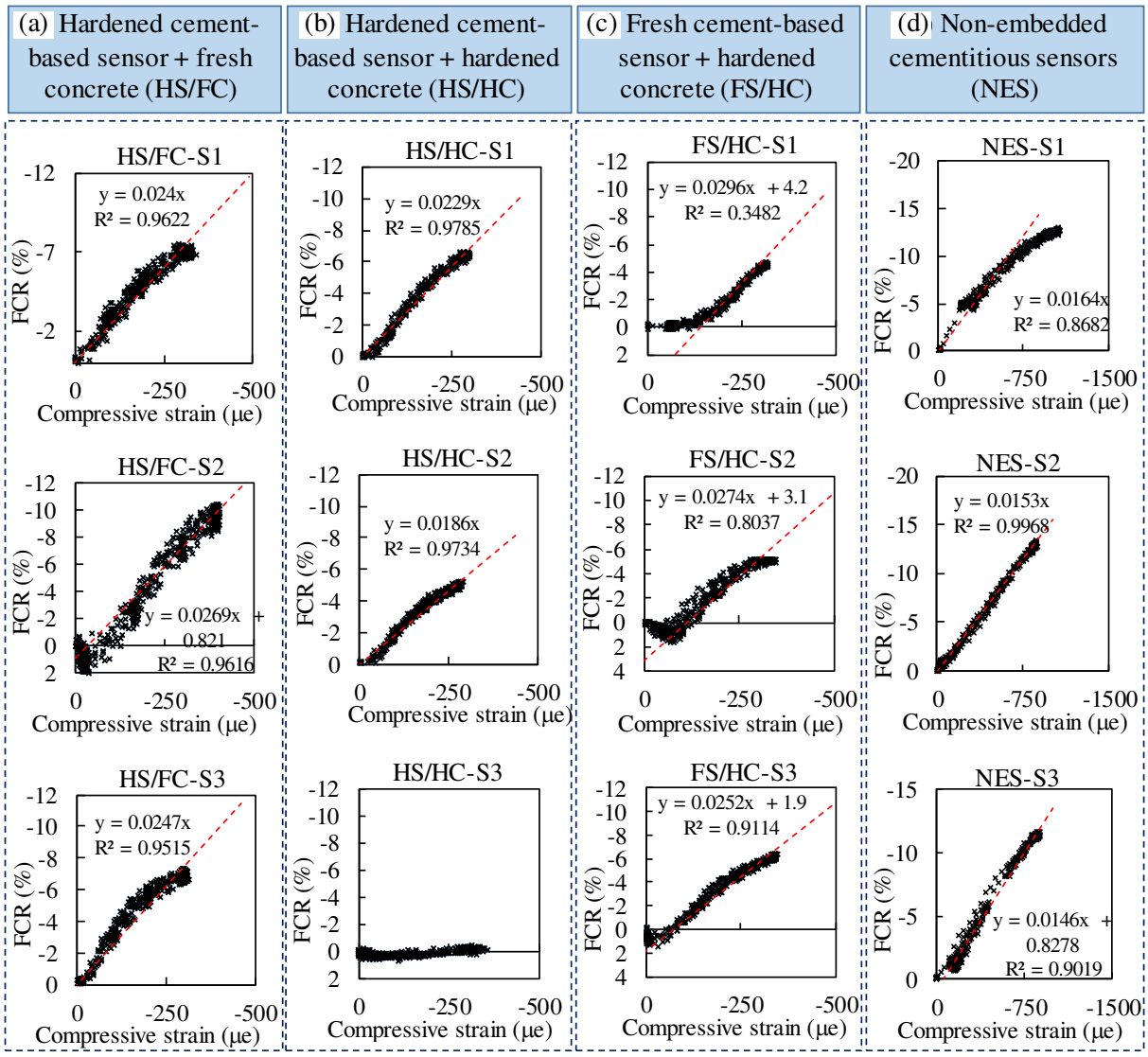

Source: Author (2024).

The gauge factor of the cementitious sensors was determined as the slope of the developed regression models. Average values of gauge factor of self-sensing cementitious composites installed using different approaches (HS/FC, HS/HC and FS/HC methods) and the average gauge factor of non-embedded cementitious sensors are present in Figure 8a. According to the statistical analyses of the APPENDIX 5A, ANOVA assumptions were met and the ANOVA provided a P-value of 5.2×10^{-4}, indicating that the type of installation statistically affected the strain-sensing response of the CBN-based cementitious composites.

Figure 8 - (a) Gauge factor and (b) compressive strength results (bars sharing an uppercase letter are not significantly different by the Tukey's test at the 5% significance level).

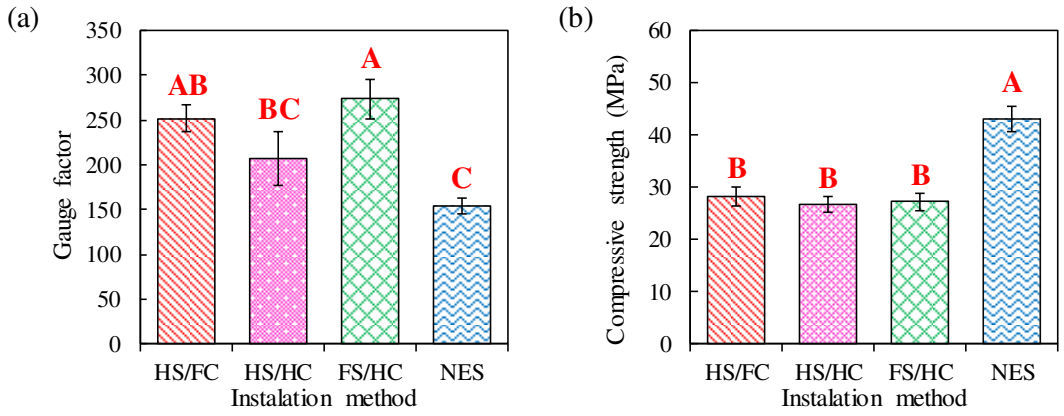

Source: Author (2024).

The results of Figure 8a indicated that the average gauge factor of non-embedded specimens (NES series) was 56.3-74.4% of the average gauge factor of the other series (HS/FC, HS/HC and FS/HC). It happened because the central zone of NES specimens was subjected to uniaxial compression, whereas the cement-based sensors embedded into the concrete units were subjected to a triaxial compression state due to two different reasons.

The solid concrete units with incorporated self-sensing mortars had a height/length ratio equal to 0.4 and a height/width ratio equal to 0.8, whereas the non-embedded specimens had height/length and height/width ratios of 3.0. The friction between the specimen and the testing machine plates causes restraining effects that decrease the lateral expansion of the specimens when the vertical compressive loading increases. If the height/length ratio of the specimen is lower than about 1.7, its central part will not be free from restraining effects of the testing machine plates, i.e., a zone of uniaxial compression does not exist within these specimens (Neville, 2011). Therefore, the cement-based sensors installed in the concrete units of the HS/FC, HS/HC and FS/HC series were significantly affected by lateral confining

stresses (height/length and height/width lower than 1.7), whereas the central zone of specimens of the NES series tended to be subjected to uniaxial compressive stress (height/length and height/width higher than 1.7).

The modulus of elasticity of the concrete units was 20.77 ± 1.45 GPa, whereas the modulus of elasticity of the self-sensing cement sensors was 14.00 ± 0.30 GPa. When the specimens of the HS/FC, HS/HC and FS/HC series were subjected to the piezoresistive tests, the cement-based sensor tended to present higher lateral deformations than the concrete units due to the different values of modulus of elasticity. Due to the strong adhesion provided by the epoxy-based structural adhesive, those differential movements were restrained and lateral stresses were mobilized in both components. The lateral deformation of both materials was an intermediate value between the amounts that each different material tended to deform. The complex states of stress and strain generated in self-sensing composites embedded into concrete elements were carefully evaluated in the finite element models developed by Cui et al. (2017). The lateral expansion of the cement-based sensor embedded into the concrete units was lower than that of the NES specimens. In addition, they were subjected to lateral compressive stresses due to the deformation restrictions provided by the stiff concrete unit.

According to previous theoretical and experimental investigations (Liu et al., 2015; Xiao et al., 2015, 2010), the piezoresistive response of cementitious composites containing randomly distributed CBN is strongly dependent on the transversal deformations of the composites subjected to vertical compressive loading. According to these studies, when the vertical load increases, the FCRs are higher when the lateral expansion of the self-sensing cementitious sensors is restrained (apparent Poisson's ratio is reduced). In the present study, the lateral expansion of the cement-based sensors embedded into the concrete units was restrained by (i) lateral confining effects provided by the machine plates due to the low height/length and height/width ratios of the units and (ii) restraining effects provided by the units due to their high stiffness. Consequently, FCR amplitudes and gauge factor values of the embedded cement-based sensors were higher than those observed in non-embedded cement-based sensors.

According to Figure 8a, the average gauge factor of the HS/HC series was slightly lower than the average gauge factor of the FS/HC and HS/FC series. An inspection of the failed specimens after the compressive strength tests revealed the reasons for this difference. As indicated in Figure 9a and Figure 9c, the cement-based sensors of the FS/HC and HS/FC series were completely covered by the cracked concrete unit matrix, so that the epoxy-based

interface was rarely visible. Figure 9b shows that the use of the HS/HC installation method caused very poor adherence between the cement-based sensor and the concrete units, so that the epoxy-based interface was clearly visible at the surface of the sensors. Mechanical stresses were only transferred from the concrete unit to the sensor in few locations where the components touched each other. Since stresses were not properly transferred to the sensors when the HS/HC approach was used, lower FCR amplitudes were observed in the curves of Figure 7 and lower values of gauge factor were reported in Figure 8a. The yellow arrow of Figure 9b indicates that the back surface of the specimen HS/HC-S3 did not touch the concrete unit. The poor contact between the sensor and the structural element being monitored explains the negligible FCR observed in the FCR *vs* strain curve of the specimen HS/HC-S3 (Figure 7).

Figure 9 - Failure modes observed in compression tests of specimens produced with the (a) HS/FC, (b) HS/HC and (c) FS/HC method of installation of cement-based sensors.

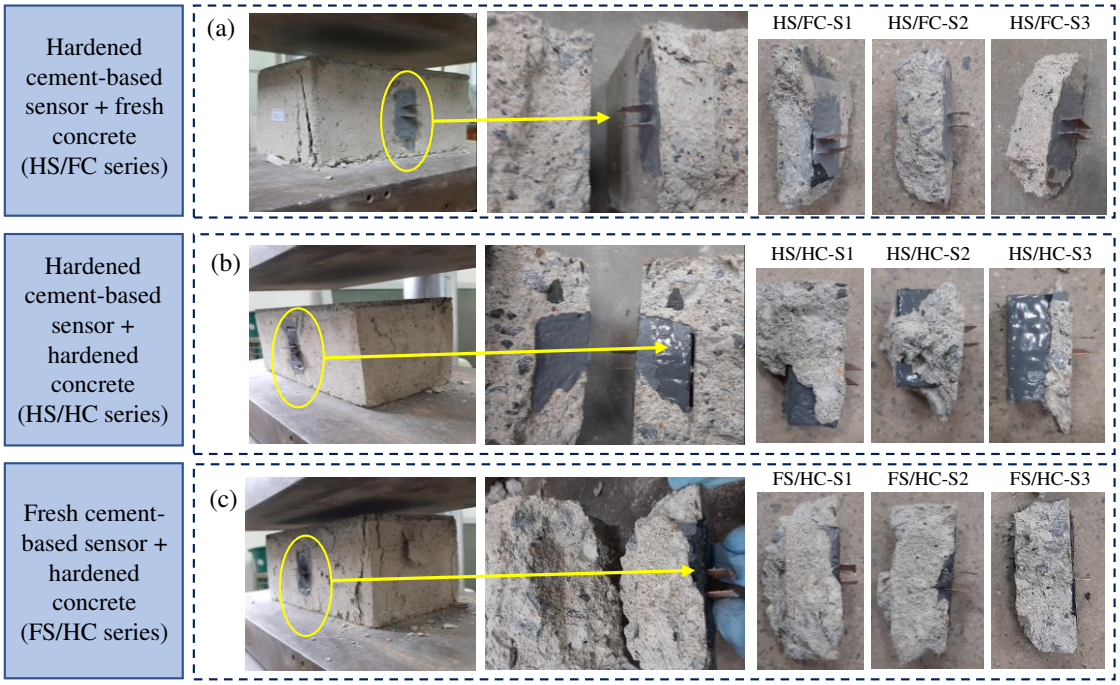

Source: Author (2024).

The gauge factors of specimens produced with the HS/FC and FS/HC series were statistically equal, according to the Tukey's test. However, it is important to highlight that the specimens of the FS/HC series did not present relevant FCRs for low compressive strain levels, which was represented by a horizontal plateau at the beginning of the FCR *vs* compressive strain curves of specimens FS/HC-S1, FS/HC-S2 and FS/HC-S3 (Figure 7). The gauge factor values were not affected by this problem because they were calculated at the

linear part of these curves, as recommended by Chung (2020). This issue was caused by the poor bonding between the cement-based sensors and the electrodes, due to the use of the FS/HC installation methodology. Since excellent bonding was verified at the interface between concrete units and self-sensing mortars in the FS/HC series (Figure 9c), drying shrinkage during the curing process of the cement-based sensors caused debonding issues at the interface between the electrodes and the self-sensing mortars (Figure 10). In the loading cycles of the piezoresistive tests of these composites, the electrical resistivity of the specimen only started to decrease when the gaps caused by shrinkage effects were closed, which abruptly formed conductive passages that enabled the measurement of the self-sensing response of the composite. Future studies are recommended to develop shrinkage control strategies that would enable the practical application of the FS/HC installation method for self-monitoring of strain in civil structures.

Figure 10 - Debonding between electrodes and self-sensing mortars of specimens of the FS/HC series.

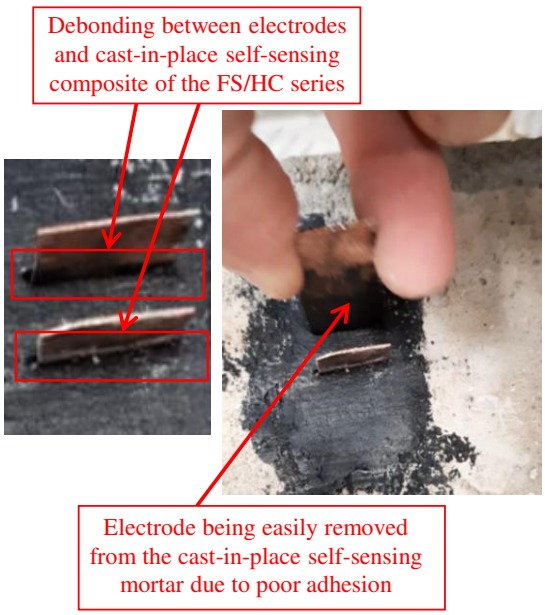

Source: Author (2024).

Field investigations and experimental results indicated that the shrinkage issues only affected the electrode/mortar bonding of specimens produced with the FS/HC installation method (HS/HC and HS/FC series were not affected). It can be attributed to the very distinct boundary conditions of these specimens during the production, curing and drying processes (Section 5.2.4). In the self-sensing mortar prisms of the HS/HC and HS/FC series, sensors were prefabricated in oiled molds (Figure 3a) and subjected to curing (20 ± 5 ℃ for 28 days) and drying (60 ± 10 ℃ for 72 h) processes without lateral restraints. Since the self-sensing

mortar prisms were not laterally restrained during these autogenous and drying shrinkage processes, the original dimensions of the prisms tended to reduce, without affecting the bonding of the electrode/mortar interface. In contrast, the self-sensing mortar of the FS/HC series was molded inside the hole of the concrete unit (Figure 3j) and then subjected to curing (20 ± 5 ºC for 28 days) and drying (60 ± 10 ºC for 72 h) processes with lateral restraints. In this distinct situation, five faces of the self-sensing mortar prism were restrained by the concrete unit during the autogenous and drying shrinkage processes. Since these faces were successfully bonded to the concrete substrate (using the epoxy-based structural adhesive), the shrinkage process inevitably affected the bonding of the electrode/mortar interface (especially during the drying process of 60 ± 10 ºC that happened after 28 days of curing, i.e., the mortar had a high tensile strength and the planes of weakness were the electrodes/mortar interfaces).

The average values of compressive strength of HS/FC, HS/HC, FS/HC and NES series are presented in the Figure 8b. The statistical analyses of APPENDIX 5A revealed that the ANOVA assumptions were also satisfied in this case. The ANOVA provided a P-value equal to 1.1×10^{-5}, which indicated a significant statistical difference between the average strength values being compared.

The Tukey's test results represented in Figure 8b indicate that the values of average compressive strength of the HS/FC, HS/HC and FS/HC series were statistically equal (these bars share the same uppercase letter "B"). In fact, Figure 9 indicates that these specimens presented the same failure mode, characterized by vertical and/or diagonal cracks at the concrete units (cracks were not visible at the cement-based sensors). Indeed, the Tukey's test results also indicated that the compressive strength of non-embedded cementitious sensors was significantly greater than the strength of the concrete units with embedded cementitious sensors.

Compressive strength results are in good agreement with recommendations of previous literature (Liu et al., 2018; Xiao et al., 2011b, 2011a) that define that the compressive strength of embedded self-sensing concretes must be equal or higher than that of the concrete substrate. This recommendation aims to avoid negative effects on the self-monitoring performance (self-sensing behavior disappears if the self-sensing material fails before the failure of the monitored concrete substrate). In addition, the incorporation of self-sensing cement sensors with high mechanical properties will not reduce the original strength of the monitored structure.

5.4. CONCLUSIONS

In the present study, self-sensing cementitious materials were embedded into concrete units for strain-monitoring using different installation approaches (HS/FC, HS/HC and FS/HC methods). The main motivation behind the development of the present experimental program was the lack of systematic comparisons between self-sensing mechanisms provided by these different installation methodologies. In addition, there was no previous investigation of bonding performance between the cement sensors and the concrete substrate. Uniaxial tensile tests were carried out to investigate the bonding performance provided by different types of agents (cement-based bonding agent, polyurethane-based interface and epoxy-based structural adhesive) applied to the interface between the self-sensing cementitious composite and the structural concrete element. In addition, self-sensing cementitious materials were embedded into concrete units using the different installation approaches and the obtained specimens were subjected to piezoresistive and uniaxial compression tests. The following conclusions derived from this work:

(1) The type of interface bond agent statistically affected the bonding between the cement sensors and the concrete substrate. Low levels of uniaxial tensile force caused partial or complete debonding in specimens without interface agent or specimens with cement-based bonding coat or polyurethane-based resin. The epoxy-based structural adhesive prevented debonding mechanisms and ensured suitable transference of stresses, so that their average maximum tensile force was up to 202.2% higher than that observed in the other specimens. The bonding improvements provided by different materials types in the present chapter can encourage future applications of interface bond agents, which will certainly improve the quality of future research in this scientific field.

(2) Tensile failure close to electrodes was verified in uniaxial tensile tests of self-sensing mortars installed with epoxy-based structural adhesive. To prevent undesirable effects related to the loss of contact between the electrodes and the self-sensing cementitious matrix, the electrodes of self-sensing composites should not be orientated in the same direction of the maximum tensile stresses. This conclusion demonstrates the importance of appropriate design of electrodes orientation in practical applications of self-sensing cementitious materials. To improve the quality of future papers in the area, electrodes should preferably be oriented in the direction of compressive strains and theoretical models of piezoresistivity of

composites under multi-axial strain can be applied to interpret the electrical response of the cement sensors.

(3) The installation of the cement-based sensors into the concrete units increased their strain sensitivity (the average gauge factor of non-embedded cement sensors was 56.3-74.4% of the average gauge factor of embedded cement). It was attributed to increases in FCRs due to lateral confining effects provided by the machine plates during compression tests and restraining effects provided by the concrete units due to their high stiffness. This conclusion elucidates the importance of evaluating the testing equipment (machine plates) used in piezoresistive analyses and measuring the elastic modulus of cement sensors and concrete substrate. If the deformation properties of the cement sensors and concrete substrate are significantly different, more complex analyses are required to properly interpret the values of FCR measured in the piezoresistive tests (complex states of stress and strain may occur close to the areas where the sensors are embedded). To improve the quality of future studies in the area, it is recommended the use of cement sensors and concrete substrate with values of deformation properties that could be considered statistically equal.

(4) Installation procedures (HS/FC, HS/HC and FS/HC methods) caused statistically significant variations in the strain-sensing response of CBN-based cementitious composites. In this experimental study, the best self-sensing performance was provided by the HS/FC method due to appropriate production procedures and stress transference mechanisms during the piezoresistive tests. Stresses were not properly transferred to the sensors when the HS/HC approach was used, whereas shrinkage issues were observed when the FS/HC method was used. Then, this chapter provided a pioneering systematic comparison between the piezoresistive response associated with the three different installation methods.

(5) Since stresses were not properly transferred to the sensors when the HS/HC approach was used, lower FCR amplitudes and lower gauge factor values were observed in specimens of this series. Therefore, the comparisons between experimental results of this work indicated that the HS/HC approach should not be used to install embedded cementitious sensors due to the possibility of serious installation issues and strain monitoring errors.

(6) When the FS/HC method was used, drying shrinkage of the cement-based sensor caused debonding between electrodes and cement sensors. Although the gauge factor was not affected by this problem, it eventually caused a horizontal plateau at the beginning of the FCR vs compressive strain curves. Thus, comparisons between the results of the present work also revealed that the FS/HC approach should only be used to install embedded cement sensors if proper shrinkage control is carried out to avoid the debonding between electrodes and cement sensors.

(7) The HS/FC, HS/HC and FS/HC installation methods did not cause statistical difference in the compressive strength of the concrete unit because the mechanical strength of the non-embedded cementitious sensors was significantly higher than the strength of the concrete units with and without embedded cementitious sensors. Regardless of the installation methodology, the experimental results of this research suggested that the compressive strength of self-sensing materials should be equal or higher than that of the monitored structure. The self-sensing material cannot fail before the monitored structure for two main reasons: (i) the cement sensor should monitor strain/stress and damage up to the failure of the monitored element and (ii) the incorporation of the cement sensor should not reduce the original strength of the monitored structure.

To complement the investigation of different interface bond agent types of this study, future works are recommended to evaluate the effects of different surface treatments (e.g., grinding, abrasive blasting, mechanical milling) on the bonding behavior between cementitious sensors and concrete substrates. Future works are also recommended to investigate the effects of cement/aggregate and water/cement ratio on the shrinkage behavior of self-sensing cementitious materials, in order to enable the practical application of the FS/HC methodology for self-monitoring of strain and stresses in existing civil structures.

REFERENCES

Abedi, M., Fangueiro, R., Gomes Correia, A., 2021. A review of intrinsic self-sensing cementitious composites and prospects for their application in transport infrastructures. Constr Build Mater 310, 125139. https://doi.org/10.1016/j.conbuildmat.2021.125139

ABNT, 2017. NBR 8522: Concrete - Determination of the static elasticity and strain modulus.

Adresi, M., Tulliani, J.-M., Lacidogna, G., Antonaci, P., 2021. A Novel Life Prediction Model Based on Monitoring Electrical Properties of Self-Sensing Cement-Based Materials. Applied Sciences 11, 5080. https://doi.org/10.3390/app11115080

ASTM, 2022. C150/C150M-22: Standard Specification for Portland Cement.

Azhari, F., 2008. Cement-based Sensors for Structural Healthy Monitoring. University of British Columbia.

Baeza, F., Galao, O., Zornoza, E., Garcés, P., 2013. Multifunctional Cement Composites Strain and Damage Sensors Applied on Reinforced Concrete (RC) Structural Elements. Materials 6, 841–855. https://doi.org/10.3390/ma6030841

Birgin, H.B., D'Alessandro, A., Meoni, A., Ubertini, F., 2023. Self-Sensing Eco-Earth Composite with Carbon Microfibers for Sustainable Smart Buildings. Journal of Composites Science 7, 63. https://doi.org/10.3390/jcs7020063

Chung, D.D.L., 2021. Self-sensing concrete: from resistance-based sensing to capacitance-based sensing. Int J Smart Nano Mater 12, 1–19. https://doi.org/10.1080/19475411.2020.1843560

Chung, D.D.L., 2020. A critical review of piezoresistivity and its application in electrical-resistance-based strain sensing. J Mater Sci 55, 15367–15396. https://doi.org/10.1007/s10853-020-05099-z

Cui, X., Wang, Y., Zeng, S., Zhou, D., Han, B., Yu, X., Ou, J., 2017. Numerical analysis on design and application of cement-based sensor for structural health monitoring. J Intell Mater Syst Struct 28, 2579–2602. https://doi.org/10.1177/1045389X17692051

D'Alessandro, A., Tiecco, M., Meoni, A., Ubertini, F., 2021. Improved strain sensing properties of cement-based sensors through enhanced carbon nanotube dispersion. Cem Concr Compos 115, 103842. https://doi.org/10.1016/j.cemconcomp.2020.103842

Deng, H., Li, H., 2018. Assessment of self-sensing capability of Carbon Black Engineered Cementitious Composites. Constr Build Mater 173, 1–9. https://doi.org/10.1016/j.conbuildmat.2018.04.031

Ding, S., Ruan, Y., Yu, X., Han, B., Ni, Y.-Q., 2019. Self-monitoring of smart concrete column incorporating CNT/NCB composite fillers modified cementitious sensors. Constr Build Mater 201, 127–137. https://doi.org/10.1016/j.conbuildmat.2018.12.203

Ding, S., Wang, X., Qiu, L., Ni, Y., Dong, X., Cui, Y., Ashour, A., Han, B., Ou, J., 2023. Self-Sensing Cementitious Composites with Hierarchical Carbon Fiber-Carbon

Nanotube Composite Fillers for Crack Development Monitoring of a Maglev Girder. Small 19, 2206258. https://doi.org/10.1002/smll.202206258

Ding, S., Wang, Y.-W., Ni, Y.-Q., Han, B., 2020. Structural modal identification and health monitoring of building structures using self-sensing cementitious composites. Smart Mater Struct 29, 055013. https://doi.org/10.1088/1361-665X/ab79b9

Ding, S., Xiang, Y., Ni, Y.-Q., Thakur, V.K., Wang, X., Han, B., Ou, J., 2022. In-situ synthesizing carbon nanotubes on cement to develop self-sensing cementitious composites for smart high-speed rail infrastructures. Nano Today 43, 101438. https://doi.org/10.1016/j.nantod.2022.101438

Ding, S., Xu, C., Ni, Y.-Q., Han, B., 2021. Extracting piezoresistive response of self-sensing cementitious composites under temperature effect via Bayesian blind source separation. Smart Mater Struct 30, 065010. https://doi.org/10.1088/1361-665X/abf992

Dong, W., Guo, Y., Sun, Z., Tao, Z., Li, W., 2021a. Development of piezoresistive cement-based sensor using recycled waste glass cullets coated with carbon nanotubes. J Clean Prod 314, 127968. https://doi.org/10.1016/j.jclepro.2021.127968

Dong, W., Li, W., Guo, Y., Sun, Z., Qu, F., Liang, R., Shah, S.P., 2022. Application of intrinsic self-sensing cement-based sensor for traffic detection of human motion and vehicle speed. Constr Build Mater 355, 129130. https://doi.org/10.1016/j.conbuildmat.2022.129130

Dong, W., Li, W., Shen, L., Zhang, S., Vessalas, K., 2021b. Integrated self-sensing and self-healing cementitious composite with microencapsulation of nano-carbon black and slaked lime. Mater Lett 282, 128834. https://doi.org/10.1016/j.matlet.2020.128834

Dong, W., Li, W., Wang, K., Han, B., Sheng, D., Shah, S.P., 2020. Investigation on physicochemical and piezoresistive properties of smart MWCNT/cementitious composite exposed to elevated temperatures. Cem Concr Compos 112, 103675. https://doi.org/10.1016/j.cemconcomp.2020.103675

Downey, A., D'Alessandro, A., Laflamme, S., Ubertini, F., 2018. Smart bricks for strain sensing and crack detection in masonry structures. Smart Mater Struct 27, 015009. https://doi.org/10.1088/1361-665X/aa98c2

Downey, A., D'Alessandro, A., Ubertini, F., Laflamme, S., Geiger, R., 2017. Biphasic DC measurement approach for enhanced measurement stability and multi-channel sampling of self-sensing multi-functional structural materials doped with carbon-based additives. Smart Mater Struct 26, 065008. https://doi.org/10.1088/1361-665X/aa6b66

Garcés, P., Fraile, J., Vilaplana-Ortego, E., Cazorla-Amorós, D., Alcocel, E.G., Andión, L.G., 2005. Effect of carbon fibres on the mechanical properties and corrosion levels of reinforced portland cement mortars. Cem Concr Res 35, 324–331. https://doi.org/10.1016/j.cemconres.2004.05.013

Garcés, P., Zornoza, E., Alcocel, E.Ga., Galao, Ó., Andión, L.Ga., 2012. Mechanical properties and corrosion of CAC mortars with carbon fibers. Constr Build Mater 34, 91–96. https://doi.org/10.1016/j.conbuildmat.2012.02.020

García-Macías, E., Downey, A., D'Alessandro, A., Castro-Triguero, R., Laflamme, S., Ubertini, F., 2017. Enhanced lumped circuit model for smart nanocomposite cement-based sensors under dynamic compressive loading conditions. Sens Actuators A Phys 260, 45–57. https://doi.org/10.1016/j.sna.2017.04.004

Han, B., Ding, S., Yu, X., 2015a. Intrinsic self-sensing concrete and structures: A review. Measurement 59, 110–128. https://doi.org/10.1016/j.measurement.2014.09.048

Han, B., Guan, X., Ou, J., 2007. Electrode design, measuring method and data acquisition system of carbon fiber cement paste piezoresistive sensors. Sens Actuators A Phys 135, 360–369. https://doi.org/10.1016/j.sna.2006.08.003

Han, B., Yu, X., Ou, J., 2015b. Self-Sensing Concrete in Smart Structures. Elsevier. https://doi.org/10.1016/C2013-0-14456-X

Han, B., Zhang, K., Burnham, T., Kwon, E., Yu, X., 2013. Integration and road tests of a self-sensing CNT concrete pavement system for traffic detection. Smart Mater Struct 22, 015020. https://doi.org/10.1088/0964-1726/22/1/015020

Han, J., Cai, J., Pan, J., Sun, Y., 2021. Study on the conductivity of carbon fiber self-sensing high ductility cementitious composite. Journal of Building Engineering 43, 103125. https://doi.org/10.1016/j.jobe.2021.103125

Han, J., Pan, J., Cai, J., Li, X., 2020. A review on carbon-based self-sensing cementitious composites. Constr Build Mater 265, 120764. https://doi.org/10.1016/j.conbuildmat.2020.120764

Han, J., Pan, J., Ma, X., Cai, J., 2022. Sensing performance of engineered cementitious composites in different application forms. Constr Build Mater 355, 129223. https://doi.org/10.1016/j.conbuildmat.2022.129223

Hassan, A., Elkady, H., Shaaban, I.G., 2019. Effect of Adding Carbon Nanotubes on Corrosion Rates and Steel-Concrete Bond. Sci Rep 9, 6285. https://doi.org/10.1038/s41598-019-42761-2

Horszczaruk, E., Sikora, P., Łukowski, P., 2016. Application of Nanomaterials in Production of Self-Sensing Concretes: Contemporary Developments and Prospects. Archives of Civil Engineering 62, 61–74. https://doi.org/10.1515/ace-2015-0083

Huang, Y., Li, H., Qian, S., 2018. Self-sensing properties of Engineered Cementitious Composites. Constr Build Mater 174, 253–262. https://doi.org/10.1016/j.conbuildmat.2018.04.129

Hussain, A., Xiang, Y., Yu, T., Zou, F., 2022. Nanocarbon black-based ultra-high-performance concrete (UHPC) with self-strain sensing capability. Constr Build Mater 359, 129496. https://doi.org/10.1016/j.conbuildmat.2022.129496

Kang, M.-S., Lee, H., Yim, H., An, Y.-K., Kim, D., 2018. Multi-Channel Electrical Impedance-Based Crack Localization of Fiber-Reinforced Cementitious Composites under Bending Conditions. Applied Sciences 8, 2582. https://doi.org/10.3390/app8122582

Laflamme, S., Cao, L., Chatzi, E., Ubertini, F., 2016. Damage Detection and Localization from Dense Network of Strain Sensors. Shock and Vibration 2016, 1–13. https://doi.org/10.1155/2016/2562949

Lee, S.-J., Ahn, D., You, I., Yoo, D.-Y., Kang, Y.-S., 2020. Wireless cement-based sensor for self-monitoring of railway concrete infrastructures. Autom Constr 119, 103323. https://doi.org/10.1016/j.autcon.2020.103323

Li, H., Xiao, H., Ou, J., 2006. Effect of compressive strain on electrical resistivity of carbon black-filled cement-based composites. Cem Concr Compos 28, 824–828. https://doi.org/10.1016/j.cemconcomp.2006.05.004

Li, W., Liu, Y., Jiang, Z., Fang, Y., Zhan, N., Long, W., Xing, F., 2020. Chloride-induced corrosion behavior of reinforced cement mortar with MWCNTs. Science and Engineering of Composite Materials 27, 281–289. https://doi.org/10.1515/secm-2020-0029

Lima, G., Nalon, G., Santos, R.F., Ribeiro, J.C.L., Franco de Carvalho, J.M., Pedroti, L.G., de Araújo, E.N.D., 2020. Microstructural investigation of the effects of carbon black nanoparticles on hydration mechanisms, mechanical and piezoresistive properties of cement mortars. Materials Research 24. https://doi.org/10.1590/1980-5373-MR-2020-0539

Liu, J., Liu, M., Xiao, H., 2015. Optimizing the Strain-Sensing Property of Cement-Based Composite Based on a Piezoresisitivity Model, in: 2015 Fifth International Conference

on Instrumentation and Measurement, Computer, Communication and Control (IMCCC). IEEE, pp. 1061–1064. https://doi.org/10.1109/IMCCC.2015.229

Liu, Q., Gao, R., Tam, V.W.Y., Li, W., Xiao, J., 2018. Strain monitoring for a bending concrete beam by using piezoresistive cement-based sensors. Constr Build Mater 167, 338–347. https://doi.org/10.1016/j.conbuildmat.2018.02.048

Machan, L., Steffan, P., 2015. Multichannel Laboratory Device for Measurement of Smart Concrete Material Properties. Adv Mat Res 1124, 249–254. https://doi.org/10.4028/www.scientific.net/AMR.1124.249

Materazzi, A.L., Ubertini, F., D'Alessandro, A., 2013. Carbon nanotube cement-based transducers for dynamic sensing of strain. Cem Concr Compos 37, 2–11. https://doi.org/10.1016/j.cemconcomp.2012.12.013

Mehta, P., Monteiro, P., 2005. Concrete: Microstructure, Properties and Materials (Portuguese version). New York.

Meoni, A., D'Alessandro, A., Cavalagli, N., Gioffré, M., Ubertini, F., 2019. Shaking table tests on a masonry building monitored using smart bricks: Damage detection and localization. Earthq Eng Struct Dyn 48, 910–928. https://doi.org/10.1002/eqe.3166

Meoni, A., D'Alessandro, A., Downey, A., García-Macías, E., Rallini, M., Materazzi, A., Torre, L., Laflamme, S., Castro-Triguero, R., Ubertini, F., 2018. An Experimental Study on Static and Dynamic Strain Sensitivity of Embeddable Smart Concrete Sensors Doped with Carbon Nanotubes for SHM of Large Structures. Sensors 18, 831. https://doi.org/10.3390/s18030831

Meoni, A., D'Alessandro, A., Kruse, R., De Lorenzis, L., Ubertini, F., 2021a. Strain field reconstruction and damage identification in masonry walls under in-plane loading using dense sensor networks of smart bricks: Experiments and simulations. Eng Struct 239, 112199. https://doi.org/10.1016/j.engstruct.2021.112199

Meoni, A., D'Alessandro, A., Mancinelli, M., Ubertini, F., 2021b. A Multichannel Strain Measurement Technique for Nanomodified Smart Cement-Based Sensors in Reinforced Concrete Structures. Sensors 21, 5633. https://doi.org/10.3390/s21165633

Monteiro, A., Loredo, A., Costa, P., Oeser, M., Cachim, P., 2017. A pressure-sensitive carbon black cement composite for traffic monitoring. Constr Build Mater 154, 1079–1086. https://doi.org/10.1016/j.conbuildmat.2017.08.053

Nalon, G., Ribeiro, J., Araújo, E., Pedroti, L., Carvalho, J., Santos, R., Aparecido-Ferreira, A., 2020. Effects of different kinds of carbon black nanoparticles on the piezoresistive

and mechanical properties of cement-based composites. Journal of Building Engineering 32, 101724. https://doi.org/10.1016/j.jobe.2020.101724

Nalon, G.H., Ribeiro, J., Pedroti, L., de Araújo, E., Franco de Carvalho, J.M., Lima, G., Oliveira, D., 2021a. Self-Sensing Mortars: Effect of Moisture and Nanocarbon Black Content. ACI Mater J 118, 131–141. https://doi.org/10.14359/51732636

Nalon, G.H., Ribeiro, J.C., Pedroti, L.G., Duarte de Araújo, E., Franco de Carvalho, J., Soares de Lima, G., de Moura Guimarães, L., 2021b. Residual piezoresistive properties of mortars containing carbon nanomaterials exposed to high temperatures. Cem Concr Compos 121, 104104. https://doi.org/10.1016/j.cemconcomp.2021.104104

Neville, A., 2011. Properties of concrete, 5th Editio. ed.

Suchorzewski, J., Prieto, M., Mueller, U., 2020. An experimental study of self-sensing concrete enhanced with multi-wall carbon nanotubes in wedge splitting test and DIC. Constr Build Mater 262, 120871. https://doi.org/10.1016/j.conbuildmat.2020.120871

Sun, M., Liew, R.J.Y., Zhang, M.-H., Li, W., 2014. Development of cement-based strain sensor for health monitoring of ultra high strength concrete. Constr Build Mater 65, 630–637. https://doi.org/10.1016/j.conbuildmat.2014.04.105

Ubertini, F., D'Alessandro, A., 2018. Concrete with self-sensing properties, in: Eco-Efficient Repair and Rehabilitation of Concrete Infrastructures. Elsevier, pp. 501–530. https://doi.org/10.1016/B978-0-08-102181-1.00018-6

Wang, H., Shen, J., Liu, J., Lu, S., He, G., 2019. Influence of carbon nanofiber content and sodium chloride solution on the stability of resistance and the following self-sensing performance of carbon nanofiber cement paste. Case Studies in Construction Materials 11, e00247. https://doi.org/10.1016/j.cscm.2019.e00247

Wang, H., Shi, F., Shen, J., Zhang, A., Zhang, L., Huang, H., Liu, J., Jin, K., Feng, L., Tang, Z., 2021. Research on the self-sensing and mechanical properties of aligned stainless steel fiber-reinforced reactive powder concrete. Cem Concr Compos 119, 104001. https://doi.org/10.1016/j.cemconcomp.2021.104001

Wen, S., Chung, D.D.L., 2007. Electrical-resistance-based damage self-sensing in carbon fiber reinforced cement. Carbon N Y 45, 710–716. https://doi.org/10.1016/j.carbon.2006.11.029

Xiao, H., Li, H., 2006. A study on the application of CB-filled cement-based composite as a strain sensor for concrete structures, in: Tomizuka, M., Yun, C.-B., Giurgiutiu, V. (Eds.), . p. 61742T. https://doi.org/10.1117/12.660787

Xiao, H., Li, H., Ou, J., 2016. Self-sensing of nano-carbon black concrete, in: Innovative Developments of Advanced Multifunctional Nanocomposites in Civil and Structural Engineering. pp. 59–78. https://doi.org/10.1016/B978-1-78242-326-3.00004-X

Xiao, H., Li, H., Ou, J., 2011a. Strain sensing properties of cement-based sensors embedded at various stress zones in a bending concrete beam. Sens Actuators A Phys 167, 581–587. https://doi.org/10.1016/j.sna.2011.03.012

Xiao, H., Li, H., Ou, J., 2011b. Self-monitoring Properties of Concrete Columns with Embedded Cement-based Strain Sensors. J Intell Mater Syst Struct 22, 191–200. https://doi.org/10.1177/1045389X10396573

Xiao, H., Li, H., Ou, J., 2010. Modeling of piezoresistivity of carbon black filled cement-based composites under multi-axial strain. Sens Actuators A Phys 160, 87–93. https://doi.org/10.1016/j.sna.2010.04.027

Xiao, H., Liu, M., Jiang, J., 2015. Effect of aligning conductive particles on the piezoresistivity of composites. Sensor Review 35, 43–50. https://doi.org/10.1108/SR-08-2013-722

Xu, J., Butler, L.J., Elshafie, M.Z., 2020. Experimental and numerical investigation of the performance of self-sensing concrete sleepers. Struct Health Monit 19, 66–85. https://doi.org/10.1177/1475921719834506

Xu, J., Yin, T., Wang, Y., Liu, L., 2021. Anisotropic electrical and piezoresistive sensing properties of cement-based sensors with aligned carbon fibers. Cem Concr Compos 116, 103873. https://doi.org/10.1016/j.cemconcomp.2020.103873

APPENDIX 5A: RESULTS OF STATISTICAL ANALYSES

5A.1. GRUBB'S TEST FOR OUTLIER DETECTION

The results of maximum tensile force, gauge factor and compressive strength of the specimens tested in the present study were subjected to Grubb's tests for detection of statistical outliers.

5A.1.1. Hypothesis and significance level

- Null hypothesis (H_0): all values belong to the same population.
- Alternative hypothesis (H_a): the smallest or the largest value is an outlier.
- Significance level (α): 5%.

5A.1.2. Results of the statistical tests

The results of the Grubb's tests are presented in Table A1, Table A2 and Table A3.

Table A1 - Grubb's test statistical summary for the maximum tensile force (in N) dataset.

Series	Mean	Standard deviation	Minimum	Maximum	Grubb's test statistic	P-value
REF	1021.2	502.3	443.4	1355.7	1.15	0.170
PUI	1499.9	429.7	1058.5	1916.9	1.03	0.906
CBC	1952.2	397.3	1599.0	2382.8	1.08	0.676
ESA	3085.2	77.9	3035.2	3175.5	1.15	0.138

Source: Author (2024).

Table A2 - Grubb's test statistical summary for the gauge factor dataset.

Series	Mean	Standard deviation	Minimum	Maximum	Grubb's test statistic	P-value
HS/FC	252.0	15.1	240	269	1.12	0.446
HS/HC	207.5	30.4	186	229	*	*
FS/HC	274.0	22.0	252	296	1.00	1.000
NES	154.3	9.1	146	164	1.07	0.756

Note: *The Grubb's test statistic and the P-value could not be calculated in this case because the specimen HS/HC-S3 did not exhibit a strain-monitoring response (Grubb's test cannot be applied to a series with only two replicates).

Source: Author (2024).

Table A3 - Grubb's test statistical summary for the compressive strength (in MPa) dataset.

Series	Mean	Standard deviation	Minimum	Maximum	Grubb's test statistic	P-value
HS/FC	28.22	1.70	26.94	30.15	1.13	0.354
HS/HC	26.67	1.48	25.13	28.07	1.05	0.827
FS/HC	27.17	1.65	25.87	29.02	1.12	0.448
NES	42.97	2.40	40.35	45.04	1.10	0.614

Source: Author (2024).

5A.1.3. Conclusions of the statistical tests

Since all analyses provided a P-value higher than 0.050, the null hypothesis was not rejected. Therefore, outliers were not found in the experimental dataset.

5A.2. SHAPIRO-WILK TEST OF NORMALITY

The results of maximum tensile force, gauge factor and compressive strength were subjected to the Shapiro-Wilk test for verification of normality of residuals, which is one of the analysis of variance (ANOVA) assumptions.

5A.2.1. Hypothesis and significance level

- Null hypothesis (H_0): residuals are normally distributed.
- Alternative hypothesis (H_a): residuals are not normally distributed.
- Significance level (α): 5%.

5A.2.2. Results of the statistical tests

The results of the Shapiro-Wilk test are summarized in Table A4.

Table A4 - Shapiro-Wilk's test statistical summary for all response variables.

Response variable	Shapiro-Wilk's test statistic	P-value
Maximum tensile force	0.943	0.533
Gauge factor	0.931	0.416
Compressive strength	0.933	0.414

Source: Author (2024).

5A.2.3. Conclusions of the statistical tests

P-values were always higher than 0.050 (null hypothesis was not rejected). Consequently, the residuals associated with all response variables were normally distributed.

5A.3. BARTLETT TEST OF HOMOSCEDASTICITY

Results of maximum tensile force, gauge factor and compressive strength were subjected to the Bartlett test for verification of homogeneity of variances, which is one of the ANOVA assumptions.

5A.3.1. Hypothesis and significance level

- Null hypothesis (H_0): all population variances are equal.
- Alternative hypothesis (H_a): at least two population variances are different.
- Significance level (α): 5%.

5A.3.2. Results of the statistical tests

Table A5 shows the results of the Bartlett test.

Table A5 - Bartlett's test statistical summary for all response variables.

Response variable	Bartlett's K-squared	P-value
Maximum tensile force	4.029	0.258
Gauge factor	1.828	0.609
Compressive strength	0.475	0.924

Source: Author (2024).

5A.3.3. Conclusions of the statistical tests

A P-value higher than 0.050 was observed in all Bartlett tests (null hypothesis was not rejected). Therefore, homoscedasticity was observed in the analyses of all response variables.

5A.4. ANALYSIS OF VARIANCE (ANOVA)

ANOVA was used to analyze differences among means of maximum tensile force, gauge factor and compressive strength.

5A.4.1. Hypothesis and significance level

- Null hypothesis (H_0): all means are equal.
- Alternative hypothesis (H_a): at least one mean is different.
- Significance level (α): 5%.

5A.4.2. Results of the statistical tests

The ANOVA results are summarized in Table A6, Table A7 and Table A8.

Table A6 - ANOVA statistical summary for the maximum tensile force dataset.

Source	Degrees of freedom	Sum of squares	Mean Square	F test statistics	P-value
Treatments	3	7019426	2339809	15.569	1.1×10^{-3}
Residuals	8	1202340	150292	-	-
Total	11	8221765	-	-	-

Source: Author (2024).

Table A7 - ANOVA statistical summary for the gauge factor dataset

Source	Degrees of freedom	Sum of squares	Mean Square	F test statistics	P-value
Treatments	3	24951.0	8317.0	23.147	5.2×10^{-4}
Residuals	7	2515.2	359.3	-	-
Total	10	27466.2	-	-	-

Source: Author (2024).

Table A8 - ANOVA statistical summary for the compressive strength dataset.

Source	Degrees of freedom	Sum of squares	Mean Square	F test statistics	P-value
Treatments	3	552.4	184.1	54.479	1.1×10^{-5}
Residuals	8	27	3.4	-	-
Total	11	579.4	-	-	-

Source: Author (2024).

5A.4.3. Conclusions of the statistical tests

P-values lower than 0.05 were obtained in all analyses (null hypothesis was rejected), indicating that at least one mean is different from the others. Tukey's multiple comparison tests (5% significance level) were applied to identify which means are statistically different from the others. Results of these post-hoc tests were tabulated in the main text of this work.

6 EFFECTS OF SHRINKAGE-REDUCING ADMIXTURES AND EXPANSIVE AGENTS ON THE SELF-SENSING BEHAVIOR OF NANOMODIFIED CEMENT-BASED MATERIALS

This chapter has been published as the following paper: Nalon, G. H.; Ribeiro, J. C. L.; Araújo, E. N. D.; Silva, R. M.; Pedroti, L. G. Effects of shrinkage-reducing admixtures and expansive agents on the self-sensing behavior of nanomodified cement-based materials. ***Journal of Building Engineering*** *78 (2023) 107648. https://doi.org/10.1016/j.jobe.2023.107648*

Abstract: *Shrinkage control is needed to ensure an appropriate installation of cementitious sensors used in the Structural Health Monitoring of concrete elements. However, the effects of shrinkage-reducing admixtures (SRAs) and expansive agents (EAs) on the self-sensing properties of the cementitious sensors is still unknown. Therefore, the present work evaluated the effects of a SRA and EAs based on calcium oxide (CaO) or calcium sulfoaluminate (CSA) on the shrinkage behavior, microstructure, self-sensing response and compressive strength of mortars containing carbon black nanoparticles (CBN). The SRA provided shrinkage reductions up to 47.4%. CaO-based EA and CSA-based EA provided an expansive behavior. The admixtures caused increases in electrical resistivity and gauge factor up to 37.1% and 71.0%, respectively. In contrast, they did not cause statistically significant changes in stress sensibility and compressive strength. A microstructural analysis suggested that portlandite and ettringite crystals provided by the inclusion of EAs caused interruptions in conductive paths inside the mortars, which decreased contact conduction mechanisms and increased the amount of insulating tunneling gaps between CBN, enhancing the gauge factor of the materials. Therefore, shrinking control admixtures were found to be promising alternatives to enable the dimensional compatibility between cement sensors and old concrete elements, and increase the self-sensing properties of smart cementitious composites.*

Keywords: *Smart cement-based composites, shrinkage control, compressive strength, piezoresistivity, microstructure.*

6.1. INTRODUCTION

Self-sensing cementitious composites are gaining significant importance in the field of integrated biomimetic Structural Health Monitoring (SHM) due to their high strain/stress sensibility, similar lifespan with concrete structures, high robustness, high scalability, easy installation and maintenance, and natural compatibility with concrete elements (Bekzhanova et al., 2021; Cassese et al., 2021; Dinesh et al., 2021). In the production process of these smart materials, conductive admixtures are dispersed in the cementitious matrix phase. Consequently, they exhibit a piezoresistive response characterized by reversible variations in electrical resistivity with changes in stress and strain, in addition to irreversible changes in electrical resistivity due to crack propagation (Bekzhanova et al., 2021; Dong et al., 2019; Han et al., 2015).

According to previous literature (Downey et al., 2018; Han et al., 2015a, 2015b), different approaches can be used to incorporate self-sensing structural materials into SHM systems, such as the bulk, coating, sandwich, bonded and embedded form. Except for the bulk form, these different approaches propose the installation of the cement-based sensors in key locations of the structural elements, such as regions of loading concentration or critical states of stress/strain, sites where progressive failure may occur and specific places of activation of failure mechanisms. These methods enable suitable monitoring efficiency with low construction cost and avoid issues of steel reinforcement corrosion.

The embedded form has been widely applied in construction of new structural elements, i.e., prefabricated cement-based sensors are placed at desired locations during concrete pouring (Ding et al., 2019; Sun et al., 2014; Ubertini et al., 2017; Ubertini and D'Alessandro, 2018). The self-sensing concretes can be applied in the embedded form to key locations of different types of structural elements, such as concrete beams (Liu et al., 2018; Xiao et al., 2011), concrete columns (Ding et al., 2019; Xiao and Li, 2006), beam-column joints (Rao et al., 2023), concrete slabs (Ding et al., 2022; Han et al., 2013); railway systems (Lee et al., 2020; Xu et al., 2020); etc.

However, cement-based sensors can also be embedded into preexisting structural elements. For example, self-sensing mortars can be applied for the SHM of heritage structures. This type of application aims to extend the lifespan of the structural elements, based on predictions of damage propagation and deterioration effects associated with

different agents (Medeiros et al., 2020; Mishra, 2021; Scuro et al., 2021). On the other hand, self-sensing concretes can also be applied for SHM of modern structures, in order to expand the concept of 'smart structures', provide information to enable the modification of the typical use of the buildings, and increase the safety level on a large territorial scale (La Mendola et al., 2021; Medeiros et al., 2020).

In the experimental program carried out by Han et al. (2013), a groove was cut in existing concrete pavement, self-sensing mortar was poured into the groove and then surface-smoothed. After one month of curing, transient and abrupt variations were observed in the voltage signal of the cast-in-place mortar sensors when vehicles passed over them, so that they could be used for real-time online traffic detection.

Self-sensing cementitious materials are commonly subjected to drying processes to avoid undesirable polarization effects on their electrical response (drying procedures mitigate ionic conduction mechanisms through the pore solution of the composites) (Downey et al., 2017; Han et al., 2015; Monteiro et al., 2017; Nalon et al., 2021; Xiao et al., 2011). In addition, they are usually produced with high cement/sand ratios to increase their electrical conductivity (Wen and Chung, 2007). Consequently, cracking and/or debonding of embedded self-sensing composites can occur when drying shrinkage is restrained by the concrete substrate (structural element to be monitored). Shrinkage issues must be resolved for appropriate application of cast-in-place cementitious sensors. When using the coating approach, McAlorum et al. (2021) also reported inappropriate bond strength between self-sensing alkali-activated concrete and concrete structures due to moisture deficit and shrinkage issues. To replace an existing structural masonry brick by a self-sensing unit in an existing masonry structure, Meoni et al. (2019), García-Macías and Ubertini (2019) recommended the use of expansive mortars to avoid shrinkage issues and ensure a reliable transmission of stresses and strains between plain and smart bricks.

When the embedded approach is applied to existing structures, the cast-in-place cementitious sensor starts to shrink soon after casting. The application of drying procedures to mitigate ionic conduction also increases shrinkage effects. To avoid cracking and/or debonding mechanisms, the shrinkage potential of the self-sensing composites should be reduced. In this context, shrinkage-reducing admixtures (SRAs) and expansive agents (EAs) can be used to mitigate the shrinkage behavior of cementitious materials.

SRAs are nonionic surfactants with functional groups that can firmly adsorb water molecules based on chemical bonding mechanisms. Relevant shrinkage decreases are

provided by these admixtures, mainly due to surface tension reductions of the pore solution (Zhang et al., 2022). On the other hand, the incorporation of EA into cementitious matrices can trigger their macroscopic bulk volume expansion, as these admixtures react with water and form expansive hydration products, thereby compensating drying shrinkage deformations (Liu et al., 2022; Tran et al., 2021a). The shrinkage control provided by SRAs and EAs is a promising alternative to avoid shrinkage cracking and improve the adherence between cement-based sensor, electrodes and the monitored concrete element.

Although the shrinkage control of cementitious materials with SRA and EA is well known in the literature, the effects of these different admixtures on the self-sensing properties of nanomodified cementitious composites is still unknown. Since there is no previous study of the influence of these admixtures on the piezoresistive response of cement-based sensors, the present research was carried out to evaluate the drying shrinkage, electrical resistivity, microstructure, self-sensing properties and compressive strength of smart mortars produced with carbon black nanoparticles (CBN) and three distinct admixtures: a SRA based on polypropylene glycol (PPG), an EA based on calcium oxide (CaO), and an EA based on calcium sulfoaluminate (CSA). Results of shrinkage, electrical and mechanical tests were explained based on microstructural mechanisms observed in field emission gun scanning electron microscopy (FEGSEM), X-ray diffraction (XRD), X-Ray Fluorescence (XRF), and Fourier transform infrared spectroscopy (FTIR) analyses. Using the appropriate shrinkage control alternatives discussed in the following sections of the present chapter, the developed self-sensing cementitious materials can be applied for self-monitoring of strain and self-detection of damage in structural elements of existing civil structures. The experimental findings of this study indicated the contributions of these admixtures to control drying shrinkage and improve the self-sensing performance of cast-in-place cementitious sensors.

This work is organized in four sections. Section 6.1 presents an introduction about the practical applications and limitations of self-sensing cementitious materials, definitions and applications of SRAs and EAs, and original contributions of the present work. Section 6.2 lists the materials and experimental methods used in drying shrinkage, electro-mechanical, compression and microstructural tests. Section 6.3 presents the results and discussions obtained from the experiments. Finally, Section 6.4 shows the conclusions and suggestions for future studies in this area.

6.2. MATERIALS AND METHODS

6.2.1. Materials

In this study, self-sensing mortars were produced with CP V-ARI Portland cement (density of 3.05 g/cm³), which is somewhat similar to the ASTM (2022) Type III cement (Mehta and Monteiro, 2005). The fine aggregates of the self-sensing mortars consisted of quartz sand with specific gravity of 2.64 and particle size < 2.38 mm. The particle size distribution curves of these different raw materials are represented in Figure 1.

Figure 1 - Particle size distribution curves of the raw materials.

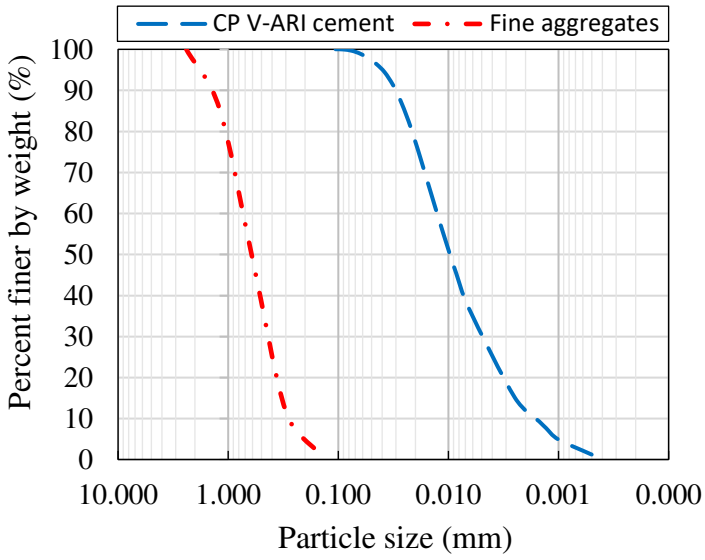

Source: Author (2024).

To construct the conductive network inside the self-sensing composites, CBN were used in this study (specific surface area of 120 m^2/g). These conductive nanomaterials were dispersed in the water used to produce the mortars, using a polycarboxylate-based superplasticizer (density of 1.12 g/cm³).

The following admixtures were used for shrinkage control: (i) a liquid SRA based on PPG, (ii) a powder EA based on CaO, and (iii) a powder EA based on CSA. The chemical composition of the EAs used in the present work was obtained using XRF analyses carried out in a Panalytical Epsilon 3^x equipment. For these analyses, samples of each type of admixture were obtained by grinding the raw materials and passing them through a #200 mesh standard sieve (75 µm opening). The chemical characterization obtained from each XRF analysis is represented in Table 1. The XRF analysis of the CaO-based EA indicated a

high content of CaO (96.68%), whereas the XRF analysis of the CSA-based EA revealed relevant contents of Al_2O_3 (11.19%), CaO (5.08%) and SO_3 (8.45%). Therefore, the tabulated data is in good agreement with the chemical characterization verified in similar EAs used in previous works (Carballosa et al., 2015; Collepardi et al., 2005; Mehdipour and Khayat, 2018; Natalli, 2017; Natalli et al., 2020; Treesuwan and Maleesee, 2017).

Table 1 - Results of XRF analyses of powder admixtures (wt.%).

Compounds	CaO	SiO_2	Al_2O_3	Fe_2O_3	MgO	Na_2O	K_2O	TiO_2	SO_3	Others
CaO-based EA	96.68	1.41	0.43	0.18	1.14	0.00	0.00	0.02	0.03	0.11
CSA-based EA	5.08	72.11	11.19	0.14	0.23	2.35	0.29	0.07	8.45	0.09

Source: Author (2024).

6.2.2. Preparation of self-sensing mortars

Three different series of self-sensing mortars were produced with distinct types of admixtures for shrinkage control, in addition to a reference series, as follows:

(i) REF series: mortar without admixtures for shrinkage control;

(ii) SRA series: mortar with 2.5% (by mass of cement) of SRA;

(iii) EA/CaO series: mortar with 2.5% (by mass of cement) of CaO-based EA;

(iv) EA/CSA series: mortar with 2.5% (by mass of cement) of CSA-based EA.

All compositions were produced with a cement/sand ratio of 0.75 (by volume) to get mortars with suitable electrical conductivity (Wen and Chung, 2007). The water/cement ratio was 0.43 (by mass). A constant CBN dosage of 6% (by mass of cement) was used to obtain cementitious composites within the percolation zone (Nalon et al. 2021). CBN were dispersed using a constant superplasticizer/CBN ratio of 0.4 (by mass) and an ultrasound sonication process (frequency of 20 kHz, power of 50 W).

The suspension of CBN, water and superplasticizer was mixed with cement and sand for about 10 minutes in a mechanical mixer. Then, the fresh mortar was poured into the molds in two equal layers appropriately compacted with a steel tamping rod (30 strokes). Each series was composed of three mortar beams of 25 mm × 25 mm × 285 mm for drying shrinkage tests (a steel gage stud was cast into each end of these specimens, providing a gage length equal to 250 mm), three 20-mm mortar cubes without electrodes for compression tests, and four mortar prisms of 20 mm × 20 mm × 60 mm for electrical resistivity and piezoresistive tests (two copper electrodes of 14 mm × 30 mm × 1 mm were embedded into these specimens, using a spacing between electrodes of about 8 mm). To evaluate the microstructural mechanisms behind the engineering properties of the materials, a cylindrical

mortar specimen (diameter of 35 mm and height of 70 mm) was also produced for each different series. After a 28-days curing period, they were oven-dried for 3 days at 60 ºC and then cooled down to room temperature, following recommendations of previous studies (Han et al., 2021; Wang et al., 2019, 2021) for elimination of the influence of ionic conduction through the pore water during piezoresistive tests.

Following the recommendations of ABNT NBR 15261 (2005), the gage stud holders were removed from the mortar beams after the compaction procedures (Figure 2a.1), in order to prevent any restraint of the gage studs during the initial shrinkage of the material. The required time to completely demold the specimens was 72 h. During this period, they were covered with a plastic film to avoid moisture losses. After that, the specimens were demolded and the plastic film was removed. According to prescriptions of the ABNT NBR 15261 (2005), the mortar beams were cured at 23 ± 2 ºC and relative humidity (RH) of 50 ± 5%.

6.2.3. Length change measurements

Length variations of the mortar beams were experimentally obtained, based on comparator readings at the ages of 3, 7, 14 and 28 days. A final comparator reading was also carried out after the final oven-drying procedure. As indicated in ABNT NBR 15261 (2005), the length change ε_i at any age i was calculated according to Equation (1), in which L_i is the difference between the comparator reading of the mortar prism (Figure 2a.2) and the reference bar (Figure 2a.3) at the age i, L_0 is the difference between the comparator reading of the mortar prism and the reference bar immediately after demolding the specimen and G is the nominal gage length (250 mm). A length comparator device with resolution of 0.001 mm was used.

$$\varepsilon_i = \frac{L_i - L_0}{G} \qquad (1)$$

Figure 2 - Methodology of (a) drying shrinkage tests, (b) compression tests, (c) DC electrical resistivity tests, and (d) piezoresistive tests.

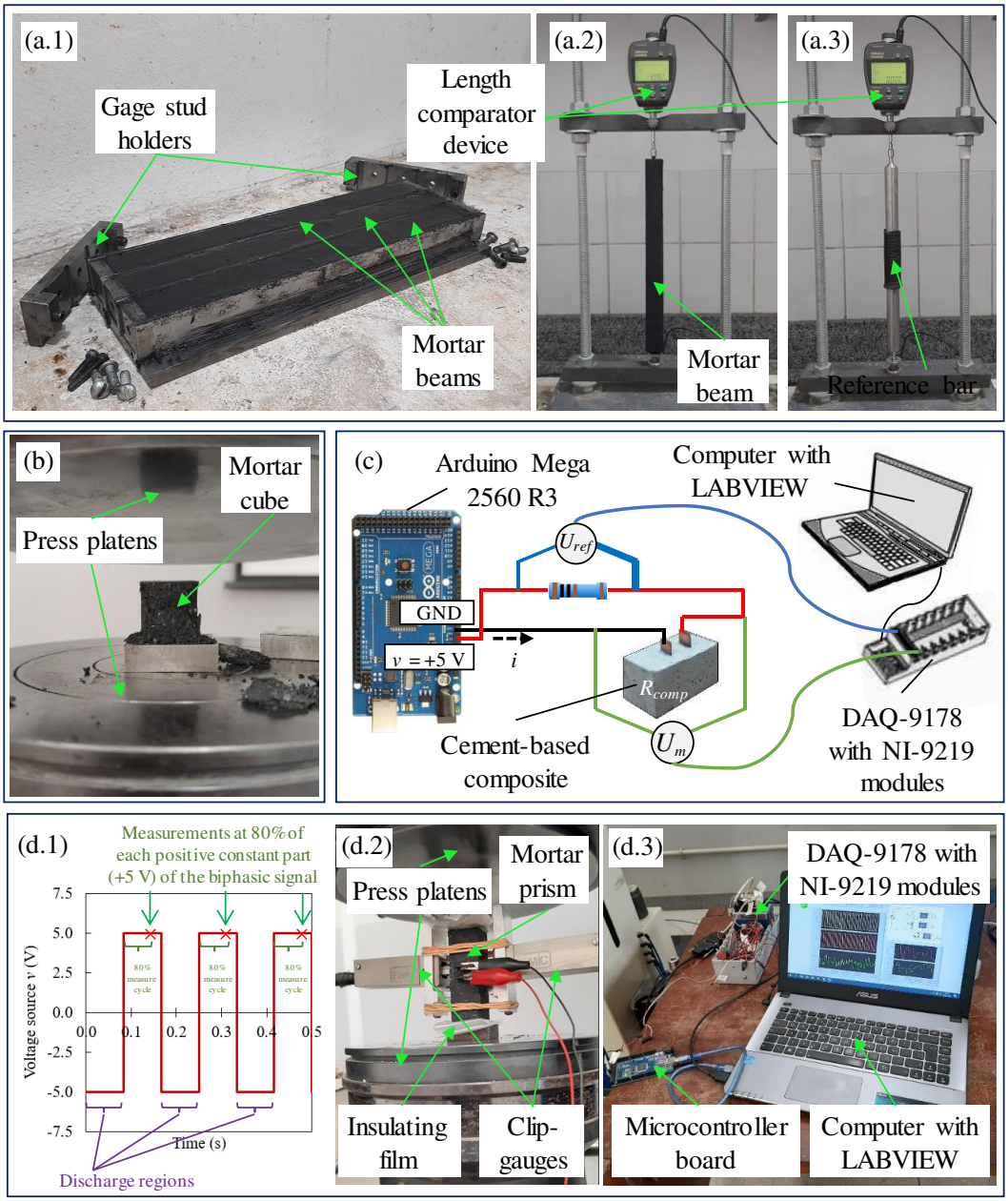

Source: Figures (a), (b), (d.2) and (d.3) were created by the author (2024); Figure (c) was adapted from Nalon et al. (2020), Copyright 2020, with permission from Elsevier; and Figure (d.1) was adapted from Nalon et al. (2021), Copyright 2021, with permission from Elsevier.

6.2.4. Electro-mechanical tests

Cubic specimens were used to determine the compressive strength of the self-sensing mortars, using an EMIC DL-60000 press and load rate of 0.5 MPa/s (Figure 2b). Mortar prisms with embedded electrodes were used to determine the direct current (DC) electrical resistivity. They were also subjected to biphasic DC measurements during piezoresistive tests

for determination of self-sensing properties, using the experimental setup illustrated in Figure 2c. In DC and biphasic DC tests, each specimen was series-connected with a resistor R_{ref} = 1000 Ω. Using an Arduino Mega 2560 R3 board, a constant 5 V voltage source was applied to the circuit in DC tests, whereas a ±5 V square wave signal (frequency = 6 Hz, duty cycle = 50%) was applied in biphasic DC tests. The potential difference across the self-sensing mortar and R_{ref} (U_m and U_{ref}, respectively) were measured with an NI compact DAQ-9178 hardware system with NI-9219 modules and the LabVIEW software.

Equation (2) was used to determine the electrical current (i) in the circuit. Using the electrodes spacing (L) and the effective area between electrodes (A), the electrical resistivity of the self-sensing mortar (ρ) was calculated with Equation (3). In biphasic DC tests, values of U_m and U_{ref} were acquired at 80% of the square wave's positive part (Figure 2d.1), following procedures described in previous works (Downey et al., 2017; Meoni et al., 2021; Nalon et al., 2021).

$$i = \frac{U_{ref}}{R_{ref}} \qquad (2)$$

$$\rho = \frac{U_m \, A}{i \, L} \qquad (3)$$

Piezoresistive tests of the self-sensing composites were carried out in the EMIC DL-60000 press, using a load rate of 0.5 MPa/s. At first, the compressive strength of one of the mortar prisms with electrodes (f_m) was obtained to define the appropriate loading amplitude for the piezoresistive tests. Then, the other three specimens were subjected to cyclic loading procedures for determination of self-sensing properties. These procedures consisted of three load-unload cycles up to 0.30 f_m followed by a final load stage applied in three steps: 0.10 f_m, 0.20 f_m and 0.30 f_m. Axial deformation during the piezoresistive tests was measured by EMIC clip-gauges symmetrically arranged at the lateral sides of the samples (Figure 2d.2). Compressive load was measured by the load cell of the EMIC DL-60000 press. Fractional changes in electrical resistivity (FCR) were continuously monitored using the NI system and the LabVIEW application (Figure 2d.3). Compressive strain, compressive stress and FCRs were used to calculate the gauge factor and stress sensibility of the self-sensing mortars.

All results of electro-mechanical tests (electrical resistivity, gauge factor, stress sensibility and compressive strength) were subjected to statistical Grubb's tests for outlier identification, Shapiro-Wilk tests for analyses of normality of residuals and Bartlett tests for analyses of homogeneity of variances. When assumptions for analysis of variance (ANOVA)

were met, this statistical technique was used to analyze the differences between average values, in addition to Tukey's tests for the comparison of the means between the groups. The significance level of the statistical tests was 0.05 and their null and alternative hypotheses (H_0 and H_a, respectively) were detailed in APPENDIX 6A.

6.2.5. Microstructural investigation

For microstructural characterization of the self-sensing composites, two slices with thickness of approximately 4 mm were cut from each different type of mortar cylinder. A circular saw was used to cut the slices and the top/bottom slices of each mortar cylinder were not used because they may not be representative (Scrivener et al., 2016). Solvent exchange with isopropanol was used to stop the hydration of the specimens.

A small sample was taken from the middle part of some slices, so that wall effects were reduced. Then, carbon double-tape was used to attach the sample to a microscope stub. Next, the sample was gold coated with a Quorum Q150RS sputtering system. Moreover, a conductive carbon-based paint was used to provide a conductive path from the stub to the sample surface. Finally, secondary electron images were obtained through FEGSEM, using a TESCAN MIRA's microscope with FEG Schottky electron emission source (resolution of 1.2 nm at 30 keV).

Powder samples of each mortar type were obtained by grinding some mortar slices, so that they could pass through a #200 mesh standard sieve (75 μm opening). These samples were subjected to XRD analysis in a Bruker D8-Discover equipment (CuKα radiation, 40 kV and 40 mA). The XRD data were collected between 2θ values of 5° and 70° with a step size of 0.05° and a scan time of 1 s/step. Using a Varian 660 spectrometer, the powder samples were also subjected to FTIR analysis in the range of 400-4000 cm^{-1} at a 4 cm^{-1} resolution.

6.3. RESULTS AND DISCUSSIONS

6.3.1. Drying shrinkage control

Length changes observed during the curing and oven-drying processes of the different types of self-sensing mortars are shown in Figure 3. Positive length changes represent expansion and negative length changes indicate shrinkage deformation. Mortars without

SRA or EA presented a maximum average shrinkage of 646 με. This value is in good agreement with previous works (Kim et al., 2019; Lea, 1970; Yeon, 2019), which reported that the ultimate drying shrinkage of cementitious materials generally ranges between 200 με and 1200 με. The removal of water held by capillary tension in small capillaries is one of the main causes of shrinkage of these systems (Mehta and Monteiro, 2005; Tran et al., 2021a).

Figure 3 - Length change of reference mortars (REF) and mortars containing shrinkage-reducing admixtures (SRA), CaO-based expansive agents (EA/CaO) or calcium sulfoaluminate-based expansive agents (EA/CSA).

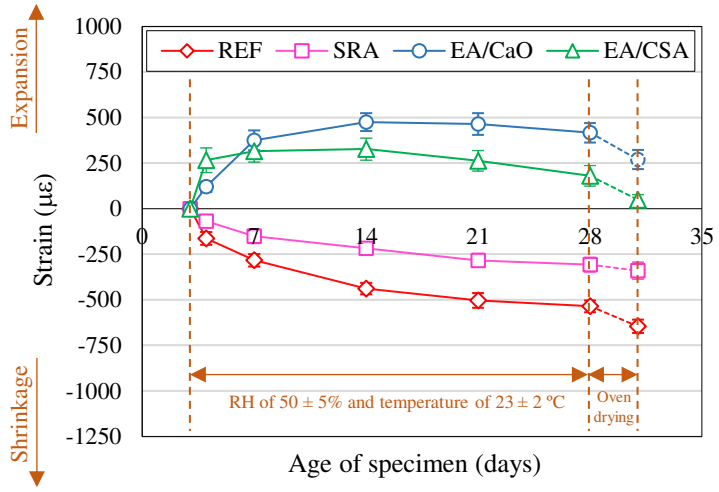

Source: Author (2024).

Although a low aggregate/cement ratio was used in this research to attain good electrical conductivity (Wen and Chung, 2007), the maximum average shrinkage of REF mortars was not significantly high, which can be attributed to some benefits provided by the inclusion of carbon-based nanomaterials. Previous studies (Donget al., 2019; Han et al., 2010; Lima et al., 2021; Zhang et al., 2019) observed that CBN adsorb significant amounts of water in the early stages of the cement matrix hydration. The water adsorbed by carbon-based nanomaterials is released in later hydration stages, which helps to maintain internal moisture for further hydration, densifying the microstructure of the system and attenuating the drying shrinkage of cementitious matrices (Tran et al., 2021a).

The moderate shrinkage values observed in REF mortars can be the major cause of debonding between self-sensing composites, electrodes and/or monitored concrete substrate. A self-sensing mortar embedded into existing concrete structures must not shrink to the extent that the imposed tensile stresses could cause (i) bond failure at the interface between the self-sensing mortar and electrodes, or (ii) bond failure at the interface between the self-sensing mortar and the old concrete element. Results presented in Figure 3 indicated that the

addition of PPG-based SRA, CaO-based EA or CSA-based EA provided significant changes in the shrinkage behavior of CBN-based mortars, so that these admixtures are promising alternatives for dimensional compatibility of patching self-sensing materials.

For example, the SRA mortars presented a maximum average shrinkage 47.4% lower than that observed in REF mortars. The main cause for this shrinkage reduction was the decrease in the surface tension on capillary walls provided by PPG-based SRAs (Mao et al., 2021; Tran et al., 2021b; Zhan and He, 2019). This percentage shrinkage decrease was very similar to the percentage shrinkage reductions reported in previous works. For example, Palacios and Puertas (2007) reported that the addition of 2% of PPG-based SRA (by mass of slag) provided shrinkage reductions up to 50% in alkali-activated slag mortars cured at RH of 50%. According to Bilim et al. (2013), the incorporation of 1% of PPG-based SRA (by mass of binder) provided maximum shrinkage reductions between 17.4% and 28.9% in Portland cement mortars and alkali-activated slag mortars cured at 23 ± 2 °C and RH of 50%. Experimental results of Ye, Fu and Lei (2020) indicated that the addition of 1% of PPG-based SRA (by mass of slag) provided shrinkage reductions up to 50% in alkali-activated slag pastes exposed to 20 ± 0.5 °C and RH of 43%.

On the other hand, Figure 3 shows that EA/CaO and EA/CSA mortars presented an expansive behavior characterized by maximum average swelling values of 475 με and 327 με at the age of 14 days, respectively. After 14 days, the length changes started to decrease, so that the EA/CaO and EA/CSA mortars presented average swelling values of 269 με and 48 με after the final oven-drying procedure, respectively. According to Figure 3, the self-sensing mortars with CaO-based EA or CSA-based EA particularly exhibited relevant expansion during the first 7 days. This expansion was able to successfully compensate the accompanied shrinkage tendency that happened when the composites were exposed to the drying procedures. The expansive behavior provided by the CaO-based EA can be attributed to the formation of CH crystals due to the hydration of free lime, whereas the expansive behavior provided by the CSA-based EA can be attributed to the formation of AFt crystals using the available source of CSA provided by the admixtures (Collepardi et al., 2005; Souza et al., 2020; Yu et al., 2021). Detailed discussions about the formation of these different expansive products and their effects on different properties of the self-sensing mortars were presented in the microstructural investigation of Section 6.3.4.

Although an expansive behavior was observed in the self-sensing mortars tested in the present research, the expansion levels were lower than those reported in the literature because

higher contents of EA have been used in the previous works. For example, length change measurements of Treesuwan and Maleesee (2017) indicated that the replacement of 15% of cement by CaO-based EA provided an approximately constant expansion of ~550 με (from 4 to 28 days) in cement mortars tested at 25 °C and RH of 40 %. After replacing 10% (by weight) of cement by an admixture with relevant sources of calcium and sulfate, Souza et al. (2020) monitored length changes during 7 days and observed an average expansion of ~150 με after this curing period. Yu et al. (2021) replaced 8% (by weight) of cement by CSA-based EA and verified an increasing expansion from 4 to 28 days when the mortars were subjected to 20 ± 2 ºC and RH of 60 ± 5%.

In the present work, the CSA-based EA provided a final average expansion of approximately 18% of the final average expansion generated by the CaO-based EA. Carballosa et al. (2015) also carried out a comparison between the expansive behavior of concretes containing different types and contents of EAs. In fact, they observed that the CaO-based EA exhibited a total longitudinal expansion higher than that obtained with the CSA-based EA, so that the CaO-based EA was more effective than the CSA-based EA to compensate the shrinkage behavior of the cementitious materials.

6.3.2. Electro-mechanical properties

The effects of SRA and EAs on the DC electrical resistivity (under unloading condition) of dried self-sensing mortars were investigated by the first time in the present study. As indicated in Figure 4, SRA, CaO-based EA and CSA-based EA caused percentage increases in average DC electrical resistivity of 22.5%, 54.0% and 37.1%, respectively. The microstructural mechanisms behind these effects were discussed in Section 6.3.4. According to the statistical analyses presented in APPENDIX 6A, the DC electrical resistivity dataset did not meet the homoscedasticity assumption at the significance level of 0.05, so that an ANOVA could not be carried out to compare the average values of DC electrical resistivity. The homoscedasticity issues can be attributed to the high standard deviation observed in mortars containing chemical admixtures compared to the standard deviation of REF mortars.

Figure 4 - DC electrical resistivity of reference mortars (REF) and mortars containing shrinkage-reducing admixtures (SRA), CaO-based expansive agents (EA/CaO) or calcium sulfoaluminate-based expansive agents (EA/CSA).

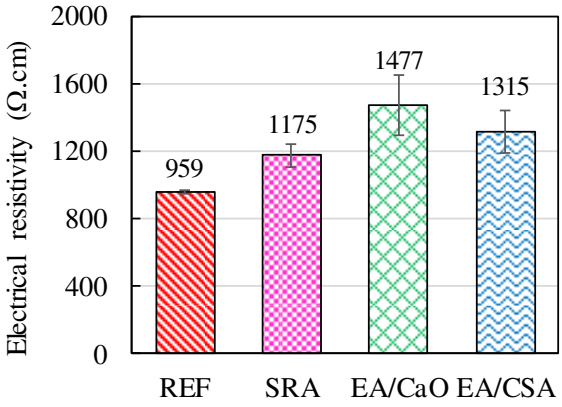

Source: Author (2024).

The self-sensing properties of conductive mortars were also investigated by the first time in the present work. The relationships between FCR, compressive strain and compressive stress verified in the piezoresistive tests of the self-sensing mortars are presented in APPENDIX 6B. Regression analyses were developed to obtain linear regression models that properly represented the data of the linear stretch of FCR *vs* strain and FCR *vs* stress curves. Based on the developed models and recommendations of Chung (2020), it was possible to determine the values of gauge factor and stress sensibility graphically summarized in Figure 5a and Figure 5b, respectively. Results of APPENDIX 6A demonstrated that the gauge factor and stress sensibility datasets satisfied the ANOVA assumptions. Thus, it was possible to carry out valid ANOVAs.

Figure 5 - (a) Gauge factor and (b) stress sensibility of reference mortars (REF) and mortars containing shrinkage-reducing admixtures (SRA), CaO-based expansive agents (EA/CaO) or calcium sulfoaluminate-based expansive agents (EA/CSA). Bars with the same uppercase letter are statistically equal, according to the Tukey's test (significance level of 0.05).

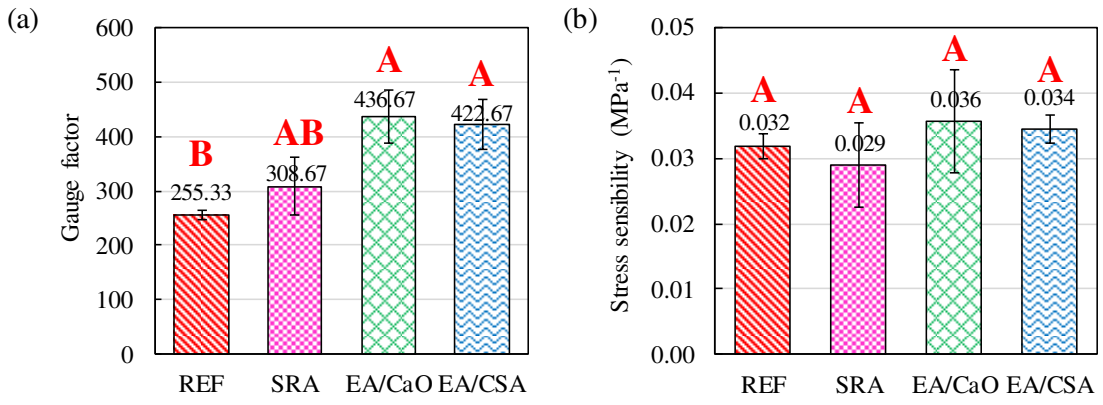

Source: Author (2024).

A P-value equal to 0.0074 was obtained in the ANOVA of the gauge factor dataset, which indicated that this self-sensing property was significantly affected by the type of shrinkage control admixture. According to the Tukey's test results represented in Figure 5a, the average values of gauge factor of CaO/EA and CSA/EA mortars (represented in the image with the uppercase letter A) were statistically higher than the gauge factor of the REF mortar (uppercase letter B). In fact, the incorporation of CaO-based EA and CSA-based EA caused percentage increases of 71.0% and 65.5% in the average gauge factor of self-sensing mortars, respectively. On the other hand, the addition of SRA did not cause significant change in the gauge factor of the nanomodified mortars because REF and SRA mortars shared the same uppercase letter (B), according to the Tukey's test results presented in Figure 5a. Section 6.3.4 discusses possible reasons for the values of self-sensing properties mentioned in the present section.

Results of Figure 5b indicated that all series of mortars presented similar values of average stress sensibility fluctuating between 0.029 MPa^{-1} and 0.036 MPa^{-1}. In fact, the ANOVA of the stress sensibility dataset provided a P-value of 0.613, which indicates that the stress sensibility was not statistically affected by the addition of SRA or EAs. Since the addition of CaO-based EA and CSA-based EA provided an enhancement in the gauge factor of self-sensing mortars and did not change their stress sensibility, it is possible to infer that the incorporation of the admixtures decreased the modulus of elasticity of the cementitious materials. Future studies are recommended to evaluate the influence of SRA, CaO-based EA and CSA-based EA on the modulus of elasticity and Poisson' ratio of self-sensing mortars.

6.3.3. Compressive strength

Figure 6 shows the effects of SRA and EAs on the compressive strength of self-sensing mortars. The information compiled in APPENDIX 6A indicated that the compressive strength dataset satisfied the ANOVA assumptions. According to the ANOVA results (P-value equal to 0.739), the values of average compressive strength of all self-sensing mortars were statistically the same. Therefore, the addition of SRA, CaO-based EA and CSA-based EA did not change the compressive strength of self-sensing mortars.

Figure 6 - Compressive strength of reference self-sensing mortars (REF) and mortars containing shrinkage-reducing admixtures (SRA), CaO-based expansive agents (EA/CaO) or calcium sulfoaluminate-based expansive agents (EA/CSA).

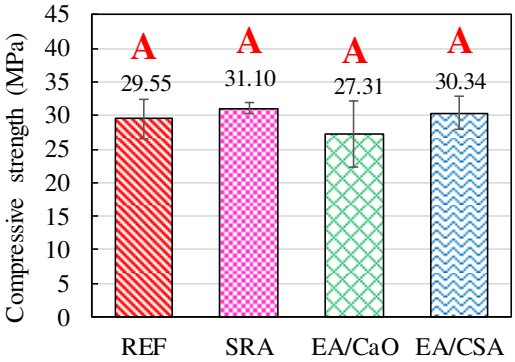

Source: Author (2024).

Some results presented in Figure 6 are similar to those reported in the literature. For example, previous studies reported negligible changes in compressive strength due to the incorporation of small contents of PPG-based SRA. Palacios and Puertas (2007) reported that alkali-activated slag mortars containing 0%, 1% or 2% of PPG-based SRAs (by mass of slag) presented similar values of 28-days compressive strength. Bilim et al. (2013) also verified that the incorporation of 1% of PPG-based SRA (by mass of binder) did not cause relevant change in the 28-days compressive strength of Portland cement mortars and alkali-activated slag mortars. Ye, Fu and Lei (2020) did not observe statistically significant variation in the 28-days compressive strength of alkali-activated slag pastes containing 0%, 0.5% or 1% of PPG-based SRA (by mass of slag).

In previous studies that reported an expansive behavior due to addition of EAs, negative and positive effects on the compressive strength due to EAs have been observed. Results of Treesuwan and Maleesee (2017) revealed that the replacement of 15% of cement by CaO-based EA caused a reduction of almost 40% in the 28-days compressive strength of cement mortars. In contrast, Souza et al. (2020) verified increases of about 25% in the compressive strength of cement pastes due to the replacement of 10% (by weight) of cement by an admixture with high contents of calcium and sulfate compounds. Carballosa et al. (2015) verified that the incorporation of CSA-based EA (contents of 15%, 17.5% and 20% by weight of cement) caused percentage decreases in 28-days compressive strength up to only 3%, whereas the use of CaO-based EA (contents of 10% or 11% by weight of cement) caused percentage decreases in the 28-days compressive strength up to 25%.

6.3.4. Microstructural behavior

According to the literature compiled in recently-published review papers (Mao et al., 2021; Tran et al., 2021b; Zhan and He, 2019), the shrinkage reductions provided by the SRA used in this study are mainly attributed to four different microstructural changes provided by SRAs: (i) decreases in the surface tension on capillary walls coupled with reductions in capillary stresses; (ii) maintenance of high RH inside the cementitious materials; (iii) reductions in the concentration of pore solution ions; and (iv) expansion effects due to the super-saturation level of silicates and formation of portlandite (CH) and ettringite (AFt) crystals that partially compensate shrinkage stresses caused by capillary pressure.

The expansive behavior observed in EA/CaO and EA/CSA composites can be attributed to the formation and growth of expansive compounds due to specific chemical reactions represented in Equation (4) and Equation (5), respectively (Collepardi et al., 2005; Souza et al., 2020; Yu et al., 2021). According to Equation (4), AFt ($C_3A \cdot 3C\bar{S} \cdot H_{32}$) is the product of the chemical reaction between the CSA ($C_4A_3\bar{S}$) of the CSA-based EA, calcium oxide (C) and anhydrite ($C\bar{S}$). On the other hand, Equation (5) shows that the expansive compound was CH, which is the product of the reaction between water and the CaO content of CaO-based EA. These expansive products caused a macroscopic bulk volume expansion, thereby compensating the drying shrinkage deformation (Tran et al., 2021a).

$$C_4A_3\bar{S} + 6C + 8C\bar{S} + 96H \rightarrow 3C_3A \cdot 3C\bar{S} \cdot H_{32} \quad (4)$$

$$C + H \rightarrow CH \quad (5)$$

In fact, results of XRF analyses of EAs (Table 1) revealed that the CSA-based EA used in this study presented high contents of Al_2O_3, CaO and SO_3 (rich CSA source), whereas the CaO-based EA exhibited high content of CaO (rich lime source).

According to the results presented in Section 6.3.2, the CSA-based EA and the CaO-based EA caused significant changes in the electrical resistivity and gauge factor of the mortars, whereas an opposite behavior was observed when the PPG-based SRA was added to the mortars. These observations can be attributed to the expansive behavior provided by the EAs and discussed in Section 6.3.1, which was not observed in mortars containing the PPG-based SRA. Since this expansive behavior was provided by the formation of CH and AFt crystals, the typical interaction between these hydration products and the CBN

aggregates that formed the conductive network inside the cementitious matrix was elucidated by the high-resolution FEGSEM images presented in Figure 7.

The FEGSEM image of CaO/EA samples (Figure 7a) evidences the presence of prismatic CH crystals of 2-3 μm (Mehta and Monteiro, 2005) obstructing the conductive path formed by CBN aggregates of 85-500 nm (ICBA, 2016). The image clearly shows that these CBN aggregates were composed of fused primary nanospheres with diameters of 10-150 nm and could be mostly found intermixed within aggregations of amorphous C-S-H gel. In contrast, the FEGSEM image of CSA/EA samples (Figure 7b) shows the ends of slender needles of AFt crystals (Mehta and Monteiro, 2005) blocking the direct contact between aggregates of CBN intermixed with amorphous C-S-H structures. It is important to highlight that the CP V-ARI Portland cement has calcite contents up to 10 wt.%. Consequently, more contents of monocarbonate tended to be stabilized instead of the monosulfate, which tended to reduce the formation of monosulfates during the hydration process of the cementitious matrix (Lima et al., 2020; Lothenbach et al., 2008; Lothenbach and Zajac, 2019).

Figure 7 - Field emission gun scanning electron microscopy (FEGSEM) images of self-sensing mortars containing (a) CaO-based expansive agents (EA/CaO) or (b) calcium sulfoaluminate-based expansive agents (EA/CSA): expansive products intercepting conductive paths of carbon black nanoparticles (CBN).

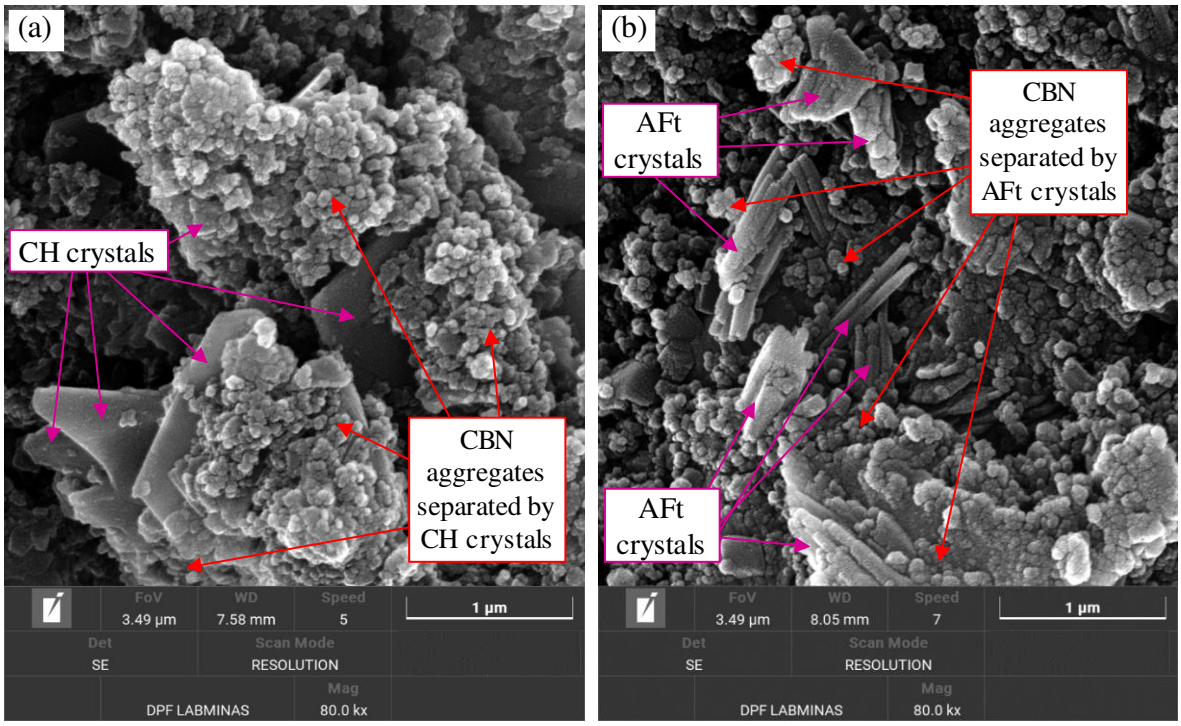

Source: Author (2024).

The plate-like CH prisms and needle-like AFt crystals provided by the incorporation of EAs caused interruptions in conductive paths, increasing the DC electrical resistivity of

the nanomodified mortars (Figure 4). The inclusion of expansive products decreased direct contact conduction mechanisms inside the matrix and increased the amount of insulating tunneling gaps between CBN. These improvements in tunneling conduction mechanisms caused increases in the FCRs associated with the application of compressive loads (Han et al., 2010, 2015; Nalon et al., 2021), so that the gauge factor of the mortars increased with the incorporation of EAs (Figure 5). The presence of these expansive products was evidenced in the XRD analyses results presented in Figure 8.

Figure 8 - X-ray diffraction (XRD) results of reference self-sensing mortars (REF) and mortars containing shrinkage-reducing admixtures (SRA), CaO-based expansive agents (EA/CaO) or calcium sulfoaluminate-based expansive agents (EA/CSA).

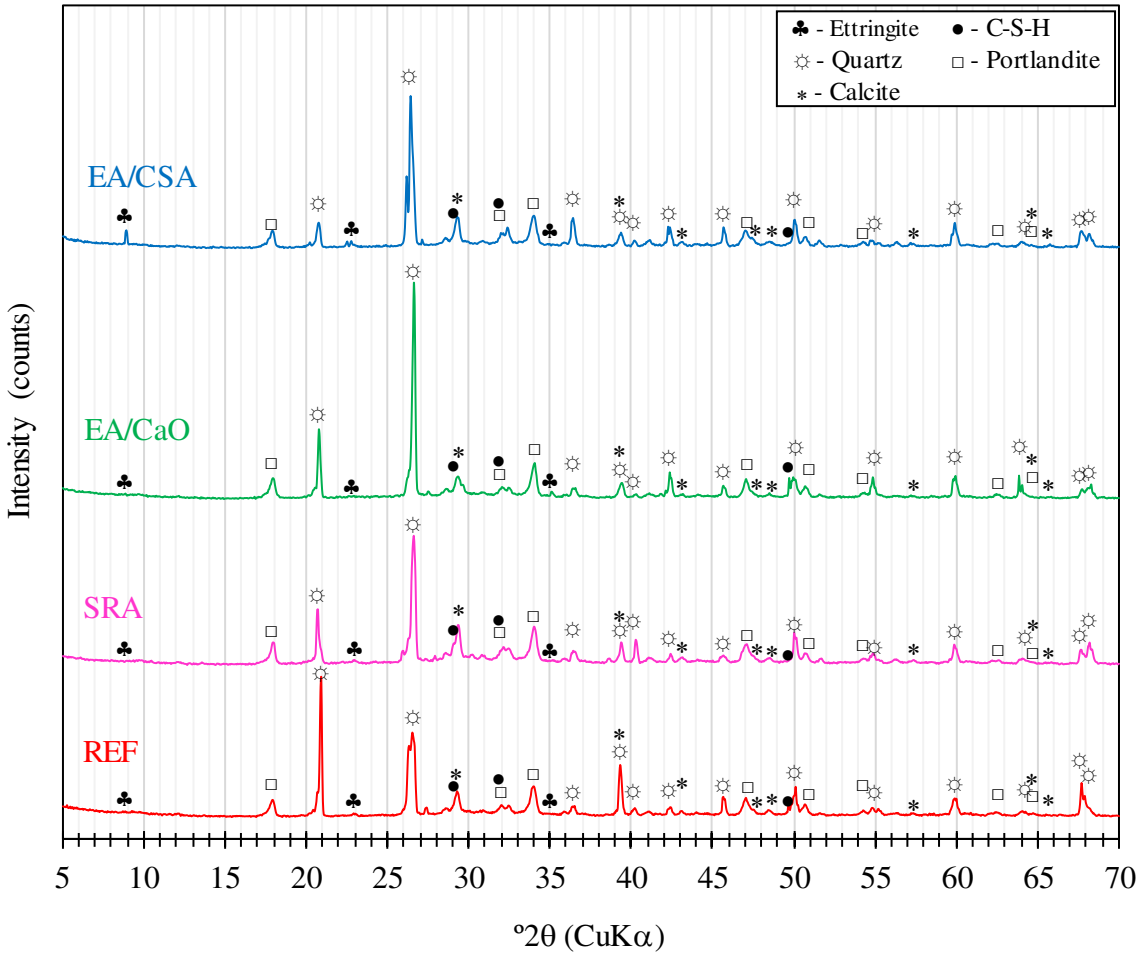

Source: Author (2024).

The XRD patterns of the different types of self-sensing mortars (Figure 8) were very similar. AFt peaks (e.g., $2\theta = 9.1^{\circ}$, 22.9° and 35.0°) were mainly observed in the XRD spectrum of the EA/CSA mortars, which is in good agreement with the observation of significant amounts of long thick needle-like structures of AFt in the FEGSEM images of

Figure 7b. XRD reflections of CH crystals (e.g., 2θ = 18.1º, 34.2º, 47.3º and 50.9º) were also observed in all composites, as CH is one of the main products of cement hydration and constitutes a significant fraction of the volume of solids of the hydrated cement paste (Mehta and Monteiro, 2005). The moderate peaks of calcite (e.g., 2θ = 29.4º, 39.5º, 47.6º and 48.7º) observed in the samples can be associated with the limestone filler typically added to the CP V-ARI Portland cement (Natalli et al., 2021). High-intensity signatures of quartz (e.g., 2θ = 20.9º, 26.7º, 50.1º) were observed in all composites, due to the high crystallinity of quartz particles of the siliceous aggregates (Marinoni and Broekmans, 2013) used in this research. Signs of C-S-H structures (e.g., 2θ = 29.2º, 49.8º) were not very evident in the XRD diffractograms due to the amorphous nature of these phases (Scrivener et al., 2016; Suh et al., 2020).

The experimental results presented in the previous sections were also supported by the spectra obtained from the FTIR analyses, which are presented in Figure 9. These microstructural analyses revealed the vibration bands that typically represent the main cement paste hydrates and siliceous aggregates that form the self-sensing mortars produced in the present research.

Figure 9 - Fourier transform infrared (FTIR) spectroscopy results of reference self-sensing mortars (REF) and mortars containing shrinkage-reducing admixtures (SRA), CaO-based expansive agents (EA/CaO) or calcium sulfoaluminate-based expansive agents (EA/CSA)

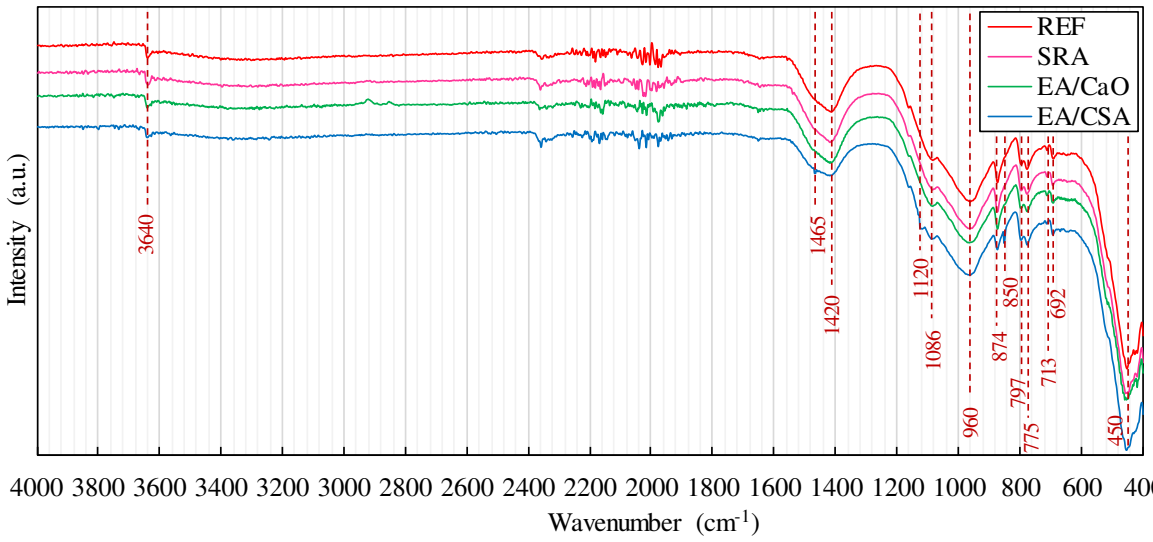

Source: Author (2024).

FTIR bands at about 850 cm^{-1}, 1120 cm^{-1} and 1465 cm^{-1} associated with the presence of relevant amount of AFt (Garcia-Lodeiro et al., 2021; Tantawy, 2017; Vaičiukynienė et al., 2013; Ylmén and Jäglid, 2013) were observed in samples containing the CSA-based EA. The

absorption band at 3640 cm^{-1} is also associated with the stretching of $(OH)^-$ in CH crystals (Horgnies et al., 2013; Tantawy, 2017; Vaičiukynienė et al., 2013; Yaseen et al., 2019; Ylmén and Jäglid, 2013). The absorption bands at about 450 cm^{-1}, 775 cm^{-1}, 797 cm^{-1}, 692 cm^{-1} and 1086 cm^{-1} can be attributed to Si-O modes of quartz particles of the aggregate fraction of the mortars (Malathy et al., 2022; Sekhaneh et al., 2020; Tyagi et al., 2006). The bands at about 1350-1500 cm^{-1}, 874 cm^{-1} and 713 cm^{-1} are attributed to asymmetric (ν_3) and symmetric (ν_2 and ν_4) vibrations of CO_3^{2-}, respectively (Medina et al., 2018; Nasrazadani et al., 2016; Tantawy, 2017; Vaičiukynienė et al., 2013). These signatures are in good agreement with the calcite reflections observed in the XRD analyses. Since all types of mortars exhibited similar compressive strength, all FTIR spectra presented a shoulder at 900-1050 cm^{-1}, which was associated with asymmetric stretching vibration of Si-O groups of the C-S-H structures (Horgnies et al., 2013; Malathy et al., 2022; Medina et al., 2018).

6.4. CONCLUSIONS

Results of the present study indicated that shrinking control admixtures are promising alternatives to ensure dimensional compatibility of patching self-sensing materials embedded into concrete elements. Some conclusions were obtained from the experimental program carried out in this work as follows:

(1) The addition of SRA provided percentage reductions up to 47.4% in the maximum shrinkage of self-sensing mortars. In contrast, the addition of CaO-based EA and CSA-based EA provided self-sensing composites with an expansive behavior characterized by maximum average swelling values of 475 με and 327 με, respectively, in addition to average swelling values after drying procedures equal to 269 με and 48 με, respectively.

(2) PPG-based SRA, CaO-based EA and CSA-based EA caused percentage increases in average DC electrical resistivity of 22.5%, 54.0% and 37.1%, respectively. These admixtures also affected the gauge factor of self-sensing mortars, but did not cause significant changes in their stress sensibility. The highest variations in gauge factor were provided by the incorporation of CaO-based EA and CSA-based EA, which caused gauge factor percentage increases of 71.0% and 65.5%, respectively. In addition, the experimental results indicated that the inclusion of PPG-based SRA,

CaO-based EA and CSA-based EA did not cause significant change in the compressive strength of self-sensing mortars.

(3) The mechanisms behind the increases in electrical resistivity and gauge factor due to the addition of EAs were investigated with microstructural analyses. Plate-like CH crystals and needle-like AFt structures were detected in these mortar types, using FEGSEM, XRD and FTIR analyses. The expansive products provided by the inclusion of EAs caused interruptions in conductive paths inside the cementitious matrix, decreasing direct contact conduction mechanisms and increasing the amount of insulating tunneling gaps between CBN aggregates. These improvements in tunneling conduction mechanisms caused increases in FCRs amplitudes, enhancing the gauge factor of the self-sensing mortars.

Based on the experimental results of this study, it was also possible to infer that the elastic modulus of self-sensing mortars changed with the addition of EAs. To complement the present experimental investigation, future research is recommended to develop a systematic investigation of the effects of SRA, CaO-based EA and CSA-based EA on the modulus of elasticity and Poisson's ratio of self-sensing mortars. A careful evaluation of these properties will be also needed to meet requirements of deformation compatibility between the embedded self-sensing mortar and the concrete structural element that will be monitored. In the present study, a combination of XRF, FEGSEM, XRD and FTIR analyses was used to get important insights into the microstructural mechanisms behind the electro-mechanical response of self-sensing nanomodified mortars. However, mercury intrusion porosimetry (MIP) and energy dispersive spectroscopy (EDS) analyses are also strongly recommended to complement the investigation of the microstructural behavior of the CBN-based mortars and explain the influence of the different types of shrinkage-reducing admixtures and expansive agents on their self-sensing behavior.

REFERENCES

ABNT. (2005). *NBR 15261: Mortars applied on walls and ceilings - Determination of dimensional changes (shrinkage)* (p. 6).

ASTM. (2022). *C150/C150M-22: Standard Specification for Portland Cement*.

Bekzhanova, Z., Memon, S. A., & Kim, J. R. (2021). Self-Sensing Cementitious Composites: Review and Perspective. *Nanomaterials*, *11*(9), 2355. https://doi.org/10.3390/nano11092355

Bilim, C., Karahan, O., Atiş, C. D., & İlkentapar, S. (2013). Influence of admixtures on the properties of alkali-activated slag mortars subjected to different curing conditions. *Materials & Design*, *44*, 540–547. https://doi.org/10.1016/j.matdes.2012.08.049

Carballosa, P., García Calvo, J. L., Revuelta, D., Sánchez, J. J., & Gutiérrez, J. P. (2015). Influence of cement and expansive additive types in the performance of self-stressing and self-compacting concretes for structural elements. *Construction and Building Materials*, *93*, 223–229. https://doi.org/10.1016/j.conbuildmat.2015.05.113

Cassese, P., Rainieri, C., & Occhiuzzi, A. (2021). Applications of Cement-Based Smart Composites to Civil Structural Health Monitoring: A Review. *Applied Sciences*, *11*(18), 8530. https://doi.org/10.3390/app11188530

Chung, D. D. L. (2020). A critical review of piezoresistivity and its application in electrical-resistance-based strain sensing. *Journal of Materials Science*, *55*(32), 15367–15396. https://doi.org/10.1007/s10853-020-05099-z

Collepardi, M., Borsoi, A., Collepardi, S., Ogoumah Olagot, J. J., & Troli, R. (2005). Effects of shrinkage reducing admixture in shrinkage compensating concrete under non-wet curing conditions. *Cement and Concrete Composites*, *27*(6), 704–708. https://doi.org/10.1016/j.cemconcomp.2004.09.020

Dinesh, A., Sudharsan, S. T., & Haribala, S. (2021). Self-sensing cement-based sensor with carbon nanotube: Fabrication and properties – A review. *Materials Today: Proceedings*, *46*, 5801–5807. https://doi.org/10.1016/j.matpr.2021.02.722

Ding, S., Ruan, Y., Yu, X., Han, B., & Ni, Y.-Q. (2019). Self-monitoring of smart concrete column incorporating CNT/NCB composite fillers modified cementitious sensors. *Construction and Building Materials*, *201*, 127–137. https://doi.org/10.1016/j.conbuildmat.2018.12.203

Ding, S., Xiang, Y., Ni, Y.-Q., Thakur, V. K., Wang, X., Han, B., & Ou, J. (2022). In-situ synthesizing carbon nanotubes on cement to develop self-sensing cementitious composites for smart high-speed rail infrastructures. *Nano Today*, *43*, 101438. https://doi.org/10.1016/j.nantod.2022.101438

Dong, W., Li, W., Lu, N., Qu, F., Vessalas, K., & Sheng, D. (2019). Piezoresistive behaviours of cement-based sensor with carbon black subjected to various temperature and water content. *Composites Part B: Engineering*, *178*, 107488. https://doi.org/10.1016/j.compositesb.2019.107488

Dong, W., Li, W., Tao, Z., & Wang, K. (2019). Piezoresistive properties of cement-based sensors: Review and perspective. *Construction and Building Materials*, *203*, 146–163. https://doi.org/10.1016/j.conbuildmat.2019.01.081

Downey, A., D'Alessandro, A., Laflamme, S., & Ubertini, F. (2018). Smart bricks for strain sensing and crack detection in masonry structures. *Smart Materials and Structures*, *27*(1), 015009. https://doi.org/10.1088/1361-665X/aa98c2

Downey, A., D'Alessandro, A., Ubertini, F., Laflamme, S., & Geiger, R. (2017). Biphasic DC measurement approach for enhanced measurement stability and multi-channel sampling of self-sensing multi-functional structural materials doped with carbon-based additives. *Smart Materials and Structures*, *26*(6), 065008. https://doi.org/10.1088/1361-665X/aa6b66

Garcia-Lodeiro, I., Carmona-Quiroga, P. M., Zarzuela, R., Mosquera, M. J., & Blanco-Varela, M. T. (2021). Chemistry of the interaction between an alkoxysilane-based impregnation treatment and cementitious phases. *Cement and Concrete Research*, *142*, 106351. https://doi.org/10.1016/j.cemconres.2020.106351

García-Macías, E., & Ubertini, F. (2019). Earthquake-induced damage detection and localization in masonry structures using smart bricks and Kriging strain reconstruction: A numerical study. *Earthquake Engineering & Structural Dynamics*, *48*(5), 548–569. https://doi.org/10.1002/eqe.3148

Han, B., Ding, S., & Yu, X. (2015). Intrinsic self-sensing concrete and structures: A review. *Measurement*, *59*, 110–128. https://doi.org/10.1016/j.measurement.2014.09.048

Han, B., Yu, X., & Ou, J. (2010). Effect of water content on the piezoresistivity of MWNT/cement composites. *Journal of Materials Science*, *45*(14), 3714–3719. https://doi.org/10.1007/s10853-010-4414-7

Han, B., Yu, X., & Ou, J. (2015). *Self-Sensing Concrete in Smart Structures*. Elsevier. https://doi.org/10.1016/C2013-0-14456-X

Han, B., Zhang, K., Burnham, T., Kwon, E., & Yu, X. (2013). Integration and road tests of a self-sensing CNT concrete pavement system for traffic detection. *Smart Materials and Structures*, *22*(1), 015020. https://doi.org/10.1088/0964-1726/22/1/015020

Han, B., Zhang, L., & Ou, J. (2010). Influence of water content on conductivity and piezoresistivity of cement-based material with both carbon fiber and carbon black. *Journal of Wuhan University of Technology-Mater. Sci. Ed.*, *25*(1), 147–151. https://doi.org/10.1007/s11595-010-1147-z

Han, J., Cai, J., Pan, J., & Sun, Y. (2021). Study on the conductivity of carbon fiber self-sensing high ductility cementitious composite. *Journal of Building Engineering*, *43*, 103125. https://doi.org/10.1016/j.jobe.2021.103125

Horgnies, M., Chen, J. J., & Bouillon, C. (2013). Overview about the use of Fourier Transform Infrared spectroscopy to study cementitious materials. *WIT Transactions on Engineering Sciences*, 251–262. https://doi.org/10.2495/MC130221

ICBA. (2016). *Carbon Black User's Guide - Safety, Health, & Environmental Information* (p. 32). International Carbon Black Association.

Kim, K. K., Yeon, J., Lee, H. J., & Yeon, J. H. (2019). Dimensional Stability of SBR-Modified Cementitious Mixtures for Use in 3D Additive Construction. *Applied Sciences*, *9*(16), 3386. https://doi.org/10.3390/app9163386

La Mendola, L., Oddo, M. C., Papia, M., Pappalardo, F., Pennisi, A., Bertagnoli, G., Di Trapani, F., Monaco, A., Parisi, F., & Barile, S. (2021). Performance of two innovative stress sensors imbedded in mortar joints of new masonry elements. *Construction and Building Materials*, *297*, 123764. https://doi.org/10.1016/j.conbuildmat.2021.123764

Lea, F. M. (1970). *The Chemistry of Cement and Concrete* (Chemical Publishing Company, Ed.; 3rd ed.).

Lee, S.-J., Ahn, D., You, I., Yoo, D.-Y., & Kang, Y.-S. (2020). Wireless cement-based sensor for self-monitoring of railway concrete infrastructures. *Automation in Construction*, *119*, 103323. https://doi.org/10.1016/j.autcon.2020.103323

Lima, G. E. S. de, Nalon, G. H., Santos, R. F., Ribeiro, J. C. L., Carvalho, J. M. F. de, Pedroti, L. G., & Araújo, E. N. D. de. (2021). Microstructural Investigation of the Effects of Carbon Black Nanoparticles on Hydration Mechanisms, Mechanical and Piezoresistive Properties of Cement Mortars. *Materials Research*, *24*(4). https://doi.org/10.1590/1980-5373-mr-2020-0539

Lima, G., Nalon, G., Santos, R. F., Ribeiro, J. C. L., Franco de Carvalho, J. M., Pedroti, L. G., & de Araújo, E. N. D. (2020). Microstructural investigation of the effects of carbon black nanoparticles on hydration mechanisms, mechanical and piezoresistive properties of cement mortars. *Materials Research*, *24*(4). https://doi.org/10.1590/1980-5373-MR-2020-0539

Liu, L., Fang, Z., Huang, Z., & Wu, Y. (2022). Solving shrinkage problem of ultra-high-performance concrete by a combined use of expansive agent, super absorbent polymer,

and shrinkage-reducing agent. *Composites Part B: Engineering*, *230*, 109503. https://doi.org/10.1016/j.compositesb.2021.109503

Liu, Q., Gao, R., Tam, V. W. Y., Li, W., & Xiao, J. (2018). Strain monitoring for a bending concrete beam by using piezoresistive cement-based sensors. *Construction and Building Materials*, *167*, 338–347. https://doi.org/10.1016/j.conbuildmat.2018.02.048

Lothenbach, B., Le Saout, G., Gallucci, E., & Scrivener, K. (2008). Influence of limestone on the hydration of Portland cements. *Cement and Concrete Research*, *38*(6), 848–860. https://doi.org/10.1016/j.cemconres.2008.01.002

Lothenbach, B., & Zajac, M. (2019). Application of thermodynamic modelling to hydrated cements. *Cement and Concrete Research*, *123*, 105779. https://doi.org/10.1016/j.cemconres.2019.105779

Malathy, R., Shanmugam, R., Chung, I.-M., Kim, S.-H., & Prabakaran, M. (2022). Mechanical and Microstructural Properties of Composite Mortars with Lime, Silica Fume and Rice Husk Ash. *Processes*, *10*(7), 1424. https://doi.org/10.3390/pr10071424

Mao, Y., Liu, J., & Shi, C. (2021). Autogenous shrinkage and drying shrinkage of recycled aggregate concrete: A review. *Journal of Cleaner Production*, *295*, 126435. https://doi.org/10.1016/j.jclepro.2021.126435

Marinoni, N., & Broekmans, M. A. T. M. (2013). Microstructure of selected aggregate quartz by XRD, and a critical review of the crystallinity index. *Cement and Concrete Research*, *54*, 215–225. https://doi.org/10.1016/j.cemconres.2013.08.007

McAlorum, J., Perry, M., Vlachakis, C., Biondi, L., & Lavoie, B. (2021). Robotic spray coating of self-sensing metakaolin geopolymer for concrete monitoring. *Automation in Construction*, *121*, 103415. https://doi.org/10.1016/j.autcon.2020.103415

Medeiros, W. A., Soriani, M. de O., & Parsekian, G. A. (2020). Innovation in flat-jack application to evaluate modern high-strength hollow concrete block masonry. *Construction and Building Materials*, *255*, 119341. https://doi.org/10.1016/j.conbuildmat.2020.119341

Medina, C., Sáez del Bosque, I. F., Frías, M., & Sánchez de Rojas, M. I. (2018). Design and characterisation of ternary cements containing rice husk ash and fly ash. *Construction and Building Materials*, *187*, 65–76. https://doi.org/10.1016/j.conbuildmat.2018.07.174

Mehdipour, I., & Khayat, K. H. (2018). Effect of shrinkage reducing admixture on early expansion and strength evolution of calcium sulfoaluminate blended cement. *Cement*

and Concrete Composites, *92*, 82–91. https://doi.org/10.1016/j.cemconcomp.2018.06.002

Mehta, P., & Monteiro, P. (2005). *Concrete: Microstructure, Properties and Materials*. McGraw-Hill Professional.

Meoni, A., D'Alessandro, A., Cavalagli, N., Gioffré, M., & Ubertini, F. (2019). Shaking table tests on a masonry building monitored using smart bricks: Damage detection and localization. *Earthquake Engineering & Structural Dynamics*, *48*(8), 910–928. https://doi.org/10.1002/eqe.3166

Meoni, A., D'Alessandro, A., Kruse, R., De Lorenzis, L., & Ubertini, F. (2021). Strain field reconstruction and damage identification in masonry walls under in-plane loading using dense sensor networks of smart bricks: Experiments and simulations. *Engineering Structures*, *239*, 112199. https://doi.org/10.1016/j.engstruct.2021.112199

Mishra, M. (2021). Machine learning techniques for structural health monitoring of heritage buildings: A state-of-the-art review and case studies. *Journal of Cultural Heritage*, *47*, 227–245. https://doi.org/10.1016/j.culher.2020.09.005

Monteiro, A., Loredo, A., Costa, P., Oeser, M., & Cachim, P. (2017). A pressure-sensitive carbon black cement composite for traffic monitoring. *Construction and Building Materials*, *154*, 1079–1086. https://doi.org/10.1016/j.conbuildmat.2017.08.053

Nalon, G. H., Ribeiro, J. C., Pedroti, L. G., Duarte de Araújo, E., Franco de Carvalho, J., Soares de Lima, G., & de Moura Guimarães, L. (2021). Residual piezoresistive properties of mortars containing carbon nanomaterials exposed to high temperatures. *Cement and Concrete Composites*, *121*, 104104. https://doi.org/10.1016/j.cemconcomp.2021.104104

Nalon, G. H., Ribeiro, J., Pedroti, L., de Araújo, E., Franco de Carvalho, J. M., Lima, G., & Oliveira, D. (2021). Self-Sensing Mortars: Effect of Moisture and Nanocarbon Black Content. *ACI Materials Journal*, *118*(3), 131–141. https://doi.org/10.14359/51732636

Nalon, G., Ribeiro, J., Araújo, E., Pedroti, L., Carvalho, J., Santos, R., & Aparecido-Ferreira, A. (2020). Effects of different kinds of carbon black nanoparticles on the piezoresistive and mechanical properties of cement-based composites. *Journal of Building Engineering*, *32*, 101724. https://doi.org/10.1016/j.jobe.2020.101724

Nasrazadani, S., Eghtesad, R., Sudoi, E., Vupputuri, S., Ramsey, J. D., & Ley, M. T. (2016). Application of Fourier transform infrared spectroscopy to study concrete degradation

induced by biogenic sulfuric acid. *Materials and Structures*, *49*(5), 2025–2034. https://doi.org/10.1617/s11527-015-0631-5

Natalli, J. F. (2017). *Desempenho do Concreto Leve em Seções Mistas (Performance of Lightweight Concrete in Composite Sections)*. Universidade Federal de Ouro Preto.

Natalli, J. F., Andrade, H. D., Carvalho, J. M. F., Defáveri, K., Castro Mendes, J., Sarmanho, A. M. C., & Peixoto, R. A. F. (2020). Performance of Lightweight Concrete with Expansive and Air-Entraining Admixtures in CFST Columns. *Journal of Materials in Civil Engineering*, *32*(6). https://doi.org/10.1061/(ASCE)MT.1943-5533.0003143

Natalli, J. F., Thomaz, E. C. S., Mendes, J. C., & Peixoto, R. A. F. (2021). A review on the evolution of Portland cement and chemical admixtures in Brazil. *Revista IBRACON de Estruturas e Materiais*, *14*(6). https://doi.org/10.1590/s1983-41952021000600003

Palacios, M., & Puertas, F. (2007). Effect of shrinkage-reducing admixtures on the properties of alkali-activated slag mortars and pastes. *Cement and Concrete Research*, *37*(5), 691–702. https://doi.org/10.1016/j.cemconres.2006.11.021

Rao, R. K., Sindu, B. S., & Sasmal, S. (2023). Real-time monitoring of structures under extreme loading using smart composite-based embeddable sensors. *Journal of Intelligent Material Systems and Structures*, *34*(9), 1073–1096. https://doi.org/10.1177/1045389X221128586

Scrivener, K., Snellings, R., & Lothenbach, B. (2016). *A Practical Guide to Microstructural Analysis of Cementitious Materials*. CRC.

Scuro, C., Lamonaca, F., Porzio, S., Milani, G., & Olivito, R. S. (2021). Internet of Things (IoT) for masonry structural health monitoring (SHM): Overview and examples of innovative systems. *Construction and Building Materials*, *290*, 123092. https://doi.org/10.1016/j.conbuildmat.2021.123092

Sekhaneh, W., Shiyyab, A., Arinat, M., & Gharaibeh, N. (2020). Use of FTIR and thermogravimetric analysis of ancient mortar from the church of the cross in Gerasa (Jordan) for conservation purposes. *Mediterranean Archaeology and Archaeometry*, *20*(3), 159–174. https://doi.org/10.5281/zenodo.4016073

Souza, M. T., Onghero, L., Repette, W. L., Raupp Pereira, F., & de Oliveira, A. P. N. (2020). Sustainable cement with Al-anodizing waste: Evaluating reactivity and feasibility as a shrinkage-compensating admixture. *Journal of Building Engineering*, *30*, 101233. https://doi.org/10.1016/j.jobe.2020.101233

Suh, H., Jee, H., Kim, J., Kitagaki, R., Ohki, S., Woo, S., Jeong, K., & Bae, S. (2020). Influences of rehydration conditions on the mechanical and atomic structural recovery characteristics of Portland cement paste exposed to elevated temperatures. *Construction and Building Materials*, *235*, 117453. https://doi.org/10.1016/j.conbuildmat.2019.117453

Sun, M., Liew, R. J. Y., Zhang, M.-H., & Li, W. (2014). Development of cement-based strain sensor for health monitoring of ultra high strength concrete. *Construction and Building Materials*, *65*, 630–637. https://doi.org/10.1016/j.conbuildmat.2014.04.105

Tantawy, M. A. (2017). Effect of High Temperatures on the Microstructure of Cement Paste. *Journal of Materials Science and Chemical Engineering*, *05*(11), 33–48. https://doi.org/10.4236/msce.2017.511004

Tran, N. P., Gunasekara, C., Law, D. W., Houshyar, S., Setunge, S., & Cwirzen, A. (2021a). A critical review on drying shrinkage mitigation strategies in cement-based materials. *Journal of Building Engineering*, *38*, 102210. https://doi.org/10.1016/j.jobe.2021.102210

Tran, N. P., Gunasekara, C., Law, D. W., Houshyar, S., Setunge, S., & Cwirzen, A. (2021b). A critical review on drying shrinkage mitigation strategies in cement-based materials. *Journal of Building Engineering*, *38*, 102210. https://doi.org/10.1016/j.jobe.2021.102210

Treesuwan, S., & Maleesee, K. (2017). Effects of Shrinkage Reducing Agent and Expansive Additive on Mortar Properties. *Advances in Materials Science and Engineering*, 1–11. https://doi.org/10.1155/2017/8917957

Tyagi, B., Chudasama, C. D., & Jasra, R. V. (2006). Determination of structural modification in acid activated montmorillonite clay by FT-IR spectroscopy. *Spectrochimica Acta Part A: Molecular and Biomolecular Spectroscopy*, *64*(2), 273–278. https://doi.org/10.1016/j.saa.2005.07.018

Ubertini, F., & D'Alessandro, A. (2018). Concrete with self-sensing properties. In *Eco-Efficient Repair and Rehabilitation of Concrete Infrastructures* (pp. 501–530). Elsevier. https://doi.org/10.1016/B978-0-08-102181-1.00018-6

Ubertini, F., D'Alessandro, A., Downey, A., García-Macías, E., Laflamme, S., & Castro-Triguero, R. (2017). Recent Advances on SHM of Reinforced Concrete and Masonry Structures Enabled by Self-Sensing Structural Materials. *The 4th International*

Electronic Conference on Sensors and Applications, 119. https://doi.org/10.3390/ecsa-4-04889

Vaičiukynienė, D., Skipkiūnas, G., Daukšys, M., & Sasnauskas, V. (2013). Cement hydration with zeolite-based additive. *Chemija*, *24*(4), 271–278.

Wang, H., Shen, J., Liu, J., Lu, S., & He, G. (2019). Influence of carbon nanofiber content and sodium chloride solution on the stability of resistance and the following self-sensing performance of carbon nanofiber cement paste. *Case Studies in Construction Materials*, *11*, e00247. https://doi.org/10.1016/j.cscm.2019.e00247

Wang, H., Shi, F., Shen, J., Zhang, A., Zhang, L., Huang, H., Liu, J., Jin, K., Feng, L., & Tang, Z. (2021). Research on the self-sensing and mechanical properties of aligned stainless steel fiber-reinforced reactive powder concrete. *Cement and Concrete Composites*, *119*, 104001. https://doi.org/10.1016/j.cemconcomp.2021.104001

Wen, S., & Chung, D. D. L. (2007). Double percolation in the electrical conduction in carbon fiber reinforced cement-based materials. *Carbon*, *45*(2), 263–267. https://doi.org/10.1016/j.carbon.2006.09.031

Xiao, H., & Li, H. (2006). *A study on the application of CB-filled cement-based composite as a strain sensor for concrete structures* (M. Tomizuka, C.-B. Yun, & V. Giurgiutiu, Eds.; p. 61742T). https://doi.org/10.1117/12.660787

Xiao, H., Li, H., & Ou, J. (2011). Strain sensing properties of cement-based sensors embedded at various stress zones in a bending concrete beam. *Sensors and Actuators A: Physical*, *167*(2), 581–587. https://doi.org/10.1016/j.sna.2011.03.012

Xu, J., Butler, L. J., & Elshafie, M. Z. (2020). Experimental and numerical investigation of the performance of self-sensing concrete sleepers. *Structural Health Monitoring*, *19*(1), 66–85. https://doi.org/10.1177/1475921719834506

Yaseen, S. A., Yiseen, G. A., & Li, Z. (2019). Elucidation of Calcite Structure of Calcium Carbonate Formation Based on Hydrated Cement Mixed with Graphene Oxide and Reduced Graphene Oxide. *ACS Omega*, *4*(6), 10160–10170. https://doi.org/10.1021/acsomega.9b00042

Ye, H., Fu, C., & Lei, A. (2020). Mitigating shrinkage of alkali-activated slag by polypropylene glycol with different molecular weights. *Construction and Building Materials*, *245*, 118478. https://doi.org/10.1016/j.conbuildmat.2020.118478

Yeon, J. (2019). Short-Term Deformability of Three-Dimensional Printable EVA-Modified Cementitious Mortars. *Applied Sciences*, *9*(19), 4184. https://doi.org/10.3390/app9194184

Ylmén, R., & Jäglid, U. (2013). Carbonation of Portland Cement Studied by Diffuse Reflection Fourier Transform Infrared Spectroscopy. *International Journal of Concrete Structures and Materials*, *7*(2), 119–125. https://doi.org/10.1007/s40069-013-0039-y

Yu, Z., Zhao, Y., Ba, H., & Liu, M. (2021). Relationship between buck electrical resistivity and drying shrinkage in cement paste containing expansive agent and mineral admixtures. *Journal of Building Engineering*, *39*, 102261. https://doi.org/10.1016/j.jobe.2021.102261

Zhan, P., & He, Z. (2019). Application of shrinkage reducing admixture in concrete: A review. *Construction and Building Materials*, *201*, 676–690. https://doi.org/10.1016/j.conbuildmat.2018.12.209

Zhang, L., Ding, S., Han, B., Yu, X., & Ni, Y.-Q. (2019). Effect of water content on the piezoresistive property of smart cement-based materials with carbon nanotube/nanocarbon black composite filler. *Composites Part A: Applied Science and Manufacturing*, *119*, 8–20. https://doi.org/10.1016/j.compositesa.2019.01.010

Zhang, W., Lin, H., Xue, M., Wang, S., Ran, J., Su, F., & Zhu, J. (2022). Influence of shrinkage reducing admixtures on the performance of cementitious composites: A review. *Construction and Building Materials*, *325*, 126579. https://doi.org/10.1016/j.conbuildmat.2022.126579

APPENDIX 6A: RESULTS OF STATISTICAL ANALYSES

6A.1. GRUBB'S TEST FOR OUTLIER DETECTION

The Grubb's test was used to detect outliers in the experimental dataset of this study.

6A.1.1. Hypothesis and significance level

- Null hypothesis (H_0): all values belong to the same population.
- Alternative hypothesis (H_a): the smallest or the largest value is an outlier.
- Significance level (α): 5%.

6A.1.2. Results of the statistical tests

Results of Grubbs' test are presented in Tables A1, A2, A3 and A4.

Table A1 - Grubb's test statistical summary for the DC electrical resistivity dataset.

Series	Mean (Ω.cm)	Standard deviation (Ω.cm)	Minimum (Ω.cm)	Maximum (Ω.cm)	Grubb's test statistic	P-value
REF	959.5	11.8	946.0	967.9	1.14	0.274
SRA	1175.3	79.8	1117.4	1266.4	1.14	0.297
EA/CaO	1477.0	219.0	1274.0	1709.0	1.06	0.770
EA/CSA	1314.8	158.0	1163.9	1479.1	1.04	0.861

Source: Author (2024).

Table A2 - Grubb's test statistical summary for the gauge factor dataset.

Series	Mean	Standard deviation	Minimum	Maximum	Grubb's test statistic	P-value
REF	255.3	11.9	247	269	1.15	0.241
SRA	308.7	64.7	238	365	1.09	0.631
EA/CaO	436.7	60.2	370	487	1.11	0.547
EA/CSA	422.7	55.9	359	464	1.14	0.326

Source: Author (2024).

Table A3 - Grubb's test statistical summary for the stress sensibility dataset.

Series	Mean (MPa^{-1})	Standard deviation (MPa^{-1})	Minimum (MPa^{-1})	Maximum (MPa^{-1})	Grubb's test statistic	P-value
REF	0.0317	0.0023	0.3030	0.0344	1.15	0.083
SRA	0.0290	0.0078	0.0223	0.0376	1.10	0.595
EA/CaO	0.0357	0.0096	0.0287	0.0467	1.14	0.298
EA/CSA	0.0344	0.0026	0.0317	0.0369	1.02	0.915

Source: Author (2024).

Table A4 - Grubb's test statistical summary for the compressive strength dataset.

Series	Mean (MPa)	Standard deviation (MPa)	Minimum (MPa)	Maximum (MPa)	Grubb's test statistic	P-value
REF	29.55	3.59	26.11	33.28	1.04	0.867
SRA	31.10	1.19	30.26	31.94	*	*
EA/CaO	27.31	6.03	23.35	34.25	1.15	0.154
EA/CSA	30.34	2.96	27.08	32.88	1.10	0.602

Note: *The Grubb's test statistic and the P-value could not be calculated for the SRA series due to technical issues during the compression test of one of its specimens (Grubb's test cannot be applied to a series with only two replicates).

Source: Author (2024).

6A.1.3. Conclusions of the statistical tests

A P-value higher than 0.050 was obtained in all Grubb's tests, which indicates that outliers were not detected at the 5% significance level.

6A.2. SHAPIRO-WILK TEST OF NORMALITY

Shapiro-Wilk tests were used to investigate the normality of residuals observed in DC electrical resistivity, gauge factor, stress sensibility and compressive strength results, as normality of residuals is an assumption of the analysis of variance (ANOVA).

6A.2.1. Hypothesis and significance level

- Null hypothesis (H_0): residuals are normally distributed.
- Alternative hypothesis (H_a): residuals are not normally distributed.
- Significance level (α): 5%.

6A.2.2. Results of the statistical tests

Results obtained from the Shapiro-Wilk's tests are listed in Table A5.

Table A5 - Shapiro-Wilk's test statistical summary for all response variables.

Response variable	Shapiro-Wilk's test statistic	P-value
DC electrical resistivity	0.946	0.580
Gauge factor	0.884	0.098
Stress sensibility	0.928	0.297
Compressive strength	0.928	0.393

Source: Author (2024).

6A.2.3. Conclusions of the statistical tests

The results indicated that the residuals were normally distributed because P-values higher than 0.050 were obtained in all Shapiro-Wilk's tests.

6A.3. BARTLETT TEST OF HOMOSCEDASTICITY

Bartlett tests were carried out to investigate homogeneity of variances in results of electrical resistivity, gauge factor, stress sensibility and compressive strength, which is another assumption of the ANOVA.

6A.3.1. Hypothesis and significance level

- Null hypothesis (H_0): all population variances are equal.
- Alternative hypothesis (H_a): at least two population variances are different.
- Significance level (α): 5%.

6A.3.2. Results of the statistical tests

Table A6 shows the results obtained from the Bartlett tests.

Table A6 - Bartlett's test statistical summary for all response variables.

Response variable	Bartlett's K-squared	P-value
DC electrical resistivity	8.261	0.041
Gauge factor	3.584	0.310
Stress sensibility	4.428	0.219
Compressive strength	2.191	0.534

Source: Author (2024).

6A.3.3. Conclusions of the statistical tests

Only the electrical resistivity dataset provided a P-value lower than 0.050 in the Bartlett tests. Then, all response variables exhibited homoscedasticity, except for the DC electrical resistivity.

6A.4. ANALYSIS OF VARIANCE (ANOVA)

Since normality of residuals and homoscedasticity of variances were observed in some response variables, ANOVAs were carried out, in order to evaluate statistical differences between the average values of gauge factor, stress sensitivity and compressive strength.

6A.4.1. Hypothesis and significance level

- Null hypothesis (H_0): all means are equal.
- Alternative hypothesis (H_a): at least one mean is different.
- Significance level (α): 5%.

6A.4.2. Results of the statistical tests

The ANOVA results are summarized in Tables A7, A8 and A9.

Table A7 - ANOVA statistical summary for the gauge factor dataset.

Source	Degrees of freedom	Sum of squares	Mean Square	F test statistics	P-value
Treatments	3	69977	23326	8.420	7.4×10^{-3}
Residuals	8	22163	2770	-	-
Total	11	92140	-	-	-

Source: Author (2024).

Table A8 - ANOVA statistical summary for the stress sensibility dataset

Source	Degrees of freedom	Sum of squares	Mean Square	F test statistics	P-value
Treatments	3	0.000079	0.000026	0.635	0.613
Residuals	8	0.000333	0.000042	-	-
Total	11	0.000412	-	-	-

Source: Author (2024).

Table A9 - ANOVA statistical summary for the compressive strength dataset.

Source	Degrees of freedom	Sum of squares	Mean Square	F test statistics	P-value
Treatments	3	21.561	7.187	0.428	0.739
Residuals	7	117.579	16.797	-	-
Total	10	139.141	-	-	-

Source: Author (2024).

6A.4.3. Conclusions of the statistical tests

A P-values lower than 0.05 was obtained in the ANOVA of gauge factor average values, so that at least one gauge factor average is different from the others. A Tukey's test at the 5% significance level was used for multiple comparisons between gauge factor averages (results of these post-hoc tests were presented in the main text of the present study). In contrast, P-values higher than 0.05 were verified in the ANOVA of stress sensibility and compressive strength averages. Therefore, the REF, SRA, EA/CaO and EA/CSA series presented average values of stress sensibility and compressive strength that are statistically equal at the 5% significance level.

Figure B1 - FCR *vs* strain curves of reference mortars (REF) and mortars with shrinkage-reducing admixtures (SRA), CaO-based expansive agents (EA/CaO) or calcium sulfoaluminate-based expansive agents (EA/CSA).

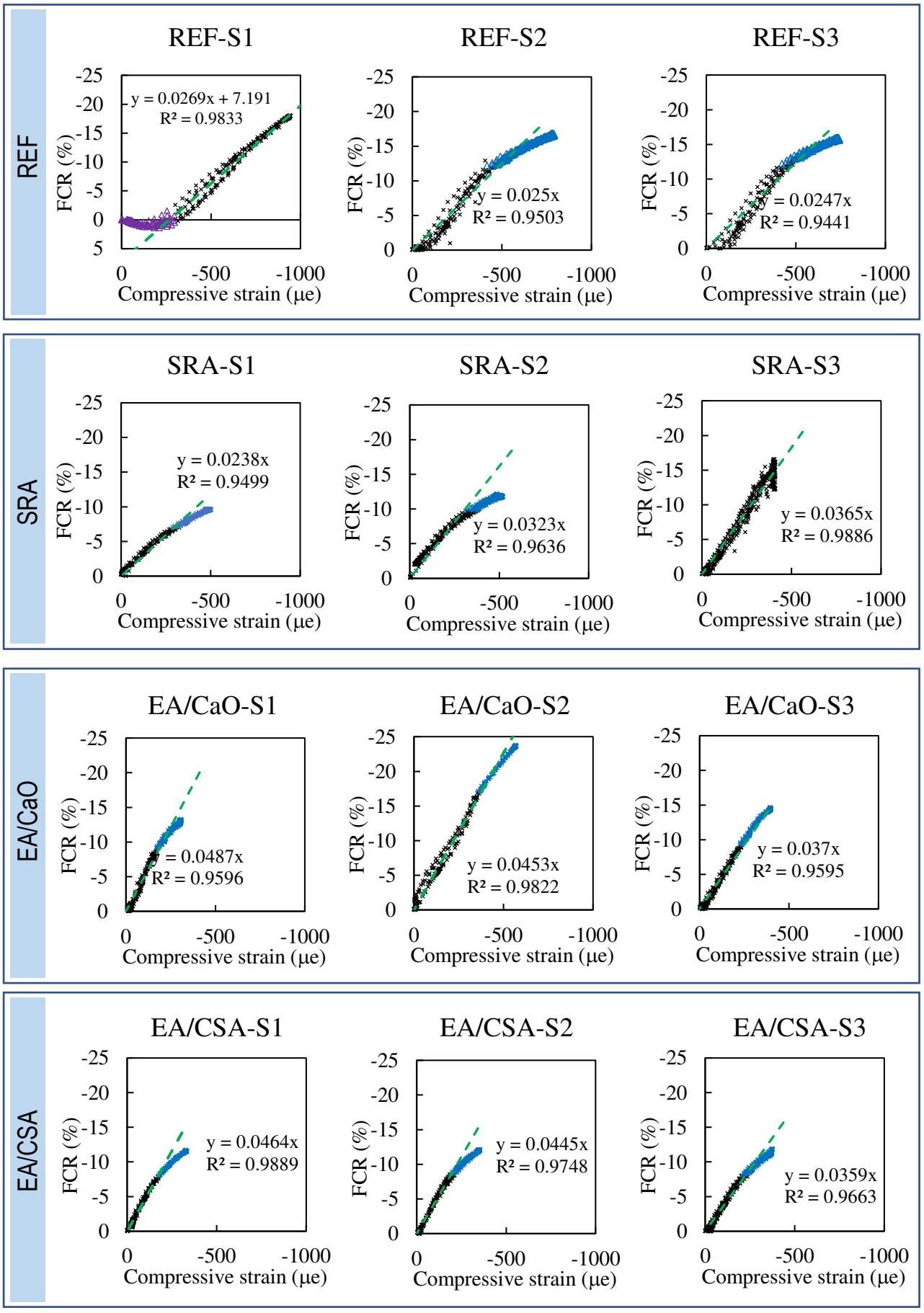

Source: Author (2024).

Figure B2 - FCR *vs* stress curves of reference mortars (REF) and mortars with shrinkage-reducing admixtures (SRA), CaO-based expansive agents (EA/CaO) or calcium sulfoaluminate-based expansive agents (EA/CSA).

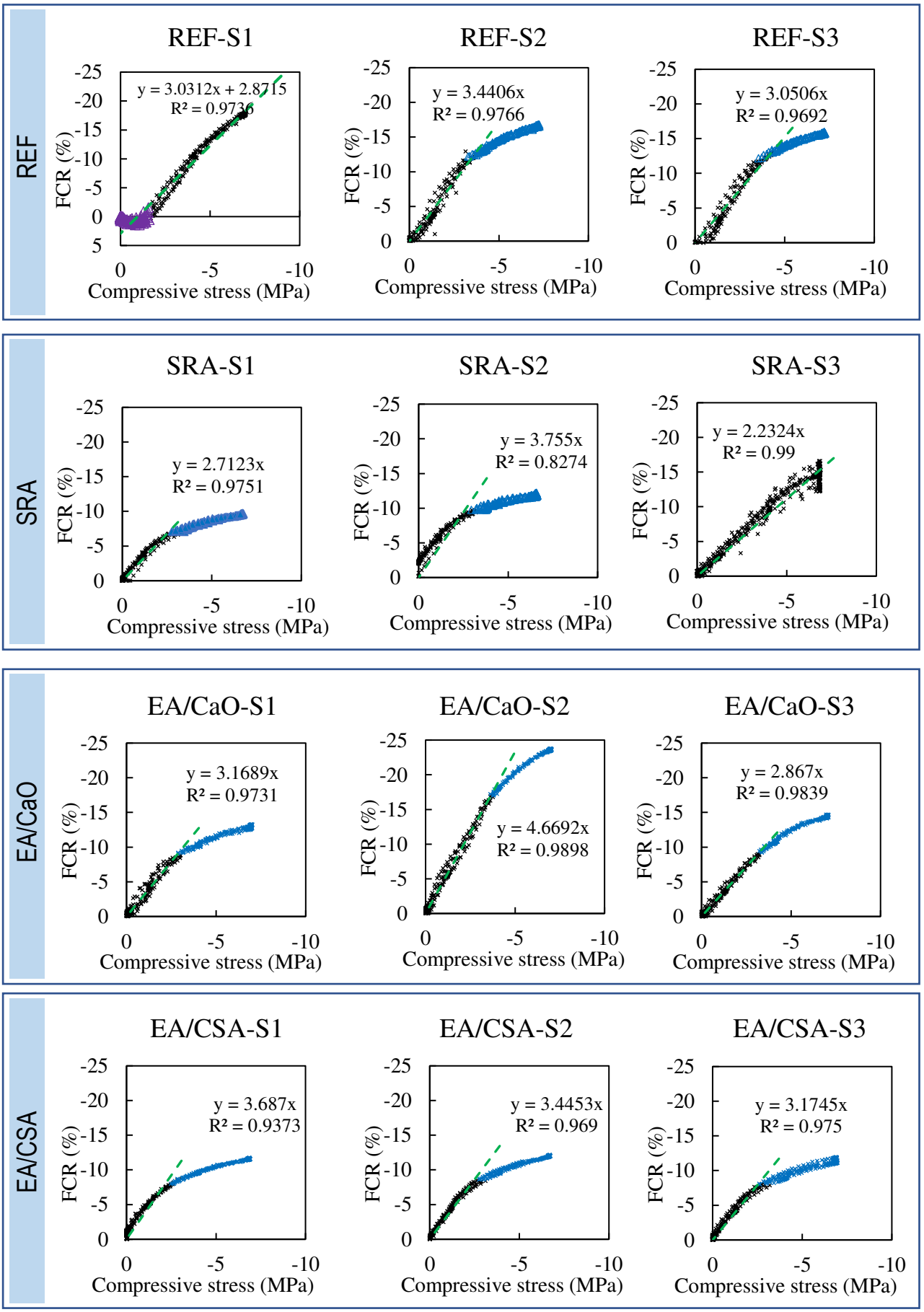

Source: Author (2024).

PART III:

VALIDATION STUDY ON SELF-SENSING MASONRY ELEMENTS AT ROOM TEMPERATURE

7 SELF-SENSING CONCRETE MASONRY STRUCTURES WITH INTRINSIC ABILITIES OF STRAIN MONITORING AND DAMAGE DETECTION

This chapter has been published as the following paper: Nalon, G. H.; Ribeiro, J. C. L.; Silva, R. M.; Pedroti, L. G.; Araújo, E. N. D. Self-sensing concrete masonry structures with intrinsic abilities of strain monitoring and damage detection. ***Structures*** *59 (2024) 105760. https://doi.org/10.1016/j.istruc.2023.105760*

Abstract: *Self-sensing cementitious materials are emerging technologies for Structural Health Monitoring (SHM) of civil structures. Their application for SHM of concrete masonry elements was not investigated in previous studies. The effects of triaxial strain/stress states of masonry joints and units on their self-sensing response are still unknown. Therefore, this work aimed to investigate mechanical and self-sensing properties of masonry elements produced with self-sensing mortar joints, solid concrete bricks and/or hollow concrete blocks fabricated with carbon black nanoparticles. The intrinsic abilities of strain monitoring and damage detection were evaluated in piezoresistive tests of masonry prisms, based on variations in the type of unit, mortar bedding approach, bonding arrangement, relative strength of mortar and units, joint thickness and location of self-sensing regions. These variations did not affect significantly the gauge factor of cementitious sensors embedded into the prism units. In contrast, the gauge factor of self-sensing horizontal or vertical joints was statistically affected by most of these variations. Stages of balance and abrupt increases in fractional changes in electrical resistivity (FCRs) during the plastic regime of the prisms provided an anticipated warming associated with the propagation of vertical and diagonal cracks associated with tensile splitting and crushing failure of units. The strong non-linearity on the electrical output of self-sensing joints evidenced the mortar pore collapse. In conclusion, the self-sensing units and mortar joints were found to be promising alternatives for strain monitoring and damage detection in smart concrete masonry structures.*

Keywords: *Masonry structures, Structural Health Monitoring, smart structures, nanomodified structural elements, piezoresistivity.*

7.1. INTRODUCTION

Different types of Structural Health Monitoring (SHM) systems have been developed for an automated assessment of deformation, loading conditions and deterioration of civil structures, after critical events or during their whole service life (Bekzhanova et al., 2021; D'Alessandro et al., 2022; Dong et al., 2020). These analyses provide improvements in the safety level, durability and preservation of the reliability of civil structures, which are some important tasks of designers, contractors, maintenance teams and operators of the construction industry. In the case of masonry structures, the application of SHM techniques requires a deep understanding of their mechanical behavior, structural morphology and interaction mechanisms between different components (Luchin et al., 2020; Nalon et al., 2022; Sarhosis et al., 2018).

SHM systems can collect different engineering parameters (e.g., strain, stress, vibration, temperature, etc.) that provide valuable information on the structural response of diverse heritage and modern masonry structures. They can detect environmental agents that can accelerate their deterioration and predict damage propagation associated with unforeseen events (Medeiros et al., 2020; Mishra, 2021; Scuro et al., 2021). The application of SHM technologies can expand the concept of "smart structures" in urban areas, enable changes in the typical use of masonry buildings, detect vulnerability factors and improve the structural safety on a large territorial scale (La Mendola et al., 2021; Medeiros et al., 2020).

Smart construction materials capable of autonomously monitoring their states of strain (or stress) and detecting damage conditions have gained increasing popularity in recent years (D'Alessandro et al., 2022; Tian et al., 2019). In this context, the present study is centered on the development and evaluation of different types of masonry components endowed with self-sensing properties, namely self-sensing mortar joints, solid concrete bricks (SCBs) and hollow concrete blocks (HCBs). When the structural elements have self-sensing properties, it is not necessary to incorporate traditional sensors in the structures. Compared to the use of traditional sensing technologies [e.g., acoustic emission sensors (Vanniamparambil et al., 2014), ceramic and capacitive sensors (La Mendola et al., 2021), accelerometers and linear variable differential transformers (Kita et al., 2019), digital image correlation equipment (Vanniamparambil et al., 2014), infrared cameras (Khan et al., 2015), etc.], self-sensing masonry components are advantageous due to their low cost, high mechanical performance,

good durability, high sensitivity and large sensing volume (Chung, 2021, 2022; Ubertini et al., 2017). In addition, the self-sensing components can be embedded into various key locations of masonry structures thus resolving scalability issues (Birgin et al., 2021; Downey et al., 2018a).

Different sensing principles have been used for real-time assessment of structural behavior. For example, some specific types of smart materials proposed for SHM applications present a strain/stress-sensing ability associated with the piezoresistive response provided by the inclusion of conductive admixtures inside their matrix. The piezoresistivity phenomenon is associated with reversible fractional changes in electrical resistivity (FCRs) due to deformation in the elastic regime. The approximation of adjacent conductive admixtures and the subsequent increase in tunneling conduction contribute to alterations in electrical conductivity, enabling a sensitive response to stress or strain under static and dynamic statuses (Liu et al., 2022; Nalon et al., 2021; Zhang et al., 2022). Moreover, crack propagation can be detected based on irreversible changes in electrical resistivity. As cracks form and propagate within the matrix of a self-sensing composite, they disrupt the continuity of the material and decrease the electronic conduction mechanisms (Bekzhanova et al., 2021; Dinesh et al., 2021; Dong et al., 2019; Jiao et al., 2020; Nalon et al., 2022). Carbon black nanoparticles (CBN) are common types of conductive admixtures used for production of self-sensing materials. Carbon black is the generic name of a family of small particles with diameter lower than 300 nm that fuse to form aggregates, whereas clusters of aggregates may connect to form agglomerates (Aparecido-Ferreira et al., 2011; Dong et al., 2019; Han et al., 2010; Monteiro et al., 2017).

Self-sensing construction materials have the potential to be utilized in various structural components, including but not limited to girders and columns (Ding et al., 2019; Liu et al., 2018; Rao et al., 2023; Xiao et al., 2011b, 2016), concrete pavements (Birgin et al., 2021; Ding et al., 2022; Han et al., 2013); railway elements (Lee et al., 2020; Xu et al., 2020); structural masonry (Downey et al., 2018a; Meoni et al., 2018, 2019, 2022); etc. Various methods have been suggested to enable the practical incorporation of these materials into SHM architectures. These approaches predominantly depend on circuit diagram configurations incorporating reference resistors and self-sensing composites. The electrical outputs of these composites are acquired through direct current (DC) (Han et al., 2007; Han et al., 2015), alternating current (AC) (Kang et al., 2018; Machan and Steffan, 2015) or biphasic DC (Downey et al., 2017; Meoni et al., 2021) measurements.

In the last years, a novel class of self-sensing construction materials was found to be a cost-effective solution for SHM of heritage masonry: smart clay bricks. These bricks are produced by mixing fresh clay with a conductive admixture (e.g., carbon nanotubes, titania or stainless-steel micro fibers (Downey et al., 2018b; Meoni, D'Alessandro and Ubertini, 2021; Ubertini et al., 2017). The homogeneous mixture is molded into prismatic oiled molds. After that, the bricks undergo drying at 90 °C for six hours and subsequent firing at 900 °C for six hours. Two external electrodes are placed on opposite horizontal faces of the fired bricks, covered with an insulating layer to prevent current flow propagation when the bricks are embedded into the masonry walls (Meoni, D'Alessandro and Ubertini, 2021; Meoni et al., 2020, 2022). Experimental results reported by D'Alessandro et al. (2018) and Meoni et al. (2021; 2019) indicated that the electrical outputs of these clay bricks allow the identification of local permanent changes in deformation and loading path of clay masonry, in addition to the risk of progressive damage. Meoni, D'Alessandro and Ubertini (2020) also developed a theoretical model to describe the strain-sensing response of smart clay bricks embedded into masonry elements subjected to eccentric axial compression load. García-Macías and Ubertini (2019) reported numerical seismic analyses of a clay masonry structure equipped with smart clay bricks and mapped the strain field throughout the structure based on their electrical outputs.

Although investigations of self-sensing clay bricks have been already reported in the literature, there is no previous evaluation of the application of self-sensing cementitious materials for SHM of masonry constructed with concrete units. Then, the present work investigates the pioneering application of SCBs or HCBs with self-sensing properties. Moreover, masonry elements containing self-sensing mortar joints were not produced and investigated in previous literature. Therefore, the piezoresistive response of nanomodified mortar joints was firstly reported in the present study. This paper also presents new findings related to the effects of conventional triaxial states of strain/stress of mortar joints and masonry units on their self-sensing response.

To fill these knowledge gaps, this paper reports a pioneering investigation of mechanical and self-sensing properties of concrete masonry elements produced with carbon-based nanoparticles. Original contributions were provided in this work, in terms of the mechanical behavior and intrinsic abilities of different masonry components to monitor strain and detect damage, based on analyses of distinct parameters (compressive strength, elastic modulus, gauge factor, FCRs amplitude, and failure modes), considering variations in

masonry elements that were never explored in previous papers that deal with evaluations of self-sensing properties (type of masonry unit, mortar bedding approach, bonding arrangement, relative strength of mortar and masonry units, joint thickness and location of self-sensing regions). The self-sensing materials developed in this work were found to be promising alternatives for strain monitoring and damage detection in smart concrete masonry structures.

This chapter is organized in four sections. Section 7.1 introduces the concept of self-sensing construction materials and assesses their applications in the field of structural masonry. Section 7.2 details the materials and methods employed for producing and testing self-sensing masonry prisms. In Section 7.3, the experimental results are presented, along with discussions related to statistical analyses of variance (ANOVA). Section 7.4 concludes with final remarks and offers suggestions for future research.

7.2. MATERIALS AND METHODS

7.2.1. Materials

Plain and nanomodified mortars were produced with CP V-ARI portland cement (density = 3.08 g/cm³) equivalent to the ASTM Type III portland cement (ASTM, 2022; Mehta & Monteiro, 2005), hydrated lime (density = 2.51 g/cm³), and siliceous sand (specific mass = 2.64 g/cm³, fineness modulus = 2.52 and maximum diameter = 2.38 mm). The self-sensing mortars also required the use of CBN to construct the conductive network inside the cementitious matrices (average diameter = 20 nm and surface area = 120 m²/g), polycarboxylate ether superplasticizer (PCE) to ensure appropriate dispersion of nanomaterials (density = 1.12 g/cm³), and CaO-based expansive agent (EA) for shrinkage control (density = 2.50 g/cm³). Masonry prisms were produced with SCBs or HCBs. These concrete units were characterized according to procedures of ABNT NBR 12118 (2013), when available. Samples of 20 mm × 20 mm × 60 mm were cut from the units to determine the static modulus of elasticity and Poisson's ratio of the material.

7.2.2. Experimental program

A completely randomized design (CRD) experiment was elaborated to investigate the effects of the following independent variables on mechanical and self-sensing properties of

masonry prisms: (i) type of concrete unit - self-sensing SCBs or self-sensing HCBs; (ii) mortar bedding approach (full bedding or face-shell bedding); (iii) bonding arrangement (stack bond or running bond); (iv) ratio between the compressive strength of mortar (f_m) and the net area compressive strength of concrete units ($f_{b,net}$); (v) mortar joint thickness (10, 15 or 20 mm); and (vi) self-sensing regions of the masonry prisms (B1, B2, J1 or J2 regions). Therefore, 12 different series of prisms (Table 1 and Figure 1) with three replicates were produced.

Table 1 - Characteristics of masonry prisms investigated in the present experimental program.

Series	Type of concrete unit	Mortar bedding approach	Bonding arrange-ment	Ratio between mortar and units' strength [a]	Mortar joint thick-ness	Use of self-sensing concrete units [b]		Use of self-sensing mortar joint [b]	
						B1 region	B2 region	J1 region	J2 region
#1	Solid concrete bricks	Full bedding	Stack bond	$0.4 < \frac{f_m}{f_{b,net}} < 0.9$ (PM-0.75 mortar)	10 mm	✗	✗	✗	✗
#2						✓	✓	✓	✗
#3	Hollow concrete blocks					✗	✗	✗	✗
#4						✗	✗	✓	✗
#5						✓	✓	✗	✗
#6						✓	✓	✓	✗
#7				$\frac{f_m}{f_{b,net}} < 0.4$ (PM-1.50 mortar)		✓	✓	✓	✗
#8				$\frac{f_m}{f_{b,net}} > 0.9$ (PM-0.25 mortar)		✓	✓	✓	✗
#9		Face-shell bedding		$0.4 < \frac{f_m}{f_{b,net}} < 0.9$ (PM-0.75 mortar)		✓	✓	✓	✗
#10		Full bedding	Running bond			✓	✗	✓	✓
#11			Stack bond		15 mm	✓	✓	✓	✗
#12					20 mm	✓	✓	✓	✗

Notes: [a] According to Parsekian, Hamid and Drysdale (2012), the compressive strength of mortar (f_m) is recommended to be between 0.7 and 1.5 of the gross area compressive strength of units ($f_{b,gross}$), i.e., 0.4 and 0.9 of the net area compressive strength of units ($f_{b,net}$).
[b] The symbol "✗" indicates that a self-sensing cementitious material was not used in the masonry prisms and the symbol "✓" indicates that it used to produce the masonry prisms.

Source: Author (2024).

Figure 1 - Position of self-sensing regions B1, B2, J1 and J2 of all series of masonry prisms (dimensions in millimeters).

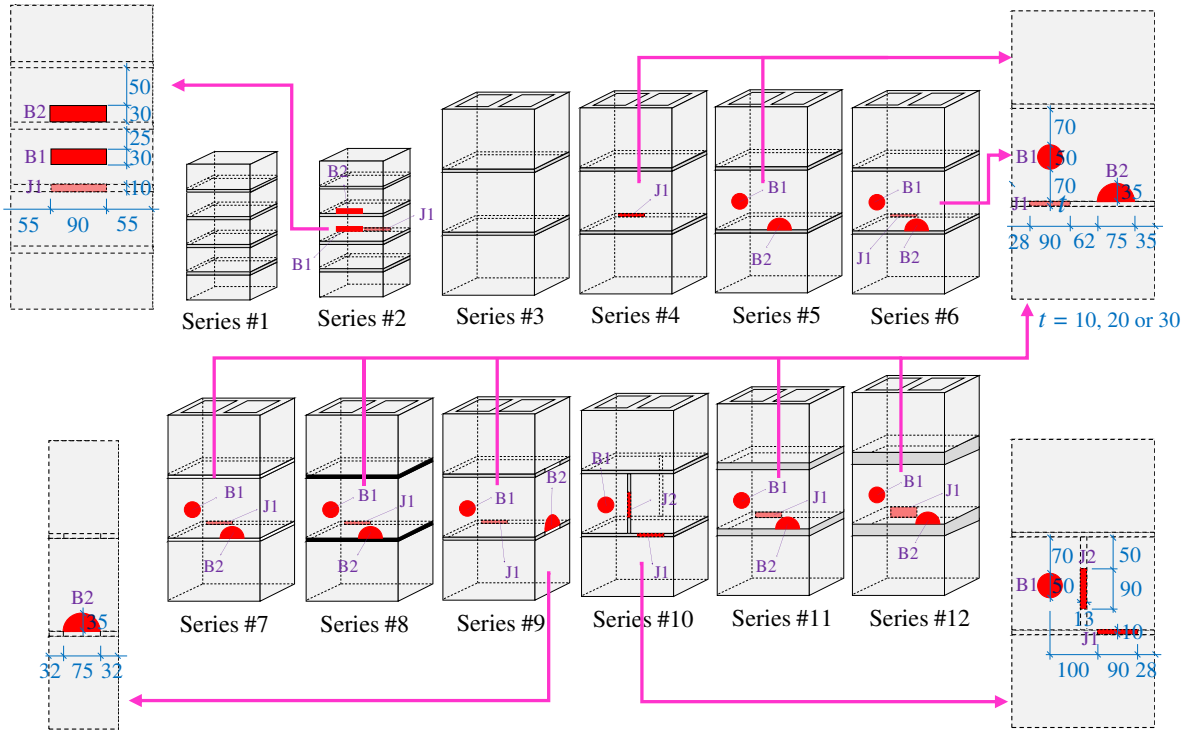

Source: Author (2024).

The embedding approach (Han et al., 2015) was used to install the self-sensing cementitious materials in the B1, B2, J1 and J2 regions of the masonry components. The B1 region was located at the middle height of the central unit of the masonry prisms. The B2 region was located at the inferior region of the central unit of the masonry prisms (close to the mortar joint). In all prisms made with HCBs, B1 and B2 regions were always located at the same face shell of the central block, except for prisms of series #9, in which the B2 region was located at the lateral web of the central block. The J1 region was located at the horizontal joint, close to the inferior central unit of the prims. The J2 region was located at the vertical joint at the middle height of the prisms. Detailed information and images of these different self-sensing regions are presented in the next subsections.

The dependent variables of the CRD experiment were the (i) compressive strength of the masonry prisms, (ii) modulus of elasticity of the masonry prisms, and (iii) gauge factor (GF) of each self-sensing region of the masonry prisms. This work also evaluated the prisms' failure modes and FCRs associated with them.

7.2.3. Production of plain and self-sensing mortars

Table 2 shows the mix proportions of plain mortars (PMs) used to produce the joints of the masonry prisms and the mix proportions of self-sensing mortars (SMs) embedded into the masonry components. They were designated as "x-y", in which "x" is the type of mortar (PM or SM) and "y" is the lime/cement ratio (in volume). PM-0.25, PM-0.75 and PM-1.50 compositions were used to produce the plain mortar joints. SM-0.00 was the composition used to produce the self-sensing units. Finally, SM-0.25, SM-0.75 and SM-1.50 compositions were used to produce the cement-lime mortar joints with self-sensing properties.

Table 2 - Mix proportions used to produce plain mortars (PMs) and self-sensing mortars (SMs).

Mortar	Lime/cement ratio (by volume)	Consumption (kg/m³)							Flow index (cm)
		Cement	Sand	Lime	Water	CBN	PCE	EA	
PM-0.25	0.25	429.58	1394.37	88.38	295.77	0.00	0.00	0.00	7.0
PM-0.75	0.75	312.11	1405.39	190.88	290.20	0.00	0.00	0.00	7.6
PM-1.50	1.50	217.87	1414.34	268.94	285.69	0.00	0.00	0.00	8.0
SM-0.00	0.00	664.28	997.06	0.00	345.30	59.78	23.91	16.61	5.5
SM-0.25	0.25	525.11	1047.16	107.05	331.85	56.90	22.76	15.80	5.8
SM-0.75	0.75	369.99	1031.36	226.29	344.03	53.67	21.47	14.91	5.8
SM-1.50	1.50	258.56	1040.67	319.17	340.64	52.00	20.80	14.44	6.0

Source: Author (2024).

The water/binder ratios used in the mortar compositions were adjusted to obtain a flow index of (7.0 ± 1.5) cm, using the Kantro-cone mold. This flow range is similar to the range of (23 ± 1) cm obtained with the conventional truncated cone mold used in the procedures of ABNT NBR 13276 (2005a). Therefore, the workability of all mortars was appropriate for use in masonry construction (Parsekian et al., 2012; Parsekian and Soares, 2010).

All PMs were produced in a mechanical mixer, using an aggregate/binder ratio of 3.00 (by volume). A lime/cement ratio of 1.50 was required to get specimens with $f_m/f_{b,net} < 0.40$, i.e., prisms with mortars significantly weaker than units (Table 1). A lime/cement ratio of 0.75 was used to obtain prisms with $0.40 < f_m/f_{b,net} < 0.90$, i.e., specimens with $f_m/f_{b,net}$ ratio within the range recommended for masonry structures (Parsekian et al., 2012). A lime/cement ratio of 1.50 provided prisms with $f_m/f_{b,net} > 0.90$, i.e., prisms produced with mortars significantly stronger than units (Table 1). The PMs were used to produce prism joints, in addition to three mortar prisms of 40 mm × 40 mm × 160 mm for characterization according to ABNT NBR 13279 (2005b), which prescribes a 28-days curing period at 23 ± 2 ºC and

relative humidity (RH) of 60 ± 5%. Three mortar prisms of 20 mm × 20 mm × 60 mm were also cast between pieces of units and cured for 28 days at 23 ± 2 ºC and RH of 60 ± 5%.

The SMs were designed to exhibit deformation properties (modulus of elasticity and Poisson's ratio) that are statistically equal to those of PMs and concrete units, as discussed in the next section. Since sand acts as an electrical insulator (Wen and Chung, 2007), low aggregate/binder ratios of 1.75 and 1.86 (by volume) were used to produce high-electrical conductivity SMs that were embedded into units and joints, respectively. A concentration of CBN of 9.00% (by weight of binders) was used to produce all SMs because previous works indicated that this concentration is above the percolation threshold and provides composites with appropriate self-sensing response before and after exposure to high temperatures (Nalon et al., 2023; 2021). The dosage of PCE was 3.60% (by weight of binders) because preliminary studies indicated that a PCE/CBN ratio of 0.40 (by weight) provided nanosuspensions with optimized dispersion. The content of CaO-based EA was 2.50% (by weight of binders) because preliminary studies indicated that this dosage provided appropriate shrinkage control (Nalon et al., 2023).

Firstly, a mixture of CBN, PCE and water was prepared with ultrasonication (sonication energy equal to 450 J/mL). Next, this nanosuspension was mixed for ~10 minutes with cement, lime, CaO-based EA and sand. The SMs were used to produce self-sensing joints and units, in addition to six mortar prisms of 20 mm × 20 mm × 60 mm cured for 28 days at 23 ± 2 ºC and RH of 60 ± 5%. Two Kanthal electrodes (iron-chromium-aluminum alloy) of 12 mm × 30 mm × 1.5 mm were embedded into the central region of three of these mortar prisms, using a distance between electrodes of approximately 1.0 cm.

7.2.4. Production of self-sensing masonry prisms

The steps of production of self-sensing masonry components and masonry prisms are presented in Figure 2. In prisms produced with self-sensing units, a hole with diameter of 5.0 cm was drilled (Figure 2a) at the middle height (B1 region) of the concrete blocks. A half hole with diameter of 7.5 cm was drilled at the inferior side (B2 region) of the concrete blocks. After that, the internal surface of the holes (Figure 2b) was covered with two thin layers of epoxy-based structural adhesive. Before the adhesive was cured, sand was sprayed on the epoxy layer and the expansive SM-0.00 mortar was poured into the hole in two layers of equal height. This epoxy-based interface was applied to provide appropriate waterproofing protection, bonding and electrical insulation to the self-sensing regions, following

recommendations of previous research (Nalon et al., 2023; Xiao et al., 2011b). After compacting each layer of self-sensing mortar with 30 strokes of a steel tamping rod (Figure 2c), electrodes were embedded into the central region of the hole (Figure 2d). The dimensions of the electrodes were 12 mm × 40 mm × 1.5 mm and the spacing between them was approximately 1.0 cm. After that, the self-sensing mortar was covered with a plastic film for three days and the concrete unit was kept at 23 ± 2 ºC and RH of 60 ± 5%.

Figure 2 - Production of self-sensing masonry components and masonry prisms.

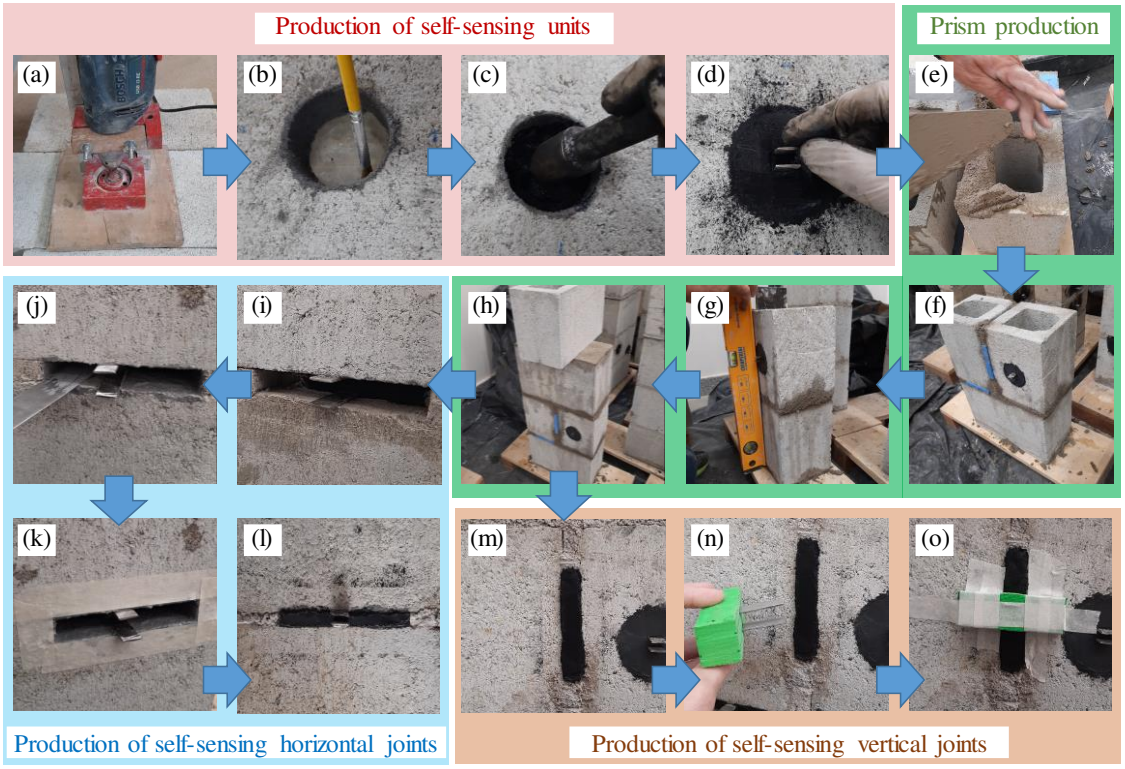

Source: Author (2024).

Using the parameters presented in Table 1, masonry prisms were constructed by an experienced mason (Figure 2e-h) when the age of the self-sensing mortar embedded into the concrete units was seven days Figure 2f shows that blue spacers were left in the J1 and J2 regions of the prisms. The concrete blocks' surface was moistened before placing the PM joints. One of the surfaces of the bottom and top units of the prisms was previously capped with a cement mortar layer with thickness of about 3.0 mm. Prisms of HCBs were produced with three courses, whereas prisms of SCBs were constructed with five courses, so that they had similar height/thickness ratios (between 4.3 and 4.5) and length/thickness ratios (between 2.0 and 2.1).

The self-sensing mortar joints were produced when the age of the prisms was seven days. The production steps of horizontal and vertical self-sensing joints were slightly different. In the case of horizontal joints, the blue spacer was removed from the J1 region and the electrodes were bonded at the appropriate location (Figure 2i), using the epoxy-based structural adhesive. After that, the internal surfaces of the J1 region were covered with two thin layers of the epoxy-based structural adhesive (Figure 2j). Again, sand was sprayed on the epoxy layer before it was cured. Then the empty space between concrete units was filled with the expansive self-sensing mortar (Figure 2k and l).

In the case of vertical joints, the blue spacer was removed from the J2 region, internal surfaces were covered with two thin layers of the epoxy-based structural adhesive were, sand was sprayed on the epoxy surface and the self-sensing mortar was embedded into the empty space between the units (Figure 2m). After that, electrodes were fixed in the green support presented in Figure 2n. Finally, the electrodes were carefully embedded into the vertical joint and the green support was bonded to the blocks' surface with adhesive tape (Figure 2o).

After casting the self-sensing joints, they were covered with a plastic film for three days and the prisms were kept immobile for 28 days at 23 ± 2 ºC, RH of 60 ± 5% and protected from rain, sun and wind. After this curing period, the specimens were dried at 60 ± 10 ºC for 72 h. This drying process was used in previous works dealing with self-sensing mortars (Han et al., 2021; Wang et al., 2019, 2021) to decrease the amount of water in the pores of the self-sensing mortars and reduce the effects of polarization on their electrical output.

7.2.5. Determination of mechanical and piezoresistive properties

The piezoresistive response of the self-sensing regions of each masonry prism was evaluated within the elastic regime of the material, using the experimental setup presented in Figure 3a. Firstly, three loading/unloading cycles up to 30% of the expected ultimate load of the specimens were carried out. Next, another loading cycle with three steps (~10%, 20% and 30% of the expected ultimate load of the prism) was applied. The loading rate was approximately 0.50 MPa/s, based on the net area of the prisms.

FCRs of the self-sensing masonry components were measured during the piezoresistive tests. At first, each nanomodified mortar was connected in series with a commercial resistor with electrical resistance of 1000 Ω. Then, they were subjected to a ±5 V square wave voltage signal generated by a microcontroller board (Arduino Mega 2560 R3). The frequency and

the duty cycle of this periodic signal were 6.0 Hz and 50%, respectively. Using a NI DAQ-9178 chassis equipped with NI-9219 modules, the voltage drops across the SM and the commercial resistor were measured during the loading/unloading cycles at specific time instants (80% of the positive part of the square wave signal), as suggested by previous researchers (Downey et al., 2017; Lima et al., 2021; Meoni et al., 2021). Given that the frequency of the square wave was 6.0 Hz, the sampling frequency used in the electrical measurements was also equal to 6.0 Hz.

Figure 3 - Experimental setup used in piezoresistive tests (a) and modulus of elasticity tests (b).

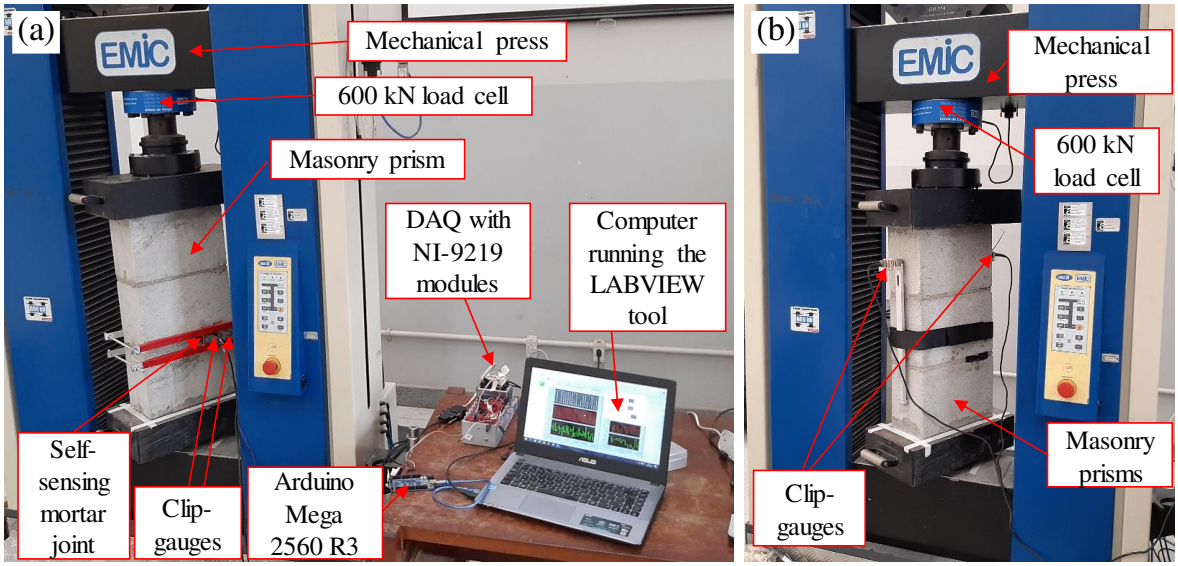

Source: Author (2024).

To measure the compressive strain during the piezoresistive tests, different apparatuses were used for symmetric arrangement of EMIC clip-gauges (model EE08 of the DL series) with respect to the central axis of the electrodes embedded into the B1, B2, J1 and J2 self-sensing regions, as shown in Figure 4a. The GF of each self-sensing region was determined using the FCR and compressive strain measurements. Values of GF were calculated using Equation (1), based on the linear stretch of FCR versus longitudinal strain (ε) curves.

$$GF = \frac{FCR}{\varepsilon} = \frac{\frac{\Delta R}{R_0}}{\varepsilon} \approx \frac{\frac{\Delta \rho}{\rho_0}}{\varepsilon} \qquad (1)$$

where R_0 and ρ_0 are the initial electrical resistance and resistivity of the self-sensing region, respectively, ε is the longitudinal strain measured by the EMIC clip-gauges, and ΔR and $\Delta \rho$ are the changes of electrical resistance and resistivity due to the uniaxial compression loading, respectively.

Figure 4 - Apparatuses used to measure compressive strain in piezoresistive tests of B1, B2, J1 and J2 regions of masonry prisms (a) and prismatic specimens of self-sensing mortars (SMs) (b).

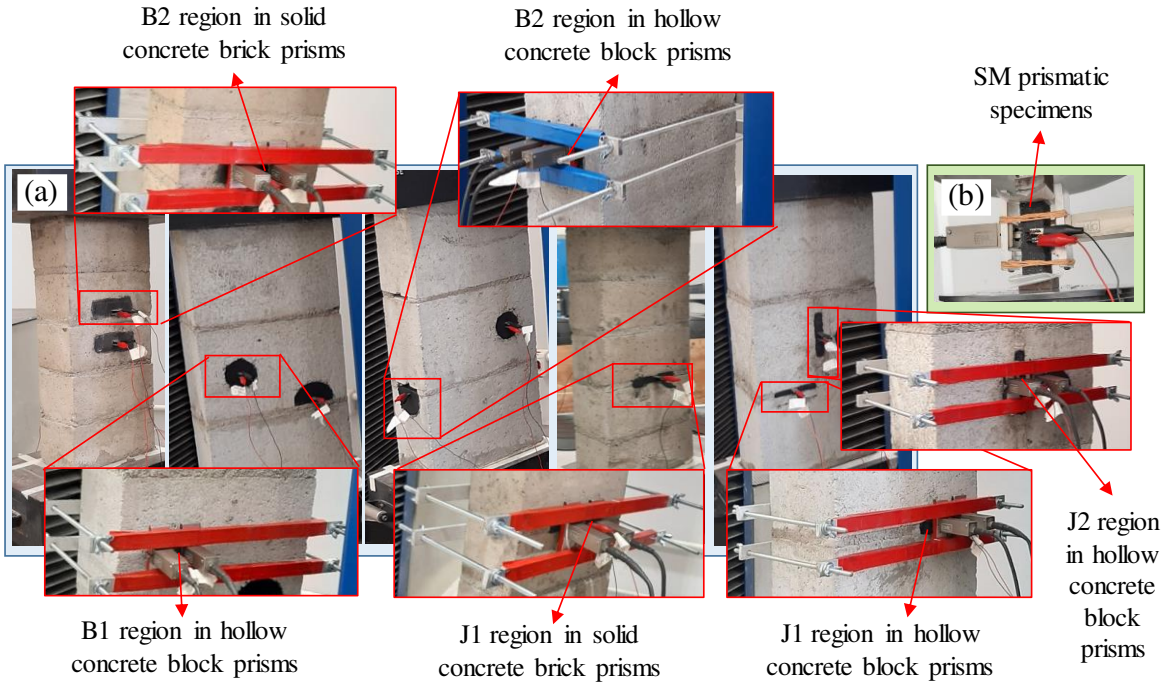

Source: Author (2024).

The same EMIC clip-gauges were used in piezoresistive tests of prismatic specimens (20 mm × 20 mm × 60 mm) of SMs containing embedded electrodes (Figure 4b), in order to calculate the GF of cement-based sensors under uniaxial compression.

According to tunnel effect theory-based piezoresistivity models applied in previous research (Liu et al., 2015; Xiao et al., 2010, 2015, 2016), the GF of cementitious composites produced with CBN is strictly related to the effects of multi-axial strain conditions. Consequently, the states of stress and strain of the self-sensing masonry components must be taken into account to understand the values of GF obtained in the present work. The results of piezoresistive tests were interpreted using formulations published in previous research (Berto, 2005; Francis et al., 1971; Hendry, 1997) for the lateral strain (in the x and z directions) induced by a vertical compressive stress σ_y (in the y direction) in a stack-bond prism produced with solid units and full mortar bedding. These formulations derived from classical continuum conditions, as indicated in Equations (2) and (3). In addition, the lateral stresses (in the x and z directions) can be obtained using Equations (4) and (5).

$$\varepsilon_{x,u} = \frac{1}{E_u}\left[\sigma_{x,u} - \nu_u\left(\sigma_y + \sigma_{z,u}\right)\right] = \varepsilon_{x,m} = \frac{1}{E_m}\left[\sigma_{x,m} - \nu_m\left(\sigma_y + \sigma_{z,m}\right)\right] \quad (2)$$

$$\varepsilon_{z,u} = \frac{1}{E_u}\left[\sigma_{z,u} - \nu_u\left(\sigma_y + \sigma_{x,u}\right)\right] = \varepsilon_{z,m} = \frac{1}{E_m}\left[\sigma_{z,m} - \nu_m\left(\sigma_y + \sigma_{x,m}\right)\right] \quad (3)$$

$$\sigma_{x,u} = \sigma_{z,u} = \frac{\sigma_y\left(-\beta\nu_m + \nu_u\right)}{1 + \alpha\beta - \nu_u - \alpha\beta\nu_m} \quad (4)$$

$$\sigma_{x,m} = \sigma_{z,m} = \frac{\alpha\sigma_y\left(\beta\nu_m - \nu_u\right)}{1 + \alpha\beta - \nu_u - \alpha\beta\nu_m} \quad (5)$$

where E_u and E_m are the modulus of elasticity of the unit and mortar, respectively; ν_u and ν_m are the Poisson's ratio of the unit and mortar, respectively; $\varepsilon_{x,u}$ and $\varepsilon_{x,m}$ are the lateral strains of the units and mortar in the x direction; $\varepsilon_{z,u}$ and $\varepsilon_{z,m}$ are the lateral strains of the units and mortar in the z direction; $\sigma_{x,u}$ and $\sigma_{x,m}$ are the lateral stresses of the units and mortar in the x direction; $\sigma_{z,u}$ and $\sigma_{z,m}$ are the lateral stresses of the units and mortar in the z direction; α is the ratio between the height of the units and the mortar joint thickness; and $\beta = E_u/E_m$.

After the piezoresistivity measurements, the masonry prisms were subjected to experimental tests for determination of static modulus of elasticity, using the experimental setup presented in Figure 3b. Two initial loading/unloading cycles up to one-half of the expected ultimate load of the prisms were applied, according to recommendations of ABNT NBR 16868-3 (2020). After that, the compressive load was increased again and the elastic modulus was calculated as the slope of the straight line between the points of compressive stress of 5% and 30% of the masonry prism's strength. These tests were carried out using the same loading rate used in the piezoresistive tests. The EMIC clip-gauges were also attached to the two smaller sides of the prism (Figure 3b) to measure the deformation between the middle height of the top unit and the middle height of the bottom unit of the prism.

Finally, the compressive stress was increased up to the rupture of the masonry prisms. FCRs were measured in all self-sensing regions of the prisms during the loading process. To enable a visual inspection of some failure mechanisms, the loading rate was 0.05 MPa/s and brief interruptions in the increased loading were eventually needed.

Prismatic specimens (20 mm × 20 mm × 60 mm) of SMs and PMs without electrodes were also subjected to experimental tests for determination of modulus of elasticity and Poisson's ratio. Following the recommendations of ABNT NBR 8522 (2017), three initial loading/unloading cycles up to 30% of the expected ultimate load of the prisms were applied, using the loading rate of 0.50 MPa/s. Then, the compressive load was increased and the static elastic modulus was determined as the slope of the straight line between the points of

compressive stress of 0.50 MPa and 30% of the specimens' strength. Deformations were measured using the EMIC clip-gauges attached to the lateral surfaces of the mortar prisms.

7.2.6. Statistical analyses

All results obtained in the characterization of masonry components (modulus of elasticity, Poisson's ratio, compressive strength and GF) and masonry prisms (modulus of elasticity, compressive strength and GF of various self-sensing regions) were subjected to Grubb's tests (outlier identification), Shapiro-Wilk tests (evaluation of normality of residuals) and Bartlett tests (evaluation of homoscedasticity). After that, an analysis of variance (ANOVA) was carried out when its assumptions were met. Tukey's tests were also used to compare average values. The significance level (α), null hypotheses (H_0), alternative hypotheses (H_a) and results of all statistical analyses are presented in APPENDIX 7A.

7.3. RESULTS AND DISCUSSIONS

7.3.1. Characterization of masonry components

Results obtained in the standard characterization of units (SCBs and HCBs) and conventional mortars (PMs) used to construct the masonry prisms are presented in Table 3 and Table 4, respectively. Results of compressive strength of mortars and units indicated that all series of prisms presented $f_m/f_{b,net}$ within the desired range defined in Table 1.

Table 3 - Standard characterization results of concrete units (SD = standard deviation).

Property [(a)]	Solid concrete bricks (SCBs)		Hollow concrete blocks (HCBs)	
	Mean	SD	Mean	SD
Length (mm)	200.4	0.3	289.3	0.3
Width (mm)	100.4	1.9	138.8	0.4
Height (mm)	80.4	0.6	189.9	0.8
Thickness of face shells (mm)	-	-	26.3	0.3
Thickness of cross webs (mm)	-	-	26.4	0.2
Net area/gross area ratio (%)	-	-	57.8	0.4
Net area compressive strength (MPa)	27.0	1.2	17.4	1.1
Water absorption (%)	8.37	0.12	5.96	0.38
Density (g/cm³)	2.14	0.07	2.16	0.03

[(a)] When available, prescriptions of ABNT NBR 12118 (2013) - similar to ASTM C140/C140M (2020) - were used in this work.

Source: Author (2024).

Table 4 - Standard characterization results of plain masonry mortars (SD = standard deviation).

Property [a]	PM-0.25		PM-0.75		PM-1.50	
	Mean	SD	Mean	SD	Mean	SD
Compressive strength (MPa)	18.54	1.13	9.70	0.48	6.52	0.39

[a] Prescriptions of ABNT NBR 13279 (2005b) - similar to EN 1015 (2019) - were used in this work.

Source: Author (2024).

As indicated in the previous section, representative specimens of masonry components (SCBs, HCBs, PM and SM) with the same shape and size (prisms of 20 mm × 20 mm × 60 mm) were tested to enable coherent comparisons. Average results of modulus of elasticity, Poisson's ratio, compressive strength and GF of these specimens are summarized in Figure 5. APPENDIX 7A indicated that all ANOVA assumptions were satisfied and statistical differences were observed in all parameters, except for the Poisson's ratio. Results of Tukey's tests were represented at the top of the bars of Figure 5 (bars sharing the same uppercase letter are statistically equal at the 5% significance level). Error bars representing the standard deviation of each series were also graphically represented.

Figure 5 - Modulus of elasticity (a), Poisson's ratio (b), compressive strength (c), and gauge factor (d) of prismatic samples (20 mm × 20 mm × 60 mm) of units, plain mortars and self-sensing cementitious materials. According to the Tukey's test (α = 5%), bars sharing the same uppercase letter are statistically equal.

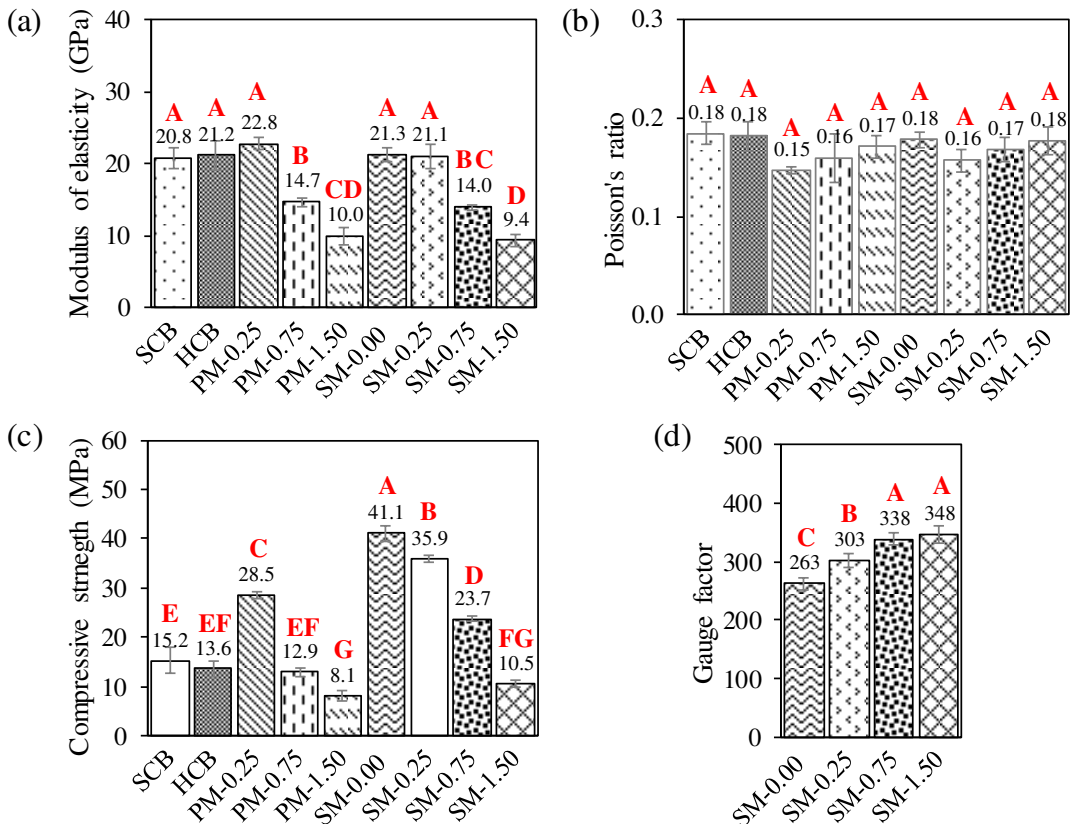

Source: Author (2024).

Figure 5a and Figure 5b indicated that SCB, HCB and SM-0.00 samples exhibited the same modulus of elasticity and Poisson's ratio. Moreover, the deformation properties of PM-0.25, PM-0.75 and PM-1.50 were statistically equal to those of SM-0.25, SM-0.75 and SM-1.50, respectively. Therefore, the self-sensing materials designed in this work presented appropriate deformation compatibility with the substrate (masonry unit or mortar joint).

Deformation compatibility is of great importance because the mismatch in the modulus of elasticity and Poisson's ratio of cementitious materials can cause stress concentration and debonding issues (Cabrera and Al-Hasan, 1997; Kiani et al., 2018; Morgan, 1996; Wang et al., 2021). Moreover, if the self-sensing material and the monitored concrete element have different stiffness, FCRs will not be only associated with the movements of the monitored structure because surrounding constraints effects will also affect the electrical output of the cement-based sensors (Han et al., 2022; Sun et al., 2014; Xiao et al., 2011b, 2011a).

Compressive strength results illustrated in Figure 5c indicated that the self-sensing materials (SMs) were always stronger than the corresponding concrete units (SCB or HCB) or mortar joints (PMs). These results are in good agreement with previous studies (Downey et al., 2018b; Xiao et al., 2011a) that reported an important aspect required for practical application of self-sensing cementitious composites in SHM systems: the smart composites should not fail before the monitored structural element.

The GFs of SMs presented in Figure 5d were calculated based on linear regression models that properly fit the experimental data represented in FCR *vs* compressive strain curves of Figure 6 (S1, S2 and S3 represent the three replicates of each different type of SM). The coefficients of determination (R^2) of the models were higher than 0.95, which indicates a piezoresistive response with good linearity and repeatability. Figure 6 shows that increases in compressive strain caused negative FCRs, which can be attributed to improvements in tunneling and/or contacting conduction between CBN aggregates due to reductions in the distance between these conductive nanoadmixtures (Dong et al., 2019; Lima et al., 2021; Nalon et al., 2021; Zhang et al., 2019). According to Figure 5d, increases in the lime/cement ratio caused slight increase in the GF of the nanomodified mortars. These results suggest that increases in porosity and $Ca(OH)_2$ contents associated with the incorporation of lime caused small interruptions in the conductive network of the composites, improving tunneling conduction rather than contacting conduction and, consequently, increasing the GF of the material.

Figure 6 - Relationship between FCR and compressive strain measured in piezoresistive tests of SMs.

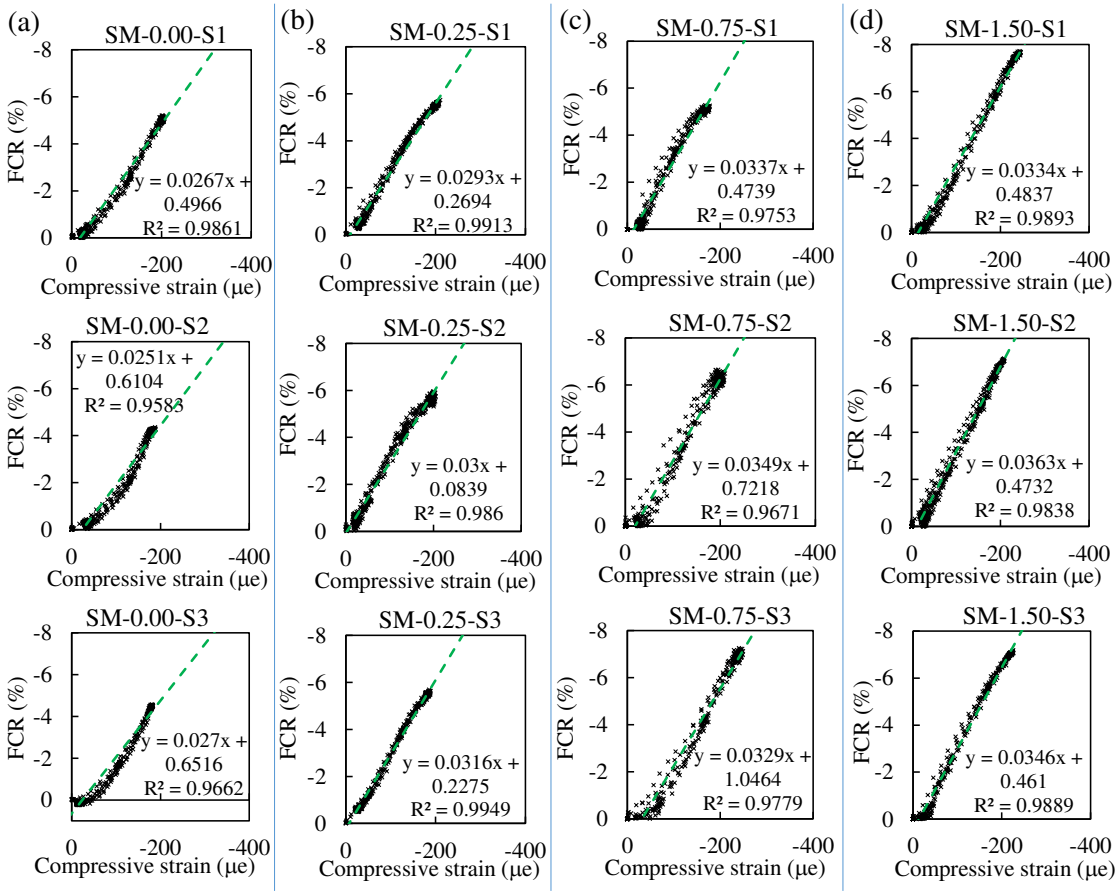

Source: Author (2024).

7.3.2. Strength, stiffness and failure modes of masonry prisms

Figure 7 shows the net area compressive strength and modulus of elasticity of masonry prisms. Statistical analyses of this dataset (APPENDIX 7A) revealed that ANOVA assumptions were satisfied for both response variables, so that Tukey's tests could be used to detect statistical differences between these parameters. Details of the failure mechanisms of specimens S1, S2 and S3 of each series of prisms are illustrated in APPENDIX 7B.

Since the series #1 and #3 were produced with units and mortars with similar deformation properties (Figure 5), they presented similar values of average modulus of elasticity (Figure 7b shows that they share the same uppercase letters "AB", according to the Tukey's test). However, the average net area compressive strength of series #1 was 24.6% lower than that of series #3. According to Zahra et al. (2021), prisms made with SCBs have higher strength than prisms produced with HCBs because an improved bonding between mortar and units is provided by solid bricks due to their larger contact area.

Figure 7 - Compressive strength (a) and modulus of elasticity (b) of the masonry prisms. According to the Tukey's test (α = 5%), bars sharing the same uppercase letter are statistically equal.

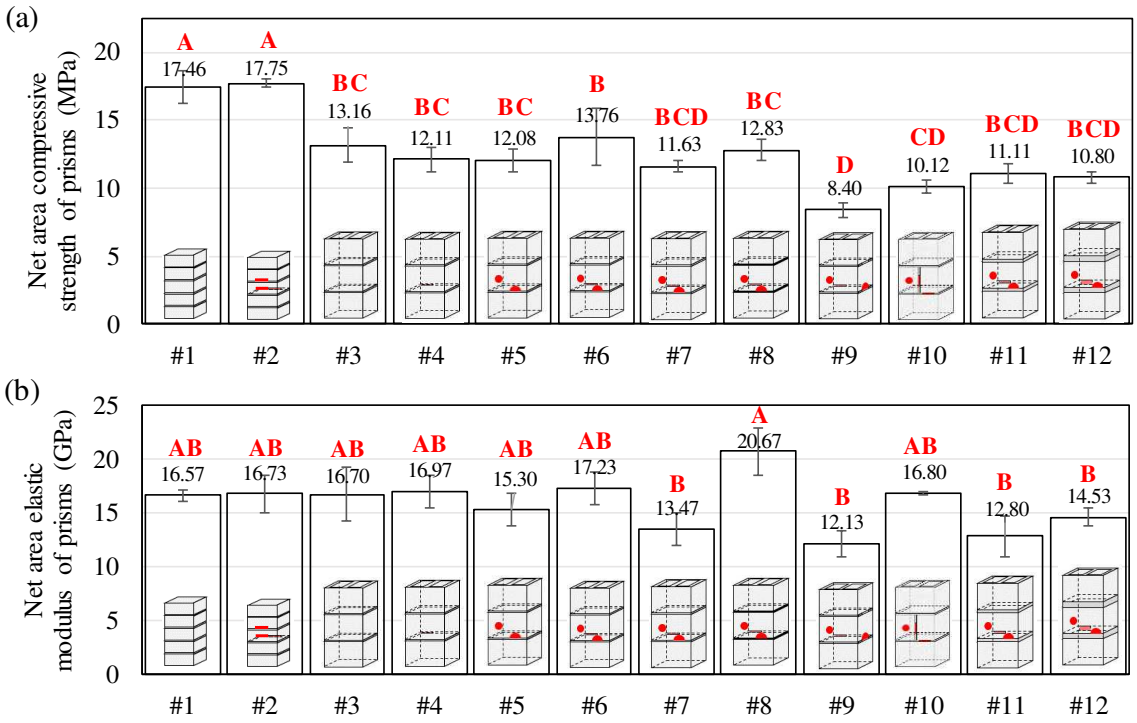

Source: Author (2024).

The incorporation of self-sensing materials into the masonry prisms did not change their mechanical behavior. For example, series #3, #4, #5 and #6 share the same uppercase letters "B" and "AB" in Figure 7a and Figure 7b, respectively. Similarly, series #1 and #2 share the same uppercase letters "A" and "AB" in Figure 7a and Figure 7b, respectively.

In series #1, #2, #3, #4, #5 and #6, the mortar was softer and weaker than the units, so that the mortar joint was confined laterally and lateral tensile stresses were induced in the units (Mohamad et al., 2007; Nalon et al., 2022; Parsekian et al., 2012). The typical failure mode observed in the prisms of these series was mainly characterized by vertical cracks (yellow arrows of Figure 8a-f) that initiated at the interface between the joints and the central unit of the prisms, when the compressive stress (σ) was around 75-85% of the strength of the prisms (f_p). This failure mode was also observed in prisms with $0.40 < f_m/f_{b,net} < 0.90$ reported in previous papers (AbdelRahman and Galal, 2020; Caldeira et al., 2020; Kazempour et al., 2017; Mahamid and Westin, 2020; Martins et al., 2018; Nalon et al., 2020; Thamboo and Dhanasekar, 2019; Zahra et al., 2021). The effects of crack propagation on the electrical output of the self-sensing regions are discussed in the next subsections.

Figure 8 - Typical failure modes of the masonry prisms

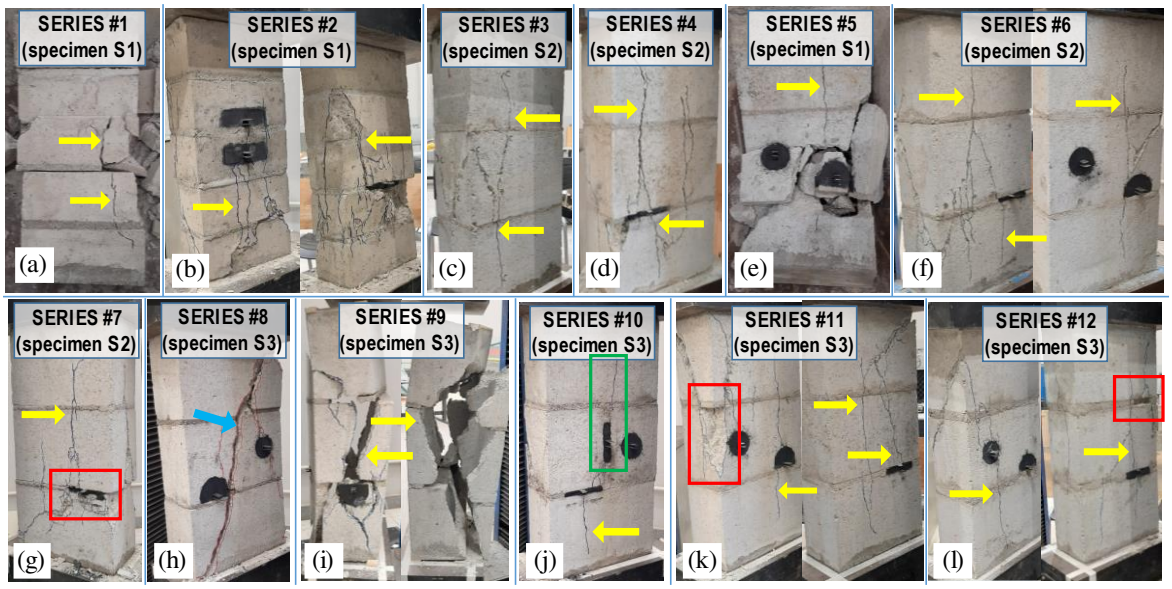

Source: Author (2024).

A comparison between the average mechanical properties of prisms of series #6 and #7 indicated that the use of mortars significantly weaker than the units caused percentage reductions of about 15.5% and 21.8% in the average compressive strength and modulus of elasticity of the prisms, respectively. Despite this, the Tukey's tests indicated that these reductions were not statistically relevant for $\alpha = 5\%$, which can be related to the high standard deviation typically observed in experimental tests of masonry elements.

Localized mortar crushing (red rectangle of Figure 8g) was observed in the joints of all prisms of series #7. The crushed mortar was expelled during the compression tests and face-shell spalling was eventually observed. These failure mechanisms are in good agreement with those verified in prisms with $f_m/f_{b,net} < 0.40$ that were tested in previous works (Caldeira et al., 2020; Mohamad et al., 2017; Nalon et al., 2020; Segura et al., 2018; Zahra et al., 2021).

When the mortar joint was stronger than the units (series #8), negligible changes in the compressive strength were observed. In fact, a literature review of previous works indicates that increases in mortar strength cause marginal increases in the compressive strength of masonry elements constructed with low-strength units (Mohamad et al., 2007; Nalon et al., 2022; Parsekian et al., 2012). In contrast, the average modulus of elasticity of series #8 was higher than those observed in all prisms investigated in this research. It happened because the modulus of elasticity of the SM-0.25 mortar was statistically higher than those observed in SM-0.75 and SM-1.50 mortars (Figure 5a).

In series #8, the unit was softer and weaker than the joint. Then, the concrete blocks were confined laterally and the joints were subjected to lateral tensile stresses. The typical rupture mode in this situation is a kind of shear failure (Berto, 2005; Hendry, 1997; Parsekian et al., 2012). In fact, the block crushing phenomenon was evidenced by the sudden propagation of diagonal cracks (blue arrow of Figure 8h) at the end of the series #8 compression tests. This brittle failure mode was also verified in prisms with $f_m/f_{b,\text{net}} > 0.90$ that were tested in previous studies (Caldeira et al., 2020; Nalon et al., 2020; Sajanthan et al., 2019; Sathiparan and Rumeshkumar, 2018; Thaickavil and Thomas, 2018).

The prisms of all series were produced with the full bedding approach (shells and webs of the blocks were fully covered with mortar), except for the prisms of series #9, which were produced using the face-shell bedding approach (mortar was only applied to the face shell areas of the blocks). The average compressive strength and modulus of elasticity of series #9 were 38.9% and 29.6% lower than those observed in series #6, respectively, when these mechanical properties were calculated on the basis of the net area of the units (Figure 7). Experimental data obtained in previous literature (Mahamid and Westin, 2020; Parsekian et al., 2012; Zahra et al., 2021) also indicated that the mechanical properties of face-shell bedded masonry is 17.0-41.4% lower than those of full-bedded masonry elements.

The failure mode of series #9 specimens was characterized by vertical cracks at some webs of the blocks (yellow arrows of Figure 8g), i.e., the prisms failed by web tensile splitting. The same rupture mode was observed in face-shell bedded prisms tested in previous research (Mahamid and Westin, 2020; Santos et al., 2017; Zahra et al., 2021), due to the deep-beam action effect developed at the center of the unmortared webs.

The running-bond arrangement of units was only used in series #10. Tukey's tests indicated that the average compressive strength of series #6 (uppercase letter "B") was statistically different from that of series #10 (uppercase letters "CD"), whereas both series exhibited average values of modulus of elasticity that are statistically equal (uppercase letters "AB"). Figure 7 indicates that the average compressive strength of series #10 was 26.5% lower than that of series #6. According to previous studies (Mohamad et al., 2011; Thaickavil and Thomas, 2018; Thamboo and Dhanasekar, 2019), the vertical joints of running-bonded prisms are weak links that contribute to an early prism rupture. As also observed in these previous studies, separation cracks propagated from the interface between the concrete blocks and the vertical mortar joint when $\sigma \approx 0.60\, f_p$ (green rectangle of Figure 8j).

Finally, prisms of series #11 and #12 were produced with an average mortar thickness of 15 mm and 20 mm, respectively. According to the Tukey's tests, these series had the same compressive strength (uppercase letters "BCD") and modulus of elasticity (uppercase letter "B"). In addition, moderate differences were observed between the average mechanical properties of these series and those of series #6 (mortar thickness of 10 mm). The increase in mortar thickness caused average strength and stiffness reductions up to 21.5% and 25.7%, respectively. In series #11 and #12, vertical cracks propagated from the mortar joints (yellow arrows of Figure 8l) and the prisms failed by tensile block splitting. Sometimes, mortar fragments were expelled from the joints (red rectangle of Figure 8l). In fact, previous research has reported that increases in the joint thickness cause decreases in the lateral confinement of the mortar and decreases in the tendency for units to fail by lateral splitting (Caldeira et al., 2020; Hendry, 1997; Nalon et al., 2022; Thamboo et al., 2013).

7.3.3. Self-sensing behavior of prisms within the elastic regime

The strain-sensing performance observed in the piezoresistive tests of the prisms (within the elastic regime) is presented in Figure 9. The GFs of all self-sensing regions were calculated as the slope of linear regression models obtained from the FCR *vs* compressive strain curves. An example of electrical signals (specimen S1 of series #6) acquired during the piezoresistive tests was taken from the Supplementary Material and represented in Figure 10. According to APPENDIX 7A, the ANOVA assumptions were also satisfied for these response variables. Therefore, Tukey's tests were eventually used to detect statistical differences between average values of GFs. The results indicated that an appropriate piezoresistive response was observed in the B1, B2, J1 and J2 regions of all types of masonry prisms, except for the B2 self-sensing region of series #9. In this case, FCRs were approximately zero when the cyclic compressive loading was applied. It happened because the main load path of face-bedded prisms was through the mortared area of the units, whereas the B2 self-sensing region was located at the lateral web of the central block of the prisms. Therefore, the applications of self-sensing cementitious material on the front side of solid concrete bricks, face shells of hollow concrete blocks and mortar joints were found to be promising strategies for strain-monitoring in SHM of masonry structures.

The GF of B1 self-sensing region of all prisms varied between 231 and 296. In the B2 self-sensing region, the gauge factor varied from 221 to 285. The ANOVAs presented in APPENDIX 7A provided P-values of 0.808 and 0.793 for the GF of B1 and B2 self-sensing

regions, respectively. These results demonstrate that the average GF of self-sensing regions embedded into masonry units are statistically equal, regardless if material was embedded into the middle height or inferior region of the masonry units. In contrast, the statistical analyses of APPENDIX 7A indicated that the GF of self-sensing regions of mortar joints changed with the type of masonry prism because a P-value of 1.7×10^{-10} was obtained in the ANOVA carried out for the experimental dataset associated with this response variable.

Figure 9 - Gauge factor of B1 (a), B2 (b), J1 and J2 (c) self-sensing regions of the masonry prisms. According to the Tukey's test ($\alpha = 5\%$), bars sharing the same uppercase letter are statistically equal.

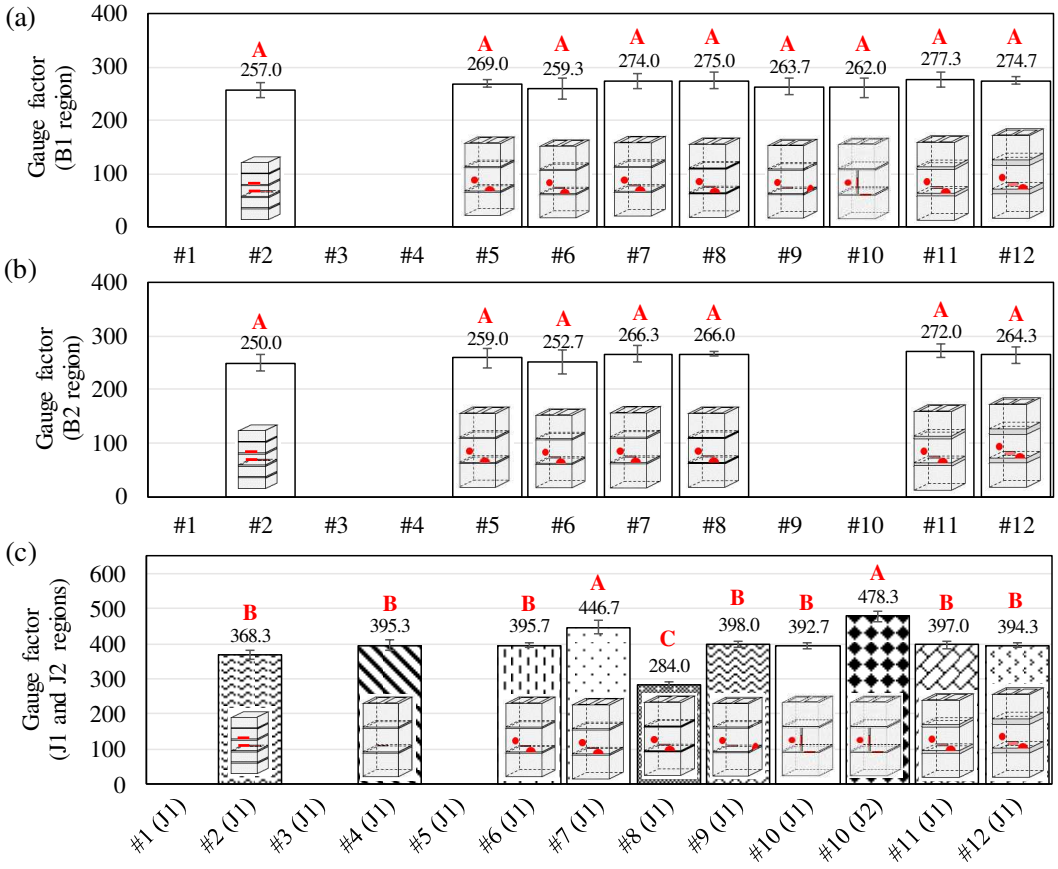

Source: Author (2024).

Figure 10 - Example of piezoresistivity results presented in the Supplementary Material: electrical output of self-sensing regions B1 (a), B2 (b) and J1 (c) of specimen S1 of series #6.

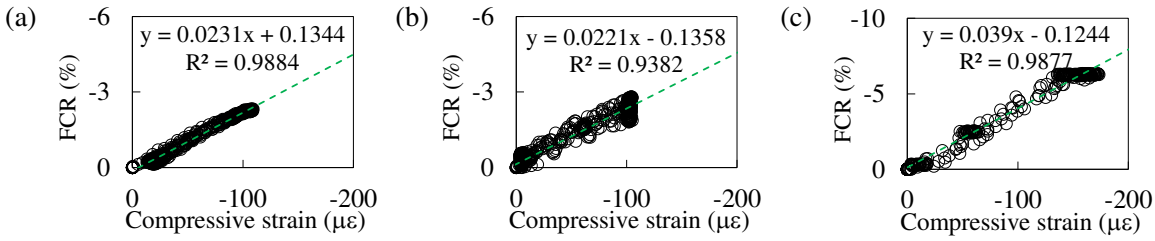

Source: Author (2024).

Based on the formulations presented in Equations (2), (3), (4) and (5) and characterization results of Figure 5, it was possible to predict a lateral strain of 32.7 με at the mortar/brick interface of series #2 prisms, considering the stress amplitude applied in the piezoresistive tests (elastic regime). If the brick was not interacting with the joint (brick under uniaxial compression), the calculated lateral strain of the brick would be 31.6 με. If the mortar was not interacting with the brick (mortar under uniaxial compression), the calculated lateral strain of the mortar would be 45.4 με. These results indicated that the mortar/unit interaction caused a small percentage increase (3.4%) in the tendency of lateral deformation of the bricks. In contrast, the mortar/unit interaction caused a significant decrease (28.0%) in the tendency of lateral deformation of the mortar. Since the α parameter of prisms of series constructed with HCBs was significantly greater than that of series #2, it is expected that the effects of mortar/unit interactions on the tendency of lateral deformations of the masonry components tend to be minimized in the case of the units and amplified in the case of the mortar.

These results indicated that the central units of the prisms tended to present lateral deformations within the elastic regime that are almost equal to those observed in uniaxial compression tests. Consequently, the GF of B1 and B2 self-sensing regions (Figure 9a and Figure 9b) were always very similar to the GF of the SM-0.00 composites (Figure 5d). In contrast, those formulations indicated that the mortar joint tended to present lateral deformations that are significantly different from those observed in uniaxial compression tests. Consequently, the GFs of J1 and J2 self-sensing regions (Figure 9c) were very different from the GFs of SM-0.25, SM-0.75 and SM-1.50 composites (Figure 5d). These results are in good agreement with previous studies (Ding et al., 2019; Liu et al., 2015; Xiao et al., 2010, 2011a, 2011b) that reported that the GF of CBN-based cementitious sensors embedded into concrete elements (beams and columns under complex states of strain/stress) may be different from the GF obtained when these cementitious sensors are calibrated under free conditions (uniaxial compression state).

According to previous works (Liu et al., 2015; Xiao et al., 2010, 2015), the GF of cementitious sensors containing randomly distributed CBN is strongly dependent on both longitudinal and transverse deformations (FCR amplitude and GF decrease with the increase in the Poisson's ratio). When the mortar was softer and weaker than the units, the joint was confined laterally, which decreased its lateral deformation. Then, the average GFs of the J1 self-sensing region of series #2, #4, #6, #9 and #10 ($0.40 < f_m/f_{b,\text{net}} < 0.90$) were 8.2-15.1%

higher than the average GF obtained when the SM-0.75 composites were subjected to uniaxial compression. In series #7, this percentage increase in average GF was amplified because the value of $f_m/f_{b,net}$ was lower than 0.40 (the average GF of J1 self-sensing region of series #7 was 22.1% higher than the average GF of SM-1.50 composites). In contrast, when the unit was softer and weaker than the mortar, the joint was tensioned laterally, which increased its lateral strain. In consequence, the average GF of the J1 self-sensing region of series #8 ($f_m/f_{b,net} > 0.90$) was 6.3% lower than the average GF calibrated when the SM-0.25 specimens were subjected to uniaxial compression.

The GF of J1 self-sensing region of the series #11 and #12 was statistically equal to those observed in series #2, #4, #6, #9 and #10 (all of them were identified with the uppercase letter "B", according to the Tukey's test). Therefore, it is possible to conclude that the increase in the joint thickness did not cause significant change in the average GF of the self-sensing horizontal joints. The decreases in the confinement level of the mortar joint associated with the increase in their thickness were too small to cause a significant change in the average GF of the joint.

Results of series #10 presented in Figure 9c also show that the average GF of the J2 self-sensing region was 41.5% and 21.8% higher than the average GF of SM-0.75 composites and J1 self-sensing region, respectively. This difference is also related to the distinct restraining conditions of the J2 self-sensing region of the prism and the SM-0.75 specimens. The surrounding concrete blocks restrained the lateral expansion of the vertical joint, whereas the SM-0.75 specimens were free to deform laterally.

7.3.4. Self-diagnosis of damage of prisms

FCRs of self-sensing regions of units (B1 and B2) were measured during monotonic compression tests of the specimens (S1, S2 and S3) of each series of masonry prisms, as presented in Figure 11. To evaluate the crack sensing ability of the cement-based sensors, the FCRs measured during the plastic regime of the masonry prisms were discussed based on the failure modes (APPENDIX 7B) described in previous subsections. The general behavior presented in Figure 11 was characterized by significant FCR decreases (increases in electrical conductivity) up to 50-70% of the compressive strength of the specimens. Sometimes, these FCRs were followed by stages of balance and abrupt increases, as also reported in subsequent experimental studies compiled in the review paper of Han et al. (2015). The stage of balance is associated with the germination of fresh microcracks that caused obstructions between

adjacent CBNs that formed the conductive network within the self-sensing regions. The progressive propagation of cracks through the cementitious matrix significantly decreased its electrical conductivity, which explains the FCR increases evidenced at the end of the compression tests of some masonry prisms. The stabilization of FCR values at higher loading levels can be interpreted as a distinctive electrical response of the self-sensing materials, as the stages of balance and abrupt increases in FCR can be associated with the germination and propagation of microcracks, providing a nuanced representation of damage evolution that may not be captured by conventional sensors like strain gauges.

Figure 11 - Fractional changes in electrical resistivity (FCR) measured in B1 and B2 self-sensing regions of masonry prims when the compressive load was increased up to the failure of the specimens.

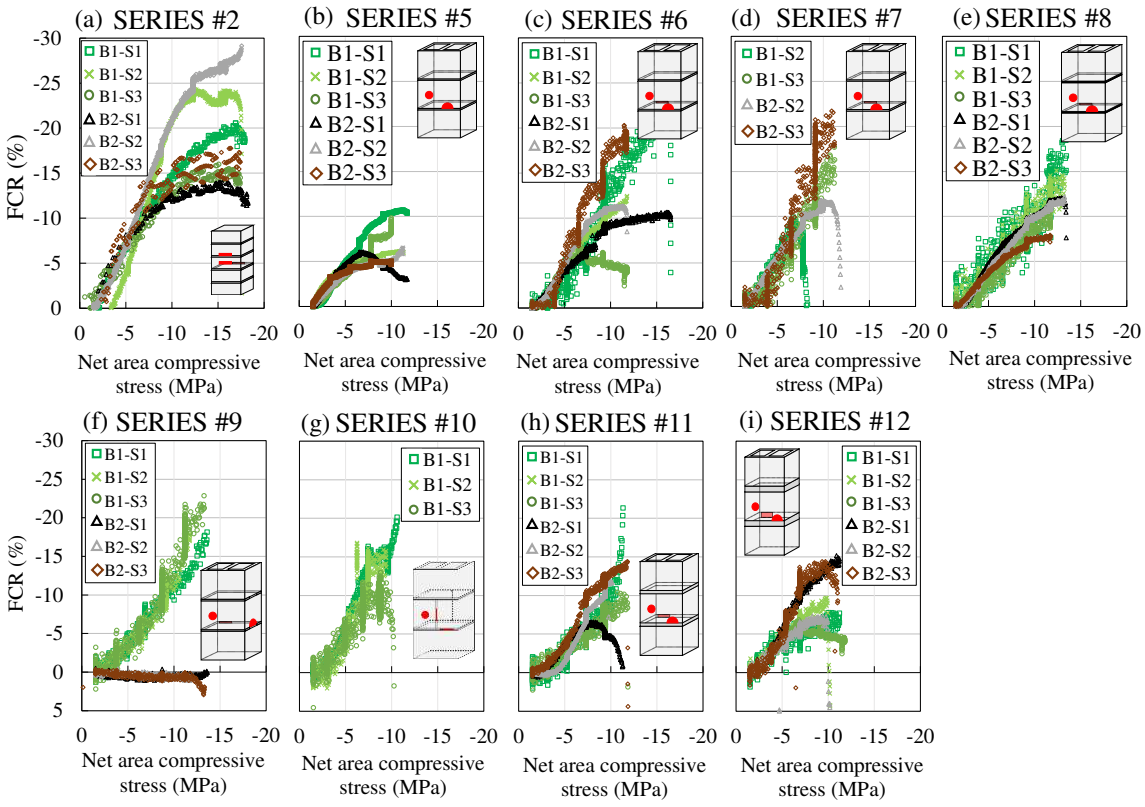

Source: Author (2024).

Propagation of vertical cracks through the B1 and/or B2 self-sensing regions were observed at the end of the compression tests of prisms with mortar weaker than the units ($f_m/f_{b,net} < 0.90$), such as specimens of series #2 (Figure 8b), #5 (Figure 8e), #6 (Figure 8f), #7 (Figure 8g), #11 (Figure 8k) and #12 (Figure 8l). Diagonal and vertical cracks were also observed around the B1 and/or B2 self-sensing regions at the end of the compression tests of prisms of series #8 (Figure 8h), i.e., prisms with units weaker than the mortar ($f_m/f_{b,net} > 0.90$).

Stages of balance and abrupt increases in FCR during the plastic regime of these self-sensing regions (Figure 11) show that their electrical output provided an anticipated warming associated with the propagation of vertical and diagonal cracks in masonry units. These stages were mainly evident in B2 self-sensing regions, where the transverse tensile stresses originated from the interaction between mortar joint and unit are more significant. These results indicate that the strong non-linearity at the end of FCR *vs* compressive stress curves can be an important evidence of the development of masonry failure mechanisms associated with tensile splitting or crushing of masonry units.

In contrast, Figure 11f shows that the B1 self-sensing region of all prisms of series #9 did not present evident non-linearity at the end of FCR *vs* compressive stress curves. It happened because these prisms failed by web tensile splitting due to the use of the face-shell bedding approach. In contrast, FCRs of the B2 self-sensing region fluctuated around zero. It happened because the B2 region was located at the lateral web of the central block (Figure 8i), whereas the main load path of these prisms was through the face shells of the blocks.

Figure 12 shows the FCRs of self-sensing regions of masonry joints (J1 and J2) during the monotonic compression tests of the masonry specimens (S1, S2 and S3) of each series investigated in the present study. The typical behavior observed in the electrical output of self-sensing masonry joints was characterized by relevant FCR decreases (increases in electrical conductivity) up to about 30% of the compressive strength of the masonry elements. After that, FCR values remained basically unchanged or slowly decreased up to the failure of the specimens. According to previous research (Caldeira et al., 2020; Mohamad et al., 2017, 2018; Nalon et al., 2022), the mortar joints govern the masonry failure process due to mortar crushing and/or localized splitting failure at the block-mortar interface. Therefore, the abrupt change in the slope of FCR *vs* compressive stress curves can be related to the propagation of prism cracks through the joint and/or the internal pore collapse of the confined mortar joint. These mechanisms caused the disruption of conductive paths between CBN due to the propagation of microcracks, decreasing the rate of FCR with increasing load.

The J1 self-sensing region of few prisms exhibited a distinct behavior in FCR *vs* compressive stress curves. For example, the J1 self-sensing region of specimens S1 and S2 of series #9 did not exhibit a descending stage at the end of the curves (Figure 12f). It happened because the face-shell bedded prisms of series #9 failed by web tensile splitting, so that the cracking propagation in their mortar joints tended to be less intense.

Figure 12 - Fractional changes in electrical resistivity (FCR) measured in J1 and J2 self-sensing regions of masonry prims when the compressive load was increased up to the failure of the specimens.

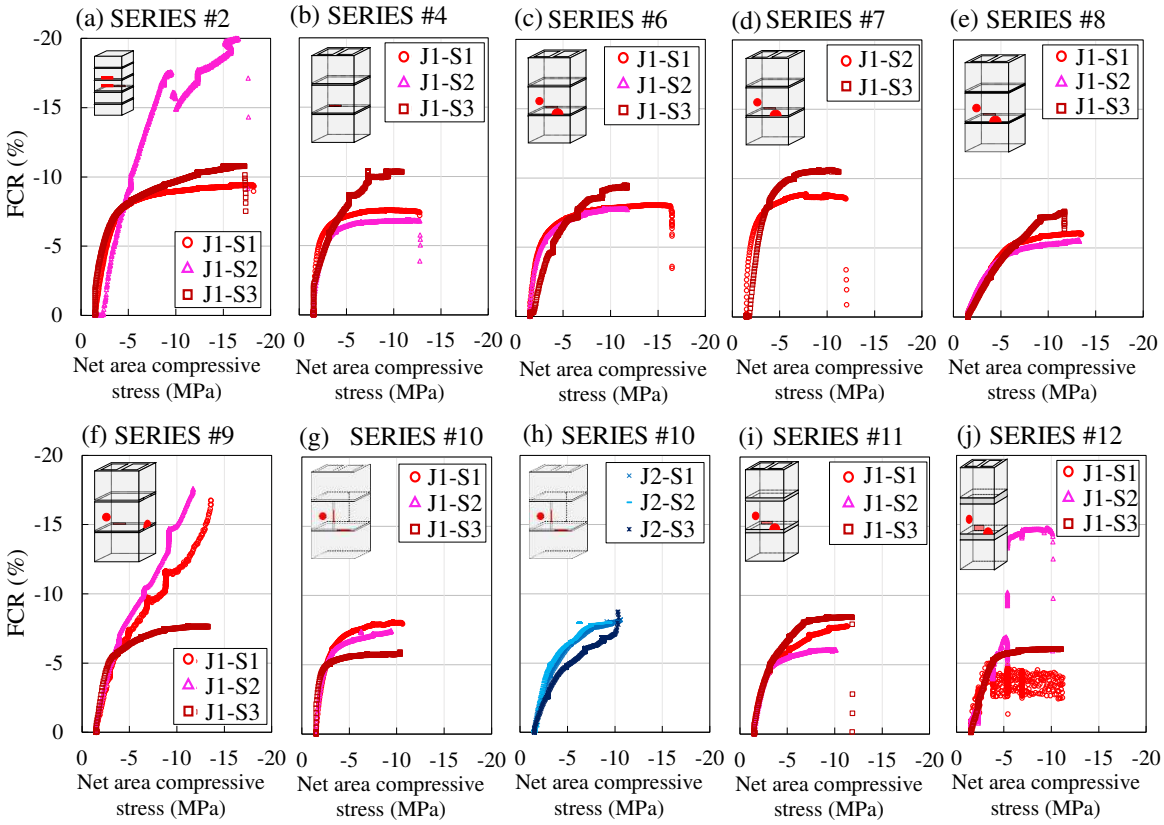

Source: Author (2024).

7.4. CONCLUSIONS

This work presents an experimental investigation of mechanical and self-sensing properties of masonry prisms produced with self-sensing mortar joints, solid concrete bricks and/or hollow concrete blocks. Self-sensing cementitious materials were designed to be compatible with existing masonry units and mortar joints. They can also be specifically designed for monitoring of next-generation smart masonry structures. The following conclusions were obtained from the results of the present work:

(1) The most appropriate locations for the embedded self-sensing mortars were the front side of solid bricks, face shells of hollow concrete blocks and mortar joints were found to be promising alternatives for strain monitoring and damage detection in the field of SHM of masonry structures. In addition, statistical analyses indicated that these applications did not cause significant changes in the compressive strength, modulus of elasticity and failure mechanism of masonry prisms. However, plain and

nanomodified components must present similar deformation properties to ensure the best self-sensing and mechanical performance.

(2) Variations in the type of masonry unit, mortar bedding approach, bonding arrangement, relative strength between mortar and units, joint thickness and location of self-sensing regions did not affect the GF of cementitious sensors embedded into the middle height and inferior region of masonry units. In contrast, the GF of cementitious sensors embedded into horizontal or vertical joints of the prisms was statistically affected by most of these variations.

(3) Effects of triaxial stress/strain states of self-sensing masonry joints on their GF were elucidated in the present work. In prisms constructed with mortar softer than units, the GF of the self-sensing masonry joint was 8.2-22.1% higher than the GF calculated when this material is under uniaxial compression. In prisms produced with units softer than mortar, the GF of the self-sensing masonry joint was 6.3% lower than the corresponding GF calculated in uniaxial compression tests. The increase in joint thickness did not cause significant GF changes. The GF of composites embedded into vertical joints of masonry prisms was 17.9% higher than the average GF of self-sensing regions embedded into horizontal masonry joints.

(4) FCRs of self-sensing regions of units and joints during the plastic regime revealed their intrinsic ability to detect damage and help in processes of prediction of masonry failure modes. Stages of balance and abrupt increases in FCR during the plastic regime provided an anticipated warming associated with the propagation of vertical and diagonal cracks associated with tensile splitting and crushing failure of units. The strong non-linearity at the end of FCR vs compressive stress curves can be an important evidence of the pore collapse phenomenon of crushed mortar joints.

Future research is needed to describe the piezoresistive responses based on theoretical piezoresistivity models available in the literature for cementitious sensors containing randomly distributed CBN and subjected to various states of multi-axial strain. Further studies on the use of different types of nanomaterials for improvement of the self-sensing response of the concrete units and mortar joints are also required.

REFERENCES

AbdelRahman, B., & Galal, K. (2020). Influence of pre-wetting, non-shrink grout, and scaling on the compressive strength of grouted concrete masonry prisms. *Construction*

and Building Materials, *241*, 117985. https://doi.org/10.1016/j.conbuildmat.2019.117985

ABNT. (2005a). *NBR 13276: Preparation of mortar for unit masonry and rendering with standard consistence index*.

ABNT. (2005b). *NBR 13279: Mortars applied on walls and ceilings - Determination of the flexural and the compressive strength in the hardened stage* (p. 15).

ABNT. (2013). *NBR 12118: Hollow concrete blocks for concrete masonry - Test methods* (p. 14).

ABNT. (2017). *NBR 8522: Concrete - Determination of the static elasticity and strain modulus* (p. 20).

ABNT. (2020). *NBR 16868-3: Structural masonry Part 3 - Test methods* (p. 39).

Aparecido-Ferreira, A., Ribeiro, G. M., Alves, E. S., & Sampaio, J. F. (2011). Determination of a soft gap in the density of states of granular carbon. *Physical Review B*, *84*(2), 024204. https://doi.org/10.1103/PhysRevB.84.024204

ASTM. (2020). *C140/C140M: Standard Test Methods for Sampling and Testing Concrete Masonry Units and Related Units* (p. 27). ASTM International.

ASTM. (2022). *C150/C150M-22: Standard Specification for Portland Cement*.

Bekzhanova, Z., Memon, S. A., & Kim, J. R. (2021). Self-Sensing Cementitious Composites: Review and Perspective. *Nanomaterials*, *11*(9), 2355. https://doi.org/10.3390/nano11092355

Berto, L. (2005). Failure mechanism of masonry prism loaded in axial compression: computational aspects. *Materials and Structures*, *38*(276), 249–256. https://doi.org/10.1617/14096

Birgin, H. B., D'Alessandro, A., Laflamme, S., & Ubertini, F. (2021). Innovative Carbon-Doped Composite Pavements with Sensing Capability and Low Environmental Impact for Multifunctional Infrastructures. *Journal of Composites Science*, *5*(7), 192. https://doi.org/10.3390/jcs5070192

Cabrera, J., & Al-Hasan, A. (1997). Performance properties of concrete repair materials. *Construction and Building Materials*, *11*(5–6), 283–290. https://doi.org/10.1016/S0950-0618(97)00049-4

Caldeira, F. E., Nalon, G. H., Oliveira, D. S. de, Pedroti, L. G., Ribeiro, J. C. L., Ferreira, F. A., & Carvalho, J. M. F. de. (2020). Influence of joint thickness and strength of mortars on the compressive behavior of prisms made of normal and high-strength concrete

blocks. *Construction and Building Materials*, *234*, 117419. https://doi.org/10.1016/j.conbuildmat.2019.117419

CEN. (2019). *EN 1015-11: Methods of test for mortar for masonry - Part 11 - Determination of flexural and compressive strength of hardened mortars*.

Chung, D. D. L. (2021). Self-sensing concrete: from resistance-based sensing to capacitance-based sensing. *International Journal of Smart and Nano Materials*, *12*(1), 1–19. https://doi.org/10.1080/19475411.2020.1843560

Chung, D. D. L. (2022). Pitfalls in Piezoresistivity Testing. *Journal of Electronic Materials*, *51*(10), 5473–5481. https://doi.org/10.1007/s11664-022-09857-4

D'Alessandro, A., Birgin, H. B., Cerni, G., & Ubertini, F. (2022). Smart Infrastructure Monitoring through Self-Sensing Composite Sensors and Systems: A Study on Smart Concrete Sensors with Varying Carbon-Based Filler. *Infrastructures*, *7*(4), 48. https://doi.org/10.3390/infrastructures7040048

D'Alessandro, A., Meoni, A., García-Macías, E., Cavalagli, N., Gioffrè, M., & Ubertini, F. (2018). Full-scale testing of a masonry building monitored with smart brick sensors. *Proceedings of 5th International Electronic Conference on Sensors and Applications*, 5764. https://doi.org/10.3390/ecsa-5-05764

Dinesh, A., Sudharsan, S. T., & Haribala, S. (2021). Self-sensing cement-based sensor with carbon nanotube: Fabrication and properties – A review. *Materials Today: Proceedings*, *46*, 5801–5807. https://doi.org/10.1016/j.matpr.2021.02.722

Ding, S., Ruan, Y., Yu, X., Han, B., & Ni, Y.-Q. (2019). Self-monitoring of smart concrete column incorporating CNT/NCB composite fillers modified cementitious sensors. *Construction and Building Materials*, *201*, 127–137. https://doi.org/10.1016/j.conbuildmat.2018.12.203

Ding, S., Xiang, Y., Ni, Y.-Q., Thakur, V. K., Wang, X., Han, B., & Ou, J. (2022). In-situ synthesizing carbon nanotubes on cement to develop self-sensing cementitious composites for smart high-speed rail infrastructures. *Nano Today*, *43*, 101438. https://doi.org/10.1016/j.nantod.2022.101438

Dong, W., Li, W., Lu, N., Qu, F., Vessalas, K., & Sheng, D. (2019). Piezoresistive behaviours of cement-based sensor with carbon black subjected to various temperature and water content. *Composites Part B: Engineering*, *178*, 107488. https://doi.org/10.1016/j.compositesb.2019.107488

Dong, W., Li, W., Tao, Z., & Wang, K. (2019). Piezoresistive properties of cement-based sensors: Review and perspective. *Construction and Building Materials*, *203*, 146–163. https://doi.org/10.1016/j.conbuildmat.2019.01.081

Dong, W., Li, W., Wang, K., Han, B., Sheng, D., & Shah, S. P. (2020). Investigation on physicochemical and piezoresistive properties of smart MWCNT/cementitious composite exposed to elevated temperatures. *Cement and Concrete Composites*, *112*, 103675. https://doi.org/10.1016/j.cemconcomp.2020.103675

Downey, A., D'Alessandro, A., Laflamme, S., & Ubertini, F. (2018a). Smart bricks for strain sensing and crack detection in masonry structures. *Smart Materials and Structures*, *27*(1), 015009. https://doi.org/10.1088/1361-665X/aa98c2

Downey, A., D'Alessandro, A., Laflamme, S., & Ubertini, F. (2018b). Smart bricks for strain sensing and crack detection in masonry structures. *Smart Materials and Structures*, *27*(1), 015009. https://doi.org/10.1088/1361-665X/aa98c2

Downey, A., D'Alessandro, A., Ubertini, F., Laflamme, S., & Geiger, R. (2017). Biphasic DC measurement approach for enhanced measurement stability and multi-channel sampling of self-sensing multi-functional structural materials doped with carbon-based additives. *Smart Materials and Structures*, *26*(6), 065008. https://doi.org/10.1088/1361-665X/aa6b66

Francis, A., Horman, C., & Jerrems, L. (1971). The effect of joint thickness and other factors on the compressive strength of brickwork. *Proceedings of the Second International Brick Masonry Conference*, 31–37.

García-Macías, E., & Ubertini, F. (2019). Earthquake-induced damage detection and localization in masonry structures using smart bricks and Kriging strain reconstruction: A numerical study. *Earthquake Engineering & Structural Dynamics*, *48*(5), 548–569. https://doi.org/10.1002/eqe.3148

Han, B., Ding, S., & Yu, X. (2015). Intrinsic self-sensing concrete and structures: A review. *Measurement*, *59*, 110–128. https://doi.org/10.1016/j.measurement.2014.09.048

Han, B., Guan, X., & Ou, J. (2007). Electrode design, measuring method and data acquisition system of carbon fiber cement paste piezoresistive sensors. *Sensors and Actuators A: Physical*, *135*(2), 360–369. https://doi.org/10.1016/j.sna.2006.08.003

Han, B., Yu, X., & Ou, J. (2015). *Self-Sensing Concrete in Smart Structures*. Elsevier. https://doi.org/10.1016/C2013-0-14456-X

Han, B., Zhang, K., Burnham, T., Kwon, E., & Yu, X. (2013). Integration and road tests of a self-sensing CNT concrete pavement system for traffic detection. *Smart Materials and Structures*, *22*(1), 015020. https://doi.org/10.1088/0964-1726/22/1/015020

Han, B., Zhang, L., & Ou, J. (2010). Influence of water content on conductivity and piezoresistivity of cement-based material with both carbon fiber and carbon black. *Journal of Wuhan University of Technology-Mater. Sci. Ed.*, *25*(1), 147–151. https://doi.org/10.1007/s11595-010-1147-z

Han, J., Cai, J., Pan, J., & Sun, Y. (2021). Study on the conductivity of carbon fiber self-sensing high ductility cementitious composite. *Journal of Building Engineering*, *43*, 103125. https://doi.org/10.1016/j.jobe.2021.103125

Han, J., Pan, J., Ma, X., & Cai, J. (2022). Sensing performance of engineered cementitious composites in different application forms. *Construction and Building Materials*, *355*, 129223. https://doi.org/10.1016/j.conbuildmat.2022.129223

Hendry, A. (1997). *Structural masonry* (2nd ed.). MACMILLAN PRESS LTD.

Jiao, P., Egbe, K.-J. I., Xie, Y., Matin Nazar, A., & Alavi, A. H. (2020). Piezoelectric Sensing Techniques in Structural Health Monitoring: A State-of-the-Art Review. *Sensors*, *20*(13), 3730. https://doi.org/10.3390/s20133730

Kang, M.-S., Lee, H., Yim, H., An, Y.-K., & Kim, D. (2018). Multi-Channel Electrical Impedance-Based Crack Localization of Fiber-Reinforced Cementitious Composites under Bending Conditions. *Applied Sciences*, *8*(12), 2582. https://doi.org/10.3390/app8122582

Kazempour, H., Bassuoni, M. T., & Hashemian, F. (2017). Masonry mortar with nanoparticles at a low temperature. *Proceedings of the Institution of Civil Engineers - Construction Materials*, *170*(6), 297–308. https://doi.org/10.1680/jcoma.15.00054

Khan, F., Rajaram, S., Vanniamparambil, P. A., Bolhassani, M., Hamid, A., Kontsos, A., & Bartoli, I. (2015). Multi-sensing NDT for damage assessment of concrete masonry walls. *Structural Control and Health Monitoring*, *22*(3), 449–462. https://doi.org/10.1002/stc.1680

Kiani, B., Liang, R. Y., & Gross, J. (2018). Material selection for repair of structural concrete using VIKOR method. *Case Studies in Construction Materials*, *8*, 489–497. https://doi.org/10.1016/j.cscm.2018.03.008

Kita, A., Cavalagli, N., & Ubertini, F. (2019). Temperature effects on static and dynamic behavior of Consoli Palace in Gubbio, Italy. *Mechanical Systems and Signal Processing*, *120*, 180–202. https://doi.org/10.1016/j.ymssp.2018.10.021

La Mendola, L., Oddo, M. C., Papia, M., Pappalardo, F., Pennisi, A., Bertagnoli, G., Di Trapani, F., Monaco, A., Parisi, F., & Barile, S. (2021). Performance of two innovative stress sensors imbedded in mortar joints of new masonry elements. *Construction and Building Materials*, *297*, 123764. https://doi.org/10.1016/j.conbuildmat.2021.123764

Lee, S.-J., Ahn, D., You, I., Yoo, D.-Y., & Kang, Y.-S. (2020). Wireless cement-based sensor for self-monitoring of railway concrete infrastructures. *Automation in Construction*, *119*, 103323. https://doi.org/10.1016/j.autcon.2020.103323

Lima, G. E. S. de, Nalon, G. H., Santos, R. F., Ribeiro, J. C. L., Carvalho, J. M. F. de, Pedroti, L. G., & Araújo, E. N. D. de. (2021). Microstructural Investigation of the Effects of Carbon Black Nanoparticles on Hydration Mechanisms, Mechanical and Piezoresistive Properties of Cement Mortars. *Materials Research*, *24*(4). https://doi.org/10.1590/1980-5373-mr-2020-0539

Liu, J., Liu, M., & Xiao, H. (2015). Optimizing the Strain-Sensing Property of Cement-Based Composite Based on a Piezoresisitivity Model. *2015 Fifth International Conference on Instrumentation and Measurement, Computer, Communication and Control (IMCCC)*, 1061–1064. https://doi.org/10.1109/IMCCC.2015.229

Liu, L., Xu, J., Yin, T., Wang, Y., & Chu, H. (2022). Improving electrical and piezoresistive properties of cement-based composites by combined addition of nano carbon black and nickel nanofiber. *Journal of Building Engineering*, *51*, 104312. https://doi.org/10.1016/j.jobe.2022.104312

Liu, Q., Gao, R., Tam, V. W. Y., Li, W., & Xiao, J. (2018). Strain monitoring for a bending concrete beam by using piezoresistive cement-based sensors. *Construction and Building Materials*, *167*, 338–347. https://doi.org/10.1016/j.conbuildmat.2018.02.048

Luchin, G., Ramos, L. F., & D'Amato, M. (2020). Sonic Tomography for Masonry Walls Characterization. *International Journal of Architectural Heritage*, *14*(4), 589–604. https://doi.org/10.1080/15583058.2018.1554723

Machan, L., & Steffan, P. (2015). Multichannel Laboratory Device for Measurement of Smart Concrete Material Properties. *Advanced Materials Research*, *1124*, 249–254. https://doi.org/10.4028/www.scientific.net/AMR.1124.249

Mahamid, M., & Westin, N. (2020). Reevaluation of fm′ for the Unit-Strength Method with Application to Lightweight Concrete Block Masonry and Face Shell–Bedded Mortar Joints. *Practice Periodical on Structural Design and Construction*, *25*(3), 04020019. https://doi.org/10.1061/(ASCE)SC.1943-5576.0000494

Martins, R. O. G., Nalon, G. H., Alvarenga, R. D. C. S. S., Pedroti, L. G., & Ribeiro, J. C. L. (2018). Influence of blocks and grout on compressive strength and stiffness of concrete masonry prisms. *Construction and Building Materials*, *182*, 233–241. https://doi.org/10.1016/j.conbuildmat.2018.06.091

Medeiros, W. A., Soriani, M. de O., & Parsekian, G. A. (2020). Innovation in flat-jack application to evaluate modern high-strength hollow concrete block masonry. *Construction and Building Materials*, *255*, 119341. https://doi.org/10.1016/j.conbuildmat.2020.119341

Mehta, P., & Monteiro, P. (2005). *Concrete: Microstructure, Properties and Materials*. McGraw-Hill Professional.

Meoni, A., D'Alessandro, A., Cavalagli, N., Gioffré, M., & Ubertini, F. (2019). Shaking table tests on a masonry building monitored using smart bricks: Damage detection and localization. *Earthquake Engineering & Structural Dynamics*, *48*(8), 910–928. https://doi.org/10.1002/eqe.3166

Meoni, A., D'Alessandro, A., Downey, A., Laflamme, S., & Ubertini, F. (2018). Strain monitoring in masonry structures using smart bricks. In H. Sohn (Ed.), *Sensors and Smart Structures Technologies for Civil, Mechanical, and Aerospace Systems 2018* (p. 66). SPIE. https://doi.org/10.1117/12.2297526

Meoni, A., D'Alessandro, A., Kruse, R., De Lorenzis, L., & Ubertini, F. (2021). Strain field reconstruction and damage identification in masonry walls under in-plane loading using dense sensor networks of smart bricks: Experiments and simulations. *Engineering Structures*, *239*, 112199. https://doi.org/10.1016/j.engstruct.2021.112199

Meoni, A., D'Alessandro, A., Mancinelli, M., & Ubertini, F. (2021). A Multichannel Strain Measurement Technique for Nanomodified Smart Cement-Based Sensors in Reinforced Concrete Structures. *Sensors*, *21*(16), 5633. https://doi.org/10.3390/s21165633

Meoni, A., D'Alessandro, A., & Ubertini, F. (2020). Characterization of the strain-sensing behavior of smart bricks: A new theoretical model and its application for monitoring of masonry structural elements. *Construction and Building Materials*, *250*, 118907. https://doi.org/10.1016/j.conbuildmat.2020.118907

Meoni, A., D'Alessandro, A., & Ubertini, F. (2021). *Recent Advances and Open Issues on the Use of Smart Bricks for Seismic Monitoring of Masonry Buildings: Experimental Tests and Numerical Simulations* (pp. 851–860). https://doi.org/10.1007/978-3-030-64594-6_82

Meoni, A., Fabiani, C., D'Alessandro, A., Pisello, A. L., & Ubertini, F. (2022). Strain-sensing smart bricks under dynamic environmental conditions: Experimental investigation and new modeling. *Construction and Building Materials*, *336*, 127375. https://doi.org/10.1016/j.conbuildmat.2022.127375

Mishra, M. (2021). Machine learning techniques for structural health monitoring of heritage buildings: A state-of-the-art review and case studies. *Journal of Cultural Heritage*, *47*, 227–245. https://doi.org/10.1016/j.culher.2020.09.005

Mohamad, G., Fonseca, F. S., Vermeltfoort, A. T., & Lubeck, A. (2018). Stiffness plasticity degradation of masonry mortar under compression: preliminar results. *Revista IBRACON de Estruturas e Materiais*, *11*(2), 279–295. https://doi.org/10.1590/s1983-41952018000200004

Mohamad, G., Fonseca, F. S., Vermeltfoort, A. T., Martens, D. R. W., & Lourenço, P. B. (2017). Strength, behavior, and failure mode of hollow concrete masonry constructed with mortars of different strengths. *Construction and Building Materials*, *134*, 489–496. https://doi.org/10.1016/j.conbuildmat.2016.12.112

Mohamad, G., Lourenço, P. B., & Roman, H. R. (2007). Mechanics of hollow concrete block masonry prisms under compression: Review and prospects. *Cement and Concrete Composites*, *29*(3), 181–192. https://doi.org/10.1016/j.cemconcomp.2006.11.003

Mohamad, G., Lourenço, P. B., & Roman, H. R. (2011). Study of the compressive strength of concrete block prisms: stack and running bond. *Revista IBRACON de Estruturas e Materiais*, *4*(3), 347–358. https://doi.org/10.1590/S1983-41952011000300002

Monteiro, A., Loredo, A., Costa, P., Oeser, M., & Cachim, P. (2017). A pressure-sensitive carbon black cement composite for traffic monitoring. *Construction and Building Materials*, *154*, 1079–1086. https://doi.org/10.1016/j.conbuildmat.2017.08.053

Morgan, D. R. (1996). Compatibility of concrete repair materials and systems. *Construction and Building Materials*, *10*(1), 57–67. https://doi.org/10.1016/0950-0618(95)00060-7

Nalon, G. H., Lopes Ribeiro, J. C., Duarte de Araújo, E. N., Marcio da Silva, R., & Pedroti, L. G. (2023). Effects of shrinkage-reducing admixtures and expansive agents on the

self-sensing behavior of nanomodified cement-based materials. *Journal of Building Engineering*, *78*, 107648. https://doi.org/10.1016/j.jobe.2023.107648

Nalon, G. H., Ribeiro, J. C. L., de Araújo, E. N. D., Pedroti, L. G., de Carvalho, J. M. F., Santos, R. F., & de Oliveira, D. S. (2021). Residual mechanical properties of mortars containing carbon nanomaterials exposed to high temperatures. *Construction and Building Materials*, *275*, 122123. https://doi.org/10.1016/j.conbuildmat.2020.122123

Nalon, G. H., Ribeiro, J. C. L., Pedroti, L. G., Silva, R. M. da, Araújo, E. N. D. de, Santos, R. F., & Lima, G. E. S. de. (2022). Review of recent progress on the compressive behavior of masonry prisms. *Construction and Building Materials*, *320*, 126181. https://doi.org/10.1016/j.conbuildmat.2021.126181

Nalon, G. H., Ribeiro, J. C., Pedroti, L. G., Duarte de Araújo, E., Franco de Carvalho, J., Soares de Lima, G., & de Moura Guimarães, L. (2021). Residual piezoresistive properties of mortars containing carbon nanomaterials exposed to high temperatures. *Cement and Concrete Composites*, *121*, 104104. https://doi.org/10.1016/j.cemconcomp.2021.104104

Nalon, G. H., Ribeiro, J., Pedroti, L., de Araújo, E., Franco de Carvalho, J. M., Lima, G., & Oliveira, D. (2021). Self-Sensing Mortars: Effect of Moisture and Nanocarbon Black Content. *ACI Materials Journal*, *118*(3), 131–141. https://doi.org/10.14359/51732636

Nalon, G. H., Santos, C. F. R., Pedroti, L. G., Ribeiro, J. C. L., Veríssimo, G. de S., & Ferreira, F. A. (2020). Strength and failure mechanisms of masonry prisms under compression, flexure and shear: Components' mechanical properties as design constraints. *Journal of Building Engineering*, *28*, 101038. https://doi.org/10.1016/j.jobe.2019.101038

Nalon, G. H., Santos, R. F., Lima, G. E. S. de, Andrade, I. K. R., Pedroti, L. G., Ribeiro, J. C. L., & Franco de Carvalho, J. M. (2022). Recycling waste materials to produce self-sensing concretes for smart and sustainable structures: A review. *Construction and Building Materials*, *325*, 126658. https://doi.org/10.1016/j.conbuildmat.2022.126658

Nalon, G., Ribeiro, J., Araújo, E., Silva, R., Pedroti, L., & Lima, G. (2023). Concrete units for strain-monitoring in civil structures: Installation of cement-based sensors using different approaches. *Construction and Building Materials*, *394*, 132169. https://doi.org/10.1016/j.conbuildmat.2023.132169

Nalon, G., Ribeiro, J., Pedroti, L., Araújo, E., Carvalho, J., Lima, G., & Ferreira, S. (2023). Effects Of Post-Fire Curing on Self-Sensing Behavior of Smart Mortars. *ACI Materials Journal*, *120*(1), 181–192. https://doi.org/10.14359/51738459

Parsekian, G., Hamid, A., & Drysdale, G. (2012). *Behavior and design of structural masonry (in Portuguese)*. EdUFSCar.

Parsekian, G., & Soares, M. (2010). *Clay blocks structural masonry - design, execution and control (in Portuguese)* (Telo Melo, Ed.; 1st ed.).

Rao, R. K., Sindu, B. S., & Sasmal, S. (2023). Real-time monitoring of structures under extreme loading using smart composite-based embeddable sensors. *Journal of Intelligent Material Systems and Structures*, *34*(9), 1073–1096. https://doi.org/10.1177/1045389X221128586

Sajanthan, K., Balagasan, B., & Sathiparan, N. (2019). Prediction of Compressive Strength of Stabilized Earth Block Masonry. *Advances in Civil Engineering*, *2019*, 1–13. https://doi.org/10.1155/2019/2072430

Santos, C. F. R., Alvarenga, R. C. S. S., Ribeiro, J. C. L., Castro, L. O., Silva, R. M., Santos, A. A. R., & Nalon, G. H. (2017). Numerical and experimental evaluation of masonry prisms by finite element method. *Revista IBRACON de Estruturas e Materiais*. https://doi.org/10.1590/s1983-41952017000200010

Sarhosis, V., Milani, G., Formisano, A., & Fabbrocino, F. (2018). Evaluation of different approaches for the estimation of the seismic vulnerability of masonry towers. *Bulletin of Earthquake Engineering*, *16*(3), 1511–1545. https://doi.org/10.1007/s10518-017-0258-8

Sathiparan, N., & Rumeshkumar, U. (2018). Effect of moisture condition on mechanical behavior of low strength brick masonry. *Journal of Building Engineering*, *17*, 23–31. https://doi.org/10.1016/j.jobe.2018.01.015

Scuro, C., Lamonaca, F., Porzio, S., Milani, G., & Olivito, R. S. (2021). Internet of Things (IoT) for masonry structural health monitoring (SHM): Overview and examples of innovative systems. *Construction and Building Materials*, *290*, 123092. https://doi.org/10.1016/j.conbuildmat.2021.123092

Segura, J., Pelà, L., & Roca, P. (2018). Monotonic and cyclic testing of clay brick and lime mortar masonry in compression. *Construction and Building Materials*, *193*, 453–466. https://doi.org/10.1016/j.conbuildmat.2018.10.198

Sun, M., Liew, R. J. Y., Zhang, M.-H., & Li, W. (2014). Development of cement-based strain sensor for health monitoring of ultra high strength concrete. *Construction and Building Materials*, *65*, 630–637. https://doi.org/10.1016/j.conbuildmat.2014.04.105

Thaickavil, N. N., & Thomas, J. (2018). Behaviour and strength assessment of masonry prisms. *Case Studies in Construction Materials*, *8*, 23–38. https://doi.org/10.1016/j.cscm.2017.12.007

Thamboo, J. A., & Dhanasekar, M. (2019). Correlation between the performance of solid masonry prisms and wallettes under compression. *Journal of Building Engineering*, *22*, 429–438. https://doi.org/10.1016/j.jobe.2019.01.007

Thamboo, J., Dhanasekar, M., & Yan, C. (2013). Effects of joint thickness, adhesion and web shells to the face shell bedded concrete masonry loaded in compression. *Australian Journal of Structural Engineering*, *14*(3). https://doi.org/10.7158/S12-035.2013.14.3

Tian, Z., Li, Y., Zheng, J., & Wang, S. (2019). A state-of-the-art on self-sensing concrete: Materials, fabrication and properties. *Composites Part B: Engineering*, *177*, 107437. https://doi.org/10.1016/j.compositesb.2019.107437

Ubertini, F., D'Alessandro, A., Downey, A., García-Macías, E., Laflamme, S., & Castro-Triguero, R. (2017). Recent Advances on SHM of Reinforced Concrete and Masonry Structures Enabled by Self-Sensing Structural Materials. *The 4th International Electronic Conference on Sensors and Applications*, 119. https://doi.org/10.3390/ecsa-4-04889

Ubertini, F., D'Alessandro, A., Materazzi, A., Laflamme, S., & Downey, A. (2017). Novel nanocomposite clay brick for strain sensing in structural masonry. *2017 IEEE International Conference on Environment and Electrical Engineering and 2017 IEEE Industrial and Commercial Power Systems Europe (EEEIC / I&CPS Europe)*, 1–4. https://doi.org/10.1109/EEEIC.2017.7977598

Vanniamparambil, P. A., Bolhassani, M., Carmi, R., Khan, F., Bartoli, I., Moon, F. L., Hamid, A., & Kontsos, A. (2014). A data fusion approach for progressive damage quantification in reinforced concrete masonry walls. *Smart Materials and Structures*, *23*(1), 015007. https://doi.org/10.1088/0964-1726/23/1/015007

Wang, H., Shen, J., Liu, J., Lu, S., & He, G. (2019). Influence of carbon nanofiber content and sodium chloride solution on the stability of resistance and the following self-sensing performance of carbon nanofiber cement paste. *Case Studies in Construction Materials*, *11*, e00247. https://doi.org/10.1016/j.cscm.2019.e00247

Wang, H., Shi, F., Shen, J., Zhang, A., Zhang, L., Huang, H., Liu, J., Jin, K., Feng, L., & Tang, Z. (2021). Research on the self-sensing and mechanical properties of aligned stainless steel fiber-reinforced reactive powder concrete. *Cement and Concrete Composites*, *119*, 104001. https://doi.org/10.1016/j.cemconcomp.2021.104001

Wang, Y., Peng, K., Alrefaei, Y., & Dai, J. (2021). The bond between geopolymer repair mortars and OPC concrete substrate: Strength and microscopic interactions. *Cement and Concrete Composites*, *119*, 103991. https://doi.org/10.1016/j.cemconcomp.2021.103991

Wen, S., & Chung, D. D. L. (2007). Double percolation in the electrical conduction in carbon fiber reinforced cement-based materials. *Carbon*, *45*(2), 263–267. https://doi.org/10.1016/j.carbon.2006.09.031

Xiao, H., Li, H., & Ou, J. (2010). Modeling of piezoresistivity of carbon black filled cement-based composites under multi-axial strain. *Sensors and Actuators A: Physical*, *160*(1–2), 87–93. https://doi.org/10.1016/j.sna.2010.04.027

Xiao, H., Li, H., & Ou, J. (2011a). Self-monitoring Properties of Concrete Columns with Embedded Cement-based Strain Sensors. *Journal of Intelligent Material Systems and Structures*, *22*(2), 191–200. https://doi.org/10.1177/1045389X10396573

Xiao, H., Li, H., & Ou, J. (2011b). Strain sensing properties of cement-based sensors embedded at various stress zones in a bending concrete beam. *Sensors and Actuators A: Physical*, *167*(2), 581–587. https://doi.org/10.1016/j.sna.2011.03.012

Xiao, H., Li, H., & Ou, J. (2016). Self-sensing of nano-carbon black concrete. In *Innovative Developments of Advanced Multifunctional Nanocomposites in Civil and Structural Engineering* (pp. 59–78). https://doi.org/10.1016/B978-1-78242-326-3.00004-X

Xiao, H., Liu, M., & Jiang, J. (2015). Effect of aligning conductive particles on the piezoresistivity of composites. *Sensor Review*, *35*(1), 43–50. https://doi.org/10.1108/SR-08-2013-722

Xu, J., Butler, L. J., & Elshafie, M. Z. (2020). Experimental and numerical investigation of the performance of self-sensing concrete sleepers. *Structural Health Monitoring*, *19*(1), 66–85. https://doi.org/10.1177/1475921719834506

Zahra, T., Thamboo, J., & Asad, M. (2021). Compressive strength and deformation characteristics of concrete block masonry made with different mortars, blocks and mortar beddings types. *Journal of Building Engineering*, *38*, 102213. https://doi.org/10.1016/j.jobe.2021.102213

Zhang, L., Ding, S., Han, B., Yu, X., & Ni, Y.-Q. (2019). Effect of water content on the piezoresistive property of smart cement-based materials with carbon nanotube/nanocarbon black composite filler. *Composites Part A: Applied Science and Manufacturing*, *119*, 8–20. https://doi.org/10.1016/j.compositesa.2019.01.010

Zhang, Q., Luan, C., Yu, C., Huang, Y., & Zhou, Z. (2022). Mechanisms of carbon black in multifunctional cement matrix: Hydration and microstructure perspectives. *Construction and Building Materials*, *346*, 128455. https://doi.org/10.1016/j.conbuildmat.2022.128455

APPENDIX 7A: RESULTS OF STATISTICAL ANALYSES

7A.1. GRUBB'S TEST FOR OUTLIER DETECTION

The results obtained from the tests conducted on masonry components and prisms were subjected to a statistical based on Grubb's tests for detection of outliers.

7A.1.1. Hypothesis and significance level

- Null hypothesis (H_0): all values belong to the same population.
- Alternative hypothesis (H_a): the smallest or the largest value is an outlier.
- Significance level (α): 5%.

7A.1.2. Results of the statistical tests

The results of Grubb's test are presented in Table A1, Table A2, Table A3, Table A4, Table A5, Table A6, Table A7, Table A8 and Table A9.

Table A1 - Grubb's test statistical summary for modulus of elasticity results of masonry components.

Series	Average modulus of elasticity (GPa)	Standard deviation (GPa)	Minimum (GPa)	Maximum (GPa)	Grubb's test statistic	P-value
SCB	20.77	1.78	19.50	22.80	1.14	0.269
HCB	21.17	2.57	19.30	24.10	1.14	0.298
PM-0.25	22.80	1.10	21.70	23.90	1.00	1.000
PM-0.75	14.70	0.70	14.00	15.40	1.00	1.000
PM-1.50	9.97	1.47	8.30	11.10	1.13	0.391
SM-0.00	21.27	1.17	20.40	22.60	1.14	0.328
SM-0.25	21.10	2.08	18.70	22.40	1.15	0.092
SM-0.75	14.00	0.46	13.50	14.40	1.09	0.637
SM-1.50	9.37	1.07	8.70	10.60	1.15	0.089

Source: Author (2024).

Table A2 - Grubb's test statistical summary for Poisson's ratio results of masonry components.

Series	Average Poisson's ratio	Standard deviation	Minimum	Maximum	Grubb's test statistic	P-value
SCB	0.184	0.014	0.172	0.200	1.11	0.537
HCB	0.181	0.018	0.167	0.202	1.13	0.420
PM-0.25	0.147	0.005	0.143	0.150	*	*
PM-0.75	0.159	0.020	0.143	0.182	1.13	0.424
PM-1.50	0.159	0.020	0.143	0.182	1.13	0.424
SM-0.00	0.178	0.009	0.170	0.188	1.09	0.637
SM-0.25	0.157	0.014	0.142	0.169	1.09	0.637
SM-0.75	0.168	0.015	0.152	0.181	1.09	0.661
SM-1.50	0.177	0.020	0.157	0.196	1.01	0.972

Note: *G and P-value were not calculated for series PM-0.25 because one of the samples was inappropriately fractured during the test. Then, it was not possible to apply the Grubb's test with only two replicates.

Source: Author (2024).

Table A3 - Grubb's test statistical summary for compressive strength results of masonry components.

Series	Average compressive strength (MPa)	Standard deviation (MPa)	Minimum (MPa)	Maximum (MPa)	Grubb's test statistic	P-value
SCB	15.24	2.74	12.31	17.73	1.07	0.729
HCB	13.56	1.50	11.98	14.96	1.05	0.815
PM-0.25	28.52	0.97	27.62	29.55	1.06	0.792
PM-0.75	12.87	1.16	11.89	14.14	1.10	0.572
PM-1.50	8.13	1.39	6.55	9.13	1.14	0.298
SM-0.00	41.09	1.87	39.49	43.15	1.10	0.584
SM-0.25	35.87	0.79	35.10	36.67	1.03	0.913
SM-0.75	23.65	0.69	22.92	24.28	1.07	0.746
SM-1.50	10.48	0.85	9.50	11.03	1.15	0.144

Source: Author (2024).

Table A4 - Grubb's test statistical summary for gauge factor (GF) results of masonry components.

Series	Average GF	Standard deviation	Minimum	Maximum	Grubb's test statistic	P-value
SM-0.00	262.7	10.2	251	270	1.14	0.281
SM-0.25	303.0	11.8	293	316	1.10	0.576
SM-0.75	338.3	10.1	329	349	1.06	0.780
SM-1.50	347.7	14.6	334	363	1.05	0.811

Source: Author (2024).

Table A5 - Grubb's test statistical summary for net area compressive strength results of masonry prisms.

Series	Average net area compressive strength (MPa)	Standard deviation (MPa)	Minimum (MPa)	Maximum (MPa)	Grubb's test statistic	P-value
#1	17.46	1.51	16.23	19.14	1.11	0.504
#2	17.75	0.43	17.37	18.21	1.08	0.675
#3	13.16	1.57	11.50	14.61	1.06	0.774
#4	12.11	1.12	10.82	12.80	1.15	0.060
#5	12.08	1.02	11.30	13.24	1.13	0.374
#6	13.76	2.54	11.82	16.63	1.13	0.382
#7	11.63	0.59	11.21	12.04	*	*
#8	12.83	0.99	11.69	13.47	1.15	0.141
#9	8.40	0.63	7.67	8.85	1.14	0.284
#10	10.12	0.62	9.42	10.59	1.14	0.348
#11	11.11	0.89	10.12	11.85	1.11	0.532
#12	10.80	0.54	10.19	11.20	1.14	0.323

Note: *G and P-value of series #7 were not calculated due to issues in the data acquisition during the compression test of one of the specimens (it is not possible to apply the Grubb's test with only two replicates).

Source: Author (2024).

Table A6 - Grubb's test statistical summary for net area elastic modulus results of masonry prisms.

Series	Average modulus of elasticity (GPa)	Standard deviation (GPa)	Minimum (GPa)	Maximum (GPa)	Grubb's test statistic	P-value
#1	16.57	0.59	15.9	17.0	1.14	0.328
#2	16.73	2.10	15.1	19.1	1.13	0.413
#3	16.70	3.04	14.7	20.2	1.15	0.157
#4	16.97	1.80	14.9	18.2	1.15	0.213
#5	15.30	1.91	13.1	16.5	1.15	0.100
#6	17.23	1.92	15.5	19.3	1.08	0.712

#7	13.47	1.85	12.3	15.6	1.15	0.103
#8	20.67	2.70	18.0	23.4	1.01	0.959
#9	12.13	1.52	10.5	13.5	1.08	0.708
#10	16.80	0.20	16.6	17.0	1.00	1.000
#11	12.80	2.31	11.0	15.4	1.13	0.417
#12	14.53	1.02	13.8	15.7	1.14	0.281

Source: Author (2024).

Table A7 - Grubb's test statistical summary for GF results of B1 self-sensing region of masonry prisms.

Series	Average GF of B1self-sensing region	Standard deviation	Minimum	Maximum	Grubb's test statistic	P-value
#2	253.7	18.6	241	275	1.15	0.206
#5	262.3	19.9	240	278	1.12	0.437
#6	259.3	24.7	231	276	1.15	0.194
#7	274.0	18.5	255	292	1.03	0.911
#8	275.0	20.1	256	296	1.05	0.835
#9	263.7	18.3	243	278	1.13	0.420
#10	262.0	22.9	236	279	1.14	0.336
#11	277.3	16.6	262	295	1.06	0.767
#12	274.7	24.0	250	298	1.03	0.908

Source: Author (2024).

Table A8 - Grubb's test statistical summary for GF results of B2 self-sensing region of masonry prisms.

Series	Average GF of B2 self-sensing region	Standard deviation	Minimum	Maximum	Grubb's test statistic	P-value
#2	250.0	19.7	232	271	1.07	0.747
#5	259.0	22.6	235	280	1.06	0.780
#6	252.7	27.5	221	271	1.15	0.174
#7	266.3	19.4	245	283	1.10	0.600
#8	266.0	5.6	260	271	1.08	0.702
#11	272.0	14.7	256	285	1.09	0.661
#12	264.3	18.1	245	281	1.07	0.756

Source: Author (2024).

Table A9 - Grubb's test statistical summary for GF results of J1 and J2 self-sensing regions of the prisms.

Series	Average GF of J1 and J2 self-sensing regions	Standard deviation	Minimum	Maximum	Grubb's test statistic	P-value
#2 (J1)	368.3	14.2	352	378	1.15	0.202
#4 (J1)	395.3	18.6	380	416	1.11	0.520
#6 (J1)	395.7	6.0	390	402	1.05	0.817
#7 (J1)	446.7	24.7	430	475	1.15	0.194
#8 (J1)	284.0	9.6	277	295	1.14	0.298
#9 (J1)	398.0	11.8	388	411	1.10	0.576
#10 (J1)	392.7	9.7	382	401	1.10	0.600
#10 (J2)	478.3	18.2	462	498	1.08	0.696
#11 (J1)	397.0	12.5	385	410	1.04	0.868
#12 (J1)	394.3	7.4	386	400	1.13	0.391

Source: Author (2024).

7A.1.3. Conclusions of the statistical tests

A P-value higher than 0.050 was observed in all series. Therefore, H_0 was not rejected, which means that outliers were not found in the experimental dataset.

7A.2. SHAPIRO-WILK TEST OF NORMALITY

Experimental results were also subjected to the Shapiro-Wilk test to evaluate the normality of residuals, which is one of the analysis of variance (ANOVA) assumptions.

7A.2.1. Hypothesis and significance level

- Null hypothesis (H_0): residuals are normally distributed.
- Alternative hypothesis (H_a): residuals are not normally distributed.
- Significance level (α): 5%.

7A.2.2. Results of the statistical tests

The results of Shapiro-Wilk's tests are shown in Table A10.

Table A10 - Shapiro-Wilk's test statistical summary for all response variables.

Response variable	Shapiro-Wilk's test statistic	P-value
Modulus of elasticity of masonry components	0.977	0.781
Poisson's ratio of masonry components	0.950	0.227
Compressive strength of masonry components	0.984	0.875
GF of masonry components	0.934	0.428
Compressive strength of masonry prisms	0.967	0.373
Modulus of elasticity of masonry prisms	0.969	0.390
GF of B1 region of masonry prisms	0.940	0.119
GF of B2 region of masonry prisms	0.927	0.123
GF of J1 and J2 regions of masonry prisms	0.959	0.292

Source: Author (2024).

7A.2.3. Conclusions of the statistical tests

P-values were always higher than 0.050 (H_0 was not rejected). Regardless of the response variable, the residuals are normally distributed.

7A.3. BARTLETT TEST OF HOMOSCEDASTICITY

Results of compression and piezoresistive tests of masonry components (SMs, PMs, SCBs and HCBs) and masonry prisms were also subjected to the Bartlett's test to evaluate homoscedasticity, which is another ANOVA assumption.

7A.3.1. Hypothesis and significance level

- Null hypothesis (H_0): all population variances are equal.
- Alternative hypothesis (H_a): at least two population variances are different.
- Significance level (α): 5%.

7A.3.2. Results of the statistical tests

The results of Bartlett's tests are shown in Table A11.

Table A11 - Bartlett's test statistical summary for all response variables.

Response variable	Bartlett's K-squared	P-value
Modulus of elasticity of masonry components	6.515	0.590
Poisson's ratio of masonry components	5.352	0.719
Compressive strength of masonry components	5.822	0.667
GF of masonry components	0.309	0.958
Compressive strength of masonry prisms	10.037	0.527
Modulus of elasticity of masonry prisms	11.279	0.420
GF of B1 region of masonry prisms	2.890	0.941
GF of B2 region of masonry prisms	3.499	0.744
GF of J1 and J2 regions of masonry prisms	5.511	0.788

Source: Author (2024).

7A.3.3. Conclusions of the statistical tests

All analyses provided P-values significantly higher than 0.050 (H_0 was not rejected). Regardless of the response variable, homoscedasticity was observed in the obtained data.

7A.4. ANALYSIS OF VARIANCE (ANOVA)

ANOVAs were carried out to compare the averages obtained in compression and piezoresistive tests of masonry components (SMs, PMs, SCBs and HCBs) and prisms.

7A.4.1. Hypothesis and significance level

- Null hypothesis (H_0): all means are equal.
- Alternative hypothesis (H_a): at least one mean is different.
- Significance level (α): 5%.

7A.4.2. Results of the statistical tests

All ANOVA results are shown in Table A12, Table A13, Table A14, Table A15, Table A16, Table A17, Table A18, Table A19 and Table A20.

Table A12 - ANOVA statistical summary for the modulus of elasticity of masonry components.

Source	Degrees of freedom	Sum of squares	Mean Square	F test statistics	P-value
Treatments	8	665.17	83.15	36.209	1.5×10^{-9}
Residuals	18	41.33	2.30	-	-
Total	26	706.50	-	-	-

Source: Author (2024).

Table A13 - ANOVA statistical summary for the Poisson's ratio of masonry components.

Source	Degrees of freedom	Sum of squares	Mean Square	F test statistics	P-value
Treatments	8	0.00359	0.000449	1.222	0.344
Residuals	17	0.00625	0.000368	-	-
Total	25	0.00984	-	-	-

Source: Author (2024).

Table A14 - ANOVA statistical summary for the compressive strength of masonry components.

Source	Degrees of freedom	Sum of squares	Mean Square	F test statistics	P-value
Treatments	8	3357.7	419.71	196.33	6.6×10^{-16}
Residuals	18	38.5	2.14	-	-
Total	26	3396.1	-	-	-

Source: Author (2024).

Table A15 - ANOVA statistical summary for the GF of masonry components.

Source	Degrees of freedom	Sum of squares	Mean Square	F test statistics	P-value
Treatments	3	13431	4477.0	32.151	8.2×10^{-5}
Residuals	8	1114	139.2	-	-
Total	11	14545	-	-	-

Source: Author (2024).

Table A16 - ANOVA statistical summary for the compressive strength of masonry prisms.

Source	Degrees of freedom	Sum of squares	Mean Square	F test statistics	P-value
Treatments	11	246.66	22.42	15.47	4.1×10^{-8}
Residuals	23	33.35	1.45	-	-
Total	34	280.01	-	-	-

Source: Author (2024).

Table A17 - ANOVA statistical summary for the modulus of elasticity of masonry prisms.

Source	Degrees of freedom	Sum of squares	Mean Square	F test statistics	P-value
Treatments	11	180.31	16.39	4.47	1.1×10^{-3}
Residuals	24	87.95	3.66	-	-
Total	35	268.27	-	-	-

Source: Author (2024).

Table A18 - ANOVA statistical summary for the GF of B1 self-sensing region of masonry prisms.

Source	Degrees of freedom	Sum of squares	Mean Square	F test statistics	P-value
Treatments	8	1405.3	175.67	0.544	0.808
Residuals	18	5810.7	322.81	-	-
Total	26	7216.0	-	-	-

Source: Author (2024).

Table A19 - ANOVA statistical summary for the GF of B2 self-sensing region of masonry prisms.

Source	Degrees of freedom	Sum of squares	Mean Square	F test statistics	P-value
Treatments	6	1135.2	189.21	0.507	0.793
Residuals	14	5226.0	373.29	-	-
Total	20	6361.2	-	-	-

Source: Author (2024).

Table A20 - ANOVA statistical summary for the GF of J1 and J2 self-sensing regions of masonry prisms.

Source	Degrees of freedom	Sum of squares	Mean Square	F test statistics	P-value
Treatments	9	67996	7555.1	36.634	1.7×10^{-10}
Residuals	20	4125	206.2	-	-
Total	29	72121	-	-	-

Source: Author (2024).

7A.4.3. Conclusions of the statistical tests

The P-value was higher than 0.05 (H_0 was not rejected, i.e., all means are statistically equal) when evaluating the Poisson's ratio of the masonry components and the gauge factor of the B1 and B2 self-sensing regions of the masonry prisms. When evaluating the other response variables, the P-value was lower than 0.05 (H_0 was rejected, i.e., all means are not statistically equal). Tukey's tests (α =5%) were used to detect the average values that are statistically different from the others. The graphs of the main text of this work indicate the results of these post-hoc tests.

APPENDIX 7B: IMAGES OF FAILURE MODES OF MASONRY PRISMS

Figure B1 - Failure modes of masonry prisms S1, S2 and S3 of series #1, #2, #3 and #4.

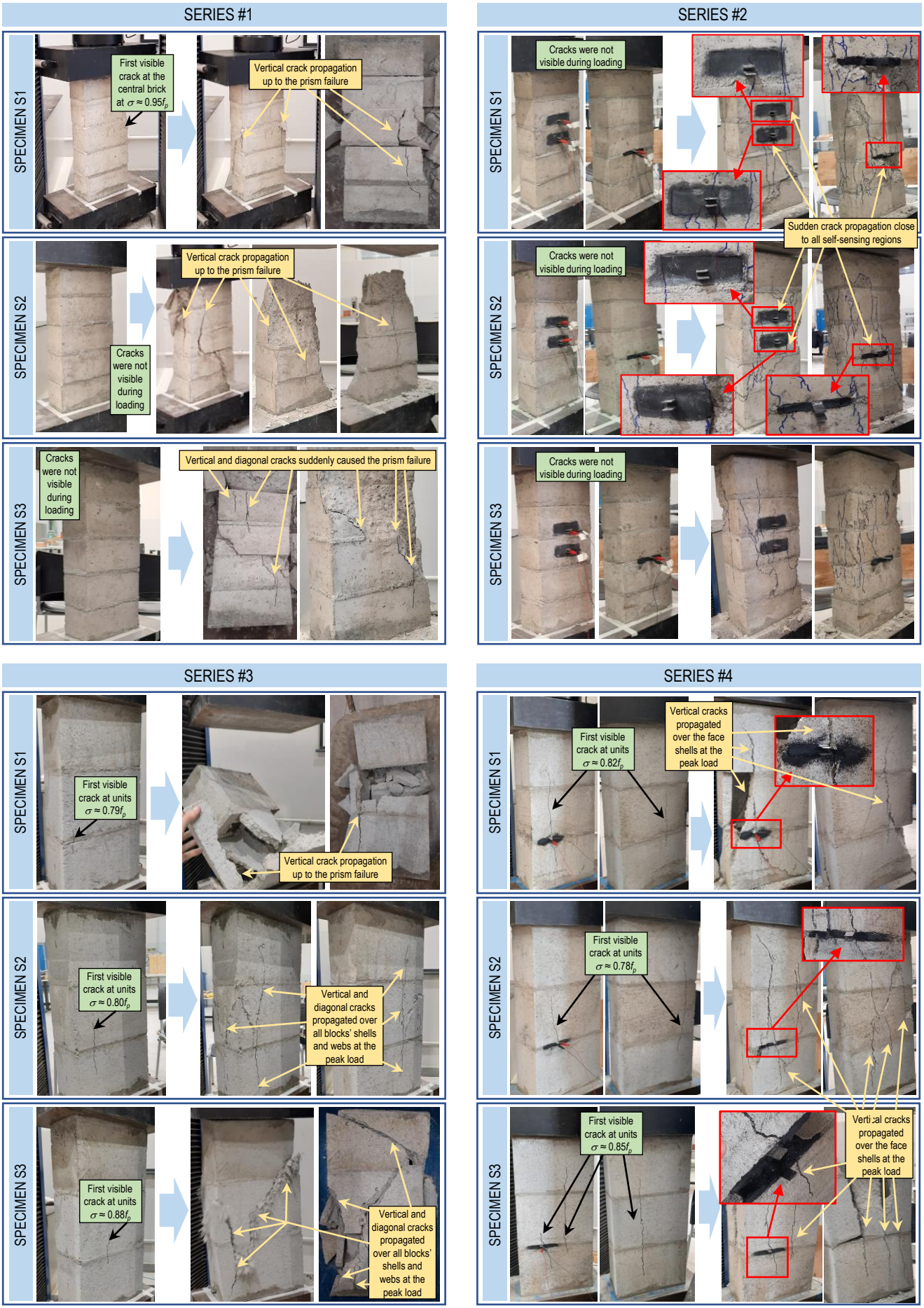

Source: Author (2024).

Figure B2 - Failure modes of masonry prisms S1, S2 and S3 of series #5, #6, #7 and #8.

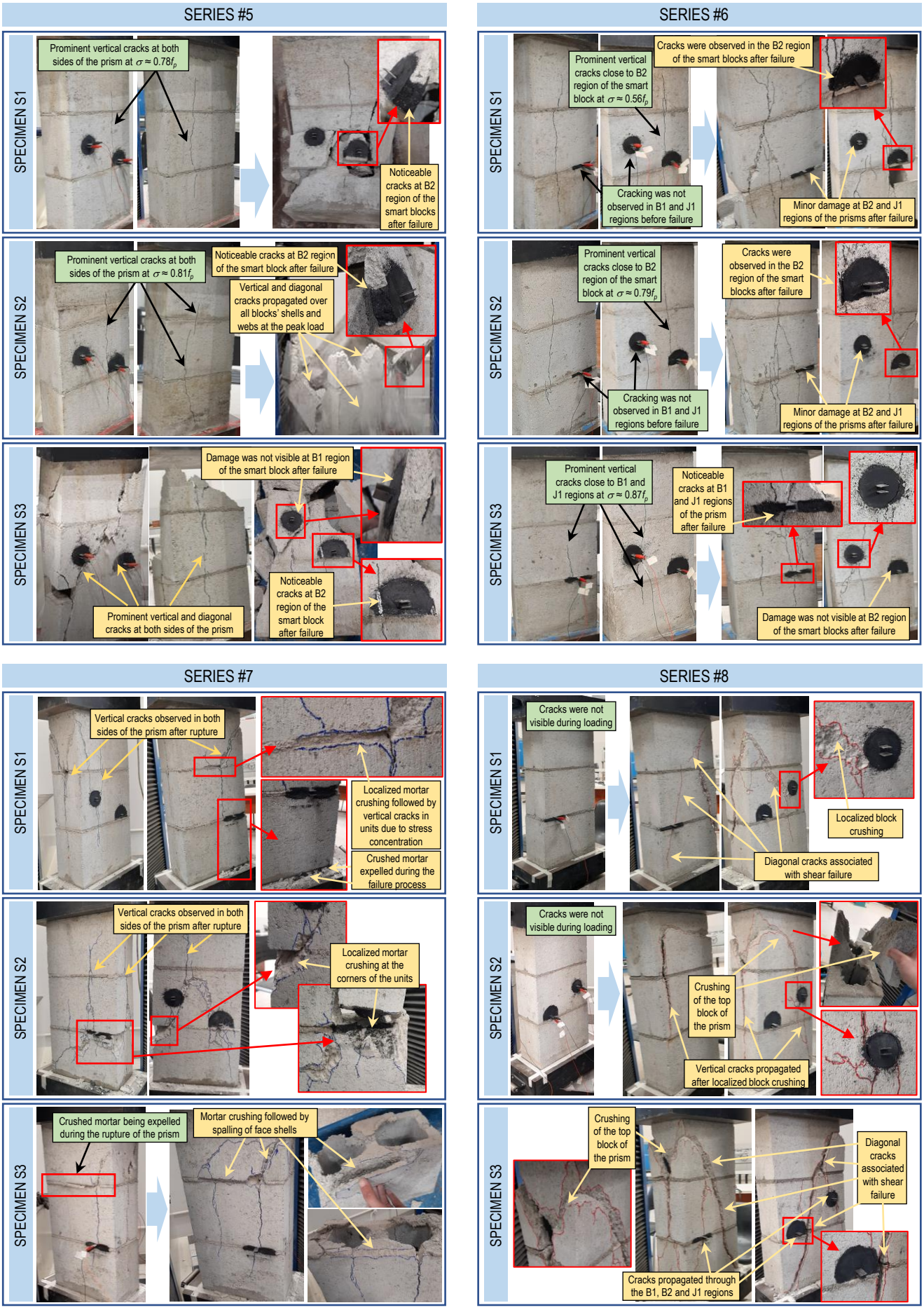

Source: Author (2024).

Figure B3 - Failure modes of masonry prisms S1, S2 and S3 of series #9, #10, #11 and #12.

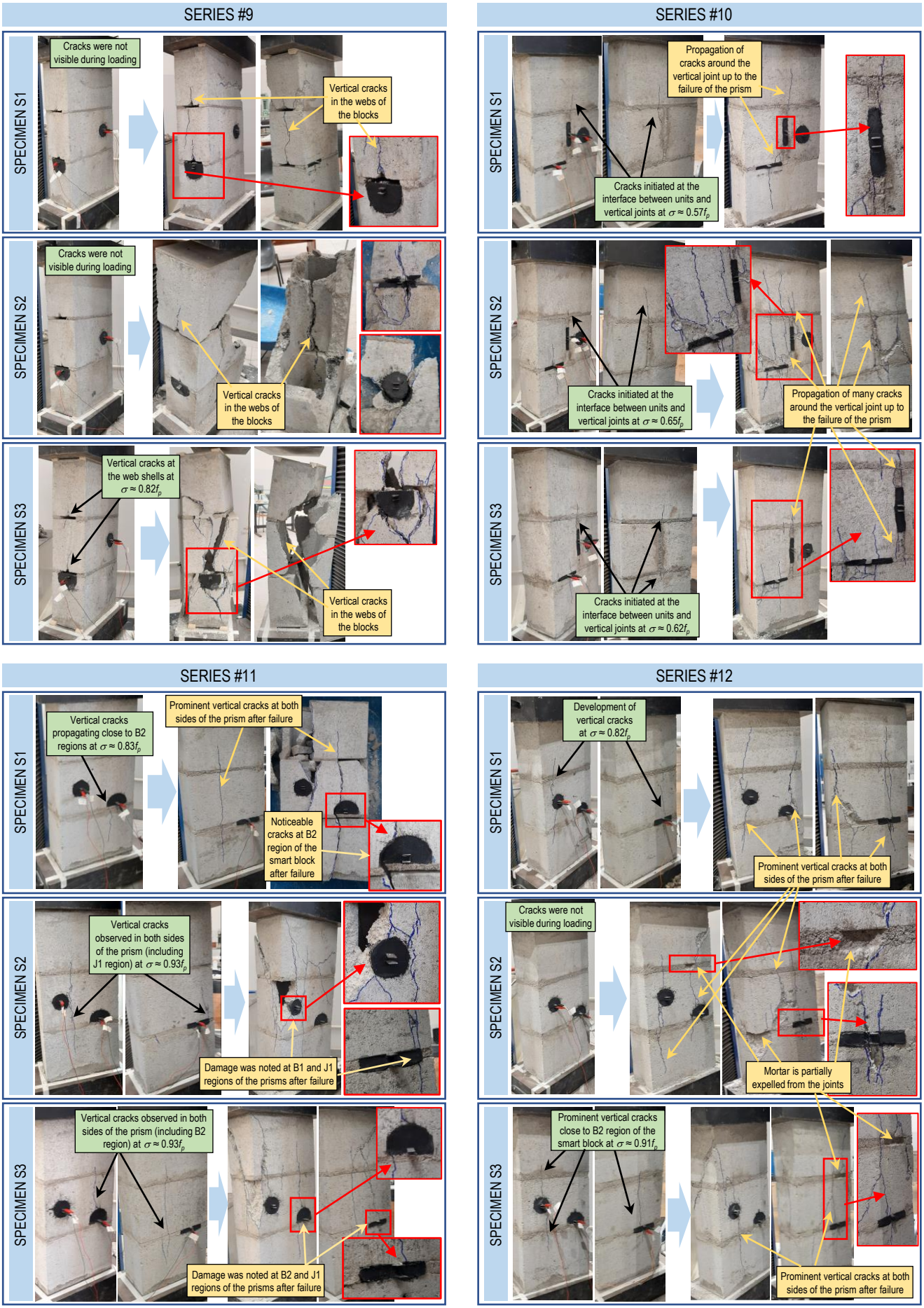

Source: Author (2024).

PART IV:

VALIDATION STUDY ON SELF-SENSING MASONRY ELEMENTS EXPOSED TO HIGH TEMPERATURES

8 THERMAL ANALYSIS OF CONCRETE BLOCKS AND STACK-BOND PRISMS UNDER DIFFERENT BOUNDARY CONDITIONS

This chapter has been published as the following paper: Nalon, G. H.; Ribeiro, J. C. L.; Pedroti, L. G.; Silva, R. M.; Araújo, E. N. D. Thermal analysis of concrete blocks and stack-bond prisms under different boundary conditions. ***Construction Materials*** *4 (2024) 58-71.*
https://doi.org/10.3390/constrmater4010004

Abstract: *Fire is a big threat to human lives and to the integrity of buildings. To better understand the complex behavior of masonry exposed to high temperatures, thermal analyses were carried out to evaluate the temperature distribution in concrete blocks and stack-bond prisms exposed to high temperature levels. The effects of distinct specimen boundary conditions (restrict or easy access to air circulation inside the voids of the block and prisms) on the thermal response of the masonry materials were investigated. Thersys 2.0 software was used to implement three-dimensional thermal analysis of distinct finite element models. Four-node tetrahedral elements and full integration were used in all models. The modeling approach was validated by experimental data obtained from thermocouples embedded into masonry components. The results indicated that the boundary conditions significantly affected the time required for homogenization of temperature in blocks and prisms. Easy access to air circulation inside the voids of the prisms provided a faster temperature homogenization. In this scenario, the prism reached temperature ranges of (300 ± 0.5%×300) ºC and (600 ± 0.5%×600) ºC after exposure times of 2 h and 2 h 10 min, respectively. When access to air circulation within the voids of the prisms was limited, the same temperature ranges were achieved after exposure times of 5 h 20 min and 6 h, respectively.*

Keywords: *masonry prisms; concrete blocks; mortars; modeling; fire; thermal properties of materials; finite element method.*

8.1. INTRODUCTION

Fire is a significant threat to the human lives and to the integrity of buildings. After exposure to elevated temperatures, masonry elements undergo a series of temperature-dependent physicochemical transformations and phase changes that degrade their original strength and stiffness (Daware and Naser, 2021; Russo and Sciarretta, 2013; Yassin et al., 2018). In the face of increasing fire incidents, a comprehensive investigation of the heat transfer mechanisms of masonry elements is essential to ensure the protection of life and masonry structures.

In fire tests of construction materials, the specimens are exposed to hot gases, so that heat transfer occurs through radiation from furnace's heating instruments and convection mechanisms (Assis and Neto, 2020). Masonry prisms have been widely used to investigate the behavior of masonry exposed to high temperatures, as they are more cost-effective specimens compared to masonry walls. Moreover, these types of samples are easier to construct and test. Fire tests of masonry prisms may provide interesting information about the masonry compressive behavior, in addition to the economic benefits associated with the small size of these types of specimens (Nalon et al., 2023).

Some fire tests of masonry prisms have been carried out in computer-controlled electrical furnaces. For example, Leal (2023) recently exposed masonry prisms to different temperatures levels (200, 400, 600 and 800 °C) in a horizontally oriented furnace with side openings and sliding doors. To optimize the convection mechanisms within the hollow spaces of the prisms, the specimens were strategically placed on supports, ensuring both elevation and central positioning inside the furnace. Then, the authors obtained normalized degradation curves of mechanical properties of concrete masonry prisms. Kiran et al. (2022) exposed prisms of solid clay brick to the standard ISO 834 (1999) curve (30, 60, 90 and 120 min) and natural cooling, using an electric furnace with inner dimensions of 700 mm × 400 mm × 400 mm. Reference prisms (without plaster) failed after a heating exposure higher than 60 min, whereas prisms coated with sand mortar, vermiculite mortar, or perlite mortar demonstrated superior fire resistance. Prisms of solid clay brick were also heated up to different temperature levels (200, 400 or 600 ºC) in a box muffle furnace by Gao et al. (2023), followed by natural cooling. They verified that the best residual strength improvements were provided by a reinforced layer of PVA (poly vinyl acetate) and steel fibers. Bittencourt and

Antunes (2019) placed hollow clay block prisms on the insulation floor of an electrical furnace and exposed them to different levels of high temperature (300, 600 or 900 ºC) and natural cooling. The high thermal resistance of hollow clay units provided excellent residual mechanical properties to the masonry prisms.

Gas furnaces with high heating capacity have been also used in fire tests of masonry prisms. For instance, Leal et al. (2021) tested concrete block prisms and small walls exposed to the standard ISO 834 curve (1999) for 70 min and natural cooling in a gas furnace with inner dimensions of 4 m × 3 m × 1.5 m. A ceramic fiber blanket was placed on the top and bottom ends of the specimens. Fire-damaged prisms and small walls exhibited a compressive strength of approximately 14% compared to their initial strength. Neto (2020) also investigated clay block prisms exposed to the standard ISO 834 curve (1999) for 120 min and fan cooling in a gas furnace. The specimens presented mechanical properties reductions up to 98.5% after exposure to 900 ºC. Dupim (2019) reported fire tests of concrete block prisms exposed to the standard ISO 834 curve (1999) for 70 and 120 min and fan cooling in a gas furnace. Specimens covered with a plaster layer and heated for 120 min presented residual compressive strength values from 6% to 9% of their initial strength.

In this context, the thermal analysis of masonry prisms is of paramount importance to understand the behavior and performance of materials under such extreme conditions. According to Torregrosa and Diez (2015), the thermal behavior of masonry elements is very complex, depending on the intrinsic characteristics of masonry units and mortar joints. Heat transfer takes place by conduction mechanisms in the components' solid parts, and by convection and radiation mechanisms on the external surfaces and surfaces of the cavities of the masonry elements. Assis and Neto (2020) verified an important role in the radiation mechanisms inside the cavities of concrete blocks. Consequently, the contribution of air convection mechanisms to heat transfer inside the voids was negligible when high emissivity values were used on the cavities surface.

The boundary conditions of the specimens during the fire tests have a substantial impact on their temperature distribution profile, as these conditions determine how heat is transferred and dissipated. Although different boundary conditions have been used in the previous fire tests of masonry prisms, there is no systematic evaluation of the thermal response associated with these distinct test methods.

Numerical analyses have been widely used for investigation of the thermal behavior of masonry structures (Oliveira et al., 2021; Prakash et al., 2020; Sciarretta, 2014), as numerical

models can provide detailed and continuous temperature distributions throughout the entire analyzed domain. Due to the limited number of thermocouples, it is hard for the experimental analyses to achieve a high level of detail in capturing the temperature distribution of complex systems. Additionally, the challenges associated with the placement of thermocouples inside the masonry specimens pose inherent difficulties. The insertion of thermocouples can change the natural thermal flow within the materials, potentially influencing the temperature distribution being measured.

For example, Russo and Sciarretta (2016) used the DIANA 9.6 (DIANA FEA BV, Delft, Netherlands) software to develop the structural analysis of heat-damaged models of stack-bond prisms produced with hollow clay blocks with different ratios between net and gross area (α), i.e., α = 1.00, 0.70, 0.55 or 0.40. Their objective was to capture the cracking behavior under both thermal and mechanical stresses. This software provided a heat flow analysis that reproduced the heat transmission throughout the specimen and its hollows. A constant density was used for blocks and mortar, the specific heat was not presented and equivalent thermal conductivity values were was used to treat the air cavities as a fictitious material and account for the heat exchange inside the voids of the blocks. Stress-strain curves were input for masonry units and mortar joints. The authors simulated the thermo-mechanical behavior of the different models during and after the standard fire exposure prescribed in ISO 834-1 (1999). However, the authors emphasized the need for further experimental validation to support the calibration of the model.

Using the finite element method (FEM) software MASA (Macroscopic Space Analysis, University of Stuttgart, Germany), Bošnjak et al. (2020; 2019) carried out thermo-mechanical numerical analyses of stack-bond prisms of masonry made of solid calcium silicate bricks. Their experimental and numerical studies aimed to provide more information for the assessment of fire-damaged masonry structures. The authors used 4-node tetrahedral elements to mesh the masonry components. The specific mass, thermal conductivity and specific heat of the materials of the numerical models were not reported. The microplane model with a relaxed kinematic constraint was used as the constitutive law for quasi-brittle materials. Additionally, the assumption of a perfect bond was made between mortar and bricks. According to the authors, their model appeared to be suitable for simulating the behavior of masonry elements exposed to elevated temperatures. According to Bošnjak et al. (2020; 2019), further validation with a more complete database (tests at both the specimen and component levels) is needed to finalize the modeling parameters.

Rodovalho and Corrêa (2019) carried out a thermal simulation of FEM models of stack-bond prisms made of hollow concrete blocks elaborated in the ABAQUS software (SIMULIA, USA). The primary objective of their work was to assess the thermal insulation capacity of concrete block masonry in a fire situation, based on numerical simulations of masonry prisms. The masonry components were generated using elements belonging to the DC3D8 "heat transfer" family. The authors modeled the fluid domain inside the cavities of the blocks using solid elements of the FC3D8 "fluid" family and applied the fluid-structure interactions. The radiation in the voids of the blocks was not represented. Variations of specific mass, thermal conductivity and specific heat with temperature were obtained from various papers published in the literature. The authors only applied the temperature increases to the external faces of the prisms that were directly exposed to the inner chamber of an oven. The numerical models were validated by comparing the average temperature increases obtained numerically with the results of a masonry experiment featuring mortar coating on the specimen's face exposed to fire.

The ABAQUS software was also used by Rodovalho, Corrêa and Neto (2020) to carry out thermo-mechanical numerical investigations of FEM models of stack-bond prisms exposed to high temperatures. The authors aimed to numerically verify the mechanical strength of concrete block prisms under compression and fire conditions. According to the authors, the thermal properties used in these models were the same used in the paper published by Rodovalho and Corrêa (2019). The stress-strain curves and damage models were obtained from various papers published in the literature. A satisfactory alignment was achieved between the experimental and numerical stress-strain curves in room temperature. Nevertheless, the results from the thermo-mechanical simulations were not validated through experimental data.

FEM models of stack-bond prisms produced with hollow clay blocks with different geometries were evaluated in thermal numerical analyses carried out by Quispe et al. (2023), using the ABAQUS software. These authors aimed to numerically analyze heat transfer mechanisms in masonry prisms under fire conditions. The DC3D8 "heat transfer" finite element was used. Three different types of numerical approaches were investigated: a homogenized model, a detailed model with constant thermal properties, and a detailed model with thermal properties varying with temperature. The authors modeled a volume of air inside the cavities of the prisms to account for radiation and convection mechanisms. The results indicated that the homogenization approach provided conservative estimates. However, its

computational demand was minimal when compared to that required by the other modelling approaches. Moreover, decreases in the value of α caused thermal insulation gains due to the low thermal conductivity of the air. Experimental studies were not carried out to validate the numerical results.

Depending on the location of masonry blocks and prims inside the furnace and the distribution of the furnace's heating instruments, the specimens will be subjected to different boundary conditions during the fire tests, which may change the heat transfer mechanisms inside their voids. Thorough attention must be given to the exposure of the open ends of hollow specimens to the heating instruments of the furnace. The specimens are sometimes placed directly on the insulating floor of the furnace. When at least one end of the specimens is covered with insulation material, the air circulation within the voids is restricted, potentially affecting the temperature distributions during the heating process because convection mechanisms are mitigated and heat conduction through the air mass emerges as the predominant mode of heat transfer. On the other hand, placing the open ends close to the heating instruments promotes relevant air circulation within the voids of the specimens, which can decrease the time required for the experimental tests. This configuration enables convective interactions between the internal surface of the specimens and the hot gases, in addition to conduction mechanisms within the air mass.

However, the existing body of research lacks both experimental and numerical investigations of the complex patterns of temperature distribution within concrete blocks and stack-bond prisms. Previous studies have not undertaken a comparison of the influence of different boundary conditions on the thermal behavior of masonry specimens during heating tests. In addition, the formation of convection currents in voids of masonry blocks and prisms was not investigated in previous research and is often overlooked in fire tests. Moreover, there is a discernible gap in the literature regarding practical guidance on the time required for temperature homogenization of masonry specimens.

To fill this knowledge gap, the present work presents thermal analyses for evaluation of the temperature distribution in concrete blocks and stack-bond prisms exposed to different temperature levels, considering the effects of distinct boundary conditions. The following contributions derived from this study: (i) new insights on the intricate patterns of temperature distribution within concrete blocks and stack-bond prisms under predefined conditions; (ii) exploration of the nuanced effects of different boundary conditions typically used in fire tests on the thermal response of masonry prisms exposed to high temperatures, which contributes

for refining fire testing methodologies; (iii) study of the impacts of the formation of convection currents inside the voids of the masonry specimens, exploring an aspect that has been neglected in fire tests carried out in previous research; and (iv) practical orientation related to the time required for temperature homogenization of concrete masonry materials subjected to elevated temperatures, contributing to the improvement of fire testing protocols for masonry materials. These contributions not only advance the current understanding of temperature distribution mechanisms but also hold practical implications, contributing to the enhancement of precision in fire testing methodologies for masonry structures.

This chapter has been organized into four sections. Section 8.1 provides an overview of previous literature regarding the thermal behavior of masonry prisms and highlights the contributions of this study. Section 8.2 shows the materials and methods used for conducting both experimental and numerical thermal analyses. Section 8.3 presents the findings derived from the experimental and numerical analyses, followed by discussions aimed at elucidating the significance of the obtained results. Section 8.4 elucidates the main conclusions drawn from this study, along with recommendations for future research in this scientific field.

8.2. MATERIALS AND METHODS

8.2.1. Experimental analysis

Hollow concrete blocks donated by BLOJAF were characterized according to ABNT NBR 12118 (2013), which is similar to the ASTM C140M (2020). The characterization of these masonry units is summarized in Table 1. These blocks were used in experimental tests for validation of the numerical analysis (Section 8.2.2) developed in the present research.

Table 1 - Characterization data of hollow concrete blocks.

Parameter	Average	SD
Length (mm)	289.3	0.3
Width (mm)	138.8	0.4
Height (mm)	189.9	0.8
Face shell's thickness (mm)	26.3	0.3
Web's thickness (mm)	26.4	0.2
α value (%)	57.8	0.4
Net area compressive strength (MPa)	17.4	1.1
Water absorption (%)	6.0	0.4
Density (g/cm³)	2.16	0.03

Notes: SD = standard deviation. α = ratio between net and gross area.

Source: Author (2024).

A K-type thermocouples was embedded into a hole drilled in the blocks' webs (diameter of 8 mm), using a bench drill machine (Figure 1a). The location and depth of the hole are indicated in Figure 1b. Then, the hole was filled with cement paste, taking special care to eliminate any gaps or fixation failures, according to recommendations provided by Medeiros, Parsekian and Moreno Junior (2022).

Figure 1 - Hole drilled in the concrete blocks (a) and position and dimensions of the hole (b).

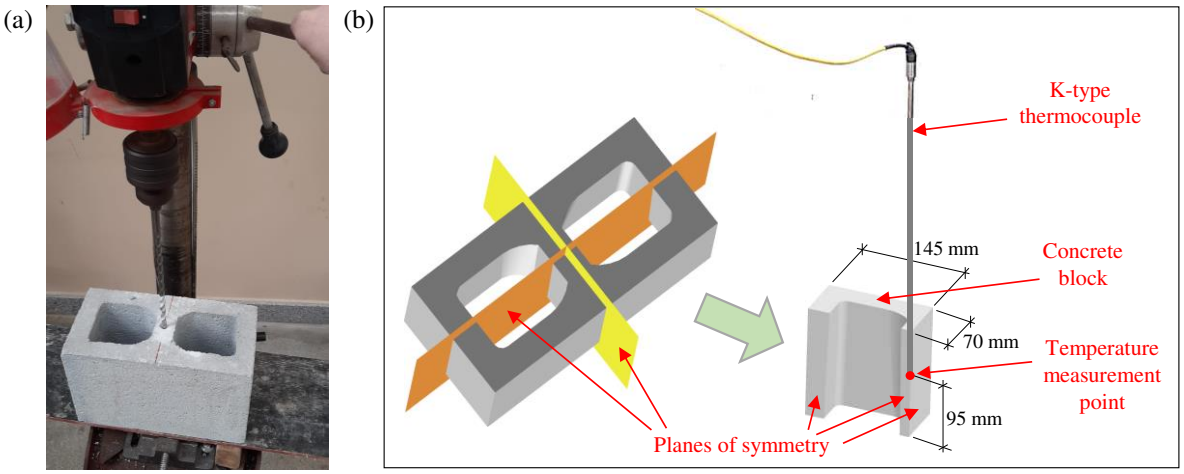

Source: Author (2024).

Dried concrete blocks were tested in a computer-controlled electrical furnace with inner dimensions of 750 mm × 750 mm × 600 mm (Figure 2a). The heating curve was defined by a linear temperature increase (rate of 7 ºC/min) up to 300 ºC, which was kept constant for 3 hours. After that, the specimens were cooled naturally inside the furnace. Two different scenarios were investigated: restrict access to air circulation inside the voids of the block (BC1), and easy access to air circulation inside the voids of the block (BC2). In the BC1 scenario, the block was placed on an insulating floor typically used in electrical furnaces (Figure 2b), as demonstrated by Bittencourt and Antunes (2019). In the BC2 scenario, the insulating floor was removed and the block was positioned upright to facilitate air circulation within its voids (Figure 2c), mirroring the experimental methods used by Leal (2023).

Temperature measurements were acquired using the NI (National Instruments) data acquisition (DAQ) system cDAQ-9178 and a NI 9219 module (acquisition rate of 1 Hz) indicated in Figure 2a. One thermocouple was used to monitor the temperature inside the furnace chamber and another thermocouple was used to monitor the temperature at the middle web and middle height of the concrete block.

Figure 2 - Experimental setup used heat the masonry components (a), according to the BC1 (b) and BC2 (c) configurations.

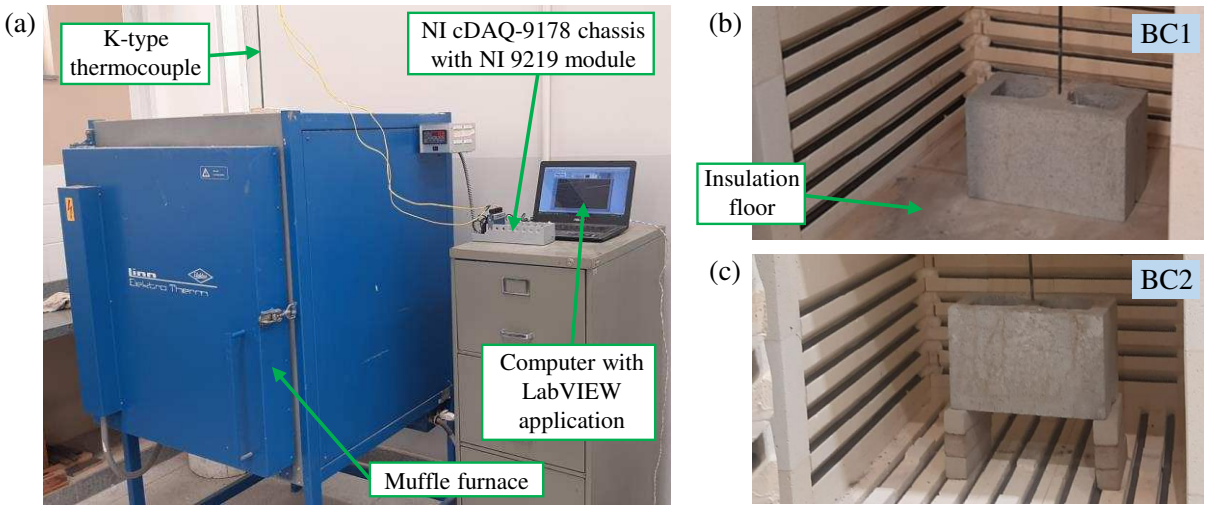

Source: Author (2024).

8.2.2. Numerical analysis

Numerical simulations of different masonry specimens were carried out in the Thersys 2.0 software (Universidade Federal de Minas Gerais, Belo Horizonte, Brazil), which is based on the FEM and enables the use of different types of bidimensional isoparametric elements (e.g., 3-node triangle element, 6-node triangle element, 4-node quadrilateral element and 8-node quadrilateral element) or tridimensional isoparametric elements (e.g., 4-node tetrahedral element, 10-node tetrahedral element, 8-node hexahedral element and 20-node hexahedral element). This software deals with conduction heat transfer in the structure domain, in addition to radiation and convection mechanisms between hot gases and the surface of the structure. It supports the utilization of different fire curves, enables the modeling of solid structures, and incorporates non-linear thermal properties of materials. Further details regarding the implementation and validation of this software are discussed in previous literature (Ribeiro et al., 2013, 2011, 2008; Ribeiro, 2009). Additionally, various researchers have demonstrated practical applications of the software (Castro, 2005; Costa, 2005; Gerken, 2007; Moreira, 2013). The elaboration of the graphical modeling environment, the generation of the FEM mesh and the visualization of results are developed using the GiD tool, a pre and post processor for numerical simulations developed by the International Center for Numerical Methods in Engineering (CIMNE, 2004).

Six distinct analyses were evaluated in the present work, whose characteristics are listed in Table 2. The heating curve of all simulations was defined by a linear temperature

increase (rate of 7 ºC/min) up to a maximum exposure temperature level (300 ºC or 600 ºC), which was kept constant until the end of each different analysis (Figure 3). The emissivity coefficient ε_m and the convection coefficient α_c were equal to 0.7 and 25 W/(m².ºC), respectively (CEN, 2005; EN 1991-1-2, 2002; EN 1996-1-2, 2010). The Galerkin scheme was used for temporal integration with a time interval Δt of 5 s.

Table 2 - Characteristics of the models evaluated in the thermal analyses.

Analysis	Model composition	Boundary conditions	Maximum exposure temperature
BC1-300	B + AM	BC1	300 ºC
BC2-300	B	BC2	
PC1-300	P + AM	PC1	
PC2-300	P	PC2	
PC1-600	P + AM	PC1	600 ºC
PC2-600	P	PC2	

Source: Author (2024).

Figure 3 - Heating curves used in the BC1-300, BC2-300, PC1-300, PC2-300, PC1-600 and PC2-600 numerical analyses.

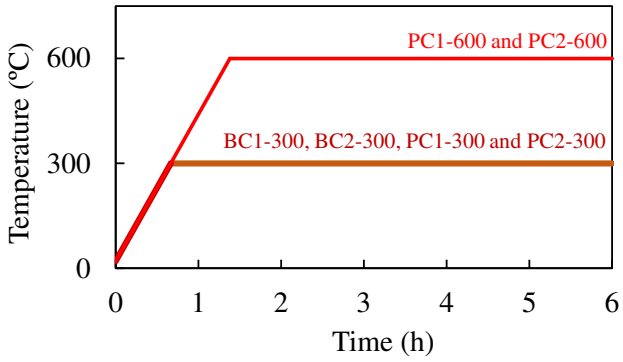

Source: Author (2024).

To reduce computational efforts, the finite element models were simplified based on thermal symmetries of hollow concrete blocks and stack-bond prisms composed of three blocks and two mortar joints. The geometry of the blocks and joints and the position of the longitudinal and transversal planes of symmetry are represented in Figure 4, in addition to the simplified models evaluated in the numerical analyses.

Figure 4 - Dimensions (in millimeters) and thermal symmetry conditions used in the definition of the numerical models.

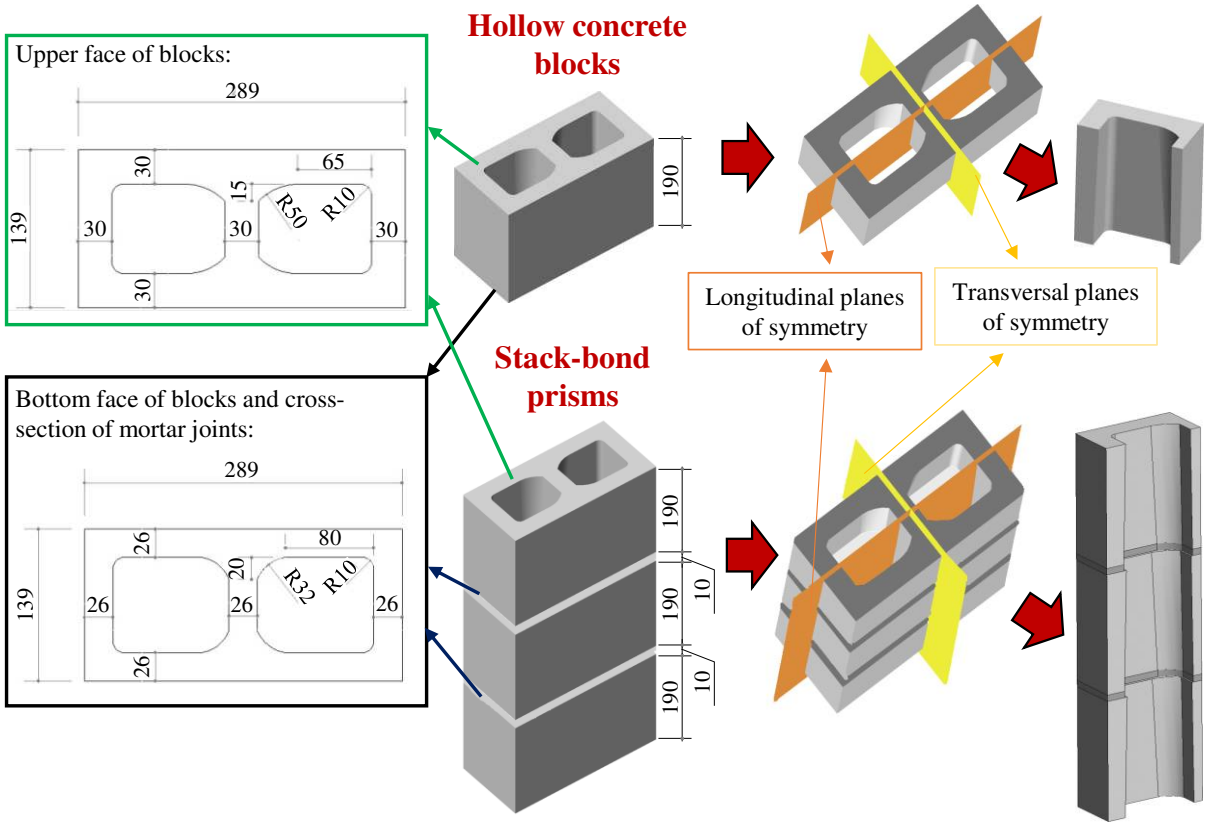

Source: Author (2024).

The models were composed of a single hollow concrete block (B), single hollow concrete block + air mass in its voids (B + AM), stack-bond prism (P), or stack-bond prism + air mass in its voids (P + AM), as indicated in Table 2 and illustrated in Figure 5. Four-node tetrahedral elements and full integration were used in all models. Full integration is commonly preferred for the development of tridimensional finite elements to address numerical instabilities and convergence problems, by providing the exact integrals for the elements' stiffness matrix (Bettaieb et al., 2015; Jain and Kapuria, 2022; Kim and Huh, 1998). Some analyses were conducted to obtain viable and useful FEM models, in terms of accuracy and computational time. They resulted in the mesh configurations, number of elements and nodes, and resolution of FEM elements indicated in the models represented in Figure 5.

Figure 5 - Finite element mesh, number of nodes and elements of the different numerical models.

B + AM (single block + air mass)	B (single block)	P + AM (stack-bond prism + air mass)	P (stack-bond prism)
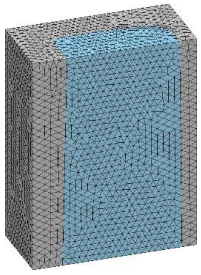	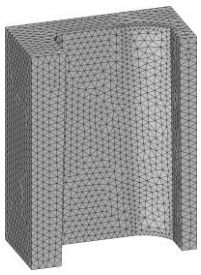	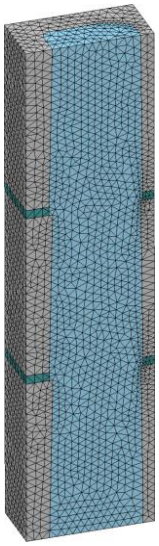	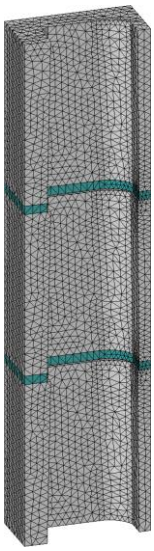
Nodes: 16297 Elements: 86644 Resolution: 6 mm	Nodes: 10412 Elements: 51167 Resolution: 6 mm	Nodes: 15701 Elements: 81185 Resolution: 10 mm	Nodes: 12172 Elements: 56955 Resolution: 10 mm

Source: Author (2024).

One of the objectives of the thermal analyses was to investigate the effects of different specimen boundary conditions due to the formation of convection currents inside the voids of blocks and prisms. Four different situations were investigated: restrict access to air circulation inside the voids of the block (BC1) and the prism (PC1), and easy access to air circulation inside the voids of the block (BC2) and the prism (PC2). Figure 6 illustrates the thermal exposure faces and thermal insulation faces of BC1, BC2, PC1 and PC2 boundary conditions, which were applied to the B + AM, B, P + AM, and P models, respectively. In the BC2 and PC2 boundary conditions, convection currents were formed inside the voids of the specimen and heat transfer also occurred by radiation between the hot gases and its internal surfaces. On the other hand, it did not happen in the BC1 and PC1 boundary conditions because only heat conduction was considered in the air mass. The insulation areas represented in Figure 6 are associated with (i) the insulation floor of the furnace or (ii) the longitudinal and transverse planes of symmetry, where there is no contact between the specimen and the hot gases of the furnace.

Figure 6 - Schematic of the boundary conditions of the finite element models.

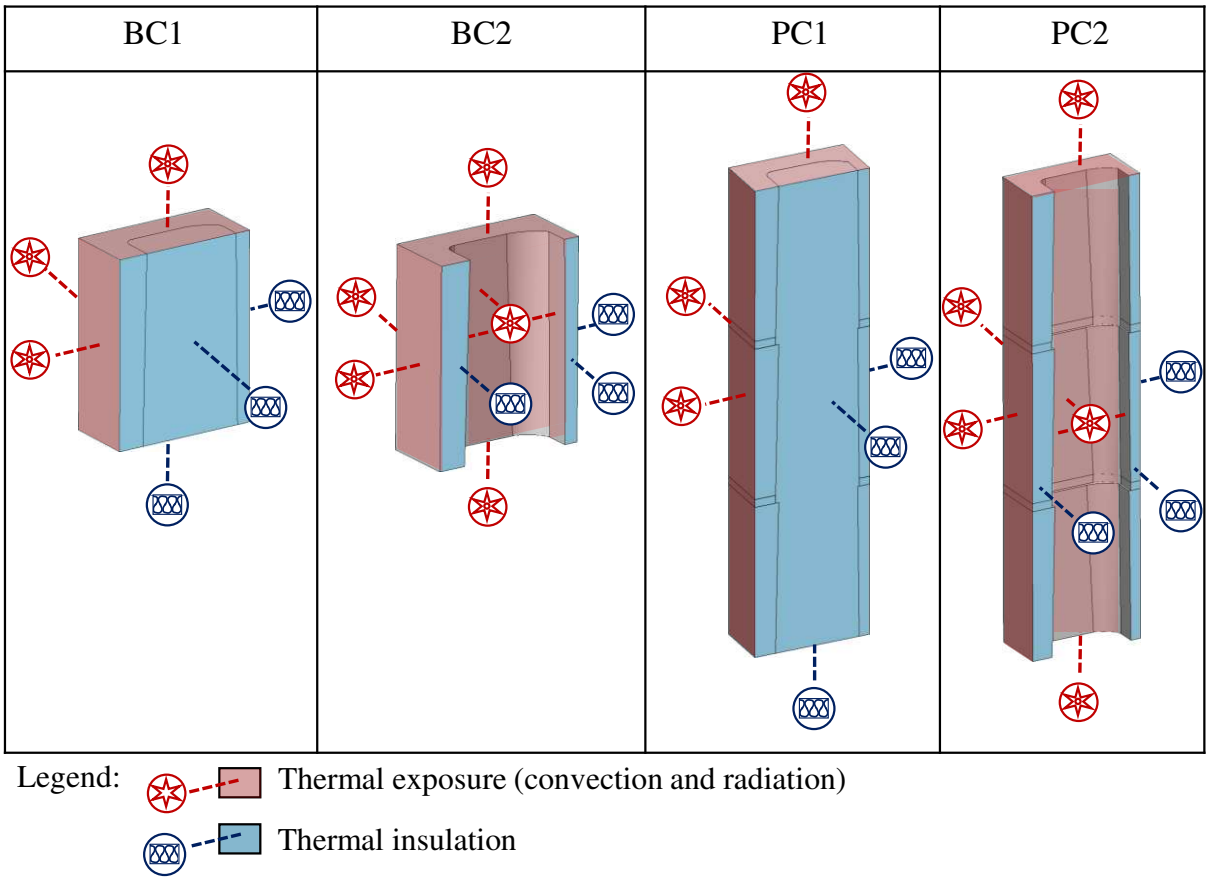

Source: Author (2024).

Values of specific heat, thermal conductivity and specific mass of the concrete units (Figure 7a) were those tabulated in EN 1992-1-2 (2004) for dry normal weight concrete with siliceous aggregates. For the mortar joints, values of specific heat, thermal conductivity and specific mass (Figure 7b) were those tabulated in previous papers (Rodovalho et al., 2017; Rodovalho and Corrêa, 2019). For the BC1 and PC1 models, data reported by Incropera and DeWitt (1992) was used to define the specific heat, thermal conductivity and specific mass of the air mass (Figure 7c) inside the hollows of concrete blocks and prisms.

Figure 7 - Variations of thermal conductivity, specific heat, and specific mass with temperature for concrete (a), mortar (b) and air mass (c).

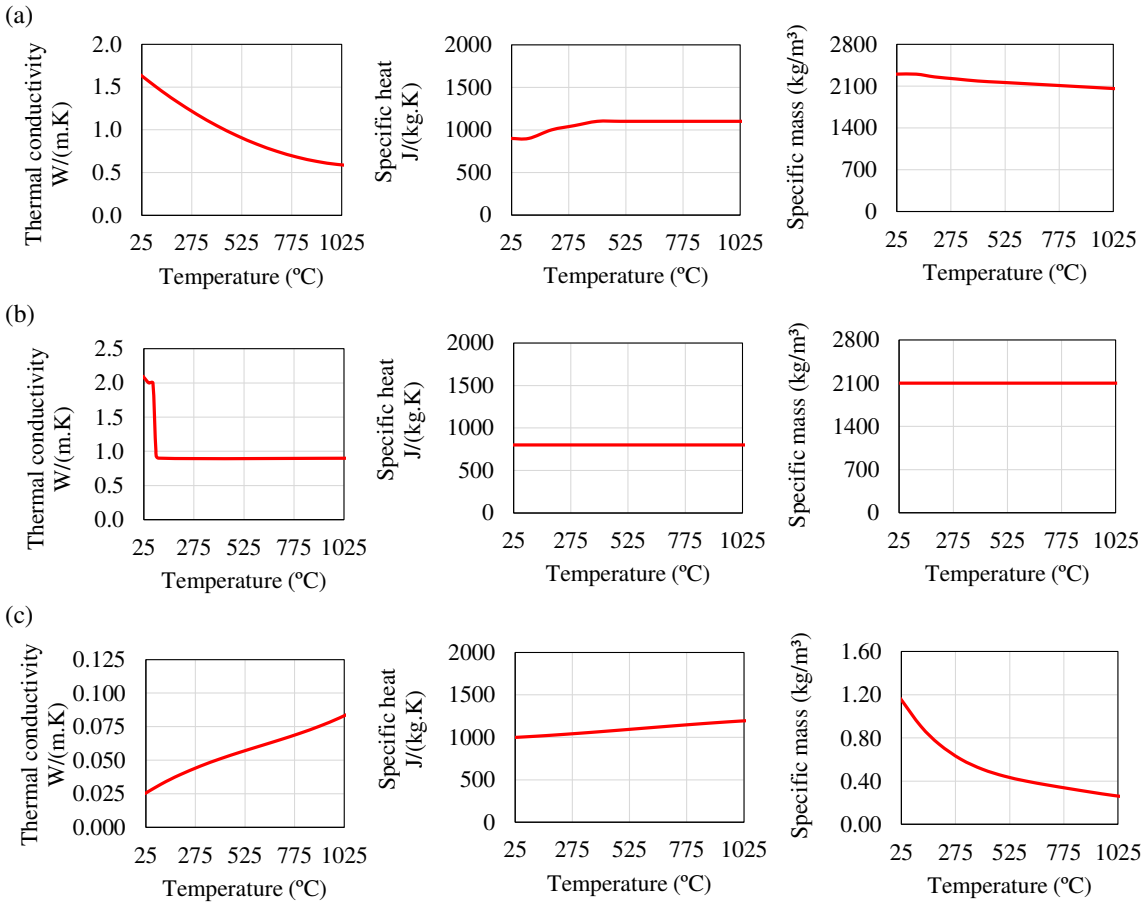

Source: Author (2024).

8.3. RESULTS AND DISCUSSION

8.3.1. BC1-300 and BC2-300 thermal analyses

Figure 8 shows a comparison between numerical and experimental results obtained in the present work. It includes the results of temperature evolution at the node located at the middle web and middle height of the numerical models BC1-300 and BC2-300, in addition to the results of the thermocouple measurements used to validate the numerical model.

Figure 8 - Experimental and numerical results of BC1-300 and BC2-300 thermal analyses.

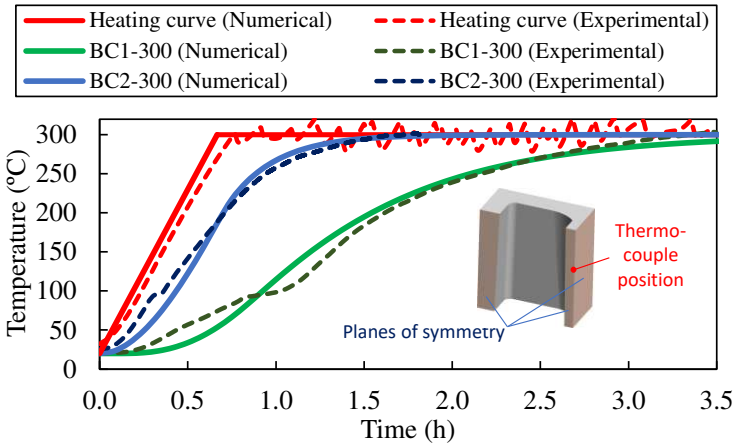

Source: Author (2024).

Before 100 ºC, the experimental model revealed a higher temperature increase rate than the numerical model. It can be attributed to the presence of some residual amount of water in the pores of the cementitious matrix around the block's thermocouples, which increased the thermal conductivity of the material. At about 100 ºC, a small plateau was observed in the experimental curves, which was associated with the pore water evaporation. After 100 ºC, the numerical and experimental models provided a very similar response, so that the temperature vs. time curves were close to each other in the range of 150-300 ºC. Results indicated that the numerical simulation approach had a high predictive ability to represent the temperature evolution of dry hollow concrete blocks.

The boundary conditions significantly affected the time required for temperature homogenization in the blocks, as results of BC1-300 and BC2-300 analyses reached the maximum temperature (300 ºC) after exposure periods of about 3 h 30 min and 1 h 45 min, respectively. Therefore, it is possible to conclude that the formation of convection currents inside the voids of blocks was able to decrease the time required for temperature homogenization.

8.3.2. PC1-300, PC2-300, PC1-600 and PC2-600 thermal analyses

Results of PC1-300, PC2-300, PC1-600 and PC2-600 thermal analyses indicated the nodes of the prisms that exhibited the highest and lowest values of temperature during the numerical simulations. The identification number and position of these nodes in the prisms and their temperature vs. time curves are presented in Figure 9.

Figure 9 - Results of (a) PC1-300, (b) PC2-300, (c) PC1-600 and (d) PC2-600 thermal analyses.

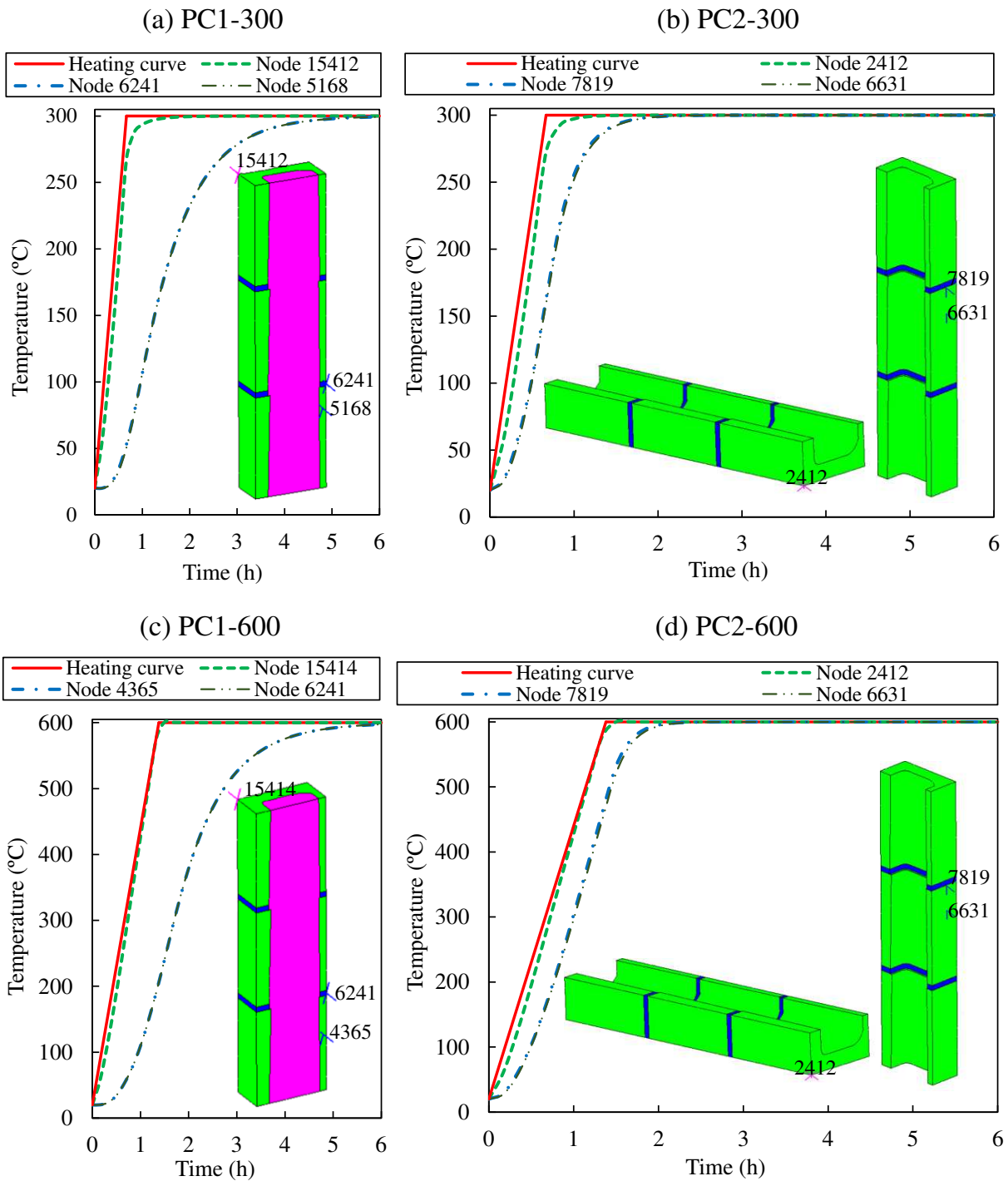

Source: Author (2024).

Figure 9 shows that the highest temperatures were observed in the hollow concrete blocks. They were always identified in the surface nodes positioned at the corner of the concrete units located at the ends of the masonry prisms (15412, 2412, 15414 and 2412 nodes in PC1-300, PC2-300, PC1-600 and PC2-600 analyses, respectively). The temperature vs. time curves for these nodes were very close to the temperature curves obtained for the hot

furnace gases, as the nodes were located at the surface of the prisms. In contrast, results presented in Figure 9 indicate that the lowest temperature levels of the prisms were observed in nodes of the interior web of blocks (5168, 6631, 4365 and 6631 nodes in PC1-300, PC2-300, PC1-600 and PC2-600 analyses, respectively) and mortar joints (6241, 7819, 6241 and 7819 nodes in PC1-300, PC2-300, PC1-600 and PC2-600 analyses, respectively).

The boundary conditions also affected the time required for temperature homogenization in the prisms. For example, the prism of the PC1-300 analysis reached (300 ± 0.5%×300) ºC after an exposure time of about 5 h 20 min, whereas the prism of the PC2-300 analysis took about 2 h to reach the same temperature range. In contrast, the prism of the PC1-600 analysis reached (600 ± 0.5%×600) ºC after 6 h, whereas the prism of the PC2-600 analysis took about 2 h 10 min to reach this temperature range. Then, the convection currents formed inside the voids also decreased the time required for temperature homogenization in the prisms, regardless of the maximum exposure temperature.

8.4. CONCLUSIONS

In conclusion, this study has advanced the understanding of temperature distribution mechanisms within masonry materials. The thermal analyses provided the temperature vs. time curves of concrete blocks and stack-bond prisms exposed to different temperature levels.

The boundary conditions (restrict or easy access to air circulation inside the voids of the block and prisms) significantly affected the time required for temperature homogenization in blocks and prisms. The examination of intricate effects arising from these distinct boundary conditions contributed to the refinement of fire testing methodologies for masonry prisms exposed to high temperatures.

The investigation into the often-neglected aspect of convection currents within voids of masonry specimens added a novel dimension to the scientific discourse, filling a critical gap in previous studies. Results indicated that the formation convection currents was able to decrease the time required for temperature homogenization.

Novel practical orientation for fire tests was offered in this study, particularly in relation to the time required for temperature homogenization in concrete masonry materials, which can improve fire testing protocols. In terms of operational aspects, easy access to air circulation inside the voids of test specimens may be recommended for fire tests, as it provided a faster temperature homogenization. When access to air circulation within the

voids of the prism was unrestricted, it reached temperature ranges of (300 ± 0.5%×300) ºC and (600 ± 0.5%×600) ºC after exposure times of 2 h and 2 h 10 min, respectively. In contrast, when the airflow within the voids of the prisms was restricted, the same temperature ranges were achieved after exposure times of 5 h 20 min and 6 h, respectively. It is essential to note that altering the heating rate would lead to variations in the time required for temperature homogenization, which is a well-established fact in the existing literature. The decision to limit the heating rate at 7°C/min in this study was intentional, focusing on facilitating the exploration of aspects not previously covered in the literature.

The present research has revealed an important perspective in the current understanding of the temperature distribution of masonry elements, based on the demonstration of the impacts of different boundary conditions on the time needed for temperature homogenization within blocks and prisms. These findings highlight the importance of evaluating the boundary conditions associated with different equipment used in fire tests, thus opening new avenues for exploration in this scientific field.

The intent of the present chapter was not to engage in a broad parametric analysis but rather to assess the effects of convection mechanisms and temperature homogenization under predefined test conditions. However, comprehensive parametric analyses could be developed to provide a deeper understanding of the underlying dynamics in fire-exposed masonry materials. In addition, the thermal analyses developed in the present work may be complemented with numerical simulations for the investigation of the effects of different boundary conditions on the thermal response of stack bond prisms made of hollow blocks with different material or thickness of coating systems. It is essential to acknowledge that the scope of this study did not encompass all possible variations in heating scenarios. Future investigations in the realm of innovative heating treatments could be developed to explore advanced techniques such as tailored heat distribution systems or innovative heating equipment for fire tests of masonry specimens.

REFERENCES

ABNT, 2013. NBR 12118: Hollow concrete blocks for concrete masonry - Test methods.

Assis, E., Neto, J., 2020. Analysis of heat transfer mechanisms on hollow concrete masonry units under standardized fire conditions, in: XLI Ibero-Latin-American Congress on Computational Methods in Engineering (CILAMCE). Foz do Iguaçu, Brazil.

ASTM, 2020. C140/C140M: Standard Test Methods for Sampling and Testing Concrete Masonry Units and Related Units.

Bettaieb, A. Ben, Velosa de Sena, J. l, Alves de Sousa, R.J., Valente, R.A.F., Habraken, A.M., Duchêne, L., 2015. On the comparison of two solid-shell formulations based on in-plane reduced and full integration schemes in linear and non-linear applications. Finite Elements in Analysis and Design 107, 44–59. https://doi.org/10.1016/j.finel.2015.08.005

Bittencourt, B., Antunes, E., 2019. Mechanical behavior of grouted prisms exposed to high temperatures: aid to future standardization (in Portuguese). Repositório UNESC 1–18.

Bošnjak, J., Gambarelli, S., Sharma, A., Mešković, A., 2020. Experimental and numerical studies on masonry after exposure to elevated temperatures. Constr Build Mater 230, 116926. https://doi.org/10.1016/j.conbuildmat.2019.116926

Bosnjak, J., Gambarelli, S., Sharma, A., Meskovic, A., 2019. Experimental and numerical studies on masonry after exposure to elevated temperatures. Otto-Graf-Journal 18, 41–52.

Castro, G., 2005. A general calculation method for the verification of concrete structures in fire situations (in Portuguese) (Dissertation). Universidade Federal de Minas Gerais, Belo Horizonte.

CEN, 2005. Eurocode 4: Design of composite steel and concrete structures - Part 1-2: General rules - Structural fire design.

CEN, 2004. Eurocode 2: Design of concrete structures - Part 1-2: General rules - Structural fire design.

CIMNE, 2004. GiD - International Center for Numerical Methods in Engineering.

Costa, R., 2005. Behavior of composite columns filled with high-performance refractory concrete at ambient temperature and in fire conditions (in Portuguese) (Dissertation). Universidade Federal de Minas Gerais, Belo Horizonte.

Daware, A., Naser, M.Z., 2021. Fire performance of masonry under various testing methods. Constr Build Mater 289, 123183. https://doi.org/10.1016/j.conbuildmat.2021.123183

Dupim, R., 2019. Resistência residual de compressão de blocos, prismas e pequenas paredes de alvenaria estrutural de blocos de concreto submetidos à situação de incêndio (MSc. Thesis). University of São Paulo, São Carlos, Brazil.

EN 1991-1-2, 2002. Eurocode 1: Actions on structures - Part 1-2: General actions - Actions on structures exposed to fire . Brussels.

EN 1996-1-2, 2010. Eurocode 6 - Design of masonry structures - Part 1-2: General rules - Structural fire design. Brussels.

Gao, S., Hao, D., Zhu, Y., Wang, Z., 2023. Compression and Shear Properties of Unreinforced Masonry Structures Reinforced by ECC/HECC subjected to High Temperatures. KSCE Journal of Civil Engineering 27, 751–768. https://doi.org/10.1007/s12205-022-1260-5

Gerken, A., 2007. Thermal protection materials for low-cost steel-structured construction systems (in Portuguese) (Dissertation). Universidade Federal de Minas Gerais, Belo Horizonte.

Incropera, F., DeWitt, D., 1992. Fundamentals of Heat and Mass Transfer, 3rd ed. Editora Guanabara Koogan S. A., Rio de Janeiro.

ISO, 1999. 834 - Fire-resistance tests - Elements of building construction.

Jain, M., Kapuria, S., 2022. Time-domain spectral finite element based on third-order theory for efficient modelling of guided wave propagation in beams and panels. Acta Mech 233, 1187–1212. https://doi.org/10.1007/s00707-021-03133-y

Kim, S.H., Huh, H., 1998. Optimum finite element for simulation of elasto-plastic bending of sheet metal. Metals and Materials 4, 685–694. https://doi.org/10.1007/BF03026381

Kiran, T., N, A., Andrushia, A.D., Kodur, V., Mathews, M.E., Arulraj, G.P., 2022. Performance of clay masonry prisms with light weight plaster exposed to standard fire exposure. Fire Mater 1–21. https://doi.org/10.1002/fam.3081

Leal, 2023. Structural masonry with concrete units: residual mechanical properties of mortars, grouts and prisms submitted to high temperatures (in Portuguese) (Thesis). Universidade Federal de São Carlos, São Carlos.

Leal, D.F., Dupim, R.H., Munaiar Neto, J., Corrêa, M.R.S., 2021. Experimental investigation on structural concrete masonry in fire: emphasis on the thermal behavior and residual strength. Revista IBRACON de Estruturas e Materiais 14, 1–16. https://doi.org/10.1590/s1983-41952021000400008

Medeiros, W.A., Parsekian, G.A., Moreno, A.L., 2022. Test methodology for determining the mechanical properties of concrete blocks at high temperatures. Mater Struct 55, 61. https://doi.org/10.1617/s11527-022-01892-1

Moreira, A., 2013. Verification of rectangular reinforced concrete sections subjected to combined oblique bending in fire conditions (in Portuguese) (Dissertation). Universidade Federal de Minas Gerais, Belo Horizonte.

Nalon, G., Ribeiro, J., Pedroti, L., Silva, R., Araújo, E., Santos, R., Lima, G., 2023. Review of Recent Progress on the Effects of High Temperatures on the Mechanical Behavior of Masonry Prisms. Infrastructures (Basel) 8, 112. https://doi.org/10.3390/infrastructures8070112

Neto, J., 2020. Estudo experimental do comportamento de elementos de alvenaria estrutural com blocos cerâmicos em situação de incêndio (MSc. Thesis). University of São Paulo, São Carlos, Brazil.

Oliveira, R.G., Rodrigues, J.P.C., Miguel Pereira, J., Lourenço, P.B., Lopes, R.F.R., 2021. Experimental and numerical analysis on the structural fire behaviour of three-cell hollowed concrete masonry walls. Eng Struct 228, 111439. https://doi.org/10.1016/j.engstruct.2020.111439

Prakash, P.R., Azenha, M., Pereira, J.M., Lourenço, P.B., 2020. Finite element based micro modelling of masonry walls subjected to fire exposure: Framework validation and structural implications. Eng Struct 213, 110545. https://doi.org/10.1016/j.engstruct.2020.110545

Quispe, A.P. da C., Rodríguez, R.Q., Lübeck, A., Lima, R.C.A. de, 2023. Análise comparativa numérica da transferência de calor em prismas de alvenaria em situação de incêndio. Ambiente Construído 23, 113–129. https://doi.org/10.1590/s1678-86212023000100652

Ribeiro, J.C.L., Fakury, R.H., Barbosa de Las Casas, E., 2013. Determinação da intensidade de um incêndio natural por meio do deslocamento plástico em vigas de aço após o resfriamento, in: Iberian-Latin American Congress in Fire Safety. Coimbra (Portugal).

Ribeiro, J.C.L., Fakury, R.H., Barbosa de Las Casas, E., 2011. Desenvolvimento de um sistema via método dos elementos finitos para simulação do comportamento de elementos estruturais de aço e mistos em situação de incêndio. Revista Sul-americana de Engenharia Estrutural 8, 20–33. https://doi.org/10.5335/rsee.v8i3.2607

Ribeiro, J.C.L., Fakury, R.H., Barbosa de Las Casas, E., 2008. Eurocode structural fire design and its application for composite circular hollow section columns. Journal of the Brazilian Society of Mechanical Sciences and Engineering 30, 39–46. https://doi.org/10.1590/S1678-58782008000100006

Ribeiro, J.C.L.R., 2009. Development and application of computational system for finite element method simulation of the behavior of steel and composite structures in fire

conditions (in Portuguese) (Thesis). Universidade Federal de Minas Gerais, Belo Horizonte.

Rodovalho, F. da S., Corrêa, M.R.S., Munaiar Neto, J., 2020. Simulação termomecânica de prismas com blocos de concreto em situação de incêndio. Matéria (Rio de Janeiro) 25. https://doi.org/10.1590/s1517-707620200001.0886

Rodovalho, F. da S., Simões, Y. de S., Correa, M.R.S., 2017. Análise térmica de alvenaria estrutural em situação de incêndio: um estudo do gradiente térmico, in: XXXVIII Iberian-Latin American Congress on Computational Methods in Engineering. Florianópolis (Brazil). https://doi.org/10.20906/CPS/CILAMCE2017-0561

Rodovalho, F.S., Corrêa, M.R.S., 2019. Thermal simulation of prisms with concrete blocks in a fire situation. IBRACON Structures and Materials Journal 12, 638–657. https://doi.org/10.1590/s1983-41952019000300011

Russo, S., Sciarretta, F., 2016. Numeric research on the mechanical properties of different masonry units during and after fire, in: Brick and Block Masonry - Trends, Innovations and Challenges. Taylor & Francis Group, London, pp. 999–1005.

Russo, S., Sciarretta, F., 2013. Masonry exposed to high temperatures: Mechanical behaviour and properties—An overview. Fire Saf J 55, 69–86. https://doi.org/10.1016/j.firesaf.2012.10.001

Sciarretta, F., 2014. Modeling of Mechanical Damage in Traditional Brickwork Walls after Fire Exposure. Adv Mat Res 919–921, 495–499. https://doi.org/10.4028/www.scientific.net/AMR.919-921.495

Torregrosa, M.E.M., Diez, J.C., 2015. Heat Transfer Mechanism and Thermomechanical Analysis of Masonry Structures (Mortars and Bricks) Subjected to High Temperatures, in: Reactions and Mechanisms in Thermal Analysis of Advanced Materials. John Wiley & Sons, Inc., Hoboken, NJ, USA, pp. 437–466. https://doi.org/10.1002/9781119117711.ch18

Yassin, Adnan, S., Shahidan, S., Ali, N., Kamarulzaman, N., Roni, N., 2018. Strength and physical properties of sustainable concrete masonry at elevated temperature: A review. Malaysian Construction Research Journal 4, 45–55.

9 BEHAVIOR OF SELF-SENSING CONCRETE MASONRY EXPOSED TO HIGH TEMPERATURES AND REHYDRATION

Abstract: *High temperatures can compromise the structural integrity of structural masonry. Therefore, assessing the post-fire mechanical behavior is crucial for selecting suitable rehabilitation methods. Recent research has proposed the application of self-sensing cementitious composites for monitoring strains, stresses, and damage of structural masonry in room temperature. No previous research has been found on the self-sensing performance of fire-damaged masonry prisms exposed to elevated temperatures, with or without subsequent rehydration. Masonry prisms with integrated self-sensing joints and blocks were produced and exposed to different maximum temperature levels, followed or not by rehydration. Then, experimental tests for determination of compressive strength, modulus of elasticity, gauge factor (GF) and damage-detection performance were carried out. The exposure to 300 ºC caused a 7.4% decrease in compressive strength and a 44.5% reduction in elastic modulus. Rehydration methods had negligible effects in this case. After 600 ºC, substantial reductions of 42.2% in compressive strength and 81.5% in elastic modulus occurred. In this case, rehydration led to a 15.9% increase in compressive strength and a 117.4% increase in elastic modulus. Regardless of the exposure temperature, the predominant rupture mode initiated by vertical cracks originating at the block-mortar interfaces. After 300 ºC, slight GF increases occurred due to the thermal decomposition of hydrates of the cementitious matrix, while exposure to 600 ºC resulted in high GF increases due to partial oxidation of nanomaterials and substantial microcracking propagation. Post-fire curing improved the GF by sealing microcracks with nonconductive rehydration products and enhancing tunneling conduction mechanisms. The self-sensing prisms also demonstrated the ability for real-time damage detection and quantification, providing valuable predictive insights into the propagation of damage.*

Keywords: *Masonry structures; fire; Structural Health Monitoring; smart structures; nanomodified structural elements; piezoresistivity.*

9.1. INTRODUCTION

Losses of life and extensive structural damage due to severe fires have stimulated new research on structural fire design and assessment. To avoid the demolition and reconstruction of structures exposed to elevated temperatures, their repair and refurbishment are interesting alternatives from the technical, ecological and economic points of view. However, a careful and precise examination of the residual conditions of the fire-damaged structure is required to ensure a suitable safety level (Cho et al., 2017; Ha et al., 2016; Nalon et al., 2021).

The construction of smart buildings is a pressing demand for an appropriate response to the continuous increase in the number of urban residents, which will be around 2.5 billion by 2050 (Qiu et al., 2023). In this context, self-sensing cementitious composites are promising technologies to produce multifunctional structures. Based on the piezoresistivity phenomenon, strain or stress of smart structural elements can be monitored based on changes in their electrical resistivity. The strain sensitivity of resistance-based self-sensing materials is estimated by their gauge factor (GF), which is defined as the fractional change in electrical resistivity (FCR) per unit strain. In addition, the FCRs in the plastic regime of the composites can be also associated with cracking propagation and damage events, which is an interesting response for Structural Health Monitoring (SHM) applications (Chung, 2023; Ding et al., 2023; Tian et al., 2019).

The self-sensing cementitious composites can be prepared by adding different types of conductive admixtures to traditional cementitious matrices. Some examples of conductive fillers used in previous literature are multi-walled carbon nanotubes (MWCNTs), carbon black nanoparticles (CBNs), carbon fibers (CFs), graphene, graphite, steel fibers (SFs), titania, etc. The addition of admixture contents within the percolation threshold of the cementitious matrix can improve the sensitivity, reversibility and repeatability of the electrical response (Bekzhanova et al., 2021; Dinesh et al., 2023; Vlachakis et al., 2020).

In their literature review paper, Mullins-Jaime and Smith (2022) identified that a promising development in the concrete nanotechnology field is the design of self-sensing cementitious matrices for strain/stress monitoring or damage detection after exposure to elevated temperatures. For example, Dong et al. (2020) investigated the self-sensing properties of cement pastes containing MWCNTs (50 mm cubic specimens), after exposure to 300 ºC or 600 ºC, and natural cooling. Pastes exposed to 300 ºC presented higher strain

sensitivity than reference specimens and pastes exposed to 600 ºC. Variations in the self-sensing response of the materials with the heating process were attributed to changes in the conductive network due to modifications in the MWCNTs' structures and damage in the cement-based matrix.

Jang et al. (2022) evaluated the residual piezoresistivity of fiber-reinforced cement pastes containing MWCNTs (50 mm cubic specimens), after temperatures of 100 ºC, 200 ºC or 400 ºC. After exposure to any maximum temperature level, the specimens exhibited a residual strain-sensing response for short- and long-term loading conditions. The thermal decomposition of hydrates of the cementitious matrix hindered connections between MWCNTs, which decreased the electrical conductivity of the materials. Cement-based sensors containing lower dosages of MWCNT were more affected by the exposure temperature than composites produced with high contents of nanomaterials, which exhibited greater stability in their piezoresistive response.

The residual capacitive response, electrical resistivity and self-sensing parameters of cement mortars containing MWCNTs or CBNs (40 mm × 40 mm × 75 mm prismatic specimens) and exposed to 200 ºC, 400 ºC or 600 ºC, and slow cooling were also investigated in two different conditions: before rehydration processes (Nalon et al., 2021) or after rehydration procedures (Nalon et al., 2023). The best piezoresistive response after exposure to high temperatures was verified in mortars produced with the highest concentration of carbon nanomaterials (9% of CBN, by weight of cement), which presented a notable sensitivity to strain, stress and damage after exposure to temperature levels up to 600 ºC. After post-fire recuring, these mortars also presented appropriate piezoresistive response and demonstrated the ability of self-detection of fire damage recovery.

Although previous studies (Dong et al., 2020; Jang et al., 2022; Nalon et al., 2023; Nalon et al., 2021) already reported the self-sensing behavior of fire-damaged pastes and mortars, the self-sensing properties of masonry components were only investigated in specimens that were not subjected to high temperatures. For example, previous works developed self-sensing clay bricks (Downey et al., 2018a; Meoni et al., 2021c; F Ubertini et al., 2017) and self-sensing masonry mortars (Dimou et al., 2022; Drougkas et al., 2023a, 2023b) using different types of conductive admixtures (e.g., MWCNTs, SFs, titania, CFs, graphene, graphite) and obtaining cost-effective solutions for SHM of heritage masonry structures. Self-sensing units embedded into masonry walls were also designed and tested in previous literature (D'Alessandro et al., 2018; García-Macías and Ubertini, 2019; Meoni et

al., 2021c, 2021b, 2020, 2019). Results indicated that could map stress/strain fields, identify loading path changes and quantify damage in masonry structures at room temperature.

There is no previous study that evaluated the piezoresistive behavior of self-sensing masonry elements after exposure to high temperatures. In addition, the ability of masonry structures to self-detect damage due to exposure to elevated temperatures has also not been evaluated in previous papers. Then, another justification for developing this research is the analysis of the applicability of self-sensing concrete blocks and mortar joints to monitor stress and strains of fire-damaged masonry elements, as well as to verify their ability to self-detect the damage associated with the exposure of the masonry to high temperatures. Moreover, the effects of post-fire rehydration on the recovery of mechanical properties of masonry prisms exposed to high temperatures are still unknown. Therefore, another motivation for the present research is the characterization of mechanical and piezoresistive properties of masonry prisms subjected to post-fire rehydration. Finally, a self-detection of masonry damage recovery due to this rehydration process is another contribution of this work.

9.2. MATERIALS AND METHODS

9.2.1. Materials

The following materials were used to prepare the plain and the self-sensing mortars: CP V-ARI portland cement [similar to the ASTM Type III high-early-strength portland cement (ASTM, 2022; Mehta and Monteiro, 2005)] with specific mass of 3.08 g/cm³; hydrated lime with specific mass of 2.51 g/cm³; and river sand with maximum particle size of 2.38 mm, fineness modulus of 2.52 and specific gravity of 2.64.

The conductive nanoinclusions used to produce the self-sensing masonry components were CBNs with average particle size equal to 20 nm and specific surface area equal to 120 m²/g. Stable nanosuspensions were obtained using polycarboxylate-type superplasticizer (PBS) with density of 1.12 g/cm³. In addition, a CaO-type expansive agent (EA) with specific mass of 2.50 g/cm³ was used for shrinkage control of the self-sensing mortars.

Masonry prisms were produced with hollow concrete blocks characterized according to ABNT NBR 12118 (2013). To enable coherent comparisons with mortar specimens, the static modulus of elasticity (E) and Poisson's ratio (ν) of the blocks was determined using samples of 20 mm × 20 mm × 60 mm extracted from the blocks. Results of basic

characterization of hollow concrete blocks are presented in Table 1. An epoxy-based structural adhesive (ESA) with density of 1.70 g/cm³ (Tecbond MF Quartzolit) was also used for construction of the self-sensing masonry elements.

Table 1 - Characterization data of hollow concrete blocks.

Parameter	Average	Standard deviation (SD)
Length (mm)	289.3	0.3
Width (mm)	138.8	0.4
Height (mm)	189.9	0.8
Face shell's thickness (mm)	26.3	0.3
Web's thickness (mm)	26.4	0.2
Ratio between net area and gross area (%)	57.8	0.4
Net area compressive strength of blocks $f_{b,net}$ (MPa)	17.4	1.1
Static modulus of elasticity (GPa)	21.2	2.1
Poisson's ratio	0.18	0.02

Note: When available, the characterization of masonry units was carried out following the standard methods of ABNT NBR 12118 (2013), which is similar to ASTM C140/C140M (2020).

Source: Author (2024).

9.2.2. Experimental design

A completely randomized design experiment with three repetitions (R1, R2 and R3) was elaborated for the present study. The designations of all series that composed this experiment are listed in Table 2. Each series was composed of self-sensing masonry prisms that were prepared and tested according to the procedures presented in Sections 9.2.3 and 9.2.4, respectively.

Table 2 - Series of prisms that composed the experimental design of the present research.

Series	Maximum exposure temperature	Rehydration procedures
REF	25 ºC	-
300WR	300 ºC	Without rehydration
600WR	600 ºC	
300R	300 ºC	24 h of water curing followed by 27 days covered by wet fabric and inside plastic bags
600R	600 ºC	

Source: Author (2024).

The factors imposed in this experimental design were the maximum exposure temperature and the application of rehydration procedures. Reference prisms that were not subjected to elevated temperatures were also tested. The response variables were the prism's compressive strength (f_p), the prism's modulus of elasticity (E_p), and the GF of three different self-sensing areas of the masonry prisms:

- B1 self-sensing area located in the middle height of the prisms' central block;
- B2 self-sensing area located in the inferior part of the prisms' central block;
- J area located in the horizontal joint, between the inferior and the middle blocks.

Many images of these self-sensing areas are presented in the next sections. The values obtained for these different response variables were subjected to statistical analyses. APPENDIX 9A shows the significance level, null and alternative hypotheses of the Grubb's tests, Shapiro-Wilk tests, Bartlett tests and analyses of variance (ANOVA) carried out in the present study. Furthermore, rupture mechanisms of the prisms were carefully observed and associated with the FCR measurements.

9.2.3. Preparation of specimens

9.2.3.1. Mixture of plain and self-sensing mortars

The mixture proportions and basic characteristics of the plain and self-sensing mortars used to construct the stack-bond prisms are summarized in Table 3. The plain mortar joint had a sand/binder ratio of 3.00 (in volume) and a lime/cement ratio of 0.75 (in volume). The water content was adjusted to obtaining a flow index of (7.0 ± 1.5) cm with the Kantro-cone mold, which provided a suitable workability for masonry construction applications. These mixture proportions provided a 28-days compressive strength of the mortar (f_m) equal to 9.7 MPa (SD of 0.5), according to prescriptions of ABNT NBR 13279 (2005), which is similar to EN 1015 (2019). Therefore, all prisms of this study had a $f_m/f_{b,\text{net}}$ ratio of 0.56, which meets the range of $0.40 < f_m/f_{b,\text{net}} < 0.90$ recommended for masonry structures (Parsekian et al., 2012).

Table 3 - Mixture proportions and characterization data of the plain and self-sensing mortars.

Mortar	Consumption (kg/m³)							Flow index (cm)	E_m (GPa)	ν_m	GF
	Cement	Sand	Lime	Water	CBN	PBS	EA				
Plain mortar joints	312.1	1405.4	190.9	290.2	0.0	0.0	0.0	7.6	14.7 (0.6)	0.16 (0.02)	-
Smart mortar of B1 and B2 areas	664.3	997.1	0.0	345.3	59.8	23.9	16.6	5.5	21.3 (1.0)	0.18 (0.01)	263 (10)
Smart mortar of J area	370.0	1031.4	226.3	344.0	53.7	21.5	14.9	5.8	14.0 (0.4)	0.17 (0.01)	338 (10)

Notes: Values of standard deviation (SD) were presented in parenthesis.

Source: Author (2024).

Lower aggregate/binder ratios (Table 3) were used for the self-sensing mortars embedded into the mortar joints and blocks (1.86 and 1.75, in volume, respectively) because the aggregates act as electrical insulation particles (Wen and Chung, 2007). The dosage of CBNs was 9% (by mass of binders) because it provides appropriate self-sensing response to cement mortars, before and after exposure to elevated temperatures (Nalon et al., 2023; Nalon et al., 2021). In addition, the PBS content was 3.6% (by mass of binders), as previous laboratory tests evidenced that improved dispersion conditions were observed in nanosuspensions with PBS/CBN = 0.4 (in mass). An EA concentration of 2.50% (by mass of binders) was added to the self-sensing mortars because previous laboratory tests revealed that it provided appropriate shrinkage control. To prepare all self-sensing mortars, a nanosuspension was initially prepared by mixing the CBNs, PBE and water, and applying an ultrasonication energy of 450 J/mL to the mixture. After that, the other raw materials were added to the nanosuspension and subjected to a mechanical mixture process for 10 min.

The mortar's elastic modulus (E_m) and Poisson's ratio (ν_m) presented in Table 3 were obtained from three prismatic mortar specimens (20 mm × 20 mm × 60 mm) that were subjected to a 28-days curing period (temperature of 23 ± 2 ºC and relative humidity of 60 ± 5%). These types of specimens were also used to determine the GF values listed in Table 3. However, the three prismatic specimens tested for determination of GF had two electrodes of 1.2 cm × 3.0 cm × 0.15 cm embedded into their central area (the spacing between the electrodes was 1.0 cm).

The modulus of elasticity and Poisson's ratio of the smart mortar of the B1 and B2 self-sensing areas (Table 3) were close to those of the concrete blocks (Table 1). In addition, the modulus of elasticity and Poisson's ratio of the smart mortar of the J self-sensing area were very close to those of the plain mortar. It happened because the self-sensing composites were designed to present suitable deformation compatibility with the substrate (masonry components).

9.2.3.2. Construction of masonry prisms

Figure 1 shows the procedures used to construct the masonry prisms. At first, a circular hole (diameter = 50 mm) was drilled in the middle height of some concrete blocks (Figure 1a) to create enough space for casting the nanomodified mortar of the B1 self-sensing area of the prisms. In addition, a half hole (diameter = 75 mm) was drilled in the inferior part of

the same blocks to create the space for molding the nanomodified mortar associated with the B2 self-sensing area of the prisms.

Figure 1 - Procedures used in construction of specimens.

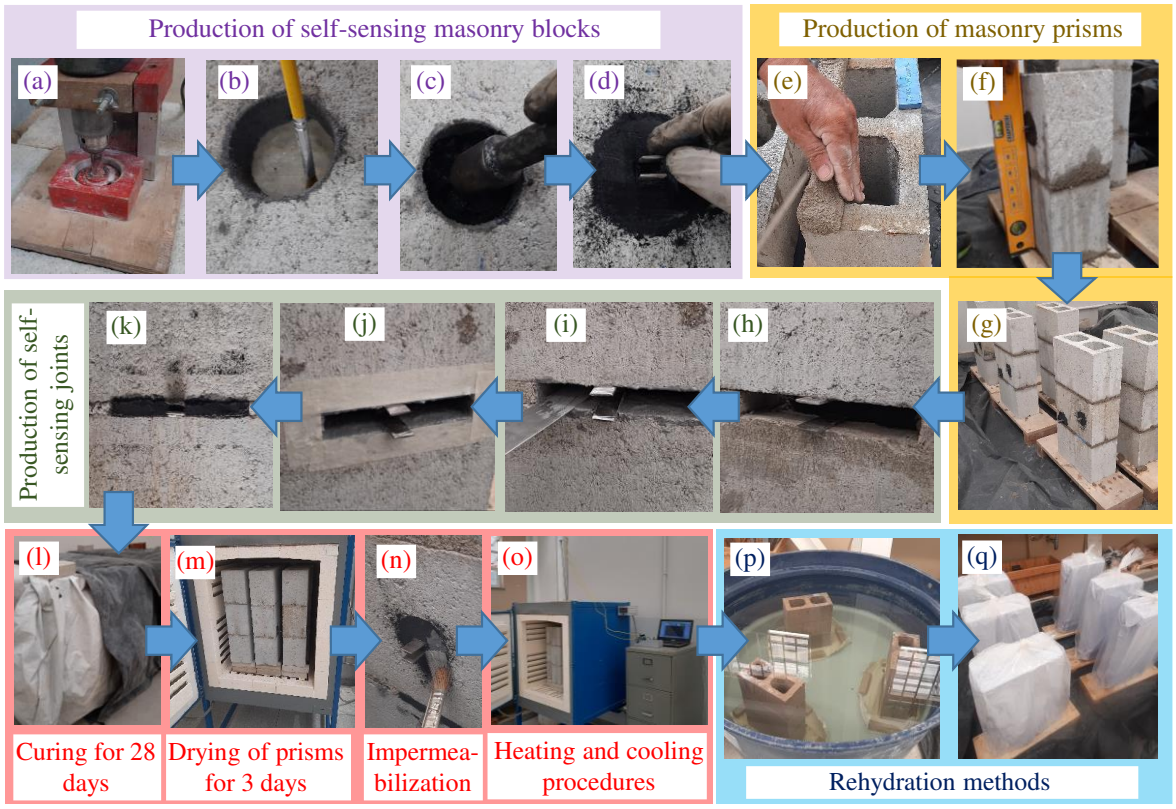

Source: Author (2024).

Following previous research findings (Nalon et al., 2023; Xiao et al., 2011), the ESA was applied to the holes' surface (Figure 1b) to ensure appropriate waterproofing and bonding performance. Fine sand was sprayed on the fresh ESA layer and the self-sensing mortar was molded in two equal layers inside the hole. After that, 30 strokes of a steel tamping rod were used to compact each layer (Figure 1c). Then, two electrodes (dimensions of 1.2 cm × 4.0 cm × 0.15 cm) were embedded into the expansive mortar (Figure 1d). The distance between the electrodes was about 1.0 cm. Next, the nanomodified cementitious matrix was covered with a plastic film for three days and the blocks were kept at 23 ± 2 ºC and relative humidity of 60 ± 5%.

The stack-bond masonry prisms were constructed seven days after preparation of the self-sensing concrete blocks (Figure 1e-g), using the full mortar bedding approach and a joint thickness of 10 ± 3 mm. The surface of the masonry units was moistened before placing the mortar. Removable rubber spacers were left in the J areas of the prism joints.

The smart mortar joint (J self-sensing area) was molded seven days after production of the masonry prisms. At first, the rubber spacer was removed from the horizontal joint and two electrodes were bonded in suitable locations using the ESA (Figure 1h). Next, the ESA was applied around the internal surfaces of the J self-sensing area (Figure 1i). After that, fine sand was sprayed on the fresh ESA layer and the expansive mortar was molded inside the empty space between the blocks (Figure 1j-k). Then, self-sensing areas were covered with a plastic film for three days. The specimens were kept immobile and protected from rain, sun and wind (Figure 1l) for additional 28 days, at temperature of 23 ± 2 ºC and relative humidity of 60 ± 5%.

After the curing process, all prisms were oven-dried (60 ± 10 ºC for 72 h) and then cooled down to room temperature (Figure 1m) to avoid undesirable effects of ionic conduction mechanisms on the self-sensing response of the nanomodified mortars (Han et al., 2021; Wang et al., 2021, 2019). The drying procedures also aimed to simulate real-life case scenarios of existing structures and avoid the formation of vapor pressure associated with the sudden rise in the temperature during the heating process (Abadel et al., 2022; Yao and Lu, 2021). After the drying process, a thin layer of ESA was also applied to the internal and external surface of the prisms' self-sensing areas (Figure 1n) to reproduce the methods of improving the sensors' waterproofing capability (Xiao et al., 2011).

9.2.3.3. Heating, cooling and post-fire recuring procedures

After the drying procedures, each series of prisms was subjected to different heating treatments. Prisms of the REF series were not exposed to elevated temperatures. The prisms of the other series were placed in a temperature-controlled chamber and heated up to the desired maximum temperature indicated in Table 2 (300 ºC or 600 ºC). A NI compact DAQ-9178 chassis, an NI-9219 module, the LabVIEW software, and type K thermocouples were used for temperature measurements (Figure 1o).

The temperature profile consisted of a 5 ºC/min ramp. After reaching the desired maximum temperature, it was kept constant. Numerical analyses presented in Chapter 8 were developed to estimate the temperature distribution in the specimens, determine the required time for temperature homogenization in the specimens, and investigate the effects of different specimen boundary conditions on the formation of convection currents inside the voids of the prisms. According to the conclusions presented in Chapter 8, it was decided to allow an

easy access to air circulation inside the voids of the prisms during the exposure to elevated temperatures. Moreover, the total exposure time was selected as 4 hours.

After the heating treatments, the masonry prisms were slowly cooled to room temperature. As indicated in Table 2, the prisms of 300R and 600R series were subjected to a rehydration process. At first, they were soaked in water for 1 day (Figure 1p). After removing the specimens from the water tank, wet fabric was placed over their surface. Then, they were covered by plastic bags (Figure 1q) and kept immobile for 27 days. The fabric was checked regularly to ensure it stayed wet. After the rehydration process, the masonry prisms were oven-dried (60 ± 10 ºC for 72 h) and cooled down to room temperature again.

9.2.4. Testing methods

9.2.4.1. Piezoresistive tests

After the different thermal treatments, the stack-bond prisms were subjected to piezoresistive tests for evaluation of the residual self-sensing response under uniaxial compressive loading. An EMIC DL-60000 universal testing machine was used to apply three load/unload cycles with a loading amplitude of approximately $0.3f_p$, followed by another loading cycle with steps at about $0.1f_p$, $0.2f_p$ and $0.3f_p$. These tests were carried out with a loading rate of 0.5 MPa/s, based on the net area of the specimens.

The experimental setup used in the piezoresistive tests is represented in Figure 2a-c. Clip-gauges (Figure 2a) were arranged with respect to the central axis of each self-sensing area of the prisms to measure the vertical strain during the piezoresistive tests. Three circuits were elaborated by connecting each self-sensing area to a specific reference resistor with electrical resistance of 1000 Ω. An Arduino Mega 2560 R3 (Figure 2b) was used to apply a ±5 V square wave voltage signal (frequency of 6.0 Hz and duty cycle of 50%) to each circuit. The NI compact DAQ-9178 chassis, two NI-9219 modules, and the LabVIEW software (Figure 2b) were used to measure the voltage drops across each self-sensing area and reference resistor at specific time instants recommended in previous works (Downey et al., 2017b; Lima et al., 2021; Meoni et al., 2021a), i.e., 80% of the positive part of the periodic signal. These measurements were used to determine the FCRs during the load/unload cycles.

Figure 2 - Testing methods: equipment used in electro-mechanical tests (a, b, c), location of self-sensing areas (d), and equipment used in elastic modulus tests (e). Dimensions were provided in millimeters.

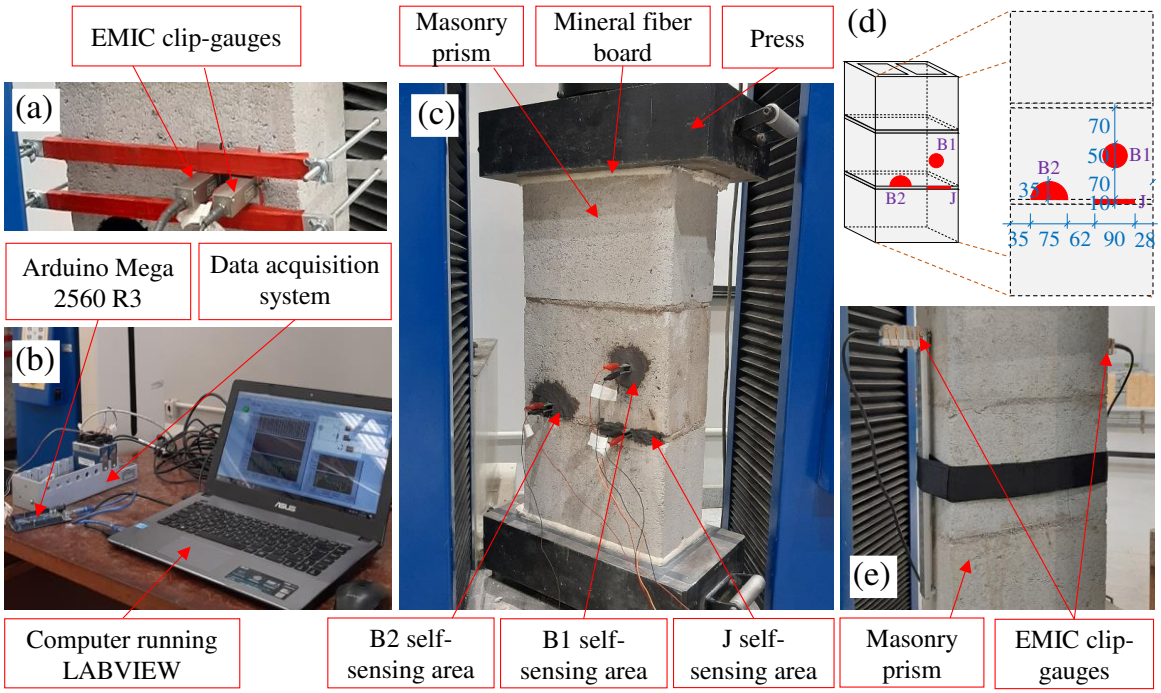

Source: Author (2024).

Mineral fiber boards (Figure 2c) were placed on the top and bottom surfaces of the masonry prism because conventional capping procedures were not recommended (plastic and cementitious materials could affect the original characteristics of fire-damaged specimens) and mechanical surface regularization was impracticable (the specimens were fragile after the heating process), according to Medeiros et al. (2022).

GF values were calculated using the experimental data related to the linear stretch of FCR *vs* longitudinal strain (ε) curves. The formulation used for determination of the GF of the B1, B2 and J self-sensing areas (Figure 2d) is presented in Equation (1):

$$GF = \frac{FCR}{\varepsilon} = \frac{\frac{\Delta R}{R_0}}{\varepsilon} \approx \frac{\frac{\Delta \rho}{\rho_0}}{\varepsilon} \quad (1)$$

where R_0 and ρ_0 are the initial electrical resistance and resistivity, respectively, and ΔR and $\Delta \rho$ are the changes in electrical resistance and resistivity due to the compression loading, respectively.

9.2.4.2. Elastic modulus tests

Experimental tests for determination of the static elastic modulus of the masonry prisms were carried out in the EMIC DL-60000 universal testing machine. Following the

prescriptions of ABNT NBR 16868-3 (2020), the specimens were firstly subjected to two load/unload cycles up to approximately $0.5f_p$, using the same loading rate applied in the piezoresistive tests. Finally, the compressive load was increased to the same level, while clip-gauges located at the lateral sides of the specimen (Figure 2e) measured its longitudinal deformation.

The elastic modulus of the material was determined as the slope of the straight line between the points with compressive stress equal to $0.05f_p$ and $0.30f_p$. In addition, the relative residual elastic modulus factor ($\psi_{c,j}$) of a specimen *j* was calculated using Equation (2):

$$\psi_{c,j} = \frac{E_{c,R,j}}{E_{cm}} \tag{2}$$

where $E_{c,R,j}$ is the residual elastic modulus of the fire-damaged specimen *j* and E_{cm} is the average elastic modulus of the reference specimens that were not exposed to high temperatures.

9.2.4.3. Compressive strength tests

The masonry prisms were also subjected to a monotonic compressive loading process in the EMIC DL-60000 universal testing machine. The loading rate was equal to 0.05 MPa/s. Brief interruptions were eventually needed for inspection of rupture modes of the specimens. To evaluate the damage-detection ability of the B1, B2 and J self-sensing areas, FCRs were measured up to the material failure using the apparatus illustrated in Figure 2b-c.

The relative residual compressive strength factor ($\Phi_{c,j}$) of a specimen *j* was determined using Equation (3):

$$\Phi_{c,j} = \frac{f_{c,R,j}}{f_{cm}} \tag{3}$$

where $f_{c,R,j}$ is the residual compressive strength of the fire-damaged specimen *j* and f_{cm} is the average compressive strength of the reference specimens that were not exposed to high temperatures.

9.2.4.4. Thermogravimetric analysis

To investigate the thermal decomposition of the conductive nanomaterials, a thermogravimetric analysis (TGA) was conducted on CBN (initial mass of 10 mg) using a DTG-60H thermogravimetric analyzer by Shimadzu. The heating rate was 10 ºC/min and the

maximum temperature was 900 ºC. To investigate the thermal stability in normal conditions, the TGA was developed in oxidizing atmosphere of dry air at a flow rate of 50 mL/min.

9.2.5. Statistical analysis

The values of compressive strength, elastic modulus and GF of all self-sensing areas were subjected to Grubb's tests for outlier detection, Shapiro-Wilk tests for assessment of the normality of residuals, and Bartlett tests for homoscedasticity evaluation. After that, an analysis of variance (ANOVA) was conducted, provided that its assumptions were met. Tukey's tests were applied for the comparison of mean values. The significance level (α), null hypotheses (H_0), and alternative hypotheses (H_a) of each statistical analysis can be found in APPENDIX 9A.

9.3. RESULTS AND DISCUSSIONS

9.3.1. Residual compressive strength and elastic modulus

Figure 3a shows the values of average compressive strength and $\Phi_{c,j}$ obtained in this research. The values of average elastic modulus and $\psi_{c,j}$ were presented in Figure 3b. The average values of compressive strength and elastic modulus were subjected to statistical analyses (APPENDIX 9A) that confirmed the fulfillment of all ANOVA assumptions. Consequently, Tukey's tests were deemed suitable for identifying any statistical distinctions between the average values of mechanical properties. In Figure 3a and Figure 3b, bars sharing an uppercase letter are not significantly different, according to the Tukey's test at a significance level of 0.05.

Figure 3 shows that the exposure to 300 ºC caused a small decrease in the compressive strength (7.4%) and relevant reduction in the elastic modulus (44.5%) of the masonry prisms. In fact, Figure 3a indicates that the Tukey's tests provided the same uppercase letter ("A") for the REF and 300WR series, whereas Figure 3b shows different uppercase letters ("A" and "BC") for these series. The mechanical properties reductions are mainly associated with the decomposition of some hydrates of the cementitious matrix of concrete blocks and mortar joints. For example, previous research (Castellote et al., 2004; Li et al., 2020; Sikora et al., 2018) reported that ettringite crystals are decomposed in the range of 60-150 ºC. Calcium silicate hydrates (C-S-H) undergo the loss of their bonded water and original structure at 100-

300 ºC, leading to the development of the first noticeable microcracks. In addition, gypsum decomposition is observed in the range of 150-170 ºC. Spalling of concrete surface layers was not observed because dried specimens were tested in this research, mitigating the pore vapor pressure inside the capillaries of the cementitious matrix.

Figure 3 - Compressive strength (a) and modulus of elasticity (b) of self-sensing masonry prisms exposed to high temperature levels. Bars sharing the same uppercase letter are statistically equal, according to the Tukey's test at a significance level of 0.05.

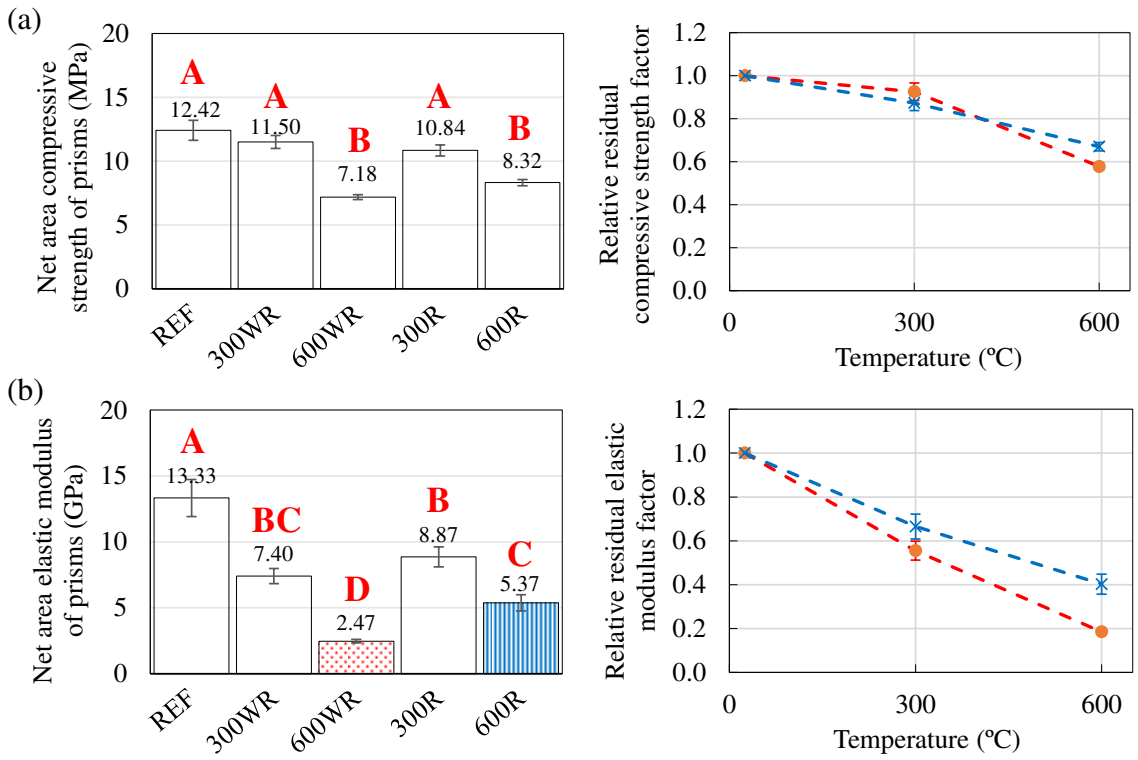

Source: Author (2024).

The exposure to 600 ºC caused significant percentage reductions in the compressive strength (42.2%) and elastic modulus (81.5%) of the masonry prisms. Consequently, Figure 3a and Figure 3b indicate that the Tukey's tests provided different uppercase letters for the REF and 600WR series. According to previous studies (Li et al., 2020; Scrivener et al., 2016; Sikora et al., 2018), the C-S-H phases also show water losses in the range of 300-600°C. In addition, the calcium hydroxide (CH) dehydrates to CaO in the range of 400-500 ºC. The quartz phase transformation (573 °C) from α-quartz to β-quartz induces volume expansion, thereby intensifying the propagation of microcracks through the aggregates, cement paste, and interface transition zone (ITZ).

In the present study, the impacts of rehydration methods on the mechanical properties of fire-damaged masonry were investigated for the first time. The results indicated that the rehydration process caused negligible changes in the mechanical properties of masonry prisms exposed to 300 ºC. According to the results of the Tukey's tests presented in Figure 3a and Figure 3b, the 300WR and 300R series presented the same uppercase letters, indicating statistical equality in average values at the 5% significance level. Two different phenomena must be considered to elucidate this result. Firstly, the heat-damaged epoxy layer caused a partial interruption in the passage of rehydration water to the interior of the self-sensing regions and limited the formation of rehydration products, as previous papers reported that exposure to temperatures of 90-200 ºC increased the porosity of epoxy materials (Wen et al., 2023) and damaged the integrity of these polymeric matrices (Altunişik et al., 2023). Secondly, the specimens exposed to 300 ºC had a limited extent of damage before the rehydration process. The smaller size of thermal microcracks limits the penetration of water during immersion. This restriction in water penetration hinders the formation of rehydration products, potentially influencing the overall rehydration efficiency. Furthermore, the limited space for formation of rehydration products may intensify the crystallization pressure from the newly generated compounds, damaging the cementitious matrix when the tensile strength is exceeded (Steiger, 2005a, 2005b; Wang et al., 2022).

The effects of rehydration methods were more significant in masonry prisms exposed to 600 °C. Figure 3 shows that the rehydration of specimens exposed to 600 ºC caused percentage increases in the residual compressive strength and elastic modulus of 15.9% and 117.4%, respectively. According to Figure 3a, the Tukey's tests provided the same uppercase letter ("B") for the 600WR and 600R series, whereas Figure 3b shows different uppercase letters ("D" and "C") for these series. The cementitious matrix of concrete blocks and mortar joints exposed to 600 ºC had greater microcracking. The higher the exposure temperature, the larger the thermal-induced microcracks, facilitating the penetration of water within the cementitious matrices during the rehydration process. Hence, the recovery of mechanical properties can be attributed to reactions between dehydrated products and water, which is responsible for reforming rehydration products like ettringite, C-S-H and CH (Li et al., 2020; Nalon et al., 2023; Suh et al., 2022; Suresh et al., 2022).

The residual strength and stiffness of concrete block prisms have been rarely investigated in previous literature. Dupim (2019) and Leal et al. (2021) recently reported the residual compressive strength of concrete block prisms exposed for 70 min to the ISO 834-1

(1999) curve. Their prisms presented a compressive strength percentage reduction (86%) significantly higher than those observed in the present work. This phenomenon can be attributed to the more severe temperature levels reached by the shells and central web of the concrete blocks during the fire simulation (approximately 400 ºC and 900 ºC, respectively). Leal (2023) recently reported the residual compressive strength and elastic modulus of concrte block prisms exposed to 200 ºC, 400 ºC, 600 ºC and 800 ºC. After 600 ºC, the compressive strength exhibited a maximum percentage reduction of 31%, a value lower than that obtained in the present study (42.2%). The elastic modulus showed a maximum reduction of 83%, a value slightly higher than that observed in the present investigation (81.5%). These findings highlight a good agreement between the results of Leal (2023) and the results obtained in this study.

9.3.2. Visual inspections

Figure 4 shows the surface of concrete blocks, surface of mortar joints, and epoxy-covered surface of self-sensing areas (before compression tests) of all series of specimens. Thermal cracks in the mortar joints of prisms from the 300WR and 600WR series were not visible to the naked eye (Figure 4a). However, previous research (Schmidt et al., 2023) reported that the mechanical properties of specimens of masonry mortars are significantly affected by elevated temperatures. To explain this contrasting behavior, Leal (2023) suggested that the minimal degradation of the mortar joints was likely associated with the confinement effects imposed by the concrete blocks. The friction effects were responsible for mitigating the free cracking of the mortar during the heating and cooling procedures, thereby delaying the decline of the mechanical properties of the prisms.

Figure 4 - Typical color of the surface of plain concrete blocks (a), surface of plain mortar joints (b) and epoxy-covered surface of self-sensing areas (c) of all series of masonry prisms.

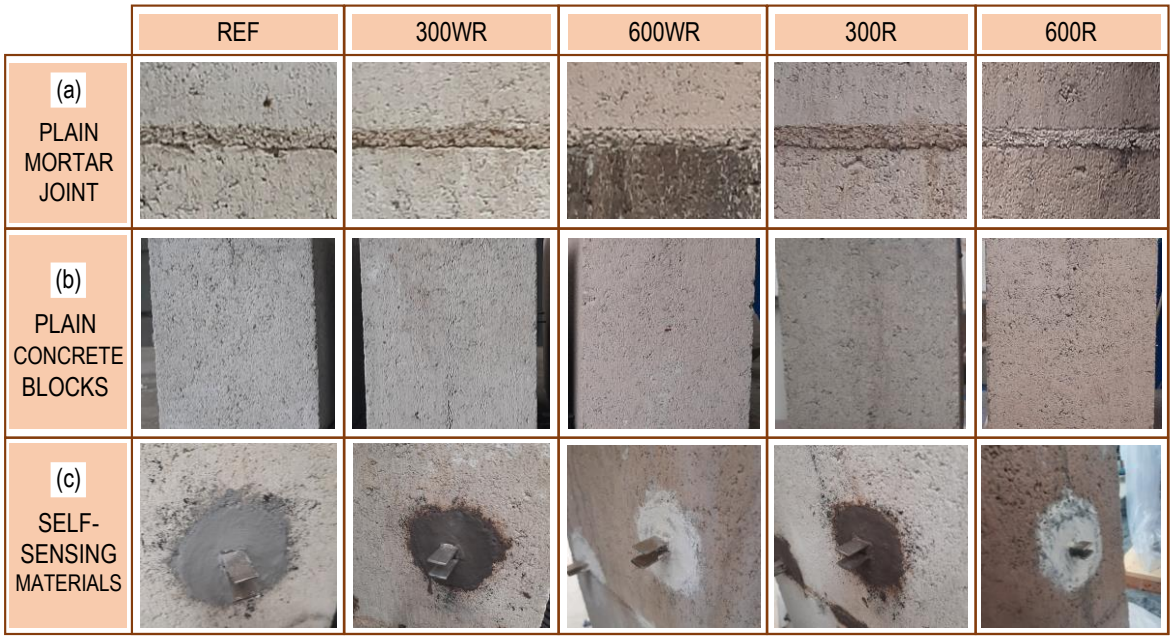

Source: Author (2024).

Figure 4a also shows that thermal cracks were not visible to the naked eye in the mortar joints of prisms of the 300R and 600R series. Despite this, the results of recent studies (Fernandes Neto et al., 2022) revealed that the expansive mechanisms associated with the rehydration of CaO induced progressive deterioration in specimens of cement-lime mortars. The findings of the present research substantiate the proposition of Leal (2023) that the minimal degradation of mortar joints is associated with the confinement effects imposed by the concrete blocks. These friction effects also contributed to mitigating potential cracks that could arise from expansive mechanisms associated with the rehydration of calcium oxide.

The heat exposure caused color changes in different materials. Figure 4a and Figure 4b demonstrate that the color of both concrete blocks and mortar joints underwent a transformation from gray to a light pink as the exposure temperature increased up to 600 ºC. Previous research (Fernandes et al., 2017; Short et al., 2001; Shumuye et al., 2021) also reported that the color of siliceous aggregate concrete changed from normal to pink or red in the range of 300-600 ºC due to the presence of iron compounds in the aggregates, which dehydrate or oxidize after exposure to high temperature levels.

The epoxy-based protection of the self-sensing areas was significantly affected by the exposure to high temperatures, which tends to compromise their waterproof performance. Figure 4c shows that the epoxy structural adhesive on the surface of the specimens appeared

gray in the REF series and black in the 300WR and 300R series. Kalyani, Joshi and Patel (2023) also observed that the color of epoxy adhesives changed from gray to black when they were exposed to 300 ºC. Figure 4c also shows that the epoxy-based insulation protection of the self-sensing areas exhibited a white color in the 600WR and 600R series. A white color was also verified in epoxy-based resins exposed to 400 ºC and 500 ºC by Kalyani, Joshi and Patel (2023). These color changes are directly related to different phenomena. Firstly, the glass transition temperature (T_g) of epoxy resins ranges from 65 °C to 120 °C (Altunişik et al., 2023; Banea et al., 2011; Carlos et al., 2018). In addition, previous studies (Boudefel and Gonon, 2006; Buch and Shanahan, 2000; Rmili et al., 2014) reported that the thermal decomposition of epoxy resins results from molecular chain scissions (thermolysis) and chemical transformations related to the oxidation of resin compounds that leave the polymer as volatiles.

Visual inspections were also conducted to verify the failure mechanisms of the self-sensing masonry prisms. Figure 5 shows the rupture mode of specimens R1, R2 and R3 of each series of the present experimental program. In these masonry prisms, the stiffness of the mortar was lower than that of concrete blocks (Table 1 and Table 3). As a result, the joints were laterally confined, inducing lateral tensile stresses in the blocks (Leal, 2023; Mohamad et al., 2007; Nalon et al., 2022; Parsekian et al., 2012). The predominant rupture mode was characterized primarily by vertical cracks that originated at the block-mortar interface when the compressive stress reached approximately 80-90% of the specimen strength.

Figure 5 - Rupture mode of specimens R1, R2 and R3 of each series of self-sensing masonry prisms.

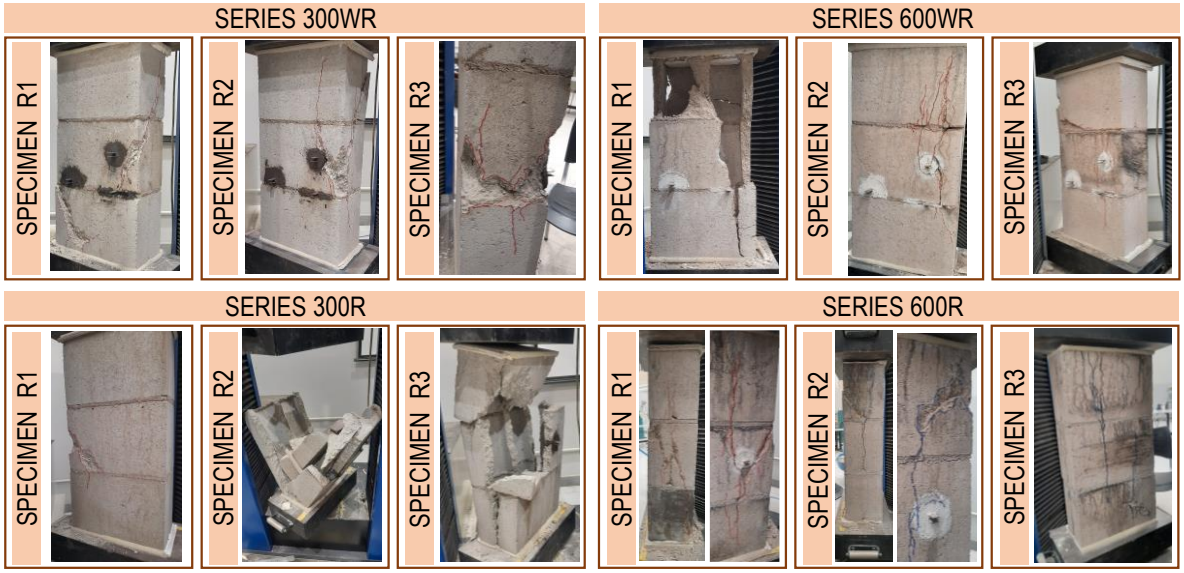

Source: Author (2024).

A similar failure mode was verified in prisms with $0.40 < f_m/f_{b,net} < 0.90$ that were not exposed to high temperatures (AbdelRahman and Galal, 2020; Caldeira et al., 2020; Kazempour et al., 2017; Mahamid and Westin, 2020; Martins et al., 2018; Nalon et al., 2020; Thamboo and Dhanasekar, 2019; Zahra et al., 2021). According to previous works, elevated temperatures cause relevant decreases on the compressive strength of both concrete blocks and masonry mortars (Amaral et al., 2023; Fernandes Neto et al., 2022; Medeiros et al., 2023; Schmidt et al., 2023). Due to the severe impact of elevated temperatures on both units and joints, slight changes occur in the difference between their residual stiffness. Consequently, previous studies have also observed that fire-damaged concrete block prisms experienced failure through tensile block splitting, accompanied by eventual spalling of block portions and mortar crushing (Dupim, 2019; Leal, 2023; Leal et al., 2021; G. H. Nalon et al., 2023).

9.3.3. Self-sensing behavior

This study introduces a pioneering exploration into the residual self-sensing behavior of masonry prisms exposed to high temperatures. In all series of prisms, the self-sensing regions B1, B2, and J demonstrated a piezoresistive response throughout the load/unload cycles. The values of GF obtained from the FCR *vs* compressive strain curves are represented in Figure 6. Statistical analyses indicated that the self-sensing properties varied significantly with the maximum exposure temperature. Therefore, Tukey's tests (5% significance level) were carried out to compare the average GF values and identify the differences among them.

Figure 6 - Gauge factor of B1 (a), B2 (b) and J (c) self-sensing areas of the masonry prisms. Bars sharing the same uppercase letter are statistically equal, according to the Tukey's test at a significance level of 0.05.

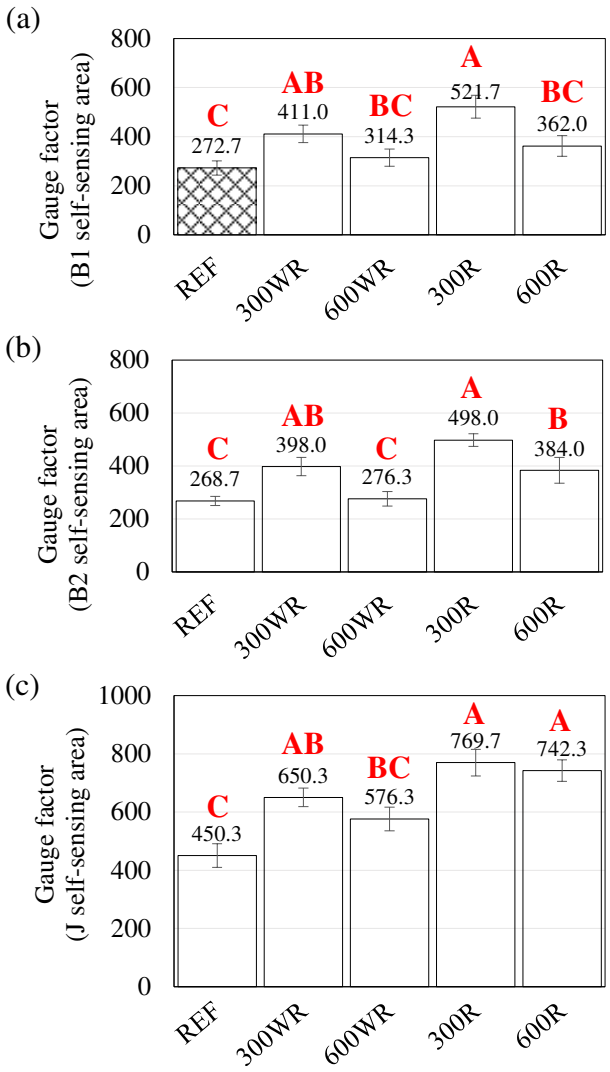

Source: Author (2024).

The exposure of the self-sensing prisms to 300 ºC caused percentage increases in the average GF of self-sensing areas B1, B2 and J equal to 50.7%, 48.1% and 44.4%, respectively. According to Figure 6, the Tukey's tests provided distinct uppercase letters ("C" and "AB") for the REF and 300WR series. The results of the TGA of CBNs (Figure 7) show that the nanoparticles are thermally stable after exposure to 300 ºC because no mass loss was verified in this temperature range. Consequently, the GF increases can be associated with microcracks resulting from the thermal decomposition of various compounds in the cementitious matrix, such as ettringite at 60-150 ºC, C-S-H at 100-300 ºC and gypsum at 150-170 ºC (Castellote et al., 2004; Li et al., 2020; Sikora et al., 2018). The microcracks interrupt some stretches of the conductive network, increase the amount of tunneling gaps

and alter the tunneling resistance between nanomaterials, improving the piezoresistivity of the material (Dong et al., 2020; Nalon et al., 2021).

Figure 7 - Results of thermogravimetric analysis (TGA) of the carbon black nanoparticles.

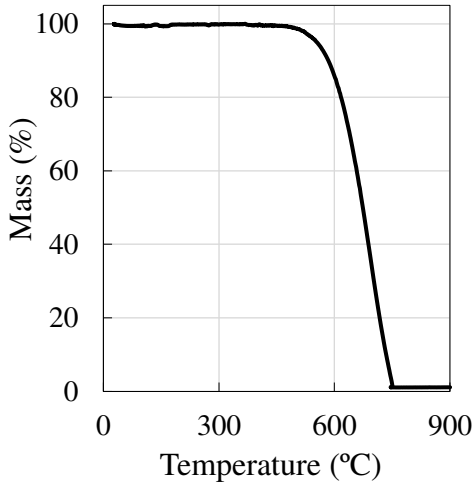

In contrast, the exposure to 600 ºC caused lower percentage increases in the average GF of self-sensing areas B1, B2 and J (15.3%, 2.8% and 28.0%, respectively). The Tukey's test results of Figure 6 provided the uppercase letter "C" for the REF and 600WR series, which indicates that they are not statistically different. The subsequent decrease in GF in the temperature range of 300-600 °C can be related to a posterior reduction in tunneling conduction mechanisms due to different factors. At first, the TGA results (Figure 7) show that a small quantity of CBNs (constituting less than 15% of the total mass) that form the conductive network can be decomposed through reactions with the oxygen available in the pores of the cement sensors. Additionally, interruption of tunneling conduction mechanisms can be attributed to the continued development of microcracks due to the dehydration of C-S-H phases at 300-600°C, dehydroxylation of CH at 400-500 ºC and expansive volumetric changes associated with the phase transition of quartz at 573 °C (Li et al., 2020; Scrivener et al., 2016; Sikora et al., 2018).

Figure 6 also shows that the rehydration process caused small increases in the GF of masonry prisms exposed to 300 ºC. According to the results of the Tukey's tests, the 300WR and 300R series presented the same uppercase letter "A" (statistically significant similarity was observed at the 5% significance level). Changes in GF values are directly related to the propagation or sealing of microcracks in the cementitious matrix (Nalon et al., 2023). Hence, the marginal changes in GF resulting from the rehydration of masonry prisms exposed to 300 ºC can be related to a modest rehydration efficiency. At first, the heat-damaged epoxy

layer causes a partial interruption in the passage of rehydration water, as increased porosity and damage occurred in epoxy materials exposed to temperatures of 90-200 ºC (Altunişik et al., 2023; Wen et al., 2023). In addition, the limited scale of thermal cracks in cementitious matrices exposed to 300 ºC hinders water penetration during the immersion process, attenuates the formation of rehydration products and compromises the recovery of strength and stiffness (Figure 3).

On the other hand, the rehydration process resulted in more significant changes in the GF of masonry prisms exposed to 600 °C. According to Figure 6, the rehydration of specimens exposed to 600 ºC caused percentage increases in the GF of self-sensing areas B1, B2 and J of 15.2%, 39.0% and 28.8%, respectively. According to Figure 6a, the Tukey's tests provided the same uppercase letters ("BC") for the 600WR and 600R series, whereas Figure 6b and Figure 6c show different uppercase letters ("A", "B" or "C") for these series. The exposure to a higher temperature level (600 ºC) led to the development of substantial thermal microcracks, facilitating water penetration during the immersion process. Consequently, rehydration products with nonconductive properties filled pores and sealed cracks in the cementitious matrix, interrupting stretches of the CBN-based conductive network within the composite. This interruption tends to enhance tunneling conduction mechanisms rather than contact conduction, increasing the GF of the self-sensing material (Nalon et al., 2023).

To assess the damage-detection ability of the self-sensing prisms, FCRs were measured during the plastic regime. Figure 8 presents the results obtained from the self-sensing areas installed in the concrete blocks (B1 and B2), whereas Figure 9 shows the values measured in the self-sensing area installed in the mortar joint (J). Regardless of the maximum exposure temperature, the FCR *vs* compressive stress curves were characterized by significant declines in FCR, eventually culminating in a phase of FCR stability followed by FCR increases. This general trend aligns with the behavior documented in previous studies for self-sensing composites that were not exposed to elevated temperatures (Han et al., 2015).

Figure 8 - Values of fractional changes in electrical resistivity (FCRs) obtained from the self-sensing concrete blocks (B1 and B2 self-sensing areas) of R1, R2 and R3 specimens tested under monotonic axial loading.

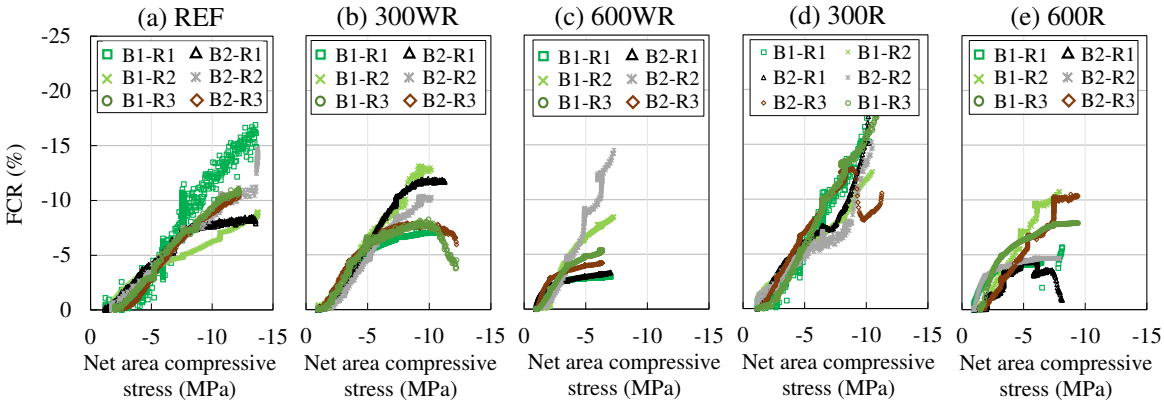

Source: Author (2024).

Figure 9 - Values of fractional changes in electrical resistivity (FCRs) obtained from the self-sensing mortar joints (J self-sensing area) of R1, R2 and R3 specimens tested under monotonic axial loading.

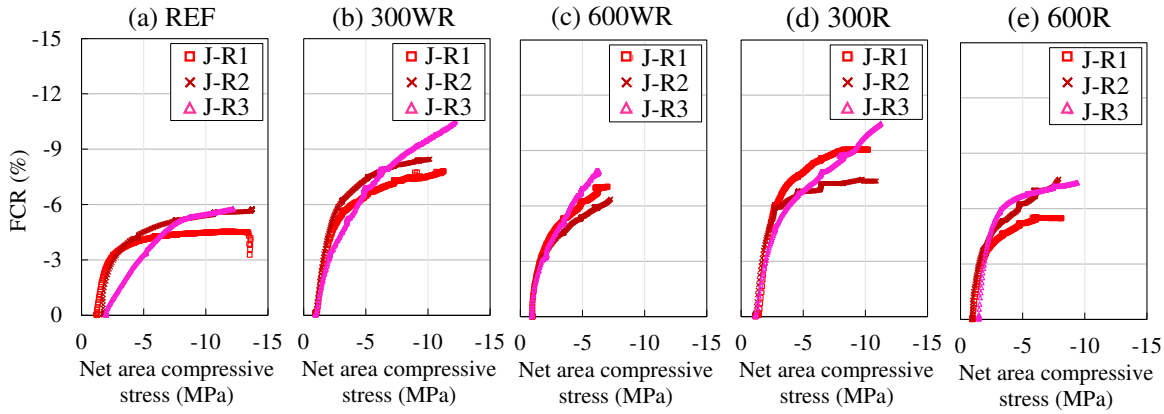

Source: Author (2024).

The FCR decreases presented in the first part of the curves of Figure 8 and Figure 9 can be attributed to decreases in the distance between CBNs due to the increased compressive loading, which improves tunneling mechanisms and decreases the electrical resistivity of the material (Bekzhanova et al., 2021; Dinesh et al., 2023; Vlachakis et al., 2020). The equilibrium phase of the curves can be associated with the emergence of intense microcracking in the self-sensing areas. The evolution of damage tends to cause an increase in the electrical resistivity because cracks are non-conducting spaces that interrupt the conductive network between neighboring conductive admixtures (Downey et al., 2018b, 2017a; Filippo Ubertini et al., 2017). The gradual propagation of cracks through the blocks and mortar joints caused notable decreases in electrical conductivity, eventually leading to FCR increases at the end of the FCR *vs* stress curves.

Stages of balance and abrupt increases in FCR of the B1, B2 and J self-sensing areas can offer a predictive insight into the development of cracks in the concrete blocks and mortar joints. Since the FCR measurements are associated with damage evolution, they can be used for the real-time localization and quantification of damage, acting as effective approaches to anticipate the evolution of failure mechanisms in fire-damaged masonry elements.

9.4. CONCLUSIONS

The present research aimed to explore the mechanical and self-sensing performance of masonry prisms exposed to different levels of elevated temperatures, with or without subsequent rehydration. The following conclusions derived from the present work:

(1) Exposure to 300 ºC led to a slight decrease (7.4%) in compressive strength and a significant reduction (44.5%) in the elastic modulus of concrete masonry prisms, primarily associated with the decomposition of hydrates in the cementitious matrix. Rehydration methods had negligible effects on these specimens due to limited damage extent and constrained water penetration.

(2) Exposure to 600 ºC resulted in substantial reductions in compressive strength (42.2%) and elastic modulus (81.5%) of concrete masonry prisms, reflecting the severe propagation of microcracks. Rehydration of these specimens led to relevant increases of compressive strength (15.9%) and elastic modulus (117.4%) due to the sealing of some microcracks with rehydration products.

(3) Visual inspections revealed that thermal cracks were not apparent in the joints of the prisms, before or after rehydration. The absence of visible cracks is probably related to the confining effects of concrete blocks on the mortar joints.

(4) Regardless of the maximum exposure temperature, the predominant rupture mode of concrete masonry prisms was characterized by vertical cracks originating at the block-mortar interface.

(5) Significant GF increases were observed after exposure to 300 ºC, which can be attributed to the thermal decomposition of matrix compounds. When prisms exposed to 300 ºC were rehydrated, marginal changes in GF were observed. This phenomenon can be attributed to the limited efficiency of the rehydration process, which was hindered by the restricted scale of microcracks.

(6) Exposure to 600 ºC caused small percentage increases in GF, which can be associated with a minor oxidation of CBNs and increased microcrack development. When prisms exposed to 600 ºC were rehydrated, the abundance of microcracks facilitated water penetration, leading to the formation of nonconductive rehydration products that tended to seal the microcracks, enhancing tunneling conduction mechanisms and increasing the GF of the self-sensing materials.

(7) The self-sensing materials enabled a real-time damage localization and quantification in the blocks and joints of fire-damaged masonry elements. Stages of balance followed by FCR increases during the monotonic compressive loading tests offered predictive insights into the propagation of damage.

The epoxy-based protection of the self-sensing areas exhibited high vulnerability to exposure to high temperatures, potentially compromising their waterproof performance. Therefore, future studies are recommended to explore alternative materials for waterproofing protection of self-sensing composites to ensure sustained functionality in extreme conditions. In addition, further research is required to investigate the effects of various rehydration methods on the mechanical and self-sensing properties of fire-damaged prisms.

REFERENCES

Abadel, A., Abbas, H., Albidah, A., Almusallam, T., Al-Salloum, Y., 2022. Effectiveness of GFRP strengthening of normal and high strength fiber reinforced concrete after exposure to heating and cooling. Engineering Science and Technology, an International Journal 36, 101147. https://doi.org/10.1016/j.jestch.2022.101147

AbdelRahman, B., Galal, K., 2020. Influence of pre-wetting, non-shrink grout, and scaling on the compressive strength of grouted concrete masonry prisms. Constr Build Mater 241, 117985. https://doi.org/10.1016/j.conbuildmat.2019.117985

ABNT, 2020. NBR 16868-3: Structural masonry Part 3 - Test methods.

ABNT, 2013. NBR 12118: Hollow concrete blocks for concrete masonry - Test methods.

ABNT, 2005. NBR 13279: Mortars applied on walls and ceilings - Determination of the flexural and the compressive strength in the hardened stage.

Altunişik, A.C., Akbulut, Y.E., Adanur, S., Kaya, A., Günaydin, M., Mostofi, S., Mosallam, A., 2023. Evaluating the high-temperature endurance of FRP-strengthened concrete using an innovative insulation system: Experimental investigation. Journal of Building Engineering 73, 106444. https://doi.org/10.1016/j.jobe.2023.106444

Amaral, R. de O., Moreno, A.L., Medeiros, W.A., Parsekian, G.A., 2023. Residual mechanical resistance of concrete blocks and laying mortars after high temperatures. Fire Mater. https://doi.org/10.1002/fam.3186

ASTM, 2022. C150/C150M-22: Standard Specification for Portland Cement.

ASTM, 2020. C140/C140M: Standard Test Methods for Sampling and Testing Concrete Masonry Units and Related Units.

Banea, M.D., de Sousa, F.S.M., da Silva, L.F.M., Campilho, R.D.S.G., de Pereira, A.M.B., 2011. Effects of Temperature and Loading Rate on the Mechanical Properties of a High Temperature Epoxy Adhesive. J Adhes Sci Technol 25, 2461–2474. https://doi.org/10.1163/016942411X580144

Bekzhanova, Z., Memon, S.A., Kim, J.R., 2021. Self-Sensing Cementitious Composites: Review and Perspective. Nanomaterials 11, 2355. https://doi.org/10.3390/nano11092355

Boudefel, A., Gonon, P., 2006. Dielectric response of an epoxy resin when exposed to high temperatures. Journal of Materials Science: Materials in Electronics 17, 205–210. https://doi.org/10.1007/s10854-006-6762-2

Buch, X., Shanahan, M.E.R., 2000. Influence of the gaseous environment on the thermal degradation of a structural epoxy adhesive. J Appl Polym Sci 76, 987–992. https://doi.org/10.1002/(SICI)1097-4628(20000516)76:7<987::AID-APP1>3.0.CO;2-1

Caldeira, F.E., Nalon, G.H., Oliveira, D.S. de, Pedroti, L.G., Ribeiro, J.C.L., Ferreira, F.A., Carvalho, J.M.F. de, 2020. Influence of joint thickness and strength of mortars on the compressive behavior of prisms made of normal and high-strength concrete blocks. Constr Build Mater 234, 117419. https://doi.org/10.1016/j.conbuildmat.2019.117419

Carlos, T.B., Rodrigues, J.P.C., de Lima, R.C.A., Dhima, D., 2018. Experimental analysis on flexural behaviour of RC beams strengthened with CFRP laminates and under fire conditions. Compos Struct 189, 516–528. https://doi.org/10.1016/j.compstruct.2018.01.094

Castellote, M., Alonso, C., Andrade, C., Turrillas, X., Campo, J., 2004. Composition and microstructural changes of cement pastes upon heating, as studied by neutron diffraction. Cem Concr Res 34, 1633–1644. https://doi.org/10.1016/S0008-8846(03)00229-1

CEN, 2019. EN 1015-11: Methods of test for mortar for masonry - Part 11 - Determination of flexural and compressive strength of hardened mortars.

Cho, H., Lee, D., Ju, H., Park, H., Kim, H., Kim, K., 2017. Fire Damage Assessment of Reinforced Concrete Structures Using Fuzzy Theory. Applied Sciences 7, 518. https://doi.org/10.3390/app7050518

Chung, D., 2023. A critical review of electrical-resistance-based self-sensing in conductive cement-based materials. Carbon N Y 203, 311–325. https://doi.org/10.1016/j.carbon.2022.11.076

D'Alessandro, A., Meoni, A., García-Macías, E., Cavalagli, N., Gioffrè, M., Ubertini, F., 2018. Full-scale testing of a masonry building monitored with smart brick sensors, in: Proceedings of 5th International Electronic Conference on Sensors and Applications. MDPI, Basel, Switzerland, p. 5764. https://doi.org/10.3390/ecsa-5-05764

Dimou, A., Asimakopoulos, G., Karatasios, I., Gournis, D., Metaxa, Z., Kourkoulis, S., Alexopoulos, N., 2022. Self-diagnostic lime-pozzolan-cement restoration nanocomposites: Effect of graphene modification and cyclic loading level under compression. Developments in the Built Environment 10, 100068. https://doi.org/10.1016/j.dibe.2022.100068

Dinesh, A., Saravanakumar, P., Rahul Prasad, B., Kilbert Raj, S., 2023. Carbon black based self-sensing cement composite for structural health monitoring – A review on strength and conductive characteristics. Mater Today Proc. https://doi.org/10.1016/j.matpr.2023.03.661

Ding, S., Wang, X., Qiu, L., Ni, Y., Dong, X., Cui, Y., Ashour, A., Han, B., Ou, J., 2023. Self-Sensing Cementitious Composites with Hierarchical Carbon Fiber-Carbon Nanotube Composite Fillers for Crack Development Monitoring of a Maglev Girder. Small 19, 2206258. https://doi.org/10.1002/smll.202206258

Dong, W., Li, W., Wang, K., Han, B., Sheng, D., Shah, S.P., 2020. Investigation on physicochemical and piezoresistive properties of smart MWCNT/cementitious composite exposed to elevated temperatures. Cem Concr Compos 112, 103675. https://doi.org/10.1016/j.cemconcomp.2020.103675

Downey, A., D'Alessandro, A., Baquera, M., García-Macías, E., Rolfes, D., Ubertini, F., Laflamme, S., Castro-Triguero, R., 2017a. Damage detection, localization and quantification in conductive smart concrete structures using a resistor mesh model. Eng Struct 148, 924–935. https://doi.org/10.1016/j.engstruct.2017.07.022

Downey, A., D'Alessandro, A., Laflamme, S., Ubertini, F., 2018a. Smart bricks for strain sensing and crack detection in masonry structures. Smart Mater Struct 27, 015009. https://doi.org/10.1088/1361-665X/aa98c2

Downey, A., D'Alessandro, A., Ubertini, F., Laflamme, S., 2018b. Automated crack detection in conductive smart-concrete structures using a resistor mesh model. Meas Sci Technol 29, 035107. https://doi.org/10.1088/1361-6501/aa9fb8

Downey, A., D'Alessandro, A., Ubertini, F., Laflamme, S., Geiger, R., 2017b. Biphasic DC measurement approach for enhanced measurement stability and multi-channel sampling of self-sensing multi-functional structural materials doped with carbon-based additives. Smart Mater Struct 26, 065008. https://doi.org/10.1088/1361-665X/aa6b66

Drougkas, A., Sarhosis, V., Basheer, M., D'Alessandro, A., Ubertini, F., 2023a. Design of a smart lime mortar with conductive micro and nano fillers for structural health monitoring. Constr Build Mater 367, 130024. https://doi.org/10.1016/j.conbuildmat.2022.130024

Drougkas, A., Sarhosis, V., Basheer, M., D'Alessandro, A., Ubertini, F., 2023b. Electromechanical Testing of Smart Lime Mortars for Structural Health Monitoring, in: European Workshop on Structural Health Monitoring. Springer, pp. 755–763. https://doi.org/10.1007/978-3-031-07254-3_76

Dupim, R., 2019. Resistência residual de compressão de blocos, prismas e pequenas paredes de alvenaria estrutural de blocos de concreto submetidos à situação de incêndio (MSc. Thesis). University of São Paulo, São Carlos, Brazil.

Fernandes, B., Gil, A.M., Bolina, F.L., Tutikian, B.F., 2017. Microstructure of concrete subjected to elevated temperatures: physico-chemical changes and analysis techniques. Revista IBRACON de Estruturas e Materiais 10, 838–863. https://doi.org/10.1590/s1983-41952017000400004

Fernandes Neto, J.A.D., Sombra, T.N., Haach, V.G., Corrêa, M.R.S., 2022. Effects of post-fire curing on the residual mechanical behavior of cement-lime masonry mortars. Constr Build Mater 327, 126613. https://doi.org/10.1016/j.conbuildmat.2022.126613

García-Macías, E., Ubertini, F., 2019. Earthquake-induced damage detection and localization in masonry structures using smart bricks and Kriging strain reconstruction: A numerical study. Earthq Eng Struct Dyn 48, 548–569. https://doi.org/10.1002/eqe.3148

Ha, T., Ko, J., Lee, S., Kim, S., Jung, J., Kim, D.-J., 2016. A Case Study on the Rehabilitation of a Fire-Damaged Structure. Applied Sciences 6, 126. https://doi.org/10.3390/app6050126

Han, B., Ding, S., Yu, X., 2015. Intrinsic self-sensing concrete and structures: A review. Measurement 59, 110–128. https://doi.org/10.1016/j.measurement.2014.09.048

Han, J., Cai, J., Pan, J., Sun, Y., 2021. Study on the conductivity of carbon fiber self-sensing high ductility cementitious composite. Journal of Building Engineering 43, 103125. https://doi.org/10.1016/j.jobe.2021.103125

ISO, 1999. 834 - Fire-resistance tests - Elements of building construction.

Jang, D., Yoon, H.N., Seo, J., Yang, B., 2022. Effects of exposure temperature on the piezoresistive sensing performances of MWCNT-embedded cementitious sensor. Journal of Building Engineering 47, 103816. https://doi.org/10.1016/j.jobe.2021.103816

Kalyani, V.J., Joshi, D.D., Patel, P. V., 2023. Study of the behaviour of FRP materials and epoxy adhesives under elevated temperature. Mater Today Proc. https://doi.org/10.1016/j.matpr.2023.08.028

Kazempour, H., Bassuoni, M.T., Hashemian, F., 2017. Masonry mortar with nanoparticles at a low temperature. Proceedings of the Institution of Civil Engineers - Construction Materials 170, 297–308. https://doi.org/10.1680/jcoma.15.00054

Leal, 2023. Structural masonry with concrete units: residual mechanical properties of mortars, grouts and prisms submitted to high temperatures (in Portuguese) (Thesis). Universidade Federal de São Carlos, São Carlos.

Leal, D.F., Dupim, R.H., Munaiar Neto, J., Corrêa, M.R.S., 2021. Experimental investigation on structural concrete masonry in fire: emphasis on the thermal behavior and residual strength. Revista IBRACON de Estruturas e Materiais 14, 1–16. https://doi.org/10.1590/s1983-41952021000400008

Li, L., Shi, L., Wang, Q., Liu, Y., Dong, J., Zhang, H., Zhang, G., 2020. A review on the recovery of fire-damaged concrete with post-fire-curing. Constr Build Mater 237, 117564. https://doi.org/10.1016/j.conbuildmat.2019.117564

Lima, G.E.S. de, Nalon, G.H., Santos, R.F., Ribeiro, J.C.L., Carvalho, J.M.F. de, Pedroti, L.G., Araújo, E.N.D. de, 2021. Microstructural Investigation of the Effects of Carbon Black Nanoparticles on Hydration Mechanisms, Mechanical and Piezoresistive

Properties of Cement Mortars. Materials Research 24. https://doi.org/10.1590/1980-5373-mr-2020-0539

Mahamid, M., Westin, N., 2020. Reevaluation of fm′ for the Unit-Strength Method with Application to Lightweight Concrete Block Masonry and Face Shell–Bedded Mortar Joints. Practice Periodical on Structural Design and Construction 25, 04020019. https://doi.org/10.1061/(ASCE)SC.1943-5576.0000494

Martins, R.O.G., Nalon, G.H., Alvarenga, R.D.C.S.S., Pedroti, L.G., Ribeiro, J.C.L., 2018. Influence of blocks and grout on compressive strength and stiffness of concrete masonry prisms. Constr Build Mater 182, 233–241. https://doi.org/10.1016/j.conbuildmat.2018.06.091

Medeiros, W.A., Parsekian, G.A., Moreno, A.L., 2023. Residual mechanical properties of hollow concrete blocks with different aggregate types after exposure to high temperatures. Constr Build Mater 377, 131085. https://doi.org/10.1016/j.conbuildmat.2023.131085

Medeiros, W.A., Parsekian, G.A., Moreno, A.L., 2022. Test methodology for determining the mechanical properties of concrete blocks at high temperatures. Mater Struct 55, 61. https://doi.org/10.1617/s11527-022-01892-1

Mehta, P., Monteiro, P., 2005. Concrete: Microstructure, Properties and Materials (Portuguese version). New York.

Meoni, A., D'Alessandro, A., Cavalagli, N., Gioffré, M., Ubertini, F., 2019. Shaking table tests on a masonry building monitored using smart bricks: Damage detection and localization. Earthq Eng Struct Dyn 48, 910–928. https://doi.org/10.1002/eqe.3166

Meoni, A., D'Alessandro, A., Kruse, R., De Lorenzis, L., Ubertini, F., 2021a. Strain field reconstruction and damage identification in masonry walls under in-plane loading using dense sensor networks of smart bricks: Experiments and simulations. Eng Struct 239, 112199. https://doi.org/10.1016/j.engstruct.2021.112199

Meoni, A., D'Alessandro, A., Mancinelli, M., Ubertini, F., 2021b. A Multichannel Strain Measurement Technique for Nanomodified Smart Cement-Based Sensors in Reinforced Concrete Structures. Sensors 21, 5633. https://doi.org/10.3390/s21165633

Meoni, A., D'Alessandro, A., Ubertini, F., 2021c. Recent Advances and Open Issues on the Use of Smart Bricks for Seismic Monitoring of Masonry Buildings: Experimental Tests and Numerical Simulations. pp. 851–860. https://doi.org/10.1007/978-3-030-64594-6_82

Meoni, A., D'Alessandro, A., Ubertini, F., 2020. Characterization of the strain-sensing behavior of smart bricks: A new theoretical model and its application for monitoring of masonry structural elements. Constr Build Mater 250, 118907. https://doi.org/10.1016/j.conbuildmat.2020.118907

Mohamad, G., Lourenço, P.B., Roman, H.R., 2007. Mechanics of hollow concrete block masonry prisms under compression: Review and prospects. Cem Concr Compos 29, 181–192. https://doi.org/10.1016/j.cemconcomp.2006.11.003

Mullins-Jaime, C., Smith, T., 2022. Nanotechnology in Residential Building Materials for Better Fire Protection and Life Safety Outcomes. Fire 5, 174. https://doi.org/10.3390/fire5060174

Nalon, G, Ribeiro, J., Araújo, E., Silva, R., Pedroti, L., Lima, G., 2023. Concrete units for strain-monitoring in civil structures: Installation of cement-based sensors using different approaches. Constr Build Mater 394, 132169. https://doi.org/10.1016/j.conbuildmat.2023.132169

Nalon, G., Ribeiro, J., Pedroti, L., Araújo, E., Carvalho, J., Lima, G., Ferreira, S., 2023. Effects Of Post-Fire Curing on Self-Sensing Behavior of Smart Mortars. ACI Mater J 120, 181–192. https://doi.org/10.14359/51738459

Nalon, G.H., Ribeiro, J.C., Pedroti, L.G., Duarte de Araújo, E., Franco de Carvalho, J., Soares de Lima, G., de Moura Guimarães, L., 2021. Residual piezoresistive properties of mortars containing carbon nanomaterials exposed to high temperatures. Cem Concr Compos 121, 104104. https://doi.org/10.1016/j.cemconcomp.2021.104104

Nalon, G.H., Ribeiro, J.C.L., Pedroti, L.G., Silva, R.M. da, Araújo, E.N.D. de, Santos, R.F., Lima, G.E.S. de, 2023. Review of Recent Progress on the Effects of High Temperatures on the Mechanical Behavior of Masonry Prisms. Infrastructures (Basel) 8, 112. https://doi.org/10.3390/infrastructures8070112

Nalon, G.H., Ribeiro, J.C.L., Pedroti, L.G., Silva, R.M. da, Araújo, E.N.D. de, Santos, R.F., Lima, G.E.S. de, 2022. Review of recent progress on the compressive behavior of masonry prisms. Constr Build Mater 320, 126181. https://doi.org/10.1016/j.conbuildmat.2021.126181

Nalon, G.H., Santos, C.F.R., Pedroti, L.G., Ribeiro, J.C.L., Veríssimo, G. de S., Ferreira, F.A., 2020. Strength and failure mechanisms of masonry prisms under compression, flexure and shear: Components' mechanical properties as design constraints. Journal of Building Engineering 28, 101038. https://doi.org/10.1016/j.jobe.2019.101038

Parsekian, G., Hamid, A., Drysdale, G., 2012. Behavior and design of structural masonry (in Portuguese). EdUFSCar, São Carlos.

Qiu, L., Ding, S., Wang, D., Han, B., 2023. Self-sensing GFRP-reinforced concrete beams containing carbon nanotube-nano carbon black composite fillers. Meas Sci Technol 34, 084003. https://doi.org/10.1088/1361-6501/accc20

Rmili, W., Deffarges, M.P., Chalon, F., Ma, Z., Leroy, R., 2014. Dynamic Mechanical Properties and Thermal Effect of an Epoxy Resin Composite, Encapsulation's Element of a New Electronic Component. J Electron Mater 43, 702–707. https://doi.org/10.1007/s11664-013-2876-5

Schmidt, R., Costa, E., Antoniazzi, J., Pinheiro, M., Lourenço, P., Favretto, S., Mohamad, G., 2023. Effect of High Temperature Exposure on Masonry Bedding Mortars. Preprint 1–31.

Scrivener, K., Snellings, R., Lothenbach, B., 2016. A Practical Guide to Microstructural Analysis of Cementitious Materials, 1st ed.

Short, N.R., Purkiss, J.A., Guise, S.E., 2001. Assessment of fire damaged concrete using colour image analysis. Constr Build Mater 15, 9–15. https://doi.org/10.1016/S0950-0618(00)00065-9

Shumuye, E.D., Zhao, J., Wang, Z., 2021. Effect of the Curing Condition and High-Temperature Exposure on Ground-Granulated Blast-Furnace Slag Cement Concrete. Int J Concr Struct Mater 15, 15. https://doi.org/10.1186/s40069-020-00437-6

Sikora, P., Abd Elrahman, M., Stephan, D., 2018. The Influence of Nanomaterials on the Thermal Resistance of Cement-Based Composites—A Review. Nanomaterials 8, 465. https://doi.org/10.3390/nano8070465

Steiger, M., 2005a. Crystal growth in porous materials-I: The crystallization pressure of large crystals. J Cryst Growth 282, 455–469. https://doi.org/10.1016/j.jcrysgro.2005.05.007

Steiger, M., 2005b. Crystal growth in porous materials-II: Influence of crystal size on the crystallization pressure. J Cryst Growth 282, 470–481. https://doi.org/10.1016/j.jcrysgro.2005.05.008

Suh, H., Im, S., Kim, J., Bae, S., 2022. Instant mechanical recovery of heat-damaged nanosilica-incorporated cement composites under various rehydrations procedures. Mater Struct 55, 5. https://doi.org/10.1617/s11527-021-01847-y

Suresh, N., Rao, V., Akshay, B.S., 2022. Evaluation of mechanical properties and post-fire cured strength recovery of recycled aggregate concrete. Journal of Structural Fire Engineering. https://doi.org/10.1108/JSFE-10-2021-0064

Thamboo, J.A., Dhanasekar, M., 2019. Correlation between the performance of solid masonry prisms and wallettes under compression. Journal of Building Engineering 22, 429–438. https://doi.org/10.1016/j.jobe.2019.01.007

Tian, Z., Li, Y., Zheng, J., Wang, S., 2019. A state-of-the-art on self-sensing concrete: Materials, fabrication and properties. Compos B Eng 177, 107437. https://doi.org/10.1016/j.compositesb.2019.107437

Ubertini, Filippo, D'Alessandro, A., Downey, A., García-Macías, E., Laflamme, S., Castro-Triguero, R., 2017. Recent Advances on SHM of Reinforced Concrete and Masonry Structures Enabled by Self-Sensing Structural Materials, in: The 4th International Electronic Conference on Sensors and Applications. MDPI, Basel Switzerland, p. 119. https://doi.org/10.3390/ecsa-4-04889

Ubertini, F, D'Alessandro, A., Materazzi, A., Laflamme, S., Downey, A., 2017. Novel nanocomposite clay brick for strain sensing in structural masonry, in: 2017 IEEE International Conference on Environment and Electrical Engineering and 2017 IEEE Industrial and Commercial Power Systems Europe (EEEIC / I&CPS Europe). IEEE, pp. 1–4. https://doi.org/10.1109/EEEIC.2017.7977598

Vlachakis, C., Perry, M., Biondi, L., 2020. Self-Sensing Alkali-Activated Materials: A Review. Minerals 10, 885. https://doi.org/10.3390/min10100885

Wang, H., Lyu, H., Liu, T., Li, Y., Hai Tan, K., 2022. Effect of post-fire curing on compressive strength of ultra-high performance concrete and mortar. Constr Build Mater 346, 128447. https://doi.org/10.1016/j.conbuildmat.2022.128447

Wang, H., Shen, J., Liu, J., Lu, S., He, G., 2019. Influence of carbon nanofiber content and sodium chloride solution on the stability of resistance and the following self-sensing performance of carbon nanofiber cement paste. Case Studies in Construction Materials 11, e00247. https://doi.org/10.1016/j.cscm.2019.e00247

Wang, H., Shi, F., Shen, J., Zhang, A., Zhang, L., Huang, H., Liu, J., Jin, K., Feng, L., Tang, Z., 2021. Research on the self-sensing and mechanical properties of aligned stainless steel fiber-reinforced reactive powder concrete. Cem Concr Compos 119, 104001. https://doi.org/10.1016/j.cemconcomp.2021.104001

Wen, J., Wu, Y., Hou, X., Yan, M., Xiao, Y., 2023. Effect of high temperature on mechanical properties and porosity of carbon fiber/epoxy composites. Journal of Reinforced Plastics and Composites 42, 990–1005. https://doi.org/10.1177/07316844221143747

Wen, S., Chung, D.D.L., 2007. Double percolation in the electrical conduction in carbon fiber reinforced cement-based materials. Carbon N Y 45, 263–267. https://doi.org/10.1016/j.carbon.2006.09.031

Xiao, H., Li, H., Ou, J., 2011. Strain sensing properties of cement-based sensors embedded at various stress zones in a bending concrete beam. Sens Actuators A Phys 167, 581–587. https://doi.org/10.1016/j.sna.2011.03.012

Yao, Y., Lu, H., 2021. Mechanical properties and failure mechanism of carbon nanotube concrete at high temperatures. Constr Build Mater 297, 123782. https://doi.org/10.1016/j.conbuildmat.2021.123782

Zahra, T., Thamboo, J., Asad, M., 2021. Compressive strength and deformation characteristics of concrete block masonry made with different mortars, blocks and mortar beddings types. Journal of Building Engineering 38, 102213. https://doi.org/10.1016/j.jobe.2021.102213

APPENDIX 9A: RESULTS OF STATISTICAL ANALYSES

9A.1. GRUBB'S TEST FOR OUTLIER DETECTION

The experimental results were subjected to the Grubb's test for outlier detection.

9A.1.1. Hypothesis and significance level

- Null hypothesis (H_0): all values belong to the same population.
- Alternative hypothesis (H_a): the smallest or largest value represents an outlier.
- Significance level (α): 0.050.

9A.1.2. Results of the statistical tests

Table A.1, Table A.2, Table A.3, Table A.4 and Table A.5 show Grubb's test results.

Table A.1 - Results of Grubb's test for results of net area compressive strength.

Series	Average net area compressive strength (MPa)	Standard deviation (MPa)	Minimum (MPa)	Maximum (MPa)	Grubb's test statistic	P-value
REF	12.42	1.23	11.32	13.75	1.08	0.685
300WR	11.50	0.63	11.03	12.21	1.13	0.356
600WR	7.18	0.24	6.95	7.42	1.03	0.881
300R	10.84	0.53	10.25	11.25	1.13	0.405
600R	8.32	0.30	8.12	8.66	1.15	0.197

Source: Author (2024).

Table A.2 - Results of Grubb's test for results of net area elastic modulus.

Series	Average modulus of elasticity (GPa)	Standard deviation (GPa)	Minimum (GPa)	Maximum (GPa)	Grubb's test statistic	P-value
REF	13.33	1.72	12.10	15.30	1.14	0.278
300WR	7.40	0.70	6.70	8.10	1.00	1.000
600WR	2.47	0.15	2.30	2.60	1.09	0.637
300R	8.87	0.93	8.10	9.90	1.11	0.520
600R	5.37	0.75	4.60	6.10	1.02	0.927

Source: Author (2024).

Table A.3 - Results of Grubb's test for results of GF of the B1 self-sensing area.

Series	Average GF of the B1self-sensing area	Standard deviation	Minimum	Maximum	Grubb's test statistic	P-value
REF	272.7	35.6	233	302	1.11	0.515
300WR	411.0	43.7	361	442	1.14	0.263
600WR	314.3	43.1	265	345	1.14	0.266
300R	521.7	56.9	475	585	1.11	0.510
600R	362.0	51.6	321	420	1.12	0.448

Source: Author (2024).

Table A.4 - Results of Grubb's test for results of GF of the B2 self-sensing area.

Series	Average GF of the B2 self-sensing area	Standard deviation	Minimum	Maximum	Grubb's test statistic	P-value
REF	268.7	21.2	246	288	1.07	0.739
300WR	398.0	42.3	351	433	1.11	0.526
600WR	276.3	34.0	251	315	1.14	0.339
300R	498.0	28.8	466	522	1.11	0.537
600R	384.0	59.1	345	452	1.15	0.162

Source: Author (2024).

Table A.5 - Results of Grubb's test for results of GF of the J self-sensing area.

Series	Average GF of the J self-sensing area	Standard deviation	Minimum	Maximum	Grubb's test statistic	P-value
REF	450.3	50.2	398	498	1.04	0.846
300WR	650.3	38.9	615	692	1.07	0.730
600WR	576.3	49.6	523	621	1.08	0.710
300R	769.7	56.4	722	832	1.10	0.567
600R	742.3	45.7	702	792	1.09	0.661

Source: Author (2024).

9A.1.3. Conclusions of the statistical tests

A P-value exceeding 0.050 was noted in all series. Consequently, the null hypothesis (H_0) was not refuted, signifying the absence of outliers in the experimental dataset.

9A.2. SHAPIRO-WILK TEST OF NORMALITY

The experimental results of masonry prisms also underwent the Shapiro-Wilk test to assess the normality of residuals, an essential assumption for the development of an analysis of variance (ANOVA).

9A.2.1. Hypothesis and significance level

- Null hypothesis (H_0): the residuals exhibit a normal distribution.
- Alternative hypothesis (H_a): the residuals do not exhibit a normal distribution.
- Significance level (α): 0.050.

9A.2.2. Results of the statistical tests

The results obtained from the Shapiro-Wilk's tests are listed in Table A.6.

Table A.6 – Results of Shapiro-Wilk's tests.

Response variable	Shapiro-Wilk's test statistic	P-value
Compressive strength	0.965	0.773
Modulus of elasticity	0.939	0.368
GF of the B1 self-sensing area	0.905	0.114
GF of the B2 self-sensing area	0.958	0.650
GF of the J self-sensing area	0.908	0.124

Source: Author (2024).

9A.2.3. Conclusions of the statistical tests

The tests provided P-values higher than 0.050 (H_0 was not rejected), which confirms that the residuals exhibited a normal distribution.

9A.3. BARTLETT TEST OF HOMOSCEDASTICITY

The experimental results underwent the Bartlett's test for detection of homoscedasticity, which is another ANOVA assumption.

9A.3.1. Hypothesis and significance level

- Null hypothesis (H_0): all population variances are equal.
- Alternative hypothesis (H_a): at least two population variances are different.
- Significance level (α): 0.050.

9A.3.2. Results of the statistical tests

The results obtained from the Bartlett's tests are summarized in Table A.7.

Table A.7 - Results of Bartlett's tests.

Response variable	Bartlett's K-squared	P-value
Compressive strength	5.506	0.239
Modulus of elasticity	6.680	0.154
GF of the B1 self-sensing area	0.423	0.981
GF of the B2 self-sensing area	1.963	0.743
GF of the J self-sensing area	0.242	0.993

Source: Author (2024).

9A.3.3. Conclusions of the statistical tests

The tests provided P-values higher than 0.050 (H_0 was not rejected), which confirms that homoscedasticity was observed in the obtained data.

9A.4. ANALYSIS OF VARIANCE (ANOVA)

ANOVAs were carried out to compare the average values obtained from the experimental tests of masonry prisms.

9A.4.1. Hypothesis and significance level

- Null hypothesis (H_0): average values are equal.
- Alternative hypothesis (H_a): at least one average is different.
- Significance level (α): 0.050.

9A.4.2. Results of the statistical tests

ANOVA results were presented in Table A.8, Table A.9, Table A.10, Table A.11 and Table A.12.

Table A.8 - ANOVA results for the compressive strength dataset.

Source	Degrees of freedom	Sum of squares	Mean Square	F test statistics	P-value
Treatments	4	58.74	14.68	31.57	1.2×10^{-5}
Residuals	10	4.65	0.47	-	-
Total	14	63.39	-	-	-

Source: Author (2024).

Table A.9 - ANOVA results for the modulus of elasticity dataset.

Source	Degrees of freedom	Sum of squares	Mean Square	F test statistics	P-value
Treatments	4	197.4	49.3	50.32	1.4×10^{-6}
Residuals	10	9.81	0.98	-	-
Total	14	207.2	-	-	-

Source: Author (2024).

Table A.10 - ANOVA results for the GF of the B1 self-sensing area.

Source	Degrees of freedom	Sum of squares	Mean Square	F test statistics	P-value
Treatments	4	111359	27840	12.72	6.2×10^{-4}
Residuals	10	21886	2189	-	-
Total	14	133245	-	-	-

Source: Author (2024).

Table A.11 - ANOVA results for the GF of the B2 self-sensing area.

Source	Degrees of freedom	Sum of squares	Mean Square	F test statistic	P-value
Treatments	4	108843	27211	17.62	1.6×10^{-4}
Residuals	10	15441	1544	-	-
Total	14	124284	-	-	-

Source: Author (2024).

Table A.12 - ANOVA results for the J self-sensing area.

Source	Degrees of freedom	Sum of squares	Mean Square	F test statistics	P-value
Treatments	4	202185	50546	21.49	6.7×10^{-5}
Residuals	10	23525	2353	-	-
Total	14	225710	-	-	-

Source: Author (2024).

9A.4.3. Conclusions of the statistical tests

P-values were always lower than 0.05 (H_0 was rejected), which means that the average values were not statistically equal. Tukey's tests were also carried out to identify the averages that are statistically different from the others. The graphs presented in the main text indicate the Tukey's tests results.

PART V:

CONCLUSIONS AND FUTURE DIRECTIONS

10 CONCLUSIONS AND FUTURE DIRECTIONS

10.1. CONCLUDING REMARKS

This thesis presented the design and testing of multifunctional concrete blocks and mortar joints with abilities to self-monitor strain/stress and self-detect damage in masonry prisms, both before and after exposure to elevated temperatures. This research has not only advanced the current understanding of masonry mechanical behavior, but also provided practical insights into the application of self-sensing materials in the fields of Structural Health Monitoring (SHM) and fire resistance of masonry structures.

This research has addressed pivotal social, economic and environmental concerns, contributing to increasing resistance and sustainability in the built environment. From a social perspective, the SHM technology developed herein significantly contributes to ensuring structural safety in buildings and urban infrastructures. On a technical-economic front, the self-sensing masonry components introduced in this study exhibit distinct advantages over traditional SHM systems, such as lower costs and enhanced values of gauge factor (GF), strength, stiffness and durability. The environmental merits of these self-sensing masonry components lie in the use of their electrical output for applying eco-friendly approaches in the maintenance and rehabilitation of masonry structures, before or after exposure to high temperatures. The dataset provided by the self-sensing masonry components can decrease the necessity for demolition and construction practices that would contribute to environmental degradation through resource consumption, energy use and waste generation.

Part I of this thesis comprised a literature review on the compressive behavior of masonry prisms, before and after exposure to elevated temperatures. This literature review elucidated the current state of knowledge on this scientific field and provided the identification of areas that merit additional investigation. The literature review presented in Chapter 2 evidenced the complexity of the compressive behavior of masonry prisms constructed with traditional and innovative components, revealing the intricate effects of different variables on the strength and stiffness of ungrouted and grouted prisms. This review also discussed case scenarios that have been neglected or not adequately addressed by current

masonry design codes. Emerging technologies used in minor-destructive and non-destructive tests of masonry prisms were also revised.

Chapter 3 presented a literature review focused on the post-fire performance of masonry prisms constructed with various types of components and subjected to different fire tests. Recommendations for enhancing masonry design codes have been proposed, considering the interdependence of variables affecting the post-fire behavior. The revised content revealed that high temperatures have induced notable changes in the failure mode of clay and calcium silicate masonry prisms, which was mainly related to the thermal degradation of the mortar joints. Less apparent effects were observed in the failure mode of concrete block prisms. The content revised also evidenced the superior fire resistance of clay and calcium silicate prisms compared to concrete block prisms. A good agreement between strength results of prisms and small walls suggested the practical relevance of prisms as simple yet insightful specimens for assessing the residual strength of fire-damaged masonry.

The literature review presented in Part I laid a solid foundation for designing the experimental programs of the other parts. They also provided a theoretical framework that guided the discussion of the mechanical behavior of the self-sensing masonry prisms tested in Part III and the evaluation of the masonry behavior after exposure to high temperatures presented in Part IV of this thesis.

In Part II, experimental investigations were developed to address crucial gaps related to the design and implementation of masonry components with self-sensing properties. At first, Chapter 4 focused on the design of self-sensing laying mortars, based on the investigation of the effects of the inclusion of different contents of lime on the electrical resistivity, microstructure, self-sensing properties and compressive strength of mortars containing carbon black nanoparticles (CBNs). A suitable self-sensing response was observed in cement-lime mortars with 6% or 9% of CBN (by weight of binders). The incorporation of lime in composites designed at the end of the percolation zone enhanced their GF and stress sensitivity (SS). In composites designed at the beginning of the percolation zone, the addition of lime reduced the GF and negligibly affected the SS of the material. The compressive strength of the mortars reduced with increases in the contents of lime or CBN.

The design of self-sensing masonry units and strategies for their practical application in the SHM of masonry structures were discussed in Chapter 5. Experimental studies revealed a significant influence of interface bond agents on the adhesion between cementitious sensors

and concrete units, with epoxy-based structural adhesive (ESA) demonstrating the most effective bonding performance. To prevent adverse effects related to the loss of contact between electrodes and the self-sensing cementitious matrix, the results indicated that electrodes should not be oriented in the same direction as the maximum tensile stresses. The results also evidenced that the methodology used for the installation of self-sensing cementitious materials can impact their strain-sensing response. The best performance was observed when hardened cementitious sensors were embedded into fresh concrete mixture (HS/FC method). Improper stress transfer was noted when hardened cementitious sensors were embedded into hardened concrete bricks (HS/HC method). In addition, shrinkage control was found to be essential to prevent electrode debonding when fresh self-sensing matrices were molded on hardened concrete substrates (FS/HC method).

Since the FS/HC method could be an effective strategy for monitoring new and existing masonry structures, the experimental research presented in Chapter 6 was developed to evaluate the potential application of different admixtures for ensuring appropriate shrinkage control for self-sensing materials embedded into concrete units or mortar joints. A shrinkage-reducing admixture (SRA) effectively provided reductions in the maximum shrinkage of self-sensing mortars. A calcium oxide-based expansive agent (CaO-based EA) and a calcium sulfoaluminate-based expansive agent (CSA-based EA) induced an expansive behavior. All admixtures caused electrical resistivity increases and improved the GF of the self-sensing mortars. Microstructural analyses revealed that calcium hydroxide and ettringite derived from the EAs interrupted conductive paths inside the cementitious matrix, enhancing tunneling conduction mechanisms and improving the sensing performance of the composites.

In Part III, the mechanical and self-sensing performance of masonry elements containing self-sensing units and joints were examined, before exposure to elevated temperatures. Chapter 7 presented a validation study based on piezoresistive and compression tests of self-sensing masonry prisms, considering different factors that affect the masonry compressive behavior revised in Chapter 2 (e.g., relative strength between units and mortar, type of unit, mortar bedding approach, bonding arrangement and joint thickness). The self-sensing mortar joints of the masonry prisms were produced using the lime/cement ratios studied in Chapter 4. Concrete units were produced using the ESA bond agent and the FS/HC installation method studied in Chapter 5. A CaO-based EA was used for shrinkage control of self-sensing mortars embedded into units and joints, following recommendations presented in Chapter 6.

The experimental results demonstrated the promising use of CBN-based cementitious materials embedded into different regions of masonry prisms (e.g., front side of solid bricks, face shells of hollow concrete blocks, horizontal or vertical mortar joints) for self-monitoring of strain and self-detection of damage in structural masonry elements. Statistical analyses indicated that the embedded self-sensing regions did not significantly impact the compressive strength, modulus of elasticity, or failure mode of masonry prisms. Variations in unit type, bedding approach, bonding arrangement, relative strength between mortar and units, joint thickness and location of self-sensing regions did not lead to statistically significant changes in the GF of cementitious sensors embedded into the masonry units. However, the GF of horizontal and vertical self-sensing joints was statistically influenced by these variations. These discrepancies were elucidated based on the influence of various triaxial stress/strain states on the electrical output of the self-sensing masonry components. Assessments of their intrinsic ability to detect damage offered new insights into the potential connection between the FCRs measured during the plastic regime and different masonry failure mechanisms, such as transverse block splitting, crushing of units, or pore collapse of mortar joints.

Part IV focused on the evaluation of the effects of high temperatures on the residual mechanical and self-sensing behavior of masonry elements produced with self-sensing units and joints. In Chapter 8, some preliminary analyses were undertaken to study the temperature distribution in masonry materials subjected to different boundary conditions that affected the air circulation within the voids of the specimens. The time needed for temperature homogenization was determined for some predefined test conditions, including those applied in the heating procedures used in the experimental campaign reported in Chapter 9.

An additional validation study was presented in Chapter 9 for analysis of the influence of elevated temperatures on the compressive strength, elastic modulus and self-sensing properties of masonry prisms that exhibited appropriate functionality in Part III. Considering the discussions presented in Chapter 3, the impacts of different maximum exposure temperatures and post-fire rehydration procedures were investigated. Masonry prisms exposed to 300 ºC presented a slight decrease in compressive strength and a significant reduction in elastic modulus. In these specimens, the rehydration procedures had minimal effects due to limited damage and constrained water penetration. In contrast, exposure to 600 ºC caused substantial reductions in compressive strength and elastic modulus due to relevant microcrack propagation. In these specimens, the rehydration methods caused notable recovery of strength and stiffness. Regardless of the maximum temperature, the predominant

rupture mode involved vertical cracks initiated at the block-mortar interface. The self-sensing areas of the masonry prisms presented relevant increases in GF after exposure to 300 ºC. On the other hand, exposure to 600 ºC caused small GF increases. The rehydration procedures led to interruptions in the conductive network due to the formation of nonconductive rehydration products, enhancing tunneling conduction mechanisms and increasing the GF of the masonry prisms. The electrical response of fire-damaged masonry prisms subjected to monotonic compression tests enabled the damage localization and quantification. Stages of balance followed by increases in FCR offered predictive insights into the development of masonry failure mechanisms.

10.2. RECOMMENDATIONS FOR FUTURE RESEARCH

The insights provided in this thesis offer valuable perspectives that can serve as a basis for guiding future research. For example, the following suggestions for future studies can be derived from the findings presented in the present research:

(1) This thesis presented the self-sensing performance of normal-strength concrete units and cement-lime mortars produced with CBNs, leaving a gap in the understanding of the piezoresistive response of other types of masonry components (e.g., high-strength units, lightweight units, polymer adhesive mortars, preblended mortars, eco-efficient masonry components) containing different types of conductive admixtures (e.g., carbon nanotubes, carbon fibers, steel fibers, graphene, graphite).

(2) The long-term performance of self-sensing masonry components was not evaluated in the present work. Future research is recommended to investigate aging effects on the self-sensing properties of smart masonry components, in order to assess the robustness and stability of the electrical response over extended periods and ensure reliability in real-world applications.

(3) The scope of the present research was limited to the design and evaluation of self-sensing units and mortar joints for SHM of masonry structures. Future research is recommended to investigate how different smart structural elements (e.g., reinforced concrete beams, columns, slabs) retain self-sensing abilities after fire conditions, extending the applicability of the findings.

(4) The effects of different types of interface bond agent on the electrical response of self-sensing materials embedded into masonry elements were reported. To complement these findings, future investigations should delve into the effects of different surface treatments (e.g., grinding, abrasive blasting, mechanical milling) on the bonding behavior between cementitious sensors and concrete substrates, along with their consequent influence on different self-sensing properties.

(5) The impacts of cement/aggregate ratio and water/cement ratio on the shrinkage behavior of self-sensing masonry components were not evaluated in the present thesis. Consequently, future research is suggested to investigate the influence of different proportions of raw materials on the shrinkage behavior of self-sensing cementitious materials. This exploration is crucial for the practical application of fresh cementitious sensors on existing buildings requiring SHM.

(6) The effects of including hydrated lime or shrinkage-control admixtures on tunnel effect theory-based piezoresistivity models were not investigated in the present work. Therefore, future studies are needed to elaborate and test theoretical models that can describe the self-sensing response of masonry components containing these types of admixtures.

(7) Although the present thesis documented the self-sensing response of masonry units and mortar joints, it did not apply theoretical piezoresistivity models to explain the electrical response of the smart materials. Consequently, future investigations should use the experimental dataset obtained in this research to support the development of theoretical piezoresistivity models that elucidate the electro-mechanical behavior of self-sensing masonry components under various states of multi-axial strain and stress.

(8) The numerical simulations developed in this thesis focused on evaluating the effects of convection mechanisms inside masonry prisms exposed to high temperatures. The time required for temperature homogenization was determined for specimens subjected to some specific predefined test conditions. Then, comprehensive parametric analyses are recommended to offer a more nuanced understanding of the effects of different boundary conditions on temperature distribution. This includes considerations of various heating scenarios, masonry

components with different properties and geometries, application of different types of coating systems, etc.

(9) The ESA interface used for construction of the self-sensing areas of the masonry prisms demonstrated high vulnerability to exposure to high temperatures, potentially compromising the waterproof performance of the smart composites. This limitation suggests a need for alternative materials that can provide effective bonding and waterproofing protection during extreme conditions. Identifying materials that not only offer robust resistance to high temperatures but also sustain waterproof integrity poses a significant challenge.

(10) Partial thermal oxidation of CBNs was observed in self-sensing masonry components exposed to 600 ºC. Future research efforts should focus on the design and testing of self-sensing masonry containing conductive admixtures with higher thermal stability. Exploring new materials becomes essential to mitigate substantial thermal decomposition of the conductive network after exposure to temperatures exceeding 600 ºC.

(11) The experimental program developed in this thesis reported the use of specific dosages of CBNs to construct the conductive network inside masonry components. Future studies are recommended to identify the most suitable type and concentration of conductive admixtures, ensuring an optimization of the residual mechanical and self-sensing properties of masonry prisms, before and after exposure to fire conditions.

(12) Compressive loading was not applied to the masonry prisms during the exposure to high temperatures. This limitation suggests a need for research that investigates the residual mechanical and electrical properties of self-sensing masonry elements subjected to thermomechanical tests. Future research should comprehensively evaluate how the combined effects of exposure to high temperatures and mechanical loading impact the residual mechanical and self-sensing behavior of the masonry prisms.

(13) This thesis focused on the self-sensing ability of nanomodified cementitious matrices to detect the effects of rehydration on the recovery of strength and stiffness of fire-damaged masonry prisms. Future research is recommended to evaluate the efficiency of these self-sensing materials for monitoring the damage

recovery of masonry elements subjected to various rehabilitation techniques after fire exposure.

(14) The present study reported the effects of some specific rehydration steps on the mechanical and self-sensing properties of fire-damaged prisms. Future works should be developed to evaluate the effectiveness of different rehydration periods on the overall performance of self-sensing masonry exposed to high temperatures.